**The Dissertation Committee for Guillermo David Huaco Cardenas
certifies that this is the approved version of the following dissertation:**

**PROCEDURES TO REHABILITATE EXTREMELY DAMAGED
CONCRETE MEMBERS USING INNOVATIVE MATERIALS AND
DEVICES**

**Committee:**

**James O. Jirsa, Supervisor**

**Sharon Wood**

**Wassim Ghannoum**

**David Fowler**

**Harovel Wheat**

# Procedures To Rehabilitate Extremely Damaged Concrete Members Using Innovative Materials And Devices

by

## Guillermo David Huaco Cardenas, B.S., M.S.E.

## Dissertation

Presented to the Faculty of the Graduate School of

The University of Texas at Austin

in Partial Fulfillment

of the Requirements

for the Degree of

## Doctor of Philosophy

## The University of Texas at Austin
## December 2013

# Dedication

To God,

who gives me life, led me here and sustained through it.


To the memory of my beloved father (†),

who passed away when I started my graduate studies here.

He always encouraged me to become a Ph.D.

His love I always carry with me.


To my beloved mother,

who always believes in my capacities,

and gives me her love and tenderness in my whole life.


To my brother,

for his protection during my childhood.


To Daniela,

the last effort was for you.

# Acknowledgements

I would like to express my most sincere thanks and appreciation to Dr. James Jirsa for his advice, guidance, and support throughout my PhD program at UT Austin. Dr.Jirsa offered his self to act as a father to me every time, especially in my quite difficult time when I started the doctoral studies. I really appreciate his kindness and I will be thankful with him always.

I am also pleased to acknowledge to my committee members Dr. Sharon Wood, Dr. Wassim Ghannoum, Dr. David Fowler and Dr. Harovel Wheat. Their contribution to my research is truly appreciated.

I especially would like to give my thanks to Dr. Richard Klingner for his advice not only about research but also about life in general.

I want to thank my family, especially to my beloved mother and father (†), my brother for their love, encouragement, and support.

To Structural Engineering and Materials Faculty, whose teachings and friendship were valuable on my behavior at graduate school.

Many colleagues at the Ferguson Structural Engineering Laboratory (FSEL) have offered useful supports during my time there. I would like to acknowledge to Eliud Buenrostro, Raul Cortez, Wanching Huang, Matthew Hommer, Matt Leborgn, Chang Hyuk Kim, Wei Sun, Jose Gallardo, Ali Yusef, David Garber, Jaime Hernandez and Jose Garcia for their help.

Technical assistance provided by the Ferguson Structural Engineering Laboratory staff is acknowledged, I would like to give thanks to Blake Stassney, Dennis Fillip, Eric Shell, John Bacon. I am also grateful with administrative staff, Barbara Howard and Michelle Damvar, your help is truly appreciated.

I would like to acknowledge my uncle Gonzalo's family, my friends and UT staff at graduate school too. I appreciate their kindness and friendship during all my time here at UT Austin.

Lastly but certainly not least, I would like to thank to ERICO and Fyfe Co.LLC for the technical contribution to the research; the Good Neighbor Scholarship for awarding me the scholarship that supported my tuition for my studies at the University of Texas at Austin.

<div align="right">

Guillermo Huaco

December 2013

</div>

# Procedures To Rehabilitate Extremely Damaged Concrete Members Using Innovative Materials And Devices

Publication No. _____

Guillermo David Huaco Cardenas, Ph.D.

The University of Texas at Austin, 2013

Supervisor: James O. Jirsa Ph.D.

Using innovative materials or devices in techniques for strengthening or repair of RC concrete members may provide interesting alternatives for structural engineers. Laboratory tests were conducted on full scale reinforced concrete columns and a masonry wall that suffered severe damage. Carbon Fiber Reinforced Polymer - CFRP sheets and anchors were used to improve shear capacity or ductility elements. CFRP jacket were installed on column hinge regions while diagonal ties (tension braces) were used on the masonry wall. Mechanical splices were used in columns where concrete crushed and bars buckled by replacing the buckled bars and providing continuity to the longitudinal reinforcement. It was found that performance of the retrofitted members was comparable to that using conventional techniques and the performance was generally better than certain "fast" retrofit procedures reported in the literature. The choice of technique depends on the degree of damage, the cost of replacement, and performance required.

Having the results of cyclic load tests of rehabilitated concrete members, envelope or backbone curves were obtained following the ASCE41-07 and proposed ASCE41-13 procedures. The backbone curves were used to develop behavioral models that can be used in the analysis and design of those types of concrete members and retrofit procedures. The inclusion of the behavioral models into current Performance Based Seismic Design procedures for strengthening of existing or repaired damaged buildings is proposed.

# Table of Contents

# List of Figures

xxiv

xxviii

xxxiii

xxxvii

xli

xlii

xlv

# List of Tables

l

li

# CHAPTER 1

## Introduction

### 1.1 INTRODUCTORY REMARKS

Natural disasters such as earthquakes and tsunamis may damage or result in collapse of concrete buildings and bridges. Some damaged structures could be restored through retrofit procedures that are cost and time effective. Using innovative materials or devices for strengthening of RC concrete members offers interesting approaches. By assessing the cost to demolish and rebuild a new column with repair of a damaged one; repair may be less expensive than replacement. However, there is very little research regarding the evaluation of structural vulnerability when innovative materials or devices are used.

Older structures and poorly constructed or badly designed structures are likely to be damaged in an earthquake. Figure 1.1 shows a building located at Port of Prince, Haiti having two columns severely damaged at the top joint of each one after the mag. 7 Earthquake in 2010. This building has a moment resisting frame system to carry lateral load induced from earthquake events. It can be observed that the reinforced concrete columns had insufficient stirrups where the shear hinge formed. It is also noticed in Figure 1.1 that the column has a small cross-sectional area compared with the beams connected at the top of those columns. The members form a weak column-strong beam system. The longitudinal bars buckled the stirrup spacing was too great to confine the longitudinal bars under the compression load from the floor above.

*Figure 1.1 Weak Column Strong Beam Join. Haiti Earthquake – 2010 Mag. 7.0*

A similar situation is evident in Figure 1.2 showing failure of a column in the 2010 Chile earthquake. Poor confinement in the column is evident in Figure 1.3. The structural system is formed by reinforced concrete columns and walls. The top of the column failed, with crushing of the column core and buckling of the bars. Large stirrup spacing resulted in poor confinement resulted in large lateral displacement across the column that extended into the wall.

*Figure 1.2  Deficient Shear Reinforcement at Reinforced Concrete Columns Chile Earthquake – 2010 Mag. 8.8*



*Figure 1.3  Deficient Shear Reinforcement in Columns and Walls Chile Earthquake – 2010 Mag. 8.8*

Masonry walls are commonly used as infills in frame structures. Figure 1.4 shows a wall damaged in the 2010 earthquake in Chile. Generally for pattern of damage consists of diagonal cracks crossing the entire section of the wall starting from a top corner extending diagonally to the opposite bottom corner.



*Figure 1.4  Masonry wall with shear cracks. Chile Earthquake – 2010 Mag. 8.8*

Traditional procedures to repair and strengthen damaged members have generally involved the use of concrete or steel jackets, adding new members to the lateral force-resisting structure, or replacing the damaged element. The current research is based on new techniques to repair severely damage reinforced concrete member such as those discussed above, with emphasis on rapid, less costly procedures.

## 1.2 OBJECTIVES

The research is aimed at determining the behavior of structured elements repaired or strengthened using innovative approaches. The intent is to provide data that designers can use to make decisions for rehabilitation of structures to meet performance based seismic design requirements.

Laboratory tests were conducted on strengthened elements. Reinforced concrete columns and a damaged masonry wall were tested with new techniques using innovative materials and devices. The test program includes a study of the use of Carbon Fiber Reinforced Polymer (CFRP) for strengthening or for creating ductile elements or for adding new shear reinforcement as a jacket for columns or diagonal ties for masonry walls. Mechanical splices or couplers were used to provide continuity to the reinforcement, in locations when bar have buckled and concrete has crushed. The mechanical couplers were used to replace the buckled bars. Behavioral models for columns and the masonry wall will be obtained from the laboratory test response of the concrete members tested.

## 1.3 METHODOLOGY

The research was divided in four general areas, the study of the properties and behavior of the CFRP and mechanical splices, the cases of reinforced columns severely damaged under axial and lateral loads, the case of the masonry wall with hollow concrete blocks damaged and retrofitted.

### 1.3.1 Mechanical couplers

A series of short and long mechanical splices (Figure 1.5) were tested under cyclic axial tension loads to assess differences in stiffness and strength of the two types

of splices. These mechanical splices were 6.8 and 10in long respectively. The number of bolts used to clamps the bars in the couplers was different in the two lengths. A second set of long mechanical splices were tested under cycle tension/compression loads. New bars were used to replace damaged bars. A third set of short mechanical splices were tested under cycle tension- compression axial load. The bars for this third set were subjected to large inelastic deformations. A work-hardened bar was coupled with a new bar using a short mechanical splice. The results of these mechanical splice tests provide a better assessment of the behavior of the mechanical splices for bars in typical older existing buildings that have been damaged or need to be strengthened.
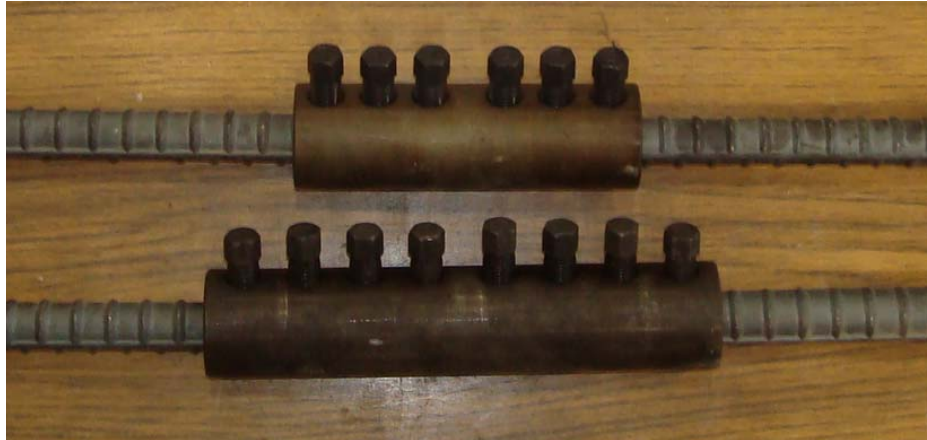


*Figure 1.5  Short and Length Mechanical Splices*

### 1.3.2  CFRP materials

In order to assess the behavior of the CFRP material used for retrofit, past research on CFRP sheets and anchors were reviewed. Results from axial tests of CFRP coupons and flexural tests of short span concrete beams with CFRP anchors were studied. Quality control of the CFRP sheets and anchors are discussed to explain the behavior of those elements and to design the rehabilitation approaches in this study. Figure 1.6 shows the CFRP sheet from the manufacturer.

*Figure 1.6  CFRP sheet for rehabilitation purposes*

### 1.3.3    Retrofit of damaged columns

Following another study conducted at Ferguson Structural Engineering Laboratory, two similar reinforced concrete columns badly damaged after being subjected to cyclic lateral loads and constant axial loads were available for use in this study. One column was tested under high axial load and the second under low axial load. The first column with low axial load failed by crushing of concrete and buckling of the bars at the bottom and spalling of the concrete cover at the top of the column. The second column with high axial load applied failed by crushing of the concrete and buckling of all the longitudinal bars at both ends of the column.

Under those patterns of failure and the severe damage obtained, the new retrofit procedures were studied. For the column case with low axial load applied, CFRP was applied at the top, where no buckling was present, and short mechanical splices were applied at the bottom joining the old and new bars. Figure 1.7 shows the column with the

CFRP materials applied at the top, and the bottom of the column having a larger cross section to accommodate the installation of the mechanical splices. For the second column with high axial load applied, where both ends of the column were damaged and the bars buckled, mechanical splices were used. The column was divided into two parts to be tested as cantilever columns using two different types of mechanical splices for each part. Figure 1.8 shows the construction columns with mechanical splices connecting new bars to the supports from the original column.



***Figure 1.7  Column damaged retrofitted by CFRP jacketing and mechanical splices***

*Figure 1.8 New columns connected to existing support with mechanical splices after buckled longitudinal bar removed.*

### 1.3.4 Retrofit of a masonry wall

One masonry wall was tested under cyclic lateral loads, and low axial load. The wall was fabricated with hollow concrete blocks and internal longitudinal and transverse reinforcement grouted through the cavities. The masonry wall was cracked diagonally

There was sliding of the wall at the base, resulting in the first two courses of concrete blocks crushing and the internal longitudinal bars buckling. To repair the wall, a reinforced concrete ring encased the base of the wall and CFRP diagonal ties with CFRP anchors were attached to both sides of the wall. The masonry was tested after the concrete ring was added in order to measure the initial stiffness of the masonry wall with a reduced aspect ratio. The second test was performed after the application of the diagonal CFRP sheets. The retrofitted wall is shown in Figure 1.9.



*Figure 1.9  Masonry wall repaired by the concrete ring and diagonal ties of CFRP*

### 1.3.5 Use of the behavioral model for non linear analysis

Having the results of cyclic load tests of rehabilitated concrete members, envelope or backbone curves were obtained following the ASCE41-07 and proposed ASCE41-13 procedures. The backbone curves were used to develop behavioral models that can be used in the analysis and design of those types of concrete members and retrofit procedures. The inclusion of the behavioral models into current Performance Based Seismic Design procedures for strengthening of existing or repaired damaged buildings is proposed.

# CHAPTER 2
# **Background**

In this chapter, past research on the retrofit of reinforced concrete columns with square cross section and masonry walls is discussed. For columns, the technique most used was jacketing, using concrete, steel plates and CFRP materials to increase the capacity and ductility of the columns. For masonry wall repair, steel plates and CFRP were used to strengthen and retrofit masonry walls carrying lateral shear forces.

## 2.1   BETT, 1985

A reinforced concrete column with 12in x 12 in cross section and reinforced with 8 #6 longitudinal bars and 6mm dia. ties @ 8" was built and tested under axial and lateral loads. The ends were restrained against rotation. The column was then repaired using concrete jacketing that increased the section to 17"x 17" by shotcrete with f'c = 4.6ksi, and adding #6 and #3 longitudinal bars and #3 ties @ 9"to the jacked. The retrofitted column, 1-1R, was tested under the same pattern of load and supports restraints. Figure 2.1 shows the cross sections of the column before and after strengthening:

Long. steel: #6's

Ties: 6mm @ 8"

Identical 12" x 12" cores used for all specimens.

Long: #3's, #6's

Ties: 6mm @ 2-1/2"

Crossties: #3's @ 9"

2-1/2" shotcrete shell
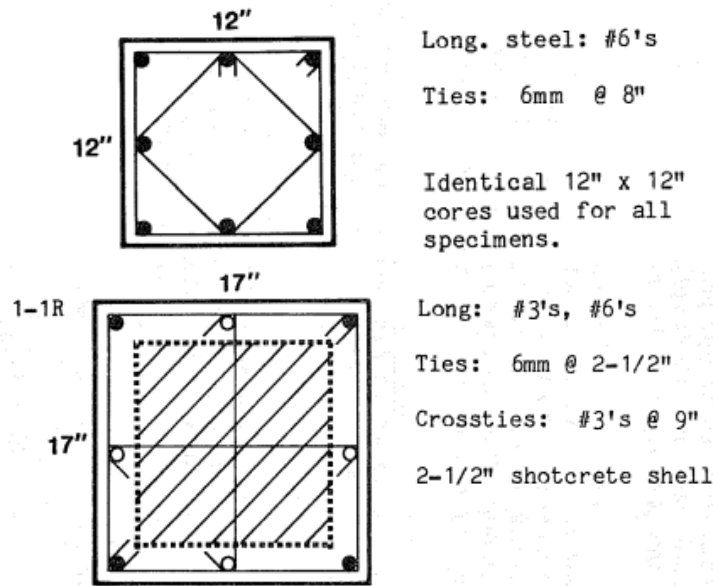
*Figure 2.1 Cross Section of the 1-1R and image of the bars for jacketing (Bett, 1985)*
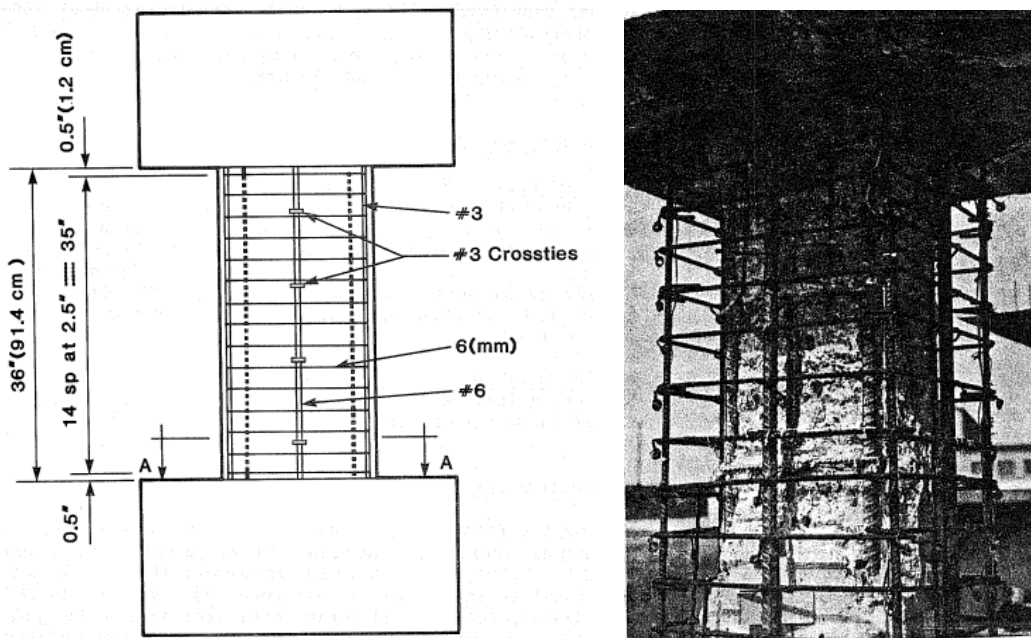


*Figure 2.2 Elevation view of the retrofitted column and image of the bars for jacketing (Bett, 1985)*

13

During the test of the retrofitted column, some slip was observed between the existing concrete and the shotcrete jacket. The retrofitted column may not have behaved monolithically, especially under flexural effects. However the behavior of the retrofitted column had 87% higher lateral load capacity, and 25% more deformation capacity than the original column.
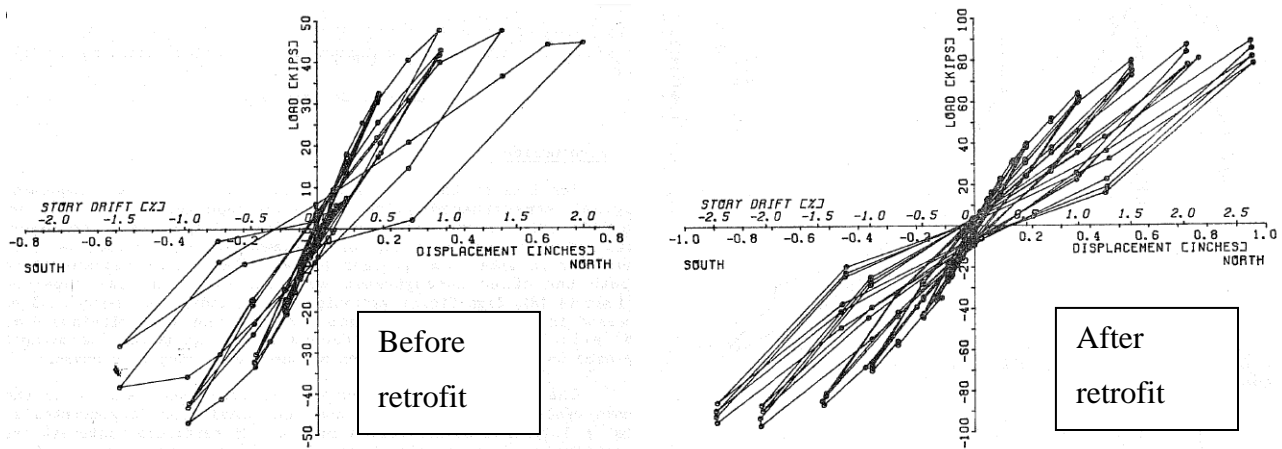


*Figure 2.3 Different responses for a column before and after retrofit (Bett, 1985)*

## 2.2  ABOUTAHA, 1994

Effects of inadequate lap splice length were studied in a laboratory test program of more than 20 cantilever columns with rectangular and square cross sections. All the columns were tested under cyclic lateral loads. Steel jackets were added to each face of the columns. One of these columns (Column FC-17) was retrofitted with the steel jackets. This column had an 18"x18" cross section, and 8 #8 longitudinal bars with #3"@16" for stirrups. The lap splice length was 24in. The ¼" thick steel was attached with steel angles at the corners. Two epoxy-grouted steel bolt anchors were added on one face to improve

14

the confinement of the splices on that face. The size of the column was increased with the addition of the jacket and the anchor bolts.
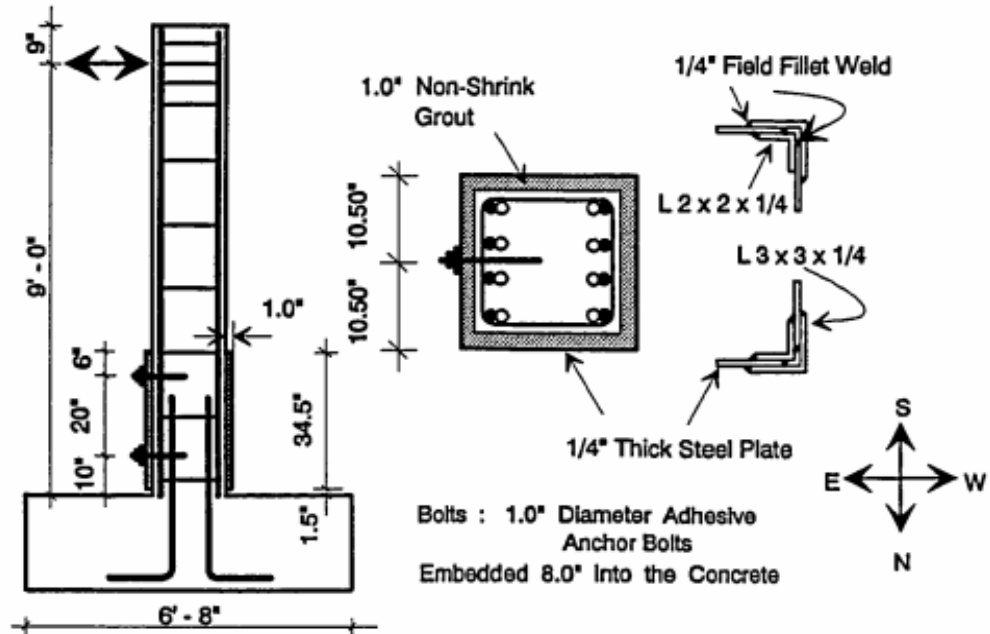
*Figure 2.4 Cross Section of the FC-17 with details of the steel jacket (Aboutaha, 1994)*

Aboutaha found that the steel jacket resulted in large improvements in the deformation capacity, more than 5% drift ratio, with little reduction of strength and stiffness. As Figure 2.5 shows, the response of the column had wide stable hysteretic loops. Flexural crack and diagonal shear cracks on the column appeared above the steel jacket. The steel jacket was removed to inspect the region of the splice area and no major damage was found.
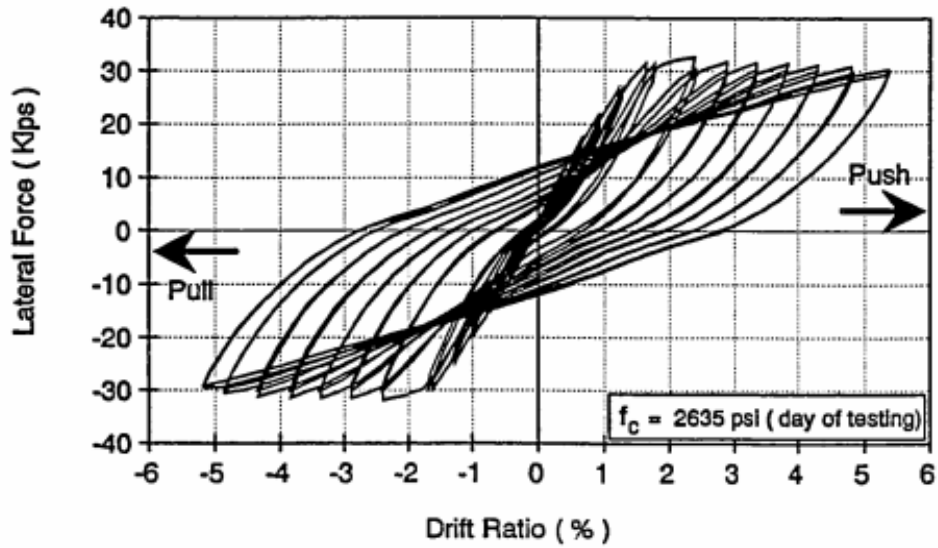
*Figure 2.5 Hysteretic response of the cycle lateral load applied to the cantilever retrofit column (Aboutaha, 1994)*



*Figure 2.6 View of the retrofitted column after the test (Aboutaha, 1994)*

## 2.3 KIM, 2008

Similar to Aboutaha, Kim studied the behaviour of columns with poorly detailed lap splices and insufficient confinement. Carbon Fiber Reinforced Polymer (CFRP) was used for strengthening the splice region. Six cantilever columns were repaired and tested with CFRP jackets and intermediate CFRP anchors. One of the columns, 2-A-S8-M, had an 18in x 18in cross section and 8 longitudinal #8 bars with #3 ties @ 16in. This column was tested under monotonic lateral load and repaired.

The test of the column before retrofit consisted of applying the load in one direction only in order to compare a column retrofitted before and after damage. The lap splice failure of the side in tension resulted in sudden drop of the lateral load. Horizontal cracks appeared on the damage side and vertical cracks along the lap splices appeared at the failure of the splice.
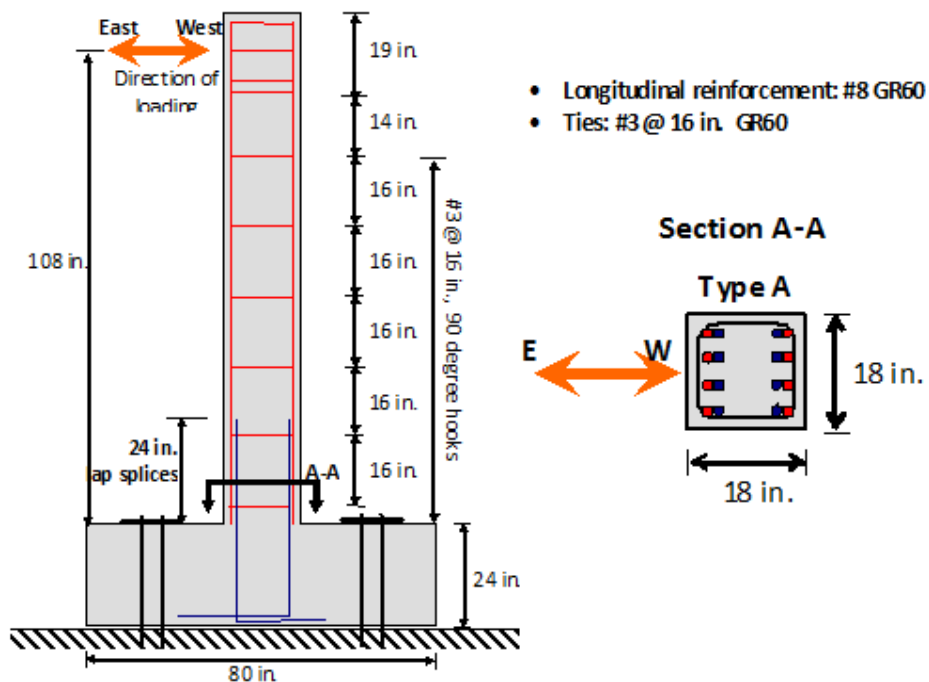


*Figure 2.7 Elevation and plan view of the column previous to the retrofit. Lap Splices are shown. (Kim, 2008)*

17

To retrofit the column cracks were injected with epoxy, the corners of the column were rounded (0.5in radius), and the CFRP jacket was installed to improve the confinement, CFRP anchors were on the faces of the column where the splices were located. The final size of the column was not increased at comparison than the steel jacketing retrofit case.
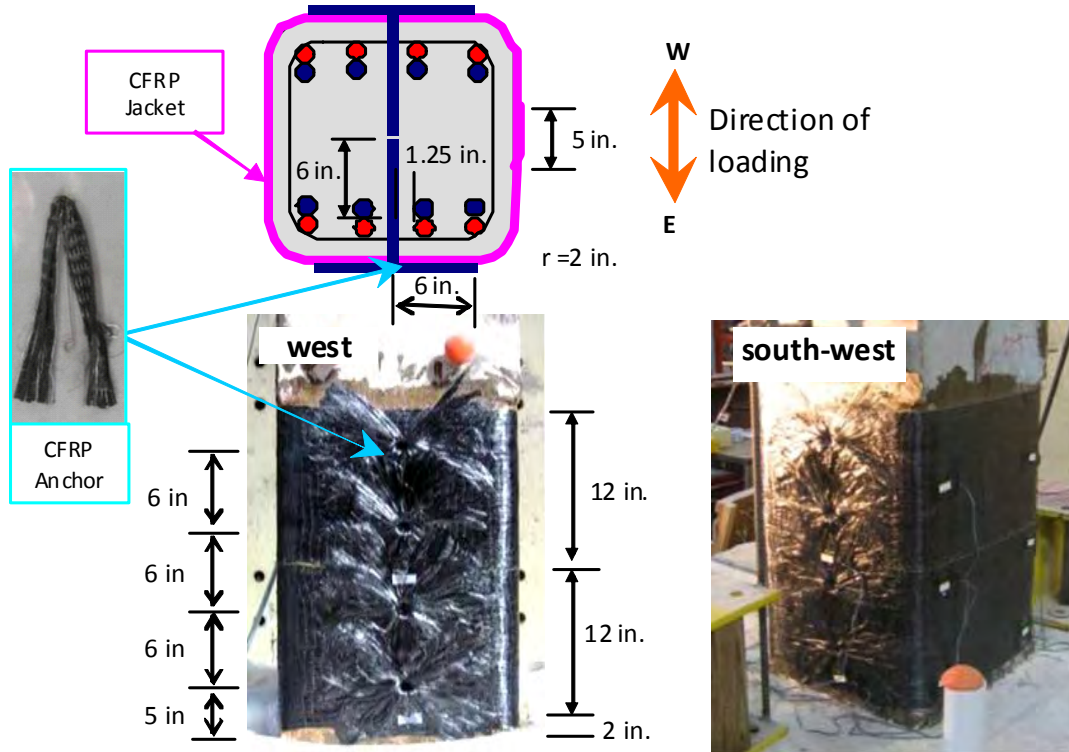


*Figure 2.8 Cross Section of the 2-A-S8-M with details of the CFRP material applied (Kim, 2008)*

The test results for the retrofitted column indicated an increase of 35% in the strength of the column, and also a greatly improved ductility. Figure 2.1 shows the performance of the column before and after retrofit. It was also observed that capacity of column before and after retrofit reached the same lateral deformation in both directions was nearly the same, indicating the effectiveness of the CFRP jacket.

18
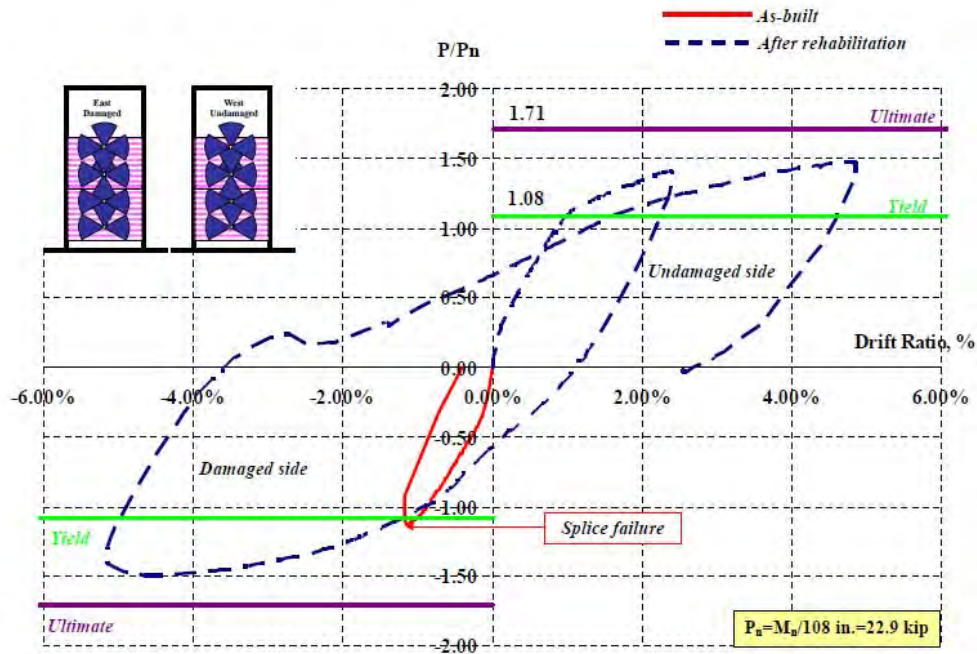
*Figure 2.9 Response of the retrofitted column for undamaged and damaged side (Kim, 2008)*

## 2.4  HE, 2013

He studied the behaviour of damaged columns at Missouri University of Science and Technology MST. Although He tested three cantilever columns, only one will be discussed here. The column was rapid repaired and tested with CFRP sheets vertically placed to act as longitudinal reinforcement and CFRP jacket were added for confinement. He used one unconventional type of anchorage using steel botls to anchor the longitudinal CFRP sheets to the base as shown in Figure 2.11. The column (Column 2-R), had a 22in x 22in cross section, with 4#9 bars in the corners and, 8#8bars. Ties were with #3 square and with octahedral shapes spaced @ 3.25in (Figure 2.10). This column

19

was tested under a constant axial load (150kips) and cyclic lateral load and repaired afterwards. Compressive strength of the concrete was 5.8ksi.

The damaged column included buckled longitudinal bars and crushed concrete. Repair mortar was used to replace the crushed concrete, the longitudinal CFRP sheets replaced the vertical buckled bars and a CFRP jacket confined the repaired section. Compressive strength of the mortar was 5.4ksi. Tensile strength of the CFRP was 110ksi.
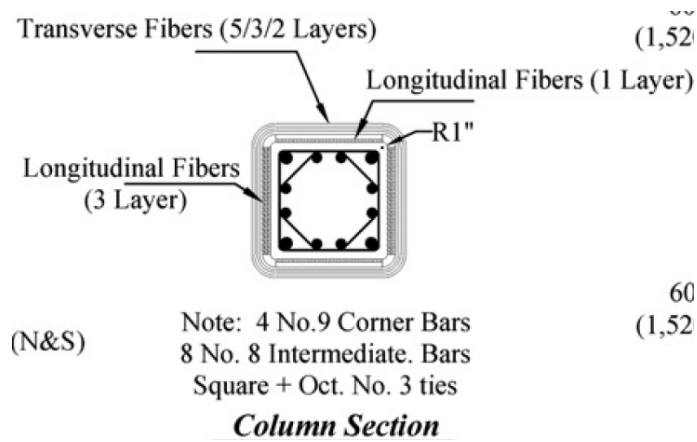


*Figure 2.10 Cross Section of the Column 2-R with details of the CFRP material applied (He, 2013)*
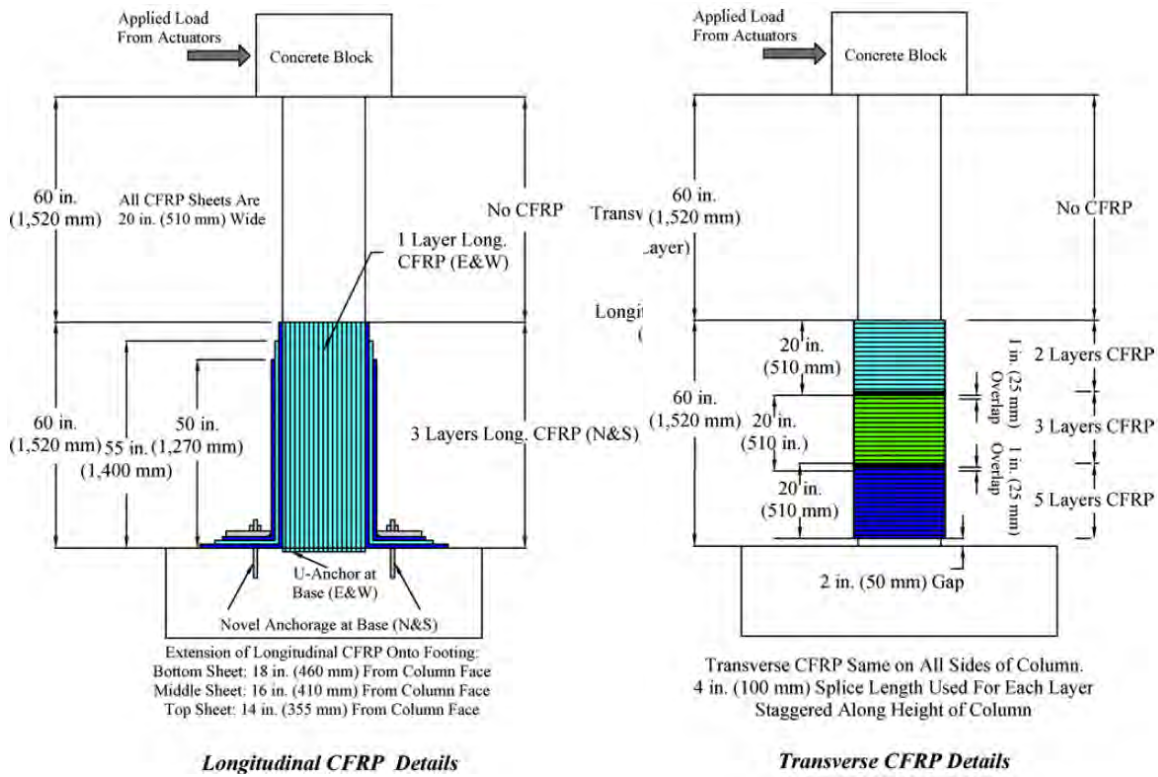
**Figure 2.11 Elevation of the column retrofitted with longitudinal CFRP and CFRP jacket. (He, 2013)**

Details of the anchorage used for the longitudinal CFRP sheets are shown in Figure 2.12 and Figure 2.13. The bolted plates were used on the north and south faces of the column (Figure 2.12)and U-anchors at the end of the strips were embedded in grooves at the bottom of the column (Figure 2.13).

21
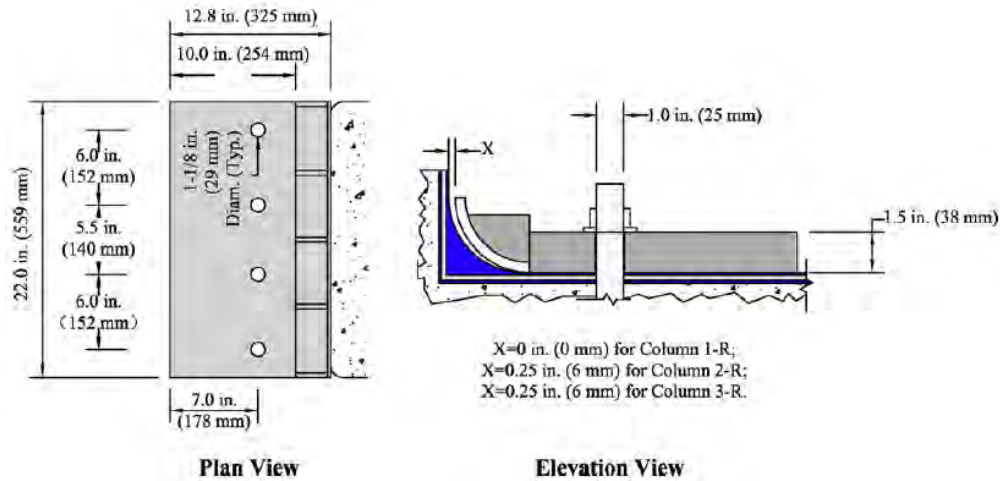
*Figure 2.12 Anchor for the north and south longitudinal CFRP (He, 2013)*
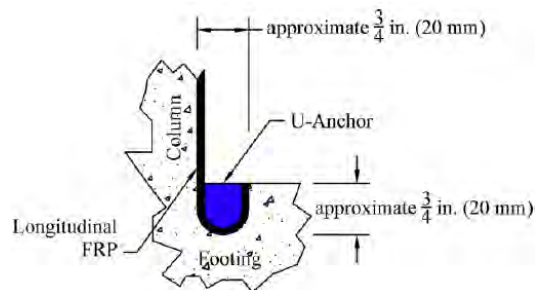


*Figure 2.13 Anchor for the west and east longitudinal CFRP (He, 2013)*

A constant axial load (150kips) was applied to the column. During the test of Column 2-R, the U-anchors on the east and west sides of the column pullet out as expected. The damaged hinge zone of the retrofitted column was located 20in above of the base. Rupture of the CFRP was also observed during test near the rounded edge for the anchor plate on the north and south faces.
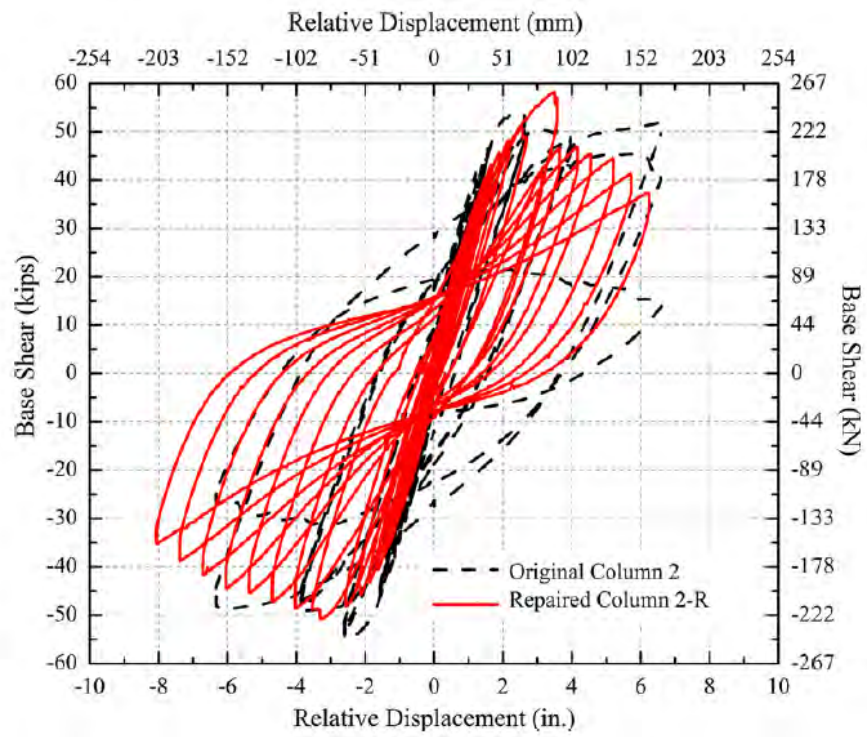
***Figure 2.14 Hysteretic response of the cycle lateral load applied to the cantilever retrofit column (He, 2013)***

## 2.5    TAGHDI, BRUNEAU, SAATCIOGLU,  2000

Two concrete block masonry unreinforced wall and two reinforced masonry walls were tested. Figure 2.15 shows the geometry of the walls and the reinforcement. One of each pair was retrofitted using steel sheets as vertical and diagonal ties as is shown in Figure 2.16. Each wall contoured hollow concrete blocks having dimensions is 7.9in x 15.7in with 7.9 in high (200mm x 400mm, 200mm high). The masonry wall was nine courses high and the aspect was 1.0 in order to ensure a shear failure. The average f'm value measured was 1.17ksi (8.1MPa) using and axial compression test of a grouted masonry prims.
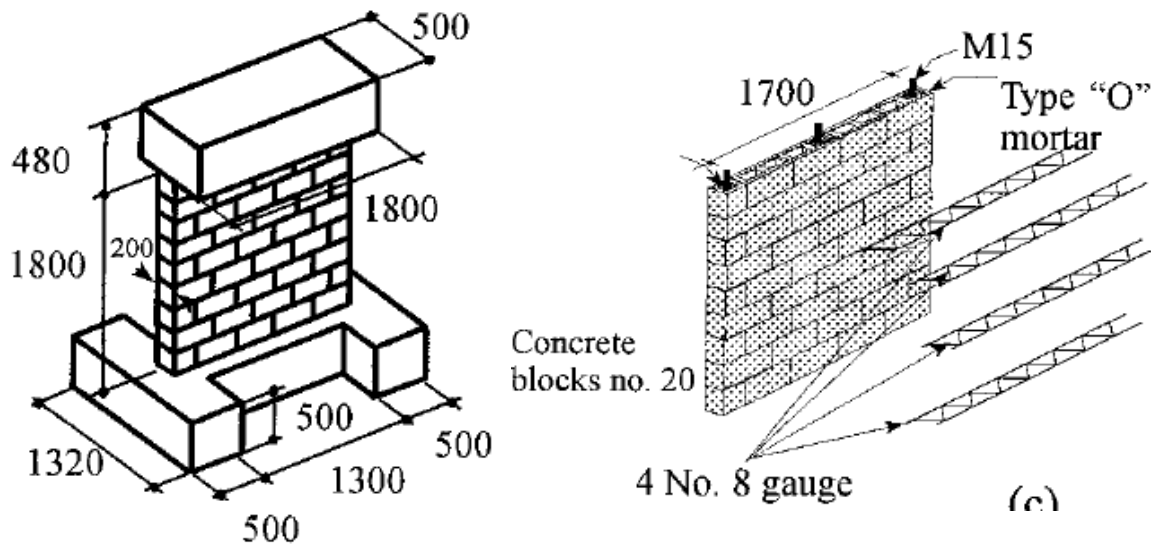


*Figure 2.15 Reinforced masonry wall design details (Taghdi, et.al. 2000)*

The retrofit process for the masonry walls consisted of adding steel plates to both surface of the wall to prevent any eccentricity in the stiffness or eccentric distribution of stress in the wall. The steel plates were placed in diagonals (Figure 2.16) forming two ties, having a thickness of 0.15in (3.91mm) and 8.66in (220mm) wide. Additional steel plates were located vertically on each extreme of the wall having a thickness of 0.15in (3.91mm) and 3.15 in (80mm) wide of the diagonals. The steel plates were attached using

24

bolts which pass through the masonry blocks so that the wall was "sandwiched" between the plates. Steel angles were placed on each of the 4 corners of the masonry wall where the diagonal ties and the vertical strips join. The elements were welded together at the joint.
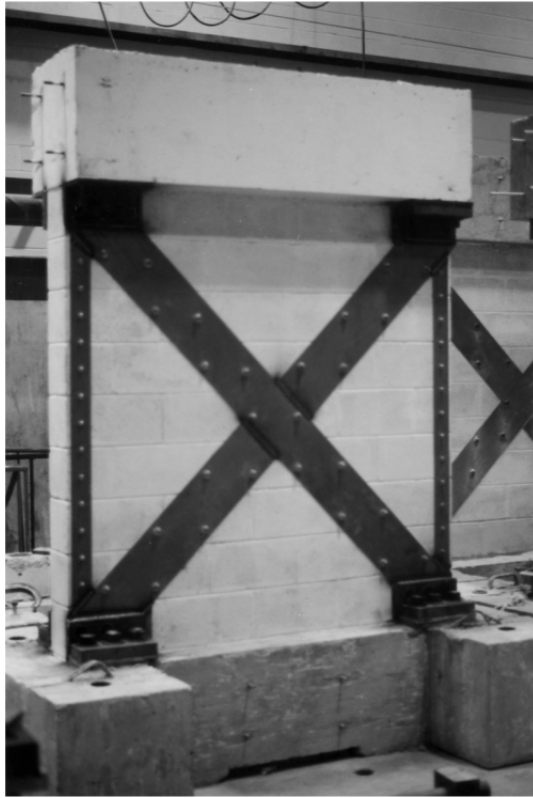


***Figure 2.16 Steel strip placed to retrofit the reinforced masonry wall (Taghdi, et.al. 2000)***

The masonry walls were tested under axial and lateral loads. The result of the test for the reinforced masonry wall without retrofit is shown in Figure 2.17. It exhibited low shear capacity and sliding at the base. The retrofitted masonry wall reached much higher shear capacity and ductility, as shown at Figure 2.17. The steel plates develop local buckling at the top and bottom corners of the masonry wall between the anchors bolts

used to attach the plates onto surface of wall. The buckling of the steel strips appeared after the yielding of the internal bars of the masonry wall.
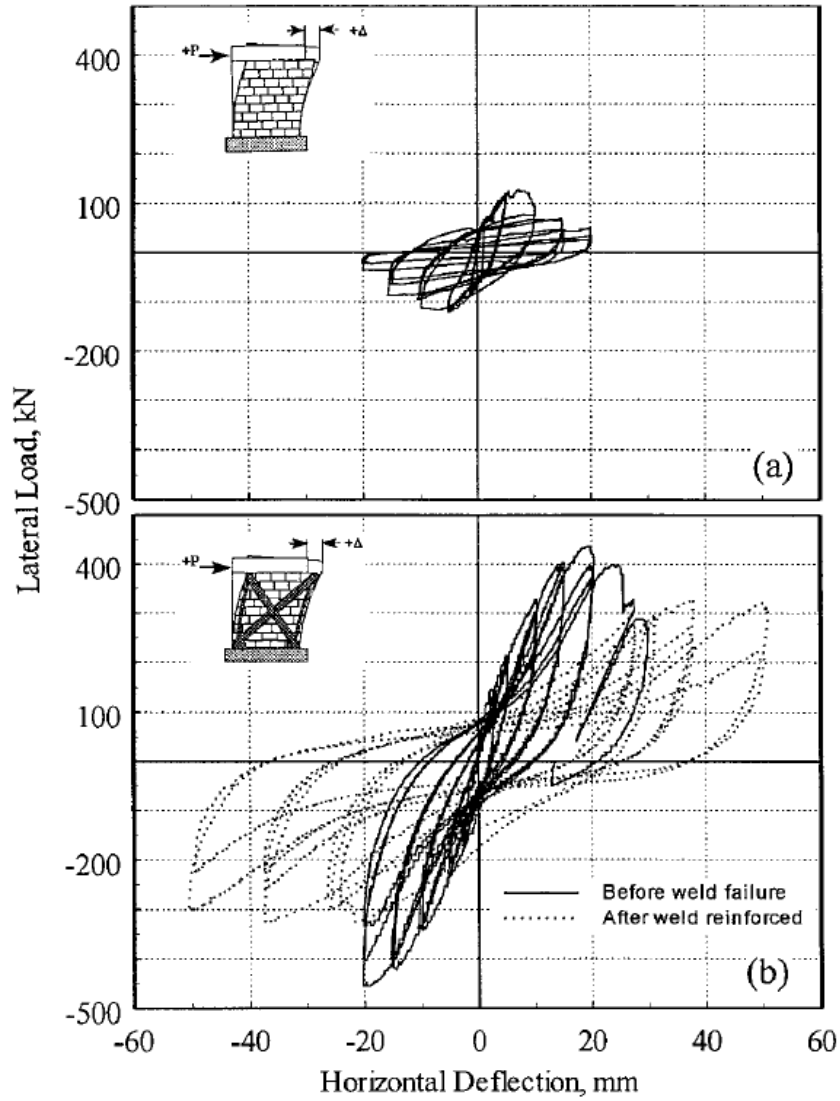


*Figure 2.17 Performance of the reinforced masonry wall un-retrofitted (a) and retrofitted (b)*

## 2.6 PAMPANIN & AKGUZEL, 2011

A set of five, 1/3 scale, one-span, two story frame specimens; with unreinforced masonry infill panels were tested. Those frames were strengthened using Carbon Fiber Reinforced Polymer - CFRP. The overlay used was in diagonal ties forming two diagonals crossing along the infill panel as Figure 2.18 shows. CFRP anchors were used to attach the strips to the wall and to improve force transfer from the strips to the wall.

After the CFRP strips were adhered to the wall with epoxy, the anchor were inserted into pre-drilled holes through the panels. CFRP U wraps were also used to cover the joints of the CFRP strips at the edges of the wall.



*Figure 2.18 CFRP materials applied to the two story frame with infill panels*
*(Pampanin & Akguzel 2011)*

The shear capacity of the wall was increased from 60kN to nearly 120kN when the braces were added. Also larger deformation capacity was developed. However the

sudden drop in the load indicated that the structural system had deficiencies that need to be addressed.
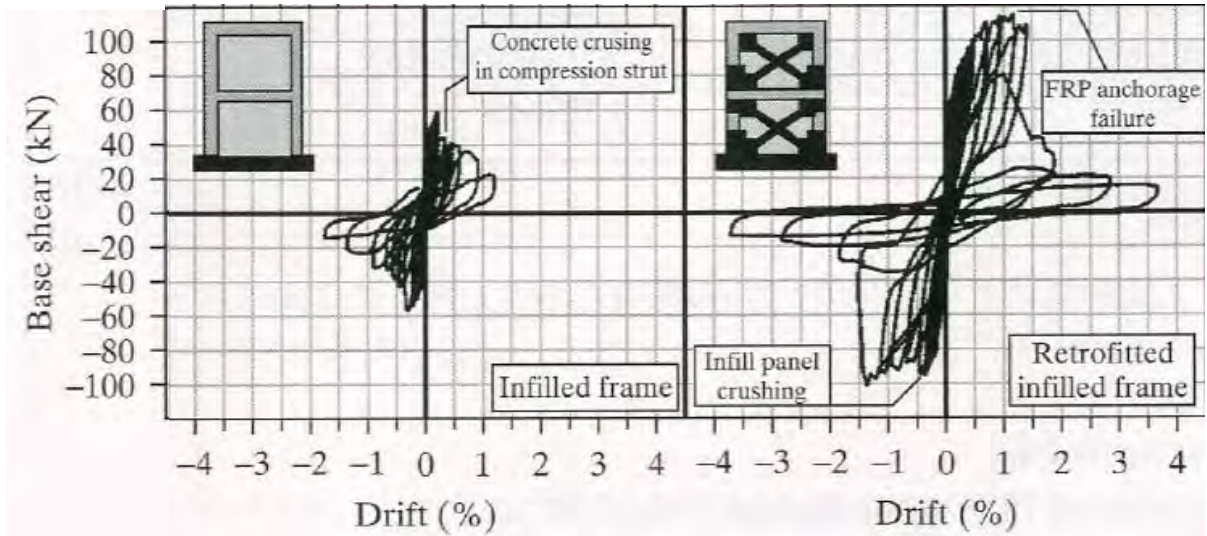


*Figure 2.19 Response of the system under lateral loads (Pampanin & Akguzel 2011)*

## 2.7    REETZ, RAMIN & MATAMOROS, 2004

A set of two reinforced concrete cantilever beams built using mechanical splices at the joint were tested to control the behavior of the plastic hinge section of the beams. Those mechanical splices were threaded at both ends to connect bars that were also threaded. The beams had 12in x 24in or 10in x 16in. Cross-section reinforcement of each beam was 4 bars #7 longitudinal bars and the same shear reinforcement. The mechanical splices were located 3in below the base of the cantilever beams and no stirrups were placed around the splices.
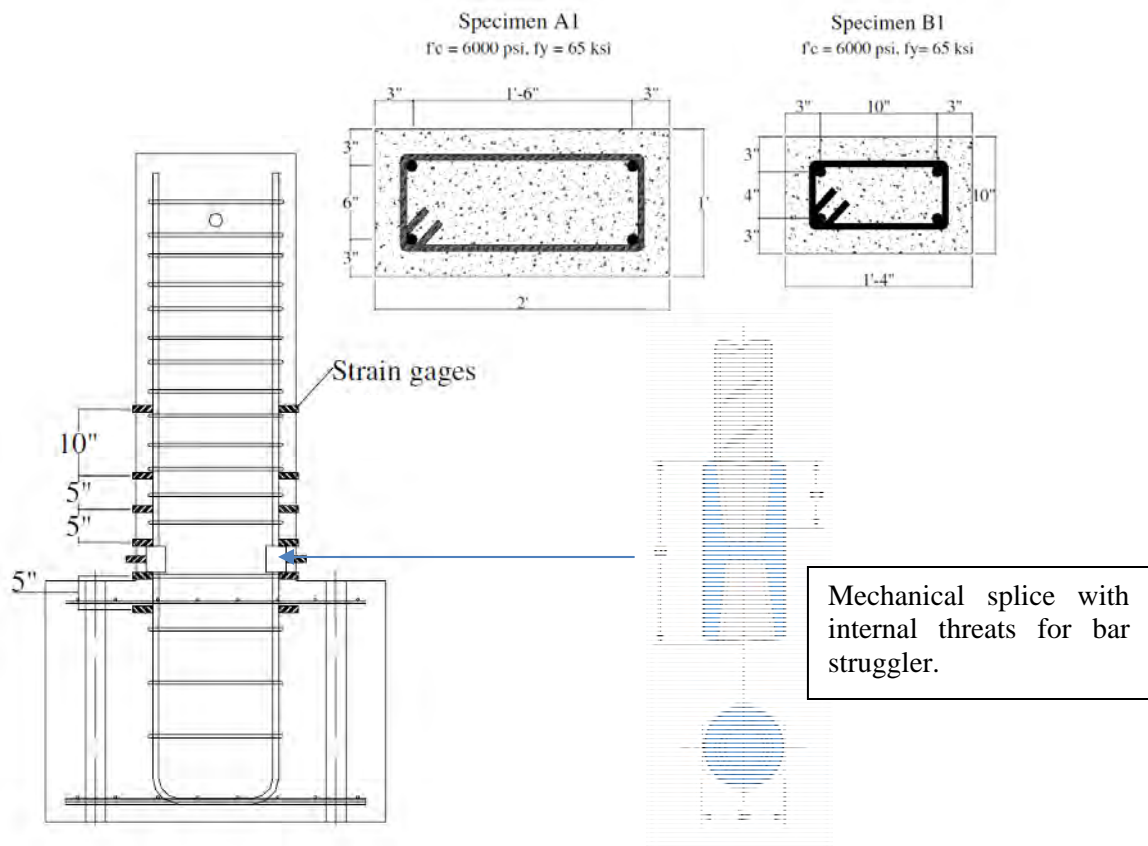
*Figure 2.20 Elevation view of the Beam with the location of the mechanical splice and the two different cross section for each beam (Pampanin & Akguzel 2011)*

Cyclic lateral load were applied to the beams that were tested as cantilever columns. The results of the test are presented at Figure 2.21 and Figure 2.22. For the specimen A1, there was no fracture of the bar near the splice, however, the core concrete inside the splice region crushed. One reason for this failure was the reduced concrete section at the level of the splices and a large spacing between the stirrups. Buckling of the longitudinal bar was also noted. Specimen B1 had same behavior and the end of the test occurred when one bar fractured near the splice.

29
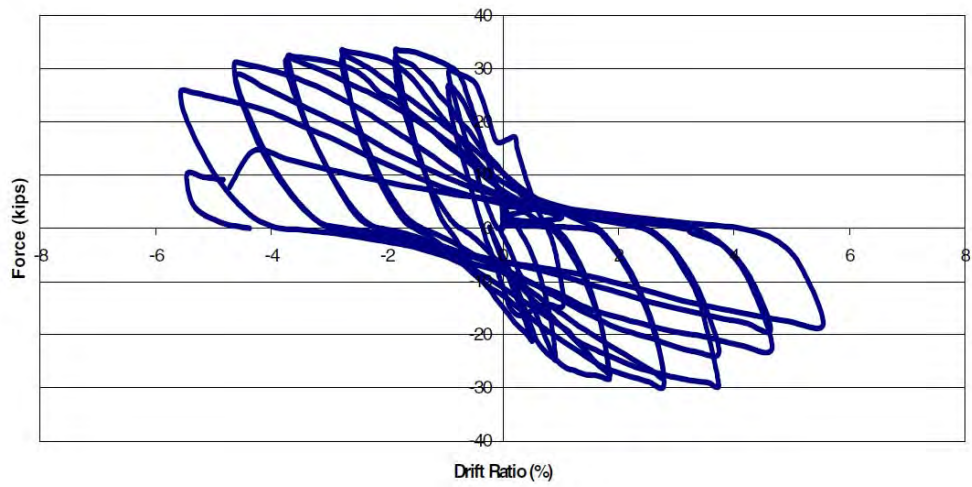
***Figure 2.21 Response of the beam with section A1 under the cycle lateral loads applied (Pampanin & Akguzel 2011)***
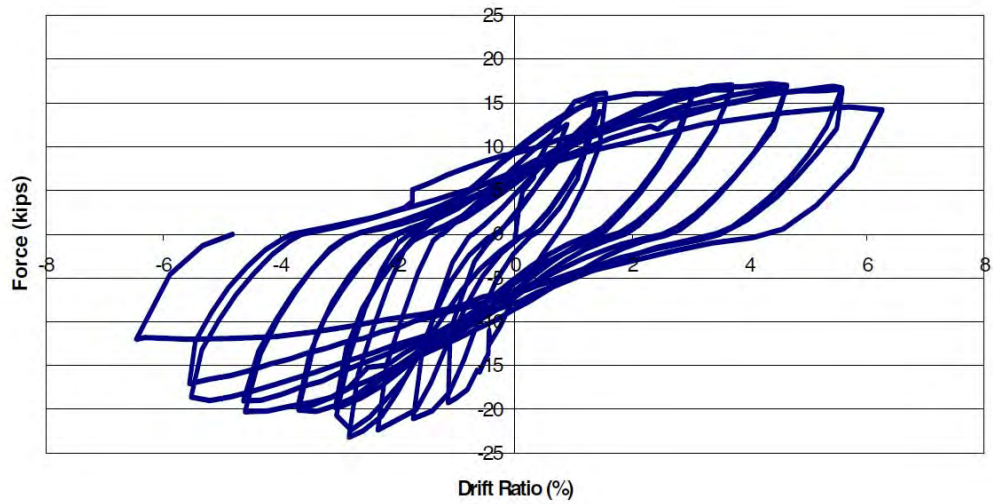


***Figure 2.22 Response of the beam with section B1 under the cycle lateral loads applied (Pampanin & Akguzel 2011)***

# CHAPTER 3

# Behavior of Mechanical Splice

## 3.1 INTRODUCTION

The main objective of this chapter is to describe the properties and behavior of mechanical splices for reinforcing bars.

## 3.2 LAP SPLICES VS. MECHANICAL SPLICES FOR NEW CONSTRUCTION USES

As an alternative to lap splicing, mechanical splices can be used for retrofit purposes. They are generally most economical than traditional lap splices when available spacing or length makes laps difficult to utilize. One type of splice is shown in Figure 3.1. There are different types of mechanical splices. The one shown in Figure 3.1 is composed of a hollow threaded steel tube to couple two reinforcing bars with threaded ends. This type of splice is not suitable for retrofit purposes since bars need to be threaded and threading bars embedded in concrete is nearly impossible.

Lap splices depend on quality of concrete and/or confinement by transverse reinforcement. Mechanical splicing provides load path continuity in the reinforcement, independent of the condition of the concrete.

*Figure 3.1  Type of mechanical splices using threaded bars*

ACI 318-11 12.14.2.1 indicates that tension lap splices are not allowed for #14 or #18 bars. Lap splices add to congestion of the concrete section in elements near beam-column joints as Figure 3.2 shows. An alternative solution is the use of mechanical splices.
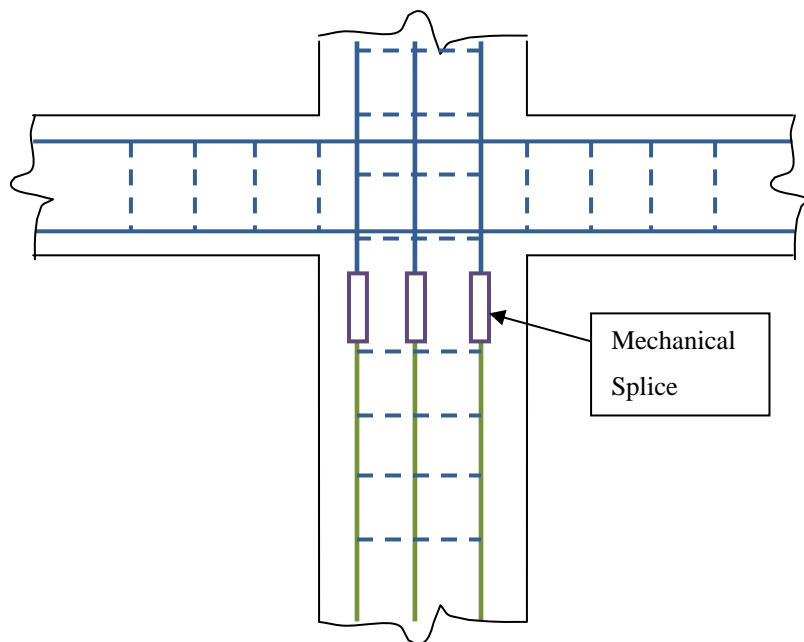


Mechanical Splice

*Figure 3.2 Mechanical Splices applied to Column-Beam joint avoiding bar congestion.*

Poorly confined lap splices cannot develop large ductility. The failure is brittle once slip between the spliced bars begins. Figure 3.3 represents the differences of deformation responses under tension axial load of a poorly confined lap splice and mechanical splice. Elwood, et.al, on the update of ASCE/SEI 41 Concrete Provisions consider also the deficiencies related to the use of lap splices, specially for cases where the splice length is shorter than required by the code.
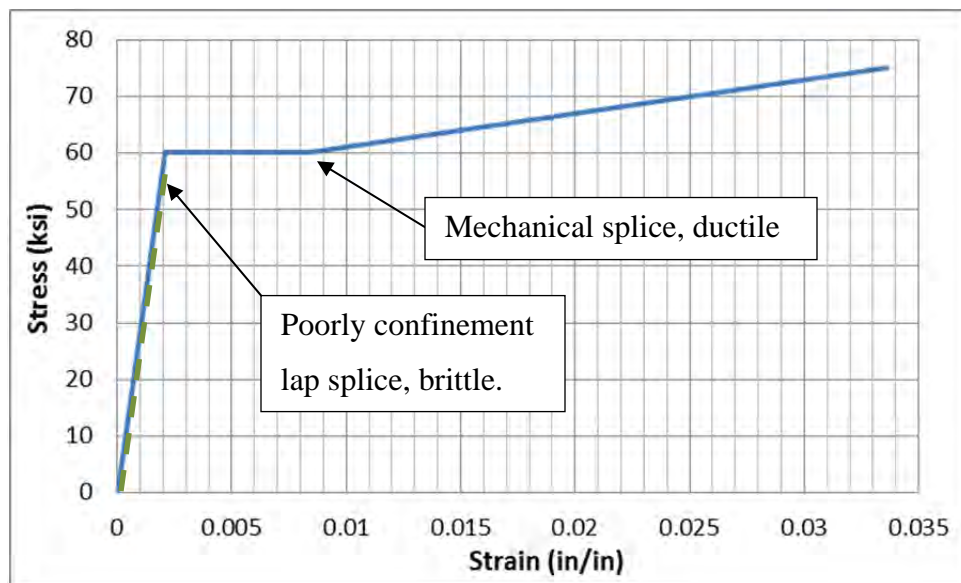


*Figure 3.3  Behavioral model for a lap splice and a mechanical splice*

ACI 318-11 code requires that mechanical splices develop at least 1.25fy (fy: nominal yield strength). For seismic applications, Type 1 splices must develop 1.25fy, however Type 2 splices must develop the specified tensile strength of the bar.

Mechanical splices are frequently used in new construction. However, their use is limited and not practical for use in retrofitted structures. However, if the bars to be joined do not need to be threaded in order to be connected with a special mechanical splice, such mechanical splices can be useful.

### 3.3 MECHANICAL SPLICE FOR RETROFITTED USES

### 3.3.1 Replacing damaged existing bars

After an event that causes damage to a structure, the damaged bars may have to be removed if they are buckled and bent. Figure 3.4 shows damaged bent bars which can be repaired by installing new bars that are mechanically spliced (coupled) to the existing bars. For this study, splices which do not need end-bar preparation were considered. Once the bar is removed the splice sleeve can be positioned over the existing bars and a new bar is introduced where the bent bar was removed. The splice sleeve is then moved to center on the location where the existing and new bars meet. The bars are held tightly in the sleeve with bolts that are torqued to a prescribed level. The system is designed to develop 100% or 125% of nominal yield strength of the bars as ACI 318-11 requires. There are different types of couplers that vary according to the process of the installation.
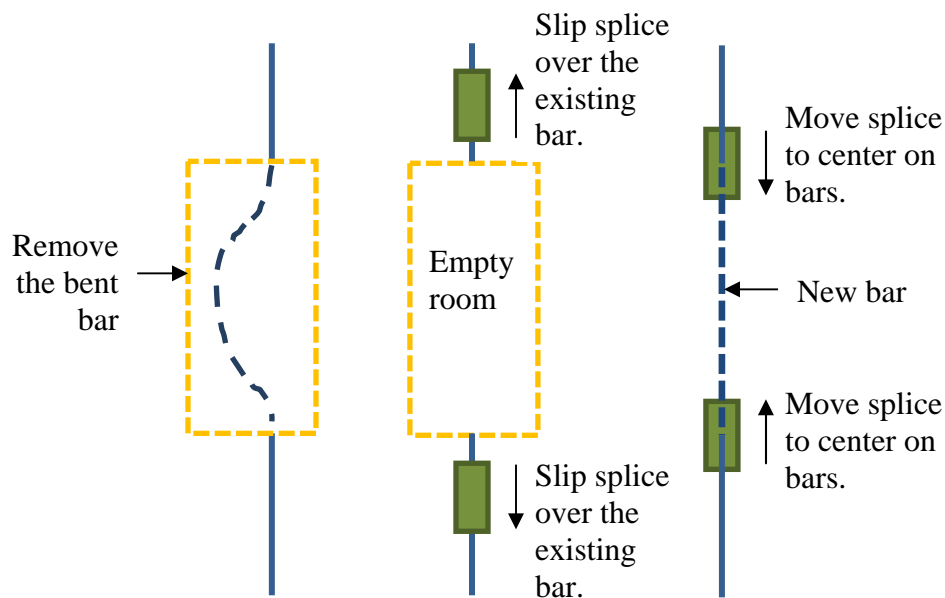
*Figure 3.4  Advantage of mechanical splice to replace bent bars*

Two different mechanical splice configurations were evaluated. The first is the Short Mechanical Splice Lenton (Type S) and Long Mechanical Splice Lenton (Type B) produced by Erico. There are different number of bolts depending on size of bar.
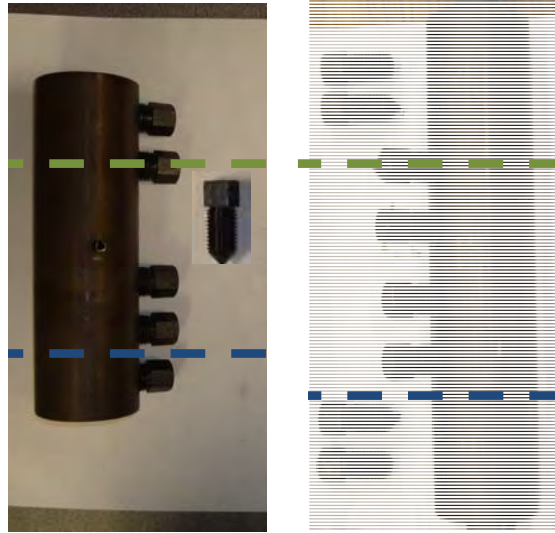


*Figure 3.5  Short (left) and Long (right) Mechanical Splices*
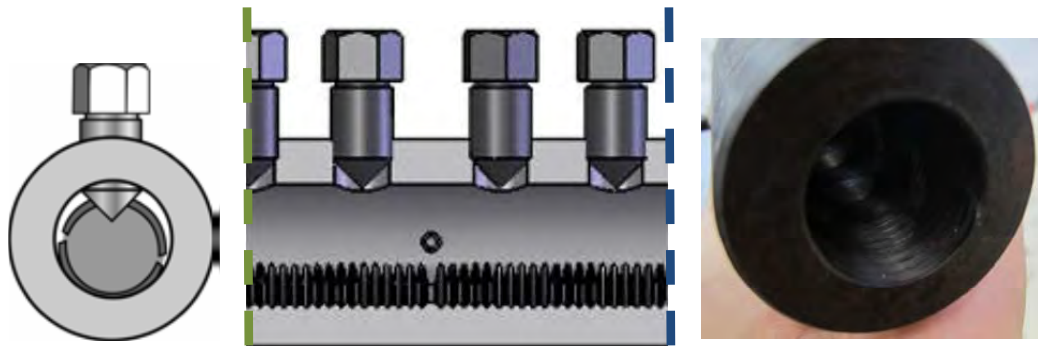


*Figure 3.6 Bolts tighten the bar with the interior sleeve of the mechanical splice.*

### 3.3.2 Mechanical splices in special moment frames in high seismic zones

When a reinforced concrete structure behaves inelastic during an earthquake, the stress in tension of the reinforcement could reach its maximum strength capacity and other cases to develop large deformations besides high strength. Seismic provisions in ACI 318 Chapter 21 classify two types of mechanical splices, Type 1 for splices located where strength is only necessary and Type 2 where large deformations and high strength are required for an appropriate behavior.

Figure 3.7 shows the allowed location for each type of mechanical splice. Type 1 mechanical splices are used in a distance out of twice the member depth from the column from the hinge zone of the column. Type 2 mechanical splices are allowed to be installed at any location. Type 1 splices are not required to provide large deformation as Type 2 splices. Besides, Type 1 is capable to resist high strength expected in yielding regions. The restriction for Type 1 splices applies to all reinforcement resisting earthquakes effects, including transverse reinforcement.
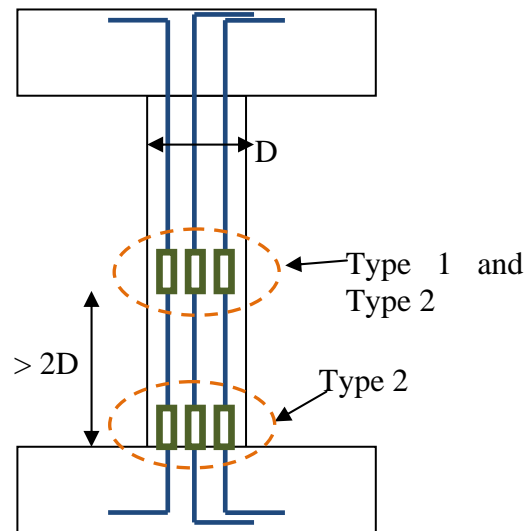


*Figure 3.7 Location of Type 1 and Type 2 mechanical splices*

Additionally, Type 2 should developed 125% of the specified yield strength (fy) of the bar, and 100% of the ultimate specified tensile strength (fu). Type 1 splice should develop 125% of the specified yield strength (fy) of the rebar.

### 3.3.3 Selection of the type of mechanical splice

The manufacture's data for the mechanical splices indicate that the long mechanical splice meets the requirements Type 2 and Type 1 splice (large deformation and high strength). The bars to be coupled should be A-615 and A-706. For short mechanical splice, it meets the requirement for Type 1 splice when the bar is A-615 (high strength), however this short mechanical splice could be used as Type 2 when the bar is A-706 (large deformation). Table 3-1 summarizes the requirements for the selection to the type of mechanical splice.

*Table 3-1  Provisions for the selection of the mechanical splices*

| Type of Splice | ASTM Specification for bars | ACI-318 Seismic Provisions Type (location) | Requirement Strength of bars (ACI 318-11) | Requirement Strength of bars (AASTHO) |
|---|---|---|---|---|
| Short Mechanical Splice | A-706 | Type 2 | 1.25 fy & 1.0fu | 1.35fy |
| Short Mechanical Splice | A-615 & A-706 | Type 1 | 1.25 fy | 1.35fy |
| Long Mechanical Splice | A-615 & A-706 | Type 1 and Type 2 | 1.25 fy & 1.0fu | 1.35fy |

For rehabilitation purposes, it should be observed that these bars can come from structures that may be quite old. Properties of the bar are very important in order to choose the appropriate mechanical splice. Table 3-2 shows comparisons of different old types of reinforcing bars. Long mechanical splices are capable to work with old bars A-615 of building build from 1968, and short mechanical splices are allowed to be used with bars used in structures build from 1974. However, if it is used a bar with the same characteristics of A-615 (min yield and tensile strength), the long mechanical splice can be applied. An example is the bar type is A432 Grade 60 which has same value for

37

minimum yield and tensile strength, then it can be repaired a structure built after 1959 using the long mechanical splices.

Short mechanical splices could be used to retrofit columns for structures build after 1974, considering the splices as Type2. However, considering the short mechanical splices as a Type 1, they can be used in the rehabilitation of structures built after 1959, similar to the long mechanical splice case.

**Table 3-2  Reinforcing bars 1911 to present, ASTM specification, minimum Yield and Tensile Strengths in psi (CRSI)**

| ASTM Spec | Years | | Steel Type | Grade 33 (Structural) | | Grade 40 (Intermediate) | | Grade 50 (Hard) | | Grade 60 | | Grade 75 | |
|---|---|---|---|---|---|---|---|---|---|---|---|---|---|
| | Start | End | | Min. Yield | Min. Tensile | Min. Yield | Min. Tensile | Min. Yield | Min. Tensile | Min. Yield | Min. Tensile | Min. Yield | Min. Tensile |
| A15 | 1911 | 1966 | Billet | 33,000 | 55,000 | 40,000 | 70,000 | 50,000 | 80,000 | | | | |
| A408 | 1957 | 1966 | Billet | 33,000 | 55,000 | 40,000 | 70,000 | 50,000 | 80,000 | | | | |
| A432 | 1959 | 1966 | Billet | | | | | | | 60,000 | 90,000 | | |
| A431 | 1959 | 1966 | Billet | | | | | | | | | 75,000 | 100,000 |
| A615 | 1968 | 1972 | Billet | | | 40,000 | 70,000 | | | 60,000 | 90,000 | 75,000 | 100,000 |
| A615 | 1974 | 1986 | Billet | | | 40,000 | 70,000 | | | 60,000 | 90,000 | | |
| A615 | 1987 | Present | Billet | | | 40,000 | 70,000 | | | 60,000 | 90,000 | 75,000 | 100,000 |
| A16 | 1913 | 1966 | Rail | | | | | 50,000 | 80,000 | | | | |
| A61 | 1963 | 1966 | Rail | | | | | | | 60,000 | 90,000 | | |
| A616 | 1968 | 1999 | Rail | | | | | 50,000 | 80,000 | 60,000 | 90,000 | | |
| A160 | 1936 | 1964 | Axle | 33,000 | 55,000 | 40,000 | 70,000 | 50,000 | 80,000 | | | | |
| A160 | 1965 | 1966 | Axle | 33,000 | 55,000 | 40,000 | 70,000 | 50,000 | 80,000 | 60,000 | 90,000 | | |
| A617 | 1968 | 1999 | Axle | | | 40,000 | 70,000 | | | 60,000 | 90,000 | | |
| A996 | 2000 | Present | Rail, Axle | | | 40,000 | 70,000 | 50,000 | 80,000 | 60,000 | 90,000 | | |
| A706 | 1974 | Present | Low-Alloy | | | | | | | 60,000 | 80,000 | | |
| A955M | 1996 | Present | Stainless | | | 40,000 | 70,000 | | | 60,000 | 90,000 | 75,000 | 100,000 |

### 3.4 SHORT MECHANICAL SPLICE

The splice consists of a 6.8 in. steel cylinder with 6 bolts. These bolts are located into one longitudinal line which go through along the splice as Figure 3.8 shows. The bolts are tightened to squeeze the bar against the grooved sleeve mechanical splice. The bolts have pointed ends that are seated into the bar as shown in Figure 3.6. Seating of the pointed bolts reduced the cross sectional area of the bar about 5%. The material used for this type of splice is also Grade 60. The interior and exterior diameters vary with the diameter of the bars to be spliced. For the current research the bar diameter used is #8, 1 in. dia. Table 3-3 provides the precise sizes for the current short mechanical splice, including the required minimum torque needed to tighten the bolt to the bars and splice.
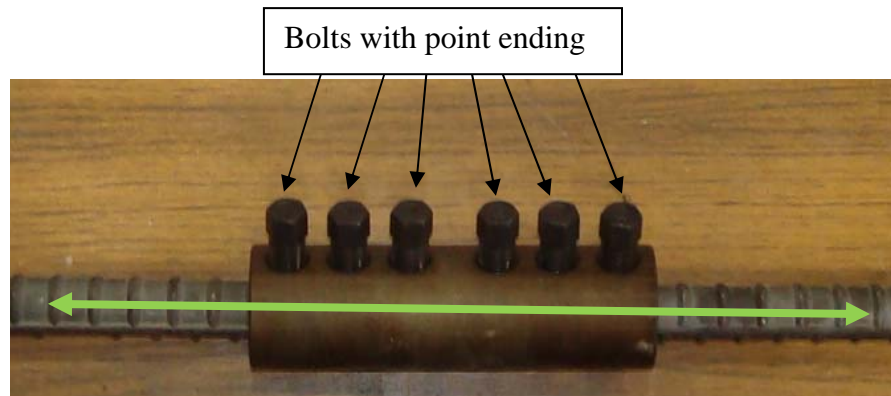


*Figure 3.8  Short Mechanical Splice for bar #8, note the green line indicating the continuity of the reinforcement.*

6.8 in.

1 in.
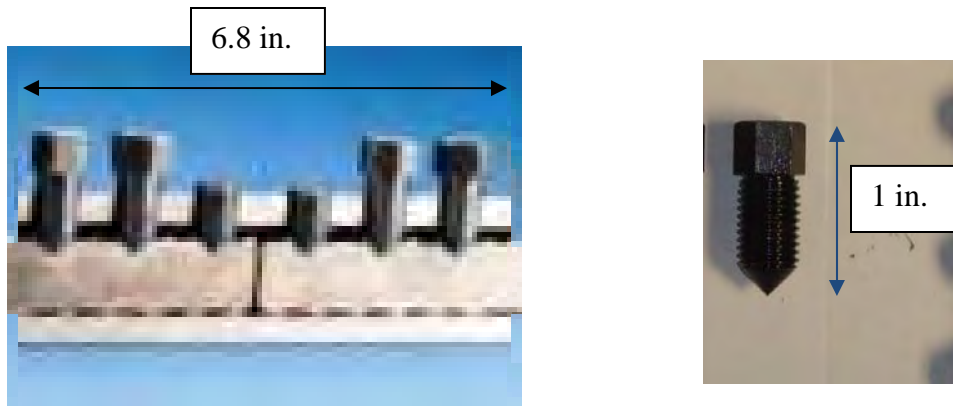
*Figure 3.9  Longitudinal cross section of the short mechanical splice (right) and length of the point ending bolt*

*Table 3-3 Dimensions and properties of the MS-S and torque needed to secure splice*

| Rebar Designation | Length (L) | Outside Diameter (d) | Inside Diameter | Weight | Socket Size | Average Torque All Bolts | Number of Bolts |
|---|---|---|---|---|---|---|---|
| units | in | in | in | lb | in | ft-lb | |
| #8 | 6.8 | 2.1 | 1.2 | 5.1 | 5/8 | 350 | 6 |

**3.5   LONG MECHANICAL SPLICES**

This mechanical splices consists of a 10 in. length steel cylinder with 8 bolts, two outer bolts with rounded ends and 6 interior bolts with pointed ends. Similar to the short mechanical splices, the rounded and pointed end bolts are located along a plane one through the splice as Figure 3.10 shows. The rounded point bolt at the end of the sleeve in intended to prevent the bars from fracturing in the splice so that the requirement for specified ultimate strength is achieved. Figure 3.11 shows dimensions and internal shape of the long mechanical splice and the bolts. Table 3-4 shows properties and dimensions also for the long mechanical splice.
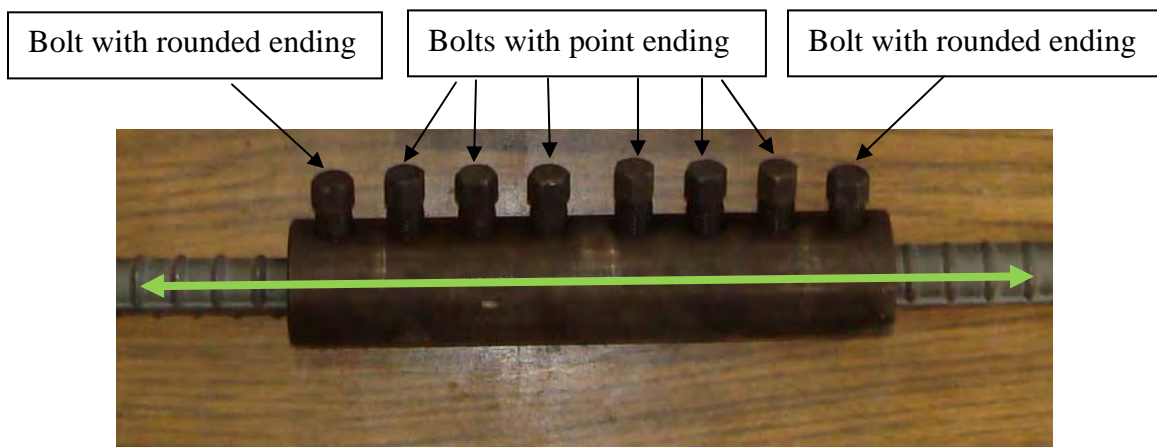


*Figure 3.10  Long Mechanical Splice*
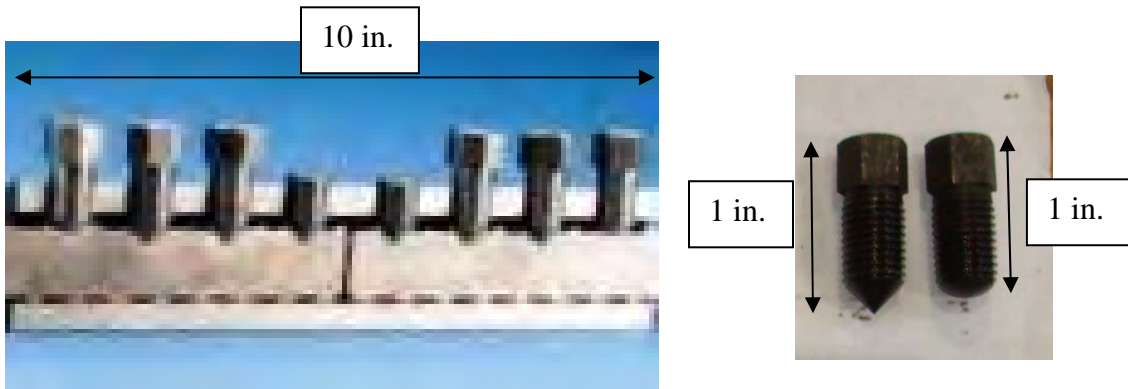
*Figure 3.11 Longitudinal cross section of the long mechanical splice (right) and length of the point and rounded ending bolts*

*Table 3-4 Dimensions and properties of the MS-L and the min Torque needed to application of the bolts*

| Rebar Designation | Length (L) | Outside Diameter (d) | Inside Diameter | Weight | Socket Size | Average Torque All Bolts | Number of Bolts |
|---|---|---|---|---|---|---|---|
| units | in | in | in | lb | in | ft-lb | |
| #8 | 10 | 2.13 | 1.2 | 7.4 | 5/8 | 350 | 8 |

**3.6    INSTALLATION OF THE MECHANICAL SPLICE**

The installation of the mechanical splices allows for the use of the splices for retrofit purposes, especially because they can be used in-situ. Other types of splices that need end-bar preparation prior to the installation are genereally not suitable for retrofit purposes. The installation requires the use of a torque wrench to reach the required torque. A simple wrench with the appropriate socket can also be used. The installations steps are explained bellow:

a) Clean the surface of the bar from any rust or concrete debris, then insert one side of the mechanical splice over the bar. Figure 3.12 shows the process. The bar should be inserted to the middle of the mechanical splice.



*Figure 3.12  Seating the bar in the mechanical splice*

b) Using an air impact or manual wrench, tighten the bolts from the center to the end of the splice (Figure 3.13). Torque is applied to the level indicated by the manufacturer or until the head of the bolt fractures as shown in Figure 3.14. The bolt penetrates into the bar approximately 1/4 in for #8bar.

*Figure 3.13  Torqueing the bolt into the mechanical splice*
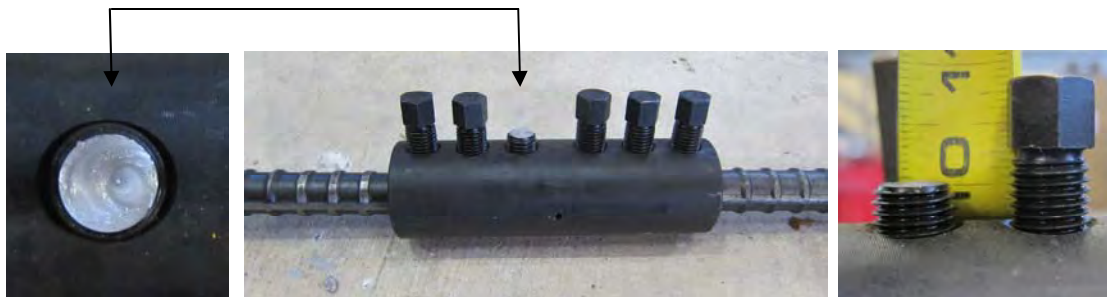


*Figure 3.14  Head of the bolt broken, depth of penetration is 1/4in*

c) The step b is repeated for the rest of bolts from the center bolt to the first bolt engaging the bar. The process is repeated for the second bar. Figure 3.15

44

shows the mechanical splice with all the bolts tightened and the heads fractured.



*Figure 3.15  Head of the bolt broken*

### 3.7    EXPERIMENTAL PROGRAM

The tests of the mechanical splices are divided in three sets:

1. Cycle tension test
2. Cycle compression-tension test
3. In situ test

### 3.7.1 Test Program: <u>First Set of Mechanical Splices</u> - Cyclic Tension Axial Load Test

In order to determine the tension properties of the system formed by the mechanical splice and the bars connected, a set of 4 spliced bars was tested under cyclic tension axial load. Two Long Mechanical Splice and two Short Mechanical Splices were tested. The nomenclature used for each specimen is MS-L1 and MS-L2 for the two long mechanical splices and MS-S1 and MS-S2 for the short mechanical splice. The modulus of elasticity, stiffness, and load and deformation capacity of each system was measured under cyclic tension. Figure 3.16 shows a general scheme of the specimen indicating nomenclature for dimensions and location of instrumentation used.
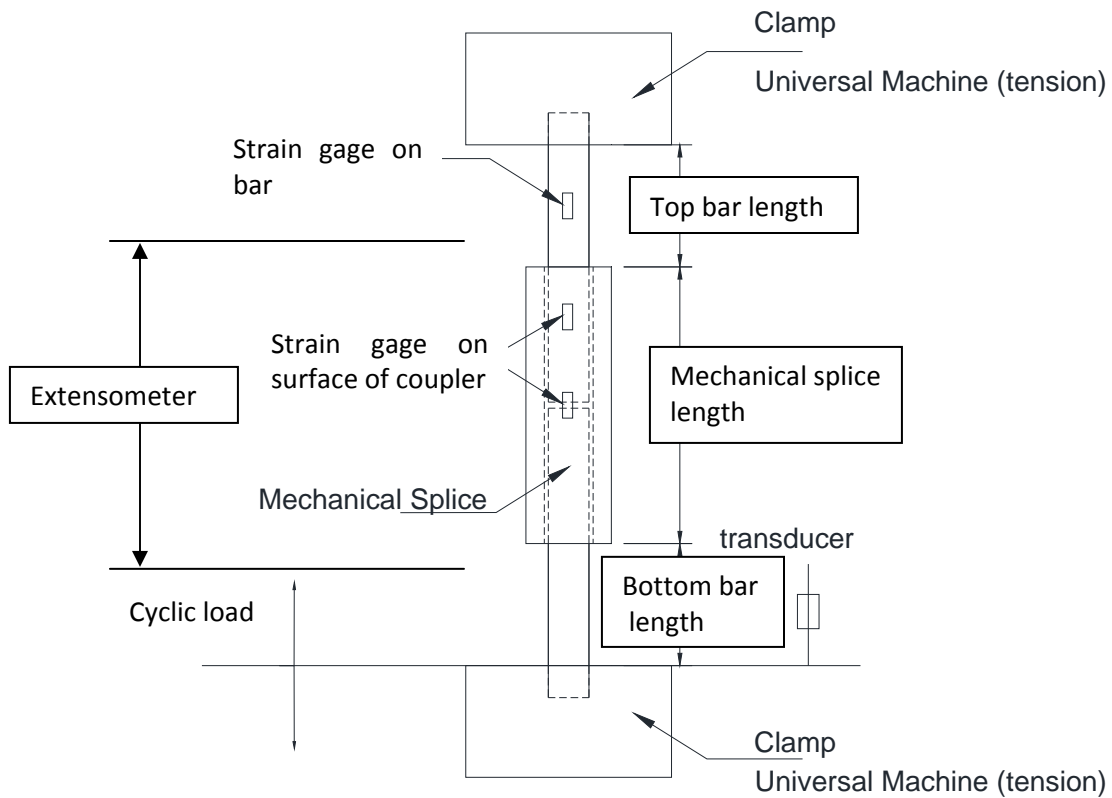


*Figure 3.16 General scheme of specimen*

Table 3-5 summarizes the specimens tested. ASTM specification of each bar is listed. Length of the specimen and extensometer used is also listed too. Table 3-6 and Table 3-7 show the application of the strain gages applied on each specimen.

The type of steel bar was A-706 Grade 60 for all the new bars used in the specimens. It was studied the Type 2 mechanical splice for Short Mechanical Splices and Long Mechanical Splices.

*Table 3-5 Specimen details for the cyclic tension test*

| Specimen | Condition | | ASTM Specification | | Length (in) | | Length (in) | Length (in) |
|---|---|---|---|---|---|---|---|---|
| | Top Bar | Bottom Bar | Top Bar | Bottom Bar | Top Bar | Bottom Bar | Specimen (*) | Extensometer |
| MS-L1 | New | New | A-706 | A-706 | 10.00 | 10.00 | 30.00 | 12.00 |
| MS-L2 | New | New | A-706 | A-706 | 10.00 | 10.00 | 30.00 | 13.75 |
| MS-S1 | New | New | A-706 | A-706 | 6.00 | 6.00 | 18.80 | 9.80 |
| MS-S2 | New | New | A-706 | A-706 | 6.00 | 6.00 | 18.80 | 9.80 |

(*) Clear space between heads of universal machine

*Table 3-6 Strain gages applied on the bar of each specimen*

| | Strain gauges on bars | |
|---|---|---|
| Specimen | Up Bar | Bottom Bar |
| MS-L1 | 2 applied each face | X |
| MS-L2 | X | X |
| MS-S1 | Applied | X |
| MS-S2 | X | X |

*Table 3-7 Strain gages applied on the mechanical splice of each specimen*

| Specimen | Strain gauges on mechanical splice | | |
|---|---|---|---|
| | Above the middle | Middle | Bellow the middle |
| MS-L1 | between 2nd and 3rd bolt | Applied | X |
| MS-L2 | X | X | X |
| MS-S1 | between 1st and 2nd bolt | Applied | X |
| MS-S2 | between 1st and 2nd bolt | Applied | X |

The test setup is shown in Figure 3.17. The universal test machine used had a maximum capacity of 100 kips for tension loads. The bars were clamped into the test machine head with wedge grips that allowed only tension loads to be applied to the specimen. An extensometer (4 in. LVDT) mounded on the splices assembly and a linear potentiometer placed between the heads on the test machine, were used to measure deformations. The universal test machine was operated under force control. Each test was controlled by increasing or decreasing the load applied.
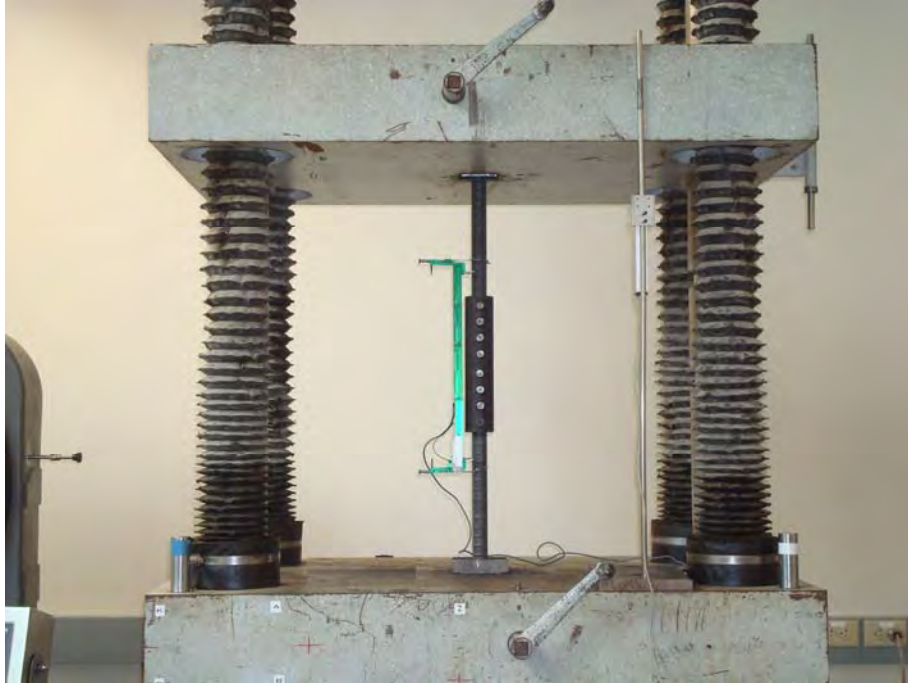
***Figure 3.17  Test Setup for the tension cycle test***

The specimen MS-L1 test procedures are presented in this chapter. The rest of the specimens are discussed in detail in Appendix I.

### 3.7.1.1 Specimen 1 - Long Mechanical Splice MS-L1

### 3.7.1.1.1 Dimensions of the specimen MS-L1

Figure 3.18 shows a sketch of specimen MS-L1. Each bar connected with mechanical splice has a length of 5in. in the splice. The total length of the specimen between clamps or the clear space between heads of the universal machine was 30 in length.
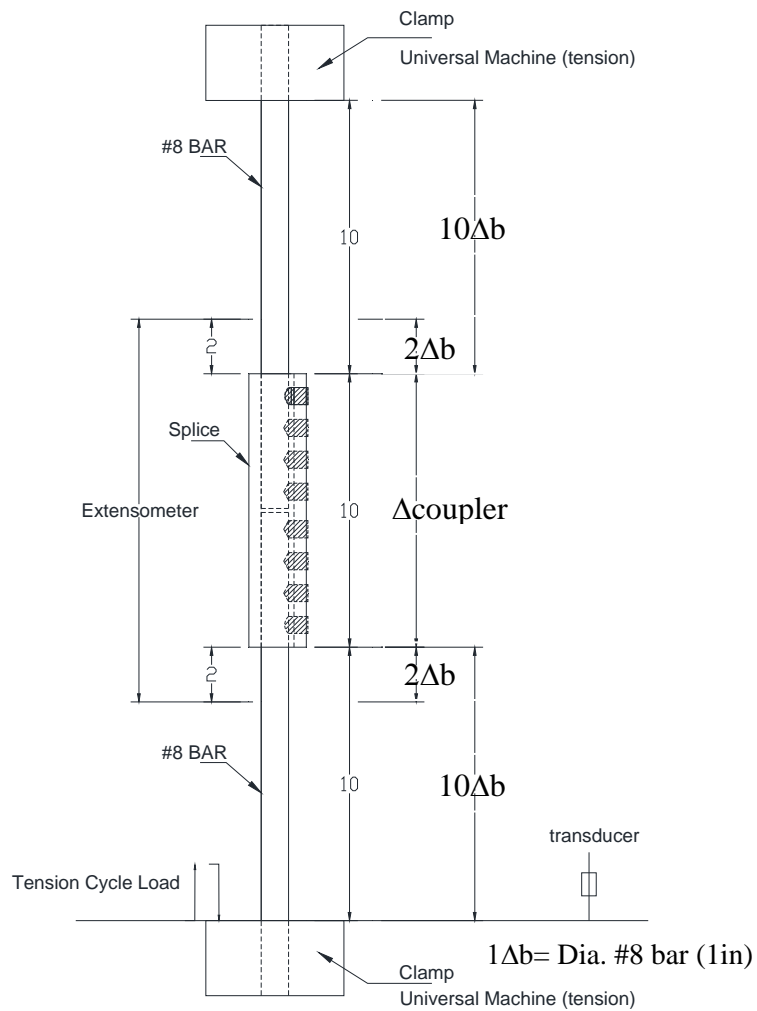


**Figure 3.18 Sketch of MS-L1 to be tested**

50

### 3.7.1.1.2 Instrumentation for the test for MS-L1

Since this was the first test, the objectives were to determine:

a) General behavior of the mechanical splice and the bar in terms of the tension axial load vs. deformation of the splice assemble.

b) Strain on opposite side of the in line with the bolts of the mechanical splice and the other at its opposite face where the bar is connected by friction. Strain in the mechanical splice, one at the middle of the splice and other of between the second and third bolts from the top of the splice. A total of four strain gages were applied on the bar and the splice. The intent was to determine how forces were transferred from the bar to the splice and to determine if the splice produced any bending to the assembly.

c) Deformation and strain along the mechanical splice. Vision System that is an optical system to follow the movement of targets attached to the test element. Results and details of the camera and target are shown in Appendix H. The targets can be seen in Figure 3.19.

51
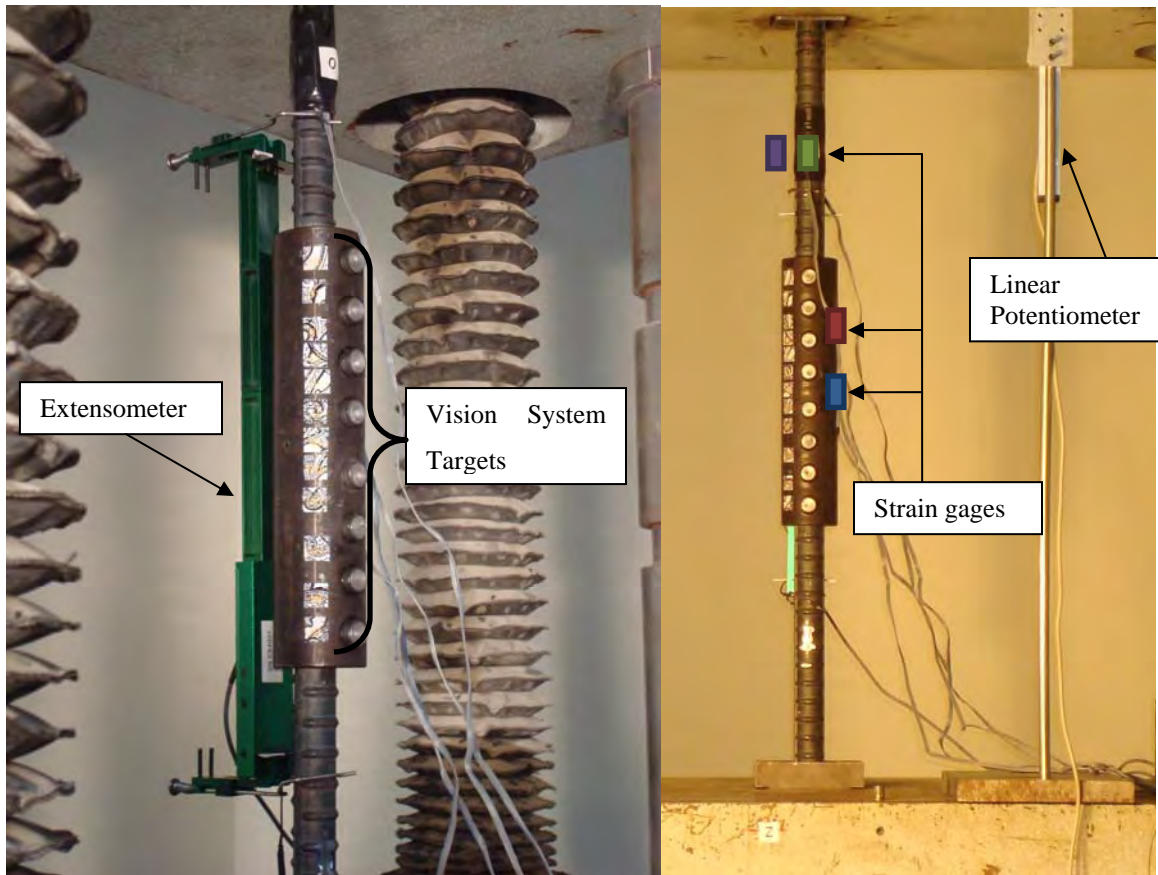
***Figure 3.19  Instrumentation for MS-L1 Test***

### 3.7.1.1.3 *Protocol of the test of MS-L1*

The specimen was subjected to two cycles of tension load to 10, 20, 30, 40 kips and a final load to failure. The loading protocol was established to capture the deformation in the linear range of the mechanical splice and bars. (Figure 3.20)
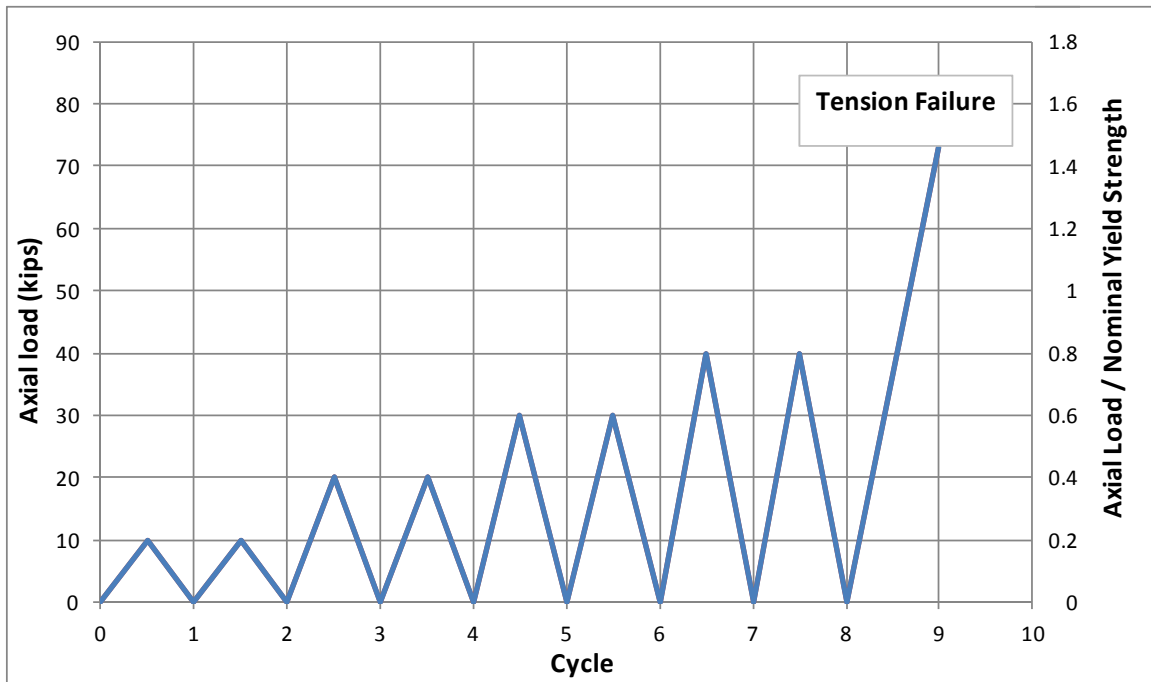
*Figure 3.20  Protocol of load to the cycle tension axial load test.*

### 3.7.1.1.4 Results of the Cyclic Tension Axial Load Test of Specimen MS-L1

The load rate applied for the two first cycles to 10kips, was 3.5 kips/min; for the second set to 20kips load, approximately 6 kips/min, the third set to 30kips was 10 kips/min; and for 40kips load the rate was 13.5 kip/min. For the last cycle, which was taken to failure, the speed was 2 kip/min. The specimen failed at the load of 76kips

Failure occurred in the wedge grips of the test machine, 4in above the splice (Figure 3.21). The load-strain relationship is shown in Figure 3.22 and Figure 3.23.
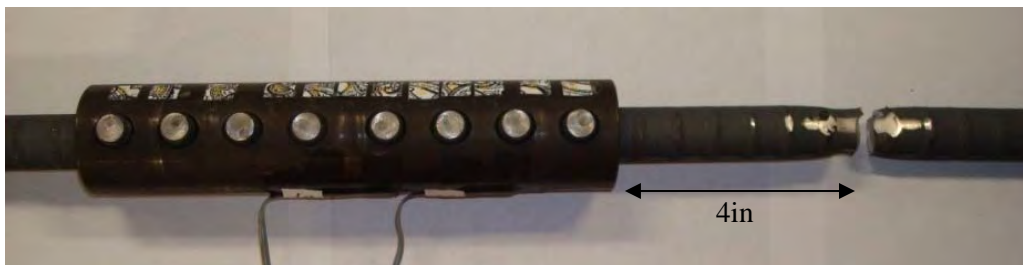
*Figure 3.21 MS-L1 failure pattern.*
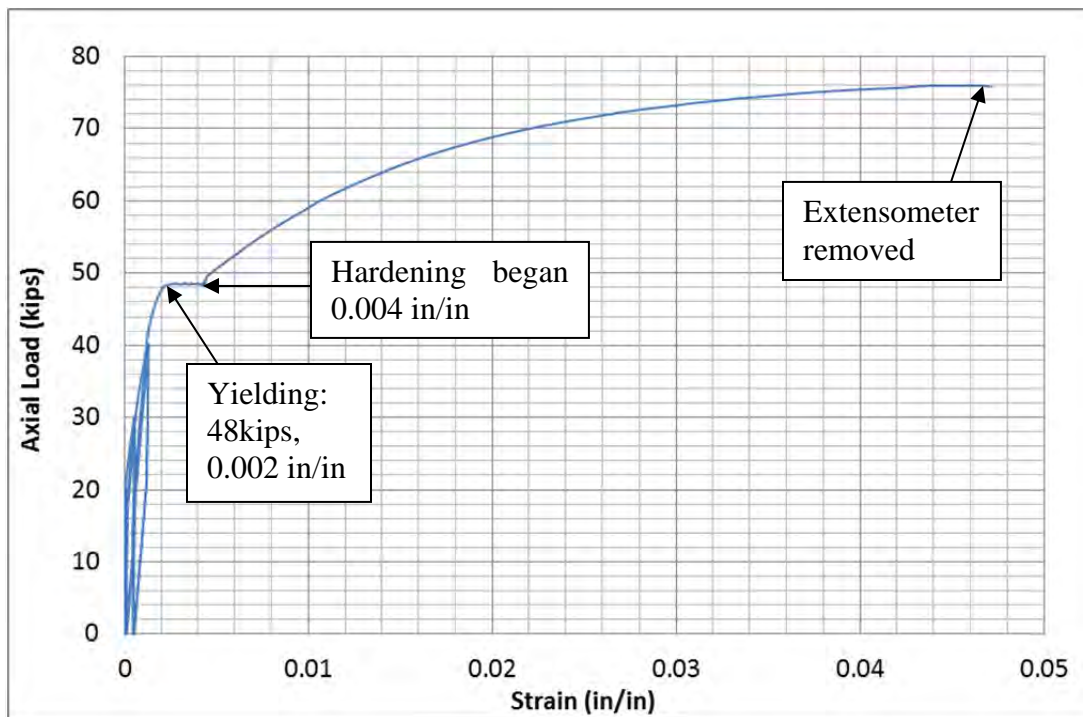


*Figure 3.22  Deformation pattern measured by extensometer for MS-L1*
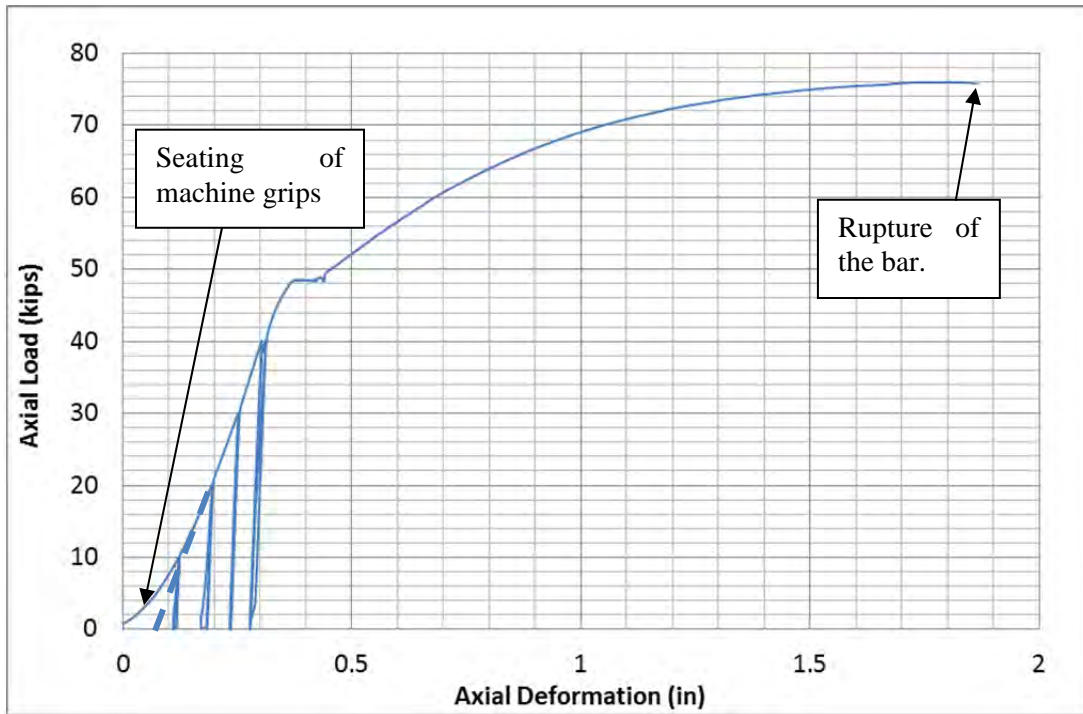
*Figure 3.23  Displacement measured by linear potentiometer for MS-L1*

Strains measured on the bar are shown in Figure 3.24, yielding occurred at 0.0019, close to the theoretical value of 0.0021 for Grade 60, and 0.0046 at the onset of strain hardening. There was no difference in the strains on opposite sides of the bar indicating that the eccentricity between the bar and the splice sleeve was insignificant.
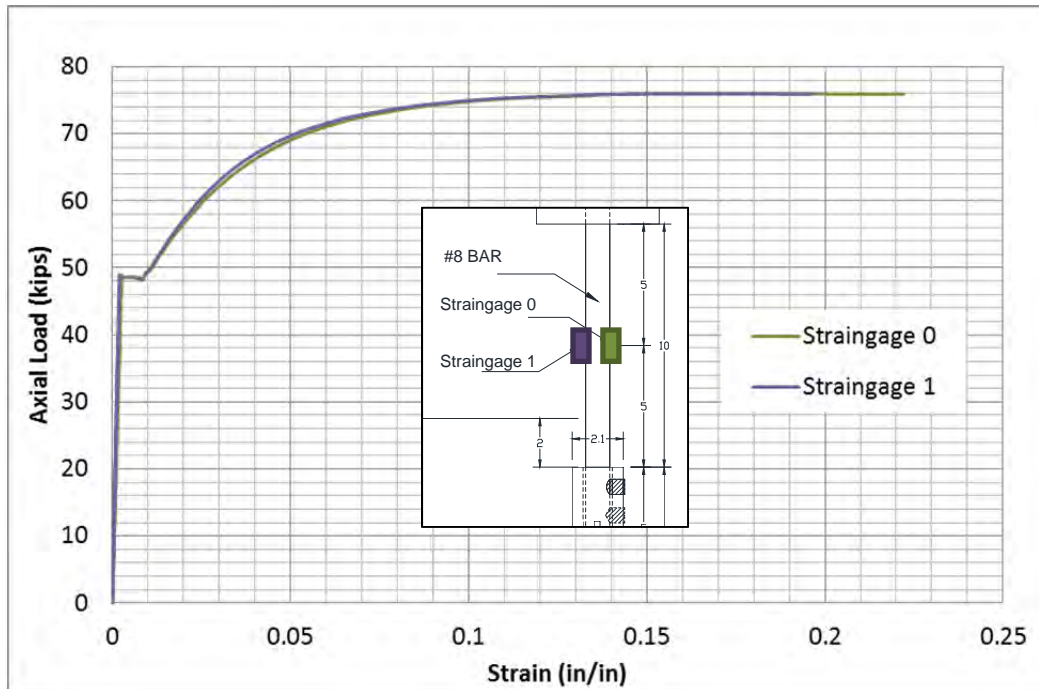
*Figure 3.24  Load-Strain measured above splice sleeve*

Strain measured on the splice indicates the different behavior on the middle of the coupler in comparison with the other location shown in Figure 3.25. Strain between the 2nd and 3rd bolts were about 60% of those at the middle of the splice. The strain between the 2nd and 3rd bolts is nonlinear indicating some redistribution of forces within the bolt group. The cross sectional area at the middle of the sleeve is large enough(about 3 times) to prevent yielding under the ultimate capacity of the bars.
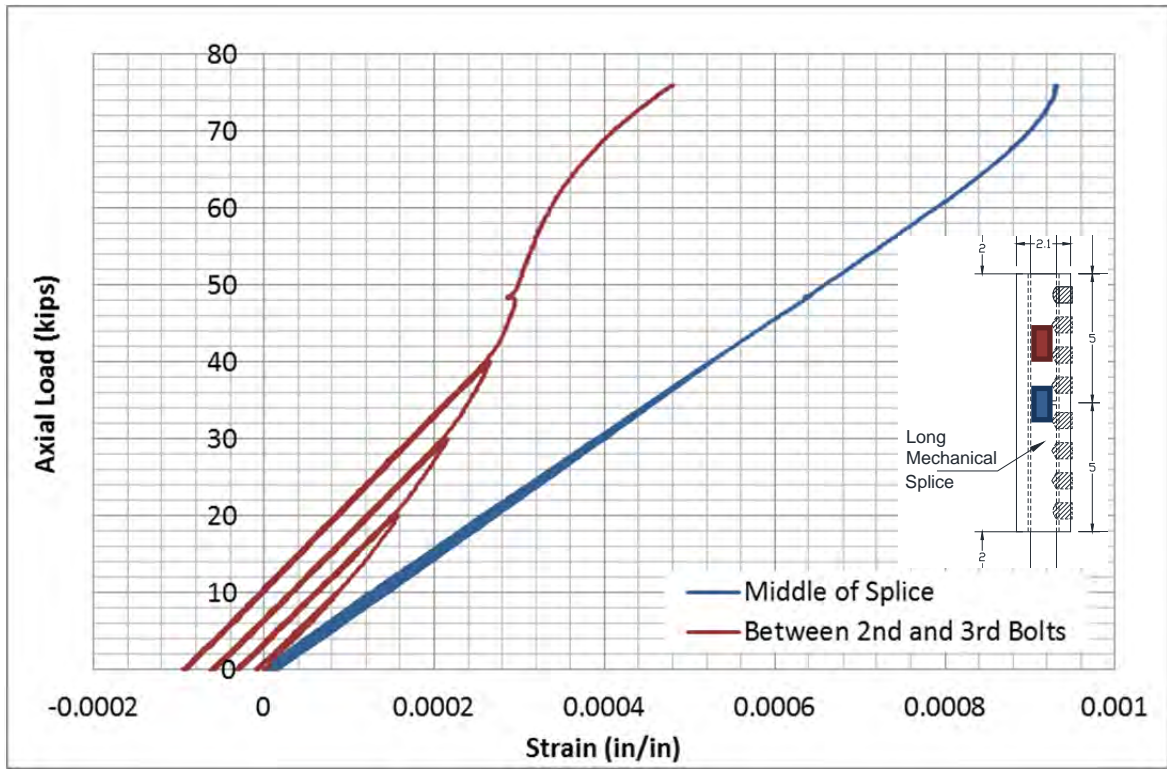
*Figure 3.25  Strain measured on the surface of the mechanical splice MS-L1*

### 3.7.1.2   Summary of results for the Tension Cycle Axial Load Test

Table 3-8 presents the different values in loads response of each case of specimen. It can be seen that the value of yielding stress is similar for long and short mechanical splice. The fractures stresses are very similar among each other because the failure of each specimen was under the rupture of the steel bar. It is also noticed that both short and long splices meet the requirements of ACI318-11 and AASTHO for Type 1 and Type 2 splices.

*Table 3-8 Results of first set of mechanical splice and acceptance criteria*

| Specimen | ASTM bar | Yield of bar Load (kips) | Max. Load Measured (kips) | Type of Failure |
|---|---|---|---|---|
| MS-L1 | A-706 | 47.85 | 75.99 | Rupture of bar 4in above the splice |
| MS-L2 | A-706 | 48.19 | 75.80 | Rupture of bar 4in above the splice |
| MS-S1 | A-706 | 48.87 | 68.98 | Rupture of bar in edge of splice |
| MS-S2 | A-706 | 49.12 | 73.30 | Rupture of bar in edge of splice |

**Area Bar ф 1"**      0.79 in2

| Specimen | ASTM bar | Yield Stress of bar (fy) (ksi) | Fracture Stress of bar (fu) (ksi) | ACI 318 - 11 fu meets Condition A? | ACI 318 - 11 fu meets Condition B? | AASTHO fu meets Condition C? |
|---|---|---|---|---|---|---|
| MS-L1 | A-706 | 60.92 | 96.75 | Yes | Yes | Yes |
| MS-L2 | A-706 | 61.36 | 96.51 | Yes | Yes | Yes |
| MS-S1 | A-706 | 62.22 | 87.83 | Yes | Yes | Yes |
| MS-S2 | A-706 | 62.54 | 93.33 | Yes | Yes | Yes |

**Condition A: measured fu > 75ksi  (1.25 x fy of ASTM bar) ?**
**Condition B: measured fu >  80ksi (fu of ASTM bar) ?**
**Condition C: measured fu > 81ksi  (1.35 x fy of ASTM bar) ?**

### 3.7.2 Test Program: <u>Second Set of Mechanical Splices</u> - Compression-Tension Cyclic Axial Load Test

Tension properties for long and short mechanical splices were found through the first set of tests. However properties of the mechanical splices under cycle compression and tension loads have not been studied.

This set of tests includes 6 mechanical splices, 2 long mechanical splices and 4 short mechanical splices. In the two first specimens, new bars were used, and in the last 4 specimens with short mechanical splices, a new bar and a bar previously yielded were used together. The nomenclature used for each specimen is MS-L3 and MS-L4 for the two long mechanical splices and MS-S3, MS-S4, MS-S5 and MS-S6 for the short mechanical splices. The modulus of elasticity, stiffness, and load vs. deformation capacity of each specimen was measured under cyclic compression-tension axial deformation.

A-615 Grade 60 bars were used. The test specimen is shown in Figure 3.26.
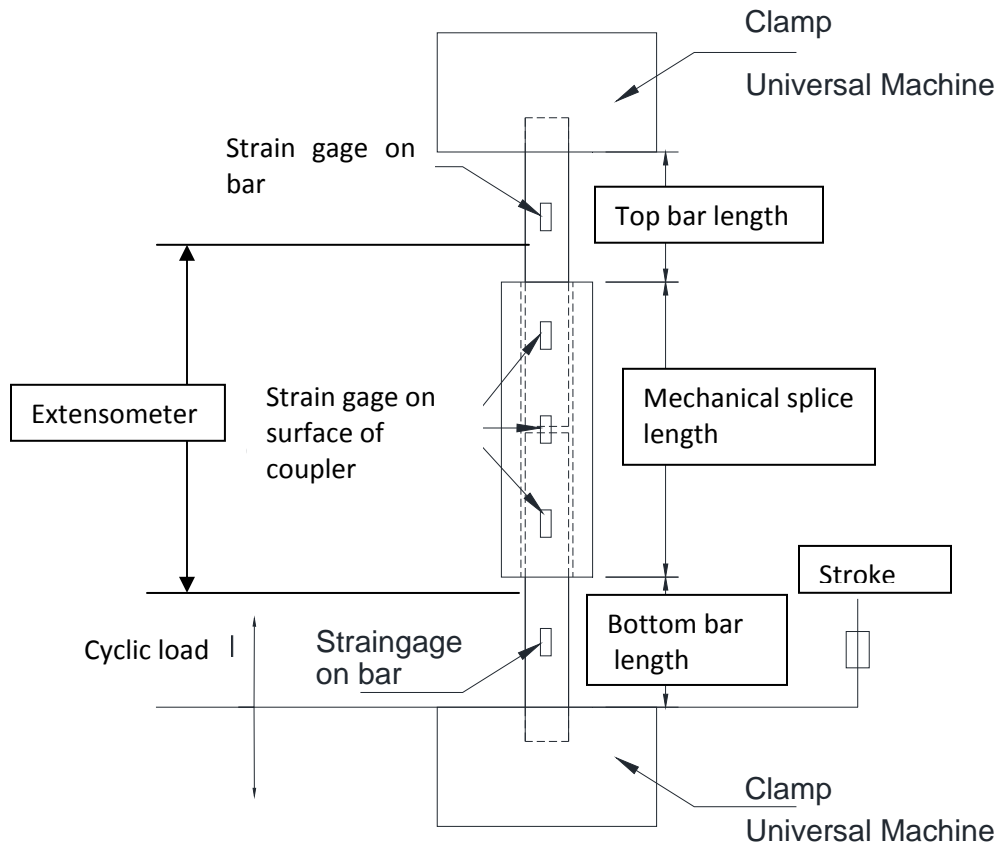
*Figure 3.26 General scheme of specimen for the compression-tension test*

In Table 3-9, specimens tested are summarized. Condition and ASTM specification of each bar is listed. Length of the specimen and extensometer used is also listed. Table 3-10 and Table 3-11 show the location of the strain gages applied on each specimen

*Table 3-9 Specimen's characteristics for the cyclic compression-tension test*

| Specimen | Condition | | ASTM Specification | | Length (in) | | Length (in) | Length (in) |
| | Top Bar | Bottom Bar | Top Bar | Bottom Bar | Top Bar | Bottom Bar | Specimen (*) | Extensometer |
|---|---|---|---|---|---|---|---|---|
| MS-L3 | New | New | A-615 | A-615 | 2.30 | 2.30 | 14.60 | 10.31 |
| MS-L4 | New | New | A-615 | A-615 | 2.00 | 2.00 | 14.00 | 10.38 |
| MS-S3 | New | 4Yield | A-615 | A-615 | 2.30 | 2.30 | 11.40 | 8.00 |
| MS-S4 | 1.5Yield | New | A-615 | A-615 | 2.00 | 2.00 | 10.80 | 8.30 |
| MS-S5 | 4Yiel | New | A-615 | A-615 | 2.10 | 2.10 | 11.00 | 8.93 |
| MS-S6 | New | 1.5Yield | A-615 | A-615 | 1.25 | 1.25 | 9.30 | No applied |

(*) Clear space between heads of universal machine

*Table 3-10 Strain gages applied on the bar of each specimen for the cycle tension test*

| | Strain Gages on Bars | |
| Specimen | Up Bar | Bottom Bar |
|---|---|---|
| MS-L3 | X | X |
| MS-L4 | X | X |
| MS-S3 | X | X |
| MS-S4 | X | X |
| MS-S5 | Applied | Applied |
| MS-S6 | X | X |

*Table 3-11 Strain gages applied on the mechanical splice of each specimen for the cycle compression-tension test*

| | Strain Gages on Mechanical splice | | |
| Specimen | Above the middle | Middle | Bellow the middle |
|---|---|---|---|
| MS-L3 | X | Applied | between 2nd and 3rd bolt |
| MS-L4 | X | Applied | between 2nd and 3rd bolt |
| MS-S3 | between 1st and 2nd bolt | Applied | between 1st and 2nd bolt |
| MS-S4 | between 1st and 2nd bolt | Applied | between 1st and 2nd bolt |
| MS-S5 | X | Applied | X |
| MS-S6 | between 1st and 2nd bolt | Applied | between 1st and 2nd bolt |

The test setup is shown in the Figure 3.27. The universal tension-compression machine used has a maximum capacity of 220kips for tension loads. The grips of the machine are flats for plate coupons. Because the steel bars have circular cross section and they are deformed, the surfaces on two sides of the bar were ground off in order to have a flat area for contact with the clamp. Figure 3.28 shows the details of grinding that portion of corrugation and bar.

The universal tension-compression machine was operated under deformation control. This deformation was measured by the internal transducer or stroke of the machine and the extensometer was installed to the system formed by the mechanical splices and the bars. Each test was controlled by applying tension or compression load to reach the peak of each cycle defined by the selected displacement history. For some tests, the displacement was controlled by the extensometer and for other tests by the stroke of the tension-compression machine.

*Figure 3.27  Test Setup for the compression-tension cycle test and details of the mechanical splices tested*
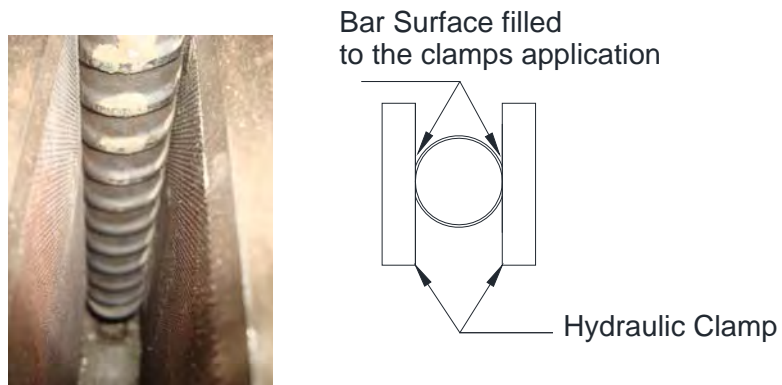
***Figure 3.28  Bar preparation for clamping into the universal compression tension machine***

The results of the test of specimen MS-S3 are presented in this chapter. The details of other specimens are discussed in Appendix I.

### 3.7.2.1 Specimen 7 Short Mechanical Splice MS-S3

### 3.7.2.1.1 Characteristics of the specimen

This specimen consisted of one new steel #8 bar, coupled to a bar yielded previously to a strain 4 times yield in tension and 3 times yield in compression. For retrofit purposes, the mechanical splice can connect an existing previously yielded bar to a new bar, replacing the buckled section of the existing bar with a new bar providing continuity of reinforcement between two couplers at the ends of the removed bar length.
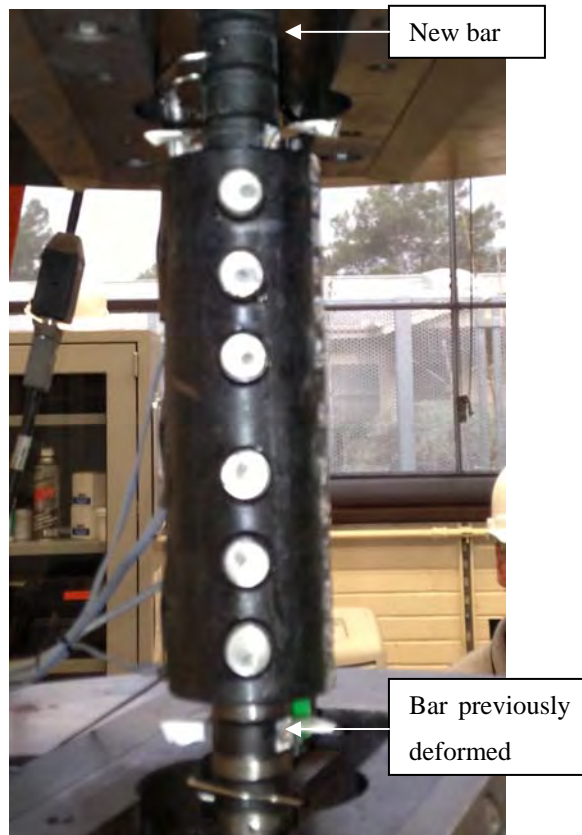


*Figure 3.29 Sketch of MS-S3 to be tested, bolts are in good conditions*

Figure 3.30 shows the scheme for specimen MS-S3. Each bar connected with mechanical splice has a length of 3.4 in into the splice. The total length of the specimen between clamps or the clear space of the universal machine was 11.4in.
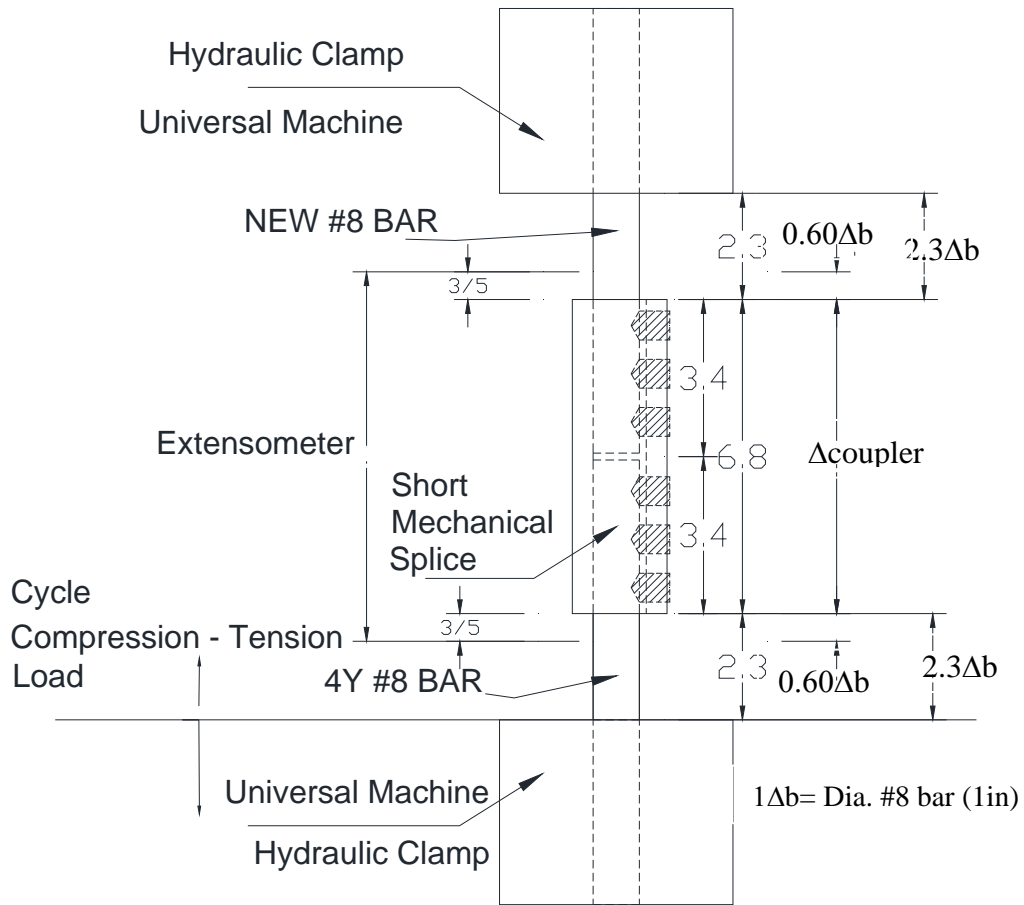


*Figure 3.30  Dimensions for MS-S3 specimen*

### 3.7.2.1.2 Instrumentation for the test

Measurement of deformation and strain located at the same locations as the previous specimen:

a) General behavior of the specimen MS-S3 in terms of axial load vs. deformation of the splice assembles. The stroke of the compression-tension machine measures the movement of the top platform of the universal test machine. The stroke is inside the bottom pump cylinder as Figure 3.27 shows.

b) Deformation pattern under cycle axial loads of the specimen considering the mechanical splice and a short length of the bars. One extensometer has been used having 8"lenght with 2" gage. The length of the stroke extended to measure the mechanical splice and bar deformation is 8in as Figure 3.30 shows. The extensometer has been keep while the entire test.

c) Strain in the mechanical splice. Strain gages were applied on the mechanical splices as Figure 3.31 also shows the location of them. One strain gage is located on the middle of this splice, 2 others at level of the gap between the first and second bolt from top and bottom part of the splice respectively. The second one between the first and second bolt from the top part of the short mechanical splice where is applied the new bar; and the third strain gage is placed between the first and second bolt of the bottom part of the short mechanical splice where is applied the previously yielded bar.
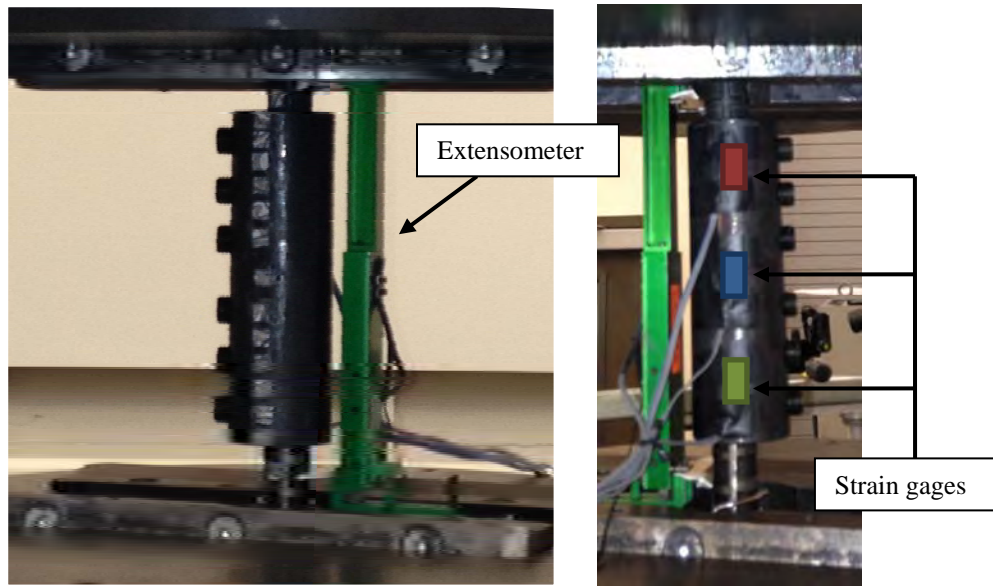
*Figure 3.31  Instrumentation for test of specimen MS-S3*


### 3.7.2.1.3 Protocol of the test to MS-S3

The objective was to measure the pattern of deformation for the linear behavior before the yielding, behavior after the yielding and hardening, as they were obtained for previous test. The tests for the second set of specimens were performed by displacement control. The graph of the protocol of deformation for this test MS-S3 is showed in Figure 3.32.


The test was controlled indirectly by the measurement of the extensometer. The universal machine operation is controlled by the increment of tension or compression loads. However the monitored displacement measured by the extensometer was used to indicate the peak of each cycle.
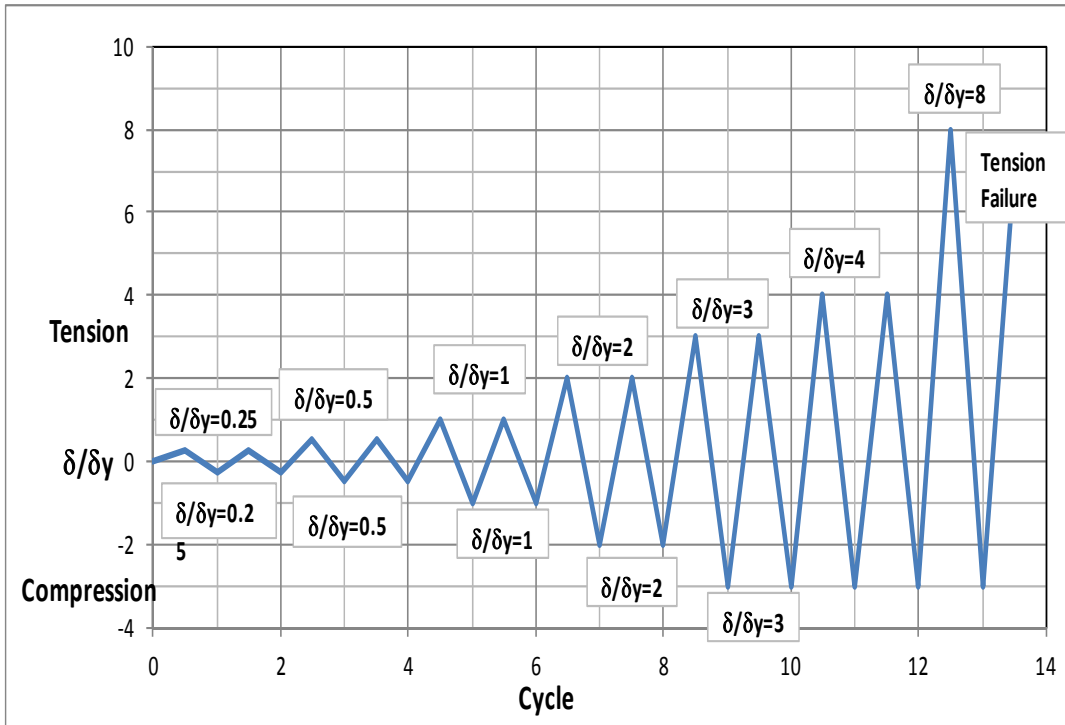
*Figure 3.32  Protocol of load for test of specimen MS-S3*

### 3.7.2.1.4 Results of the Cyclic Compression-Tension Axial Load Test

There was not disruption while the application of the load. The speed load average of the application of the load on the test was 27 kips/min, and measured by displacement 0.046in/min. During the test, there was no fracture of any part of the long mechanical splice. The bolts behaved as one piece together with the mechanical splice. However buckling of the bars appeared at the 9<sup>th</sup> cycle when the deformation reached -3δy at compression loads, Figure 3.33 shows the specimen MS-S3 after buckling of the bar that had been previously yielded. The mechanical properties of this bar were changed under the previous compression-tension axial load test explained in Appendix I, as it was expected also.

The system reached yielding under a tension load of 51 kips. Under compression load, the yielding occurred at a load of 50 kips. The maximum load measured in tension was 81.75 kips (+8δy) and under compression 73.17 kips (-3δy).

The specimen failed by the fracture of the previously yielded bar in the contact zone with the last bolt of the mechanical splice as Figure 3.34 shows. The failure occurred after the second tension loads to +8δy (cycle #13) as Figure 3.32 shows. The tension load value at fracture was 76kips.

Bar previously yielded buckled at -3δy
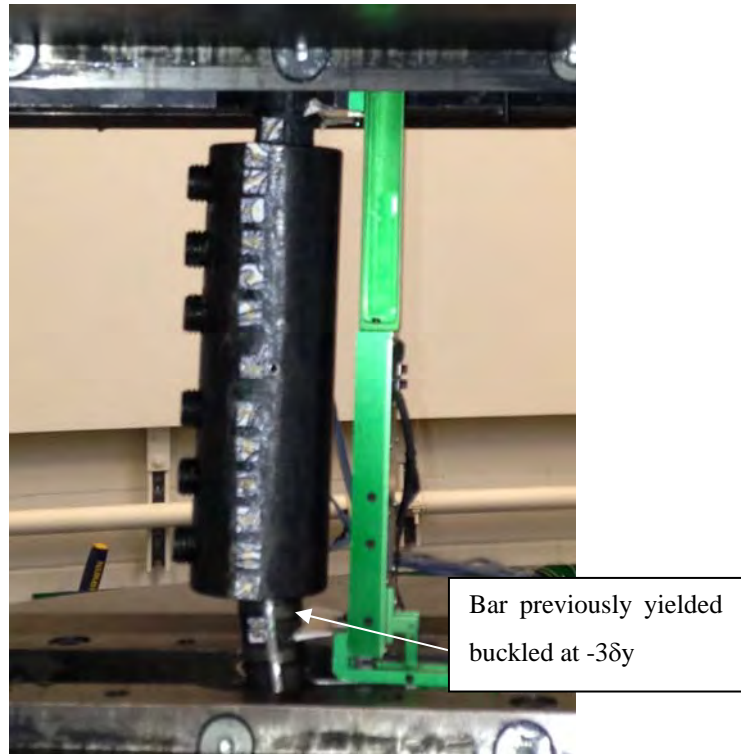
*Figure 3.33 Buckling failure under compression load*



*Figure 3.34 Failure under tension load: previously bar yielded was fractured*
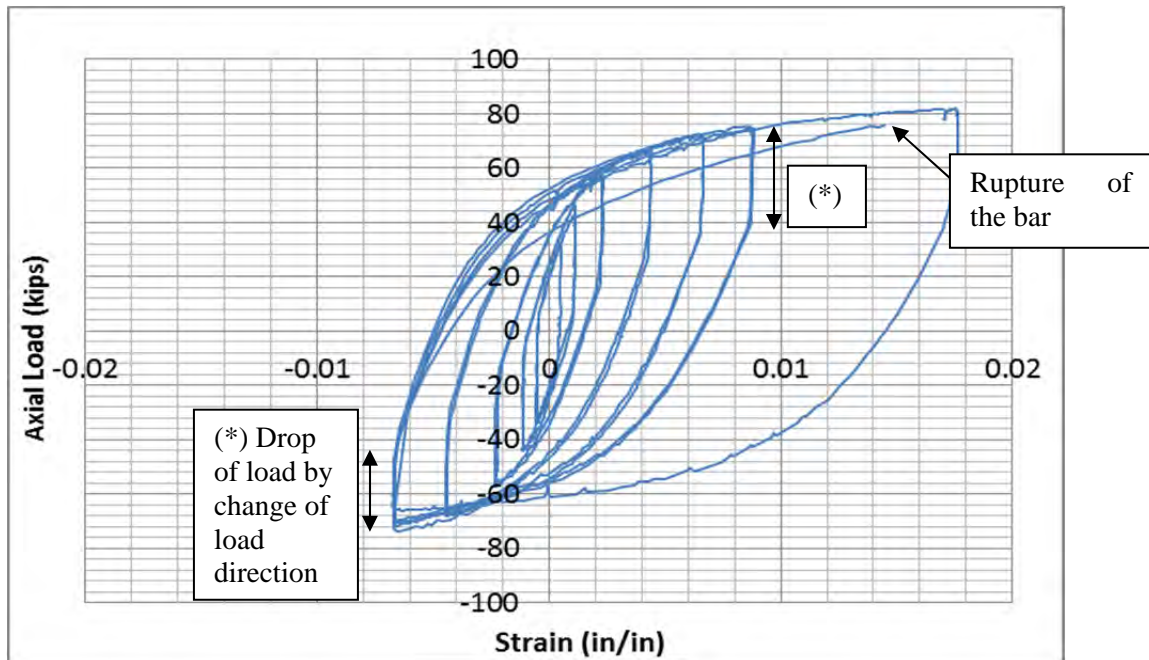
*Figure 3.35  Strain Deformation of the system measured by the Extensometer*

The strain at top and bottom of the coupler exhibited different pattern than at the middle one. The strain above and below the middle exhibited some no-linearity probably due to some slip inside the coupler. The strain measured at the middle of the splice is linear; throughout the test.
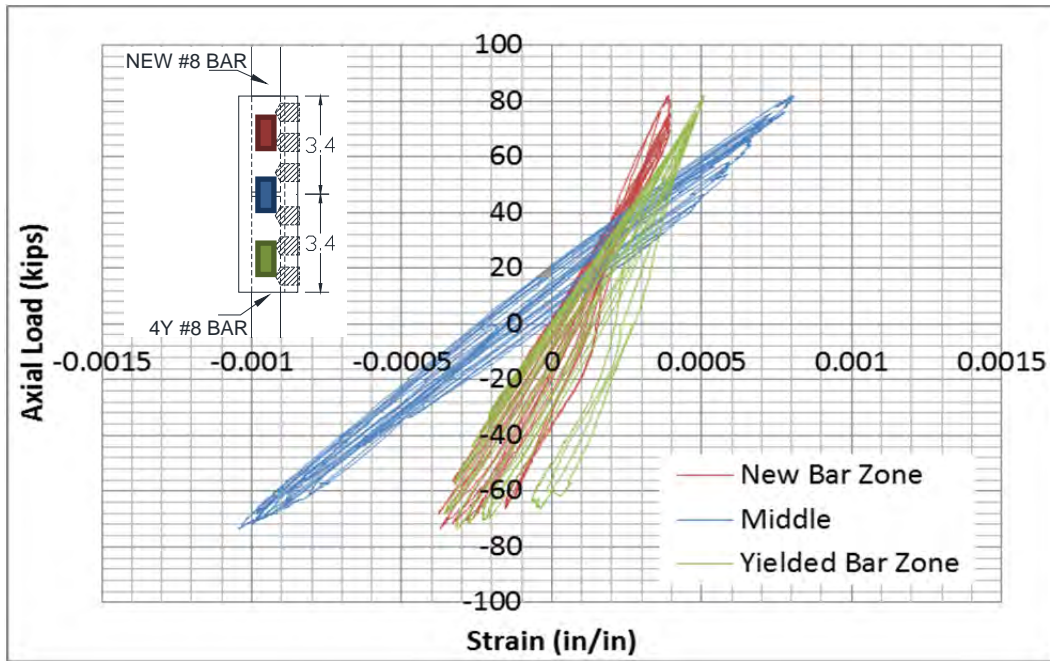
*Figure 3.36  Strain at the three different locations on the mechanical splice of MS-S3.*

73

### 3.7.2.2 Summary of results for the Compression Tension Cycle Axial Load Test

Under cyclic tests, the compression behavior was similar to that in tension. Good performance of the couplers would be expected in concrete members.

Figure 3.37 shows the measurements of the top platform of the universal machine, considering the deformation of the total length of each mechanical splice up to the failure. It can be seen that the elongation of the long mechanical splices is greater than the short mechanical splices.
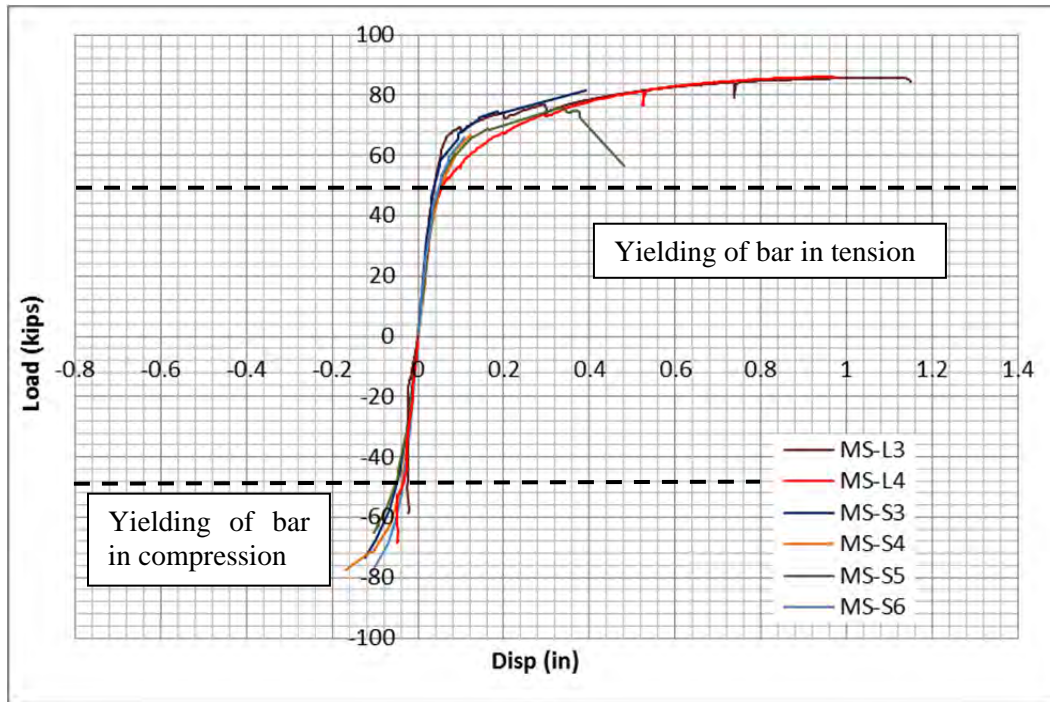


**Figure 3.37  Peak cycles displacement of the universal machine**

Figure 3.38, Figure 3.39 and Figure 3.40 show the different responses in strain deformation from each test. Strain in the middle of the splices presented linear response primarily. However for the zone of contact with the new bar, the responses for the strain

74

at level of the gap between the last two bolts of the splice presented linear response at the first loads and afterwards they presented nonlinear responses under higher tension loads applied. For the strain measured in the contact zone with the previous yielded bar is not clear the tendency of the stiffness in compression; however in tension the responses in stiffness are comparable among each other.
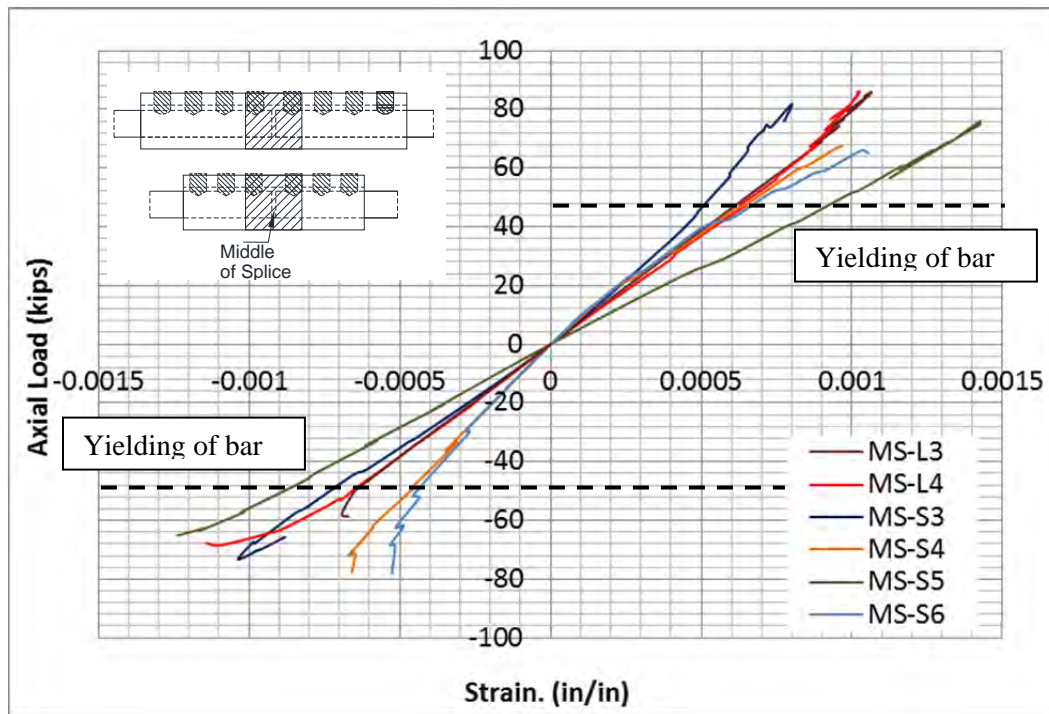


*Figure 3.38  Peak cycle strain deformation at the middle of the mechanical splices*
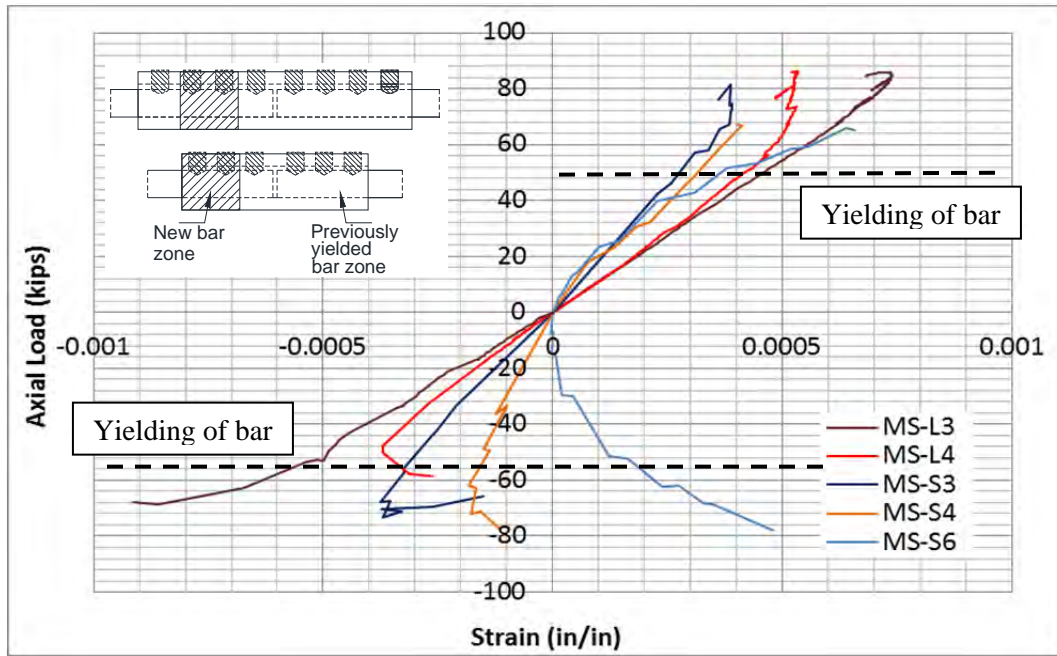
*Figure 3.39  Peak cycle strain deformation measured between bolts of the mechanical splices at new bar zone contact*
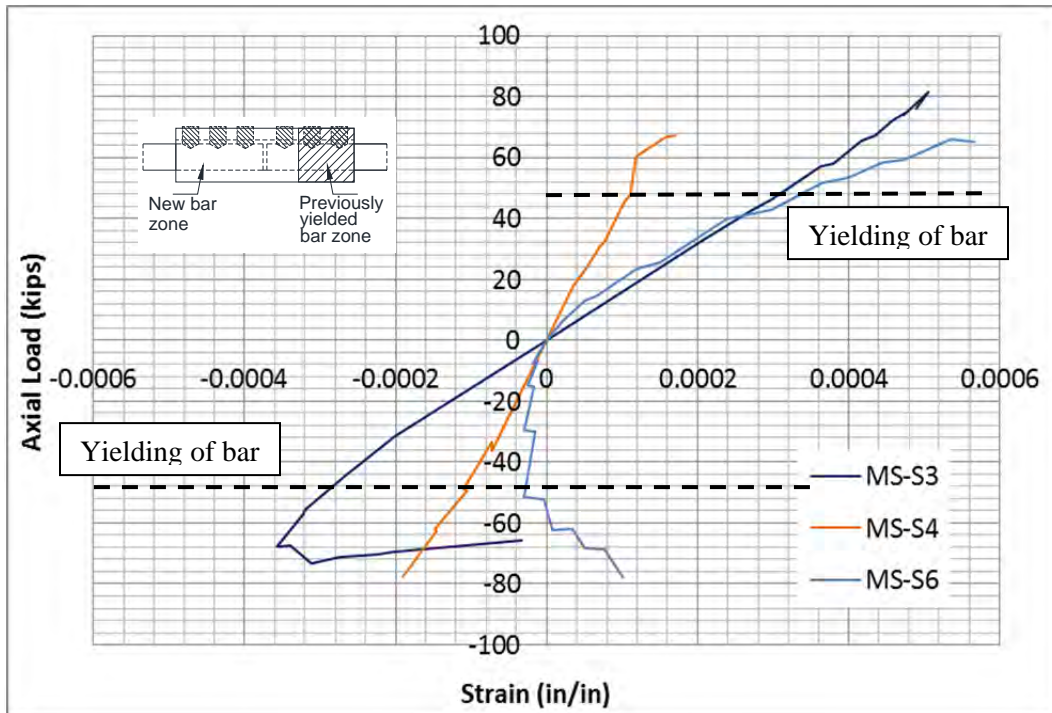
***Figure 3.40  Peak cycle strain deformation measured between bolts of the mechanical splices at previously yielded zone contact***

Table 3-12 summarize the values of axial load and strain for tension and compression yielding loads and strain values

***Table 3-12 Loads measured from the cycle compression-tension cycle test***

| Specimen | Max. Load Measured (kips) | Type of Failure |
|---|---|---|
| MS-L3 | 85.80 | Rupture of bar above the splice |
| MS-L4 | 86.03 | Rupture of bar above the splice |
| MS-S3 | 76.00 | Rupture of 4Yield bar on the edge of splice |
| MS-S4 | 67.35 | Rupture of 1.5Yield bar on the edge of splice |
| MS-S5 | 56.62 | Shear failure of the bolts on the new bar zone |
| MS-S6 | 65.00 | Rupture of 1.5Yield bar on the edge of splice |

| Specimen | ASTM bar | Fracture Stress of bar (fu) (ksi) | ACI 318 - 11 fu meets Condition A? | ACI 318 - 11 fu meets Condition B? | AASTHO fu meets Condition C? |
|---|---|---|---|---|---|
| MS-L3 | A-615 | 109.24 | Yes | Yes | Yes |
| MS-L4 | A-615 | 109.54 | Yes | Yes | Yes |
| MS-S3 | A-615 | 96.77 | Yes | Yes | Yes |
| MS-S4 | A-615 | 85.75 | Yes | No | Yes |
| MS-S5 | A-615 | 72.09 | No | No | No |
| MS-S6 | A-615 | 82.76 | Yes | No | Yes |

**Condition A: measured fu > 75ksi (1.25 x fy of ASTM bar) ?**
**Condition B: measured fu > 90ksi (fu of ASTM bar) ?**
**Condition C: measured fu > 81ksi (1.35 x fy of ASTM bar) ?**

### 3.7.3   Test Program - In Situ Tests

The results of the coupled bar tests will be compared with the test results of the same type of mechanical splices used in retrofitted concrete columns in Chapter 4.

### 3.8   SELECTION OF MECHANICAL SPLICE FOR THE REHABILITATION OF COLUMNS

The short mechanical splice behavior proved to be suitable for hinge areas with large deformations and high forces especially where there may be difficulty installing the long couplers. These splices can satisfy Type 2 and Type 1 splice requirements if A-706 is used.

However, the long coupler should be used wherever there is sufficient room for installation and are suitable for both A-615 and A-706 bars.

<div align="center">

CHAPTER 4

# Rehabilitation with Carbon Fiber Reinforced Polymer CFRP

</div>

## 4.1 CFRP AS MATERIAL FOR REHABILITATION

Rehabilitation techniques based on Fiber Reinforced Polymer (FRP) materials appear to be innovative alternatives to traditional solutions because of their high tensile strength, lightweight, and ease of installation. Application of composite materials does not change the geometry of the structure. In some cases, it can be installed without interrupting the use of the structure. Carbon Fiber Reinforced Polymer (CFRP) sheets and anchors attached to a member can add tensile strength at critical locations. Carbon fibers are not affected by harsh conditions such as exposure to high humidity, acids, bases or other solvents and they can withstand direct contact with concrete. The use of CFRP sheets in the construction industry has increased in recent years, especially for seismic retrofit applications.

Despite the good tensile performance of Carbon Fiber Reinforced Polymers (CFRP) and the potential for improvement of the capacity of retrofitted RC members, anchorage between CFRP and reinforced concrete (RC) members is a weak link that limits the performance of retrofitted RC members. CFRP sheets debond from the surface of reinforced concrete members (Figure 4.1). To avoid this failure, CFRP anchors can be applied to provide a "mechanical" anchor. The CFRP anchors allow the CFRP sheets to reach tensile capacity (Figure 4.2) and to maximize the efficiency of the CFRP retrofit. The number and size of anchors are critical parameters.

<div align="center">

80

</div>

*Figure 4.1  Debonding of CFRP sheet before strength of sheet is reached (Kim 2006)*



*Figure 4.2  CFRP sheet rupture when anchor used. (Kim 2006).)*

## 4.2    CFRP Sheets

### 4.2.1    Definition and importance

The carbon fiber reinforced polymer is formed by combining the carbon fiber and resin. The fiber is a textile made with carbon and the resin is a high strength epoxy. Figure 4.3 shows a microscope image of a CFRP strand, where the filaments that form a single carbon fiber strand can be seen. The CFRP sheet is made by placing carbon fibers in one direction and threads of nylon or glass woven in the other direction. (Kobayashi, et.al). The CFRP sheet is saturated with epoxy so that the composite behaves as a unit with high tensile capacity in the direction of the carbon fibers (Figure 4.4).
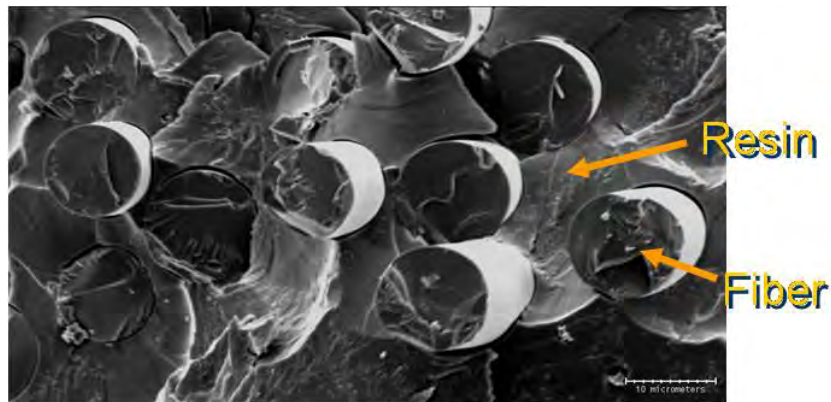


*Figure 4.3  Scanning electron microscope image of CFRP (Yang, 2007)*
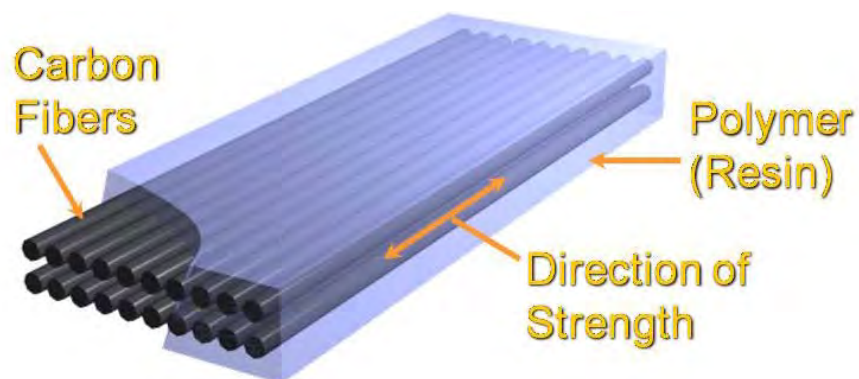


*Figure 4.4  Schematic diagram of a CFRP sheet (Yang, 2007)*

82

The resulting installation is anisotropic. CFRP is an elastic material up to failure having an ultimate tensile strain of 0.01 or higher. Figure 4.5 shows the stress-strain curves for CFRP and Grade A60 reinforcement. Details of the tests of coupons are shown in Appendix E. It can be seen that the tensile capacity of the CFRP is 50% greater than the steel bar; however the CFRP sheet is a brittle material having no ductility and a brittle failure. Those curves were obtained by axial monotonic test of CFRP sheet coupons and a Grade 60 reinforcing bar (Appendix D) that were conducted in the current research.
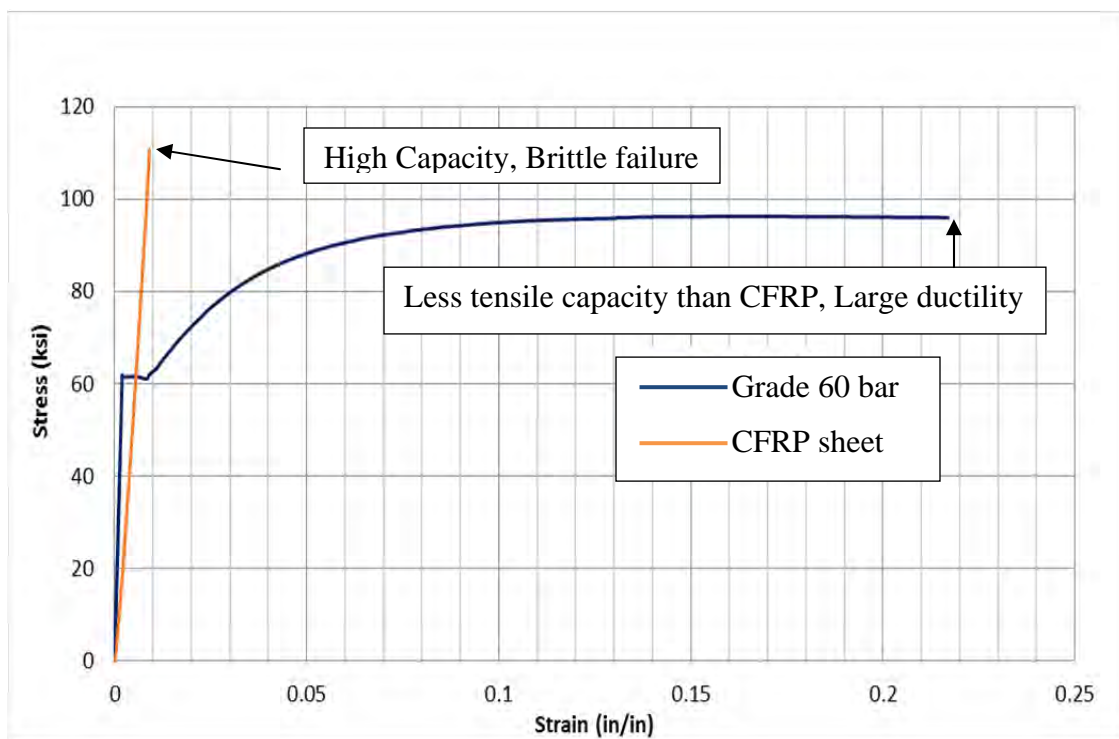


*Figure 4.5  Differences in material tensile properties of Grade 60 reinforcing bar and CFRP sheet coupons*

### 4.2.2 Capacity of the CFRP sheet under tension loads

As discussed in 4.2.1, a CFRP sheet has a high tensile strength in one direction and little strength in the transverse direction. Several coupons made with the CFRP sheet and epoxy were tested under axial tension loads (Appendix D). The number of test did not meet the ACI 440.2R recommendation to test at least 20 coupons to define the elastic modulus and ultimate strength. The mechanical properties of the CFRP materials depended on the volume fraction of fiber and the amount of resin although the dry fiber properties of materials were identical. (Kim, 2011)

Since designers are likely to use CFRP properties as provided in manufacturer's specifications, such data was used in this research. A typical manufacturer reported mechanical properties of CFRP laminates are presented in Table 4-1.

*Table 4-1 CFRP sheets properties provided by the manufacturer*

| Property | ASTM Method | Typical Test Value | Design Value |
|---|---|---|---|
| Ultimate tensile strength (ksi) | D-3039 | 143 | 121 |
| Elongation at crack failure | D-3039 | 1.00% | 0.85% |
| Tensile modulus (ksi) | D-3039 | 13900 | 11900 |
| Laminate thickness (in) | D-3039 | 0.04 | 0.04 |

The results of coupons tests were close to the ultimate strength determined using the manufacturer's values for elastic modulus and rupture strain. The properties shown in the Table 4-1 were used to evaluate the contribution of the CFRP sheet under tension loads in the test program. A procedure to calculate the thickness or width needed is explained below and includes safety factors as recommended by ACI 440.

$$T_b = 1.25 f_y A_s \qquad\qquad \textbf{\textit{Equation 4-1}}$$

$$T_f = f_{fu} w_f t_f \qquad\qquad \textbf{\textit{Equation 4-2}}$$

$$T_f / T_b \geq 1.5 \qquad\qquad \textbf{\textit{Equation 4-3}}$$

$$w_f = \frac{1.5 \times (1.25 f_y A_s)}{f_{fu} t_f} \qquad\qquad \textbf{\textit{Equation 4-4}}$$

$T_b$: expected tensile strength of the reinforcement, lb

$T_f$: tensile strength of CFRP sheet, lb

$f_y$ : yield strength of reinforcement bars, psi

$A_s$: area of the reinforcement, in$^2$

$f_{fu}$: tensile strength of CFRP, psi

$t_f$: Effective thickness of CFRP sheet, in.

$w_f$ : width of CFRP beam sheet, in.

### 4.2.3   Capacity of the CFRP sheet for confinement of reinforced concrete columns

For strengthening purposes, the use of the CFRP for confining concrete elements is very effective, providing larger ductility and improving shear capacity. The application of the CFRP jacket is an easy and clean process.
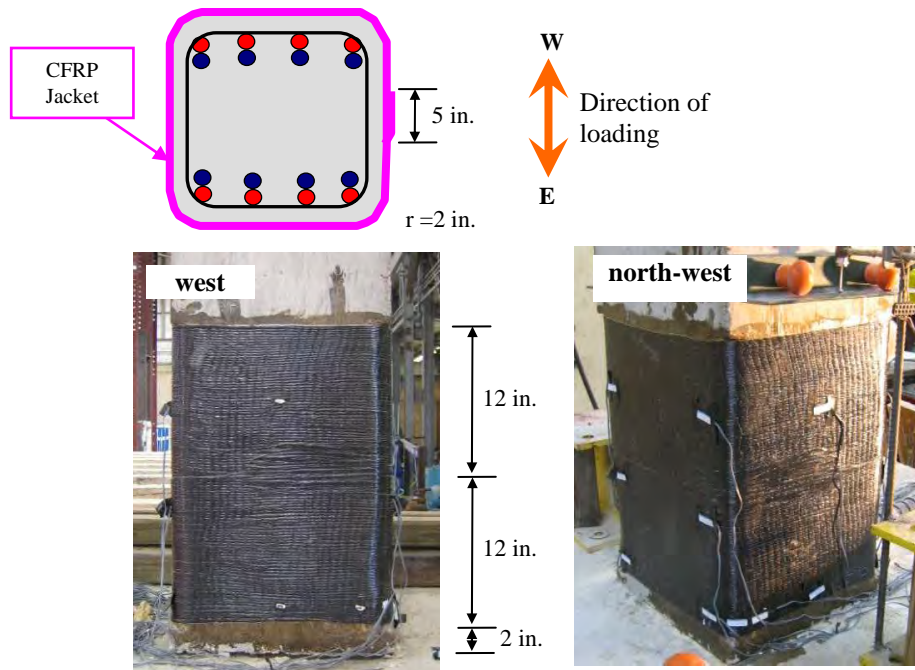
*Figure 4.6  CFRP jacket for column with poor lap splices (Kim, 2008)*

As discussed in Chapter 2, Kim (2008) studied the effect of CFRP jacketing of a column with inadequate lap splicing. Some columns were partially damaged before strengthening with CFRP sheets as confinement (Figure 4.6).
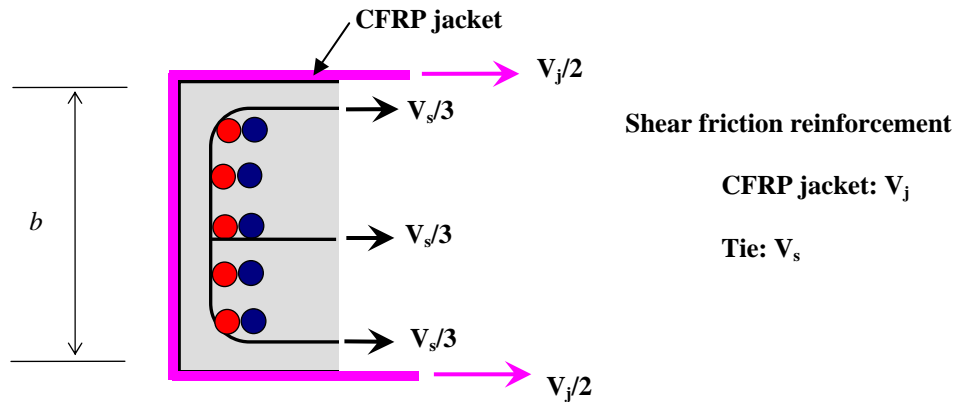
*Figure 4.7  Shear load pattern for column confined with steel ties and CFRP jacketing*
*(Kim, 2008)*

In Figure 4.7, the shear contribution of the CFRP jacket is similar to that the steel stirrups, and acts as an additional reinforcement. The total shear force of the cross section is proposed as:

Vc + Vs + Vj = Total Shear Capacity               *Equation 4-5*

> *Vc:* Shear capacity of the concrete.
> *Vs:* Shear contribution of the stirrups
> *Vj:* Shear contribution of the CFRP jacket.

After determining the needed value of Vj, the area of the CFRP sheet needed to jacket the concrete member can be determinated. For retrofitting purposes is difficult to define the value of Vc because internal cracks, may cross the core of the transversal section. The CFRP jacket provides extra shear capacity making the column stronger in shear than the original column. Figure 4.8 shows the shear force vs. lateral displacement (normalized by nominal shear force and height respectively) behavior. It can be seen that the retrofitted column had higher shear capacity than the column without the jacketing.
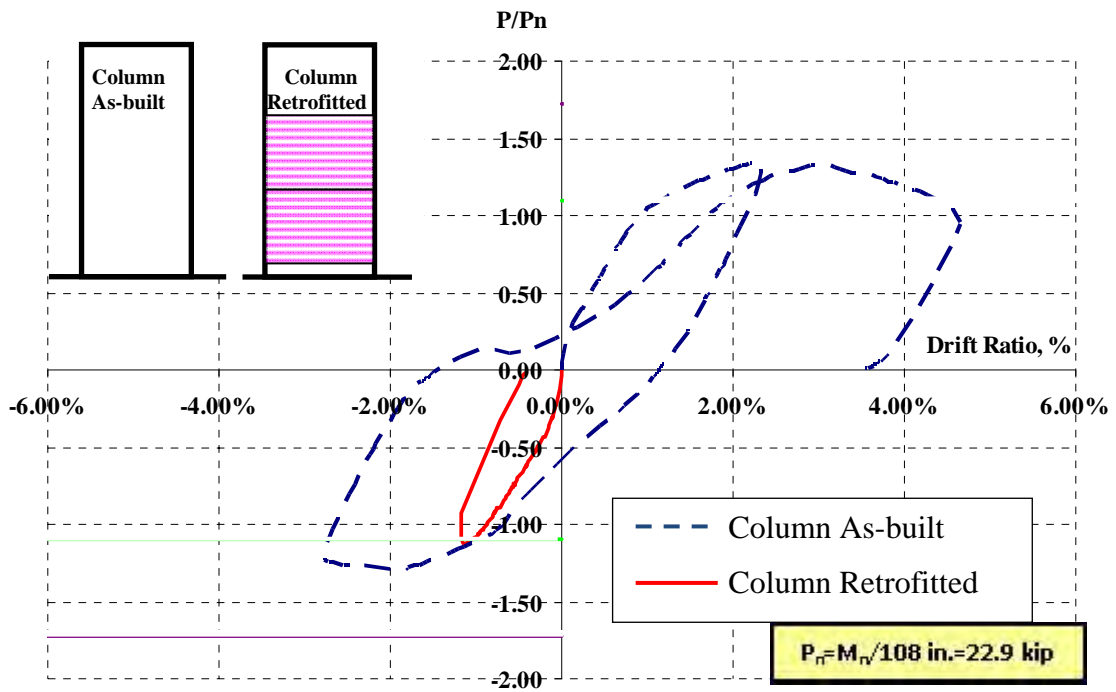
*Figure 4.8  Comparison between one column with and without CFRP jacketing (Kim, 2008)*

## 4.3    CFRP ANCHORS

### 4.3.1    Definition and importance

The CFRP anchor consists of a CFRP sheet folded as shown in Figure 4.9. The anchor is saturated with epoxy and inserted into the concrete. The remaining material is splayed out over the CFRP sheet. The performance of CFRP sheets used to strengthen concrete in tension depends on the attachment with the concrete member surface. Under high force and deformations of the concrete member, the adhesion between the sheet and the concrete surface will not be sufficient to prevent debonding of the CFRP sheet. CFRP anchors provide an alternate means of transferring tension from the sheet to the concrete so that debonding does not control the mode of failure.
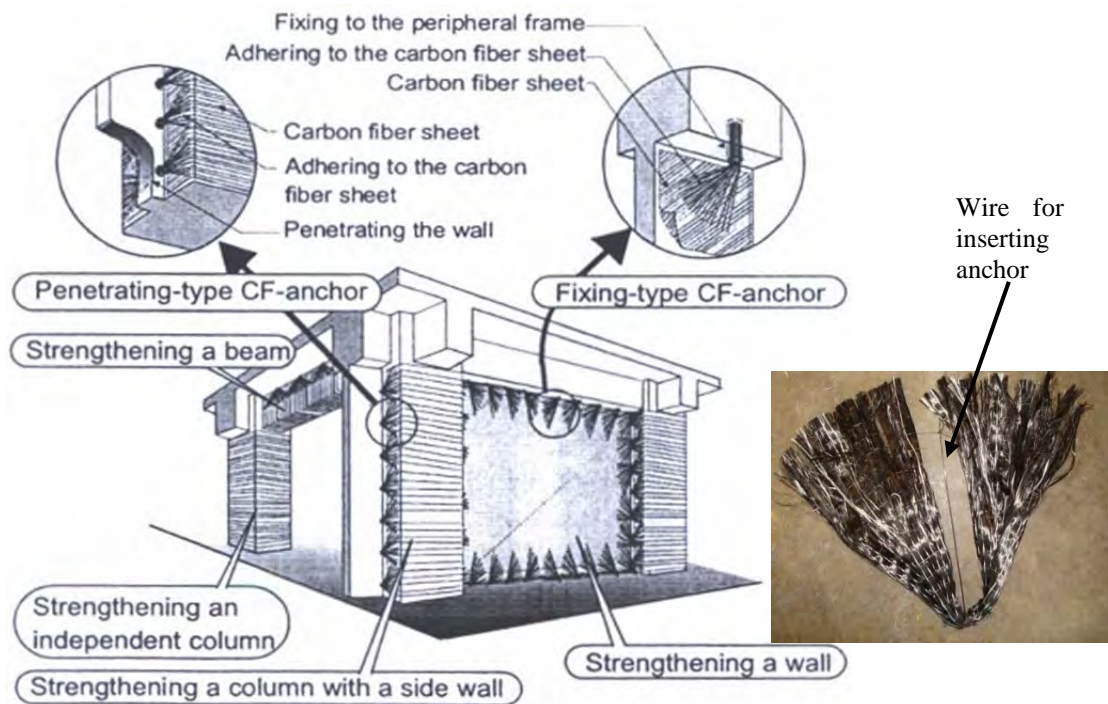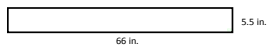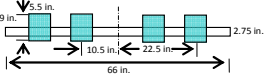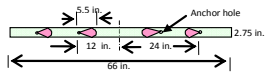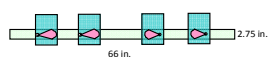


Figure 4.9    CFRP anchors applied to columns and wall for better attachment of the CFRP sheets (Kobayashi, 2001) and CFRP strip for installation

Kim (2008) demonstrated that the strength and deformation capacity of a concrete member is increased as the type of anchor improved. The CFRP sheet developed its full tensile capacity with a combination of CFRP anchors and wraps (CFRP sheet over the CFRP materials used for retrofit). The force and displacement increased more than 100% over the beam without anchors. Table 4.2 shows a matrix of different combinations of a reinforced concrete beam strengthened using CFRP sheets with and without anchors or wraps. The simply-supported beams were tested under a concentrated load at the center span. The maximum load applied increased as the amount of CFRP material in the anchor increased.

*Table 4.2 Characteristics of type of anchorage on Beams (Kim 2008)*

| No. | Configuration of CFRP Materials | Number of Layers of CFRP sheet | Type of Anchorage | Failure Mode | Maximum Applied Load |
|-----|---------------------------------|-------------------------------|-------------------|--------------|----------------------|
| 1 |  | 1 layer | None | Delamination of CFRP sheet | 14.57 kip |
| 2 |  | 2 layers | CFRP U-wrap | Delamination of CFRP U-wrap | 15.38 kip |
| 3 |  | 2 layers | CFRP Anchor | Concrete Failure around Anchor Holes | 25.78 kip |
| 4 |  * Location of the anchors and U-wraps are the same as specimen No. 2 and No. 3 | 2 layers | CFRP Anchor & CFRP U-wrap | Fracture of CFRP Sheet | 31.94 kip |

Anchor geometry is shown in Figure 4.10 and Figure 4.11. The force transferred from the CFRP sheet to the fan of the anchor is transmitted as a shear force applied to the root of the anchor as Figure 4.11 shows. The capacity of the anchor will be defined by the

shear capacity of the root of this anchor as Equation 4-6 shows. The anchor is usually installed at perpendicular to the CFRP sheet but slight inclinations to avoid reinforcement in the concrete will not impair the performance of the anchor.
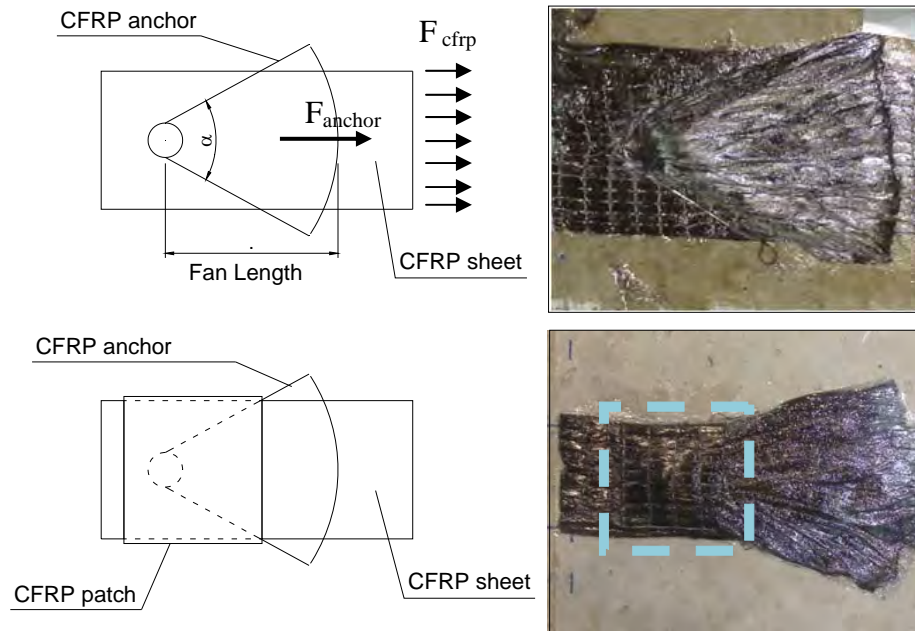


***Figure 4.10  Details of CFRP anchor installation***
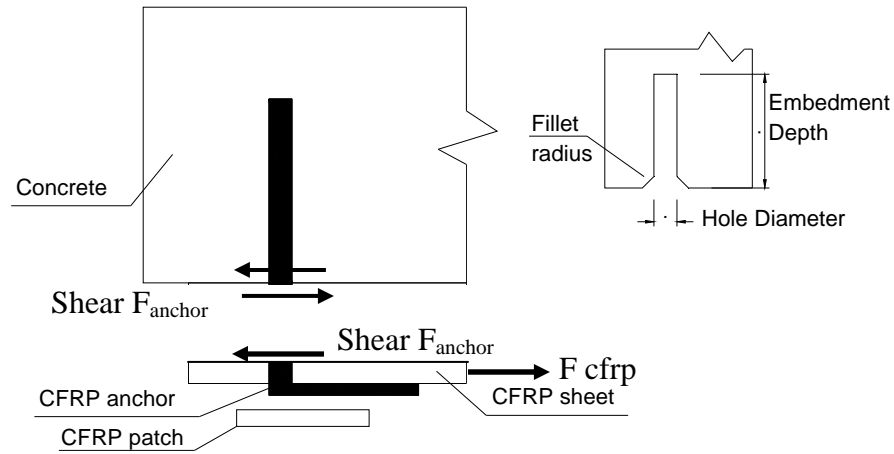
*Figure 4.11  Plan View details of CFRP anchor and CFRP patch*

$$F\,cfrp = F\,anchor = Shear\,F\,anchor \qquad\qquad \textit{Equation 4-6}$$

For CFRP in direct tension, the anchors are generally installed parallel to the plane of the CFRP sheets. However, it can be lightly deviated (<10deg) as Figure 4.12 shows. It is impossible to drill at the right angle to keep the anchor in the plane of the sheet. The force transferred from the CFRP sheet ($F_{cfrp}$) to the fan of the anchor ($F_{anchor}$) is transmitted to the root, which must resist pull out ($F_{pull\ out}$). Considering the equilibrium of this system, there is a lateral force at the corner between the concrete member retrofitted with the CFRP sheet and inclined anchor. The capacity of the anchor will be defined by the tension strength of the root of the anchor and the adherence between the interior surface of the hole and the root of the anchor. As Equation 4-7 shows, the strength of the anchor should be greater than the tensile force in the CFRP (Fcfrp).

92
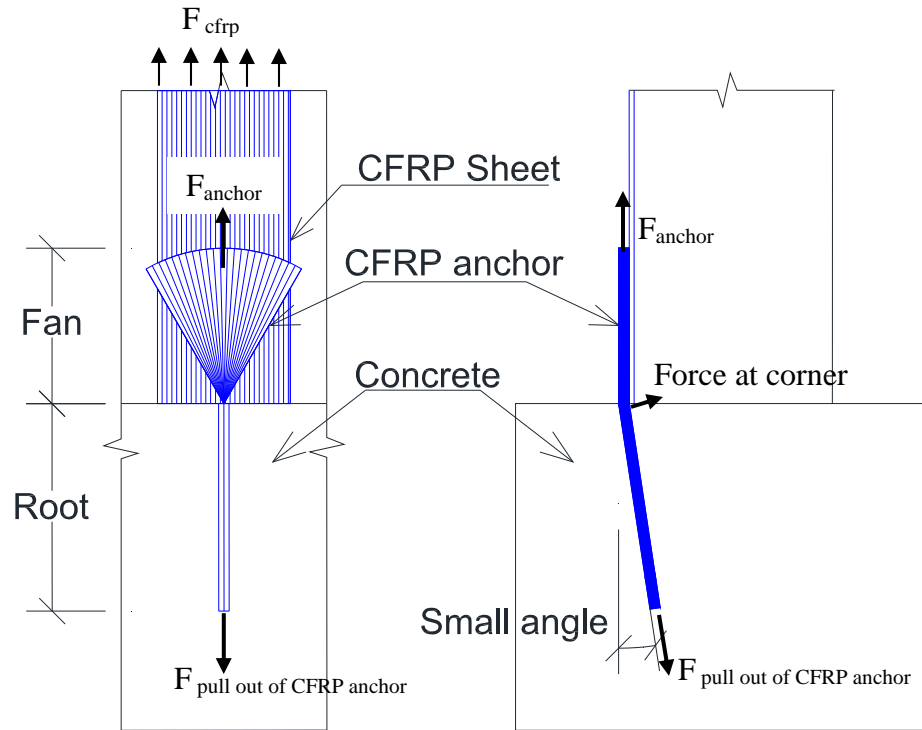
*Figure 4.12 CFRP anchors applied to columns and wall for better attachment of the CFRP sheets*

$$F\,cfrp = F\,anchor \leq F\,pull\,out \qquad\qquad \textbf{\textit{Equation 4-7}}$$

### 4.3.2    Capacity of the CFRP anchor

#### *4.3.2.1    Method developed to measure the capacity of CFRP anchor under shear force*

A method for assessing the strength of anchors was developed by Huaco (2009) using plain concrete beams reinforced externally with CFRP sheets attached with epoxy and CFRP anchors. Under loading on the beam, a tensile force was developed in the CFRP sheets and a shear force on the CFRP anchors. The forces in the CFRP anchors were defined by the load applied to the beam and compared with forces based on measured stress in CFRP sheets. The strength of the concrete was very high (11.4 ksi) in order to avoid shear failure of the concrete. It was used plastic wrap to apply the CFRP sheet unbonded to the concrete surface; this way, the CFRP anchors received the total tensile force from the CFRP sheet.
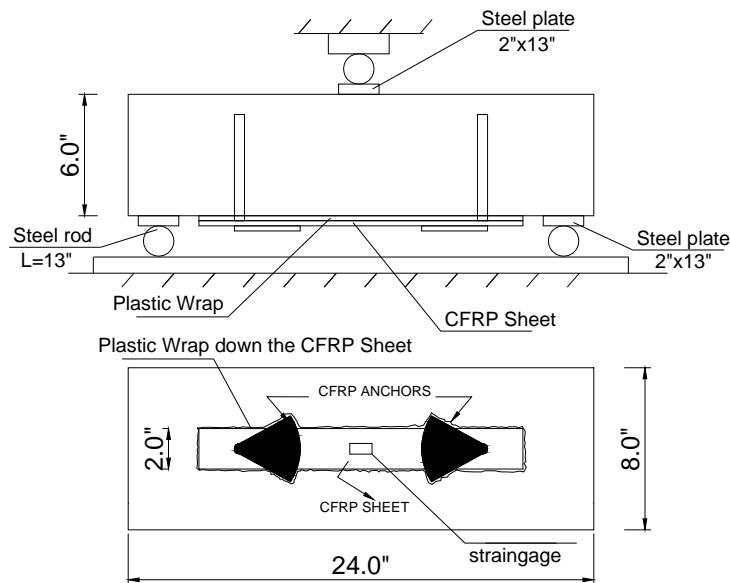


***Figure 4.13   Sketch of specimens for cases using plastic wrap (Huaco, 2009)***

All the tests were performed in a universal test machine. The beam was supported by a roller and pin as shown in Figure 4.14. In most tests, the load and reactions were applied through bearing plates attached to the surface of the concrete. Deflection at the beam midspan was measured. Strain gages were attached to the CFRP sheet.



*Figure 4.14  Specimen in test machine (test setup)*

Huaco (2009) tested more than 30 beams having different amounts of CFRP materials, changing the values of width for the CFRP strips for sheet and anchor; and different diameters for the holes into the concrete. The specimens described below belong to the last set of tests (4 beams). For those specimens the width of CFRP sheets was 2 in and the width of CFRP anchors was less than 1in so that anchor failure would occur before the concrete failed in shear or the CFRP sheet ruptured. Additionally half of specimens had a sheet of plastic placed between concrete surface and CFRP sheet to create a debonded interface so that. The tensile force in the CFRP sheets was carried only by the CFRP anchors.

### 4.3.2.1.1 Observations from tests

Debonding did not have a significant influence on the capacity of the anchors. In two cases anchor failure was observed at nearly the same beam load. The strains in the CFRP sheet at anchor failure were quite different even though the ultimate loads were about the same. The maximum strain values measured were less than 1%. Anchor failures are shown in Figure 4.15.
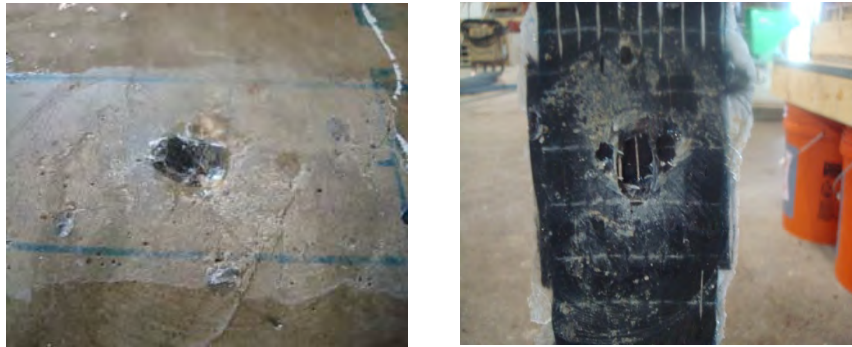


***Figure 4.15  CFRP anchor fracture with bonded sheets (Huaco, 2009)***

Anchor failures were also observed in specimens with plastic wrap (unbonded). In these tests, there is little difference in loads at failure, once again indicating that adhesion was not important for achieving anchor failure of the 2 x 0.8 in wide CFRP anchors. The maximum measured strain was close to 0.6%. The appearance of the specimen after fracture is shown in Figure 4.16. There was a shear block failure when the CFRP sheet fractured similar to bolted connections in steel joints. All four tests with anchor failures are shown in Figure 4.17, and key values for those tests are summarized in the Table 4-3.

*Figure 4.16  CFRP anchor fracture with unbonded sheets (Huaco, 2009)*

*Table 4-3 Specimen Notation (Huaco, 2011)*

|  | SPECIMEN | Max. strain in CFRP (in/in) | Beam load (kips) Initial craking of concrete | Failure |
|---|---|---|---|---|
| **Bonded** | S6A-2-2 x 0.8-0.375-4-0.375 | 0.0084 | 7.61 | 9.83 |
| **Debonded** | S6B-2-2 x 0.8-0.375-4-0.375 | 0.0053 | 7.18 | 8.25 |
| **Bonded** | S6A-2-2 x 0.6-0.375-4-0.375 | 0.0056 | 7.32 | 9.06 |
| **Debonded** | S6B-2-2 x 0.6-0.375-4-0.375 | 0.0058 | 8.34 | 7.17 |



*Figure 4.17  Fracture of CFRP anchors in all 4 tests*

### 4.3.2.1.2 Calculation of Shear Force on the CFRP anchor

The tension in the CFRP sheet is produced by flexure on the beam and is transferred to the CFRP anchor thereby producing a shear force on the anchor (Figure 4.18). The forces transferred to the anchor can be determined from the measured CFRP strain and compared with the force computed using measured beam loads.
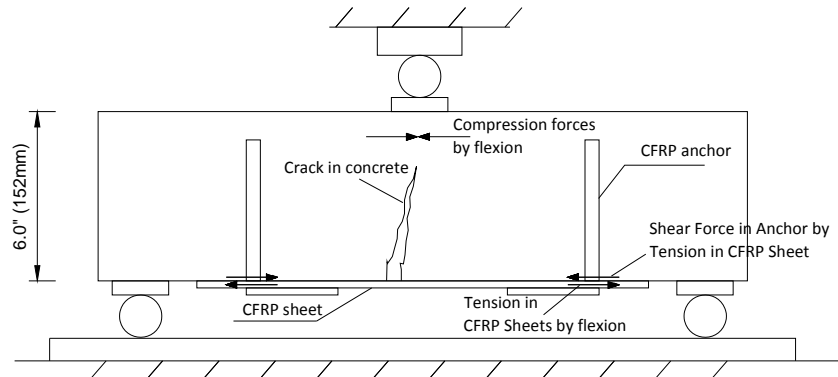


*Figure 4.18  Beam used in calculations*

For the first method (force from strain measured on CFRP sheet), the shear force on the anchors is calculated using the value of the ultimate strain measured in the CFRP sheet ($\varepsilon$) and the elastic modulus provided from the manufacture of the CFRP which is E manufacturer = 13900ksi, as Equation 4-8 shows.

ε x E x (Transversal Area CFRP sheet) =

Tension CFRP sheet = Shear Force CFRP anchor   *Equation 4-8*

For the second method (using values of measured beam load P), the force transferred to the anchor can be determined from the load considering that the most reliable data are the measured loads. The moment in the beam is:

$$M = \frac{PL}{4} = T \; x \; Z \qquad\qquad \textit{Equation 4-9}$$

98

$$Z = h + t/2 - \frac{a}{2} \qquad\qquad \textit{Equation 4-10}$$

$$\frac{PL}{4} = T\,x\,(h + t/2 - \frac{a}{2}) \qquad\qquad \textit{Equation 4-11}$$

Because the strength of concrete is high, it was observed that the value of "a" is small (about 0.1 in). in comparison with the moment arm "Z". The formulation of arm Z can be simplified as follows:

$$Z = h + \frac{t}{2} - \frac{a}{2} \cong h \qquad\qquad \textit{Equation 4-12}$$

The terms used in, are defined in Figure 4.19,
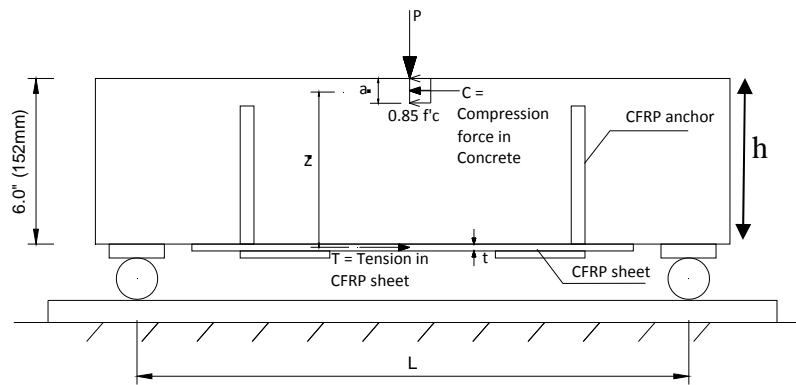


*Figure 4.19 Shear beam due P load*

Differences between the shear force computed from measured stresses in the CFRP sheet and the calculated value using beam load are indicated in Table 4-4. Since strains may vary considerably across a CFRP sheet, the values shown are deemed acceptable.

*Table 4-4 -- Comparison among shear force on anchor*

| SPECIMEN | Calculated by measured beam load - kips (kN) | Computed by strain measured - kips (kN) |
|---|---|---|
| S6A-2-2 x 0.6-0.375-4-0.375 | 7.97 (35.87) | 6.23 (28.04) |
| S6A-2-2 x 0.8-0.375-4-0.375 | 8.65 (38.93) | 9.34 (42.03) |
| S6B-2-2 x 0.6-0.375-4-0.375 | 6.29 (28.31) | 6.45 (29.03) |
| S6B-2-2 x 0.8-0.375-4-0.375 | 7.25 (32.63) | 5.89 (26.51) |

The size of CFRP sheets and anchors and/or strength of concrete were studied in order to find a reliable procedure for quality control of CFRP anchors. It was possible to develop anchor fracture using less material in the anchor than in the CFRP sheet. Sheet fracture and concrete fracture were thereby eliminated. For a 2-in.-wide CFRP sheet the width of the material in the CFRP anchor had to be less than 1.6 in or 80% of sheet width.

The forces transferred to the anchor were determined from the measured CFRP strain, and were found to compare favorably with the force computed using measured beam loads. The measured load is considered to be more reliable than measured strain in the CFRP sheet since stress can vary considerable across the sheet.

### 4.3.2.2 *Method to measure the capacity of CFRP anchor under pull out force*

The effect of concrete compressive strength, anchorage diameter and depth, and amount of fibers on the tensile strength of CFRP anchors was studied by Ozdemir and Akyuz (2005). Tensile capacity of the CFRP anchor increased linearly until the depth reached an effective bond length of 100mm as embedment depth increased. Beyond this length the tensile capacity did not increase. In Figure 4.20 the test setup used by Ozdemir and Akyuz (2005) is shown. The load is applied to the CFRP anchor using a pipe clip to clamp the anchor to the loading rod.
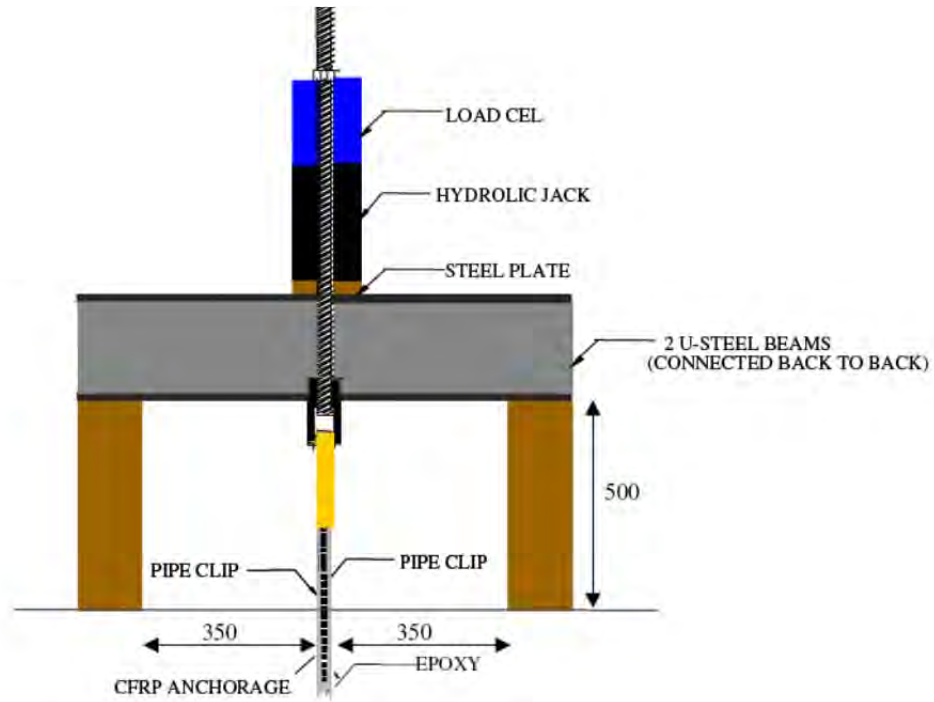
***Figure 4.20 Test setup used by Ozdemir and Akyuz (2005)***

### 4.3.2.2.1 Observations from tests

Three failure modes were observed depending on the depth of the CFRP strip of the anchor into the hole in the concrete. The first type was shallow concrete cone failure at h less than 2 in. Compressive strength of the concrete did not affect the tensile capacity of the CFRP anchor if its embedment depth was less than 2 in. However, as embedment depth increased, the effect of concrete compressive strength became more significant. The second type was cone-bond failure for depths between 2.5 to 4 in. They also observed that as embedment depth increased, tensile capacity of the CFRP anchor also increased linearly until the depth reached 4in. Beyond this length the tensile capacity did

101

not increase. The rupture of the CFRP strip or root was observed for depths higher than 150mm. The tensile capacity of the CFRP anchor increased with an increase in the amount of CFRP materials, but the increase was not proportional to the increase in the material. The diameter of the anchor hole did not have a significant effect on the tensile capacity of the CFRP anchor.

### 4.3.2.2.2 Calculation of Pull –out force on the CFRP anchor

Ozedmir and Akyuz proposed formulas for predicting tensile capacity of CFRP anchors under this pull out effects. These equations were based on their experimental study and a cone-bond failure model proposed by Cook et al. (1998). Ozedmir and Akyuz found that the concrete cone depth, $h_c$, in which shallow cone failure occurs, is 2in for all embedment length of the anchors. Equation 4-13 was proposed for the tensile capacity of an anchor when shallow cone failure occurs ($h \leq 2$in). It can be seen in Equation 4-14 that a equation was proposed for the tensile capacity of an anchor when a shallow cone is followed by a slip along the anchor length below the cone (cone-bond failure, $h > 2$in).
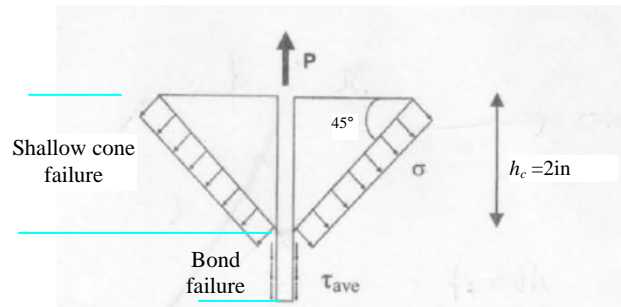


**Figure 4.21**    *Stress distribution along the embedment depth of CFRP anchor (Ozedmir and Akyuz, 2005)*

102

$$P_n = 4\sqrt{f_c} \times h \times (d + h) \times \pi \qquad\qquad h \le 2\,in. \qquad\qquad \textbf{\textit{Equation 4-13}}$$

$$P_n = 4\sqrt{f_c} \times h_c \times (d + h_c) \times \pi + 22\sqrt{f_c} \times h_c \times (h - h_c) \quad h > 2\,in. \qquad \textbf{\textit{Equation 4-14}}$$

$P_n$ : tensile strength of CFRP anchor, lb

$f_c$ : compressive strength of concrete, psi

$d$ : hole diameter, in.

$h$ : embedment depth of CFRP anchor, in.

$h_c$ : concrete cone depth, 2 in.

They concluded that compressive strength of the concrete did not affect the tensile capacity of the CFRP anchor if its embedment depth was less than 50mm. However, the effect of concrete compressive strength became more important as embedment depth increased as indicated by the term that include $f_c$.

## 4.4    QUALITY CONTROL

For optimal use of the CFRP materials, quality control of implementation are important to the performance of the application of the CFRP. Without high quality installation, the capacity of the CFRP is compromised and may not reach the capacity desired.  For example, poor quality of epoxy (older than expiration date on material) is likely to result in poor performance of the retrofitted section (anchor for/ sheet failure interface failure) as shown in Figure 4.22.



*Figure 4.22 Anchor fan debonding due to poor quality epoxy*

### 4.4.1    Quality of implements for installation

Appropriate installation tools are needed to realize the inherent strength of CFRP materials (Figure 4.23)

*Figure 4.23 Installation tools*

Procedures for preparing the materials (epoxy and CFRP elements), tool selection, and time of installation (pot life) should follow manufacturer's recommendations closely.



*Figure 4.24 Preparation of the epoxy: Mixing of the epoxy component (left) and Epoxy ready to use (right)*

## 4.4.2 Installation of the CFRP materials for a good performance

Although the anchor was intended to carry the force developed in the CFRP sheet, the concrete surface in contact with the CFRP sheet was cleaned. And a hole was drilled for the CFRP anchor. A roller was used to apply the epoxy on the surface of the concrete beam. Epoxy was also inserted into the holes drilled for the CFRP anchors. (Figure 4.25)



*Figure 4.25  Application of the epoxy into drilled holes for CFRP anchor.*



*Figure 4.26  Application of epoxy to CFRP materials.*

Next the CFRP materials were saturated with epoxy (Figure 4.26) and applied to the concrete. It was necessary to eliminate excess epoxy on the CFRP materials by squeezing it out. The CFRP sheets were positioned before the installation of the CFRP anchors. The CFRP anchors were inserted using a wire to push the CFRP anchor into the drilled hole as shown in Figure 4.27. The remaning material from the hole was splayed as shown in Figure 4.28. After the installation of the CFRP sheets and CFRP anchors was completed, the wire used to insert the anchor was cut.



*Figure 4.27  -- Installation of CFRP anchor in concrete beam.*



*Figure 4.28  -- Spreading out of the CFRP anchor fan.*

A small square patch of CFRP was placed over the root of the anchor (or fan). The patches which cover the CFRP anchor are shown in Figure 4.29. The direction of the filament of the CFRP was the same as in the CFRP sheet. The dimensions of the patches were based on the width of CFRP sheet being anchored. Finally a roller saturated with the epoxy was passed over the sheet and anchor fan. The length of the patch was the same as the width of CFRP sheet.



*Figure 4.29  Application of the patch on the CFRP anchor*

The fan had to be large enough to ensure sufficient bond area was present between the anchor and the strengthening sheet. The fan angle affected the force transfer from the CFRP to the anchor.

# CHAPTER 5

# Experimental Program – Rehabilitation of Severely Damaged Reinforced Concrete Columns

## 5.1 INTRODUCTION

Procedures using mechanical couples or CFRP materials to retrofit severely damaged concrete columns are presented and explained in this chapter. The rehabilitation process and evaluation of two identical reinforced concrete columns is described. The columns had different patterns of damage, including spalling of cover, crushing of the concrete, buckling of the longitudinal bars and cracking along the columns. Both columns were rehabilitated following the retrofit procedures proposed in this research. Constant axial load and lateral cyclic loads were applied until collapse of each column was reached. One column was subjected to a 150 kips axial load (RC-1) and the other to a 350 kips axial load (RC-2).

## 5.2 TEST SPECIMENS BEFORE REHABILITATION

### 5.2.1 Properties of the two columns tested

Two identical reinforced concrete columns (Figure 5.1) were built by Leborgne, (2012). The columns had 16 in x 16 in cross section and 8-#8 longitudinal bars with three bars in each face. Column ties were #3 @ 6 in with 90 degrees hooks. Clear cover was 1.5 in. At each spacing, one perimeter tie was placed along with a smaller square tie that confined the middle bars on each side as shown in Figure 5.2. The compressive strength was  f'c = 3ksi and the bars were A-615 Grade 60.
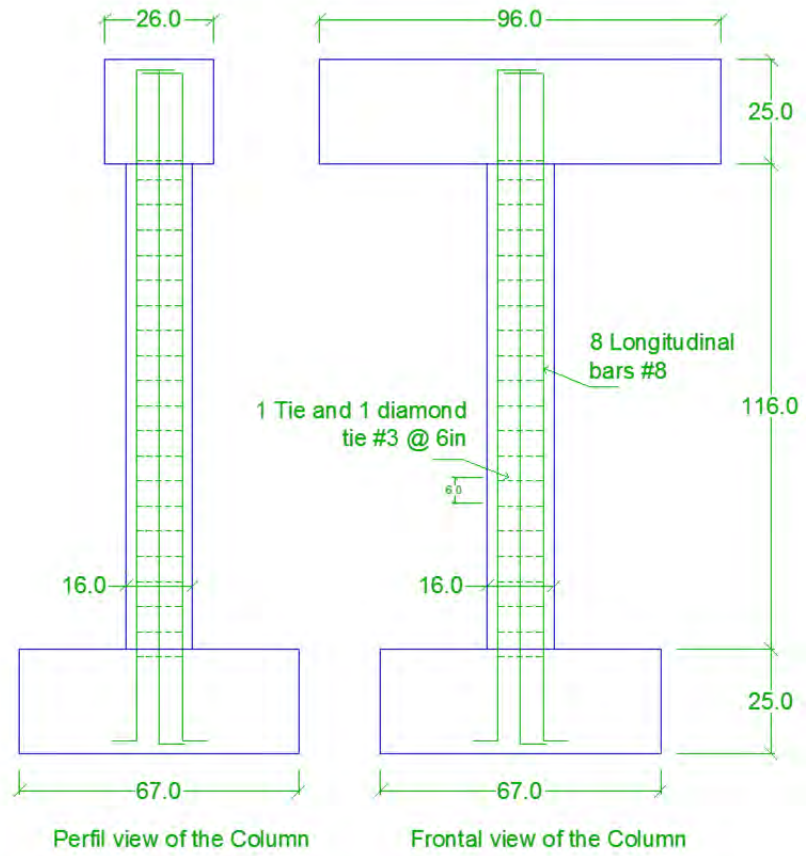
*Figure 5.1 Geometry of the column before test*
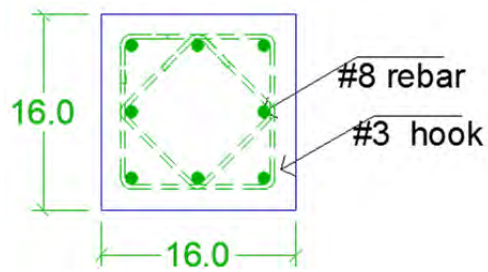


*Figure 5.2 Cross section of the columns*

110

**5.2.2    Test Setup for the column – Pattern of deformations**

In the test setup, the bottom support of the columns was fixed and at the top, the rotation was restrained to produce a column in double curvature as shown in Figure 5.3.



Double Curvature Deformation
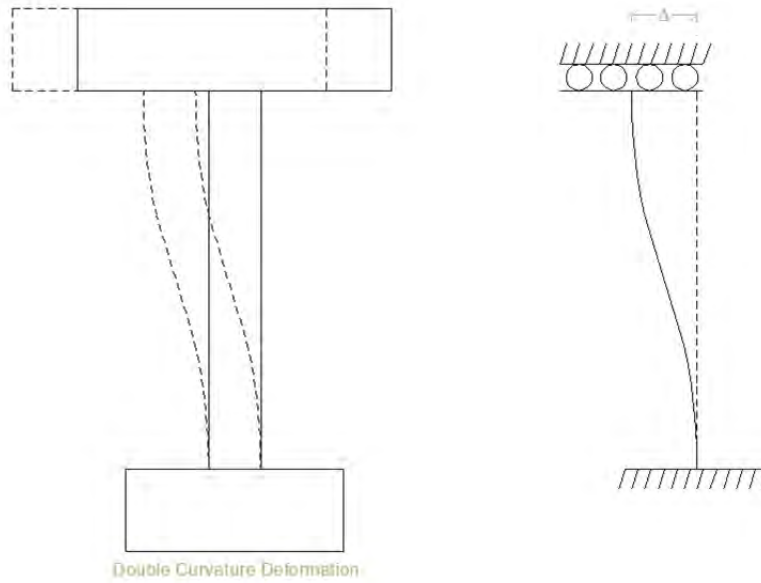
*Figure 5.3 Pattern of Deformation for columns tests its structural model*

The loads were applied by hydraulic shown in Figure 5.4 actuators with capacities of 320 kip in compression and 220 kips in tension and 50 in stroke. Two hydraulic actuators were used to apply the axial loads and a third was used for lateral load.

*Figure 5.4 Actuator – Hydraulic Machine*

To transmit the loads from the hydraulic actuators to the column, an L-shape steel frame was fabricated. This frame was made using two W 33x130 beams. Those beams were welded to form an L-shape as shown in Figure 5.5. Shear plates were added to avoid possible local buckling. The capacity of the vertical leg of the L frame is 330 kips applied at the bottom of the leg. Figure 5.5 shows the L frame before attachment to the test specimen.



*Figure 5.5 Steel L-Frame for loading columns*

The entire test setup is shown in Figure 5.6. The two vertical actuators are connected at the bottom at the strong floor and to the L frame at top. The horizontal actuator is connected to the L-frame and bears against the reaction wall. The vertical actuators apply a total constant axial load to the column; however each actuator will have different axial loads applied to produce the moment needed to prevent rotation of the top concrete beam, and creating double curvature deformation of the column. Each vertical actuator is displacement controlled to maintain constant rotation of the top concrete beam. The horizontal actuator is located at mid height of the column in order to transmit a cyclic lateral load so that a point of inflection is will occur at mid height.

Figure 5.8 and Figure 5.9 show the direction of the lateral and vertical loads for displacement in each direction. When the horizontal actuator is pushing in the north direction, the compressive load in north vertical actuator will be lower than that of the south actuator to produce a resisting moment and maintain the condition of no rotation of the top concrete beam. The column is deformed in double curvature pattern with an inflection point around the mid-height of the column. For loading in the south vertical actuator the condition is reversed.
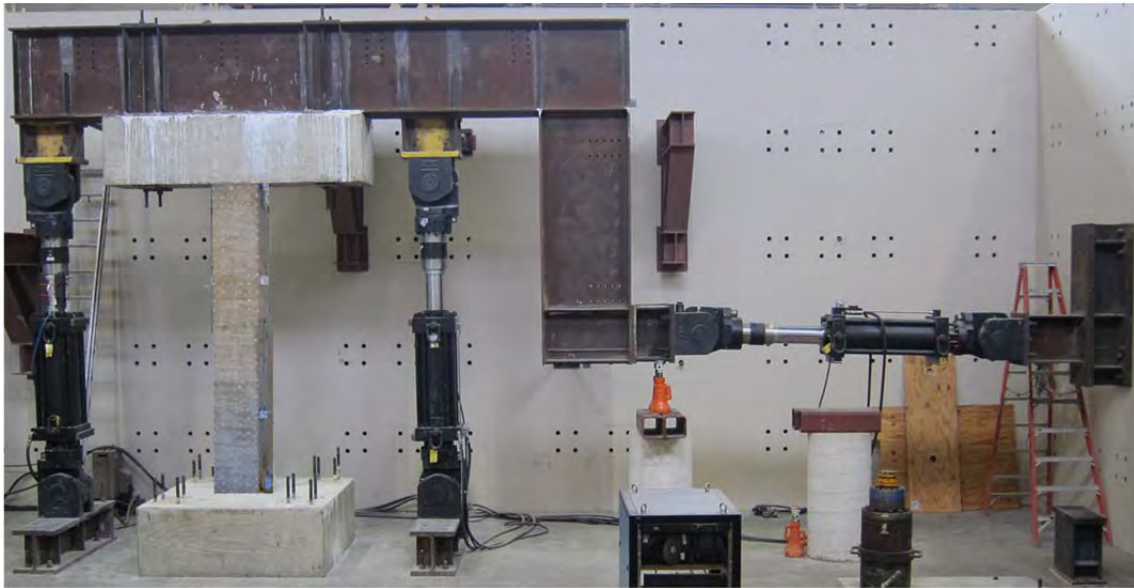
*Figure 5.6 Test setup for the fix bottom – top rotation restrained column*
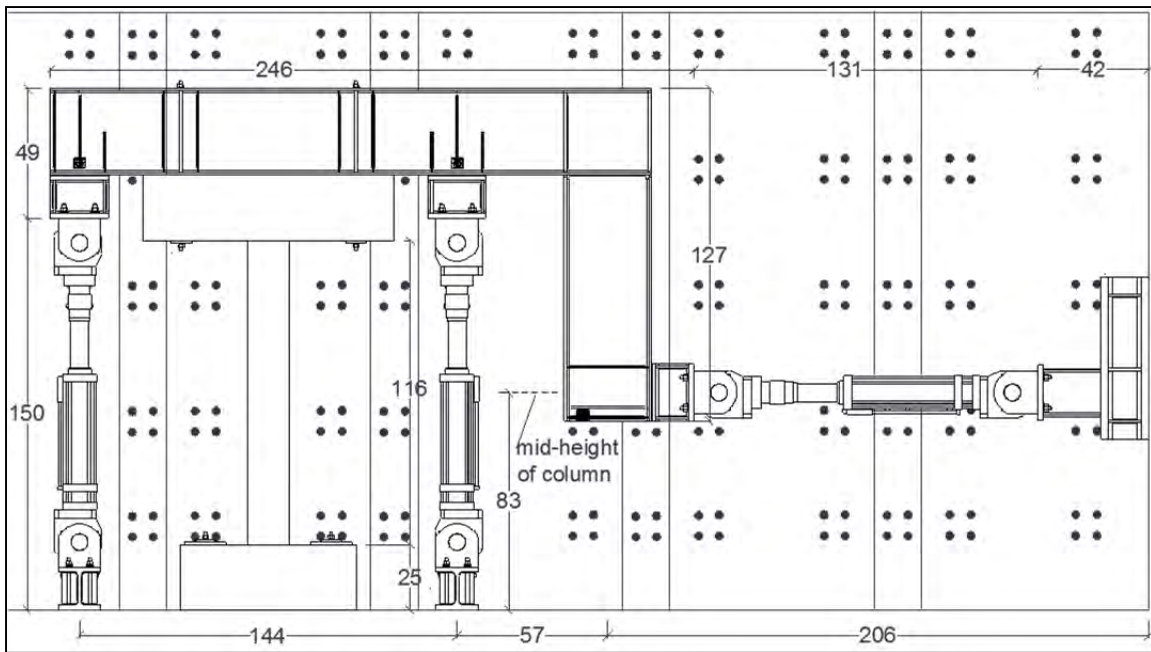


*Figure 5.7 West-East view of the reaction wall and dimensions of the test setup and the column*

114

North

Mid-height level of the column
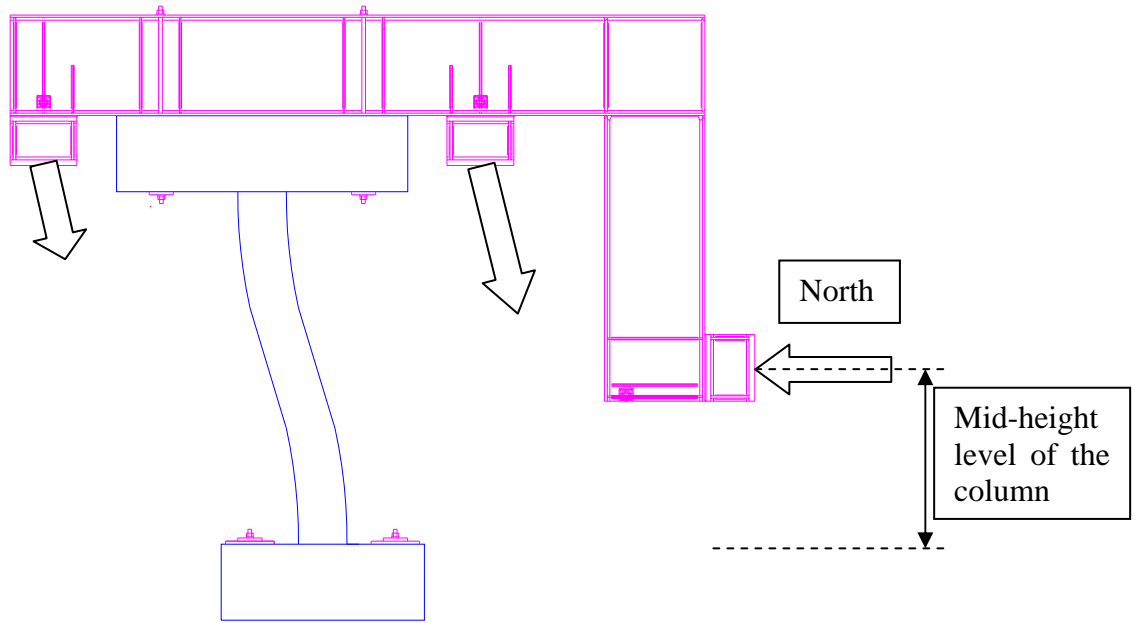
*Figure 5.8 Application of loads to the specimen through the steel L-frame for lateral displacement to North.*



South

Mid-height level of the column
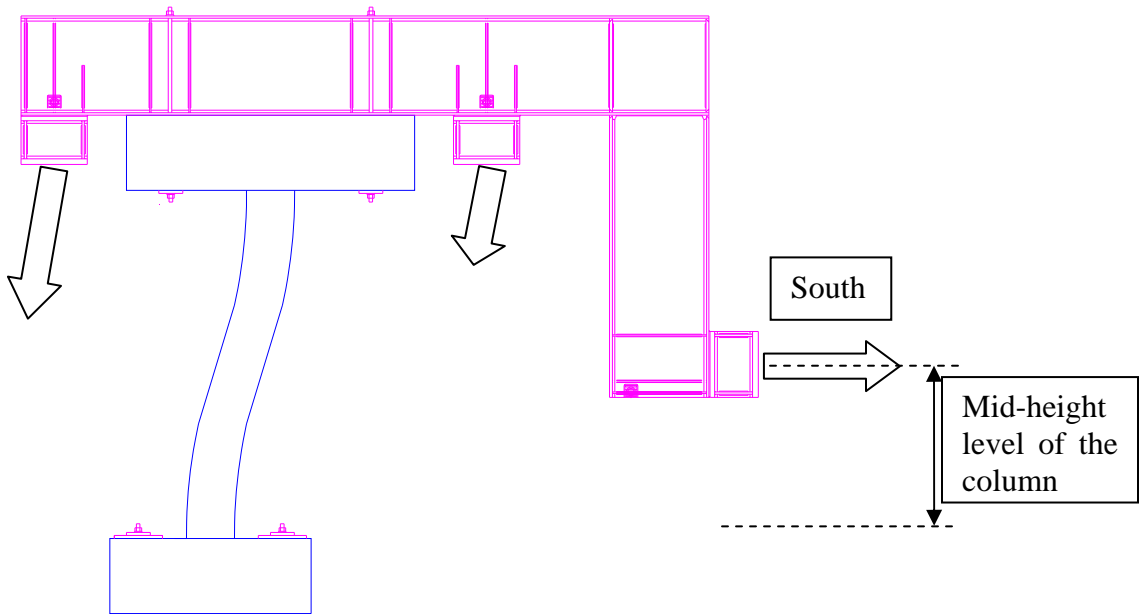
*Figure 5.9 Application of loads to the specimen through the steel L-frame lateral displacement to South.*

### 5.2.3 Instrumentation

Deformation linear potentiometer and wire potentiometers were used to measure the column response. Linear potentiometers with 2 in. and 4 in. gage lengths; and 25 in.in gage wire potentiometers were used; the first one were used for local deformation of the column and the second ones were used to measure global displacement of the column and the test setup. Figure 5.10 and Figure 5.11 show the location of each linear potentiomer to measure local deformation and Figure 5.12 show the linear potentiometer to global displacement of the specimen.
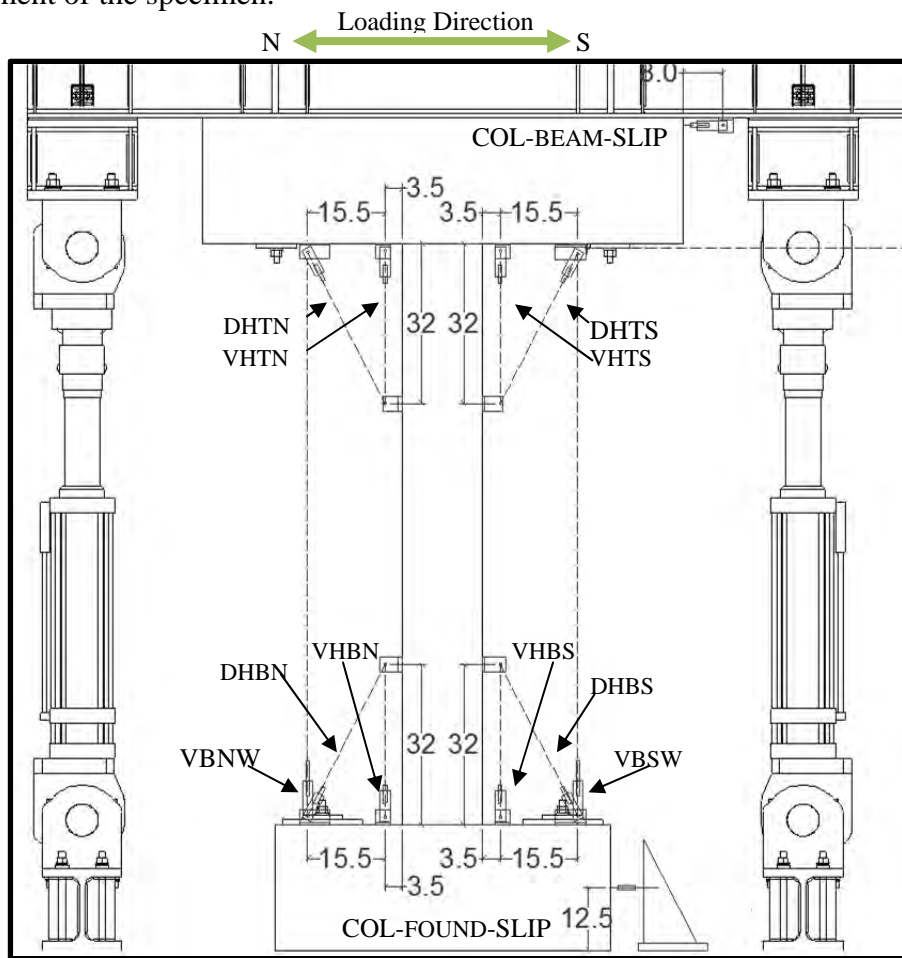


**Figure 5.10 Location of the linear potentiometers for local deformation of the column (west side view)**
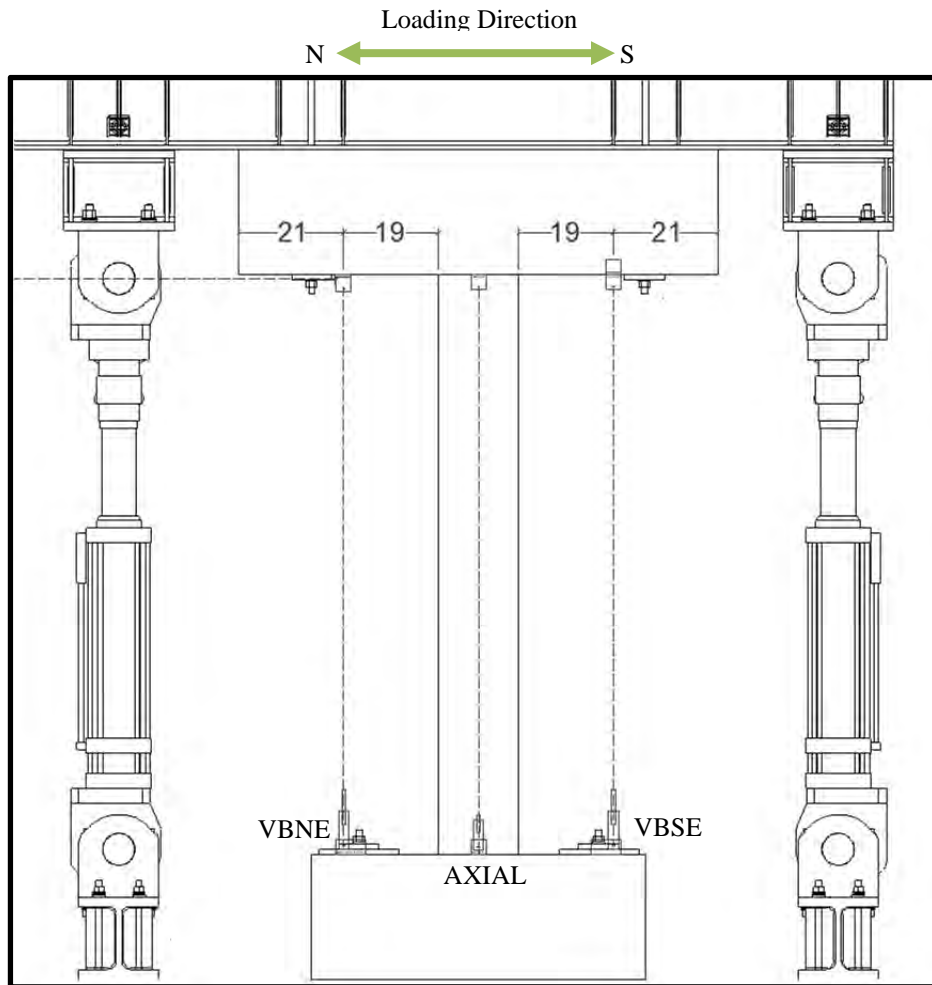
*Figure 5.11 Location of the linear potentiometers for local deformation of the column (east side view)*
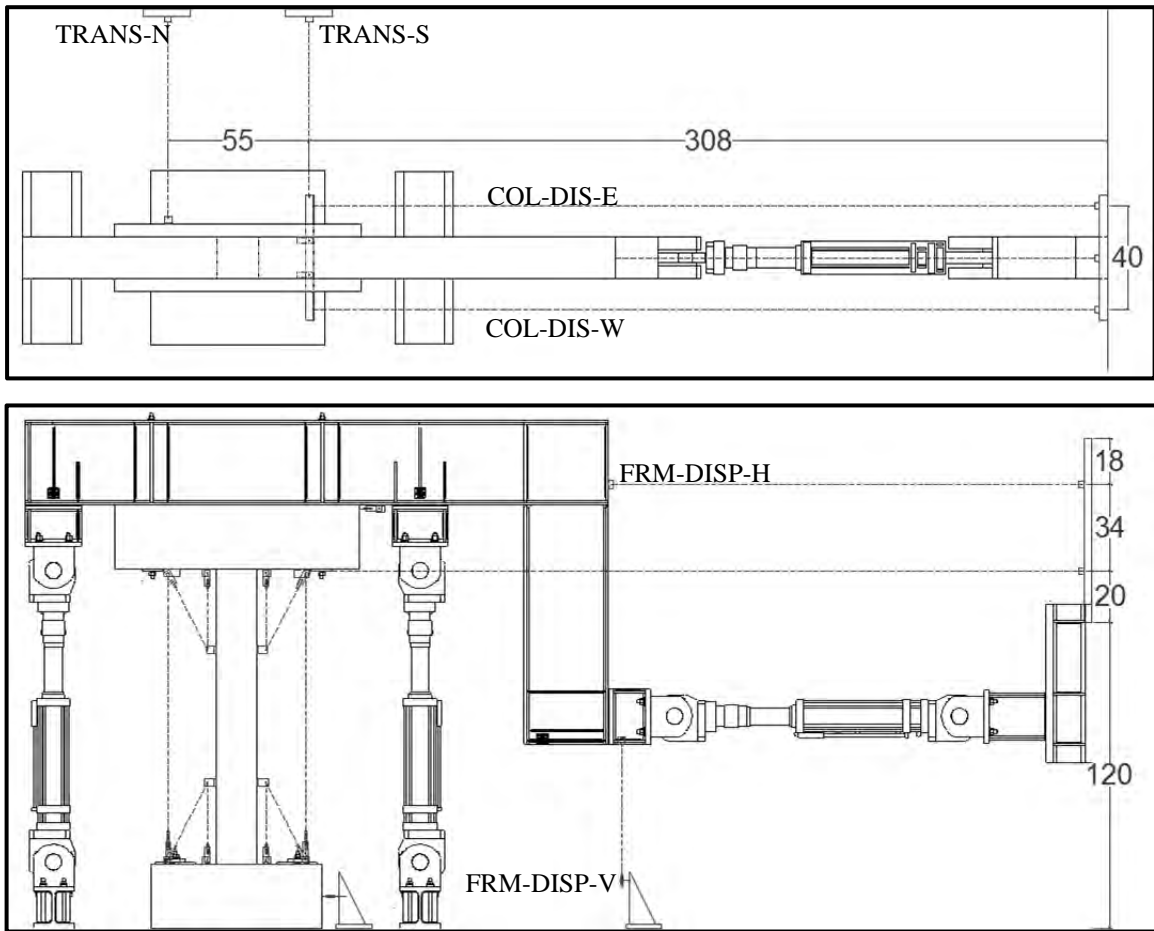
*Figure 5.12 Location of the wire potentiometers for global deformation of the column and the displacement of the frame setup*

Strain gages were installed at critical locations on the longitudinal and transversal reinforcement of the column as shown in Figure 5.13 and Figure 5.14.

Loading Direction

N ⟷ S

Concrete Beam

TLNW, TLNE | TLSW, TLSE
TWRH1, TWRH1
TWRH2, TWRH2
TWRH3, TWRH3
6 in. spa.typ
TWRH3, TWRH4

TERH1
TLNE | TLSE
TLNW | TLSW
TWRH1
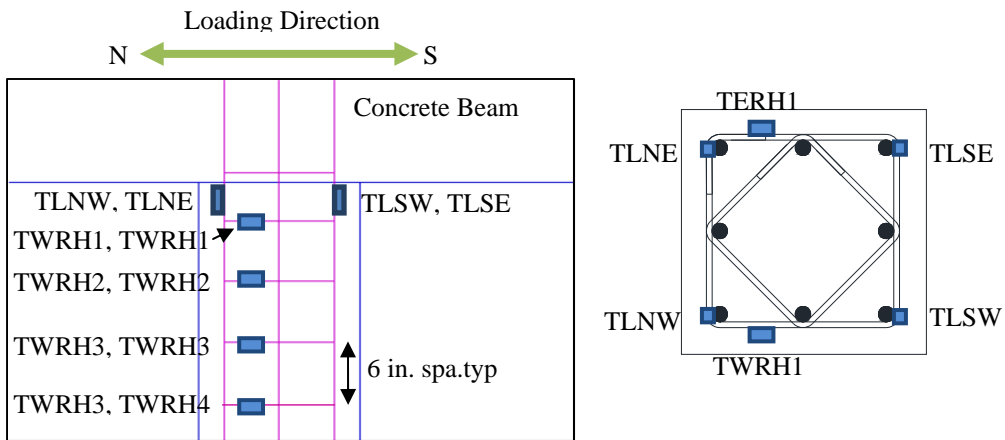
**Figure 5.13 Location of the internal strain gages at the top of column.**

Loading Direction

N ⟷ S

BWRH4, BWRH4
BWRH3, BWRH3
6 in. spa.typ
BWRH2, BWRH2
BWRH1, BWRH1
BLNW, BLNE | BLSW, BLSE

BERH1
BLNE | BLSE
BLNW | BLSW
BWRH1
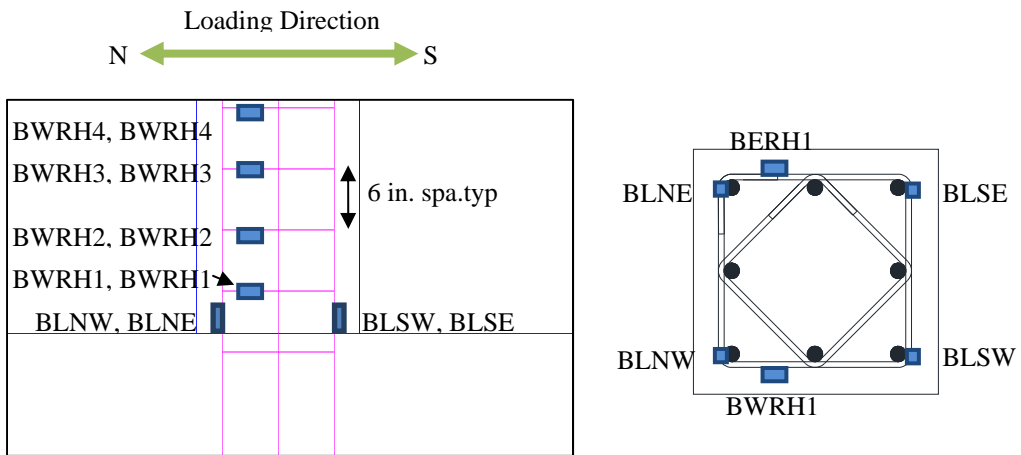
**Figure 5.14 Location of the internal strain gages at the bottom of column.**

## 5.3 TEST OF THE ORIGINAL COLUMNS

### 5.3.1 RC-1, Axial Load Applied 150kips

The test was conducted under deformation control. An axial load of 150 kips, was applied before the lateral load history was imposed.

#### 5.3.1.1 *Lateral Cycle Displacement Protocol*

In the cyclic loading test, the specimen RC1 was subjected to three cycles of lateral displacements to drifts shown in Figure 5.15.
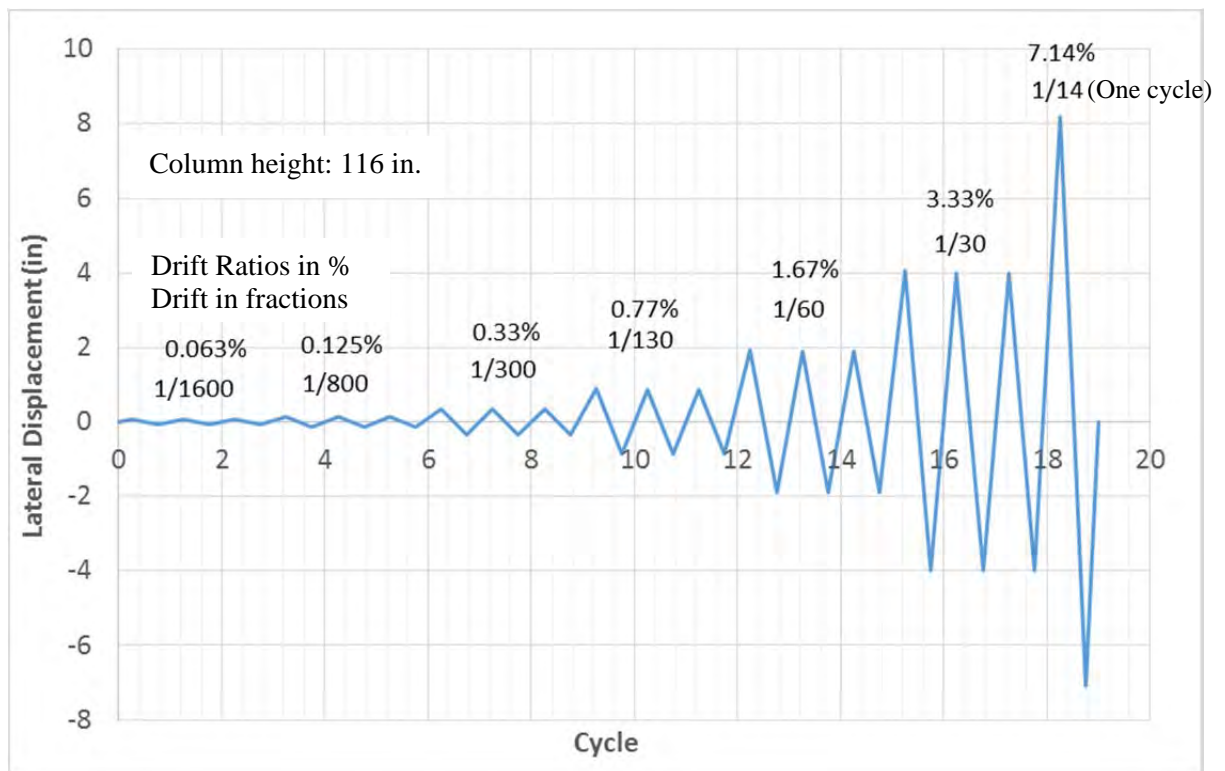


*Figure 5.15 History of cycles after axial load applied*

### 5.3.1.2  *Results of the test for RC-1*

Yielding in tension of the longitudinal bar was noted at a lateral deformation of 0.8 in. (0.77% drift ratio) at both ends of the column. The lateral load measured was 44.6kips. The yielding in compression of the bars was reached in the 13th cycle at 59kips lateral load. Figure 5.16 (left) shows the deflection shape of the column at the 10th cycle loading to north when the yielding occurred. The double curvature shape of the column can be seen. Shear and flexural cracks developed, especially at bottom right side of the column (tension side). Shear cracks developed 15 in. above the column base, with the largest crack at the bottom of the column (Figure 5.16-right). Flexural cracks appeared on the top of the column as well.
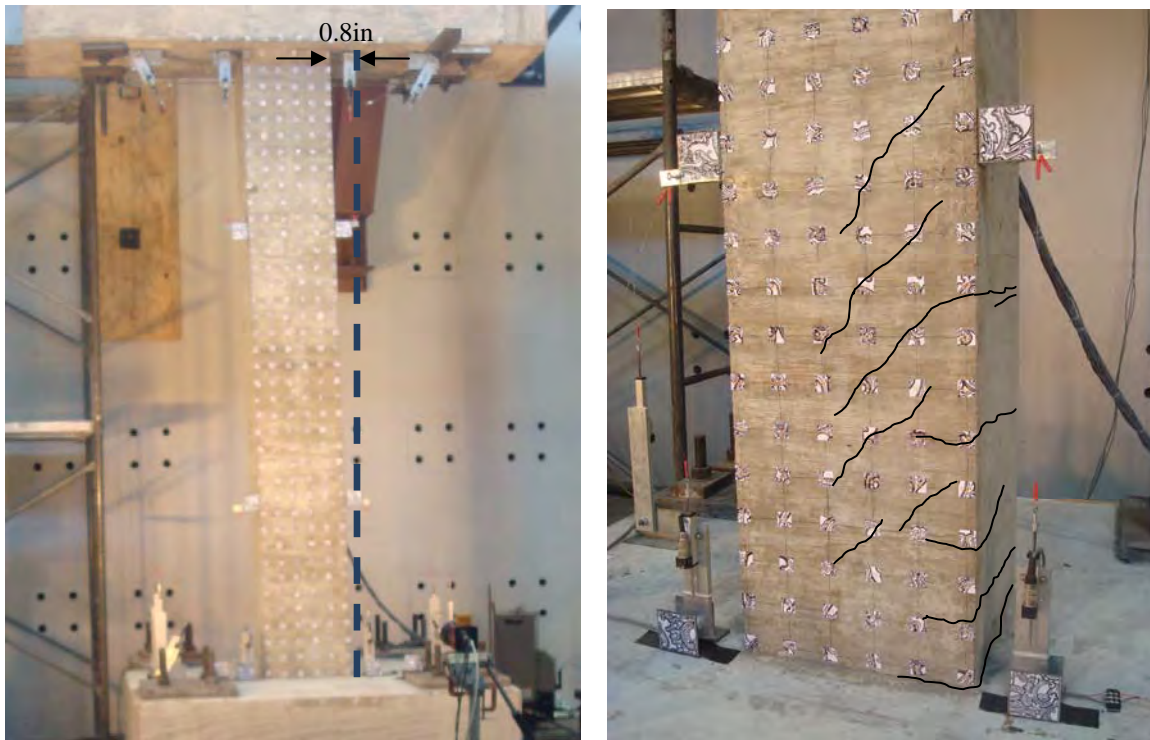


***Figure 5.16 Shape of the column at 0.8 in. lateral deformation to north direction (left). Shear and flexural cracks appeared (right)***

Cracks became wider as larger lateral displacement was applied to the column. A hinge started to form at the bottom and other hinge at top of the column as well. At the top of the column, flexural cracking and spalling of the cover was observed. At the bottom of the column, the core of the concrete started to be damaged as it can be seen in Figure 5.18. Figure 5.17 shows a sudden drop of the axial load to 10kips during the 19$^{th}$ cycle of loading to north due to hydraulic shut down of the actuator. The concrete core at bottom of the column was severely damaged (Figure 5.18) and the longitudinal bars carried most of the axial load. The column was reloaded to 150kips and pushed to north until an axial failure was reached at 8.2 in. lateral deformation (7.14% drift ratio).

Severe damage occurred at both ends (Figure 5.18). The cover at the top of the column (Figure 5.19) spalled over a 12 in. height of the column. No buckling bar was presented. Crushing of the concrete and buckling of every longitudinal bar was observed at the bottom of the column (Figure 5.20), the horizontal ties also were opened in that zone of buckling. Several diagonal and horizontal cracks were through the bottom and top of the column. The maximum shear capacity of the column was 61.8kips in both direction of loading (north and south).
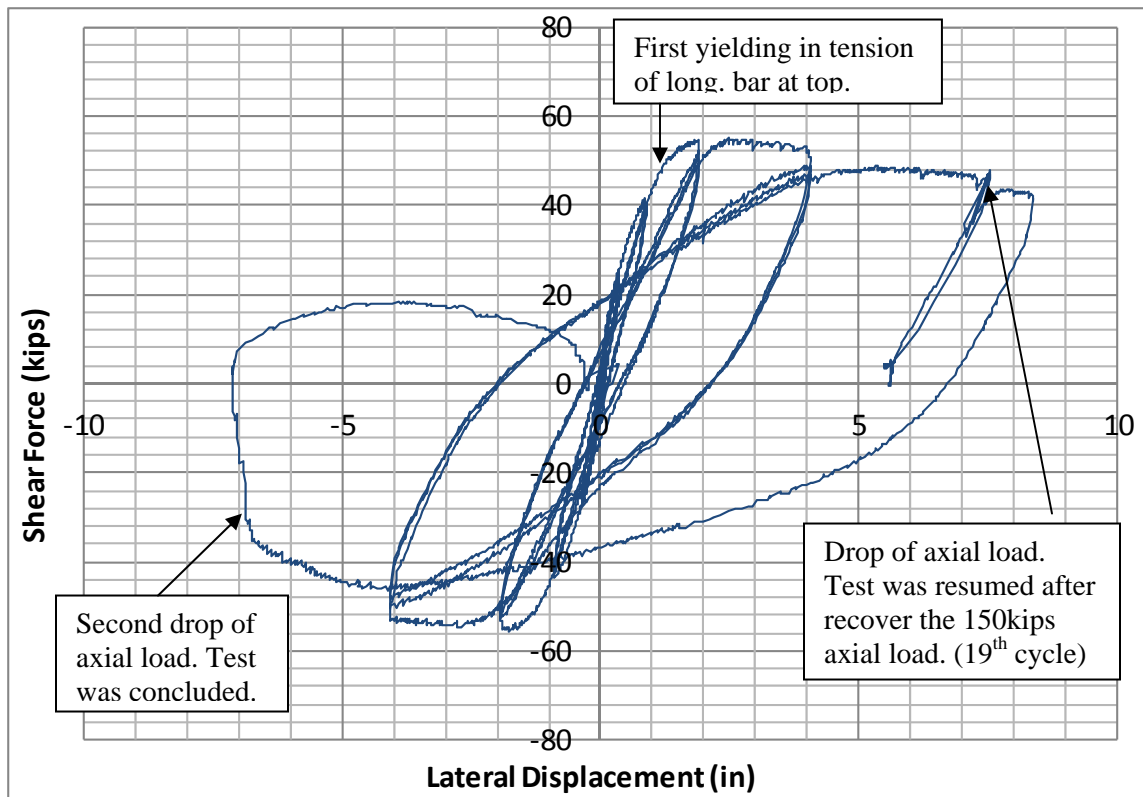
*Figure 5.17 Shear Force vs. Lateral Displacement of RC-1. Axial Load 150kips*

*Figure 5.18 RC-1 at 19<sup>th</sup> cycle loading to south. Spalling of the cover at top of column. Concrete crushing and buckled bars at bottom of column.*



*Figure 5.19 Spalling of the cover at top of column.*

*Figure 5.20 Concrete crushing,  bars buckling, and opening of the transverse reinforcement at the bottom of column.*

Strains in the longitudinal steel reinforcement are shown in Figure 5.23. The strains were higher at the bottm of column indicating that the base provided more resistance that the beam at the top.

The horizontal reinforcement formed by the ties and the diamonds developed well behavior at top of the column, confinement the core and avoiding the buckling of the longitudinal bars. They reached the yielding at $16^{th}$ cycle (Figure 5.23 left). The bottom lateral reinforcement also reached the yielding; however, the ties were opened because the effect of the buckling on the longitudinal bars (Figure 5.23 right). They pushed out the ties being opened as it can be seen in Figure 5.20.
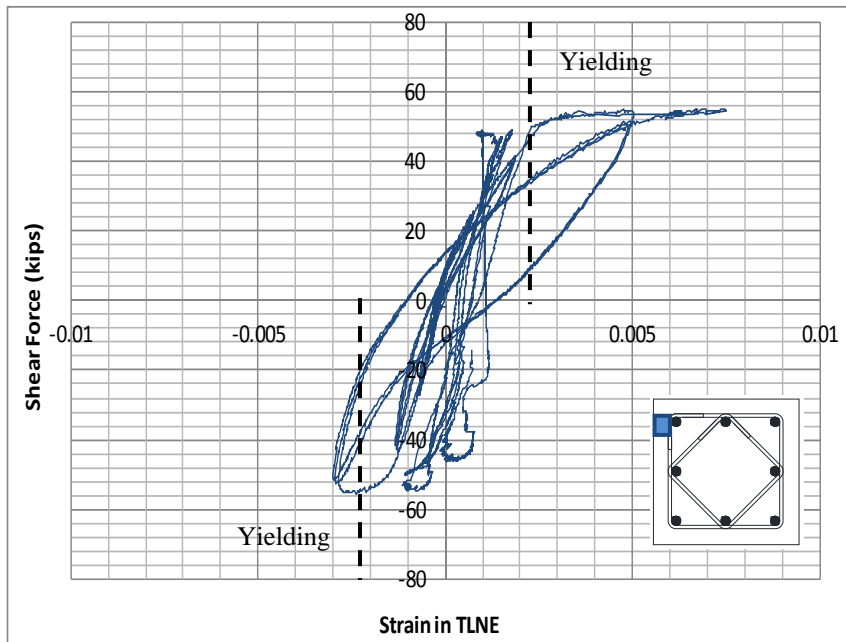
*Figure 5.21 Strain in the longitudinal bar located at north-east corner of column at top*
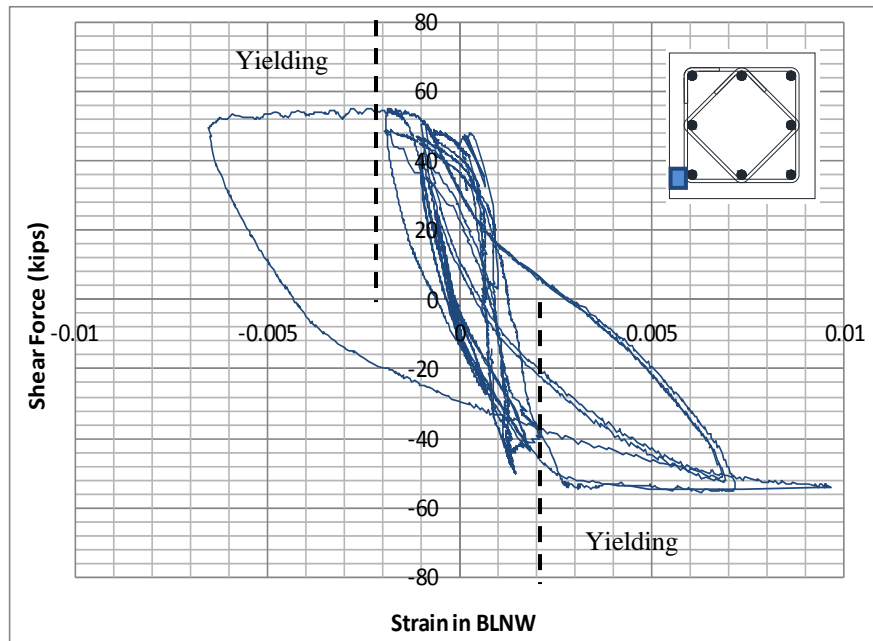


*Figure 5.22 Strain for the longitudinal bar located at north-west corner of bottom of column*

126
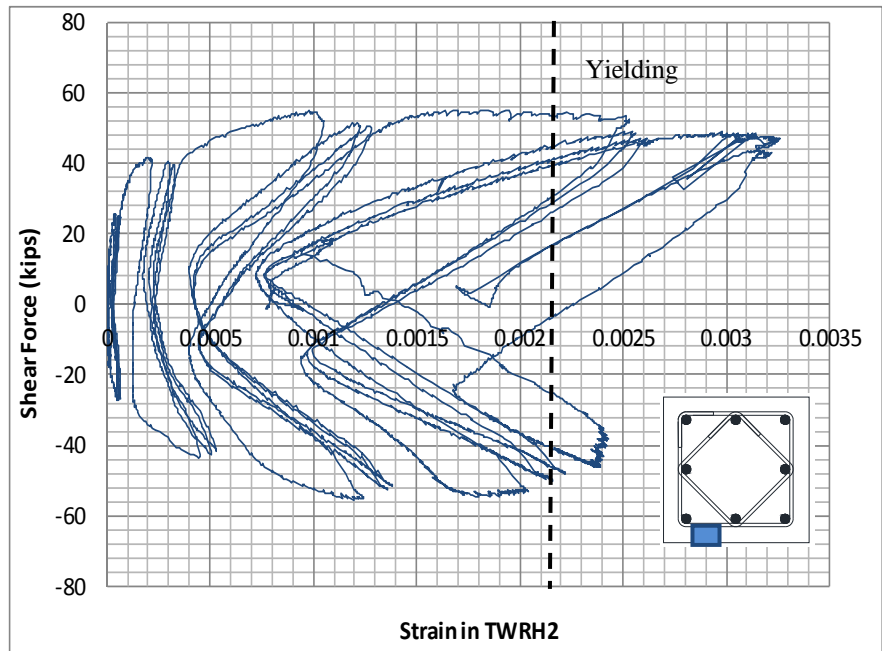
*Figure 5.23 Strain in tie at top of column.*
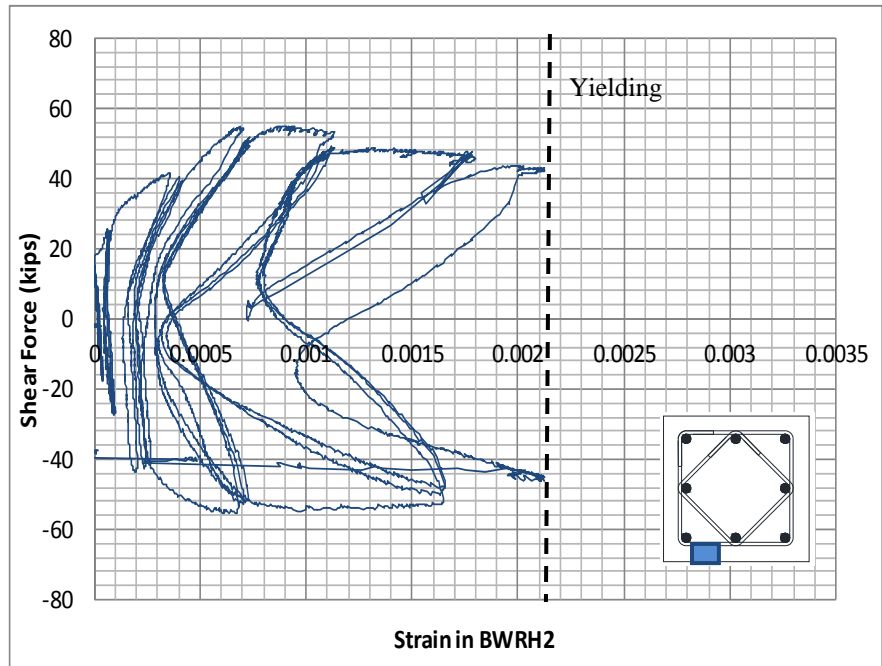


*Figure 5.24 Strain in tie at bottom of column.*

127

### 5.3.2 RC-2, Axial Load 350 kips

The test was conducted under lateral deformation control. The axial load applied on the column was 350 kips and it was imposed before the lateral cyclic load.

#### 5.3.2.1 *Protocol of Load for the Lateral Cycle Load Test*

In the cyclic loading test, the specimen RC2 was subjected to three cycles of tension compression lateral to drifts shown in Figure 5.15.
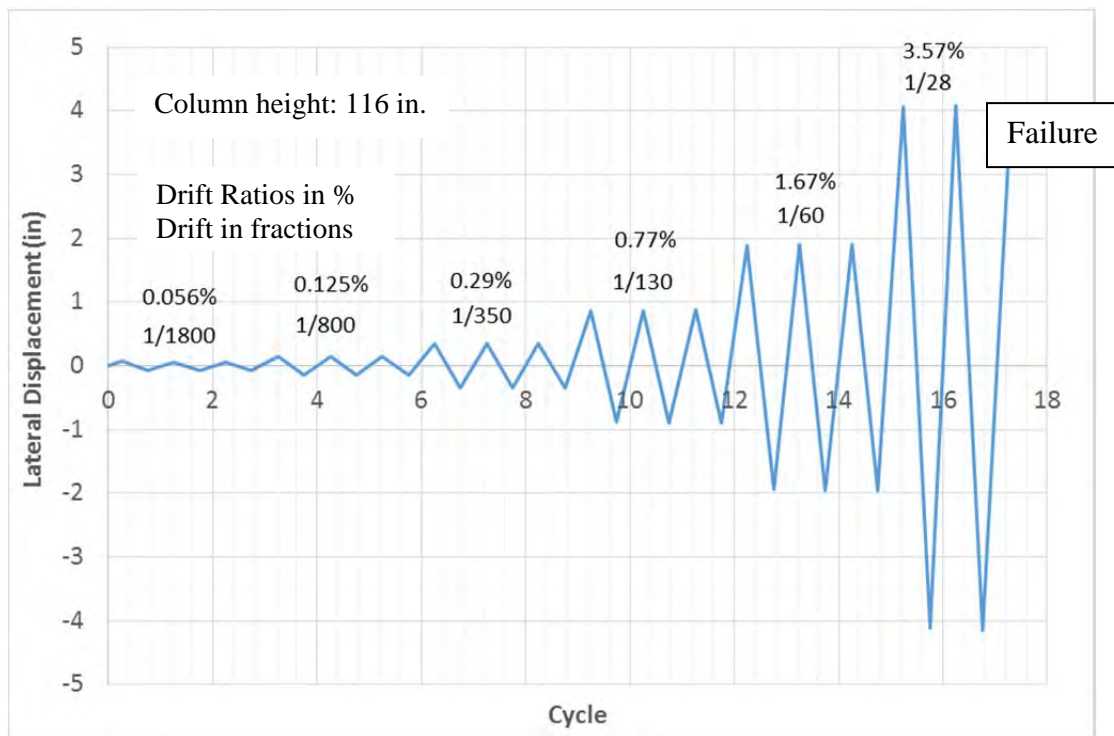


*Figure 5.25 History of cycles after axial load applied*

5.3.2.2  *Results of the test for RC-2*

At 0.86 in. (0.77% drift ratio) lateral deformation, yielding in compression of the longitudinal bar at the top of the column was noted. Horizontal cracks on the north face of top of column and south face of bottom of column appeared by flexion effects. The yielding in tension of the longitudinal bar at top and bottom of column was reached on the 13th cycle, at 1.90in (1.67% drift ratio) of lateral deformation. The column appeared in reasonable condition (Figure 5.26). Diagonal cracks on west and east faces of column appeared by shear effects, observing also wider horizontal flexural cracks. The shear cracks developed 15in above the bottom and top base of the column as well. Cover spalling on the corners and faces of column perpendicular to the lateral load was observed (Figure 5.27). The maximum shear capacity of the column was 53.07kips reached at the 13th cycle as well.
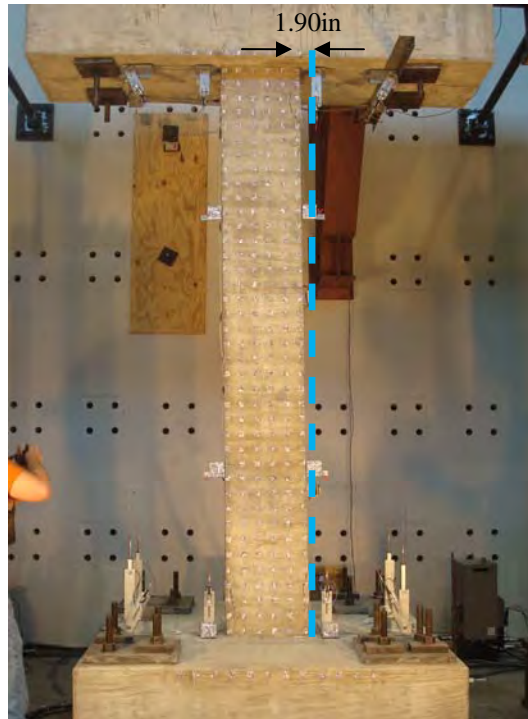


***Figure 5.26 RC-2 at 1.8 in. (1.67%drift ratio) of lateral deformation to North***

*Figure 5.27 Top(left) and bottom (right) of the column. Cracks and some spalling of cover are observed on both extremes of the column.*

The maximum lateral displacement reached was 4.14in (3.57% drift ratio) at 15th cycle. However the failure was reached at the 18th cycle. The lateral displacement to north 3.76 in. The column exhibited severe deterioration at both ends presenting buckling of all longitudinal bars with crushing of the concrete as it can be seen in Figure 5.28. Also diagonal and horizontal cracks were presented through the rest of the column also. Damage was more severe on the bottom of column (Figure 5.29). The concrete was crushed from base to more than 20in height. Top of column presented the crushed of concrete until 16in down the top joint (Figure 5.30).

*Figure 5.28 Condition of the column at the failure.*



*Figure 5.29 Concrete crushed, buckled longitudinal bars in the top of column*

131

*Figure 5.30 Concrete crushed, buckled longitudinal bars and opened ties in the corner of the column's bottom.*
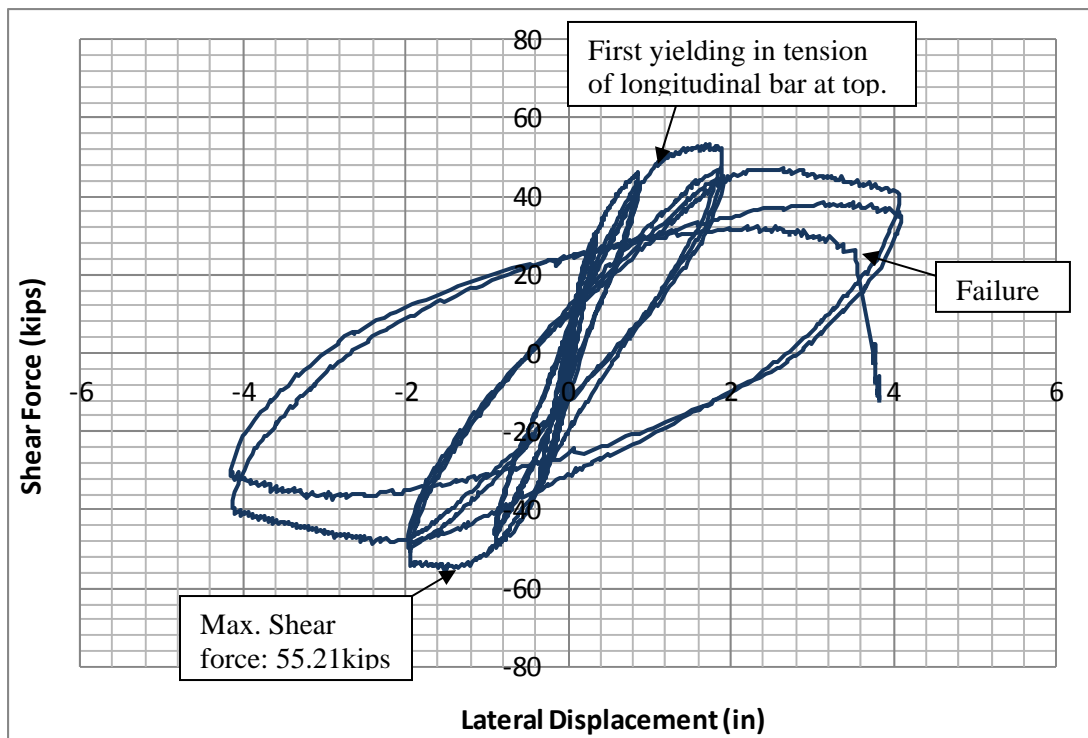


*Figure 5.31 Shear Force vs. Lateral Displacement of RC-1. Axial Load 350kips.*

The longitudinal steel reinforcement received tension and compression axial load through the vertical and lateral load applied to the column (Figure 5.32). The bars had compression a strain of 0.0006in/in by the 350kip axial load imposed previous the hysteretic axial load. Figure 5.32 also shows that the yielding in compression of the bars at top appeared in the $10^{th}$ cycle when the lateral load was 46kips (to south), while the first bar yield in tension occurred in the $13^{th}$ cycle when the load was 50kips (to north). The longitudinal bars on the bottom yield in compression and tension in the $13^{th}$ cycle as well, having lateral load of 53kips (to south) and 51 kips (to north) respectively. No hardening presented, measuring a plateau of 0.006in/in, larger than the observed on the bars of specimen RC-1. Every longitudinal bar buckled on top and bottom of the column.

The rectangular and diamond ties had tension strain, reaching the yielding the ties on the top of the column (Figure 5.34). Because the longitudinal bars pushed out the ties under the high axial load on them, from the second to the fourth levels of ties the column's bottom were opened on the hook, showing that the 90deg arrangement is not enough to keep the longitudinal bar straight.
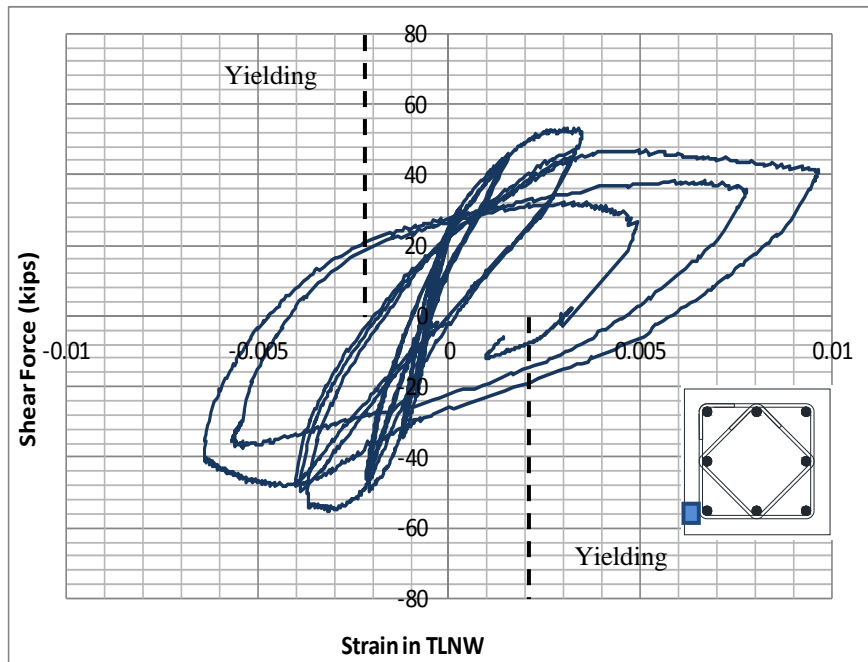
*Figure 5.32 Strain in the longitudinal bar located at north-west corner top of column*
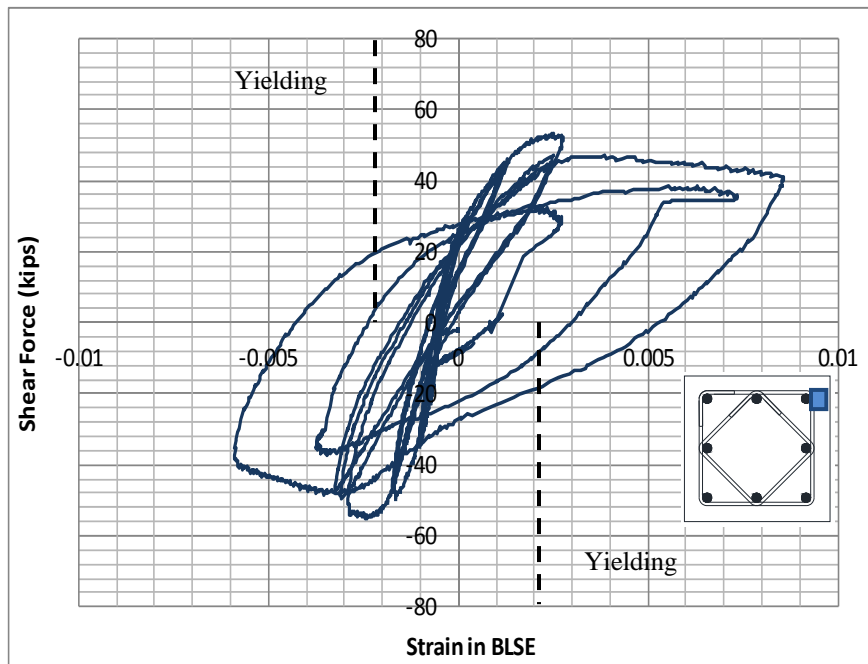


*Figure 5.33 Strain for the longitudinal bar located at south-east corner bottom of column*
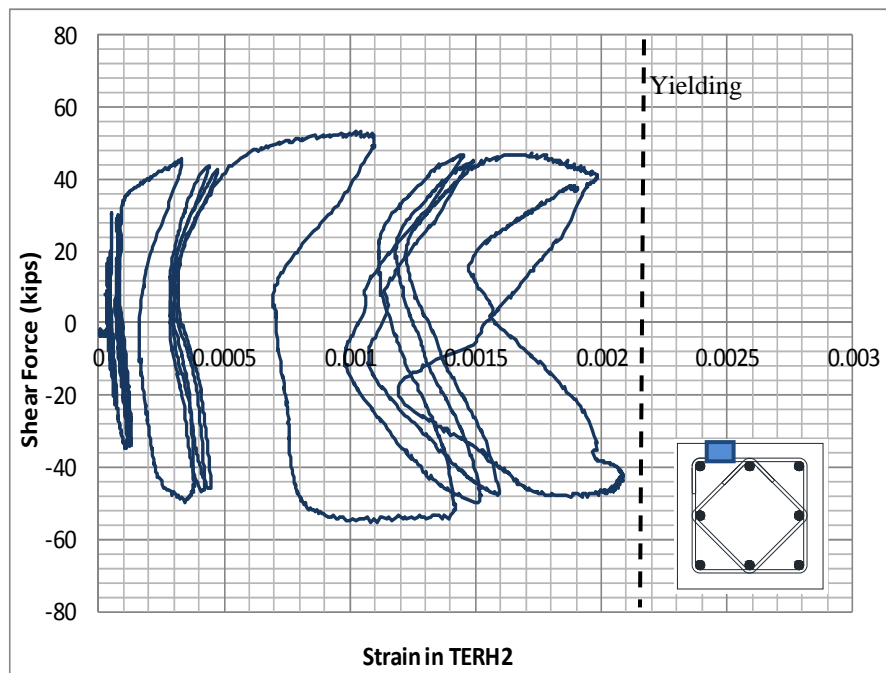
*Figure 5.34 Strain in tie at top of column.*

135
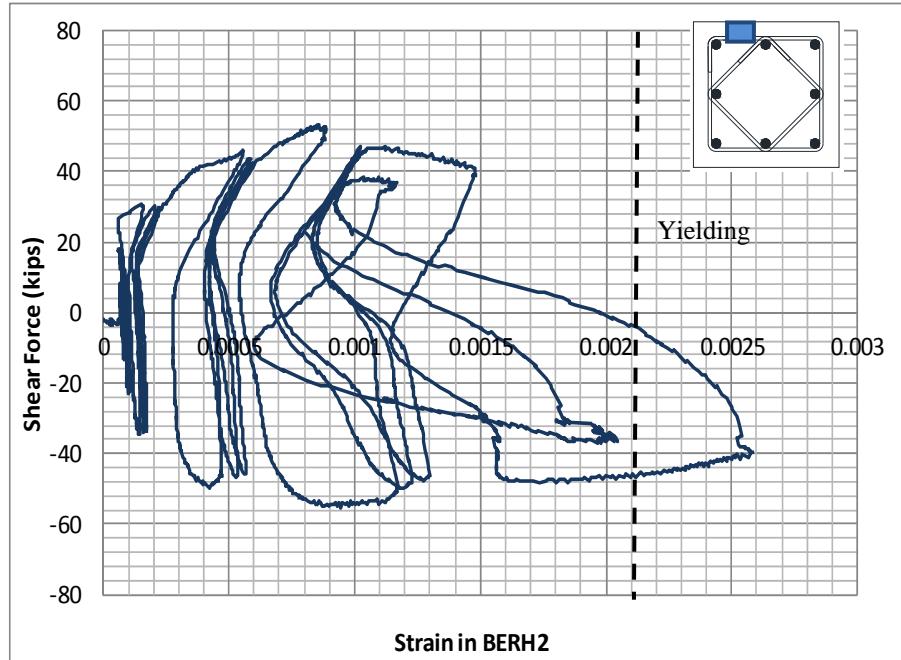
*Figure 5.35 Strain in tie at bottom of column.*

## 5.4    COLUMN RETROFIT PROCEDURES FOR RC-1

### 5.4.1    Overview of RC-1 retrofit

Figure 5.36 shows the damaged column after the first test, buckled bars at the bottom and the cover spalled at the top. Loose concrete was removed in the bottom hinging region. Top of column was straightened using jacks in order to made the column has a vertical alignment with the foundation.



*Figure 5.36 Condition of column prior to retrofitting*

The two hinging zones of the column had different patterns of damage, therefore two retrofit procedures were used. Figure 5.37 shows the two different types of repair used for RC-1. A CFRP jacket was installed in the top hinge zone of the column and concrete and reinforcement were replaced in the heavily damaged bottom hinging region. Mechanical splices were used to replace the buckled bars.
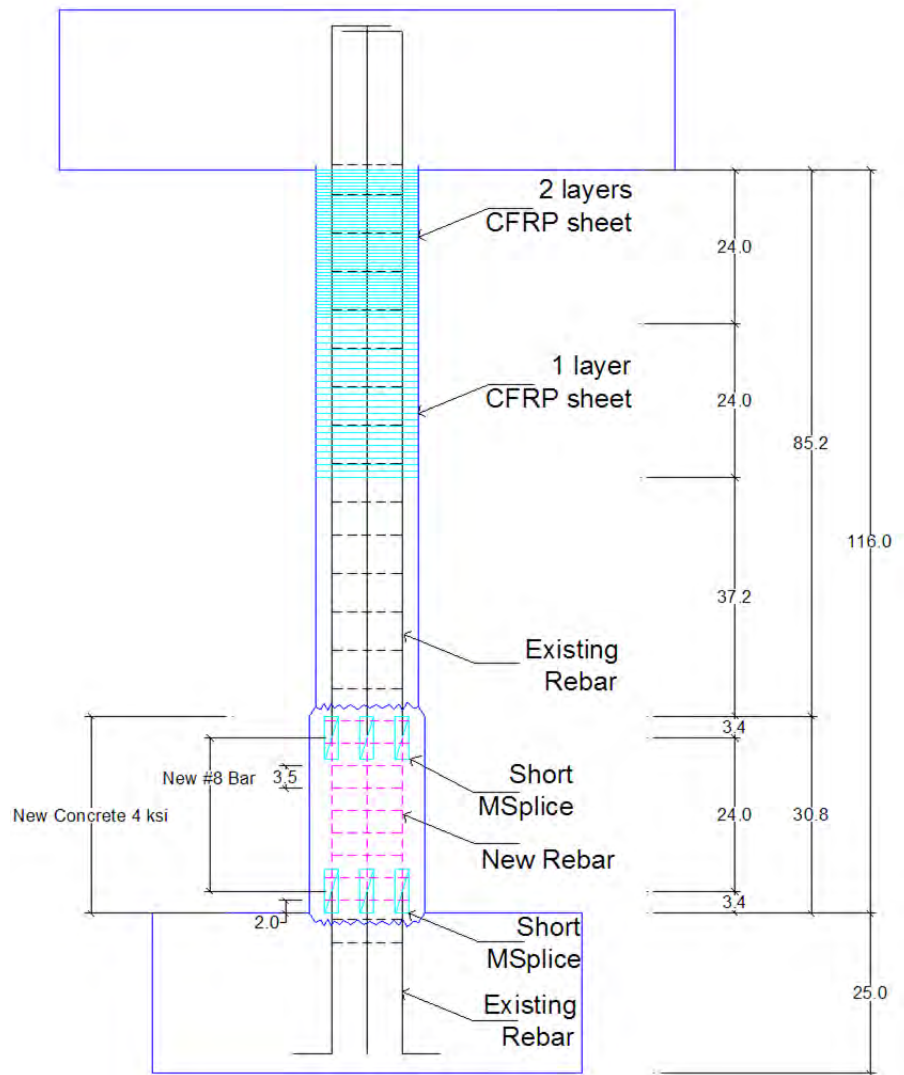


*Figure 5.37 Retrofitting using short mechanical splices and CFRP materials*

138

For RC-1 the top end of the column where the cover spalled but no buckling occurred, loose concrete was removed and repair mortar (properties in Appendix E) was used to replace the concrete removed. There was no attempt to inject epoxy into the cracks at the top of the column. The damaged region was wrapped with two layers of CFRP sheets that extended 24in from the top of the column and one layer on the 24in below. Intermediate CFRP anchors were installed midway between the corners. Figure 5.39 shows details of the jacketing procedure.
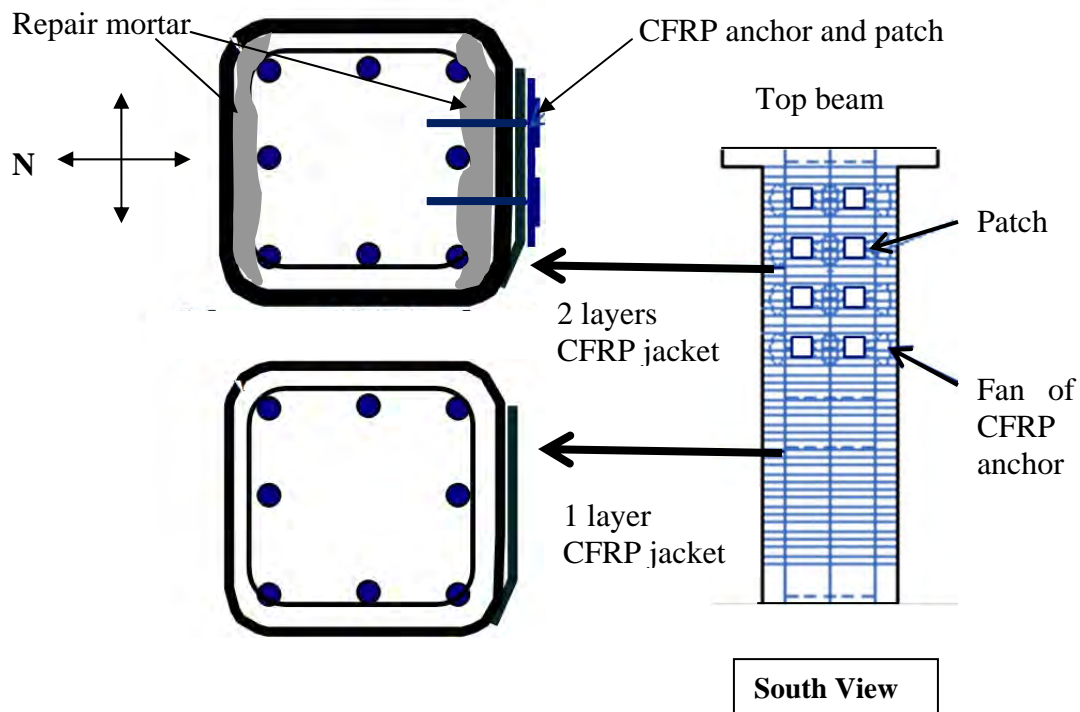


*Figure 5.38 Details for the retrofit of top of column*

The anchors were formed by CFRP strips of 17in length folded in two and 2in wide. The hole drilled into the column had a diameter of 1/2in with a depth of 4in. The edge of the hole had a fillet of ½ in.. A square patch of CFRP (4inx4in) was placed over the center of the CFRP anchor.

139
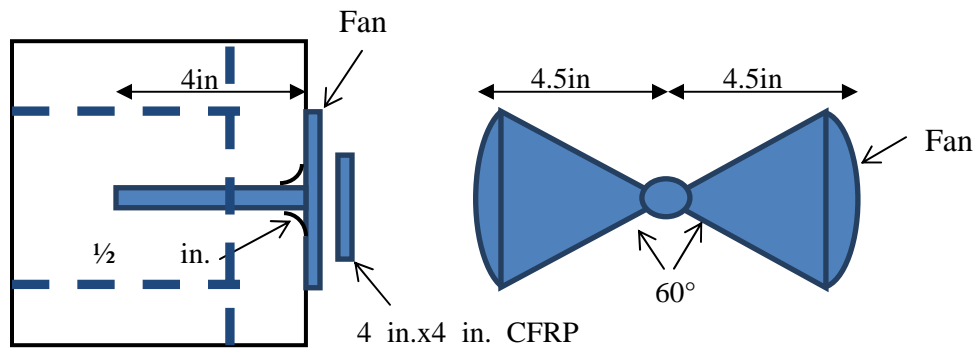
*Figure 5.39 Details of the CFRP anchor*

At the bottom of the column, short mechanical splices were used to replace the buckled bars and to provide continuity to the longitudinal bars. The strength of the new concrete was higher than the original column concrete. The cross section was increased 1 in per side to provide sufficient cover over the mechanical splices. The new reinforced was the same type of the existing bar: A-615 Grade 60 steel. Figure 5.40 shows details of the jacketing procedure used. The process is explained in Appendix B.

**West View**

2.08

2.08

18

Short
mechanical
splices

#8 bar

#3 hook
@ 3.5in

18

18in x 18in

New #8 Bar   3.5

New Concrete 4 ksi

2.0

Short   mechanical
splices

New reinforcement

Short   mechanical
splices

Existing bars
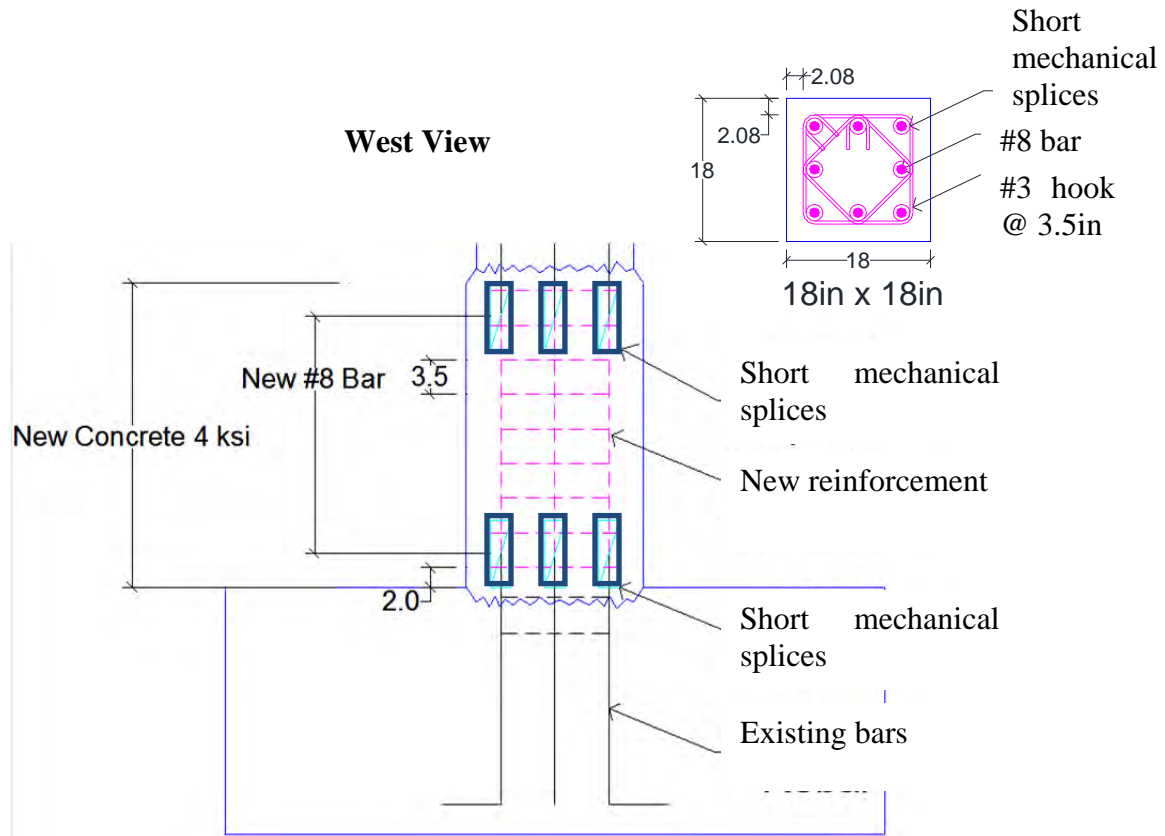
*Figure 5.40 Details for the retrofit at bottom of column*

### 5.4.2  Preparation of the bottom and top hinges zones

The top and bottom of the column exhibited of concrete crushing. And bar buckling. All damaged concrete was removed. Figure 5.41 and Figure 5.42 show details of the damage to the top and bottom of column.
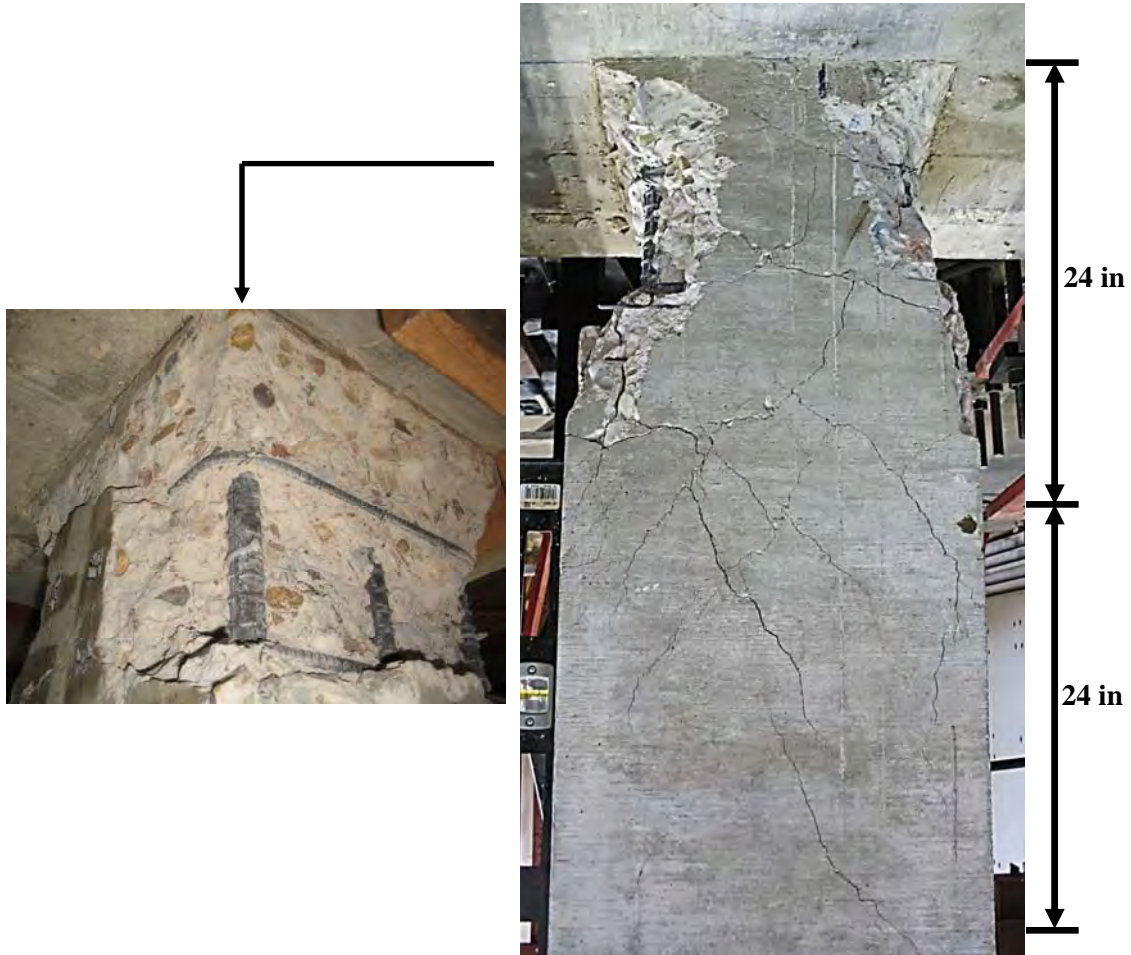


*Figure 5.41 Condition of column top hinge*

The crushed concrete was removed from the bottom zone of the column, however it was necessary to remove more concrete in order to have enough clear space for installation of the short mechanical splices. The removal was done carefully to avoid further damage to the column. Figure 5.42 shows that lateral buckling was more dramatic in the direction of lateral loading.

**Loading Direction**
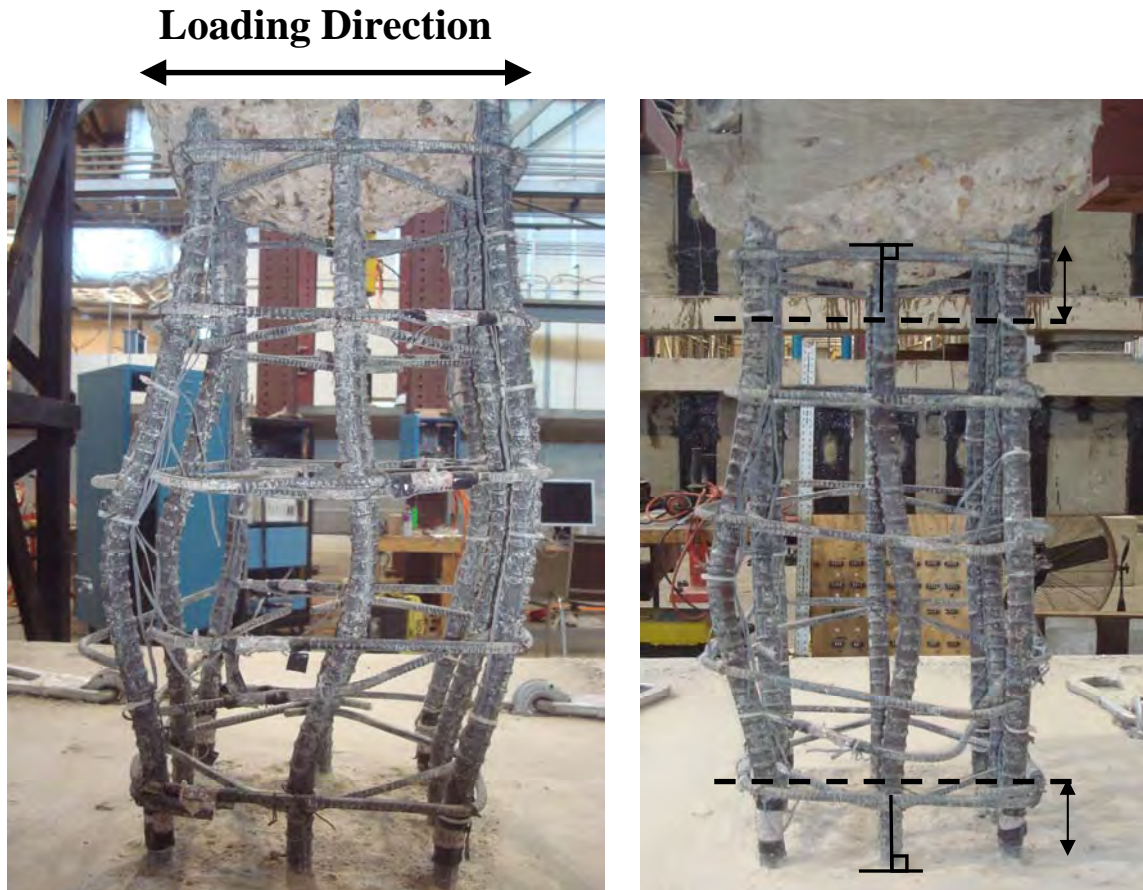


*Figure 5.42 Buckled bar at bottom of column*

### 5.4.3 Retrofit of the top of the column with CFRP materials

After the top hinge zone was prepared by removing the spalled concrete and using compressed air to remove dust, the cover was replaced using a commercial mortar (Quikrete), which had a compressive strength of 4ksi. The properties of this type of mortar are listed in Appendix E. Figure 5.43 shows mortar applied on the surface of the cross section of the column. The right image shows the damaged area after the mortar was placed. The mortar covered essentially the top 24 in of the top cover of the column. The four corners of the column were rounded to a radius of 1/2in. to avoid a stress concentration on the corners of the CFRP wrap. In the remaining areas to be wrapped with CFRP, the corners of the existing concrete were rounded.



*Figure 5.43 Application of repair mortar and CFRP at top*

To better confine the concrete in the hinging region, anchors were added to the faces that were subjected to compression due to bending under lateral loading. Holes were drilled as shown in Figure 5.44 to insert the CFRP anchors. The holes were 4in deep

and had a diameter of ½ in. More details are presented in Appendix B. Anchors were installed only on the south face of the column.



*Figure 5.44 Holes drilled for the CFRP anchor installation*

The application of the CFRP materials was done in the following order. The anchor holes were filled with the epoxy before the sheets were applied. The CFRP sheets for the top 24 in. of the column were saturated with the epoxy and applied. The sheets overlapped on the face where the anchors were installed (south side of the column). Immediately after the application of the CFRP jacket on the first 24 in., the second 24 in. zone of the column top was jacketed with one layer of CFRP overlapped on the south face. Finally the CFRP anchors were installed. Details are shown in Appendix B.

*Figure 5.45 Application of the CFRP sheet (jacket) on top of column.*



*Figure 5.46 Application of the CFRP anchors.*

CFRP anchor's fans

CFRP patches

Top 24 in., CFRP jacket with the CFRP anchors and patches

Second Top 24 in., CFRP jacket without anchors
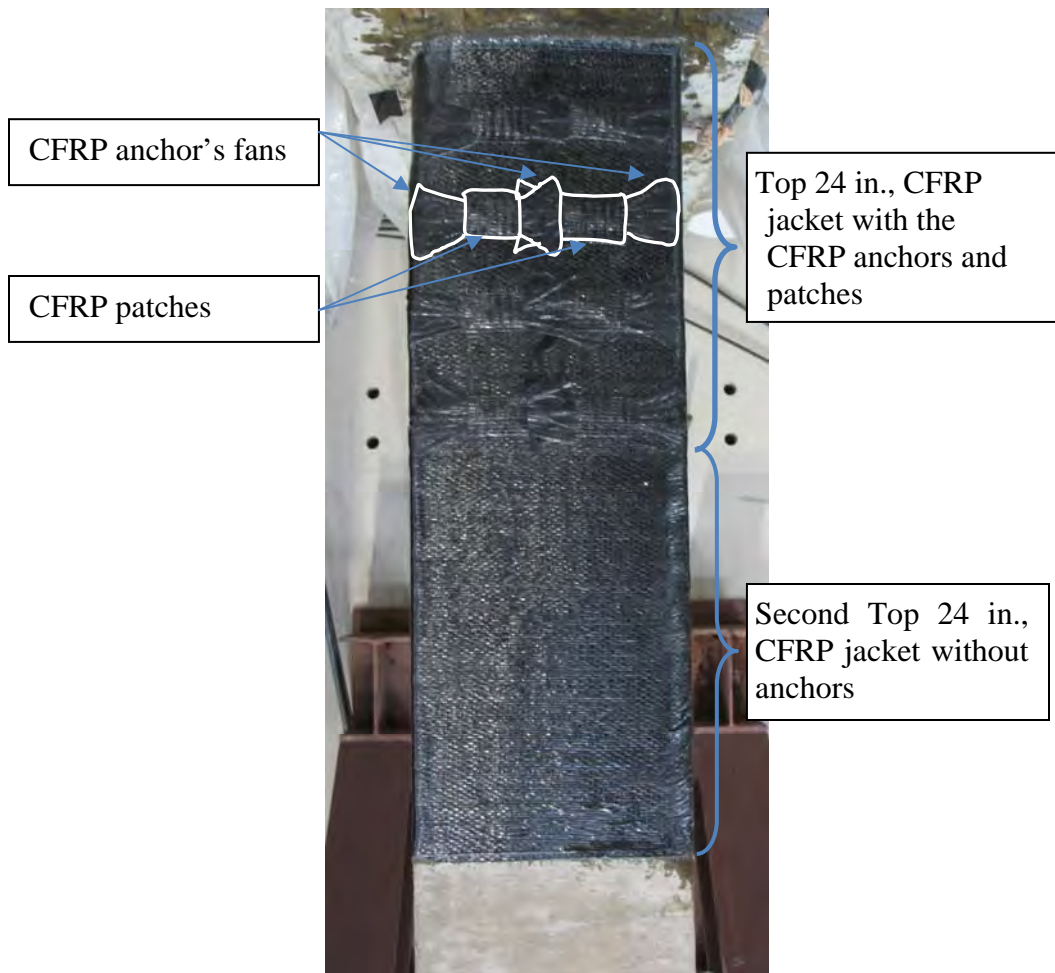
*Figure 5.47 Top of column after installation of CFRP sheets and anchors.*

### 5.4.4 Retrofit of the bottom of the column using Mechanical Splices

The procedure proposed in this study was to replace the bent bars with new bars. The new bars were joined to the existing bars by short mechanical splices. The shear reinforcement was also strengthened increasing the number of ties and using 135 deg hooks as Figure 5.40 shows. Also, the column section was increased 2 in. in each direction to provide an enough clear cover over the mechanical splices. The compression strength of the concrete for the spliced section was 4ksi.

The repair involved cutting of the bent bars; however, leaving sufficient enough bar length to permit installation of the mechanical splice as shown in Figure 5.40. Figure 5.48 shows a bar protruding about 3 ½ in from the concrete. Details of the installation are presented in Appendix B.

After removing the bent bars, the mechanical splices were located on the protruding bars as shown in Figure 5.48. The new bars and column ties were assembled with the bottom mechanical splices in place at the column base. The mechanical splices at top of the new bars were located to engage the bar protrusions from the column. Bolts in the splices were tightened and the columns ties are spaced as required. Details of those steps are shown in Appendix B.

**3.5in**

*Figure 5.48 Installation of replacement bars using the Short Mechanical Splices*

A special form was constructed with a chute for casting the concrete (Figure 5.49). No special additive was used, however, the maximum size of aggregate was 1/2in diameter and a high slump was specified (6 ½ in.) in order to place the concrete and consolidate it around the reinforcement and splices. Figure 5.49-left shows the columns prior to the formwork application and the right image shows the concrete placement. The top of the form was 1in above than the bottom of the existing concrete. In this way, the new concrete could be placed without leaving a gap. The strength of concrete was 4ksi. Details are in Appendix C.

*Figure 5.49 Column with the Mechanical Splices Applied (left) and placement of concrete (right)*

A fillet of repair mortar was applied at the top of the new concrete to improve the appearance of the retrofitted column (Figure 5.51).
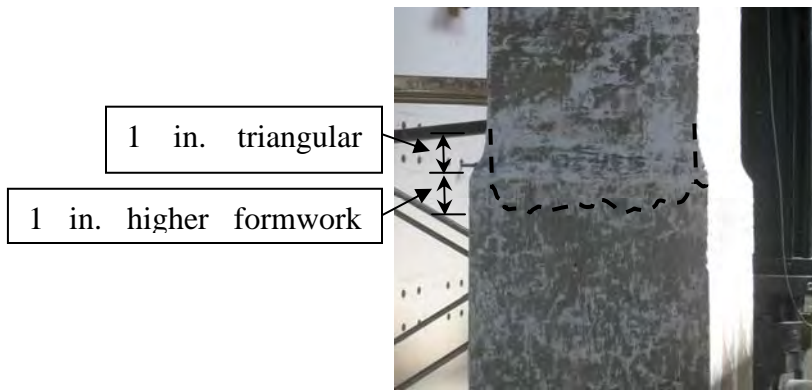
*Figure 5.50 Fillet made with repair mortar*
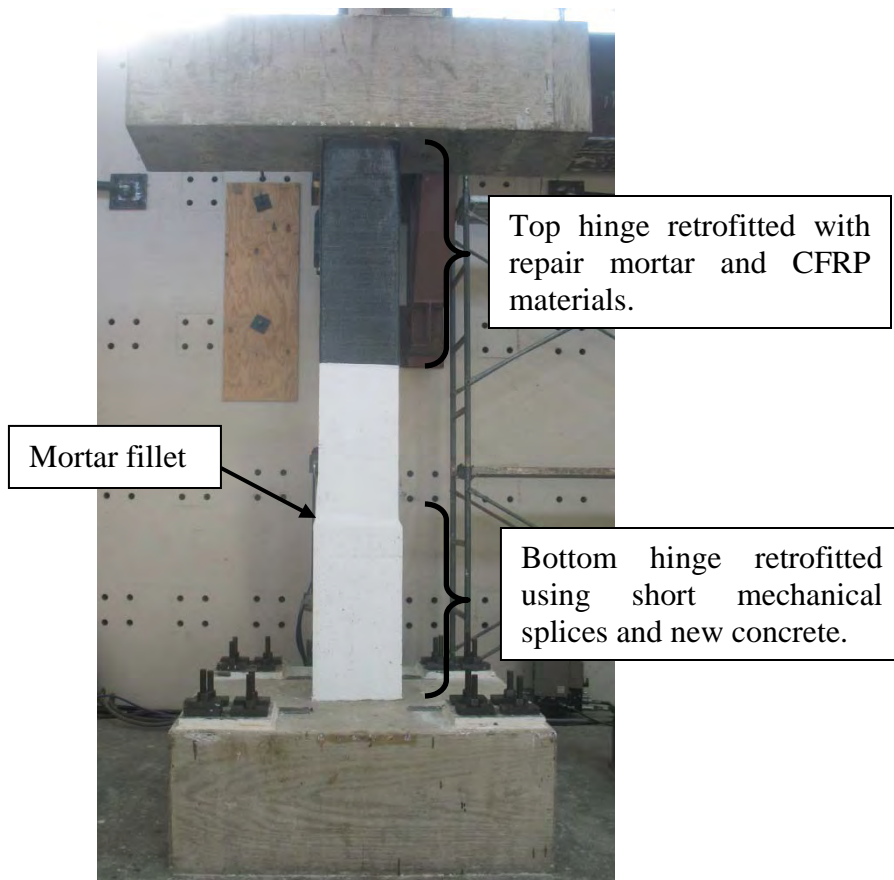


*Figure 5.51 Column retrofitted*

### 5.4.5 Laboratory Test of RC-1R

#### 5.4.5.1 *Test Setup for the test and Data Acquisition System*

Figure 5.52 shows the repaired specimen after installation into the L-frame.



*Figure 5.52 Test Setup for RC-1R*

#### 5.4.5.2 *Instrumentation for the Test*

Linear and wire potentiometers were placed to measure the global and local deformation of the column. External strain gages were installed on the CFRP sheets. Internal strain gages were installed to measure the strain of the short mechanical splices and the new longitudinal transversal reinforcement. Figure 5.53 shows the locations of the external linear and wire potentiometer used
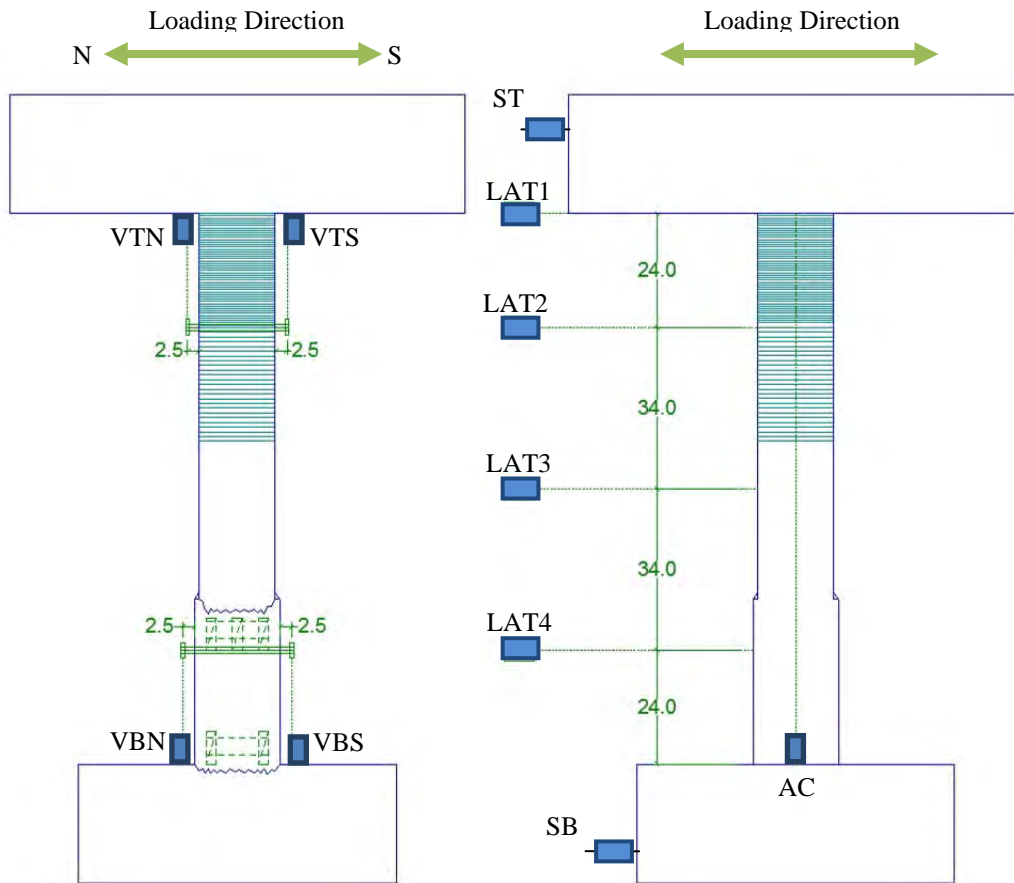
***Figure 5.53 Location of linear and wire potentiometer for local (left) and global deformation (right)***

Figure 5.54 shows the location of each strain gage for the internal reinforcement at the top of the column. The strain gages located on the longitudinal bars were located 2in above the base. The strain gage locations on the CFRP layers are shown in Figure 5.55. Those four gages were placed on the east side of the column. Finally, the strain gages installed on the reinforcement of the bottom of column are shown in Figure 5.56 and Figure 5.57. Gages were installed at the mid-height of the splices as shown in Figure 5.56 and Figure 5.57.
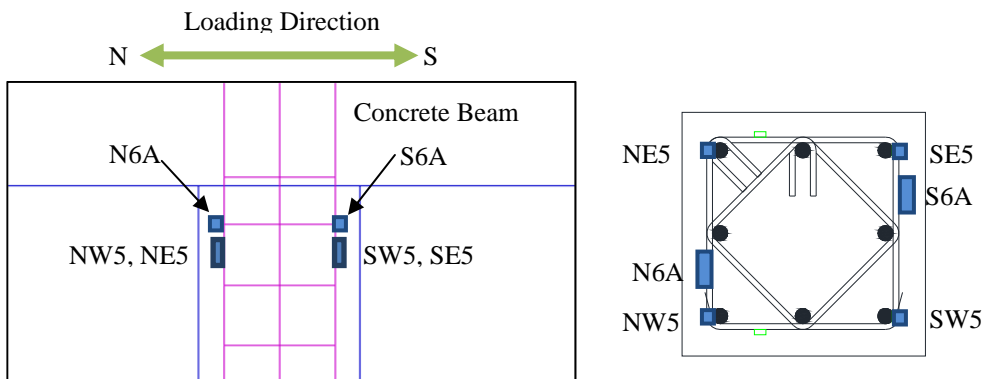
*Figure 5.54 Location of the internal strain gages at the top of the column*
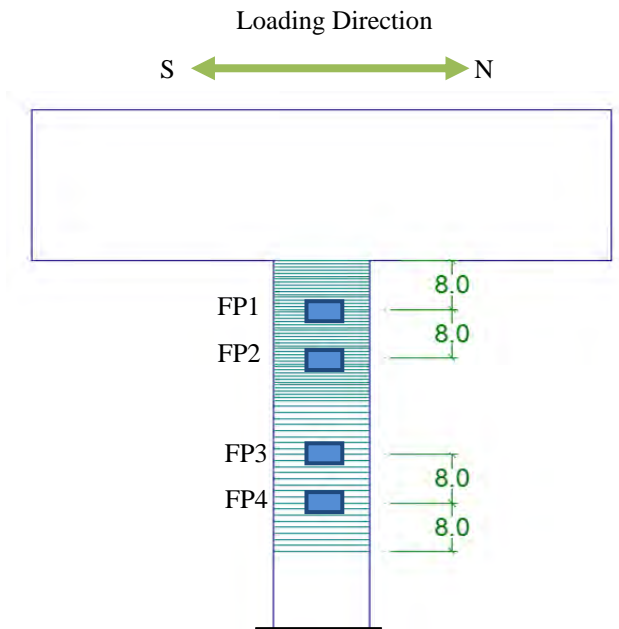


*Figure 5.55 Location of the external strain gages on the CFRP jacket*

154
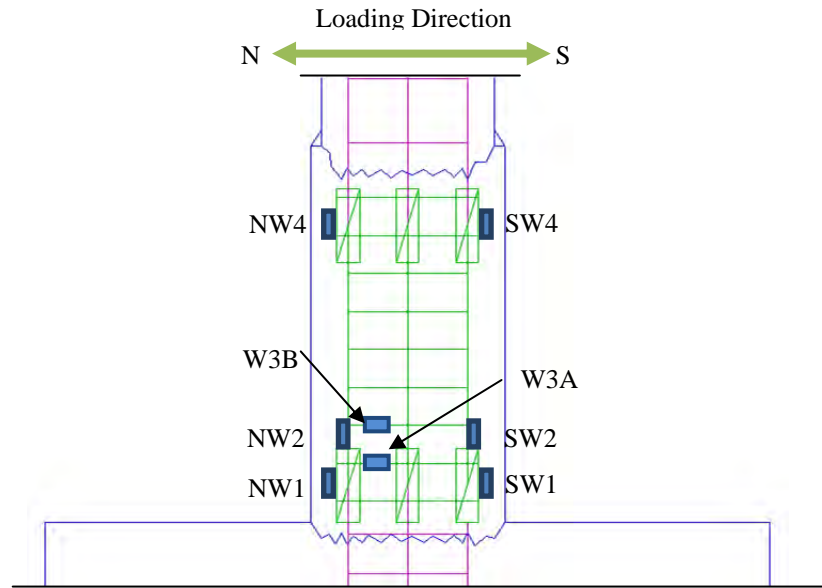
*Figure 5.56 Location of the internal strain gages for the West face of bottom of the column*
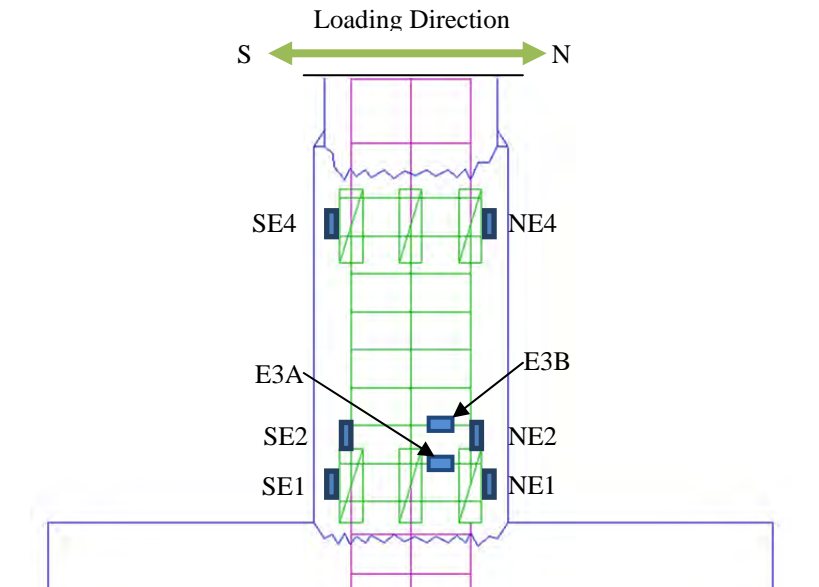


*Figure 5.57 Location of the internal strain gages for the East face of the bottom of the column*

155

The Vision System was used to measure the local deformation on this test. Targets were spaced at 3 in. on the entire west surface of the specimen. Details of the Vision System method are explained in Appendix H.
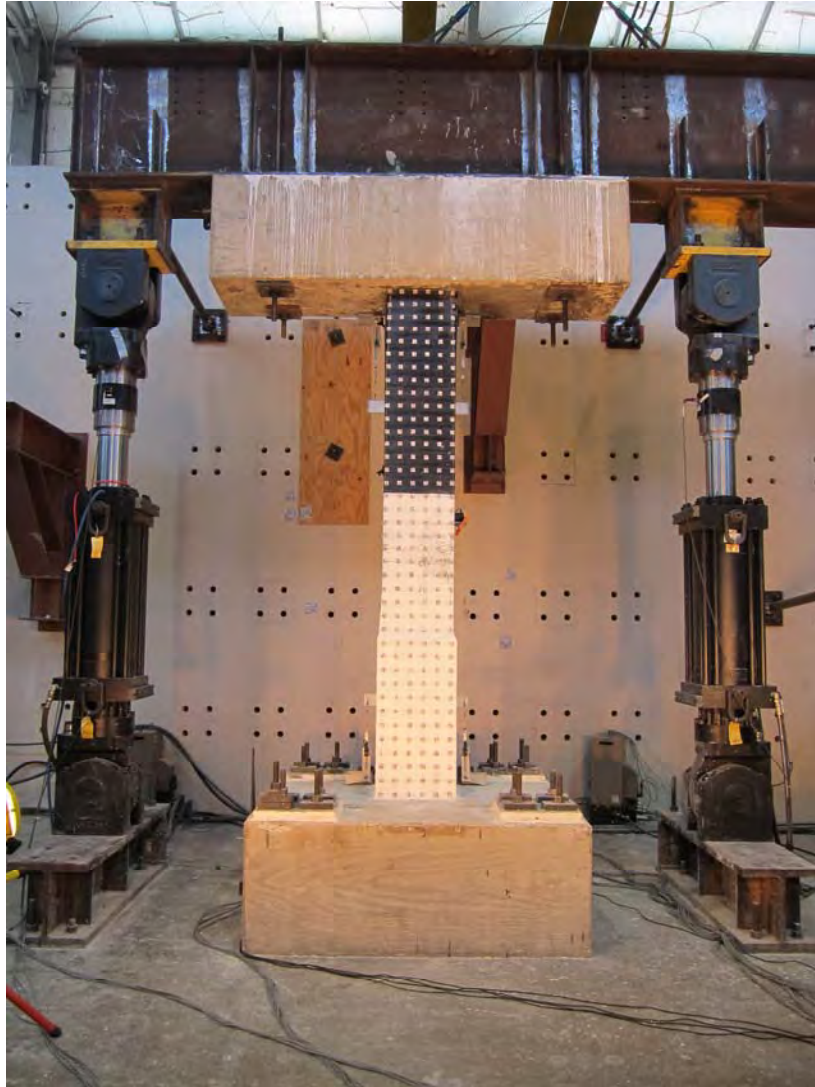


*Figure 5.58 Targets for Vision System placed on specimen*

5.4.5.3  *Protocol of load*

Loading was controlled by displacement. In the cyclic loading test, specimen RC-1R was subjected to cycles of lateral displacements at drifts shown in Figure 5.15 and finally was pushed north until the column could not sustain the axial load applied. Afterwards the axial load applied to the column was reduced in order to measure the lateral load capacity of this column with lower axial load. The result of this last procedure is explained in Appendix G. Protocol of load was following the procedures of FEMA 461.
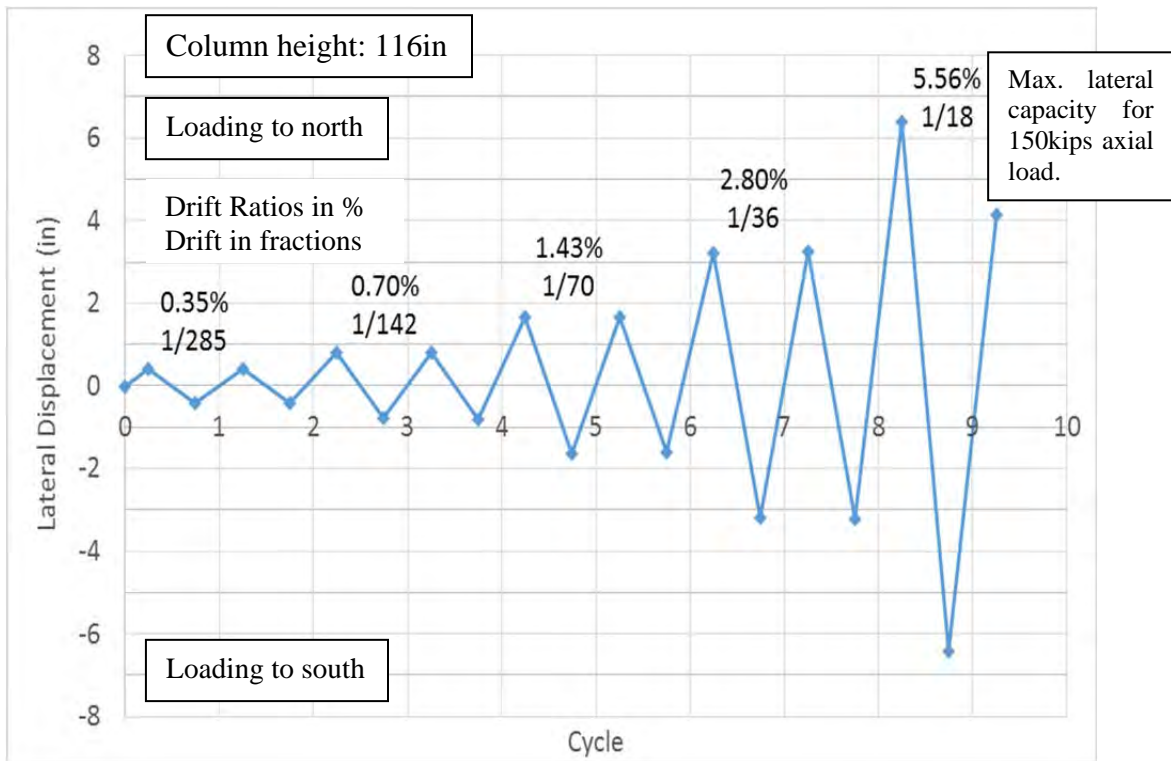


*Figure 5.59 Load cycling for specimen RC-1R*

### 5.4.5.4  *Test Results – Global Behavior of the RC-1R*

The test for RC-1R began with the application of a 150kips axial load to the column.

The behavior of the member finished was nearly linear up to lateral displacement of 1.66in or 1.43% drift ratio (6th hysteretic cycle). The shear force to the North was 46.85kips, and to the South was -38.55kips (Figure 5.60). The strain of the new bars on the bottom of the column reached yield value for Grade 60 steel.
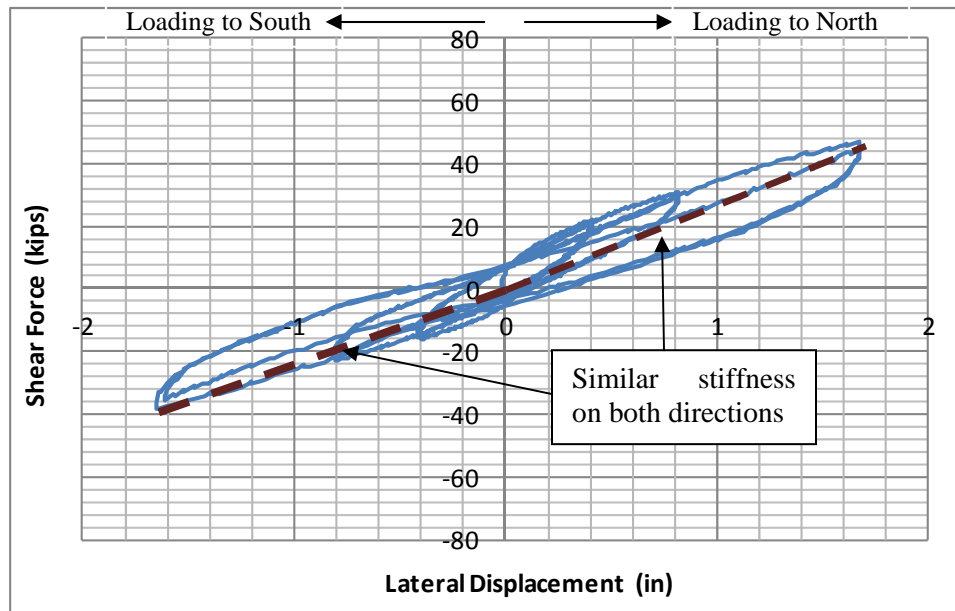


***Figure 5.60  Shear force vs. Lateral displacement of the first 6 hysteretic cycles***

The maximum shear capacity was reached in the 6th and 7th cycles of the column: 60.9kips North and 56kips South. The lateral deformation was 2.80% drift ratio in both directions. The column dissipated more energy in 6th hysteretic cycle than the 7th cycle. There was some degradation of shear capacity in the 7th cycle. (Figure 5.61)

158
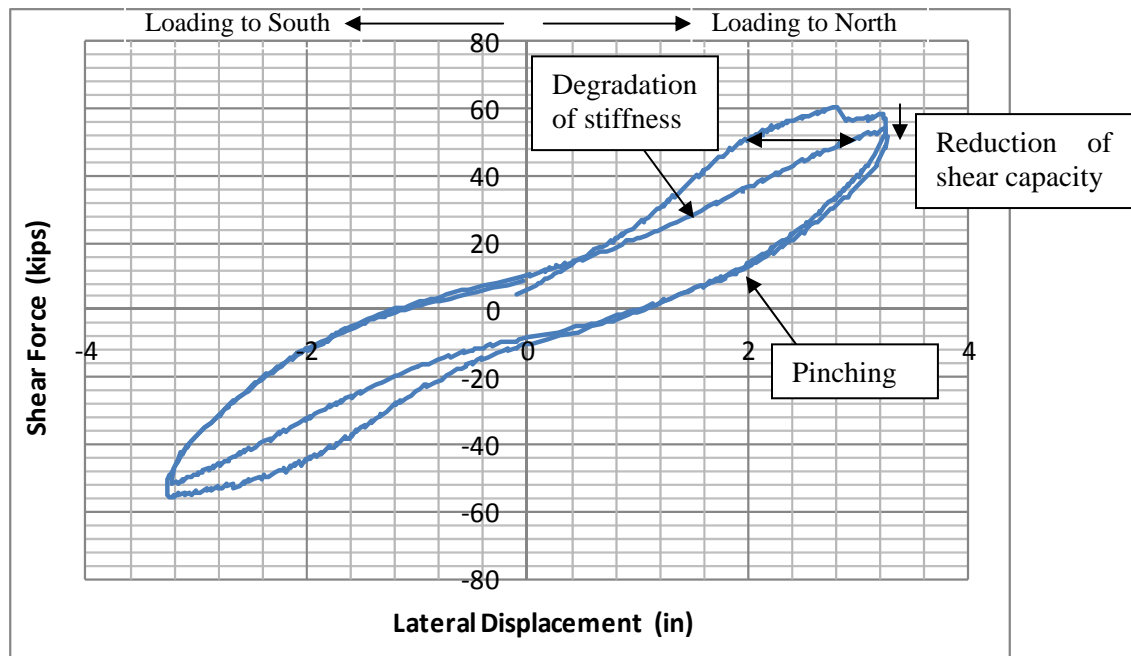
*Figure 5.61 Shear force vs. Lateral displacement on the 6th and 7th hysteretic cycle*

Degradation of stiffness and strength was seen in the $8^{th}$ cycle (Figure 5.62) deformation (5.5% drift ratio) both directions. Pinching effect seemed to be appeared for pushing loading when the lateral load was dropped as can be seen in Figure 5.62. Figure 5.63 shows the column deformed under loading to north (left) and south (right) directions. The cracks appeared near the bottom became wider, while on top the CFRP started to debond.
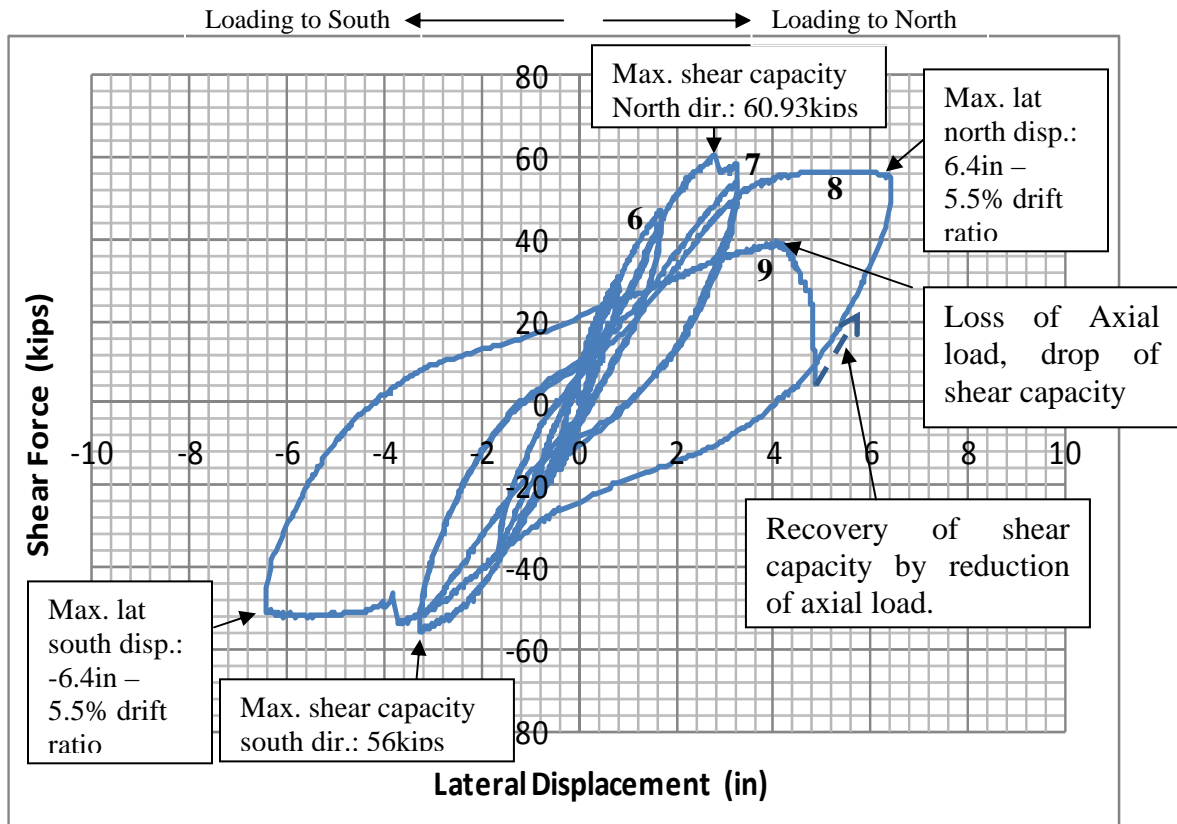
*Figure 5.62 Load cycling for specimen RC-1R*
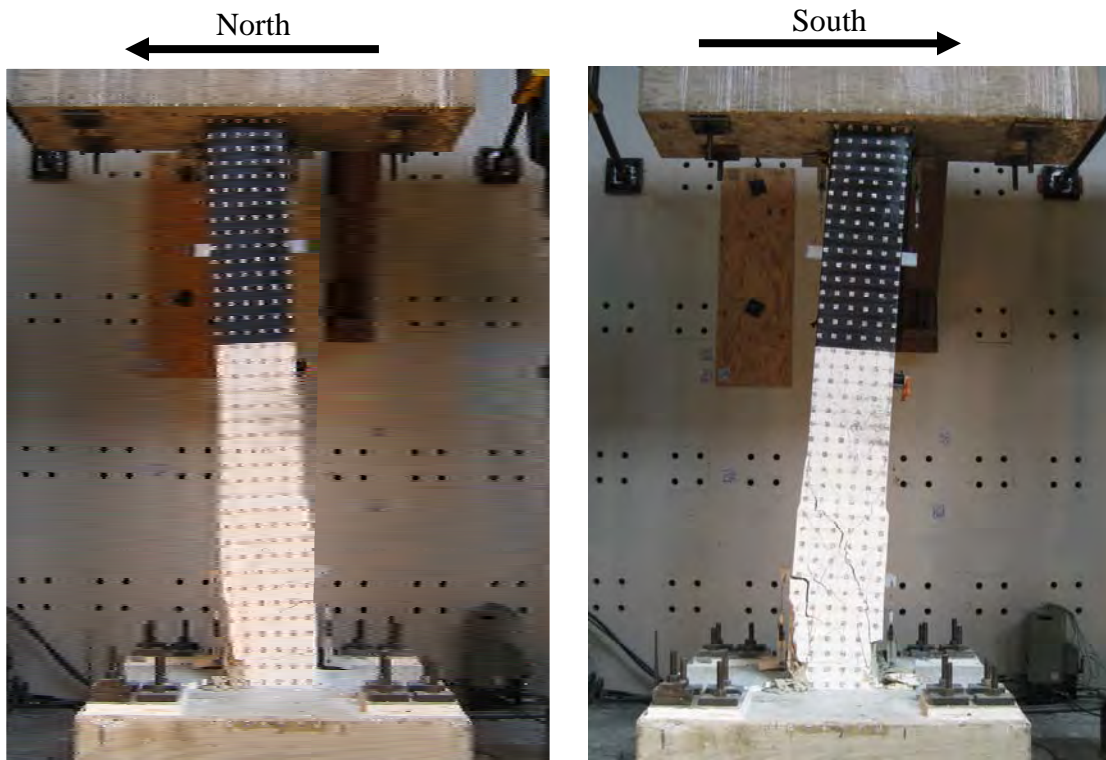
*Figure 5.63 Condition of specimen RC-1R after pushing (left) and pulling (right)*
*displacement applied for 1/17drift ratio*

The specimen was not able to sustain the 150kips axial load in the 9th cycle and the test was stopped when the lateral load dropped by 30kips. Shear failure developed in the existing concrete above the mechanical splices zone as can be seen in Figure 5.64.
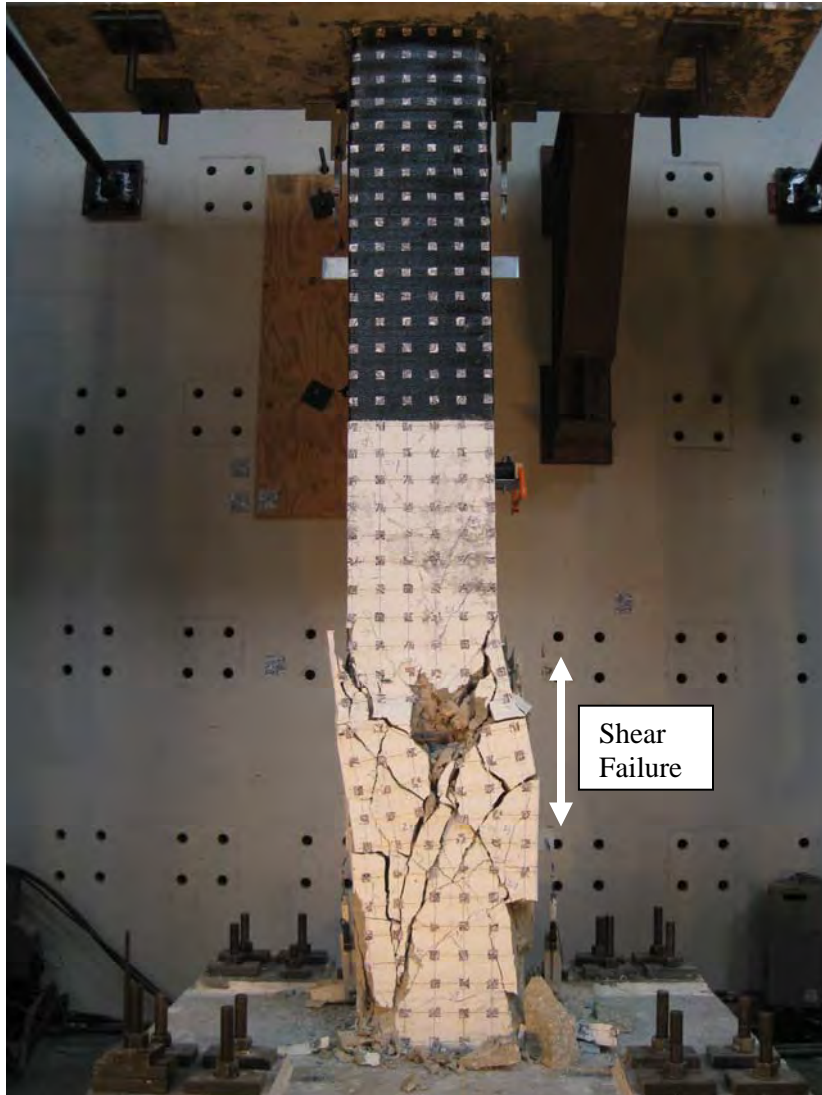
***Figure 5.64 Condition of RC-1R at the drop of the axial load.***

The axial load was reduced in order to increase the lateral deformation. Results of these adjustments are explained in Appendix G.

### 5.4.5.5  *Behavior of Bottom Hinging Region*

Flexural cracks began to appear in both faces when a lateral displacement of 0.8in (0.70% drift ratio) was applied to the specimen.

Yielding of the new longitudinal reinforcement occurred at 1.66in lateral displacement (1.43% drift ratio) in cycles 5 and 6. Table 5-1 shows the values for compression and tension strains. No significant strains were measured on the mechanical splices.

**Table 5-1 Strains values at peak lateral displacement for 5$^{th}$ cycle in bars located in each corner of bottom of column**

|  | Pushing toward North | Pulling toward South |
| --- | --- | --- |
| NW2 | -0.0010 | 0.0028 |
| NE2 | 0.0000 | 0.0000 |
| SW2 | 0.0032 | -0.0010 |
| SE2 | 0.0027 | -0.0011 |

Damage after loading to north and south direction for the 5$^{th}$ and 6$^{th}$ cycle is shown in Figure 5.65. Flexural cracks 0.025in wide on the north and south face propagated through the column, and diagonal cracks on those faces indicated a shear distress. The shear distress began to form above the new concrete (4ksi) in the existing concrete (3ksi). Additionally large cracks (0.03in width) appeared at the base of the column (cold joint between the foundation and the new concrete in the column)

*Figure 5.65 Crack pattern appeared at 1.6in lateral deformation (1.43% drift ratio)*

In the 8th cycle, crack widths increased and new diagonal cracks propagated through the core of the column. Spalling of the cover was observed at the north and south faces of the bottom of column.

In the 9th cycle, the test was stopped because the column lost the capacity to carry 150kips axial load. Concrete crushed above upper splices and the cover spalled at this level as shown in Figure 5.66.

Figure 5.67 shows the response in shear force and lateral displacement at the mid-height of the column.
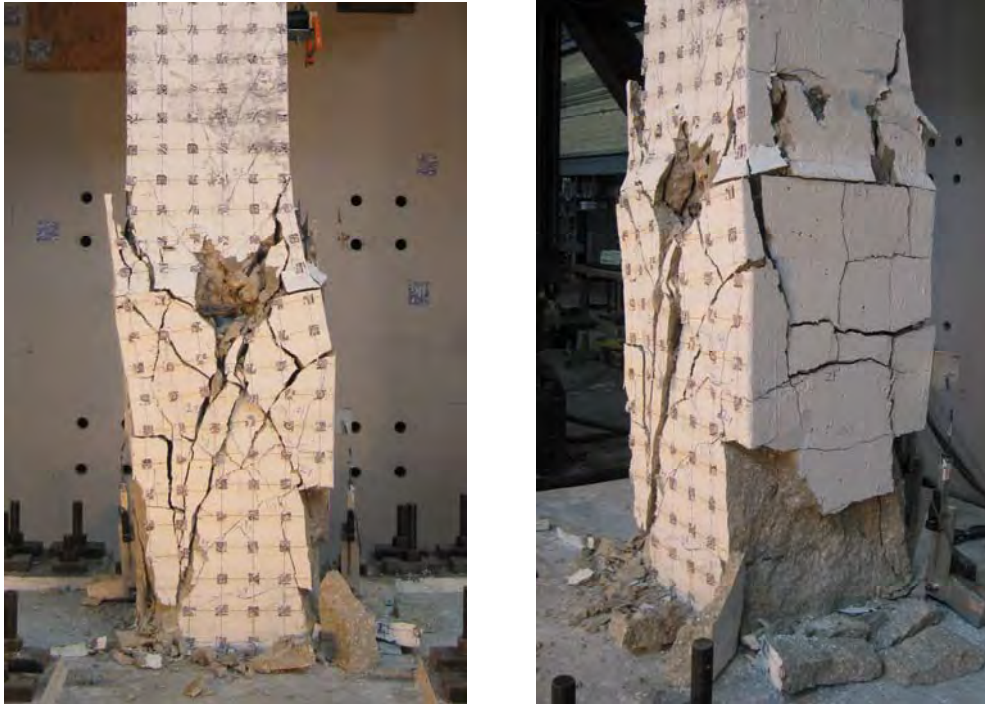
*Figure 5.66Condition of specimen at failure: cracks pattern producing the spalling of the 2in cover*
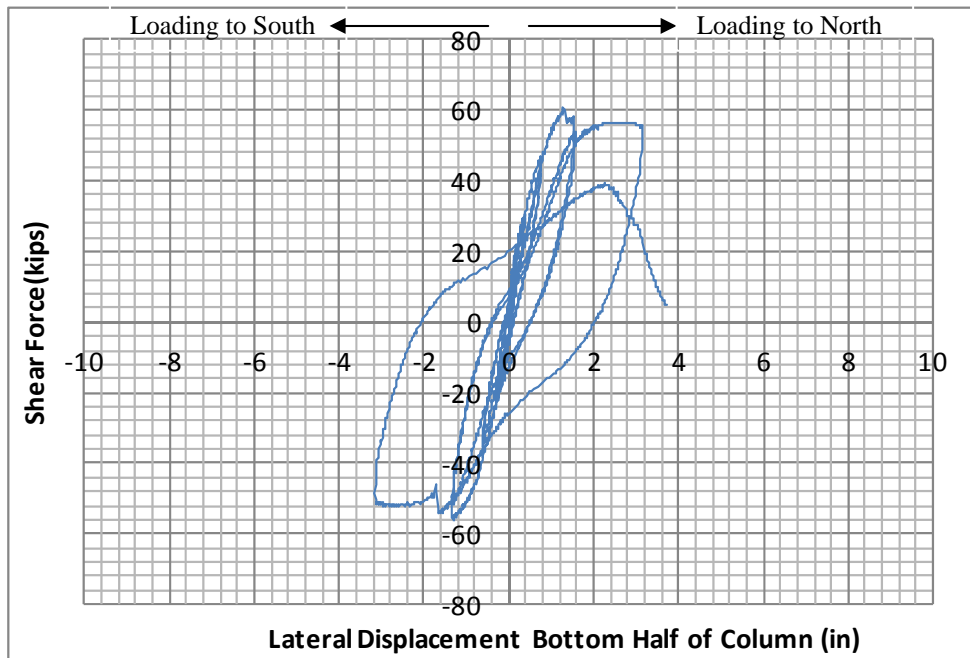


*Figure 5.67 Shear force vs. Lateral Deformation at mid-height of column*

165

The short mechanical splices behaved similar to the axial cycle load tests of the splices explained in Chapter 3. For tension stress the splices behaved linearly however for compression the splice behaved nonlinearly as Figure 5.68 and Figure 5.69 show. Both the superior and inferior set of splices shown similar responses under the axial load induced through the flexion by the lateral load applied to the specimen. It can be also appreciated that the strain for the inferior set (NW1 and SW1 in Figure 5.68 and Figure 5.69) is larger than the superior set (NW4 and SW4). Since the flexural moment is biggest at the base of the column, it was expected to have larger strain for the splice located in the inferior level.
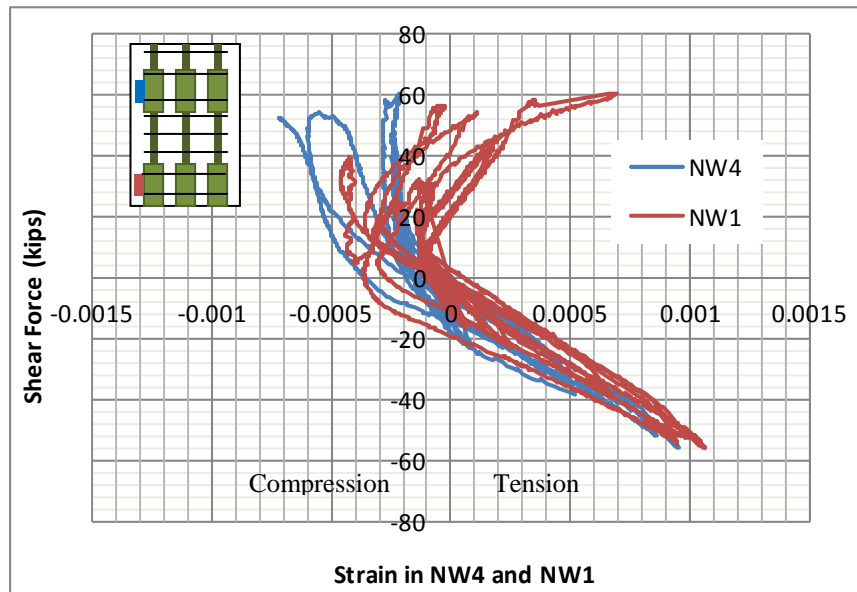


*Figure 5.68 Strain in upper and lower splices (north-west corner)*
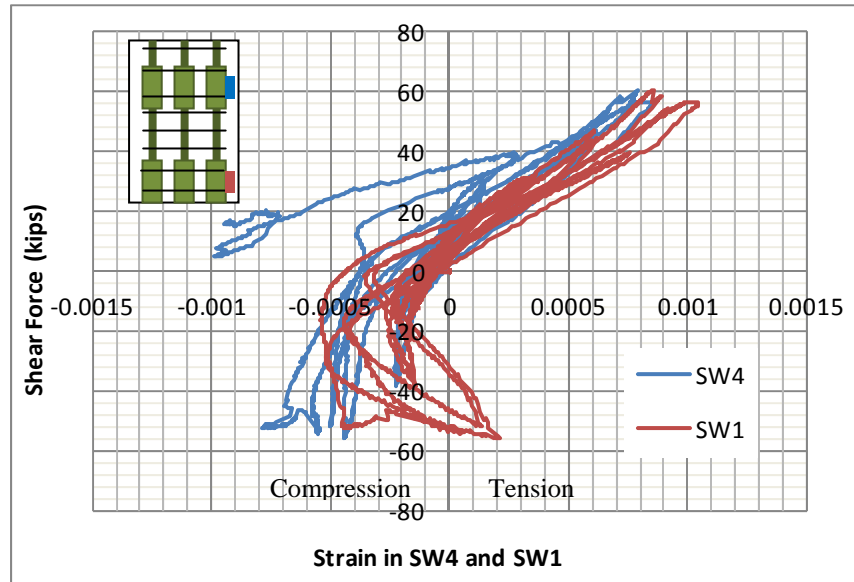
*Figure 5.69 Strain in upper and lower splices (south-west corner)*

The new longitudinal bars reached the capacity of the strain gages (strain > 0.009) at the peak of the 5th cycle as shown in Figure 5.71. For the new longitudinal bars located in the south face, it is seen a drop of strain for compression strain (Figure 5.71 left). Those longitudinal bars worked under tension stress since the neutral axis at that level of the column (7in above the base) moved to the south, making all the bars in the section work for tension stress and having the 2.1in concrete cover working under compression stress. The transverse reinforcement around the mechanical splices and new longitudinal bars confined the core and allowed the column to reach large ductility. Behavior of the new longitudinal reinforcement is shown in Figure 5.73. Those bars were in tension through the loading history with strains increasing as the lateral deflection increased. The largest strain measured was 0.0011

.

167
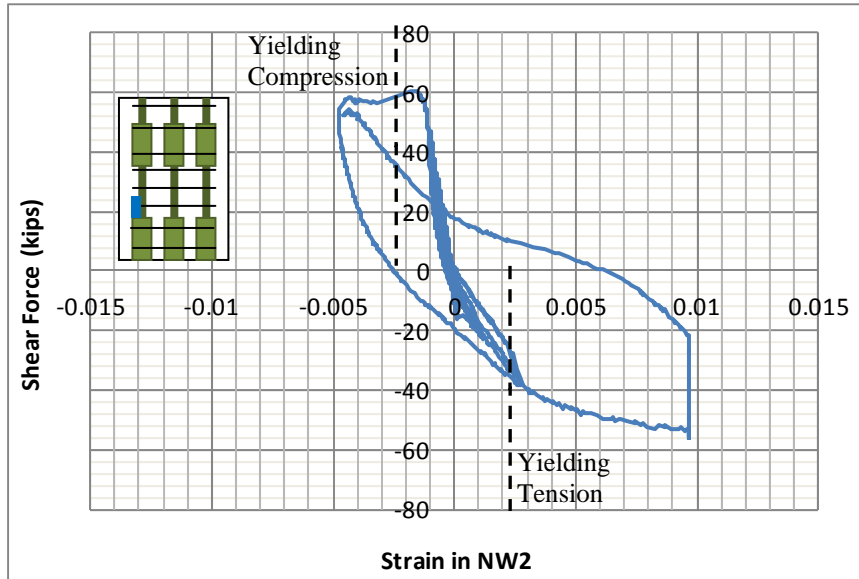
*Figure 5.70 Strain in new long. reinforcement at north-west corner*
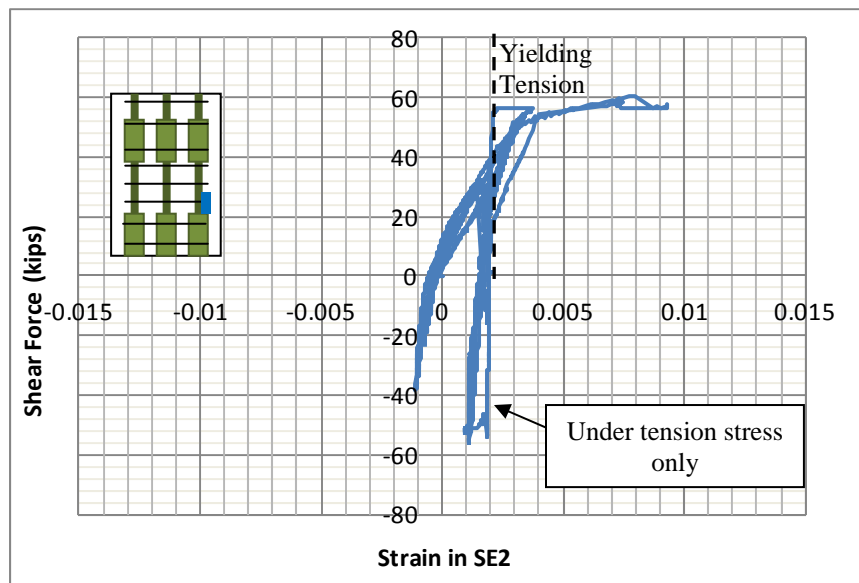


*Figure 5.71 Strain in new long. reinforcement at south-east corner*

168
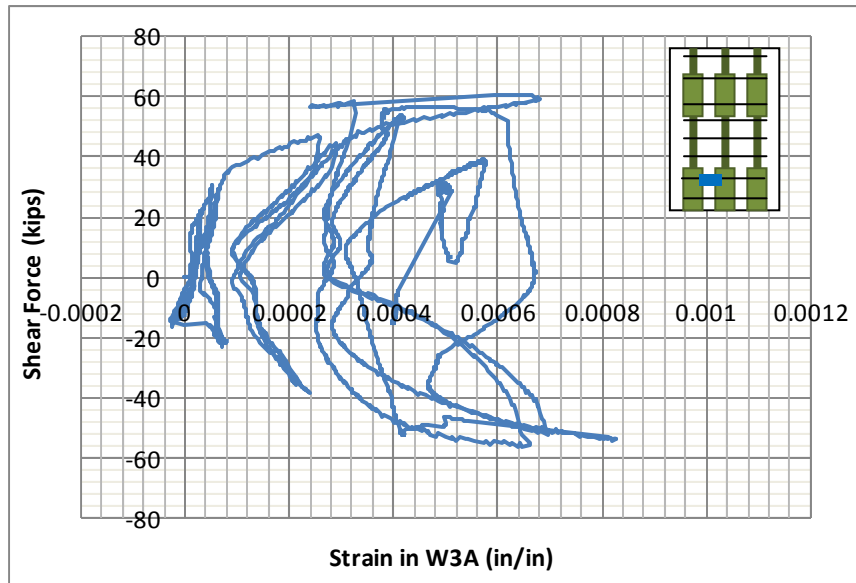
*Figure 5.72 Strain measured in confinement on inferior set of splice – west side of column*
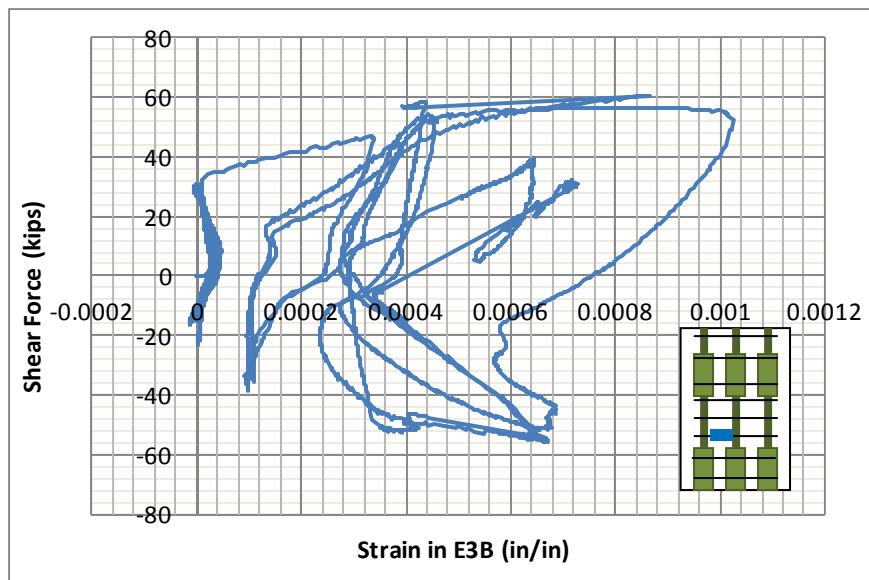


*Figure 5.73 Strain measured in confinement on new longitudinal reinforcement – east side of column*

5.4.5.6  *Behavior of Top Hinging Region*

On the 5th cycle, the strain on the original longitudinal bars reached or exceeded the yielding value for Grade 60 steel (0.0021). Table 5-1 shows the values of compression and tension strains.

*Table 5-2 Strain values at peak lateral displacement for 5th hysteretic cycle for bars located in each corner of top of column*

|  | Pushing toward North | Pulling toward South |
|---|---|---|
| NW5 | 0.0000 | 0.0000 |
| NE5 | 0.0023 | -0.0017 |
| SW5 | -0.0027 | 0.0019 |
| SE5 | -0.0030 | 0.0021 |

There was no observable damage after loading to north and south direction in the 5th and 6th cycles. However, during loading some pops were heard indicating debonding of some areas of the CFRP jacket. The 2 layer CFRP jacket was inspected by tapping on the surface. Hollow sounds confirmed that debonding had occurred. The 1 layer CFRP jacket remained bonded. A large lifting was observed at the column and top beam interface.

Although force and stiffness degradation occurred in 8th cycle (6.4in lateral deformation and 5.56% drift ratio); the CFRP jacketing system at top of the column performed well without rupture of anchor or jackets. In the 9th cycle when the specimen lost axial capacity, the CFRP jacket remained intact.

Figure 5.75 shows shear force vs. lateral displacement of the top half of the column. This response of the top of column indicates that it did not contribute to loss of axial load capacity.

170

*Figure 5.74  Good condition of CFRP sheets and anchors after the 9ᵗʰ hysteretic cycle*
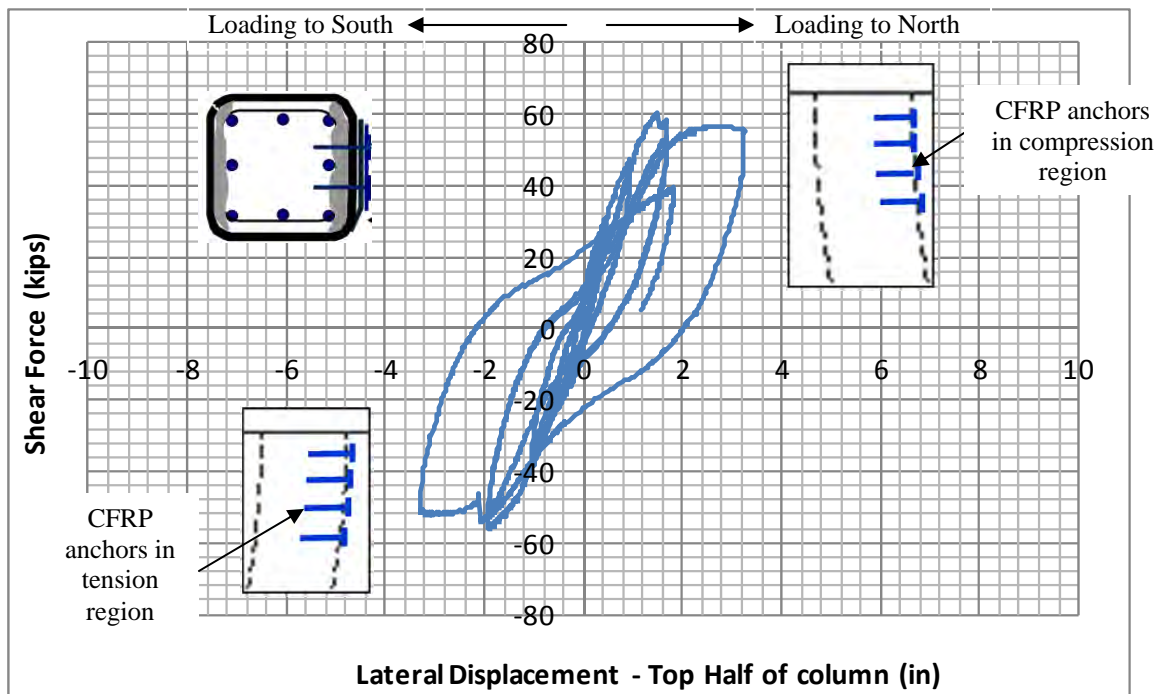


*Figure 5.75 Shear force vs. Lateral Deformation of top half of specimen*

171

Figure 5.76 shows the envelopes of the behavioral response for top of column when it was loaded to north and south directions. It can be noticed that the Loading-to-North curve is stiffer than Loading-to-South. The reason is the presence of the CFRP anchors in the south face of the specimen. When the specimen is loaded to north, the CFRP anchors is in the compression region of stress, the anchors provided compression strength capacity. However, the specimen is loaded to the opposite side, the CFRP anchor is in the tension stress region. The anchors do not provide important tension capacity to the section.
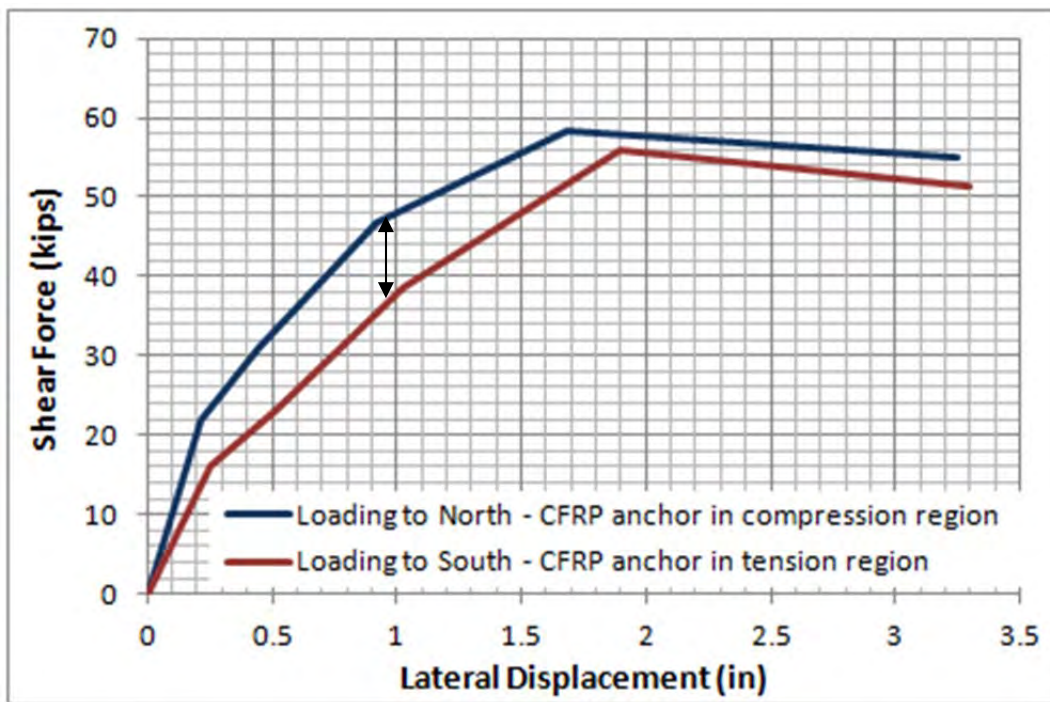


*Figure 5.76 Envelopes curves of RC-1R Top Half for loading to North and South*

The strains measured on the CFRP jacket are shown in Figure 5.77 and Figure 5.78. The maximum strain reached on the 2 layers CFRP jacket was 0.0038 (strain gage FP1); and 0.0014 on the 1 layer CFRP jacket well below the fracture strain of the CFRP. The larger strain in the 2 layer jacket indicates that the CFRP was providing both confinement and shear capacity in that region. Since there was extensive cracking in the top part of column, the concrete contribution to shear was reduced and the CFRP and steel transverse reinforcement had to carry the applied shear. In the 1 layer CFRP jacket zone, cracks there were fewer the CFRP did not contribute as much to shear capacity as indicated by the lower strains in the 1 layer jacket.
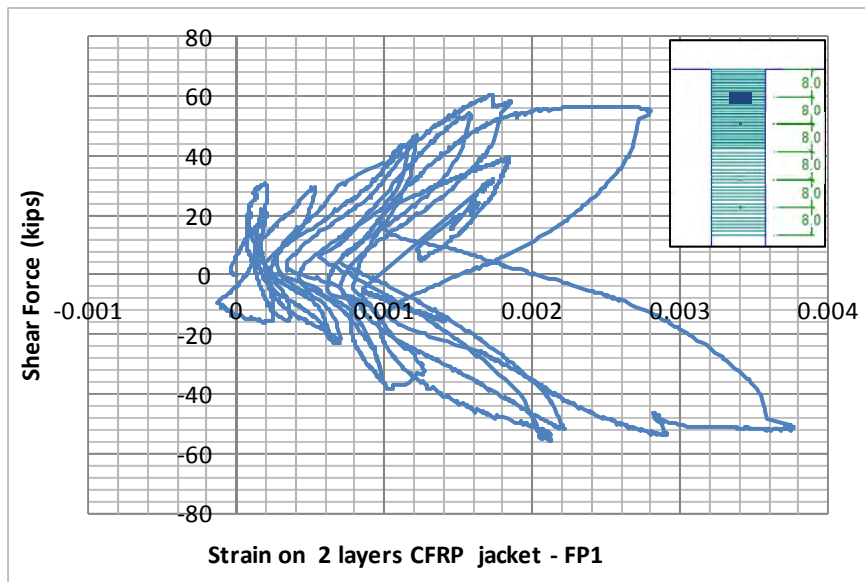


*Figure 5.77 Strain measured 8in bellow the top edge of column*

173
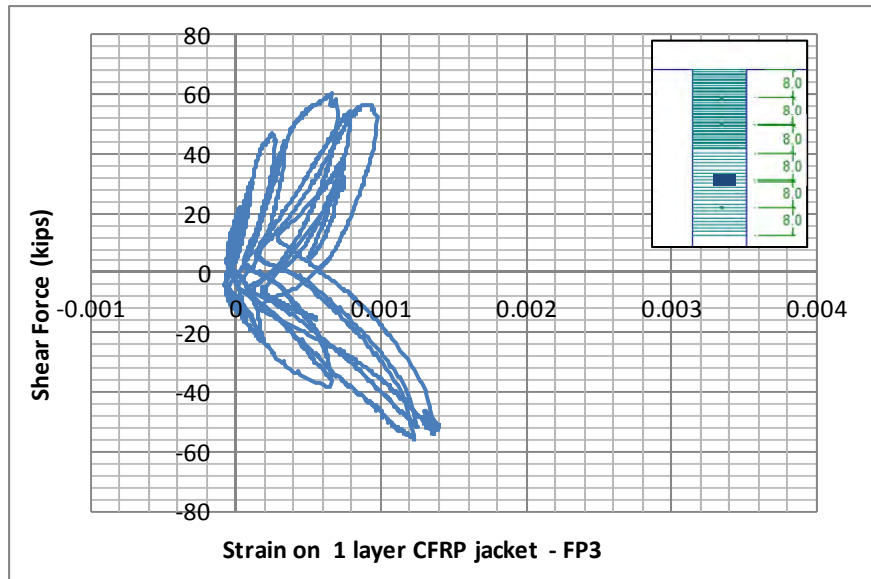
*Figure 5.78 Strain measured 32in bellow the top edge of column.*

Strains in most of the longitudinal bars in the top of the column yielded as shown in Figure 5.79 and Figure 5.80 where strains are plotted against the applied shear on column. The portion of the CFRP anchors into column core provided flexural capacity indirectly since those anchor helped confined the core. A flexural hinge at top of column formed after the formation of the shear hinge at bottom. The tie in the north face of the column reached a strain 0.0014 (Figure 5.81), however in the south face, the tie yielded reaching strain of 0.0042 (Figure 5.82).
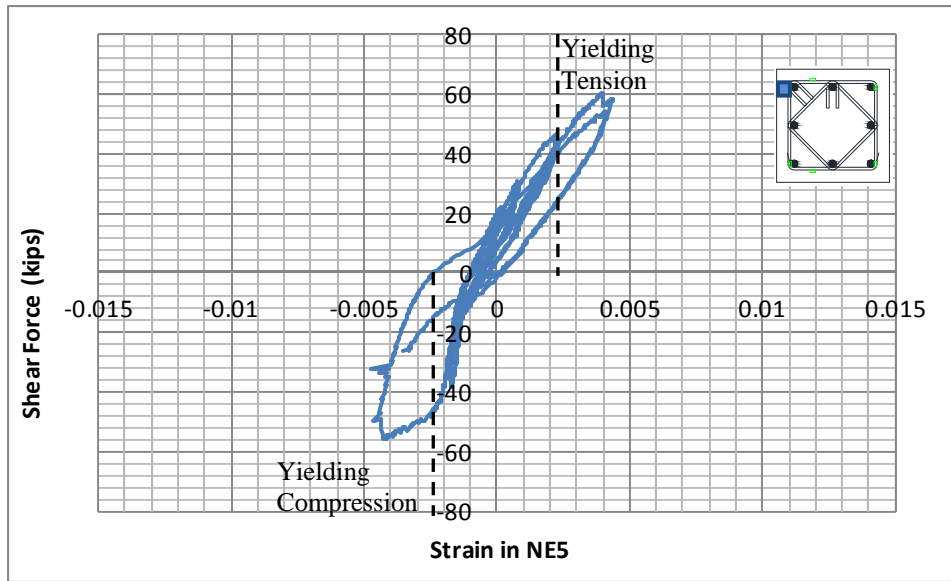
*Figure 5.79 Strain on the longitudinal bar at the top of column – north-east corner*
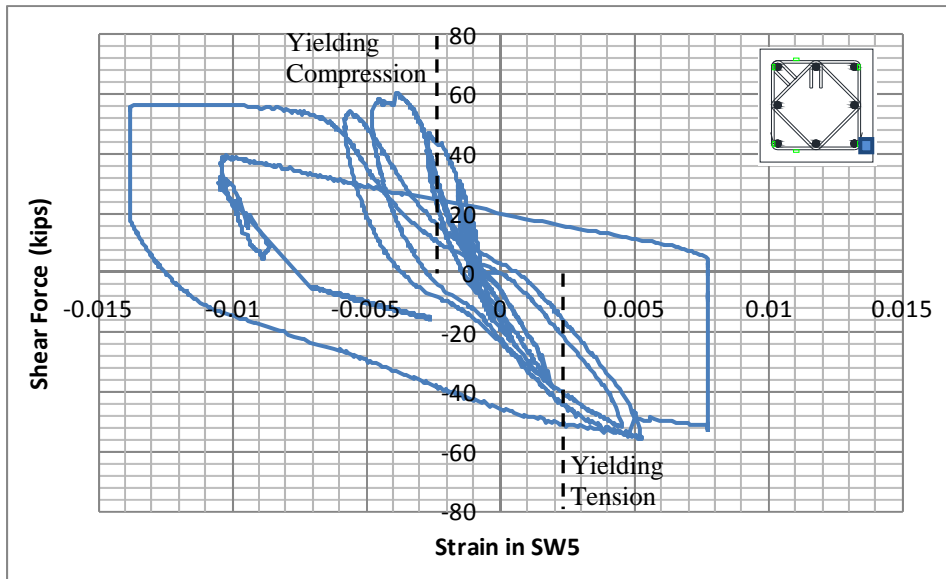


*Figure 5.80 Strain on the longitudinal bar at the top column – south-west corner*

175
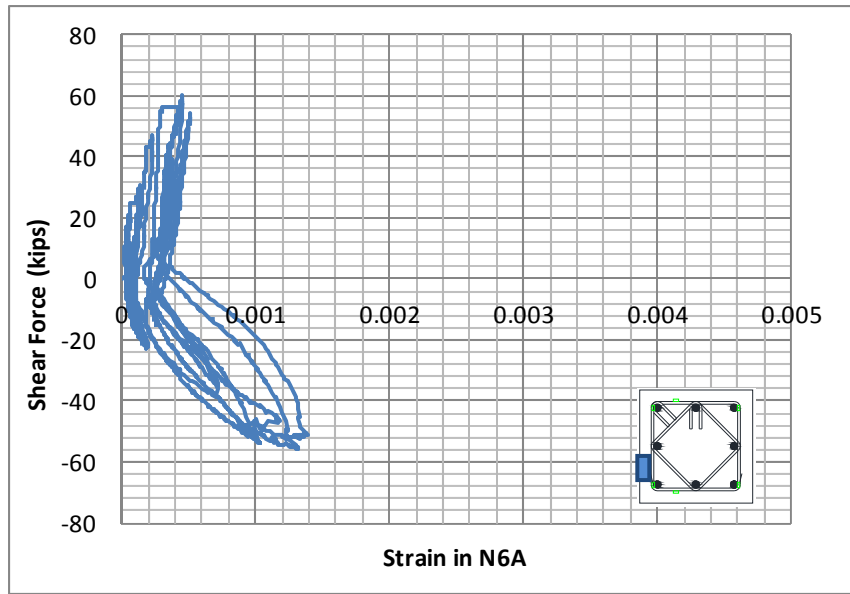
*Figure 5.81 Strain measured in the tie - north face*
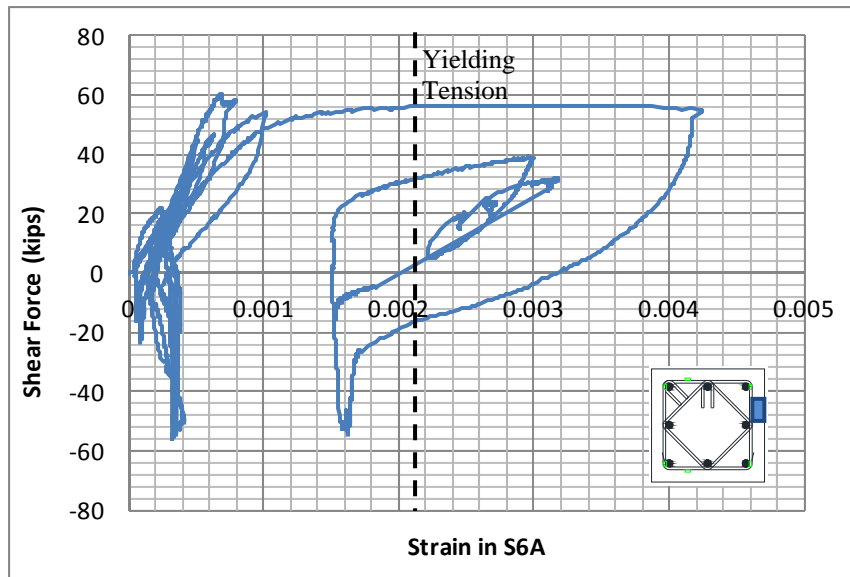


*Figure 5.82 Strain measured on the tie - south face*

176

## 5.5 Column retrofit procedures for RC-2

### 5.5.1 Overview of RC-2 retrofit

Figure 5.83 shows the column RC-2 at 3.6in lateral deformation. The column exhibited a double curvature with an inflection point near mid-height. A horizontal line represents the level of the inflection point.
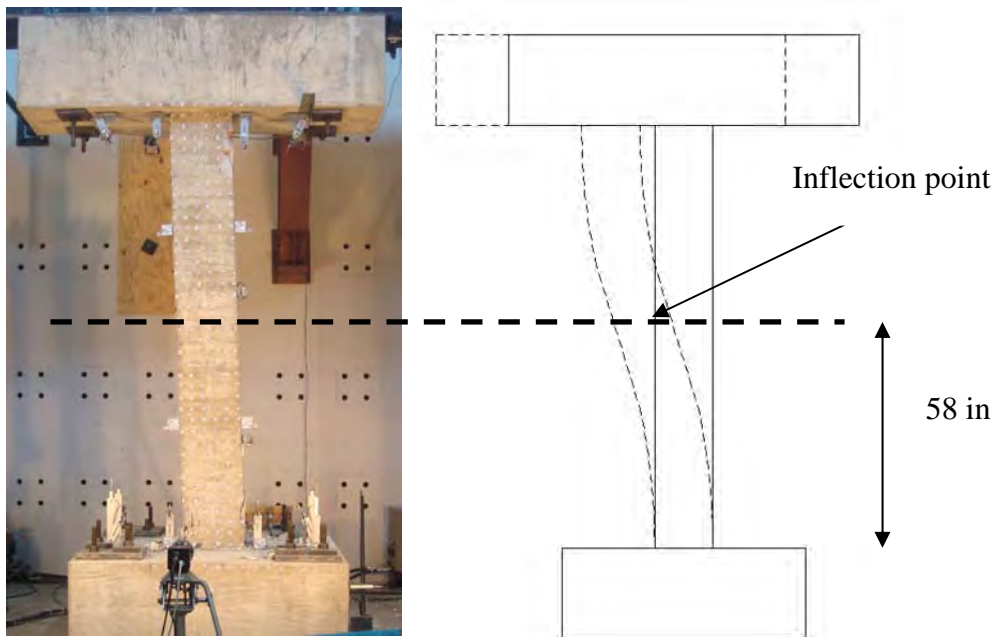


*Figure 5.83 Inflection Point*

The column was cut into two parts to be tested as cantilever columns by applying lateral load at the mid-height of the original column. One of the half-columns was repaired using long mechanical couplers described above and the other using shorter couplers. The half column retrofitted using short mechanical splices was named RC-2R-SMS, and the second half column which used the long mechanical splices were named RC-2R-LMS.

177

The yielded bars, which buckled and bent during the test RC-2, were removed and replaced with new longitudinal bars connected by the mechanical splices as shown in Figure 5.84. The new tie configuration in the region where the bars are coupled will have 135° hooks as recommended for constructions in high seismic zones. The space between the ties was decreased from 6in to 3.5in following the provisions in Chapter 21 of ACI 318.
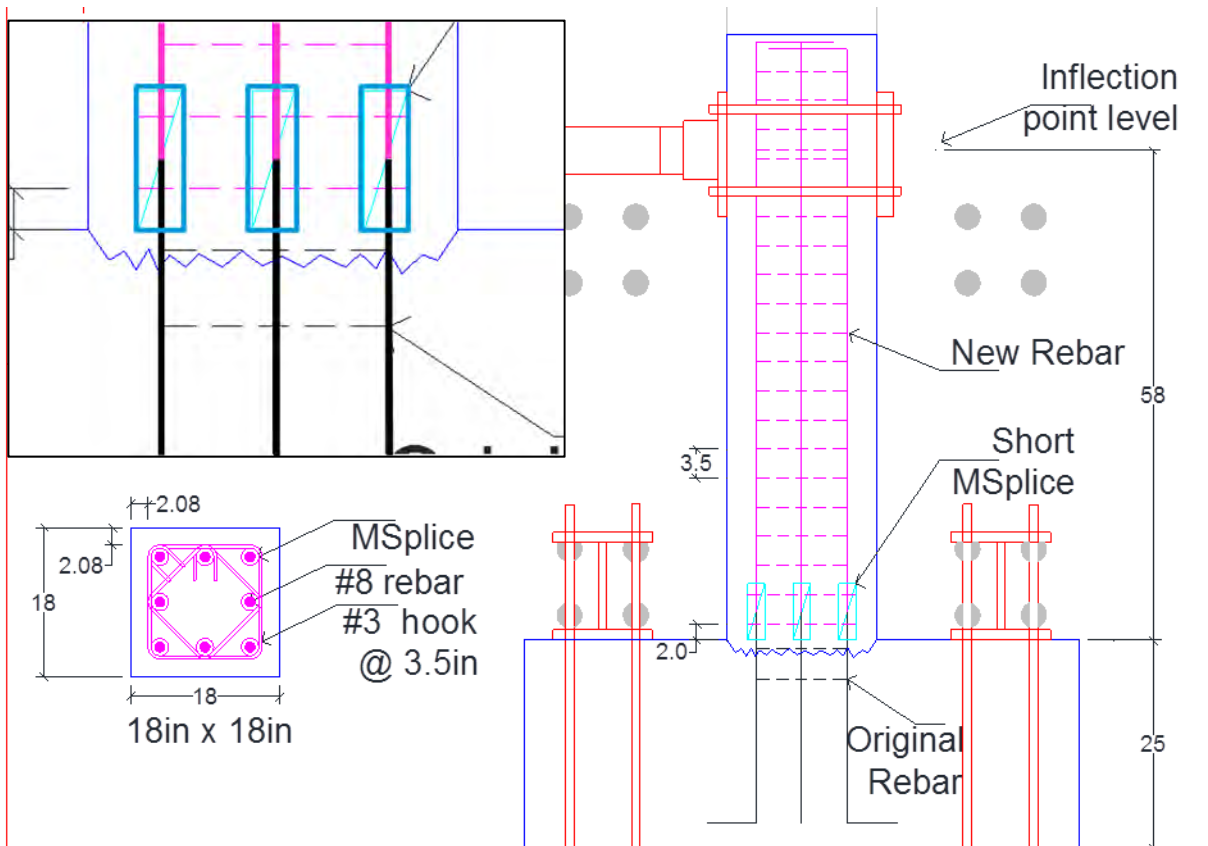


*Figure 5.84 Retrofitting using mechanical splices*

### 5.5.2 Preparation of the bottom and top hinge zones

The existing damaged column from test RC-2 was removed leaving only the base and the top beam.

For the specimen RC-2R-SMS (bottom hinge of RC-2), a 3.3 in. of bar protruded from the concrete for installing the short mechanical splice (6.8 in. length). As shown in Figure 5.85, removal penetrated into the base where there was less damage to the concrete and to have a enough space to manipulate the impact wrench for tightening the splice's bolts. It was also necessary to remove the base concrete to get a straight length of bar for installing the mechanical splice. Buckling of the bars at the base left bent bars just above the column-base interface.

Long mechanical splices (10 in. length) were used to retrofit the specimen RC-2R-LMS (top hinge of RC-2). The buckled bars were below the bends in the bars and concrete was removed to leave a 5 in., protrusion for installation of the long mechanical splice Figure 5.86.
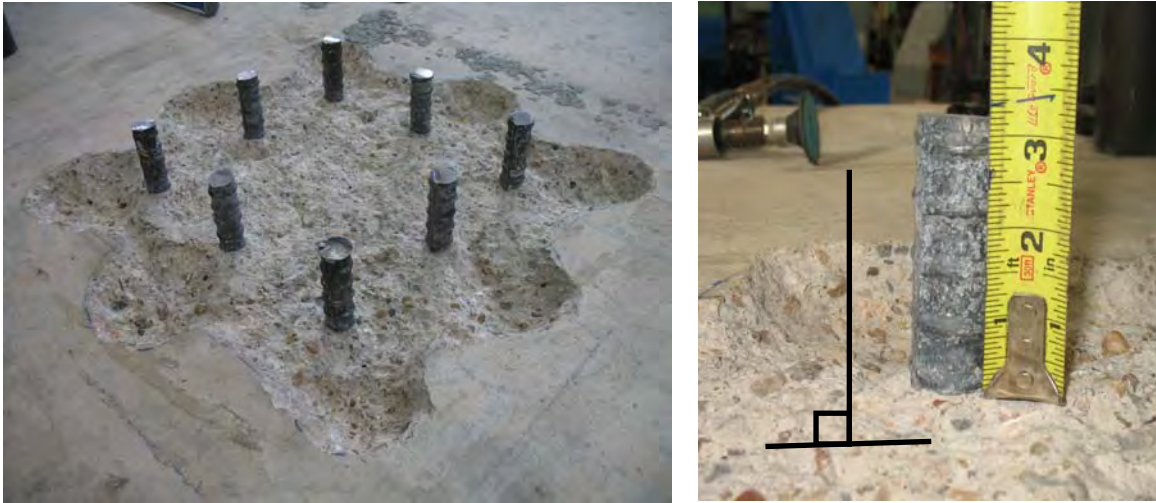
*Figure 5.85  Base with existing bars removed for the installation of the short mechanical splice*



*Figure 5.86  Top beam with the existing bar removed for the application of the long mechanical splice*

180

### 5.5.3 Application of the Mechanical Splices

The mechanical splices were placed on the protruding bars of each cantilever column as is shown in Figure 5.87 and Figure 5.88. The splice's bolts were tightened lightly by hand manually to orient the splices properly.



*Figure 5.87 Short mechanical splices placed on protruding bars*



*Figure 5.88 Long mechanical splices placed on protruding bars*

The bolts of the splices were removed leaving only the bolt on the bottom of the splice in order to locate easily the ties around the mechanical splices. Afterwards, the ties were installed; the longitudinal bars were placed into the mechanical splices. The end which goes into the splice was removed ground flat.

The rest of ties were then placed around the longitudinal bars at a 3.5in spacing (maximum space following the provisions of Chapter 21 ACI 318-2011). After the longitudinal bars were aligned properly (Figure 5.89), some bolts were replaced in the mechanical splice and tightened by hand. Those bolts did not interrupt the tie around the mechanical splice as Figure 5.89 also shows.
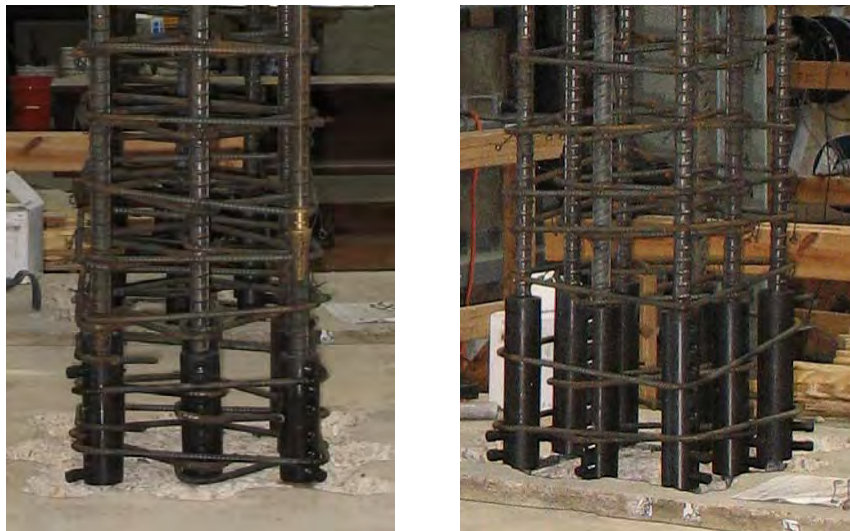


*Figure 5.89 Long mechanical splices placed onto the old bars*

The rest of the bolts were inserted into the splices. Finally, all the bolts were tightened using an impact wrench. As can be seen in Figure 5.90 and Figure 5.91, the region where the mechanical splices are located was very congested and ties had to be arranged so they would not interface with the bolts and the tightening procedure.

182

*Figure 5.90 Short mechanical splices completely installed for specimen RC-2R-SMS*



*Figure 5.91 Long mechanical splices completely installed for specimen RC-2R-LMS*

Figure 5.92 to Figure 5.94 show the formwork, concrete placement and finished replacement columns.



***Figure 5.92  Internal reinforcement and formwork for each specimen***

The strength of the concrete was 4.1 ksi. and had a slump of 3.5in. Details of the cylinder test results are in Appendix E.

*Figure 5.93 Placement the concrete into the formwork*



*Figure 5.94 Finished replacement columns RC-2R-LMS (left) and RC-2R-SMS (right)*

### 5.5.4 Laboratory Test of RC-2R-SMS

#### 5.5.4.1 *Test Setup*

One actuator was used to apply lateral cycle loads to the column. The actuator was connected to reaction wall. Figure 5.95 shows the test setup.

The base specimen RC-2R-SMS was attached to the strong floor with steel rods, as shown in Figure 5.95. Hydro-stone was placed between the base and the strong floor to improve friction bearing between the base and the lab floor.
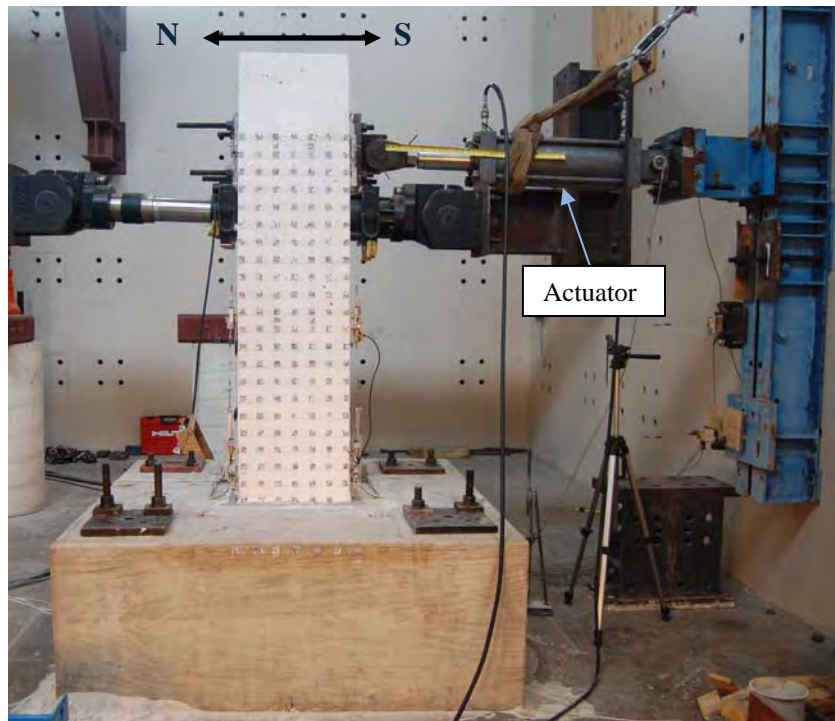


*Figure 5.95 Test Setup for RC-2R-SMS*

## 5.5.4.2  *Instrumentation for the Test*

A set of external linear and wire pots was installed to measure the local and global displacements as shown in Figure 5.96 and Figure 5.97. Internal strain gages were installed on the mechanical splices and bars as shown in Figure 5.98, Figure 5.99 and Figure 5.100.
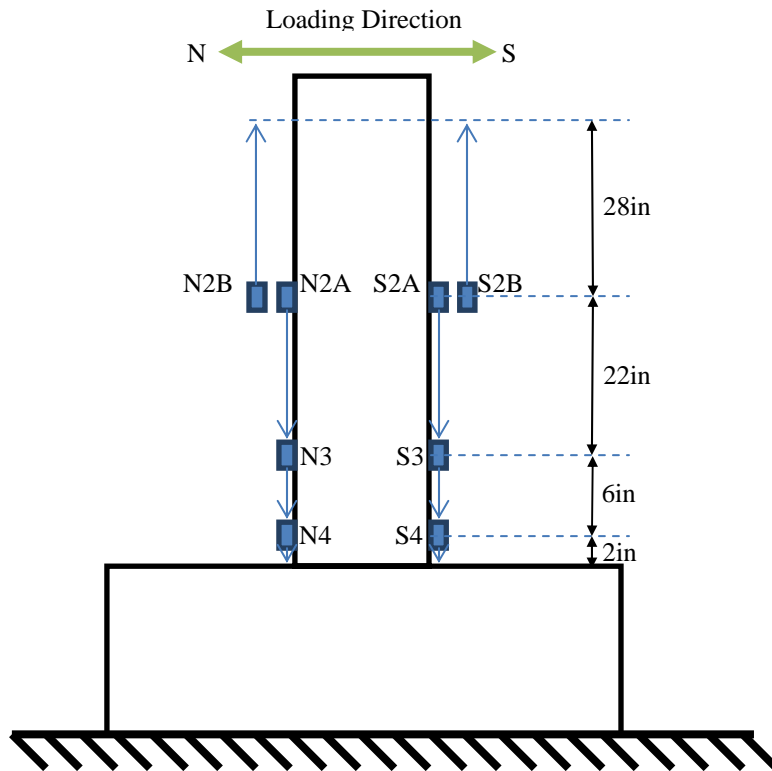


***Figure 5.96 Location of the linear and wire potentiometers for column flexural deformation***
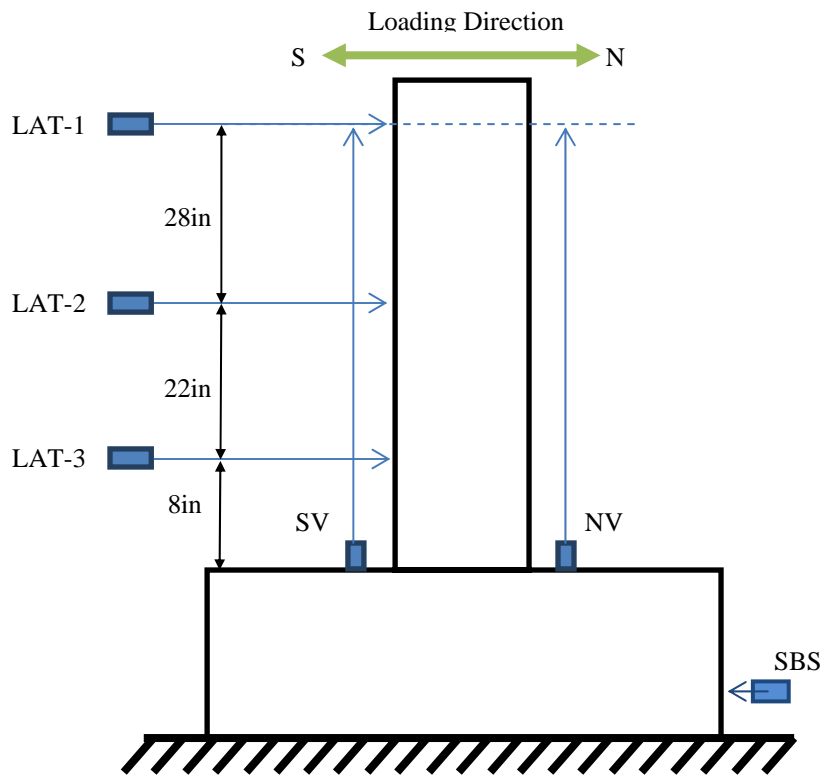
*Figure 5.97 Location of the linear and wire potentiometers for global displacement*
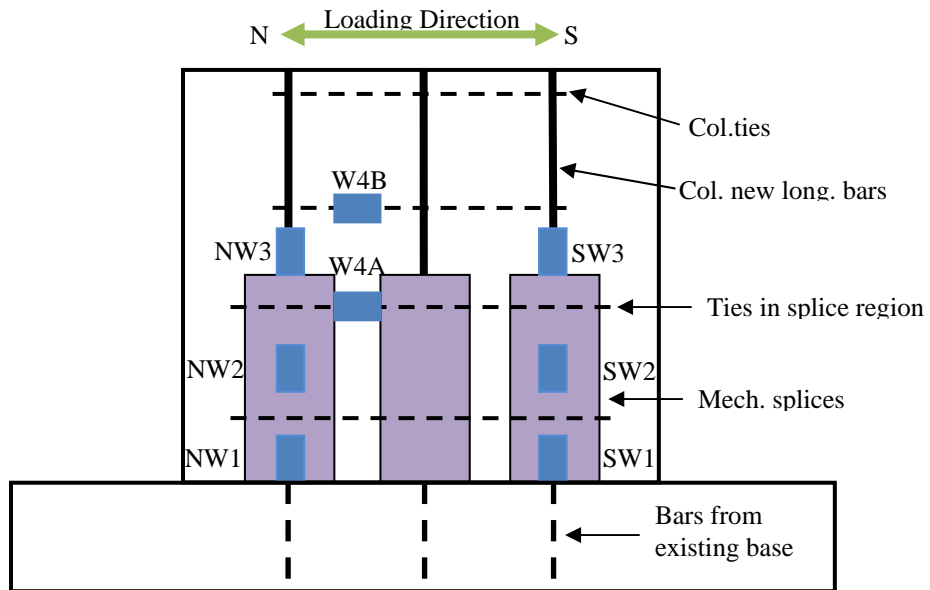
*Figure 5.98 Location of the strain gages on the west side of the specimen*
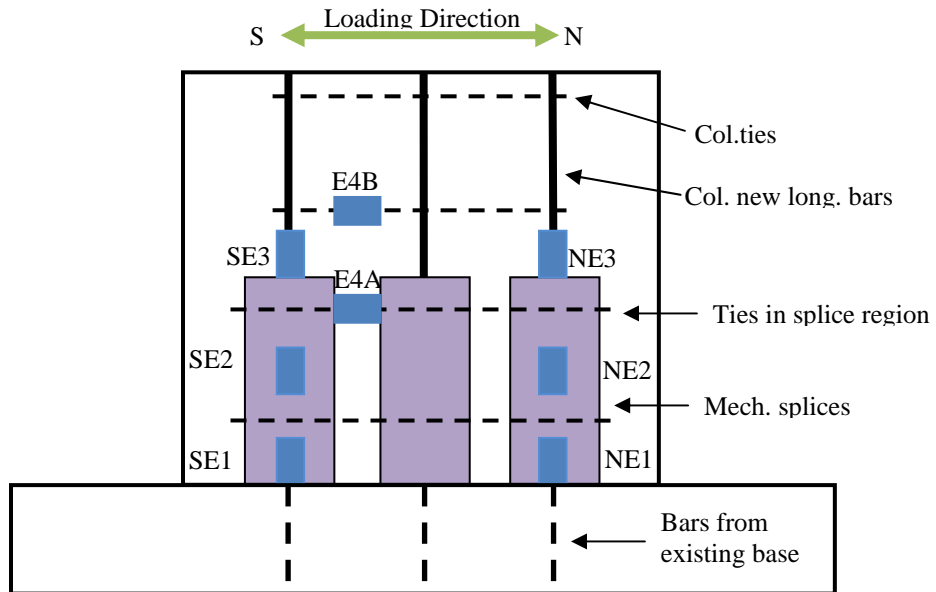
*Figure 5.99 Location of the strain gages on the east side of the specimen*
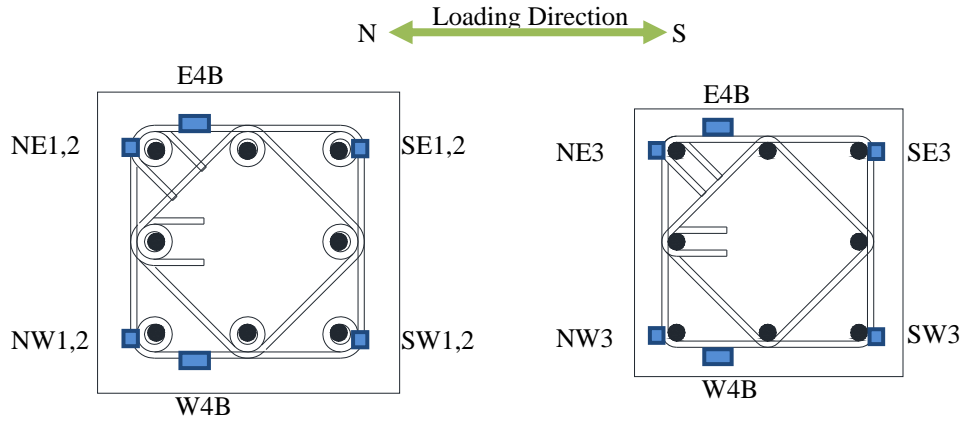


*Figure 5.100 Location of the strain gages*

The use of the Vision System to measure the local deformation was also used on this test. Targets were placed on the entire west surface of the specimen. Details of the Vision System method are explained in Appendix H.

5.5.4.3 *Protocol of load*

In the cyclic loading test, the specimen RC-2R-SMS was subjected to two cycles of tension compression increasing lateral displacements as shown in Figure 5.101. Protocol of load was following the procedures of FEMA 461 until 2.10% drift ratio which is above the maximum allowed drift recommended in the ASCE-07-05 seismic design provisions.
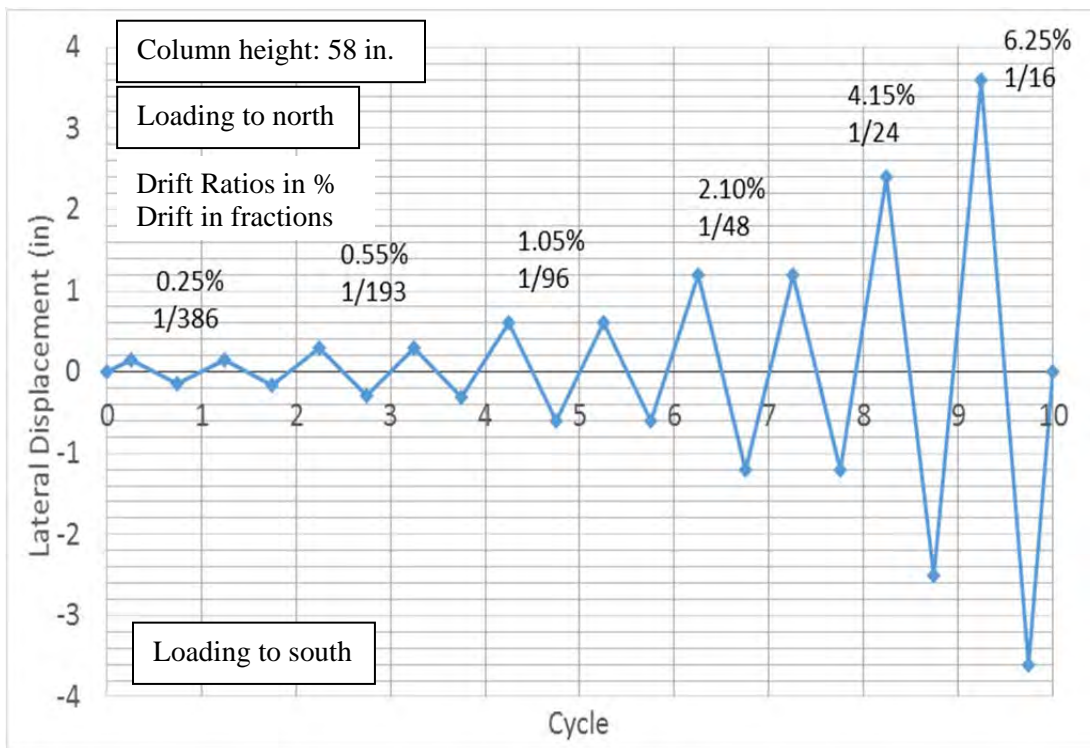


***Figure 5.101 Cycle history for specimen RC-2R-SMS***

5.5.4.4  *Test Results*

### *5.5.4.4.1 Global Behavior*

Flexural cracks developed at 1/193 (0.55%) drift or 0.30in (lateral displacement) in both faces of the column at the base. The lateral load was 32kips in the north direction and 27kips in the south direction. At the cold joint between the new column and the existing foundation, a crack with of 0.027in was measured.

Yielding occurred at 1.1% drift ratio or 0.60in lateral displacement ($5^{th}$ cycle). At a lateral load of 50kips in the north direction and 46kips in the south direction. The behavior of the specimen was in the linear range through the $6^{th}$ cycle (Figure 5.102). Flexural cracks propagated through the column from the north and south face of the specimen (Figure 5.103) shows. The crack at the base opened to 0.05 in. The strain measured in the mechanical splices was 0.0009 in tension and 0.00015 in compression. The longitudinal bars strain was between 0.0025 and 0.003 in tension and 0.00008 to 0.00015 in compression. No concrete spalling was observed. None of the ties reached yield. Pinching was observed also.
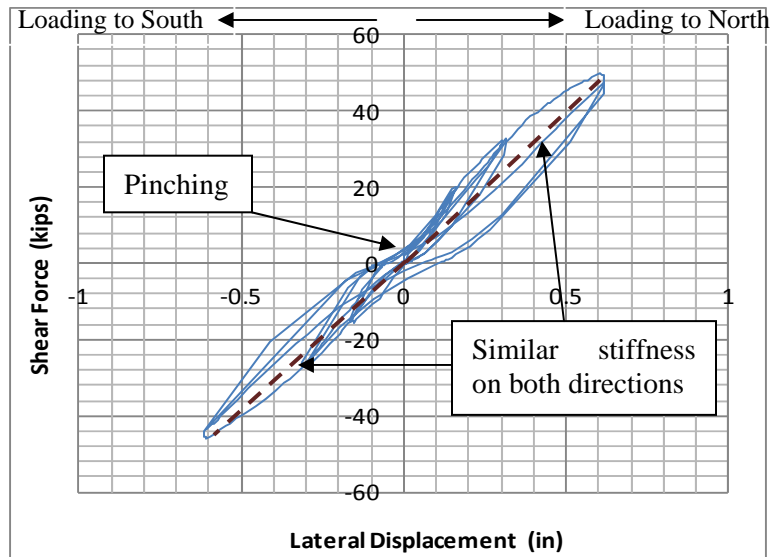
*Figure 5.102  Linear response of the specimen – First 6 cycles*



*Figure 5.103  Propagation of cracks on north (left) and south (right) face of the specimen at yielding (1.05% drift ratio)*

In the 7th and 8th cycles to 1.20in lateral deformation (Figure 5.104), the flexural crack widths increased further but the lateral load increased to about 60kips. Pinching was more pronounced in the 7th cycle. Energy absorption greater was the 7th hysteretic loop than the 8th cycle. There was a slight degradation of stiffness and strength.

Loading to South ◄─────    ─────► Loading to North
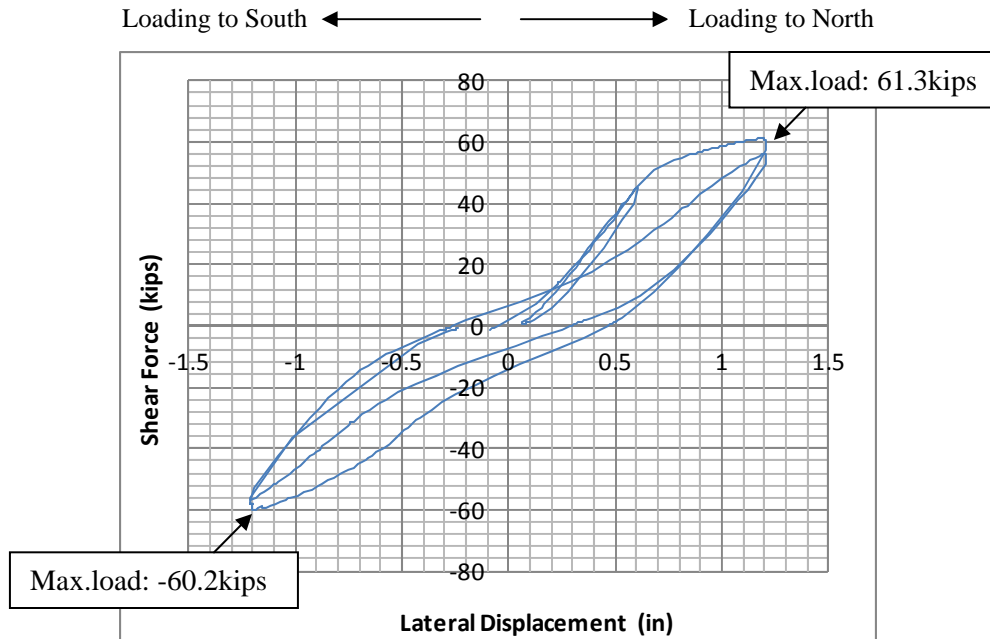


*Figure 5.104 Response of specimen at 7th and 8th cycle*

In cycle 9 the lateral load dropped from 60kips to 47kips after a loud noise was heard. The lateral deformation prior to rupture was 1.40in and jumped 1.46in (Figure 5.105). One of existing longitudinal bars fractured at the south-east corner of the specimen. The strain in the splice at this location dropped indicating bar rupture as is indicated in Figure 5.113 (strain gage SE1). A similar drop in strain was observed in the new longitudinal bar above the splice as shown in Figure 5.116 (strain gage SE2). Further increases in deformation resulted in failure of a second bar produced at 53kips and 2.0in lateral displacement. The load after rupture, dropped to 28kips and the lateral deformation increased to 2.2in (Figure 5.105). The fractured existing bar was located at

the south-center of the column and was recognized because the strains measured in SW corner showed no drop. Since there was not continuity of the longitudinal reinforcement, the splice and new bar in this south-east corner worked under compression deformation only. Displacing the column to 1/24 (4.15% drift ratio) or 2.5 in, a load of 30kips was reached. The strain measurements are shown in Appendix C.

The column was loaded south to finish the 9th cycle of lateral load. The response was comparable to the north loading. There was a similar reduction of stiffness and rupture of two existing longitudinal bars in the north face with reductions in load and change in deformation. The first existing bar that fractured was located at the north – east corner and the second was the north-center bar. The column began to twist (Figure 5.106) due to the rupture of the bars creating an eccentric moment at the base. The change in strain in the mechanical splice indicated rupture of the bars.
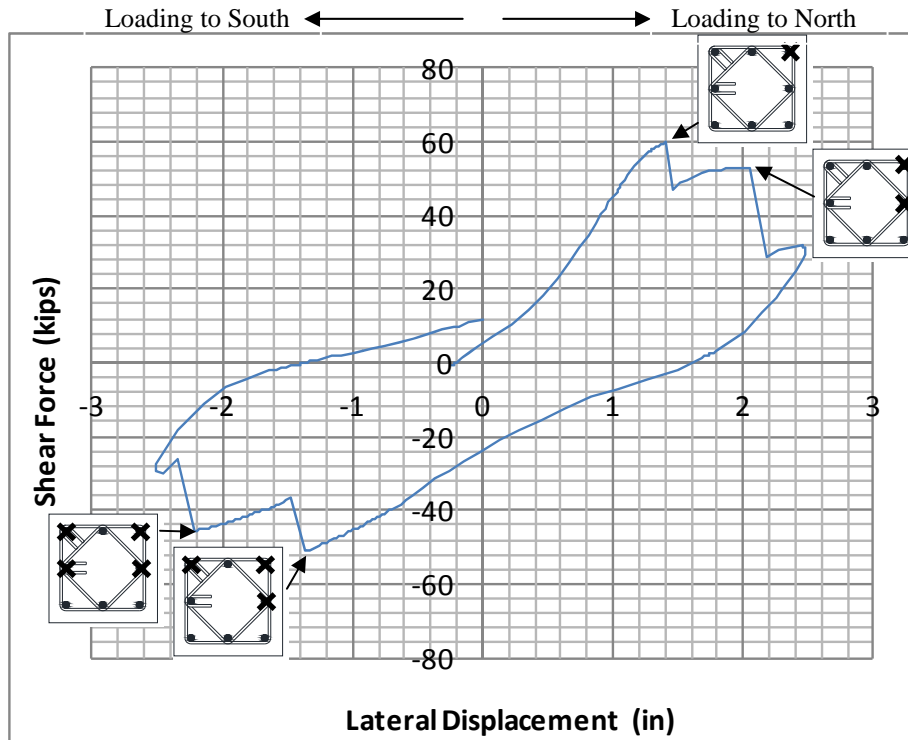
*Figure 5.105 Response of specimen in 9<sup>th</sup> hysteretic cycle. Notice the location of the*
*fractured bar where shear capacity dropped*
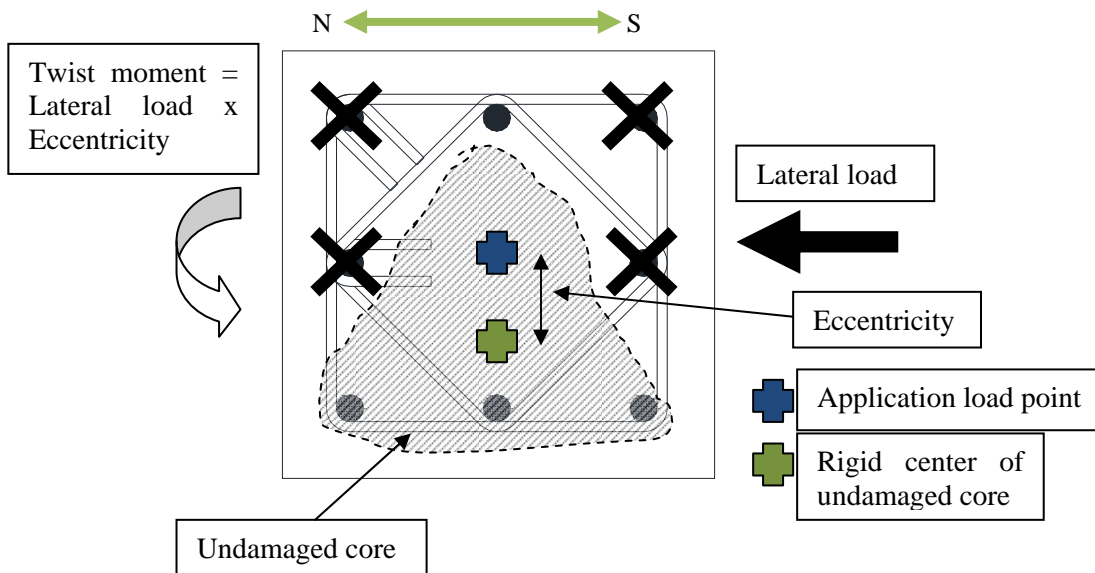


*Figure 5.106 Eccentricity of load which produce twisting of column*

196

Loading was continued until all bars at the base fractured. In the 10th cycle, going to 3.6in lateral deformation (6.2% drift ratio) the behavior was similar in both directions. Degradation on strain and force were presented also by the rupture of the remained existing longitudinal bars (at south-west and north-west corners). For north direction displacement, the rupture occurred when the lateral load was 18.64kips and dropped to 5.87kips to north and the lateral displacement was 2.70 in jumping to 2.82in because the rupture. The maximum lateral displacement applied to load 3.60in having 8.90kips for lateral load to north (deformation shape Figure 5.107). It can be seen in Figure 5.108 the lifting as result of the rupture of the three existing longitudinal bars indicating that the torsion was increased for this level of deformation.
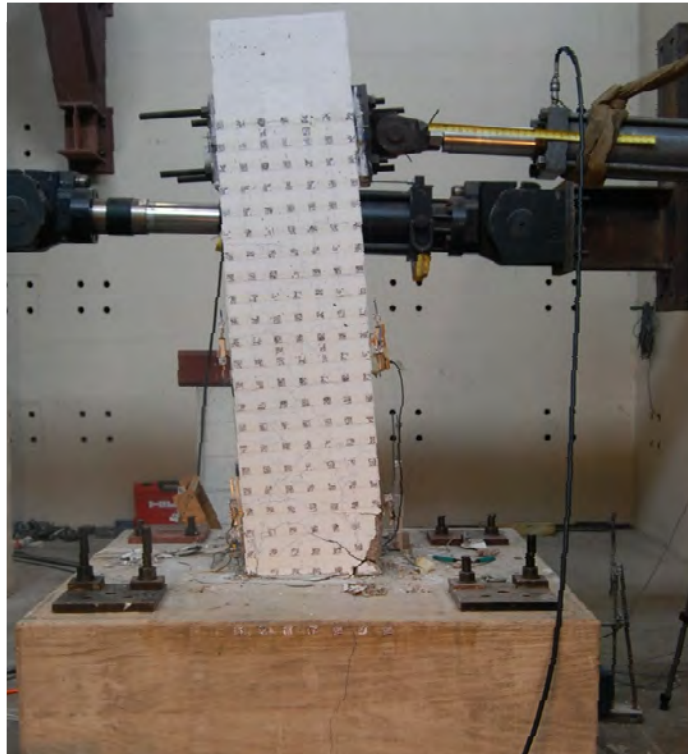


*Figure 5.107 Maximum deformation of the column under loading to North*

*Figure 5.108 Rupture of original south longitudinal bars pushing to north direction.*

For south direction the rupture of the north-west existing bar was at 2.78in lateral deformation jumping to 3in and lateral load 27kips dropping to 7.93kips. The torsion was also increased for this level of deformation as it can be seen in Figure 5.109. The maximum deformation reached was 3.62 in obtaining an ultimate load of 9.5kips (deformation shape Figure 5.110). It can be seen in Figure 5.110 the lifting as result of the rupture of 3 existing longitudinal bars of north face.

*Figure 5.109 Specimen twisting at the base before rupture of NW existing bar. The column is inclined to the south-west corner since only NW bar is carrying tension.*
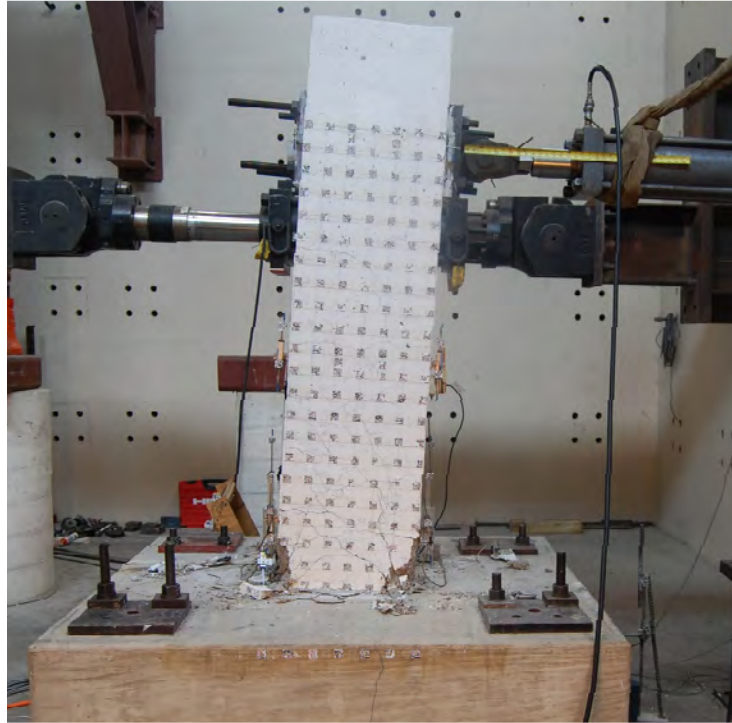
*Figure 5.110 Maximum deformation of the column under loading to South direction.*



*Figure 5.111 Rupture of existing north longitudinal bars loading to south*

Finally, the shear force vs. lateral deformation of the specimen is shown in Figure 5.112, indicating the moment when the existing longitudinal bars ruptured. The behavior of the specimen was symmetric on both direction of loading, having similar initial stiffness, maximum load capacity and ductility.
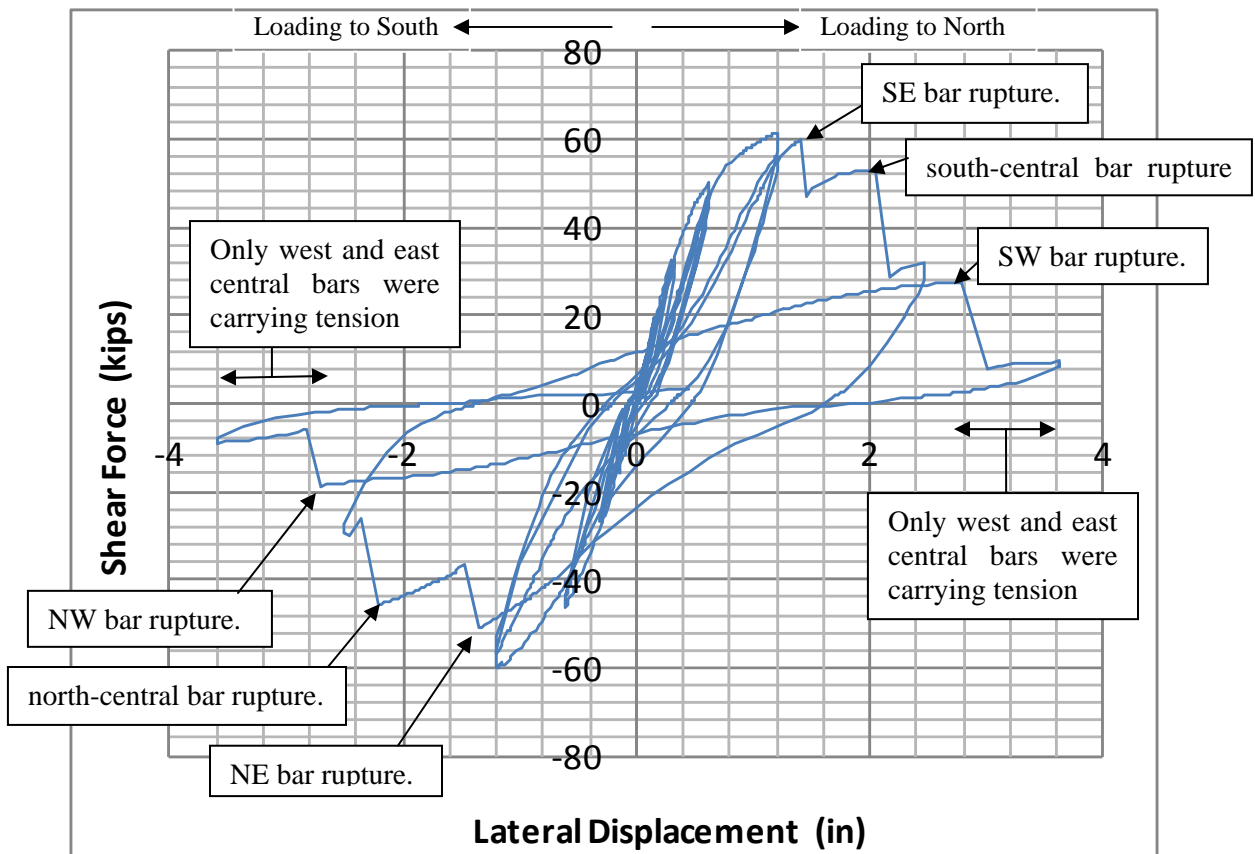


*Figure 5.112 Shear force response for specimen RC-2R-SMS.*

### 5.5.4.4.2 *Behavior of mechanical splices and bars*

The mechanical splices behaved linearly under tension deformation, however, the compression deformation was nonlinear. This pattern was very similar to that in axial test of the short mechanical splices as explained in Chapter 3. In Figure 5.113, this pattern of behavior for the short mechanical splices is shown. It is observed also the differences of strain measured between the middle strain gage (SE2) and the lowest level strain gage (SE1) for the South-East mechanical splice. SE2 deformed larger than SE1 as is seeing in Figure 5.113. Similar pattern was observed on the axial cycle load test performed for the splice only. No mechanical splices reached the yielding being the higher deformation 0.0014 in/in.
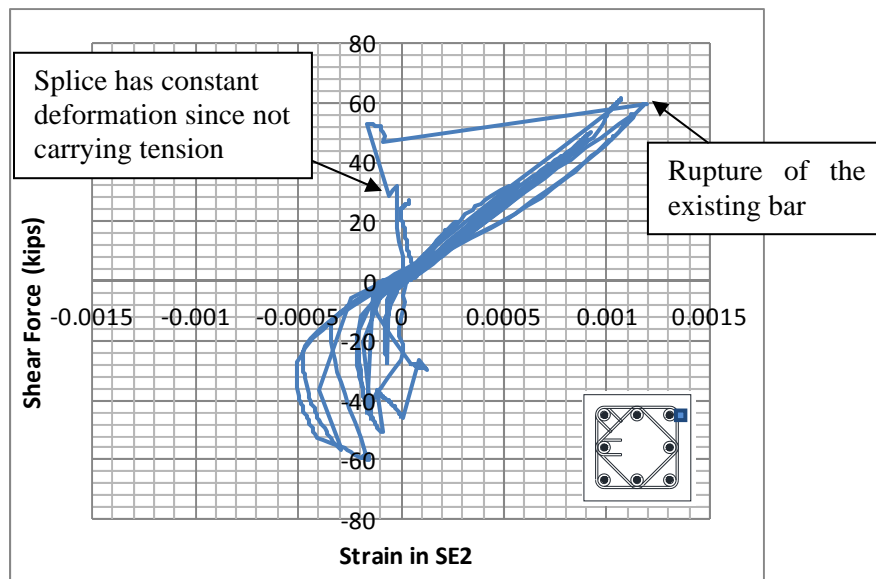


*Figure 5.113  Strain on the middle-height of south-east corner splice*
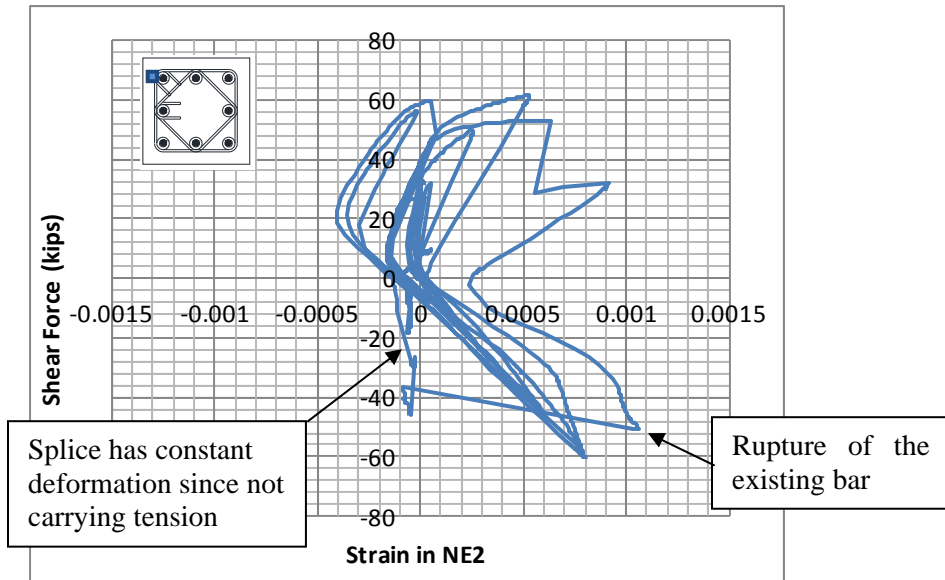
*Figure 5.114 Strain on the base of north-east corner splice*

The new longitudinal bars exhibited tensile strains for nearly all loading as shown in Figure 5.115 and Figure 5.116. Since the cover was more than 2in, the neutral axis was located in this concrete cover. All the longitudinal bars were in tension. Bars in both faces reached the yield. The NE bar strains exceed the range of the strain gage, 0.012 (Figure 5.116).

The strains in the ties indicate twist on the specimen due the rupture of the existing bars. As can be seen in Figure 5.117 and Figure 5.118, the strain on the east tie (E4A) is larger than the measured in the west tie (W4A). The original bars that fractured first were on the east face of specimen inducing a higher strain than the west transverse bars. The east transverse bars reached yield.
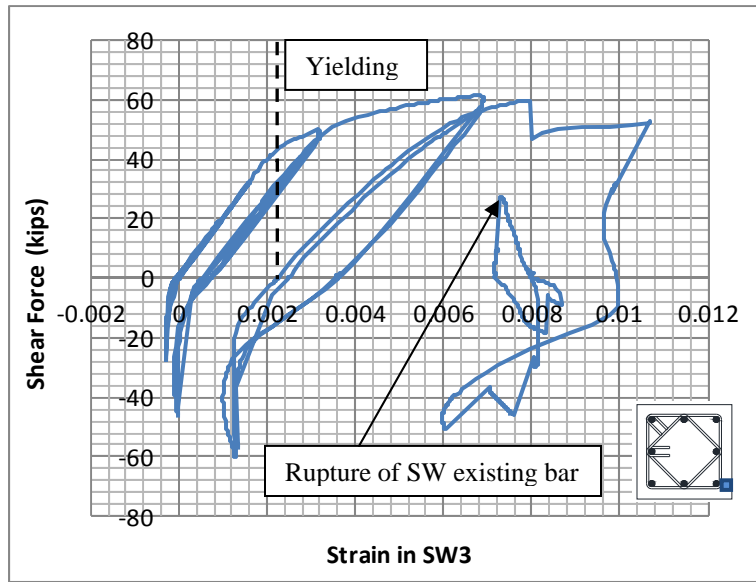
*Figure 5.115 Strain in the south-west longitudinal new bar.*
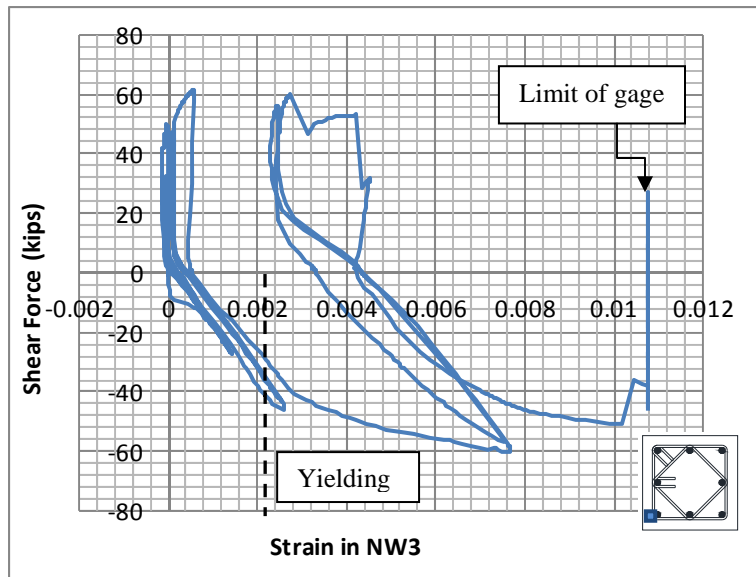


*Figure 5.116 Strain in the north-west longitudinal new bar.*
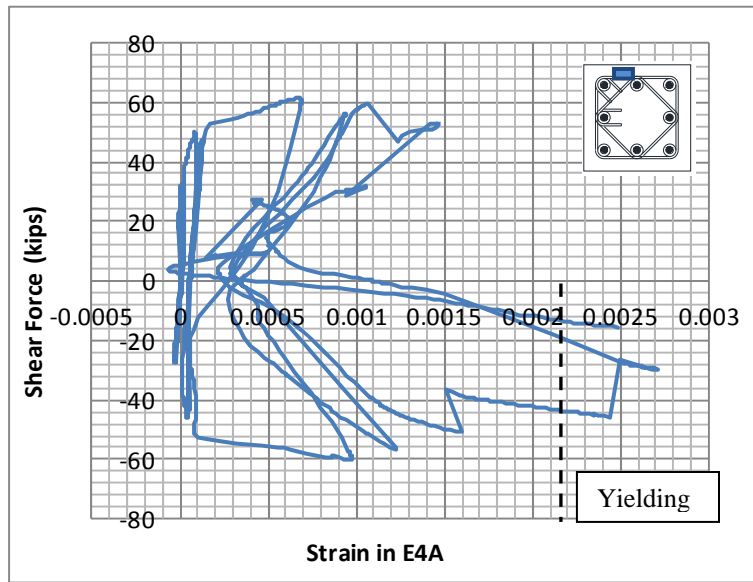
***Figure 5.117 Strain in the tie around the mechanical splice-east side.***
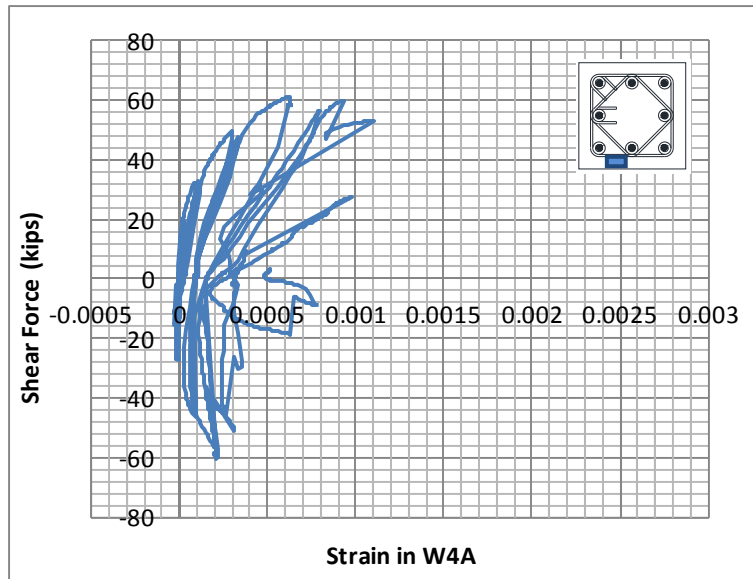


***Figure 5.118 Strain in the tie around the mechanical splice–west side.***

205

### 5.5.5  Laboratory Test of RC-2R-LMS

#### 5.5.5.1  *Test Setup*

The test procedures were similar to RC-92R-SMS. Since top beam from the existing column was smaller than the base, the attachment to the strong floor consisted on 2 steel beams (Figure 5.119) connected to the strong floor by post tensioned rods. Hydrostone was placed between the concrete base and the strong floor surface to improve the friction between the surface of the top beam and surface avoiding the sliding.
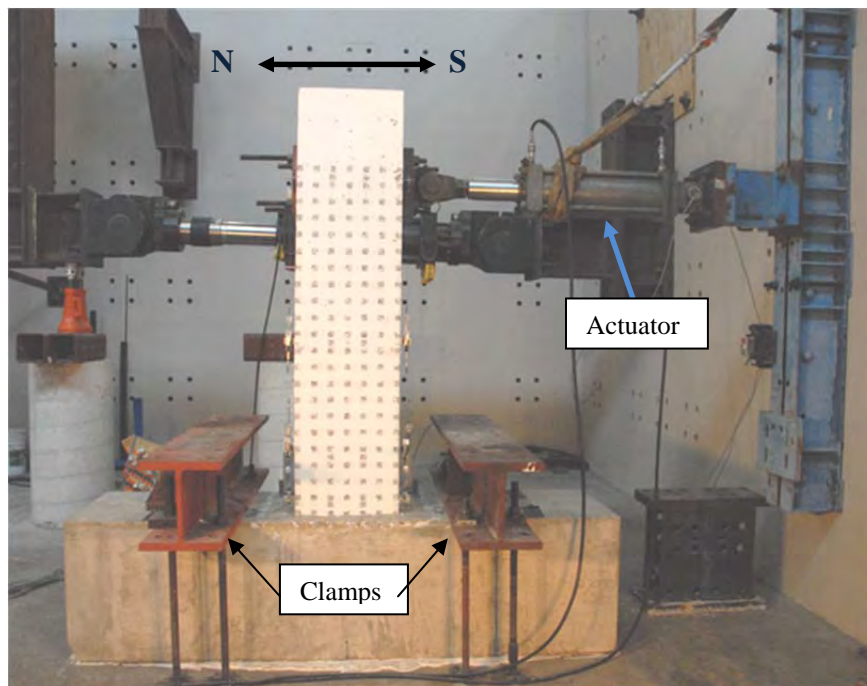


*Figure 5.119 Test Setup for RC-2R-LMS*

### 5.5.5.2 *Instrumentation for the Test*

The disposition of external linear and wire potentiometer was similar than previous specimen. However, for global displacement LAT3, the instrument used was a linear potentiometer because the difficult access to the area between the two steel clamps beams.
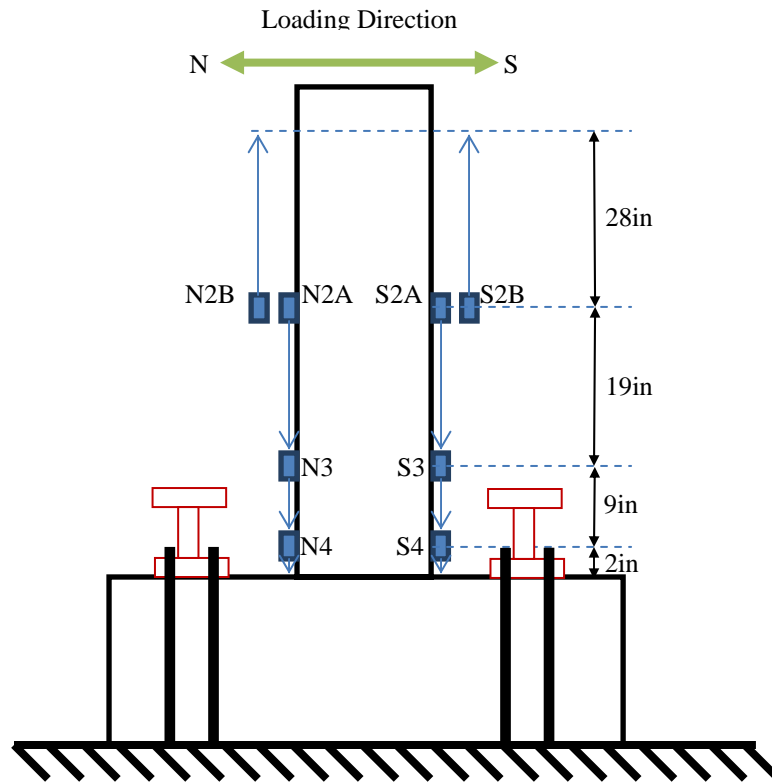


*Figure 5.120 Location of the linear potentiometers for column flexural deformation*
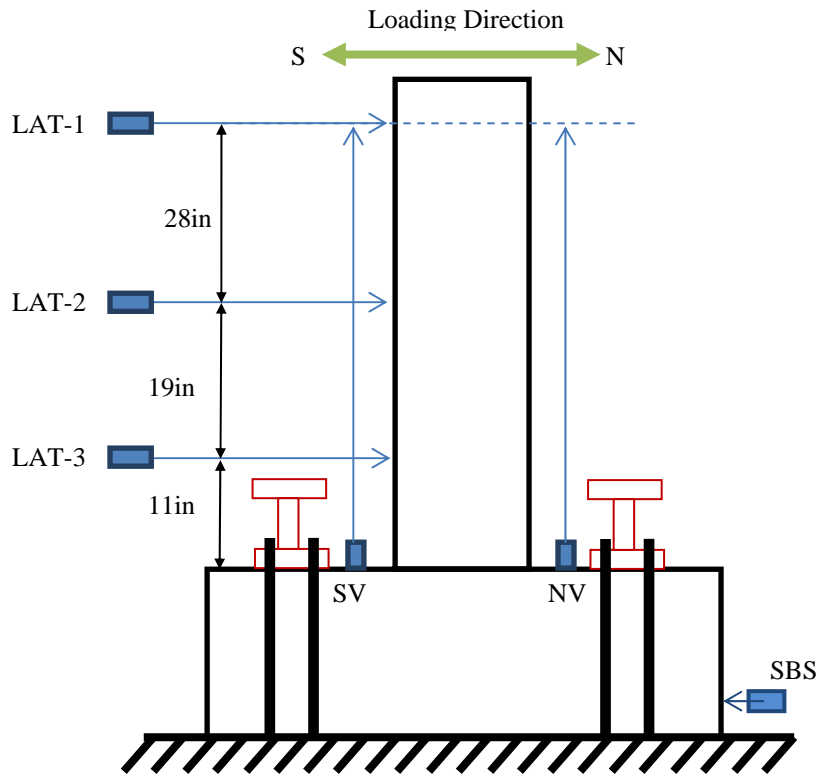
***Figure 5.121 Location of the linear and wire potentiometers for global displacement***
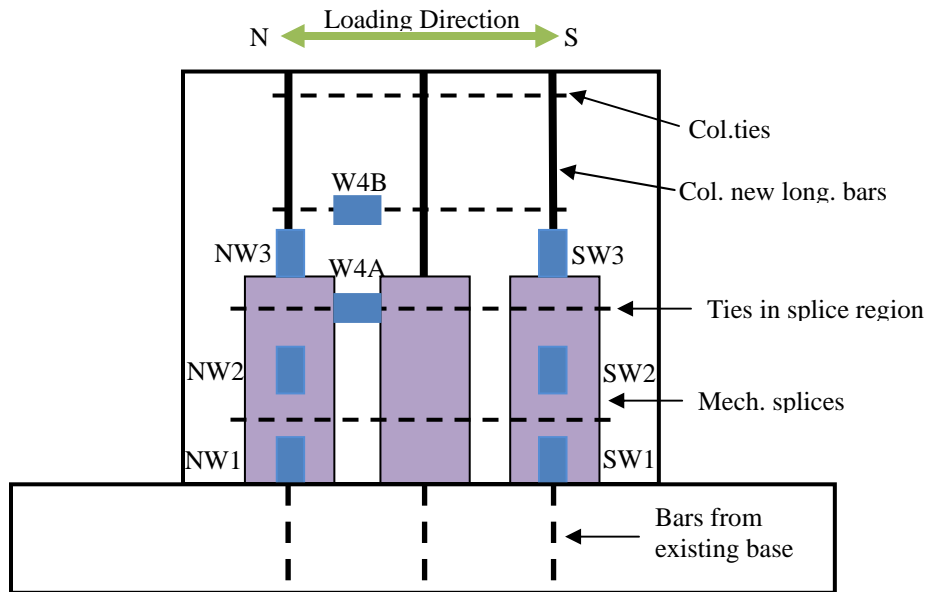
*Figure 5.122 Location of the Strain gages on the west side of the specimen*
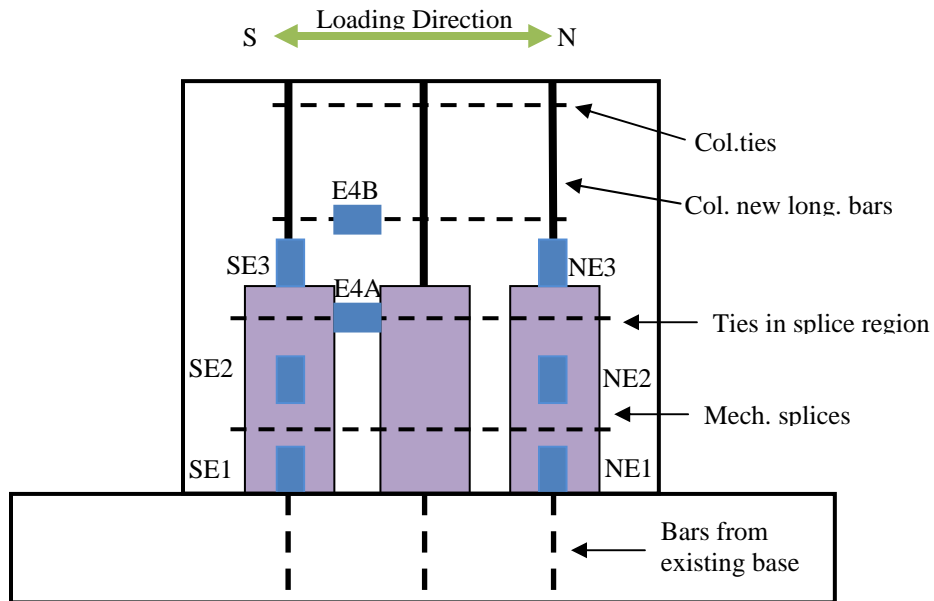


*Figure 5.123 Location of the strain gages on the east side of the specimen*

209
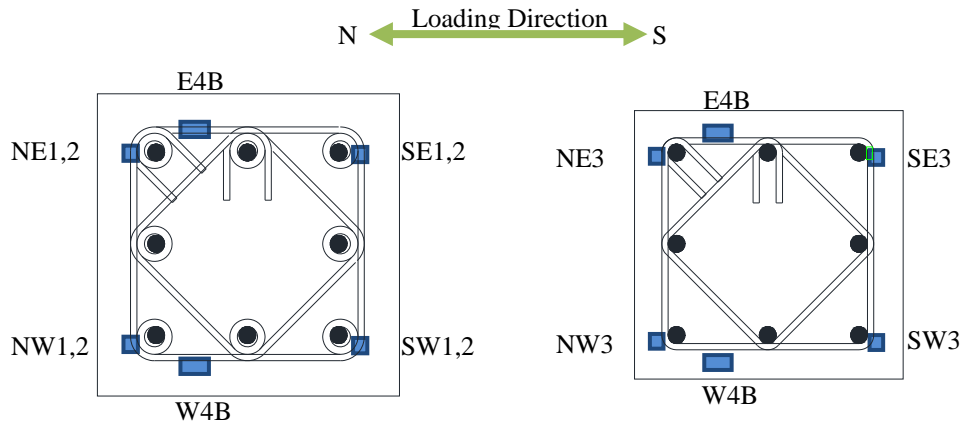
***Figure 5.124 Location of the strain gages on ties***

The optical deformation measuring system was used to measure deformations of the specimen, similar than previous specimen. Targets were placed on the surface of the specimen covering. Details of the Vision System method are explained in Appendix E.

### 5.5.5.3 *Protocol of load*

In the cyclic loading test, the specimen RC-2R-SMS was subjected to two cycles of tension compression increasing lateral displacements as shown in Figure 5.125. The positive values of displacement was defined for pulling loads toward South direction, and the negative values for pushing loads toward North direction. Protocol of load was following the procedures of FEMA 461 until 2.10% drift ratio which is above the maximum allowed drift recommended in the ASCE-07-05 seismic design provisions.
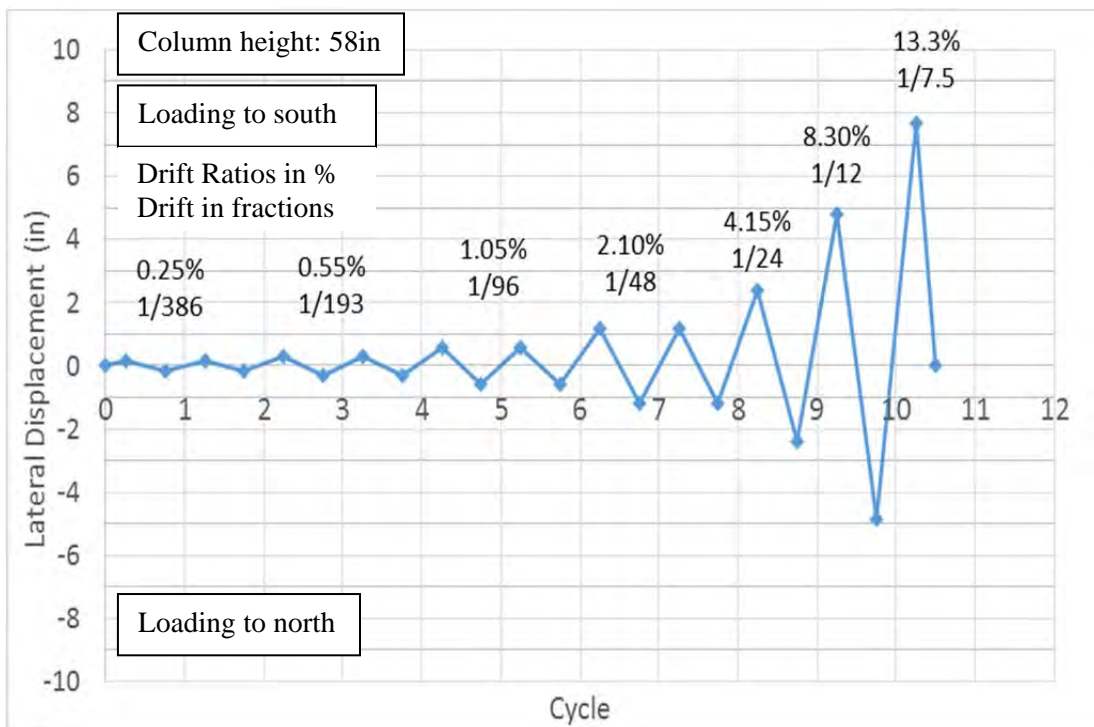


*Figure 5.125  Cycle load history for specimen RC-2R-LMS*

5.5.5.4  *Test Results*

### 5.5.5.4.1 Global Behavior

No crack appeared while the firsts 4 hysteretic cycles. The maximum load of the first cycle (0.15in lateral displacement) was 17.5kips to south and -17.82kips to north. The peak load at $3^{rd}$ cycle was 27.67 kips to south and 27.92 kips loading to north. The specimen had a linear behavior (Figure 5.126).

Figure 5.126 shows the response of the specimen until the $6^{th}$ hysteretic cycle. The specimen behaved also in linear range at $5^{th}$ and $6^{th}$ hysteretic cycles, having 0.60in lateral displacement (1.05% drift ratio). The lateral load to south direction measured was 46.17 kips and -46.87 kips loading to north. Degradation of shear capacity was also noticed, measuring drop of 3kips. Pinching effect was observed too. This figure shows also the pinching effect presented and the lightly load drop measured. Flexural cracks width of 0.025in was measured (Figure 5.127). Lifting appeared lightly, the cold joint between the new column and the existing concrete beam base started to separate, being this lifting 0.066in. The new longitudinal bars reached the yield in tension. The strain were 0.00277 (NE3) and 0.0030 (NW3) in tension, and 0.0006 (NE2), 0.0007 (NW2) in compression, both when the specimen was loading to south. The strain on the new longitudinal bars were 0.0031(SE3) and 0.0037(SW3) in tension and 0.0007 (SE2 and SW2) in compression loading the specimen to north. No spalling was presented despite that the cover was taking all the compression internal force by the flexural load. The splices were in tension deformation indicating that the neutral axis was located in the concrete cover zone. The ties neither the long mechanical splices did not reach the yield.
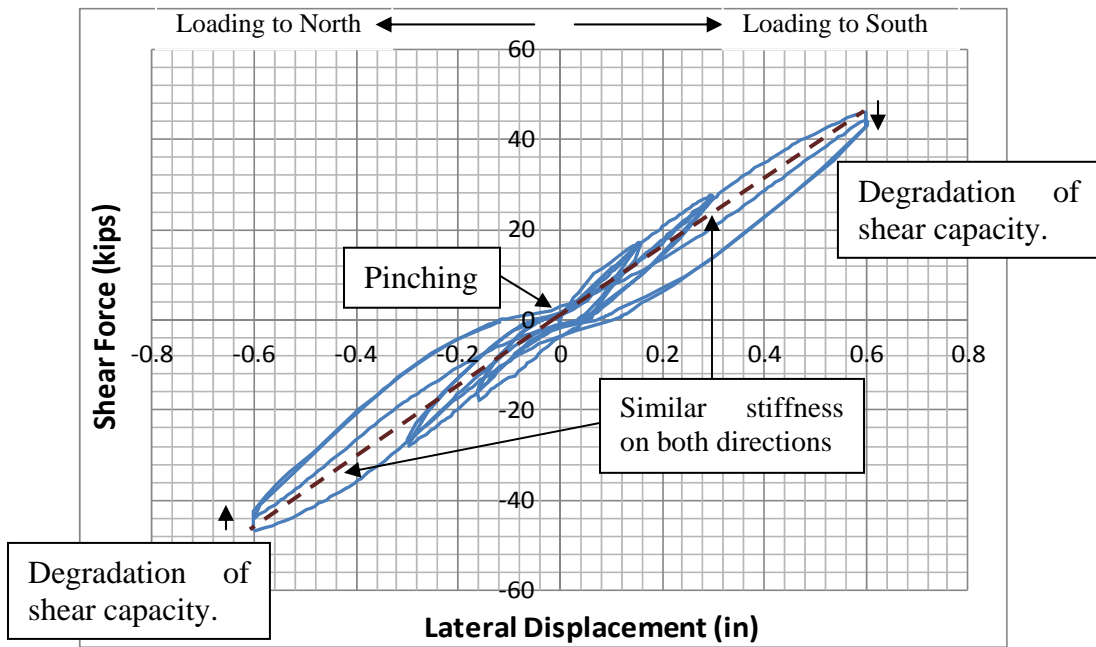
*Figure 5.126  Behavior in first 6 cycles*
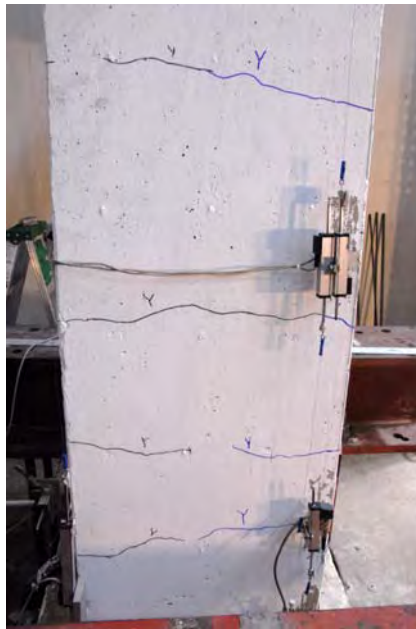


*Figure 5.127 Flexural cracks on north face of specimen*

Figure 5.128 shows behavior of the specimen in the 7th and 8th cycle. It can be seen that the specimen's response was on the no-linear range. It was expected because the new longitudinal bars exceed the yield strain. The width of the cracks increased until 0.040in and new cracks appeared and extended in the specimen. The lifting of the base reached 0.18in. The shear force obtained for 1.20in lateral displacement was 60kips in both direcctions. Pinching and degradation of shear force were noticed. The strain of the splices was varying in compression and tension indicating that the neutral axis moved into de column core zone.
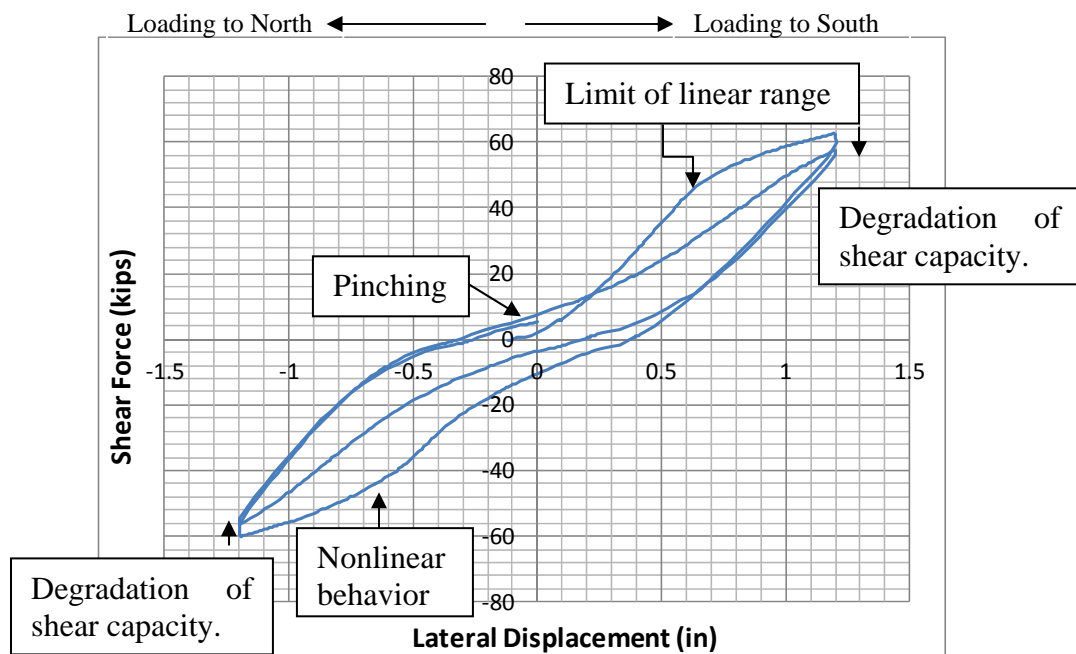


*Figure 5.128 Response of the specimen at 7th and 8th cycle*

In the 9th cycle the specimen reached its maximum shear capacity -67.38kips loading to north and the lateral deformation was -2.39in correspondent to the peak displacement for this cycle having a lifting of 0.33in at south base. Crack's wide increased until 0.125in, and shear cracks appeared in the East face of the column. Spalling at south face began by the compression stress in the concrete cover.

214

In the 10<sup>th</sup> cycle loading to south the specimen reached its maximum shear capacity 71.65 kips and the lateral deformation was 4.72in. The lifting at north measured was 0.64in. The cracks propagated to west and east face of the specimen. There was spalling of the concrete cover at the south face of the column at its bottom base where the deformation strain was governed by compression stress. Figure 5.129 shows the spalling of the cover and also it can be seen part of the central mechanical splice of the south face of the column and it can be seen that the cover fallen was on the first 13in from the base.



*Figure 5.129 Spalling of the cover at bottom south face of the specimen*

In cycle 10<sup>th</sup> loading to north the lateral load dropped 61.40kips to 47.40kips after a loud noise was heard. The lateral displacement prior the rupture was 2.96in. One of the existing longitudinal bars fractured. This bar was located at the south-center. The strain in the SE neither SW splices did not dropped indicating that the south-center existing bar ruptured. Further increases in deformation resulted in the lateral deformation of 4.83in (8.3% drift ratio) which was the maximum lateral north displacement, measuring a load of 54kips. The internal area between the curves of the hysteretic loops became larger

indicating mayor energy released at comparison than previous loops correspondent for the linear behavior of the specimen.
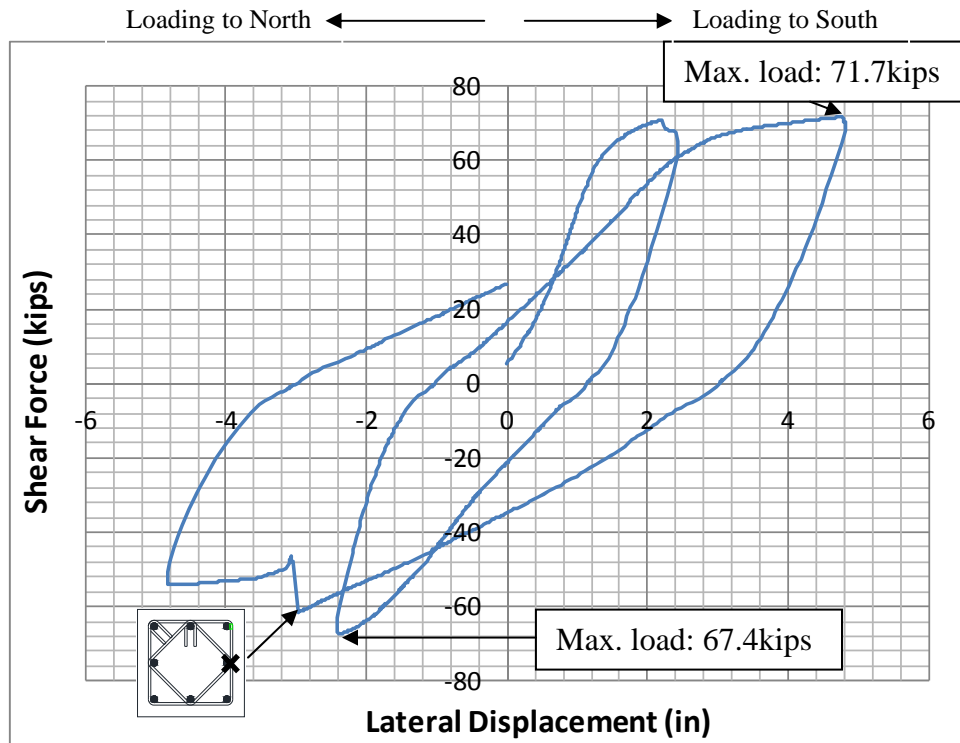


*Figure 5.130 Response of the specimen at 9$^{th}$ and 10$^{h}$ hysteretic cycle*

Figure 5.131 shows the rest of cover below the first 13in from the base spalled The linear potentiometer S4 was removed. The wide of the flexural cracks increased and the shear cracks propagated through the west and east faces of the column forming a shear hinge at 15in height from the base as is shown in Figure 5.131.
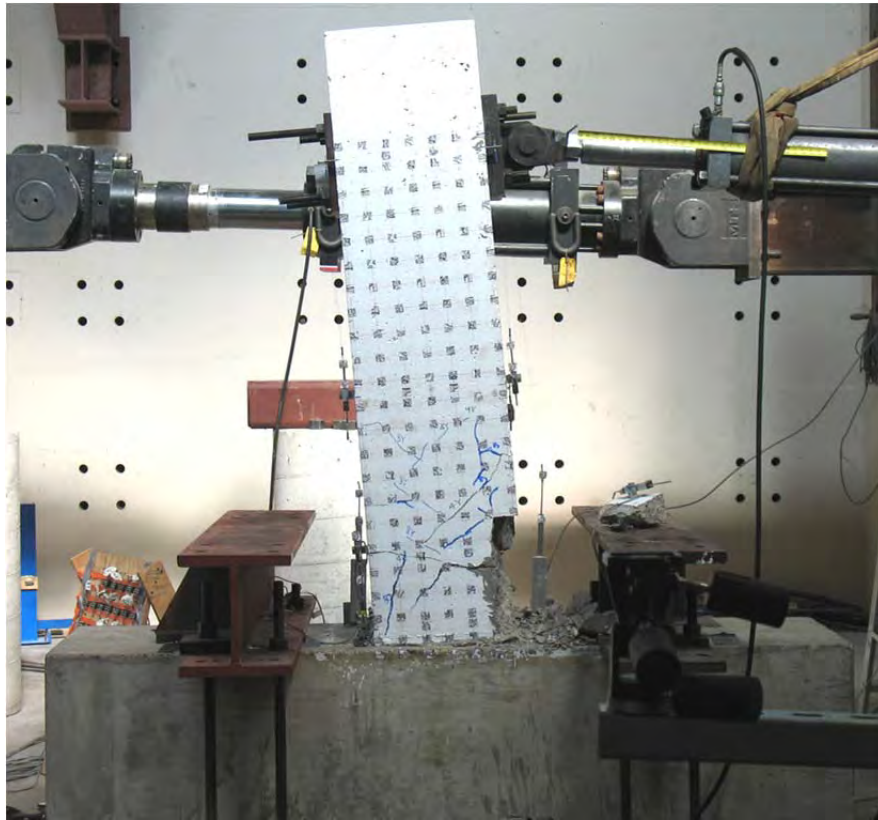
*Figure 5.131  Maximum deformation of the column in north direction*



*Figure 5.132  Flexural and shear cracks on east face of the specimen*

In the 11$^{th}$ hysteretic cycle the column was loading to south until the rupture of one existing longitudinal bar. This failure was noticed by the loud noise. Figure 5.133 shows the specimen deflected. The cover of the south face until 15in above the base spalled Figure 5.134 (left). The lifting increased considerately on north-west corner as is shown in Figure 5.134 (right), however it was been measured because linear potentiometer N4 was removed for the spalling of cover. This lifting and the strain dropped in the splice in the north-west corner indicated the location of the existing bar fractured. The lateral shear force prior the bar's fracture was 68.05kips dropping to 51.99 kips. The lateral displacement prior the rupture was 7.62in jumping to 7.68in. as is shown in Figure 5.135. Energy was released in mayor amount at comparison than other hysteretic loops as it can be seen also in Figure 5.135.
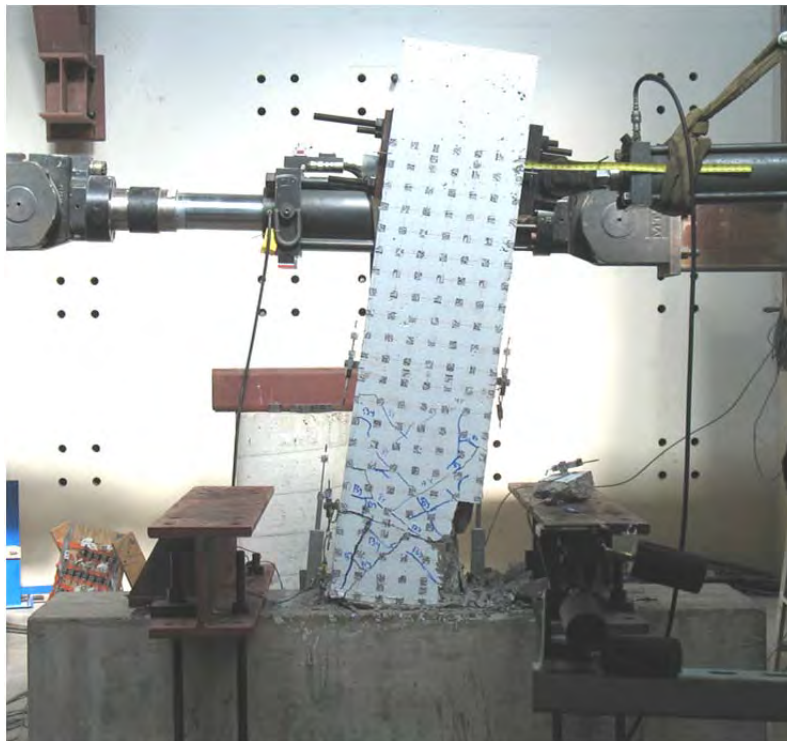


*Figure 5.133 Maximum deformation of column in south direction*

*Figure 5.134 Close-up view of the column base. Exposed mechanical splices under compression stress at south face (left) and lifting on the north face (right)*
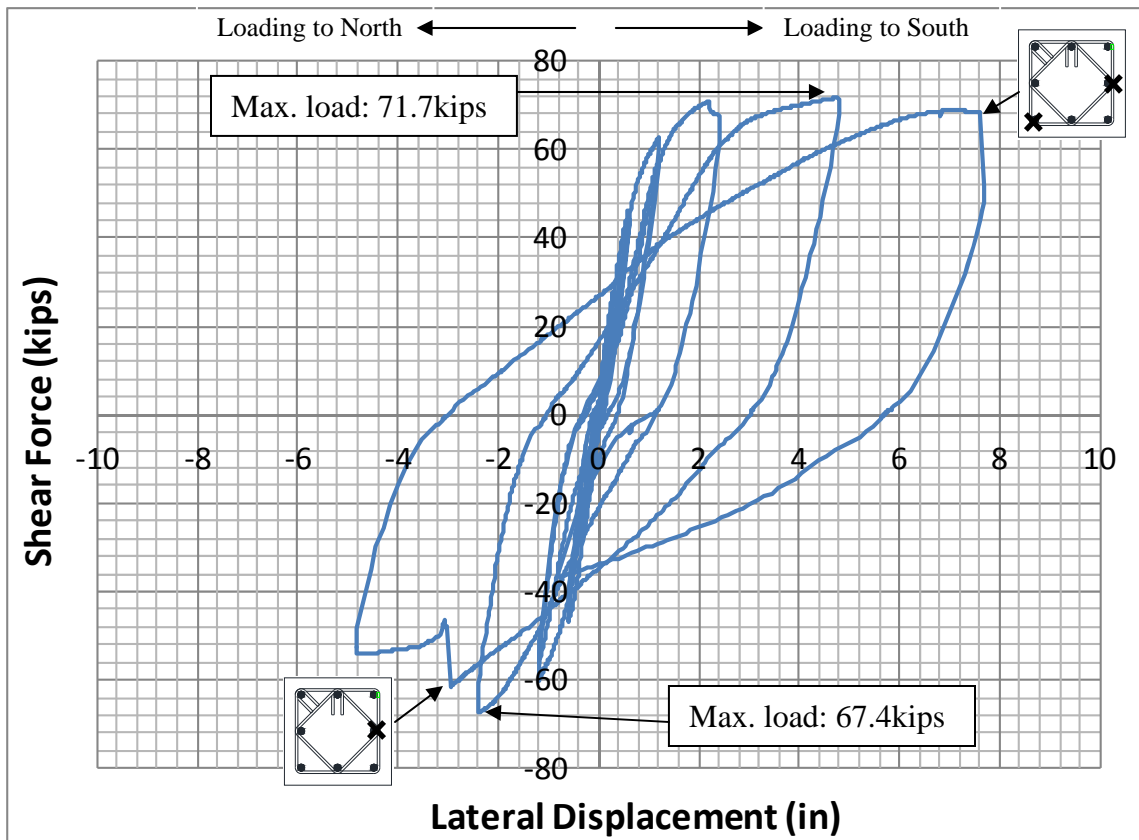


*Figure 5.135 Flexural cracks in north face of specimen*

### 5.5.5.4.2 Behavior of mechanical splices and bars

The long mechanical splices behaved in the linear range for tension axial loads and no linearly for compression axial load measured by the two strain gages located in each splice. No splice reached the yield being the largest strain measured 0.0013 in the middle of the splice located at north-west (Figure 5.136) and south-east corner (Figure 5.139). Splice's behavior under compression loads has similar pattern than splices tested under axial cycle load test. For high compression axial load received for the splice, the strain measured was governed by tension deformation as is appreciated in Figure 5.136 and Figure 5.139. No mechanical splices damage was noticed, neither the bolts broken while they applied to the bars.
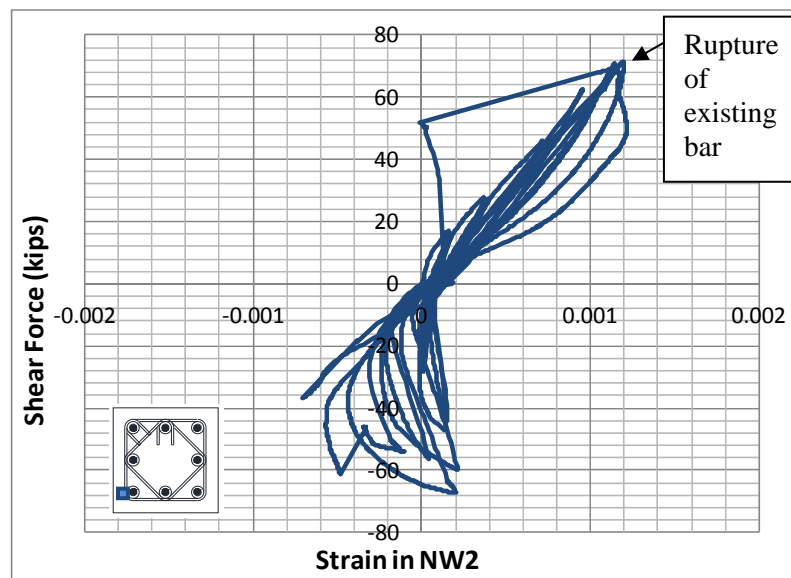


***Figure 5.136  Strain on the middle-height of north-west corner splice***

220
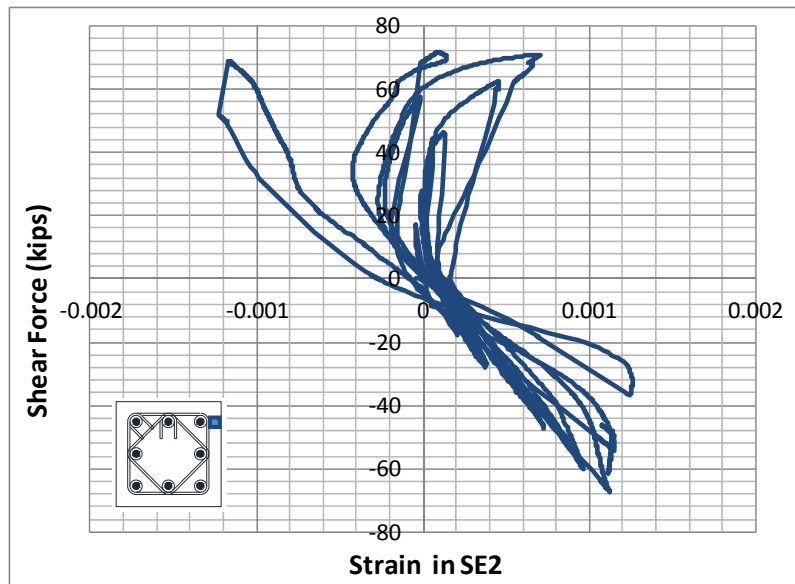
*Figure 5.137  Strain on the middle-height of south-east corner splice.*

The behavior of the new longitudinal bars was predominant in tension deformation. This indicates that the neutral axis was located on the concrete cover zone. All bars on both faces of specimen reached the yield and exceeded the range of the strain gage (0.012) as is shown in Figure 5.138 and Figure 5.139.

The transversal reinforcement remained in good condition performing very well. They made to the specimen to have an effective confinement of core. The strain of the ties around the splices and the new longitudinal bars reached the yield and exceed the limit of the gage. Figure 5.140 and Figure 5.141 show the strain for the ties around the splices on west and east face. Despite there appeared shear diagonal cracks on the column forming a shear hinge, the core remained in good shape after the test finished as is shown in Figure 5.142.

221
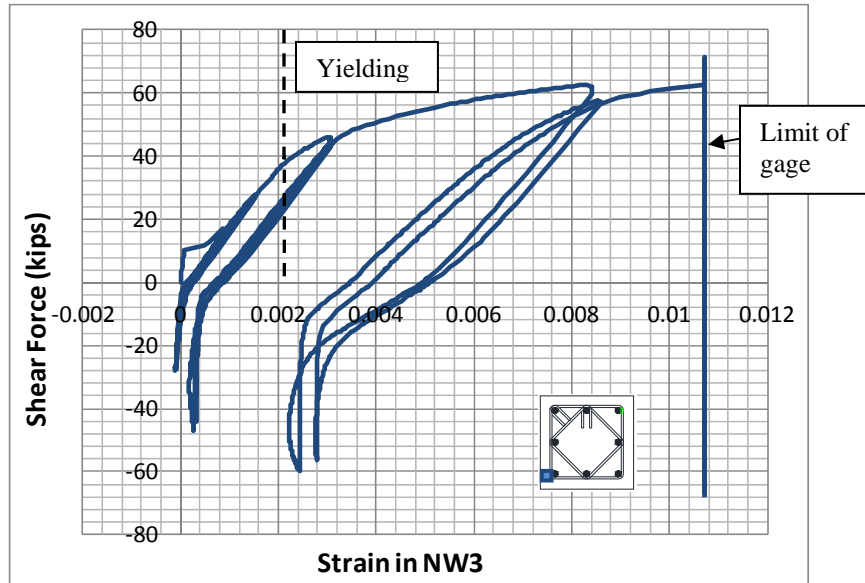
*Figure 5.138  Strain in the north-west new longitudinal bar.*
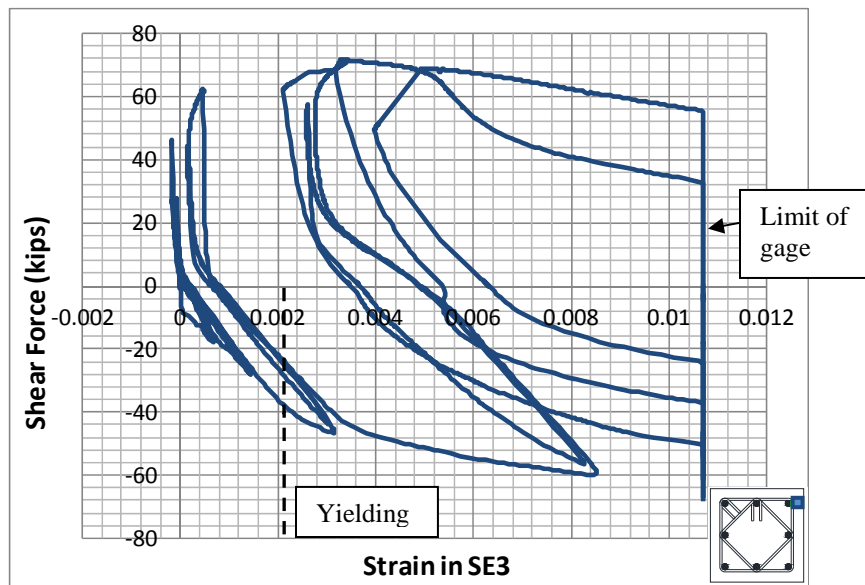


*Figure 5.139  Strain in the south-east new longitudinal bar.*
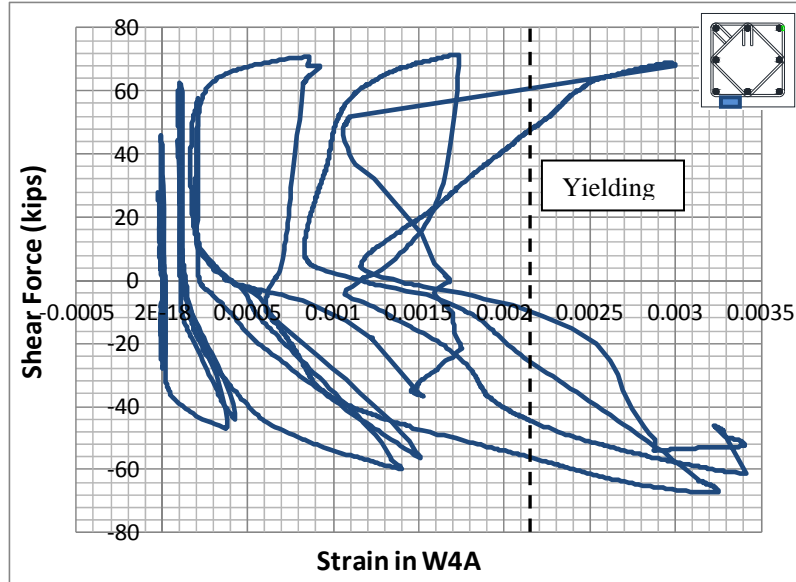
*Figure 5.140  Strain in the tie around the mechanical splice-west side.*
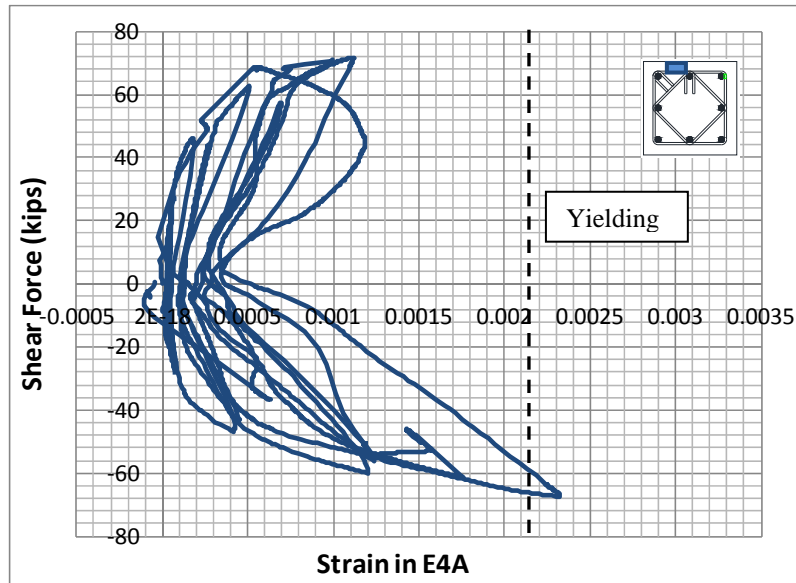


*Figure 5.141  Strain in the tie around the mechanical splice-east side.*

*Figure 5.142  Final condition of the specimen after the test showing well-confined core.*

## 5.6  SUMMARY

The histories of shear force vs. drift for each specimen are presented. Further detailed comparisons are shown and explained in chapter 7.

Figure 5.143 shows the behavior of the as-built column RC-1 and after retrofitting RC-1R. Values of displacement are normalized by drift ratios. It was observed that RC-1R had less stiffness than the as-built column, even though the retrofitted column had a larger cross sectional area at the bottom. This was more evident when the column was loaded in the south direction. Since large cracks opened at top and bottom of the column, it can be assumed that the existing bars were deformed more than in the original test. RC-1R had slighter higher lateral capacity than RC-1 and values of ultimate drift ratio are comparable.
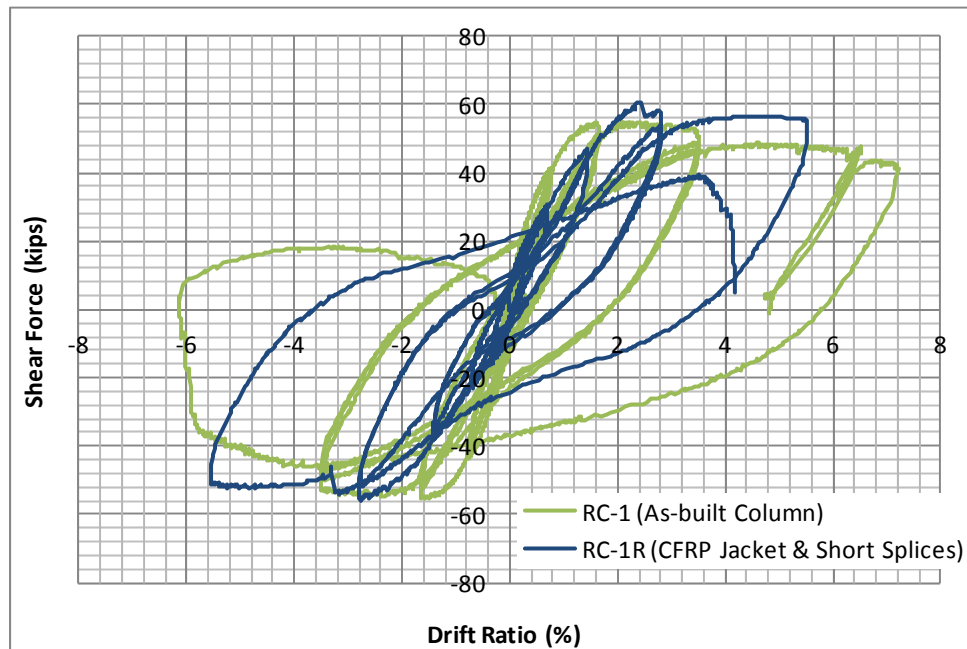


***Figure 5.143  Shear force vs. drift ratio of RC-1 and RC-1R***

225

Figure 5.144 shows the comparisons of the response of the as-built column RC-1 and the bottom half of the retrofitted column RC-1R bottom half (short mechanical splices). Lateral deformation was using drift ratios. The stiffness of RC-1R bottom half under loading on both directions was slightly less than RC-1 even though the clear cover was increased. Ultimate drift ratios were also comparable. There was progressively greater drop in the shear capacity of RC-1R as drift increased. RC-1R Bottom Half contained the hinge zone where the failure of the as-built column occurred.
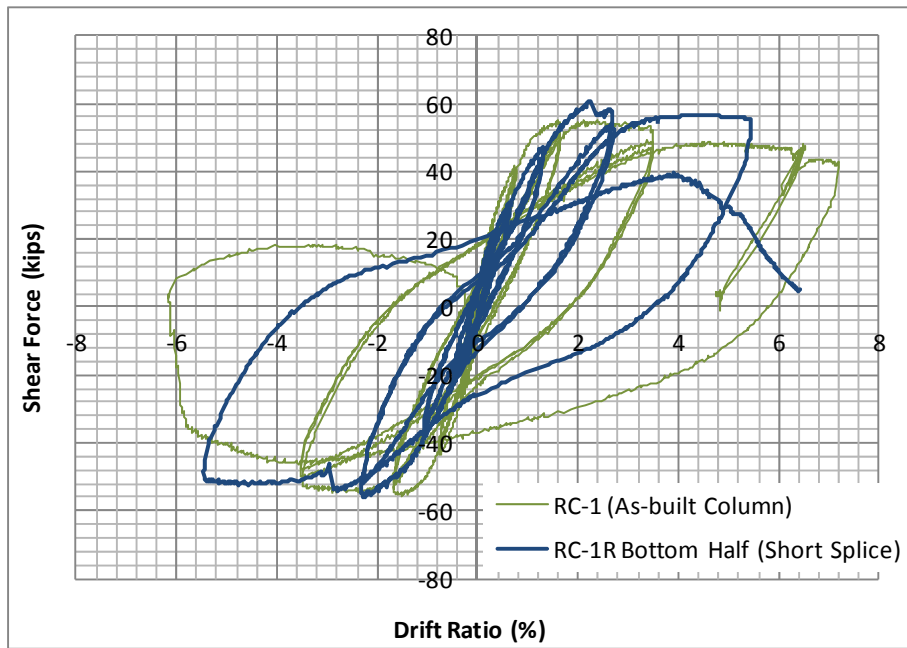


*Figure 5.144  Shear force vs. drift ratio of RC-1 and RC-1R Bottom Half*

Figure 5.145 shows the response of RC-1 and RC-1R top half (CFRP jacket). Lateral displacements are normalized by drift ratios. Slighter higher shear forces were observed in RC-1R top half but the stiffness at low drifts was greater for the retrofitted column, especially the specimen was loaded to the south. The CFRP anchor on one face of the jacketed hinge zone increased the stiffness in the south direction. The displacement capacity of RC-1R (top half) was no evaluated since the failure of RC-1R occurred in the bottom half and the top half was in good condition after the bottom half failed.
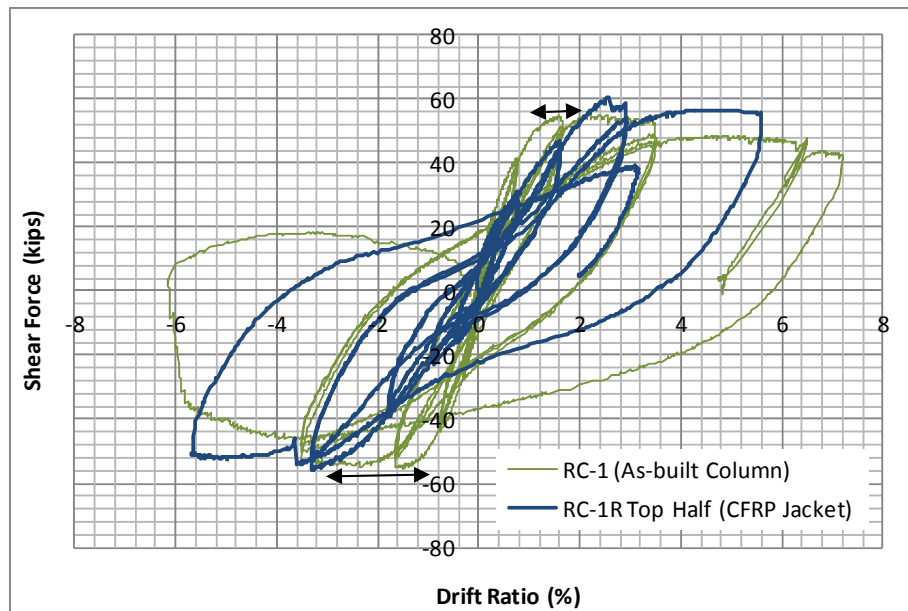


*Figure 5.145  Shear force vs. drift ratio of RC-1 and RC-1R Top Half*

Figure 5.146 shows a comparison of behavior for the two retrofitted halves of RC-2. Values of lateral displacement were normalized with drift ratios. It can be seen that both halves had the same behavior in the linear range. However, the half retrofitted with long mechanical splices reached higher lateral capacity and developed larger lateral displacement. The end point bolt of the short mechanical splice in RC-2R-SMS produced the rupture of the existing bar at lower drift ratios than in RC-2R-LMS, which had long mechanical splices with rounded bolt and fracture outside of the mechanical splice.
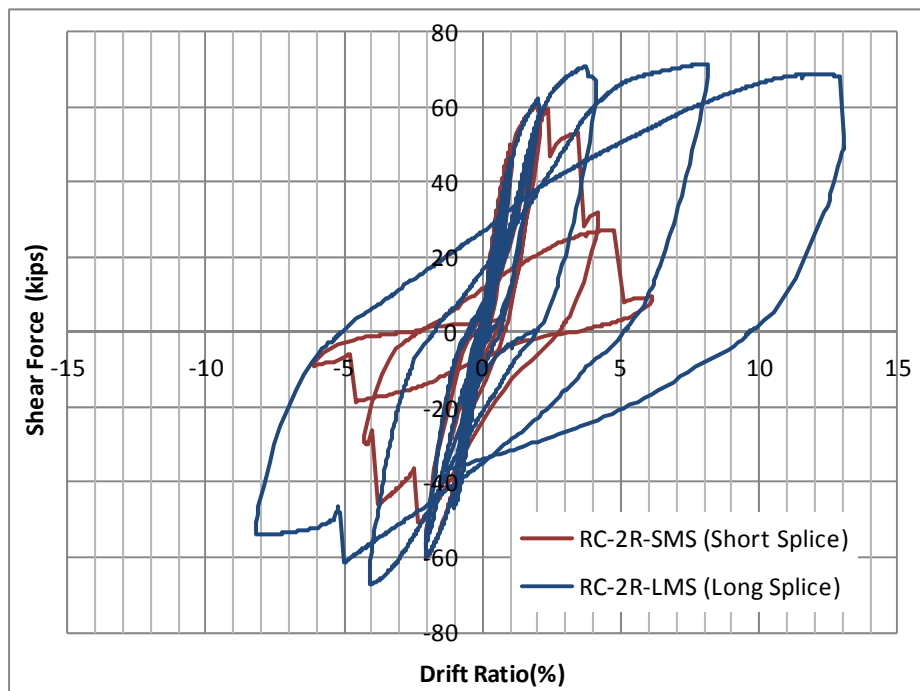


***Figure 5.146  Shear force vs. lateral displacement of RC-2R-SMS and RC-2R-LMS***

# CHAPTER 6

# Experimental Program – Rehabilitation of Severe Damaged Masonry Wall

## 6.1  INTRODUCTION

Masonry walls are frequently damaged by natural disasters such as earthquakes or tsunamis. The pattern of damage commonly seen in walls is shear cracking, and sliding between the wall foundation interfaces or between the courses of the wall. Sliding between courses occurs often when the masonry wall interface has no internal reinforcement.

The objective of this program was to evaluate the effectiveness of rehabilitation of a severely damage reinforced masonry wall with CFRP materials to improve the shear capacity of the wall and reduce sliding at the top and bottom interfaces of the wall and the reinforced concrete structure.

## 6.2 SHAKE-TABLE TEST OF FULL-SCALE THREE-STORY SPECIMEN

A full-scale three-story reinforced masonry structure was tested at the large high-performance outdoor one-direction shake table at the University of California in San Diego (UCSD). The structure had structural members composed of masonry CMU walls with internal vertical and horizontal reinforcement. Figure 6.1 shows side and elevation views of the specimen. The specimen was tested under 14 major time-history dynamic loads.

The objective for the rehabilitation research was to evaluate the damage one wall located at the middle of the first story and its influence on the response of the whole structure. Under different dynamic loads imposed on the specimen using time-history acceleration in one direction, most of the observed damage for this wall was sliding at the base. Diagonal shear cracks were observed in the rest of masonry walls on the first story.



Wall to study

***Figure 6.1  Full-Scale three-story reinforced masonry structure. Side and elevation view.***

### 6.2.1 Properties of the Three-Story Specimen

Figure 6.2 shows the plan view and dimensions of the full-scale specimen which is the same for each of the three stories. The structural members are composed of two T-walls located at each extreme and one longitudinal wall called W-2 that was studied for this project.
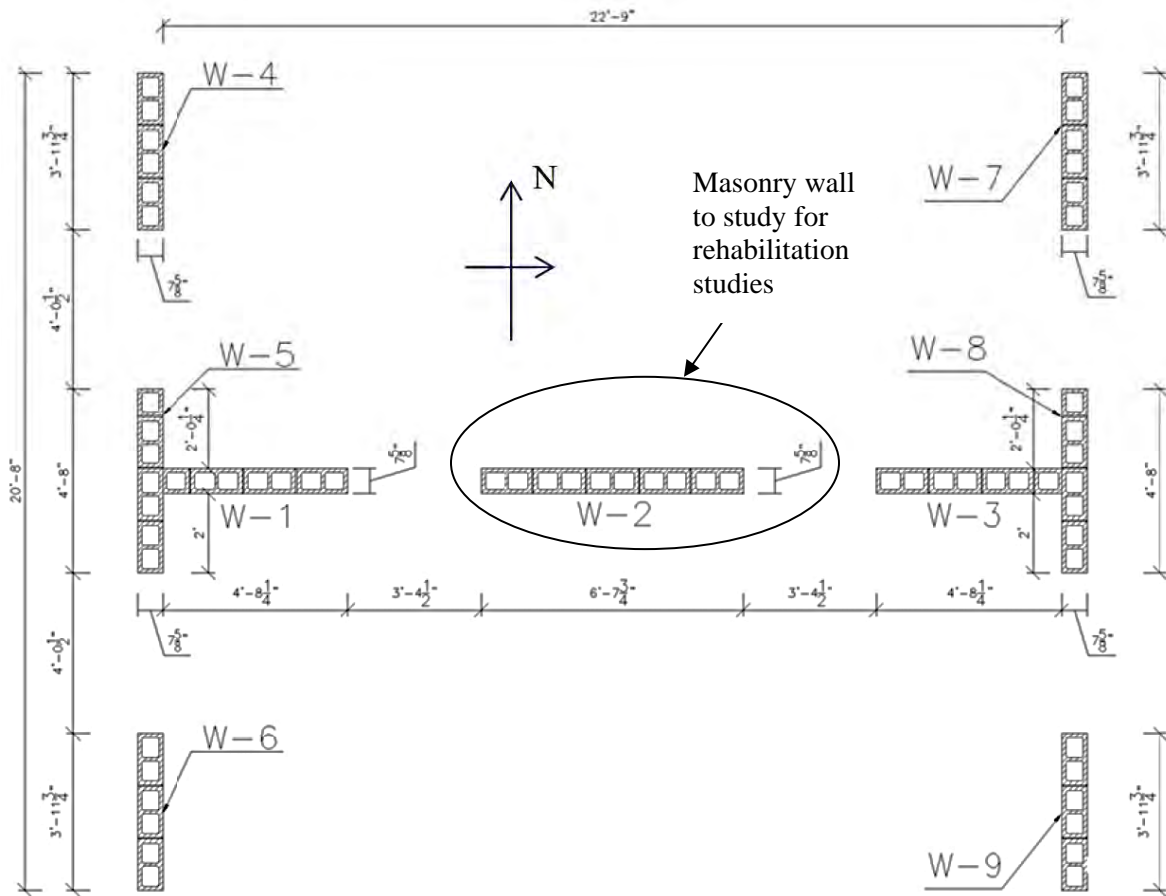


*Figure 6.2  Plan view of wall layout of the three-story specimen (Stavridis 2011)*

Figure 6.3 shows the elevation view of the three-story specimen. The dimensions of the masonry walls and the concrete hollow slab are the same for each story. The location of W-2 is also shown in Figure 6.3. There is a lintel in each story which works as an extension of the rigid floor. This lintel resulted in W-2 having an 80 in. height. Therefore, W-2 wall had an 80 in. length and 80in height and a thickness of 7.6 in. corresponding to the CMU's width. The slender L/H ratio of this wall was 1.
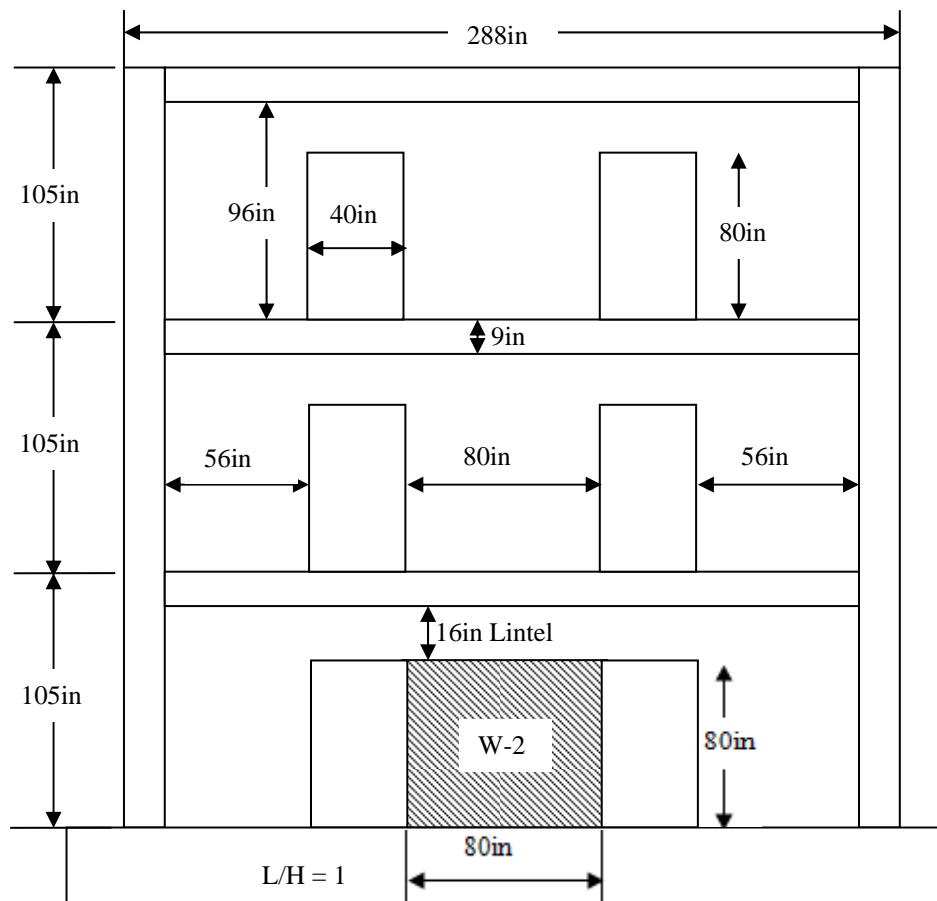


**Figure 6.3  Elevation view of the three-story specimen. Masonry wall W-2 is shown.**

Figure 6.4 shows the internal reinforcement for W-2. This wall was reinforced internally with #4 bars spaced vertically at 8 in. through the voids in the concrete blocks and grouted. One #4 horizontal bar was placed between each two courses of the wall to form a mesh of #4bars @ 16 in. All the bars were Grade 60 (Stavridis, 2011). Lap splices of 16in length were located at the bottom of the wall as is shown in Figure 6.4. It should be noted that ASCE-7 provisions don't allow lap splices to be located in the hinge zones as the bottom of a wall as in W-2. Because of this, W-2 was a potential example of a masonry wall that might be severely damaged and that would be a candidate for rehabilitation.

The compressive capacity of a concrete masonry unit (CMU), made with a grouted 8x8x8in block, was 3.05ksi. This grout had a compressive strength of 3.82ksi and the mortar between courses was 5.11ksi. The CMU properties were determined for a group of masonry walls constructed by Stavridis, 2011.
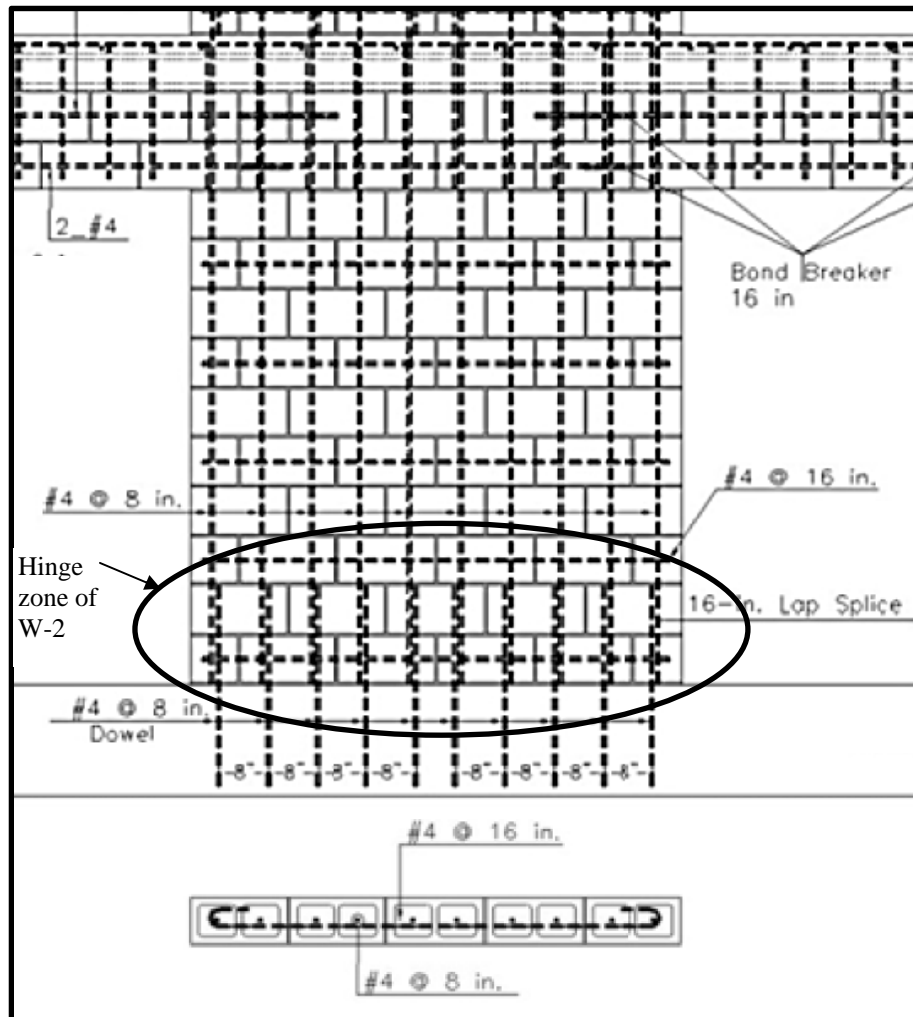
*Figure 6.4  Internal reinforcement of W-2 and location of hinge zone (Stavridis, 2011)*

### 6.2.2 Test program for the Full-Scale Specimen

#### 6.2.2.1 *Test Setup*

The tests were performed on the Large High Performance Outdoor Shake Table (LHPOST) is one of the test facilities of the University of California, San Diego (UCSD). This shake-table reproduces the ground motions for the seismic testing of very large structures. The LHPOST is a 25 ft. wide by 40 ft. long single degree of freedom (DOF) system. This shake-table has a stroke of ±2.45 ft., a peak horizontal velocity of 5.9 ft/s, a horizontal force capacity of 1500kips and a vertical capacity of 4500kips. The testing frequency range is 0-20 Hz.
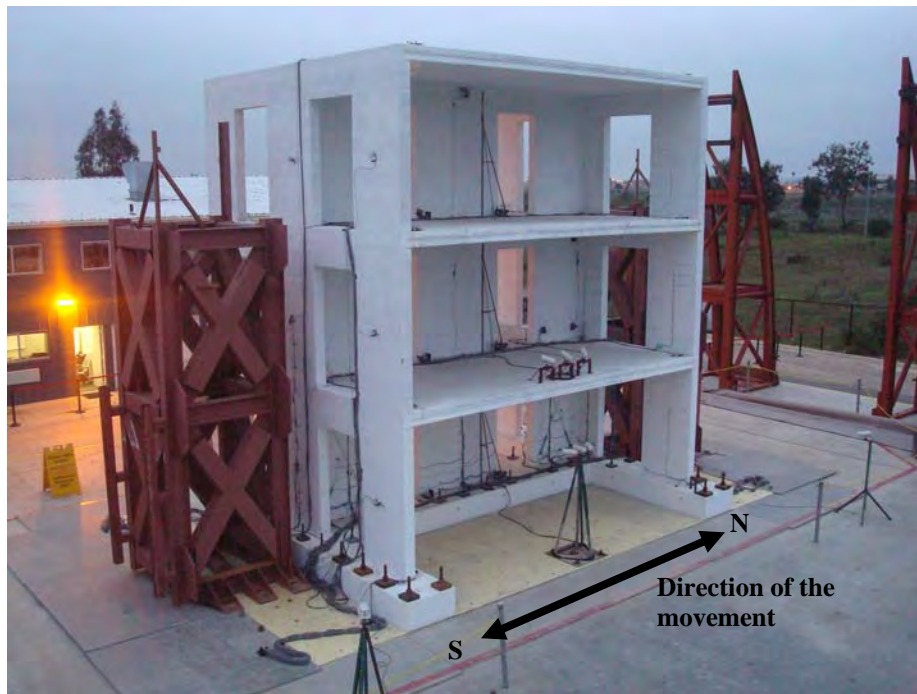


*Figure 6.5  UCSD one direction Shake-Table.*

6.2.2.2 *Instrumentation*

A set of 90 accelerometers, 133 linear potentiometers and 266 strain gages were used to monitor the global response of the full-scale specimen, its members and internal reinforcement.

Figure 6.6 shows the accelerometers located on some of the floors of the specimen and on the middle of W-2. The accelerometers A0F2NX, A1S2NX and A3S2NX monitored the acceleration response of the specimen at its base, $1^{st}$ story and roof. The accelerometer A1S2NX monitored the acceleration response of W-2 ($1^{st}$ story).

In Figure 6.7 the linear potentiometers used to monitor the behavior of W-2 through all the tests are shown. The names of each instrument is labeled and indicated in the figures. Linear potentiometers L1S2W1 and L1S2E1 monitored the sliding in both directions at the base for W-2. Instruments L1S2M2, L2S2M2 and S3S2M2 measured the global lateral displacement of the specimen at $1^{st}$, $2^{nd}$ and $3^{rd}$ story respectively.



| $1^{st}$ story slab | $2^{nd}$ story slab | Roof of Specimen |
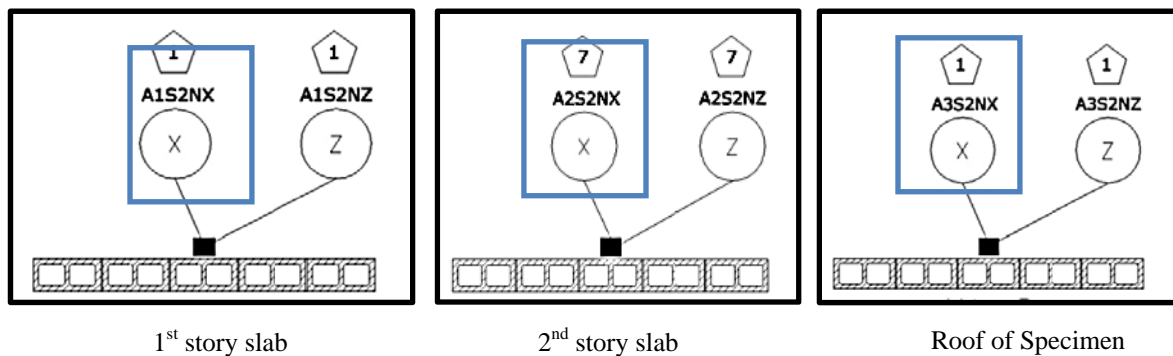
**Figure 6.6 Accelerometers on the full-scale specimen and W-2. (Stavridis,2011)**

236
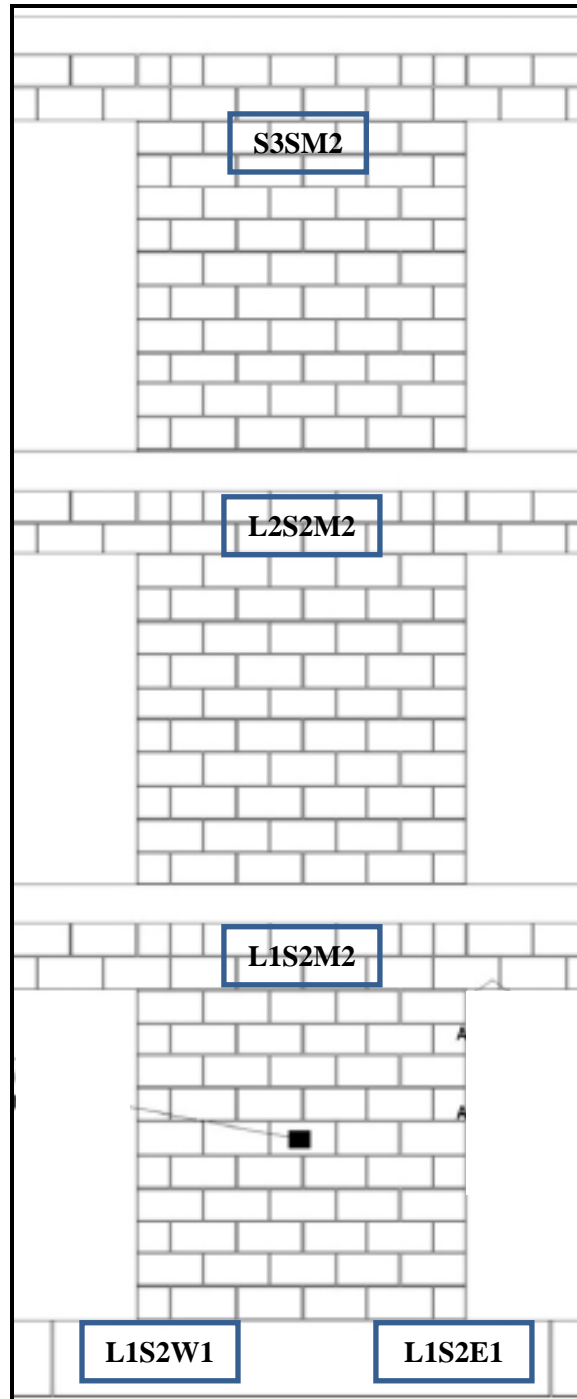
***Figure 6.7  Linear potentiometers located for measuring global response of specimen and local behavior of W-2. (Stavridis,2011)***

6.2.2.3 *Protocol of the times-history strong ground motion records applied*

The specimen was subjected to 14 time-history tests. However they were used 5 ground motion records. Table 6-1 shows the list of the ground motion records used, the magnitude and their PGA. Those records were chosen because of they produced the maximum pseudo accelerations for the natural period of the specimen as is shown in Figure 6.8. The natural period of the specimen before testing was 0.09sec and it was increased as each test was performed. Figure 6.8 shows also the Design Basis Earthquake (DBE) which represent the demand of an event with 10% probability of occurrence each 50years, and the Maximum Considered Earthquake (MCE) which represent the demand of an event with 2% probability of occurrence each 50years. DBE and MCE were considered for risk occupancy of an idealized structure (hospital or school).

*Table 6-1 Ground motion records used*

| Earthquake Event | Magnitude | Station-Record | PGA |
|---|---|---|---|
| Imperial Valley - California - USA 1940 | 6.9 Mw | El Centro | 0.519 g |
| Imperial Valley - California - USA 1979 | 6.4 Mw | El Centro | 0.313 g |
| Northridge - California - USA 1994 | 6.7 Mw | Sylmar | 0.843 g |
| Northridge - California - USA 1994 | 6.7 Mw | Rinaldi | 0.838 g |
| Chi Chi - Taiwan 1999 | 7.7 Mw | Chi Chi | 1.01 g |
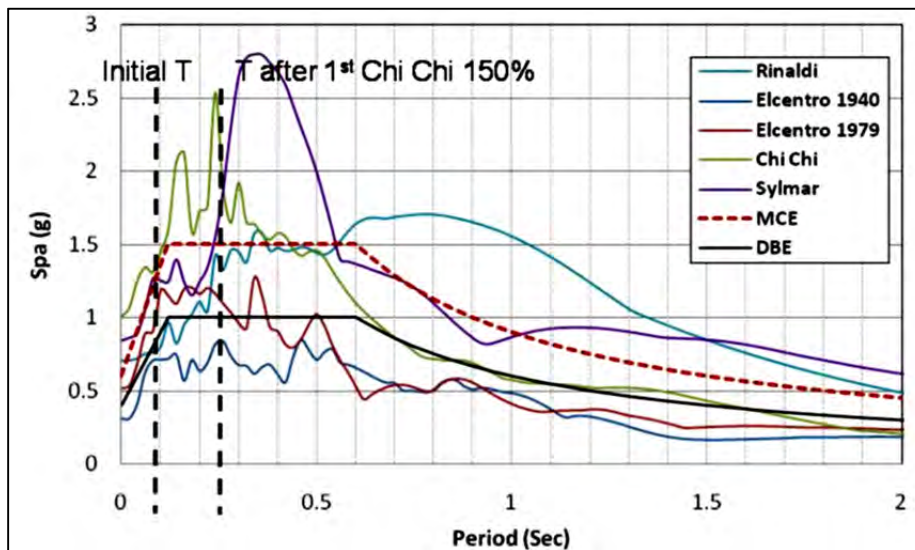
***Figure 6.8  Response Spectrums of the ground motion records used, DBE and MCE***
***spectrums (Ahmadi, 2012)***

Table ***6-2*** shows the list of 14 time-history tests performed. The ground motion records were scaled by different parameters for each test as the natural period of the structure was degraded. The ground motion records used the scaled PGA for each test are shown. Comments related with DBE and MCE are included also. Between each time-history test, a white-noise excitation was applied that produces less than 0.03g acceleration in order to determine the degraded natural period.

239

*Table 6-2 Summary of tests*

| | | Note | Ground Motion Record | PGA |
|---|---|---|---|---|
| Friday, 11 January | Test 1 | | 20% of El Centro 1979 | 0.103 g |
| Monday, 12 January | Test 2 | | 45% of El Centro 1979 | 0.234 g |
| Thursday, 13 January | Test 3 | Expected DBE | 90% of El Centro 1979 | 0.493 g |
| Monday, 18 January | Test 4 | Realized DBE | 120% of El Centro 1979 | 0.623 g |
| | Test 5 | Slightly below MCE | 150% of El Centro 1979 | 0.778 g |
| Wednesday, 19 January | Test 6 | Slightly above MCE | 180% of El Centro 1979 | 0.934 g |
| | Test 7 | | 250% of El Centro 1979 | 1.295 g |
| | Test 8 | | 250% of El Centro 1940 | 0.782 g |
| Thursday, 20 January | Test 9 | Slightly above MCE | 125% of Sylmar | 1.053 g |
| Tuesday, 26 January | Test 10 | Above MCE | 160% of Sylmar | 1.349 g |
| | Test 11 | Slightly above MCE | 140% of Rinaldi | 1.173 g |
| | Test 12 | Above MCE | 100% of Chi Chi | 1.010 g |
| Tuesday, 8 February | Test 13 | About 2 times MCE | 150% of Chi Chi | 1.515 g |
| | Test 14 | About 2 times MCE | 150% of ChiChi | 1.515 g |

6.2.2.4 *Results of Tests*

The discussion will focus on the behavior of W-2. However, some general information regarding the behavior of the three-story structure and the progressive damage trough the different ground motion on to this specimen will be mentioned.

For the first tests, 20% and 45% El Centro 1979, there was no visible damage. Flexural cracks began to appear on the base of the two T-walls at 90% El Centro 1979. No sliding was observed or measured on W-2 and the natural period of the specimen remained 0.09sec. Some flexural cracks in the lintels appeared at 120% El Centro 1979 motion. The drift of the first story was 0.05% when the Design Basis Earthquake DBE level was reached.

At 150% El Centro 1979 and 180% El Centro 1979, horizontal cracks between the first course of CMU in W-2 and its foundation appeared. A sliding deformation of 0.04in was measured at the base of W-2. The drift ratio reached 0.14% or 0.15in maximum lateral deformation. At 250% El Centro 1979, the sliding deformation of 0.12in constituted almost the 50% of the maximum lateral displacement of 0.26in for the first floor. Additionally, diagonal shear cracks appeared on the T-walls and the lintels. Figure 6.9 shows the location of the cracks in W-2, near the lintels and sliding at toe of the wall. The natural period of the specimen increased to 0.20sec indicating further degradation of the structure. At this level, the behavior was non-linear.
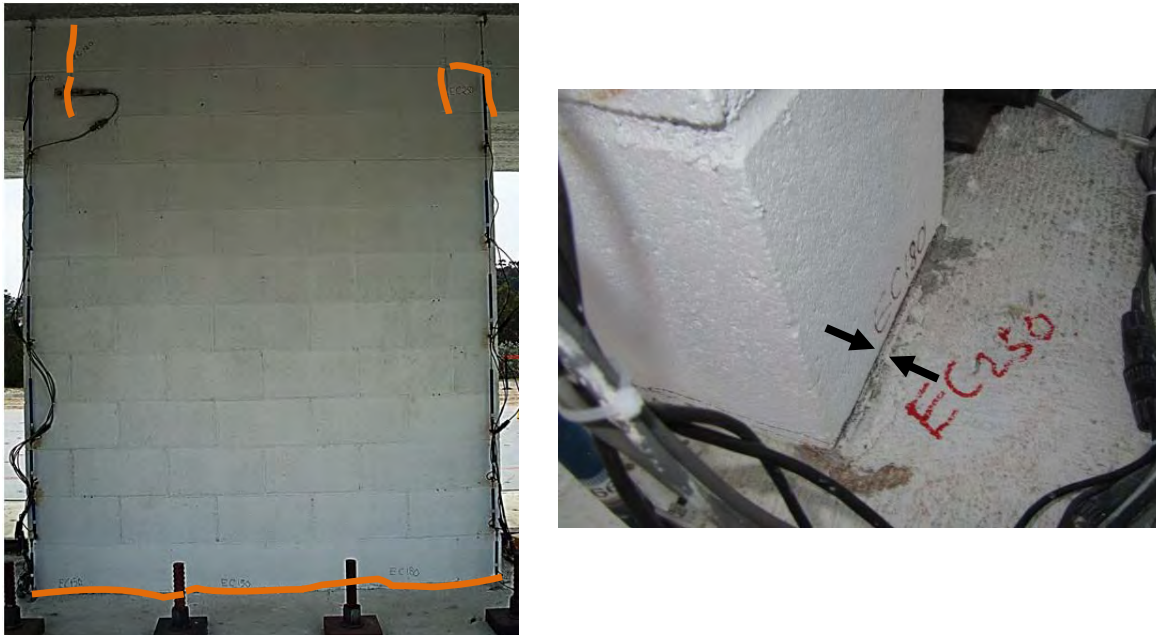
***Figure 6.9  Condition of W-2 after apply the motion 250% El Centro 1940***

In Table 6-3, the maximum values for displacement of first story, sliding at the base of W-2, and base shear correspondent for the first floor and the masonry wall W-2 are summarizes. Values of PGA are shown. The displacement increased nearly linearly as with the factored El Centro 1979 ground motion.

*Table 6-3 Summary of maximum values of measured response parameters of three-story structure and W-2 in the linear range.*

| | | H (in) | 105 | Max. Drift 1st Story | Max.Disp. 1st Story | Max.Sliding 1st Story | Max. Base Shear | Max. Base Shear W-2 |
|---|---|---|---|---|---|---|---|---|
| | | | PGA (g) | (%) | (in) | (in) | (kip) | (kip) |
| Test 1 | 20% El Centro 1979 | | 0.10 | X | LVDT malfuntioning | no sliding | x | x |
| Test 2 | 45% El Centro 1979 | | 0.23 | X | LVDT malfuntioning | no sliding | x | x |
| Test 3 | 90% El Centro 1979 | | 0.49 | 0.04 | 0.037 | no sliding | 127.86 | 42.62 |
| Test 4 | 120% El Centro 1979 | | 0.62 | 0.05 | 0.056 | 0.008 | 172.79 | 57.60 |
| Test 5 | 150% El Centro 1979 | | 0.78 | 0.09 | 0.097 | 0.016 | 208.83 | 69.61 |
| Test 6 | 180% El Centro 1979 | | 0.93 | 0.14 | 0.148 | 0.036 | 246.39 | 82.12 |
| Test 7 | 250% El Centro 1979 | | 1.30 | 0.25 | 0.261 | 0.120 | 278.01 | 92.67 |

Figure 6.10 shows the hysteretic loops for base shear vs. displacement for W-2 for the ground motion records at 90%, 120% and 150% El Centro 1979 reflect behavior up to the DBE. Ground motion records at 180% and 250% of El Centro 1979 reflect response at the MCE. The shear- displacement response of W-2 for 250% El Centro 1940 indicates that the structure behaved in the nonlinear range. The natural period of the specimen increased after the Test 7 (250% El Centro 1979).
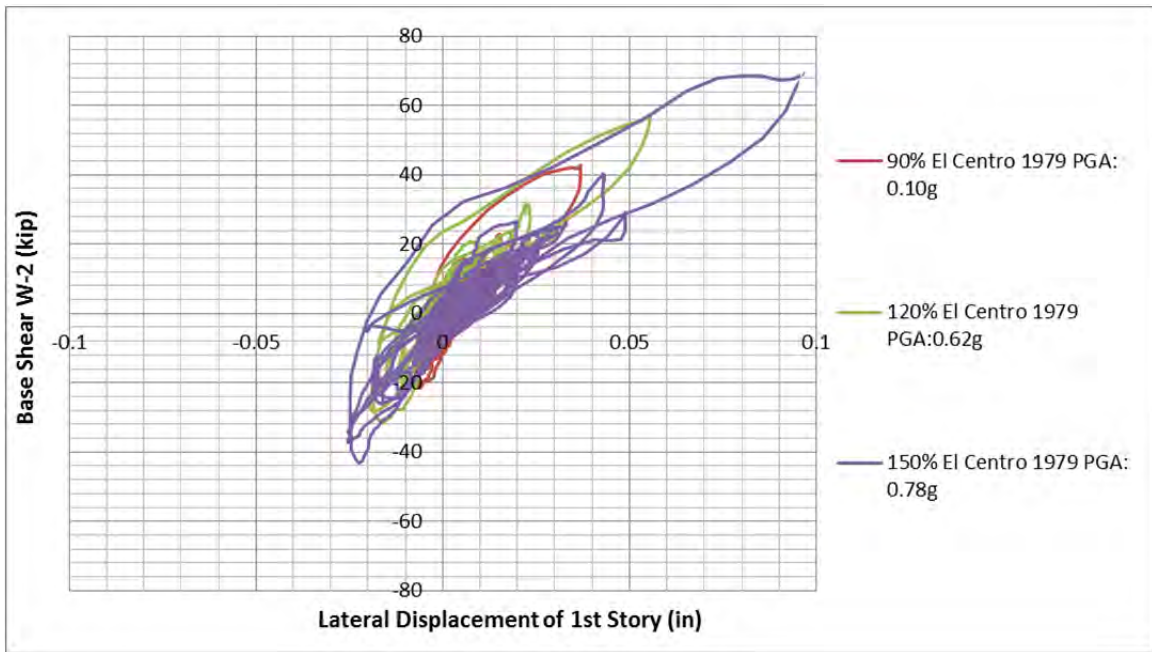
*Figure 6.10  Base shear vs. lateral displacement hysteretic loops of W-2 for Test 3 to 5*
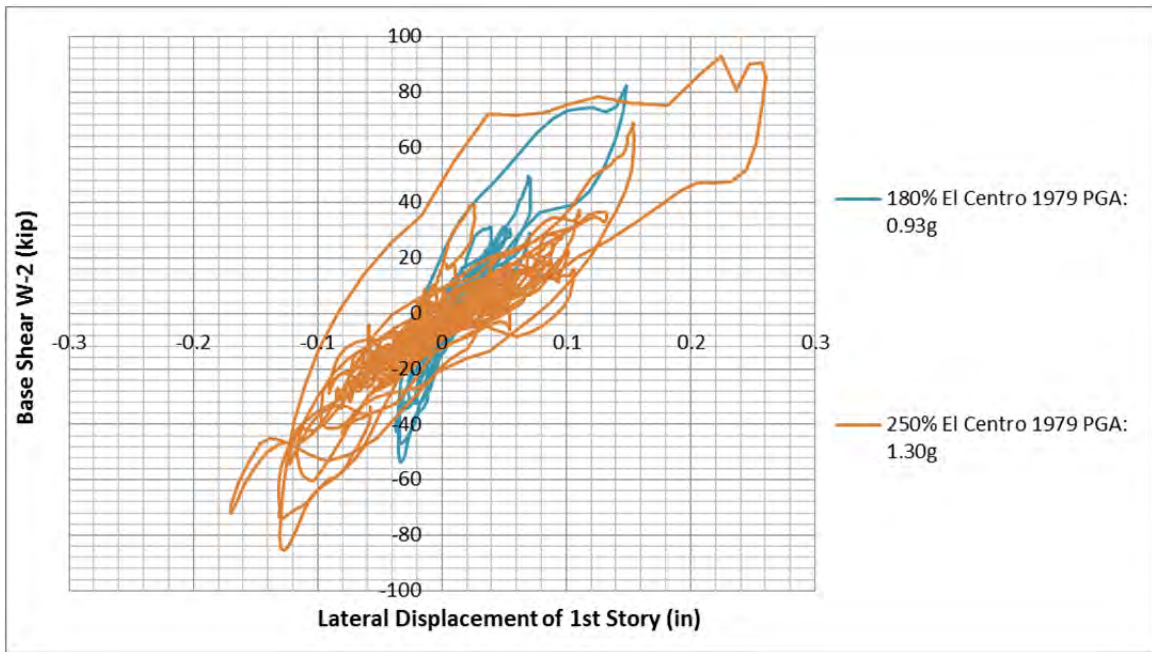


*Figure 6.11  Base shear vs. lateral displacement hysteretic loops of W-2 for Test 6 to 7*

244

The nonlinearity was due to the sliding, flexural and shear cracks in the T-walls, and the formation of the hinges in the lintels.

When the maximum lateral displacement of the first floor was 0.15in, which is less than or under 250% El Centro 1979 case. Test 8 did not change the natural period of 0.20sec. Cracks on the 1st story slab appeared perpendicular to the longitudinal direction of the specimen indicating the forming of hinges in lintels.

For 125% and 160% Sylmar, the diagonal shear cracks extended in the T-walls. Also, sliding at bottom of W-2 increased to 0.25in, or 63% of the maximum lateral displacement of 0.40in for the first floor. Horizontal cracks developed in the top course CMUs of W-2.

At 140% Rinaldi, the maximum lateral displacement of 0.26in (0.25% drift ratio) was reached and was less than the 160% Sylmar movement. However, sliding of W-2 was 0.18in which represents 78% of the maximum lateral displacement of the first floor. The natural period increased to 0.22 sec indicating stiffness degradation of the specimen. This event was considered to represent the MCE and sliding at base of W-2 constituted a very important fraction of the degradation of the structure. For rehabilitation purposes, W-2 represented very stiff member, with high shear and flexural resistance and low restraint against sliding.

To evaluate behavior above the MCE level, 100% Chi Chi ground motion was applied. The maximum lateral deformation of the first story was 0.38in and sliding of W-2 0.26in or 71% of the total maximum lateral displacement of the first story. Figure 6.12 shows the base of W-2 and the sliding observed. In this test, sliding was governed the behavior of W-2. Additionally, cracks on the T-walls of 2nd story appeared. These

flexural and shear cracks developed at the bottom of the T-walls. No further degradation of the natural period of specimen was observed.



*Figure 6.12  Sliding in W-2 after 100% Chi Chi event (Stavridis)*

Figure 6.13 shows the hysteretic loops for base shear vs. displacement of W-2 for 125% and 160% Sylmar, and 100% Chi Chi. Degradation of base shear capacity was observed in these tests.
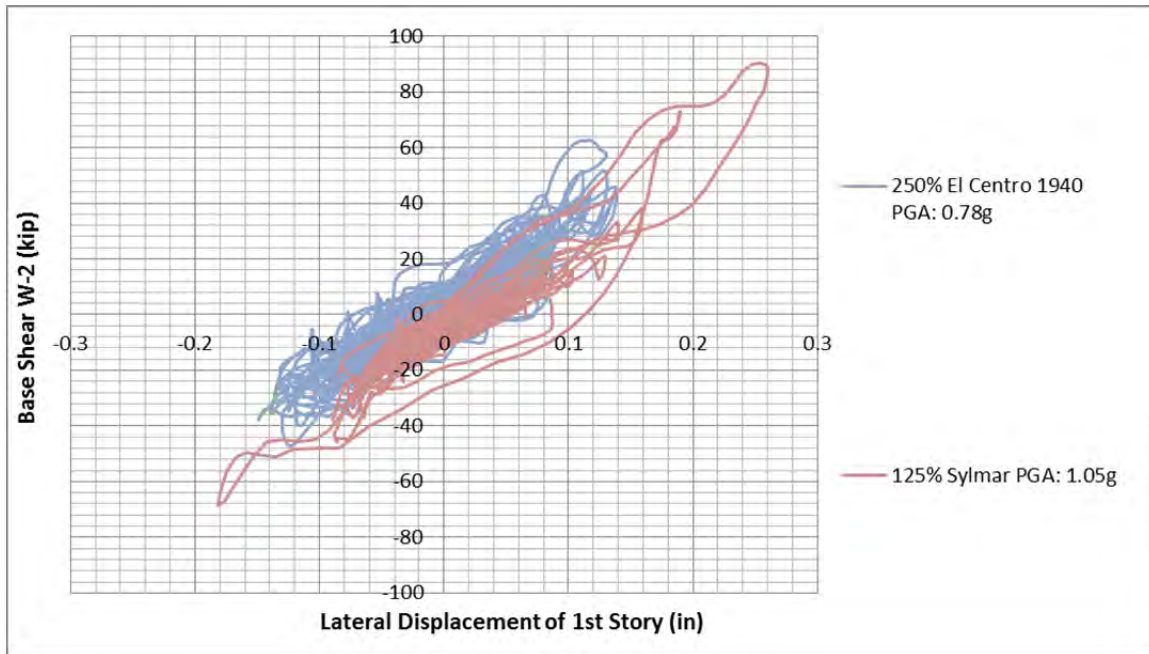
*Figure 6.13  Base shear vs. lateral displacement hysteretic loops of W-2 for Test 8 to 9*
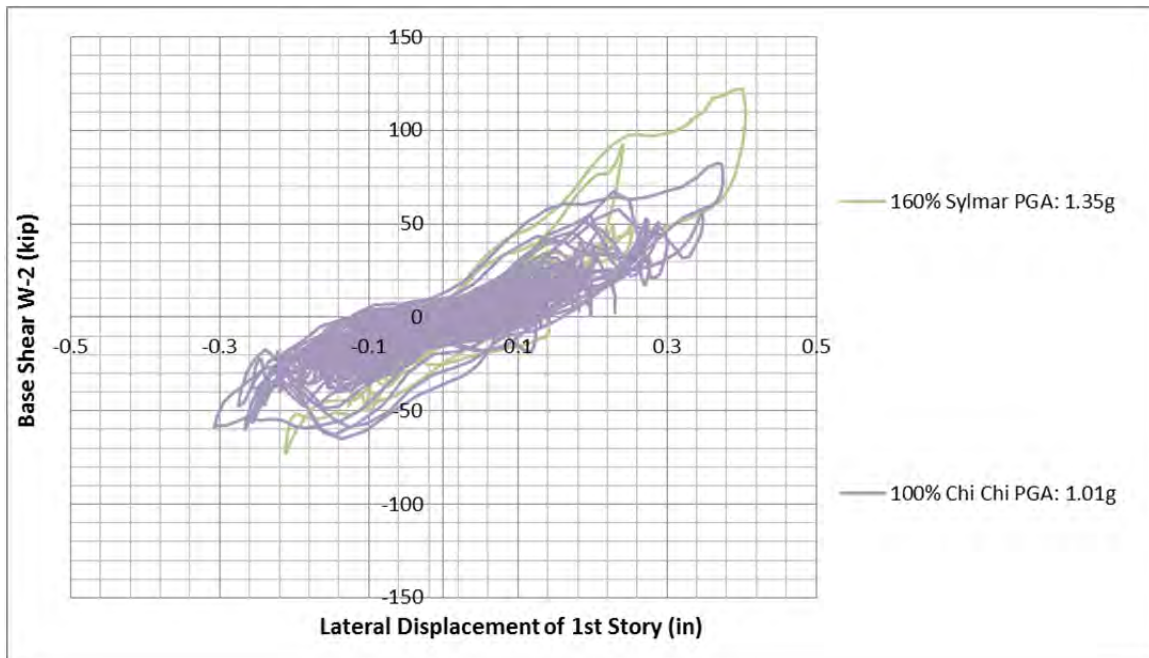


*Figure 6.14  Base shear vs. lateral displacement hysteretic loops of W-2 for Test 10 to 11*

247

The 150% Chi Chi ground motion was applied twice. The 150% Chi Chi event was considered 2 times MCE. For the first application of 150% Chi-Chi motion, W-2 had a sliding of 0.27in or 74% of the total maximum lateral displacement at first story 0.77in (0.73% drift ratio). No additional cracks were presented on W-2. However the existing diagonal shear cracks in the T-walls became wider (1.5mm), and new diagonal cracks appeared. After this test, the natural period of the structure was increased to 0.25sec. Finally, 150% Chi Chi motion was applied to the degraded structure, resulting in a maximum lateral displacement of 1.68in (1.6% drift ratio) in the first story. It is very important to notice that this lateral displacement was two times larger than the lateral displacement in the first 150% Chi Chi test. T-walls developed new diagonal shear cracks and the existing ones increased the width to 10mm (Figure 6.15). No additional cracks appeared on W-2, however the sliding at W-2 was 1.12in, which was 71% of the total displacement of the 1$^{st}$ story and therefore of W-2 too. (Figure 6.16).
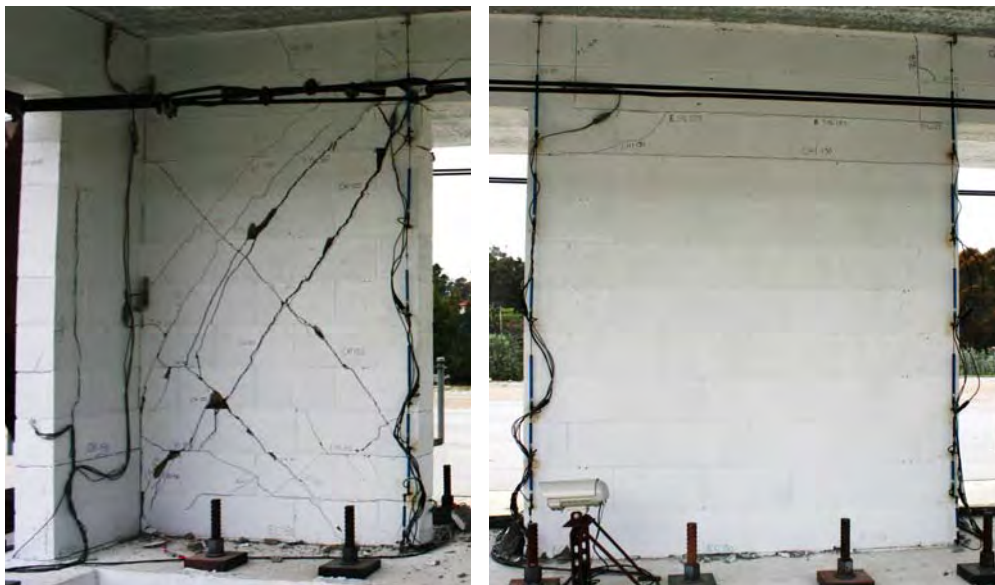


*Figure 6.15  Condition of one T-wall and W-2 after 2$^{nd}$ 150% Chi Chi motion (Stavridis, 2011)*

***Figure 6.16  Sliding in W-2 after 2<sup>nd</sup> 150% Chi Chi motion (Stavridis, 2011)***

Figure 6.17 shows the hysteretic loops for base shear vs. displacement for the first and second 150% Chi Chi tests. Further degradation of shear capacity and stiffness occurred when the same ground motion was imposed a second time.
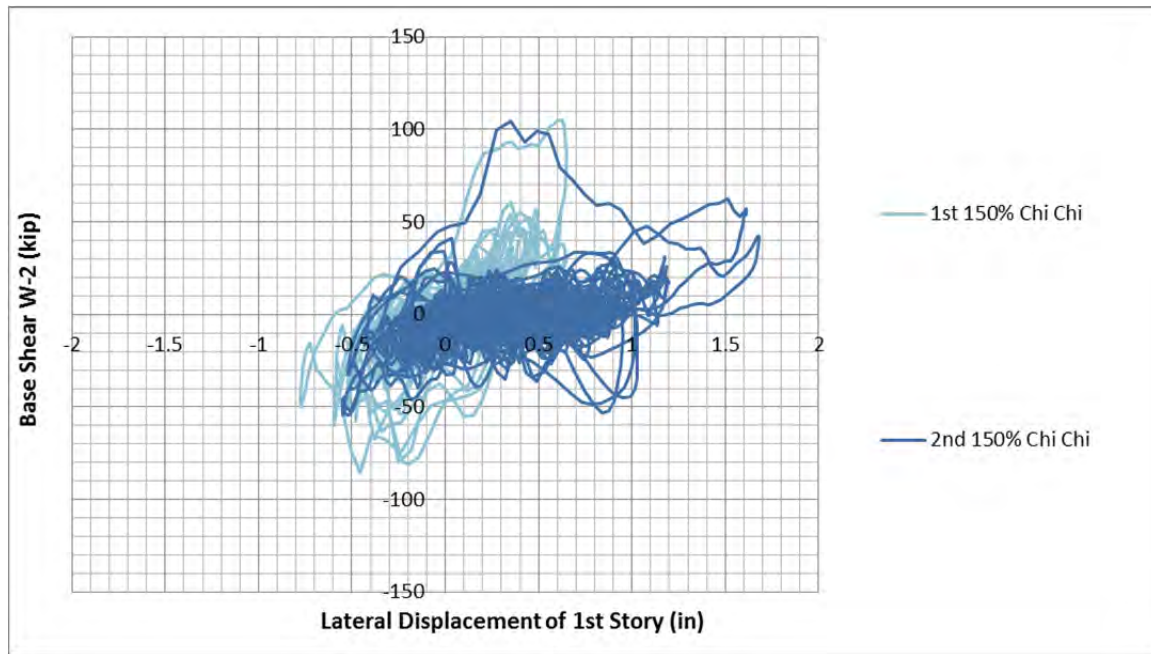
***Figure 6.17 Base Shear vs. Lateral Displacement Hysteretic Loops of W-2 for Test 13 and Test 14***

Table 6-4 summarizes the maximum values for displacement of first story, sliding at the base of W-2, and base shear correspondent for the first floor and the masonry wall W-2. Values of PGA are included. The three-story structure behaved on the nonlinear range for all of those tests presented in the table.

| | | H (in) | 105 | Max. Drift 1st Story | Max.Disp. 1st Story | Max.Sliding 1st Story | Max. Base Shear | Max. Base Shear W-2 |
|---|---|---|---|---|---|---|---|---|
| | | | PGA (g) | (%) | (in) | (in) | (kip) | (kip) |
| Test 8 | 250% El Centro 1940 | | 0.78 | 0.14 | 0.147 | 0.087 | 187.95 | 62.65 |
| Test 9 | 125% Sylmar | | 1.05 | 0.25 | 0.260 | 0.146 | 270.00 | 90.20 |
| Test 10 | 160% Sylmar | | 1.35 | 0.38 | 0.404 | 0.246 | 366.97 | 122.32 |
| Test 11 | 140% Rinaldi | | 1.17 | 0.25 | 0.260 | 0.177 | 313.76 | 104.58 |
| Test 12 | 100% Chi Chi | | 1.01 | 0.36 | 0.375 | 0.259 | 247.71 | 82.60 |
| Test 13 | 1st 150% Chi Chi | | 1.52 | 0.73 | 0.770 | 0.630 | 314.65 | 104.88 |
| Test 14 | 2nd 150% ChiChi | | 1.52 | 1.60 | 1.680 | 1.115 | 313.76 | 104.58 |

During testing, it was observed that the deformation of W-2 was similar to double curvature deformation, due to restrained rotation at the top and bottom of this wall. Additionally, a constant gravity load was acting on W-2 by the self-weight of the correspondent tributary area of the slab, and the self-weight of W-2 plus the masonry walls in the two stories above this W-2. The gravity load on W-2 estimated is to be 56kips.

Figure 6.18 shows the hysteretic loops of the base shear – lateral displacement of W-2 for all the 14 tests. Degradation of stiffness and shear capacity is apparent   as explained on 6.2.2.4. By joining the peaks of lateral displacement, to a backbone or envelope curve for W-2 shear force- lateral displacement is obtained. Peaks of the 250% El Centro 1940, 125% Sylmar, 140% Rinaldi and 100% Chi Chi hysteretic loops were not included because they are inside the areas formed by the rest of the hysteretic loops (their base shear and displacement peaks values were lower). The envelope curve was plotted to represent the response of W-2 for retrofit purposes.
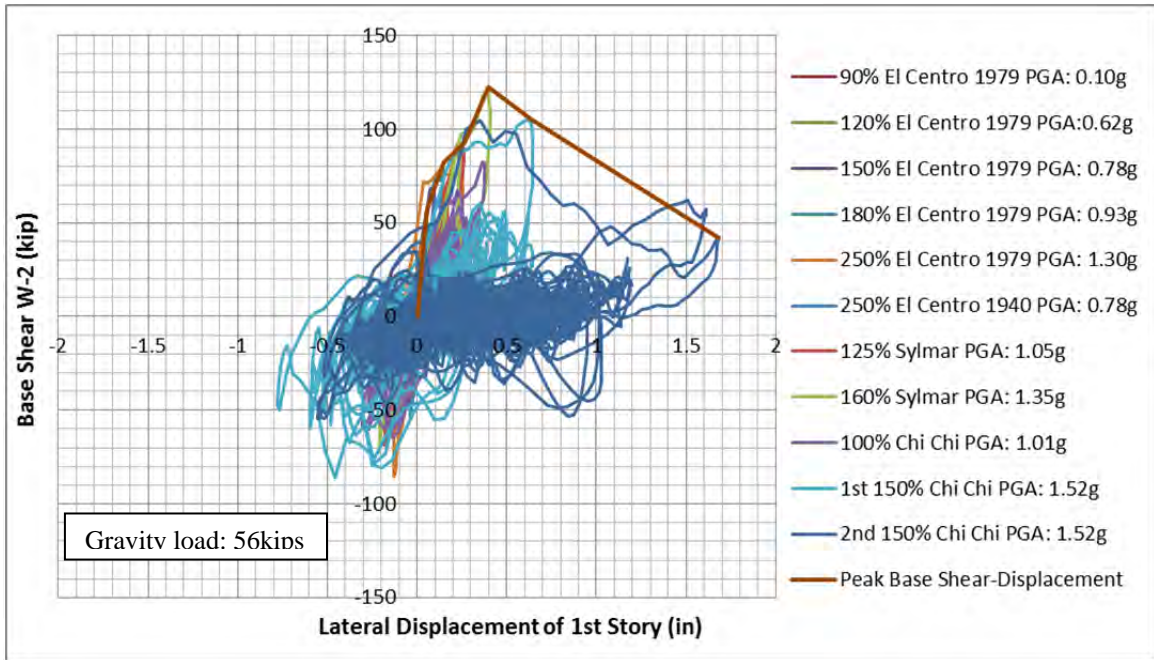
*Figure 6.18  Base Shear vs. Lateral Displacement Hysteretic Loops of W-2 for the 14 different ground motions imposed to the specimen.*

### 6.2.3 Comments of the test result of W-2 for rehabilitation research

Figure 6.19 shows comparisons of the sliding at W-2 (red bars), with the total displacement of the first floor (blue + red bars) for each test. The total length of the bar represents the maximum total displacement presented in the first floor. It can be seen that sliding governed the behavior of W-2 after the 250% El Centro 1979 test and represented 63% of the total displacement. Sliding was involved in the degradation of the stiffness of the structure and reduced the shear capacity of the specimen as well. For rehabilitation purposes, the strengthening of W-2 to reduce the sliding is important for future DBE and MCE events.
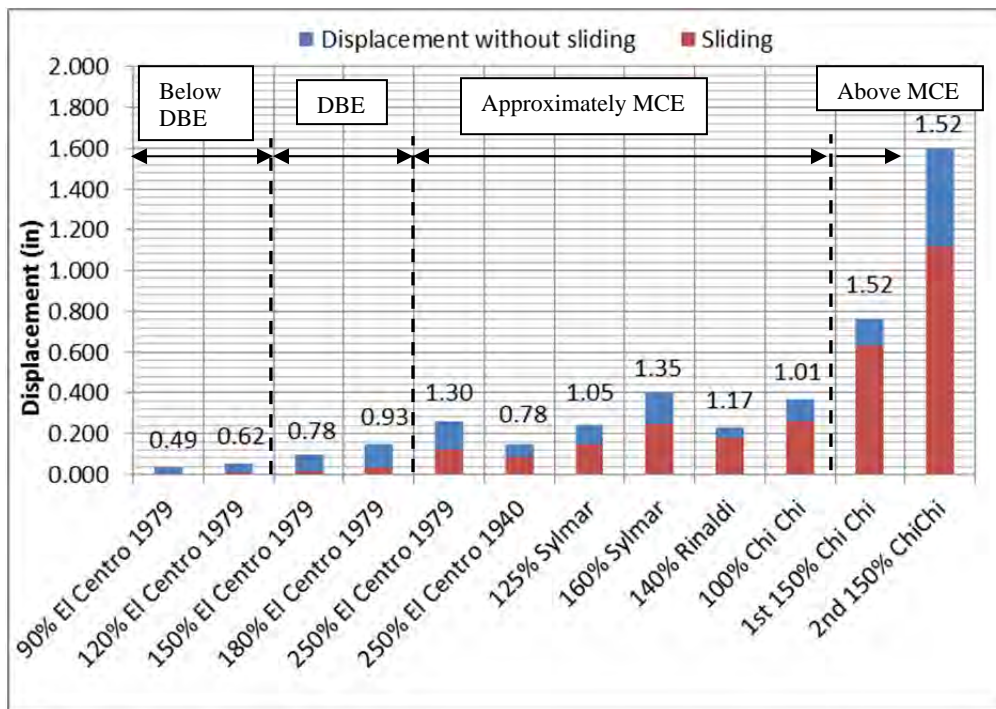


*Figure 6.19  Maximum displacement of 1$^{st}$ story and sliding in W-2 for each test. PGA of each event is on top of bars*

Figure 6.20 shows a comparisons of the maximum base shear on W-2, measured through the different tests. It is observed that the shear capacity increased progressively in the linear range (first 5 tests until 250% El Centro 1979).
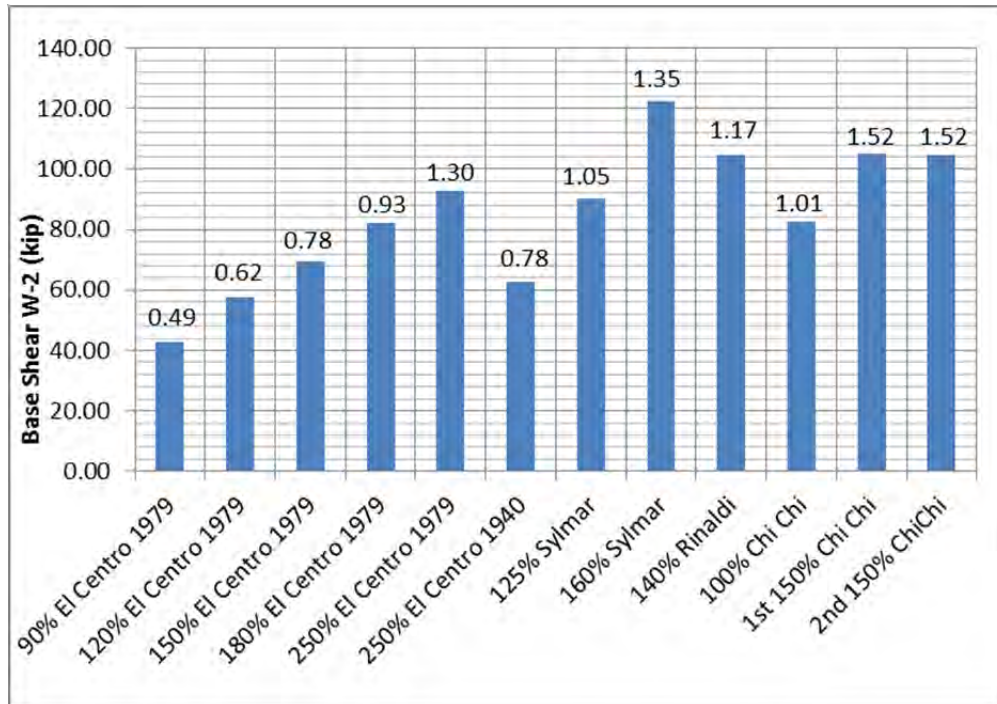


***Figure 6.20  Maximum base shear of W-2. Peak Ground Acceleration PGA of each event is on top of bars***

The three-story structure and W-2 were severely damage after that MCE event was exceeded in the 140% Rinaldi ground motion. Without appropriate rehabilitation of W-2 after the 140% Rinaldi event, the structure suffered more damage. Figure 6.19 indicates that the structure had a progressive increase in lateral displacement under a similar level (similar PGA for 125% Sylmar and 100% Chi Chi). This effect was evident during the two last tests (1$^{st}$ and 2$^{nd}$ 150% Chi Chi event). The reinforced masonry structure degraded significantly under the same ground motion (the maximum lateral

displacement was increased by 2) as a result of the increased sliding on W-2 and the shear cracking of the T-walls.

For cases such as hospitals or schools, rehabilitation is essential for protecting occupants. The study of the shake-table test of the three-story structure helped to define the type and level of damage which could be observed on reinforced masonry wall.

In the next section, the behavior of a reinforced masonry wall with an aspect ratio similar to that of W-2 and 2.5 times higher axial load. Then that imposed on W-2 is presented and discussed before and after rehabilitation.

**6.3    QUASI-STATIC TEST OF MASONRY WALL**

A reinforced masonry wall similar that in the three-story reinforced masonry structure was tested. This was subjected to constant axial load, lateral cyclic load and rotations at the top and bottom of the wall were restrained. The boundary conditions were similar to those of the middle wall in the shake-table test.

### 6.3.1    Properties of the original masonry wall

The hollow concrete masonry units used to build the wall had normal dimensions16x8x8in (the measured dimensions were 15.6x7.6x7.6in and a 1.25in wall thickness). The wall cross-section is shown in Figure 6.21. The compressive capacity of a concrete masonry unit (CMU), made with a grouted 8x8x8in block, was 3.5ksi. The grout had a compressive strength of 6ksi and the mortar between courses had strength of 2.4ksi. The compression resistance of a grouted prism formed by 2 blocks was 3.1ksi. The CMU properties were reported for the group of masonry walls constructed by Ahmadi, 2012.

The wall was reinforced internally with #4 bars spaced vertically at 8in through the hollow cores in the concrete blocks and grouted. One #4 horizontal bar was placed between each course of the wall to form a mesh of #4bars @ 8in. All the bars were Grade 60 (Ahmadi, 2012).

The height of this wall was 72 in (9 courses of CMU). The length of the wall was 71.6in. Figure 6.21 shows an elevation of the wall and the cross section with the location of the internal reinforcement shown. The dimensions of the concrete base foundation and top concrete loading block are also shown (Ahmadi, 2012)
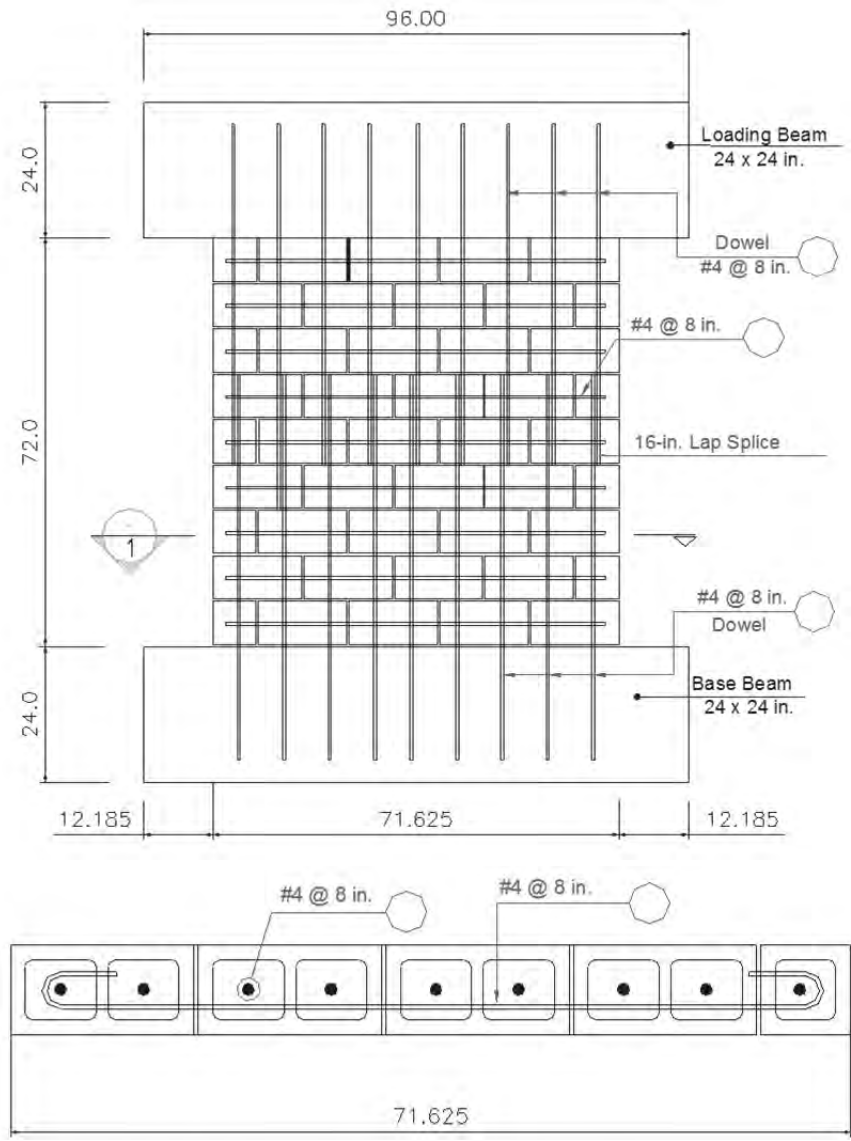
*Figure 6.21  Dimensions of the original masonry wall and its internal reinforcement (Ahmadi 2012)*

257

### 6.3.2 Test Setup for the Quasi-Static Test

The masonry wall was tested under the same pattern of lateral loads applied to the columns described in Chapter 4. The constant axial load and cyclic lateral loads were applied to the masonry wall through the L-frame with three hydraulic actuators. However, a concrete block supported the base of the wall and a steel spacer beam was added above the concrete loading beam at the top of the masonry wall to position the masonry wall properly within the L-frame as shown in Figure 6.22. Both the concrete block and the spacer beam were 23in deep. The bolts and the rods connecting the loading elements to the test specimen and to the lab floor can be seen in Figure 6.22.



*Figure 6.22 Test setup for the fix bottom – top rotation restrained masonry wall*

### 6.3.3 Instrumentation

For the test of the masonry wall, deformation transducers, wire potentiometer and strain gages on the internal reinforcement were used to monitor the behavior as shown in Figure 6.23
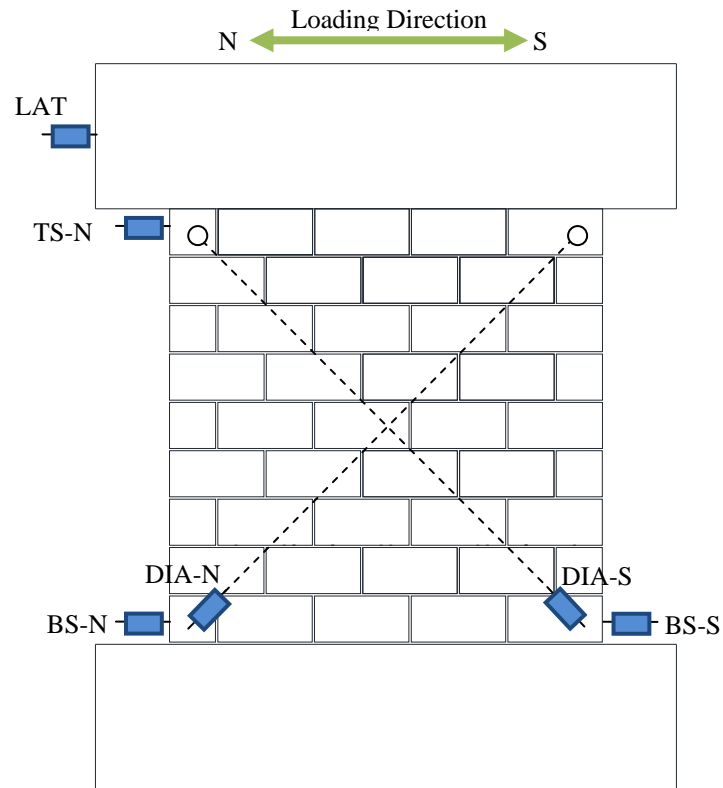


*Figure 6.23 Instrumentation used for current research*

### 6.3.4 Protocol of Load for the Lateral Cycle Load Test

The loading history was applied under displacement control as shown in Figure 6.24. An axial load of 140kips was applied prior the application of any lateral load.
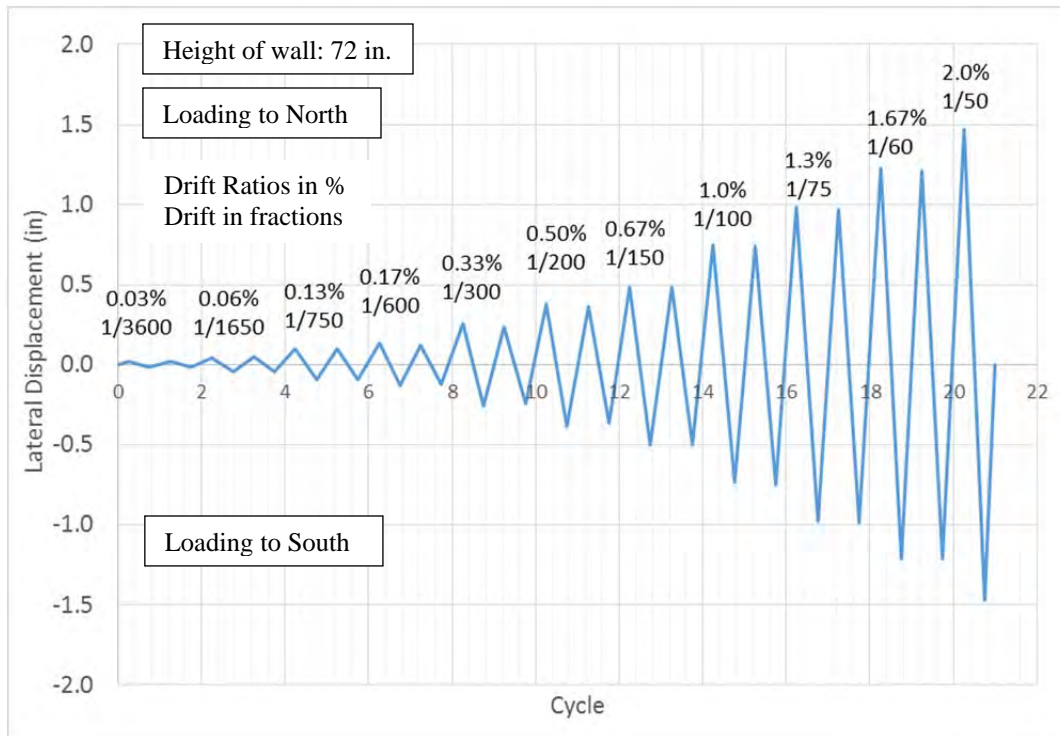
*Figure 6.24 Protocol for lateral displacement*

## 6.3.5 Results of the test for RMW

In the 5th and 6th hysteretic cycles, at a lateral deformation of 0.095in (0.13% drift ratio), the first flexural and diagonal shear cracks were observed as shown in Figure 6.26. The peak lateral load was 126kips marked the end of the linear range of behavior because the internal vertical reinforcement reached yield and the CMUs.
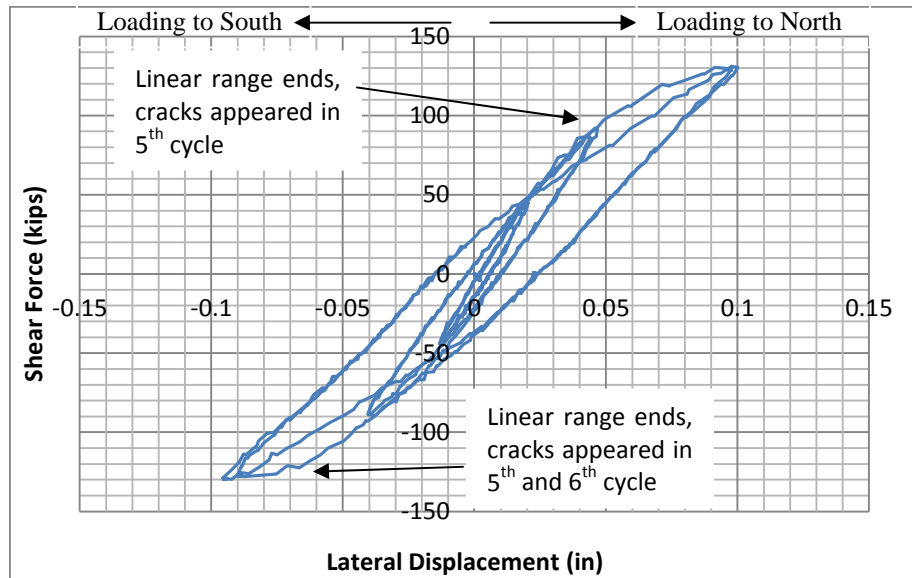
*Figure 6.25  Shear force vs. lateral displacement response of specimen until the 6th cycle*



*Figure 6.26 Horizontal, flexural and diagonal shear cracks*

261

Further lateral displacement to the masonry wall produced more flexural and diagonal cracks especially in the 9th and 10th cycle (0.24in lateral deformation or 0.33% drift ratio) and the width of the existing cracks increased. The maximum shear capacity of the specimen in the south direction was 171kips measured at the peak of the 9th cycle as shown in Figure 6.27. In the 11th cycle to the north, the maximum shear capacity of 179kips for that direction was reached.

Sliding was noticed in the 13th cycle. The shear force was 175kips to the north and 161kips to the south direction. The shear force vs. lateral displacement response pattern reflected sliding at the base as seen in Figure 6.27. Larger and wider diagonal shear cracks developed through the wall in both faces as is shown in Figure 6.28. Toe crushing appeared on the bottom corners of the wall as a result of sliding.
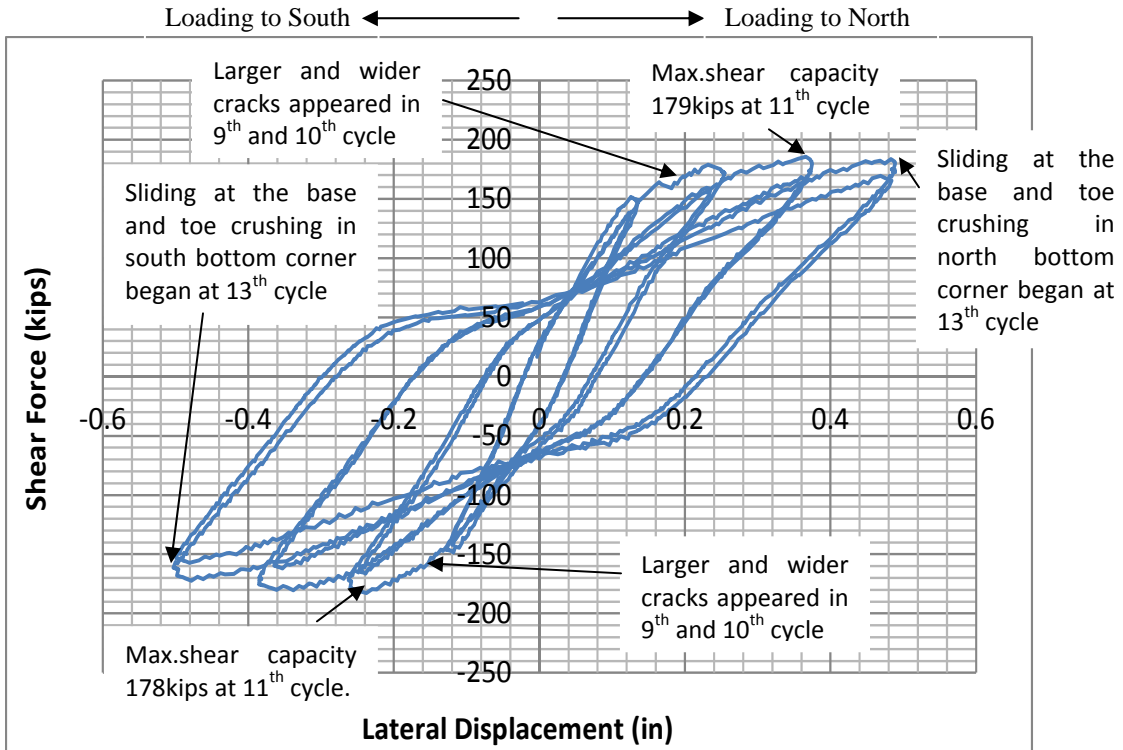
Figure 6.27 Shear response of the specimen for the 7th to 14th hysteretic cycle
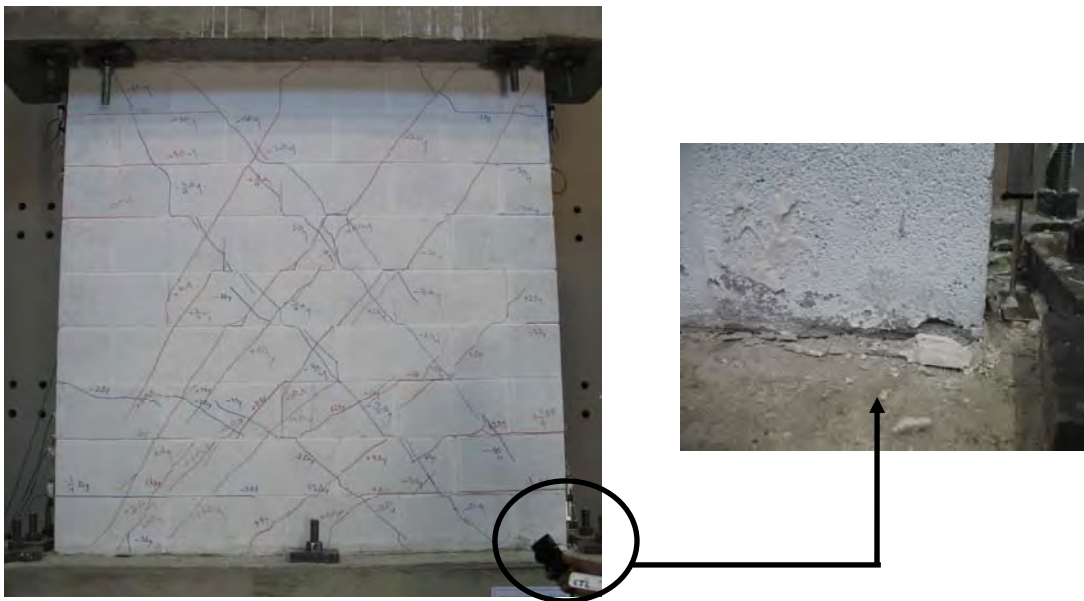


Figure 6.28 Flexural and shear cracking and toe crushing at south bottom corner of wall

263

As deformations increased, additional diagonal cracks formed in the wall and large sliding deformations were noted at the bottom of wall. The crushing occurred in the bottom in two courses of the wall. The vertical bars in the wall were bent due the high shear deformation. After the wall began to crush, the specimen was not able to support the 140kips axial load producing a collapse at 1.4 in. lateral deformation (2% drift ratio). The shear capacity degraded to 80kips loading north and 61kips loading south, less than half the peak capacity.
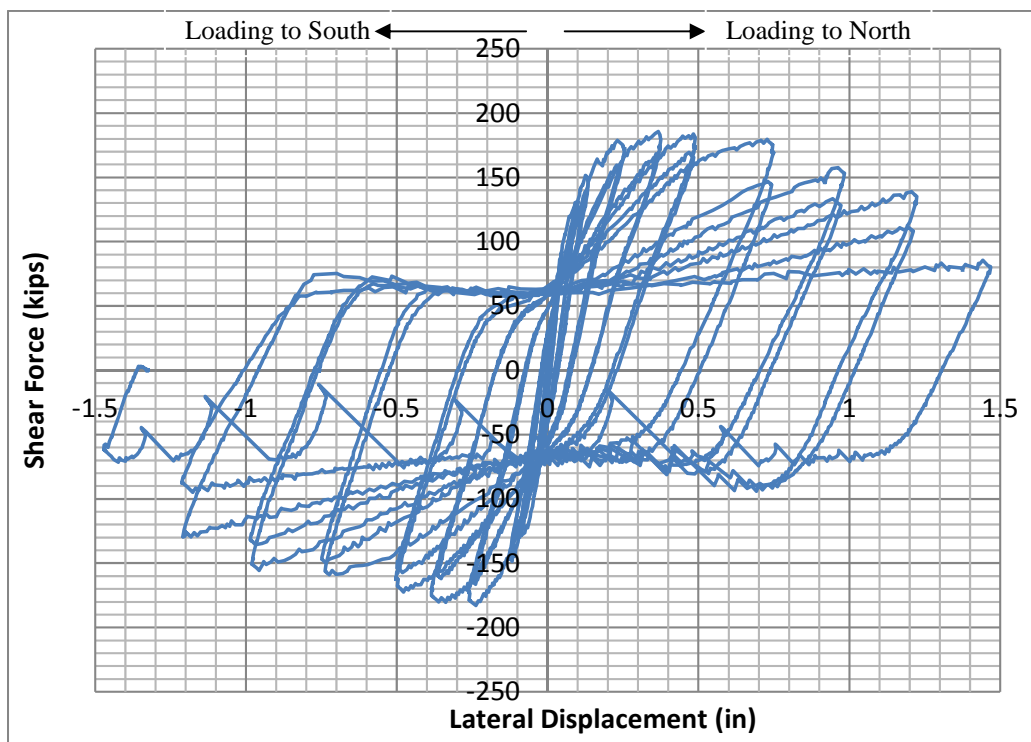


*Figure 6.29 Shear Force Response of the masonry wall*

*Figure 6.30  Crushing of masonry wall at end of the test*



*Figure 6.31 Toe crushing of the inferior right corner of the masonry wall.*

Sliding at the base was the predominant feature of behavior at large deformations, and represented more than 70% of the total deformation of the specimen as it can be seen in Figure 6.32. Sliding at the top was less than 1% of the total deformation of the specimen (Figure 6.32). Figure 6.33 shows the response of the specimen with the top and bottom sliding displacement removed. The maximum displacement to north without the sliding is 0.39 in. (0.54% drift ratio) and 0.43 in. (0.6% drift ratio) to south direction.
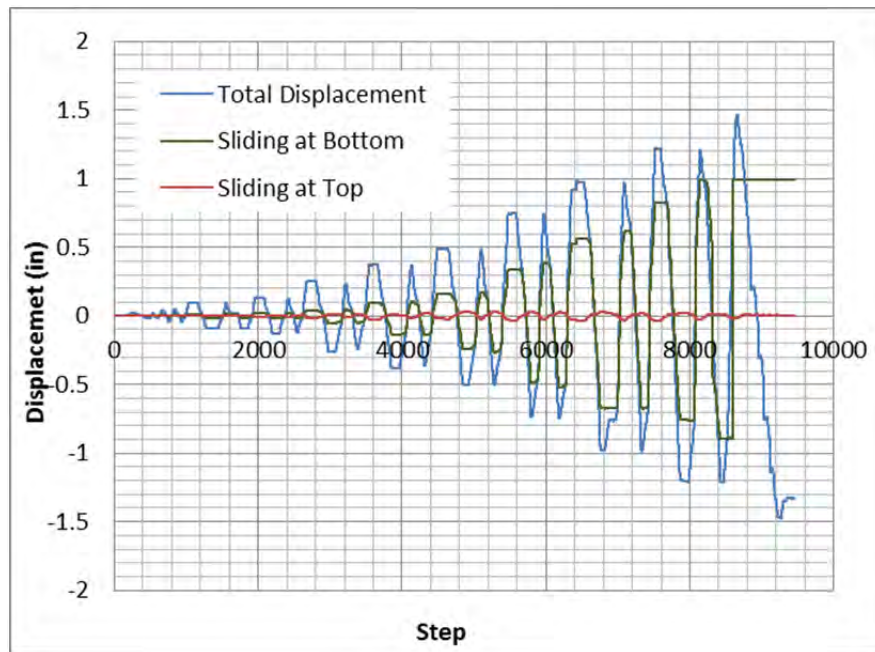


*Figure 6.32 Shear Force Response of the masonry wall*
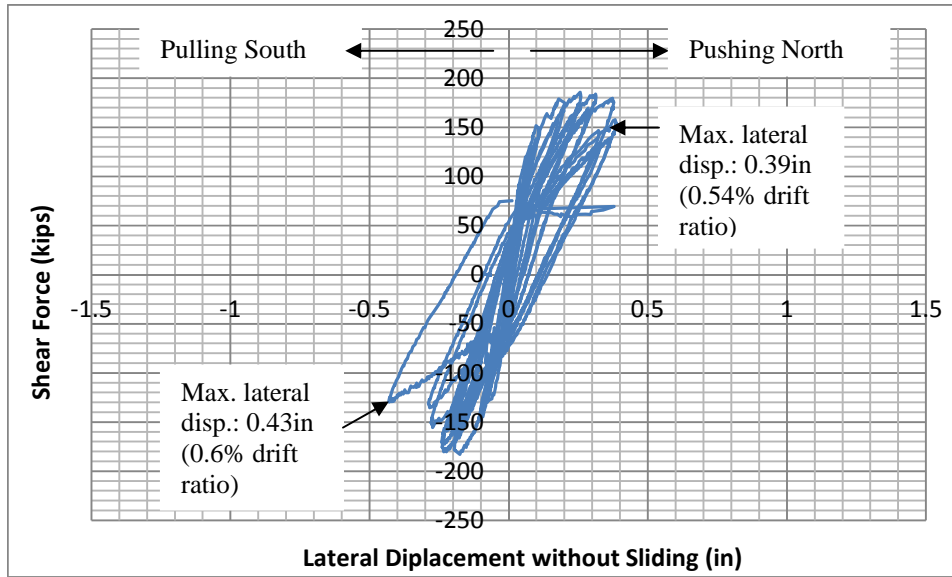
*Figure 6.33 Shear force vs. lateral displacement response of the masonry wall without sliding*

**6.4    REHABILITATION OF THE MASONRY WALL**

The rehabilitation of the masonry wall was divided into two phases. The first phase consisted of adding a reinforced concrete ring above the base foundation to encase the two badly-damaged bottom courses of CMU. The concrete ring reduced the height of the wall. In the second phase, CFRP sheets were attached to the wall along the diagonals to produce a tension brace or tie, and. CFRP anchors were installed to at the ends of the sheets. Figure 6.34 shows the location of the concrete ring and the CFRP materials for the two phases of the repair process.
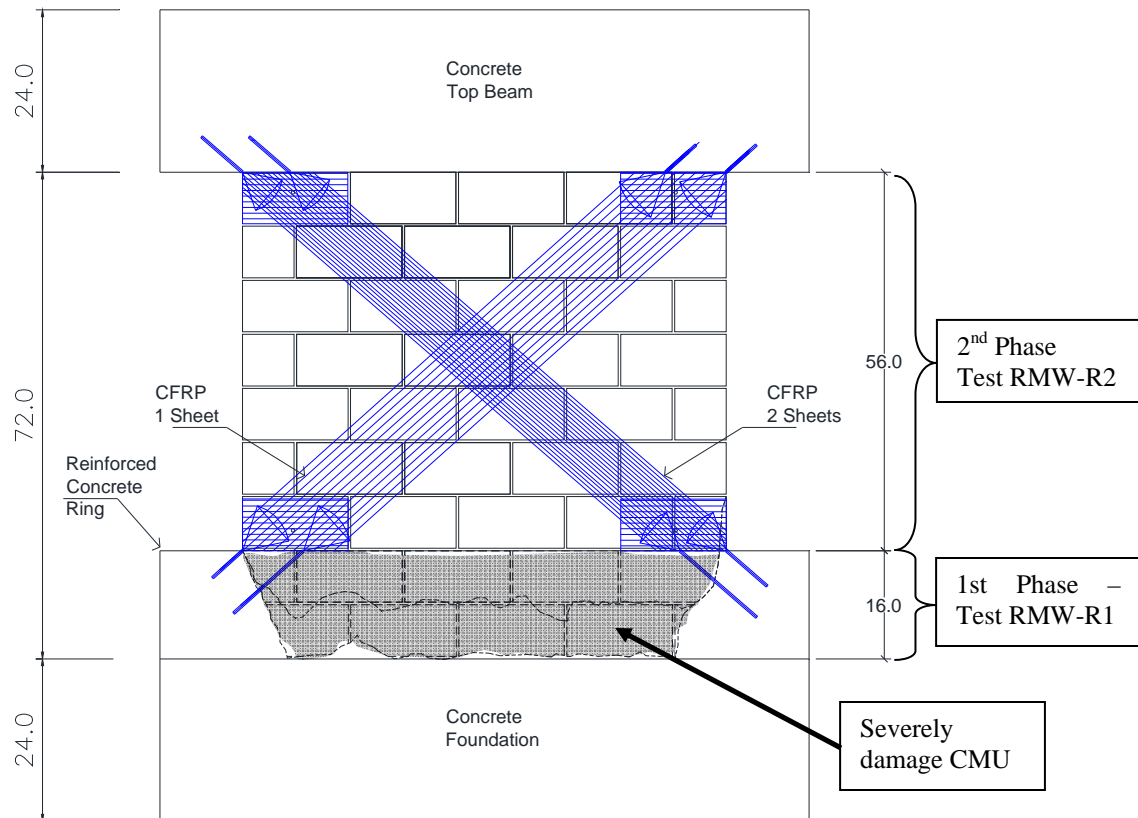


*Figure 6.34 Details for the retrofit of the masonry wall*

### 6.4.1 Phase 1: Addition of Concrete Ring

A reinforced concrete beam was cast to encase the original base and two bottom CMU courses that were severely damaged. Some damage to the end CMU wall in third course of the wall was repaired with a mortar patch. The concrete beam or ring also eliminated sliding at the base. The concrete ring reduced the clear height of the masonry wall from 72 in. to 56 in., and the aspect radio from 1 to 0.78. Internal reinforcement was provided in the concrete ring as shown in Figure 6.35 to connect the concrete foundation of the original masonry wall the new concrete ring. Eight #5 Grade 60 steel bars were anchored into holes drilled in the concrete foundation as shown in Figure 6.35. Also 4 #5 bars were placed horizontally through the 2nd course level (Figure 6.36), in order to tie the masonry wall to the concrete.
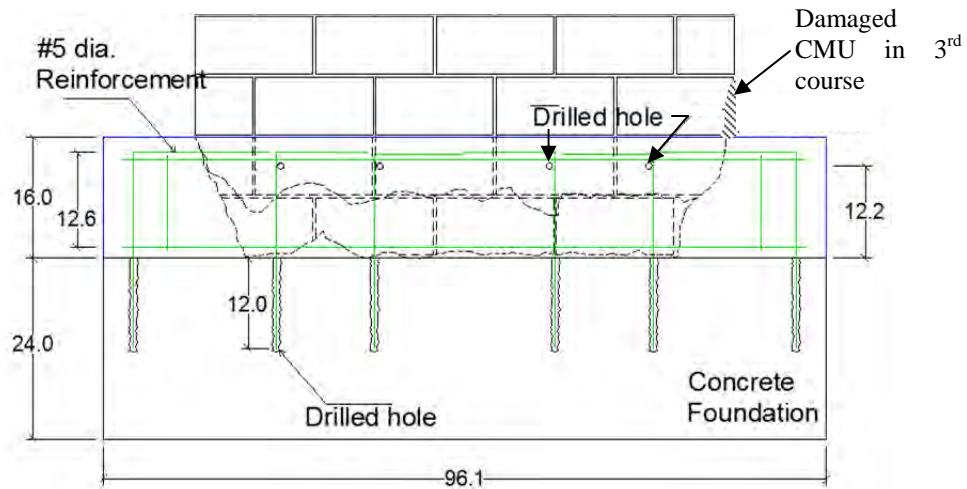


*Figure 6.35 Internal reinforcement for the concrete ring. Side view.*
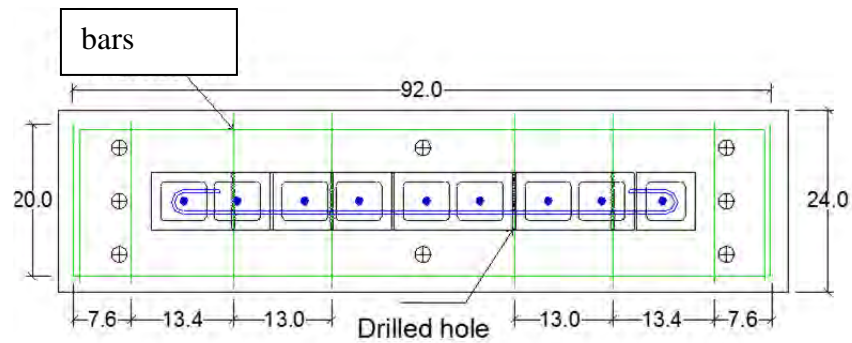
*Figure 6.36 Cross section of the concrete ring.*

6.4.1.1 ***Procedure of the retrofit technique***

### 6.4.1.1.1 *Removal of damaged wall elements*

First the crushed material from the bottom two courses was removed. Bent steel bars bended were not removed. Holes more drilled vertically into the existing concrete foundation and horizontal in through on the second curse of the wall. Core was taken to avoid damage to the remaining masonry wall. Figure 6.37 shows the bottom part of the masonry wall after removal of crushed concrete.
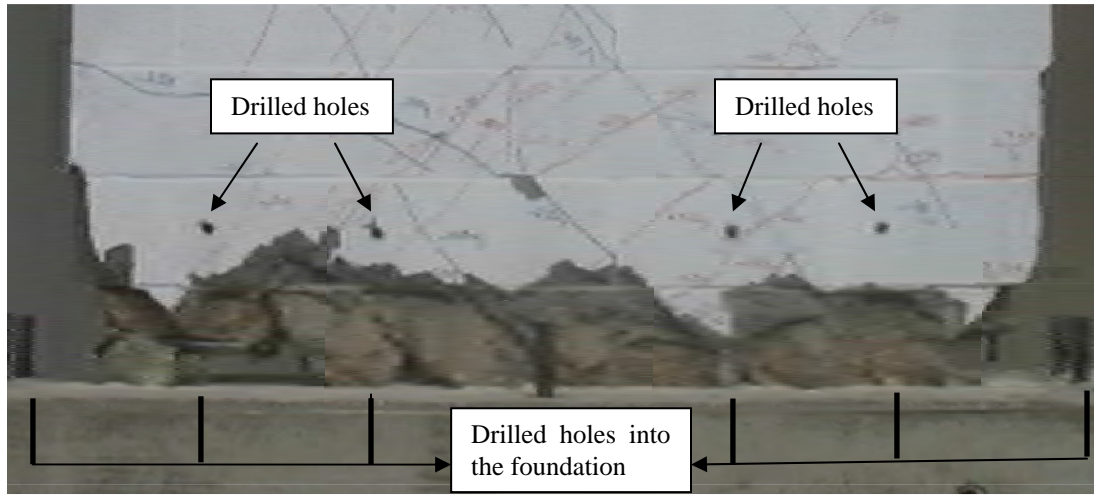
*Figure 6.37 After removal crushed concrete*

In Figure 6.38 steel bars placed for the concrete ring are shown. The holes in the foundation were saturated with epoxy before #5 bars were inserted. The horizontal holes in the masonry wall were saturated with epoxy and the horizontal bars were inserted through the wall. The rest of the cage was tied to the bars in the foundation and wall. Finally the formwork was located.

*Figure 6.38 Cage of the concrete ring placed.*

### 6.4.1.1.2 Placement of the concrete

The concrete casted had a slump of 6.5 in. for ease of transportation and consolidation. In Figure 6.39, the casting operation is shown. The damaged corner of the 3$^{rd}$ course was filled using repair mortar as shown in Figure 6.40 shows.



*Figure 6.39 Casting of the concrete ring beam.*

*Figure 6.40 Repair mortar to fill the damaged south corner of the wall*



*Figure 6.41 Masonry wall with concrete ring applied.*

6.4.1.2 *Test of masonry wall partially retrofitted RMW-R1*

The purpose of this test was to establish the performance of the severely damaged wall partially retrofitted with a concrete ring prior to installation of the CFRP materials. The wall was loaded to about the half of the expected lateral capacity.

### 6.4.1.2.1 Instrumentation for the Test

The instrumentation used for this test consisted of linear potentiometer to measure the lateral displacement at the top of the wall, diagonal shear deformation in each direction, and vertical deformation at north and south ends of the wall. Figure 6.42 shows the location of the linear potentiometers on the masonry wall.
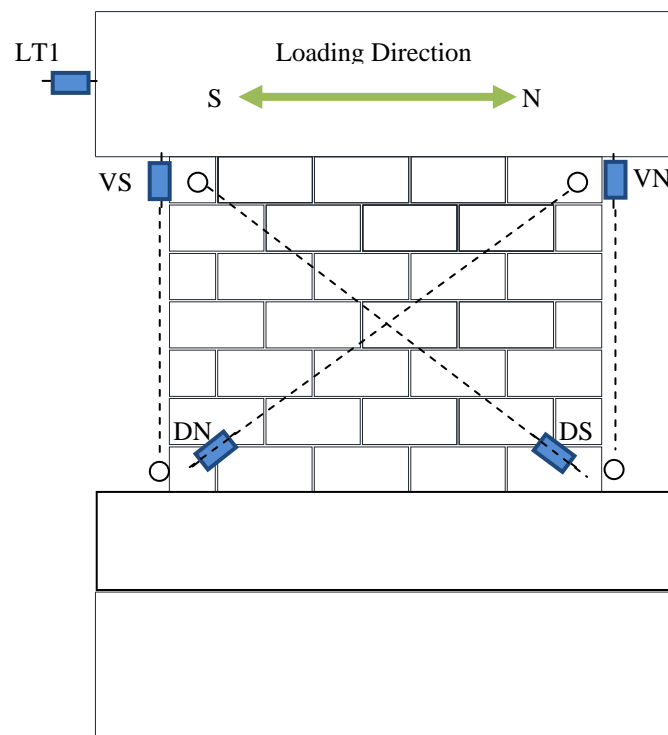


*Figure 6.42 Instrumentation used for current research, back view of the specimen*

### 6.4.1.2.2 Protocol of displacement

The test was displacement controlled. The protocol of displacement consisted of three hysteretic cycles of displacement increasing progressively as shown in Figure 6.43. The values of the drift are expressed as a fraction and percentage of the wall height. A constant axial load of 140kips was applied as in test RMW. The rate of displacement was 0.022 in/min.
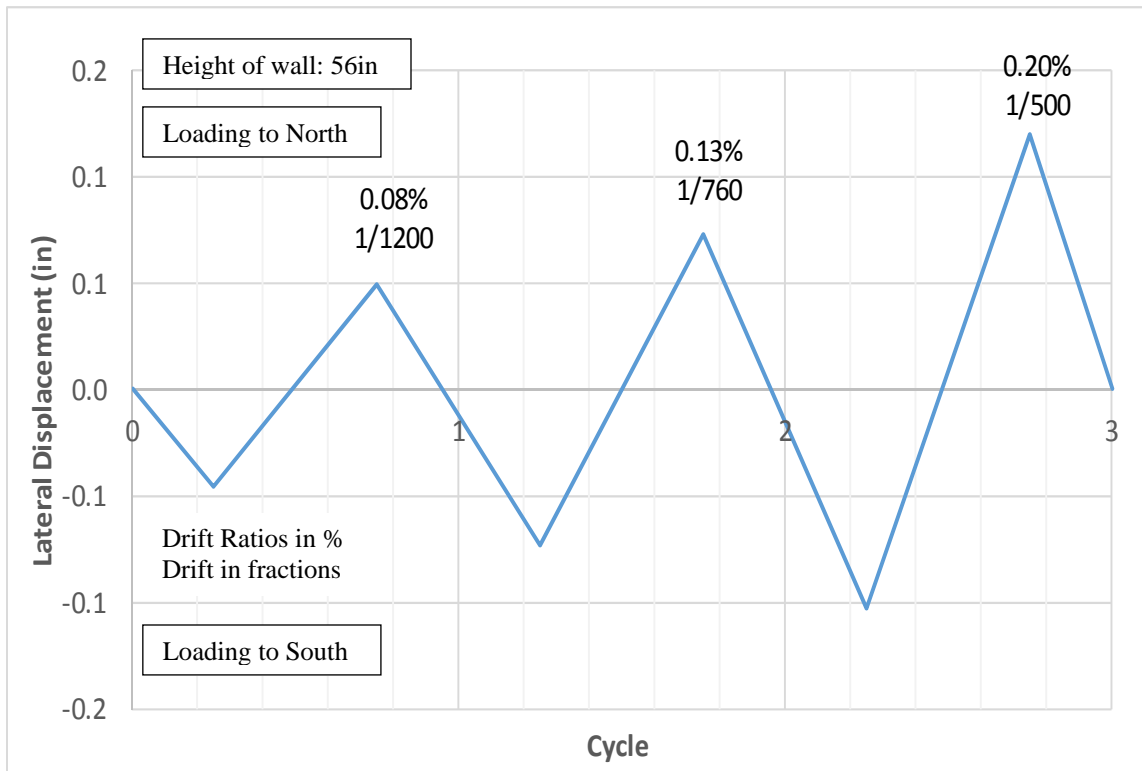


**Figure 6.43 History of cyclic displacement applied to the wall.**

### 6.4.1.2.3 *Test of the masonry wall retrofitted RMW-R1*

After the 140kips axial load was applied, lateral deformations to 0.045in were imposed in both directions. Diagonal cracks opened to a width of 0.020in. The measured lateral load was 70kips. For the second cycle of the test, the existing cracks opened to 0.025 in. and load reached was 84 kips in the south direction and 99 kips to the north. The peak displacement in both directions was 0.073 in. In the third cycle, the lateral load reached 119 kips at 0.10 in. south displacement and 118kips for 0.12in to north displacement. The diagonal cracks opened to 0.030 in. Shear force vs. lateral displacement is shown in Figure 6.44.

The behavior of the specimen was nearly linear. As can be seen in Figure 6.44, the hysteretic loops were similar in both directions. From the diagonal deformation measured by DN and DS linear potentiometers (Figure 6.45), the stiffness in both directions was observed similar. It can be concluded that the pattern of damage for both directions was the same. The stiffness calculated was 1060kip/in for pushing (north) displacement and 1190 kip/in for pulling displacement (south).
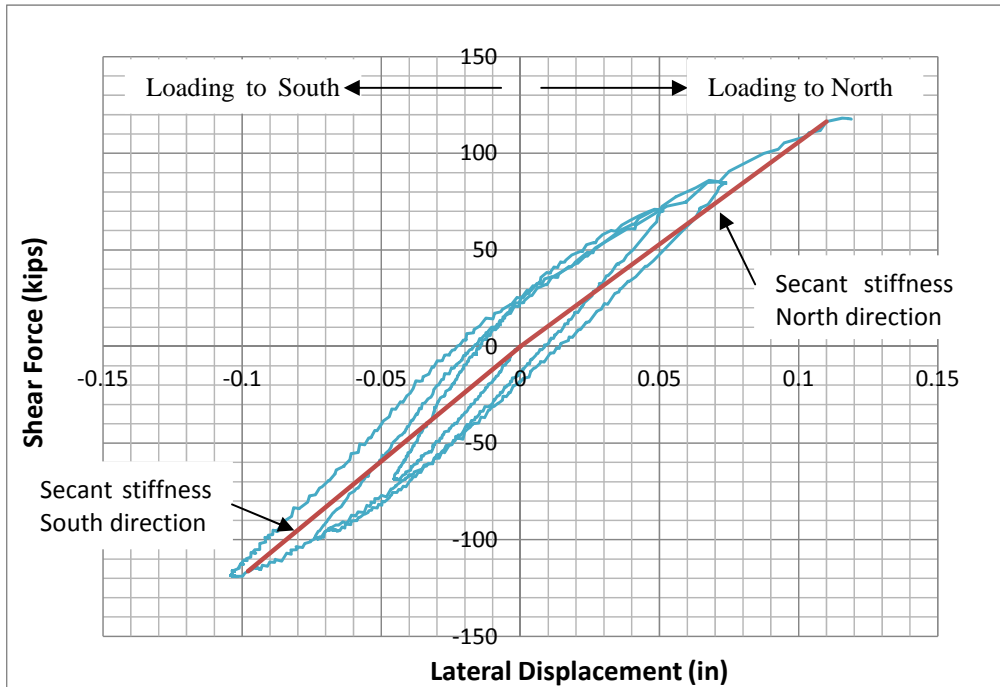
*Figure 6.44 Shear response of the specimen*



277
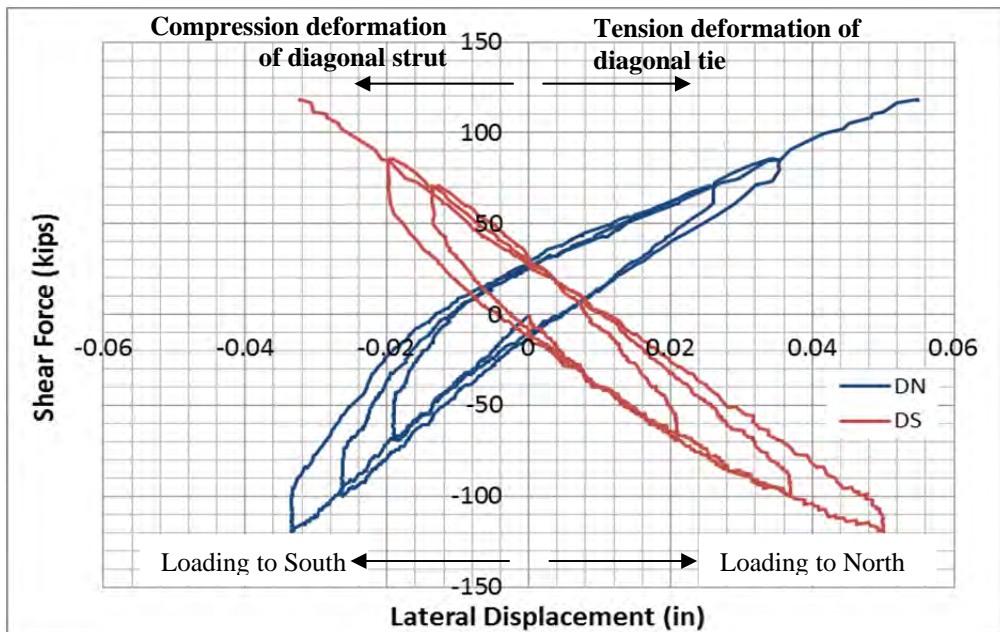
*Figure 6.45 Deformation of the diagonal ties and struts*

The retrofitted masonry wall was tested again in order to review the parameters obtained and to also check the sliding deformation between the concrete beam and the CMUs. The test consisted of one lateral cycle displacement to 1.25 in. in both directions.

The maximum lateral loads were 121 and 119kips in the north and south directions. The lateral stiffness measured was 970 kip/in and 1003 kip/in for north and south direction respectively. Load-deformation is plotted in Figure 6.46. The test was stopped when the specimen was returned to its initial position. After the axial load applied was removed, the specimen movement to the north direction by 0.066in and the lateral load dropped to 23 kips. The specimen was pulled 0.066 in. south to its initial position.
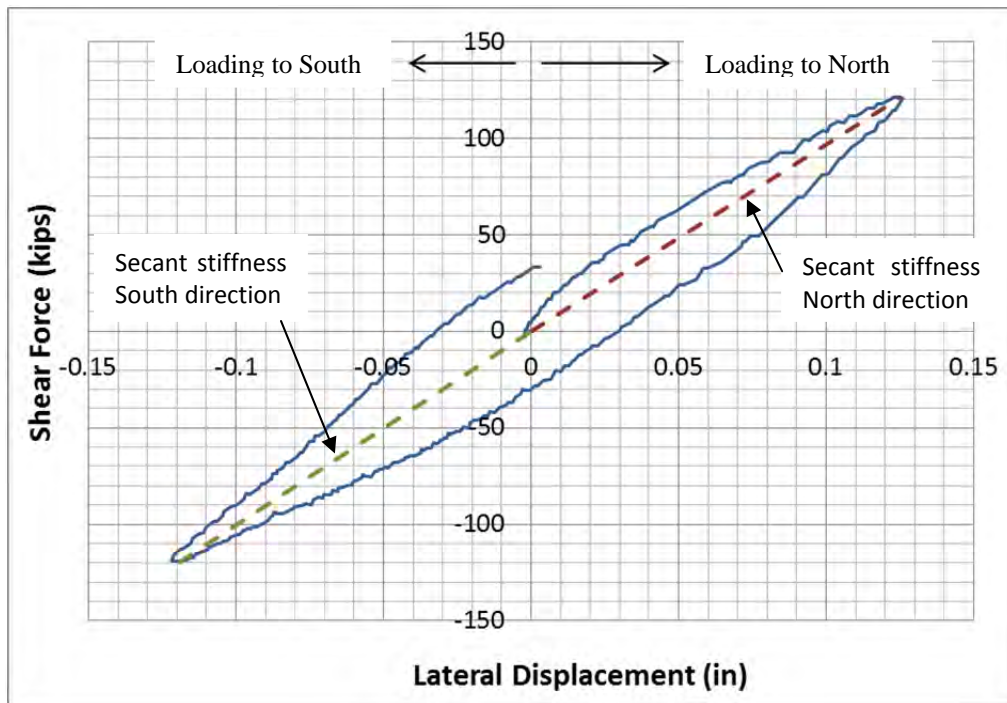
*Figure 6.46 Shear response of the specimen for the second test of RMW-R1*
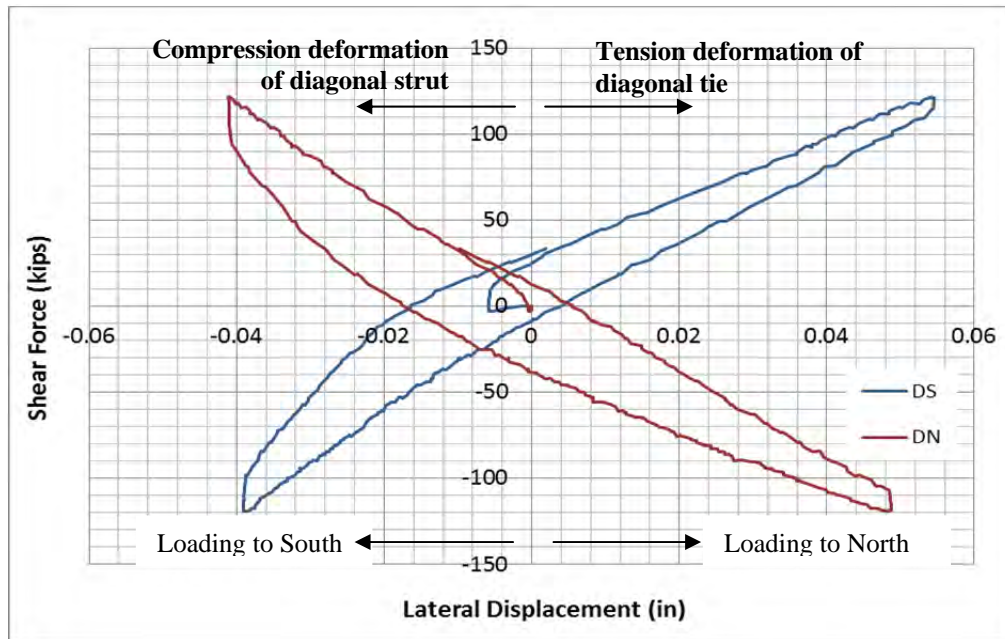


*Figure 6.47 Deformation of the diagonal ties and struts for the second test of RMW-R1*

It was concluded that the actual stiffness of RMW-R1 is less compared from the test of the as-built specimen(RMW), even when the masonry wall retrofitted had lower aspect ratio (from 1 for the as-built case to 0.78 for the retrofit case). The diagonal shear cracks represented important keys to work for rehabilitation purposes as well.

### 6.4.2 Phase 2: Installation of CFRP materials

Although the base of wall suffered major damage in the original test, there was extensive diagonal cracking in the wall. After the initial loading described earlier was completed CFRP sheets and anchors were installed. CFRP diagonal ties, anchors and U-wraps were applied on both faces of the masonry wall as shown in Figure 6.49 and Figure 6.50.

Since there was the same pattern of damage in both directions, it was decided to use two different amounts of CFRP in the diagonal ties to evaluate the efficiency of the rehabilitation system. Two layers of CFRP 9in wide were applied along one diagonal and one layer of CFRP 12in wide was placed along the other diagonal on both faces. The anchors at the top and bottom extreme of each diagonal tie were installed. The angle of inclination of the diagonal CFRP strips was about 40°.

The two 9 in.wide layers of CFRP diagonal ties provided a tension brace produced for loading to the north (Figure 6.48 left). The CFRP diagonal ties provided tension resistance to the strengthened masonry wall. The total amount of CFRP material was 4 strips 9 in. wide and 0.04 in. thick, with a total transverse area of 4x9x0.04= 1.44sq.in. Both CFRP diagonal ties were also attached by a total of 4 CFRP anchors in their extremes and wrapped by U-patchs. Details are shown in Figure 6.49 and Figure 6.50.

The one 12 in.wide layer of CFRP diagonal ties provided a tension brace for loading to the south (Figure 6.48 right). The total amount of CFRP material was 2 strips of 12 in. wide and 0.04in. thickness, having a total transversal area of 2x12x0.04=0.96sq.in. being 50% less than the other diagonal ties. The CFRP diagonal

ties were attached the base and the upper load beam by a total of 4 CFRP anchors. Details are shown in Figure 6.49 and Figure 6.50.

Loading Direction
N ← S

Loading Direction
N → S

Tension Tie, two 9in.wide layers of CFRP

Tension Tie, one 12in. wide layer of CFRP
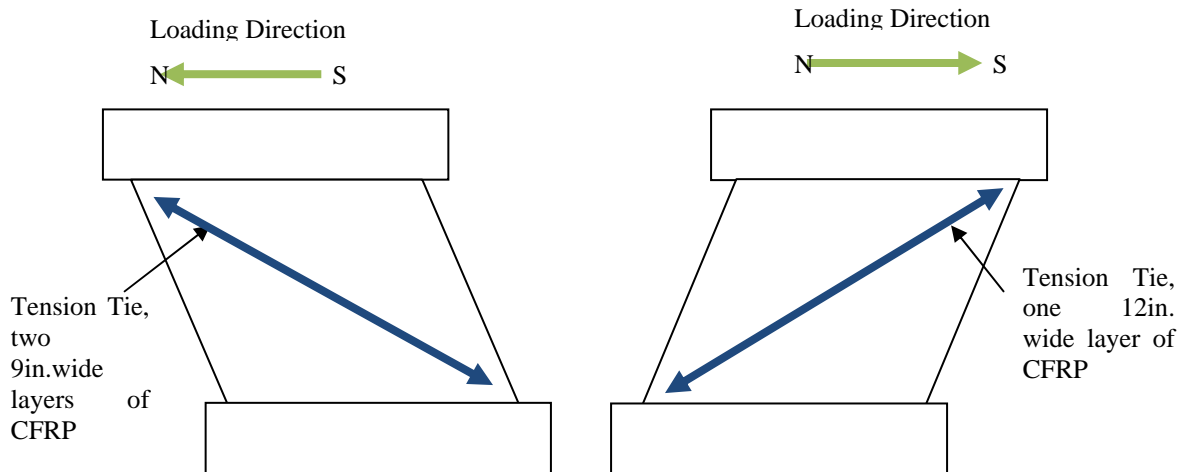
*Figure 6.48 CFRP diagonal materials.*

For both types of diagonal ties, the CFRP anchors were installed at the same inclination as the CFRP diagonal strips. The holes for the installation of the anchors at bottom of the diagonals were deeper than at the top to engage sound concrete in the ring beam. Figure 6.49 and Figure 6.50 show, the embedment length of each anchor. They had 60°, 7 in. fan's radius for south resistance tension tie and 60°, 7in fan's radius for north resistance tension tie. U-Wraps made with CFRP sheets were also located at each end of the diagonal to cover the fans of the anchors. Each U-Wrap provided a patch over 4 CFRP anchors. Figure 6.51 shows details of CFRP anchorage.
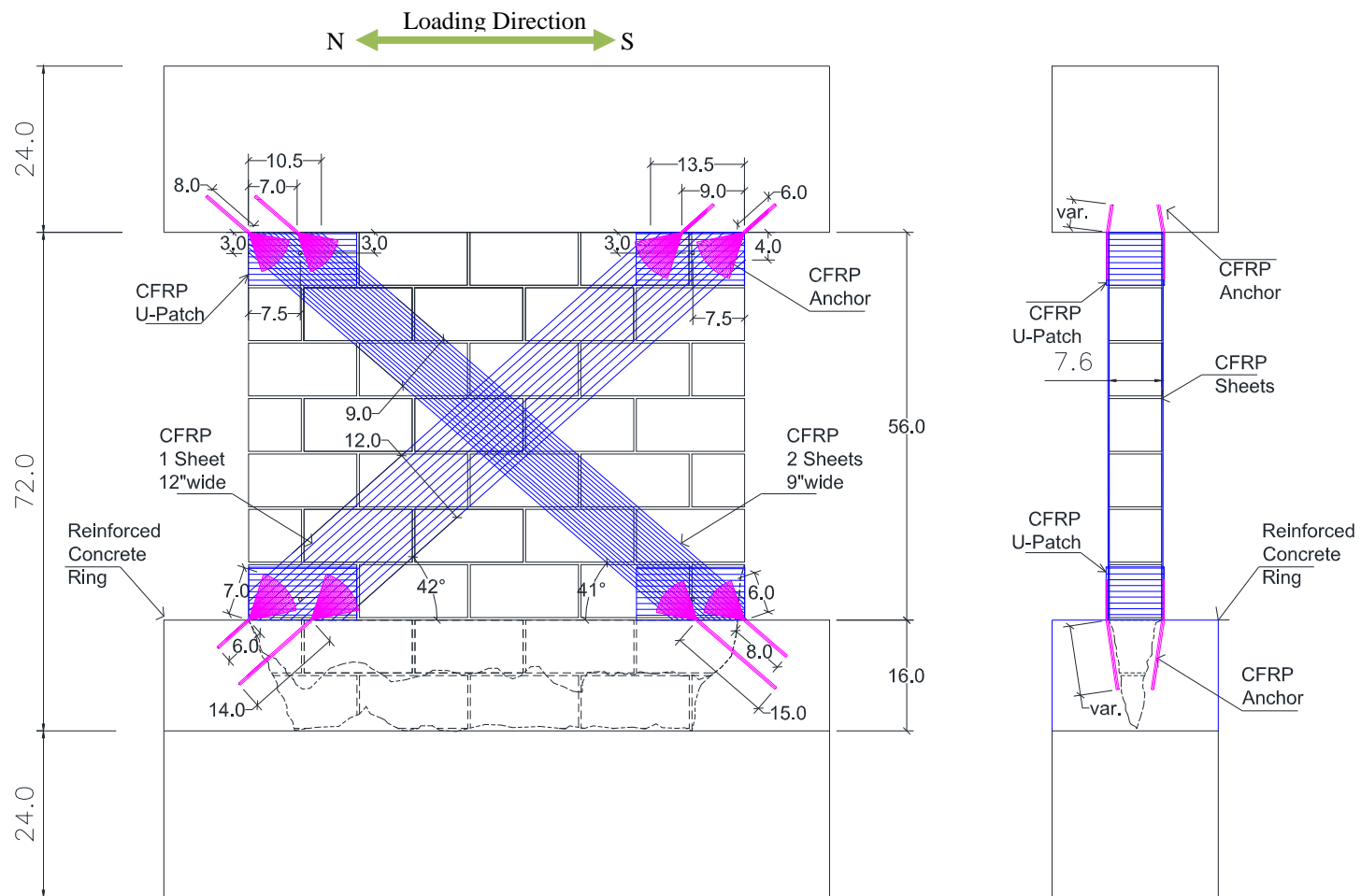
*Figure 6.49 Front view (left) and side view (right) of the details of the application of the CFRP materials. Units in inches*
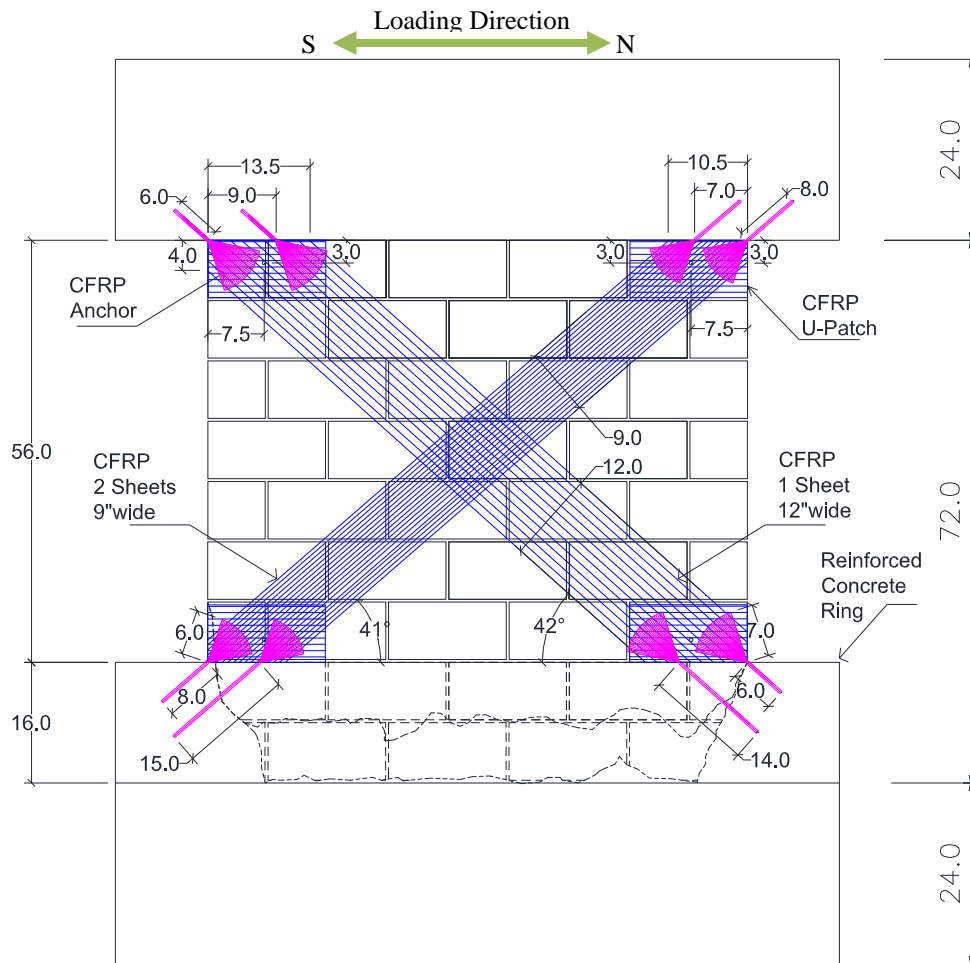
*Figure 6.50 Back view of the details of the application of the CFRP materials Units in inches*
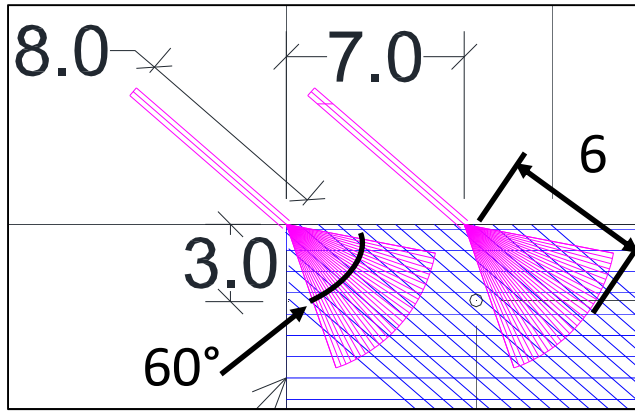
*Figure 6.51 Details of CFRP anchors. Units in inches.*

6.4.2.1 *Procedure of the retrofit technique*

*6.4.2.1.1 Preparation of the surface and concrete ring and beam for the application of the CFRP materials*

The surface of the masonry wall was cleaned for good adherence of the CFRP sheets. A surface grinder was used for cleaning the surface of the CMUs. Figure 6.52 (left) shows surface preparation. Figure 6.52 (right) shows the drilling of one hole in the concrete ring for an anchor. Finally, the surface of the wall and the holes was vacuumed to remove dust.



*Figure 6.52 Drilling of the surface (left) and the holes (right)*

*6.4.2.1.2 Application of the CFRP materials*

The epoxy is applied to the surface of the wall with as it can be seen in Figure 6.53 (left). After saturating the CFRP sheets with the epoxy, they were applied to the masonry wall. One 9in.CFRP diagonal strip was applied first, second the 12in. wide CFRP strip was placed, and finally the second 9in.wide CFRP strip was applied over the previous 9'wide CFRP strip. Figure 6.53 and Figure 6.54 show the steps of the process. After the strips were placed the roller was used to ensure saturation of the epoxy into the

CFRP sheets. The roller also removed air pockets between the surface of the wall and the layers of CFRP.



*Figure 6.53 Application of epoxy to the surface of the masonry wall (left) and first 9in.wide CFRP strip (right) afterwards*



*Figure 6.54 Application of the 12in.wide CFRP strip (left) and second 9in.wide CFRP strip (right) later.*

The CFRP anchors were installed after the diagonal CFRP sheets were installed. The process of the installation followed the procedures explained in section 3.3.4 (Chapter 3). The internal surface of the drilled holes was saturated with epoxy prior to inserting the CFRP anchors. For the holes into the concrete ring, half of the hole was filled with epoxy. However for the holes into the top concrete beam, the surface was saturated with epoxy. CFRP strips for the anchors also were saturated with epoxy before installing them into the holes. A small aluminum bar was used to push the CFRP anchor into the hole as shown in Figure 6.55 (left). The remaining portion of the anchor was spread out forming the triangle shaped fan shown in Figure 6.55 (right). A roller was used to coat the fan with epoxy.
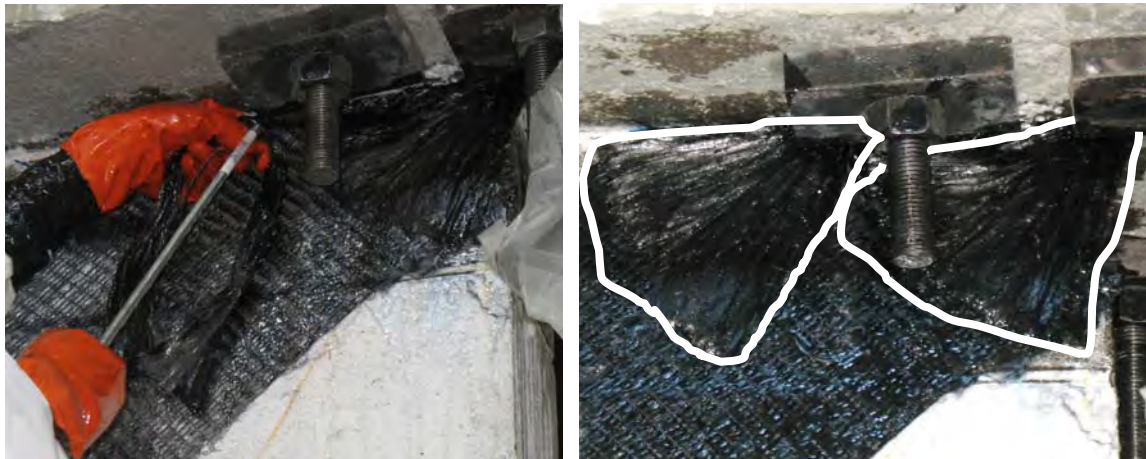


*Figure 6.55  Application of the CFRP anchor into the top concrete beam (left). CFRP anchors installed (right)*

The last step of the application of the CFRP materials was the placement of the CFRP U-Wrap. The CFRP strips for the u-wrap were saturated with epoxy, placed over the end of the masonry wall to cover the CFRP anchor fans as shown in Figure 6.56 to Figure 6.58

*Figure 6.56 Application of the CFRP U-Wrap*

Both sides of the retrofitted wall are shown in Figure 6.57 and Figure 6.58.

One 12in.wide layer CFRP

Two 9in.wide layers CFRP diagonal tie.
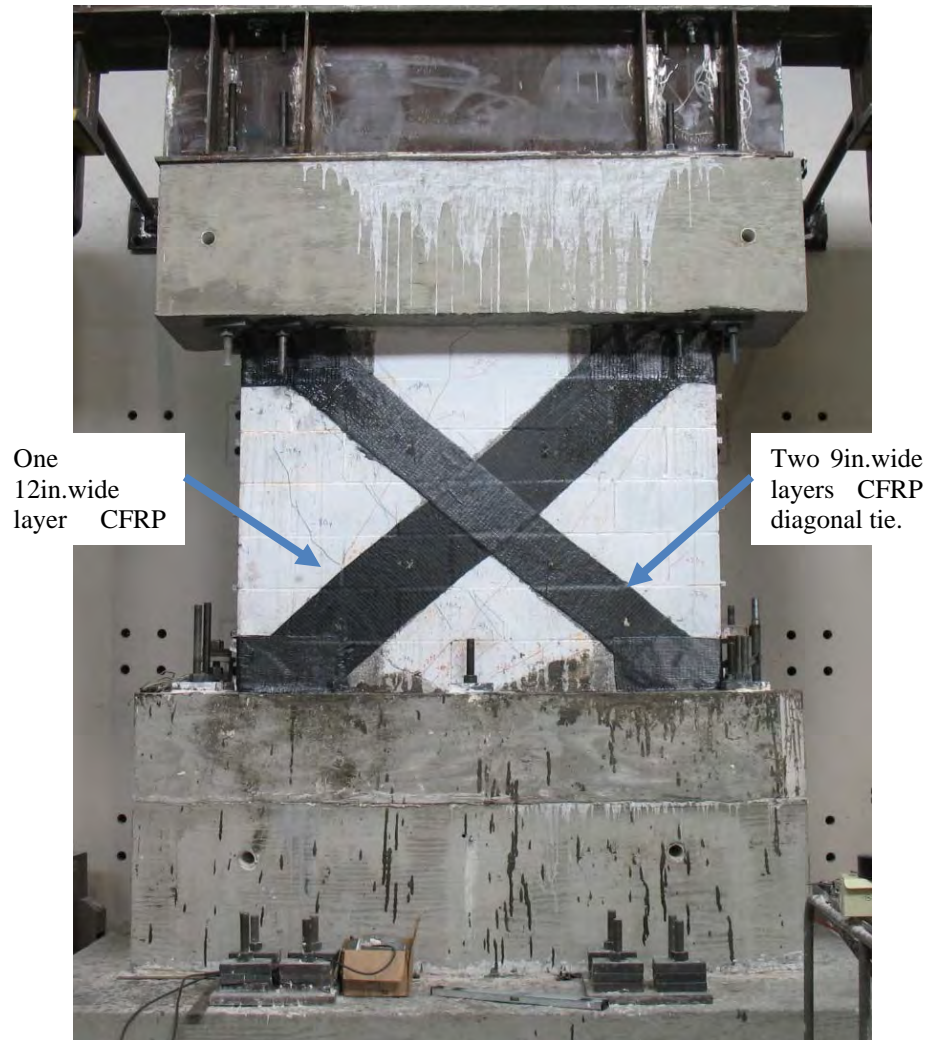
*Figure 6.57 Front view (West side) of the masonry wall retrofitted*

Two 9in.wide layers CFRP diagonal tie.

One 12in.wide layer CFRP

*Figure 6.58 Back view (East side) of the masonry wall retrofitted*

6.4.2.2 *Test of masonry wall retrofitted RMW-R2*

### 6.4.2.2.1 Instrumentation for the Test

A set of linear potentiometers were used to measure the global displacement and local deformation of the masonry wall and also the sliding of the top concrete beam and bottom concrete foundation. Figure 6.59 and Figure 6.60 shows the location of the linear potentiometers used. LAT1 was used to control the hysteretic cycle lateral displacement. Those instruments were placed on the back side and lateral edges of the masonry wall as shown in Figure 6.61.

In addition, a set of strain gages was placed on the CFRP diagonal sheets. Four on the west face of the wall located at the center of each half of each the diagonal tie (Figure 6.62). The strain gages located on the back CFRP diagonal sheets (east face of the masonry wall) were located at third points of each tie (Figure 6.63).

The strain on the internal bars of the masonry wall could not be measured. The leads for the strain gages on the bars were damaged during the test of the as-built wall.
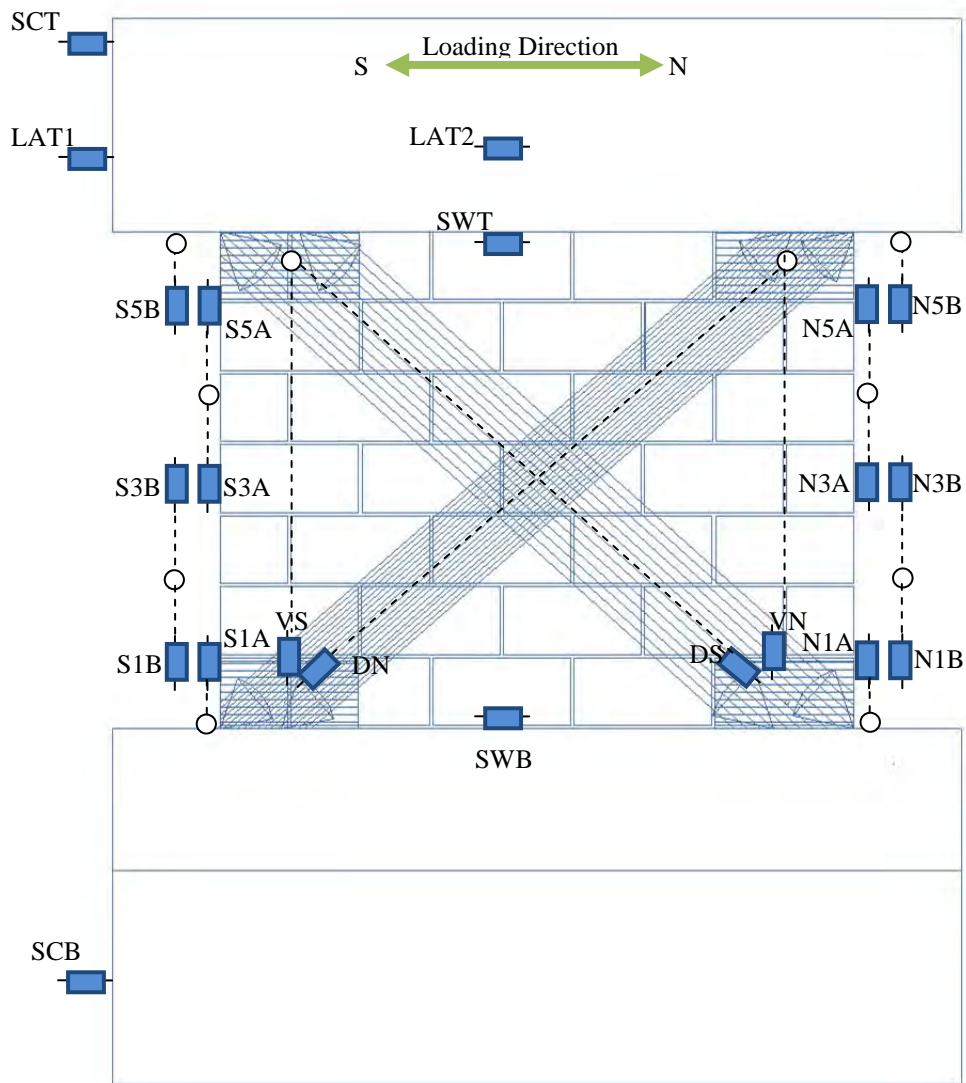
***Figure 6.59 Linear potentiometer for local and global deformation measurement***
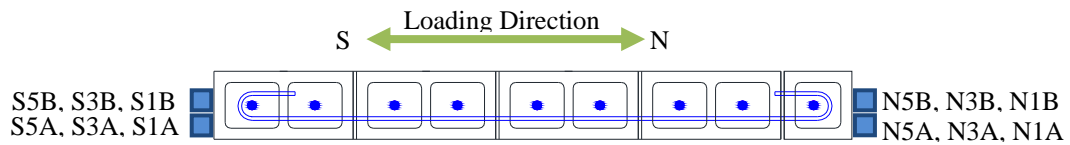


***Figure 6.60 Cross section of the masonry wall showing the location of the linear
potentiometer at north and south extreme.***

*Figure 6.61 Linear potentiometer for local and global deformation measurement*
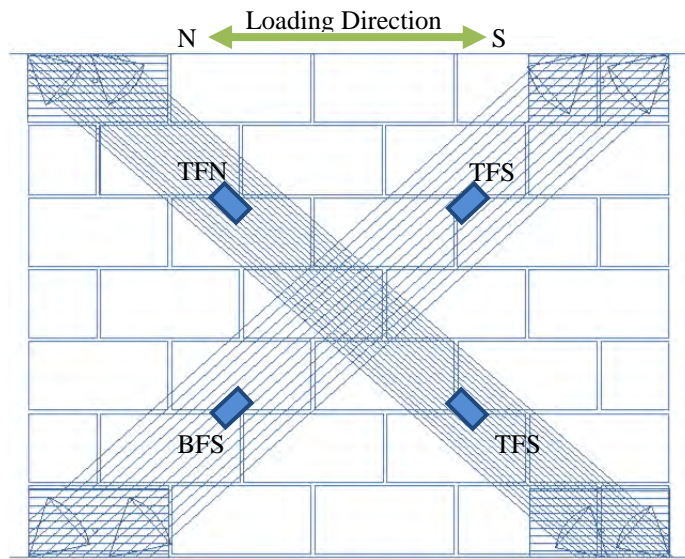
*Figure 6.62 Location of the strain gages on the CFRP diagonal ties - Front view (west side)*
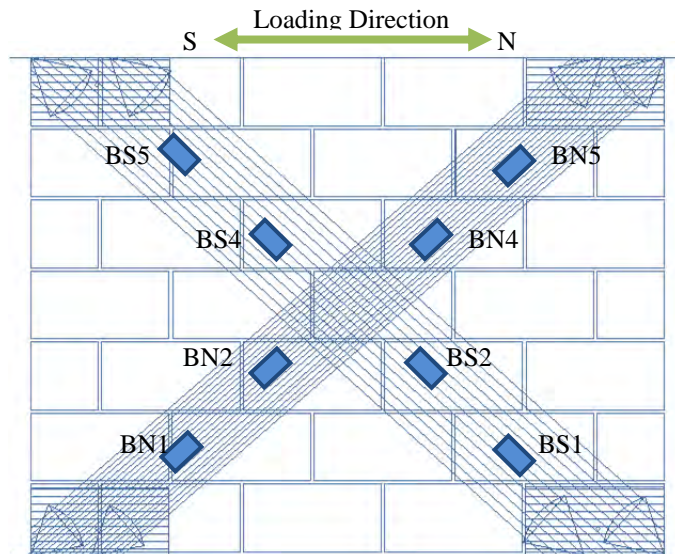


*Figure 6.63 Back Location of the strain gages on the CFRP diagonal ties – Back view (east side)*

### 6.4.2.2.2 Protocol of load

The history of hysteretic displacement cycle applied to the masonry wall is shown in Figure 6.64. It is noticed that different displacements for north and south peaks resulted from control of peak lateral force to south level. The axial load applied during the experiment was 140kips. Protocol of load was following the procedures of FEMA 461 until 0.80% drift ratio for loading to north direction, which is above the maximum allowed drift recommended in the ASCE-07-05 seismic design provisions for masonry walls.
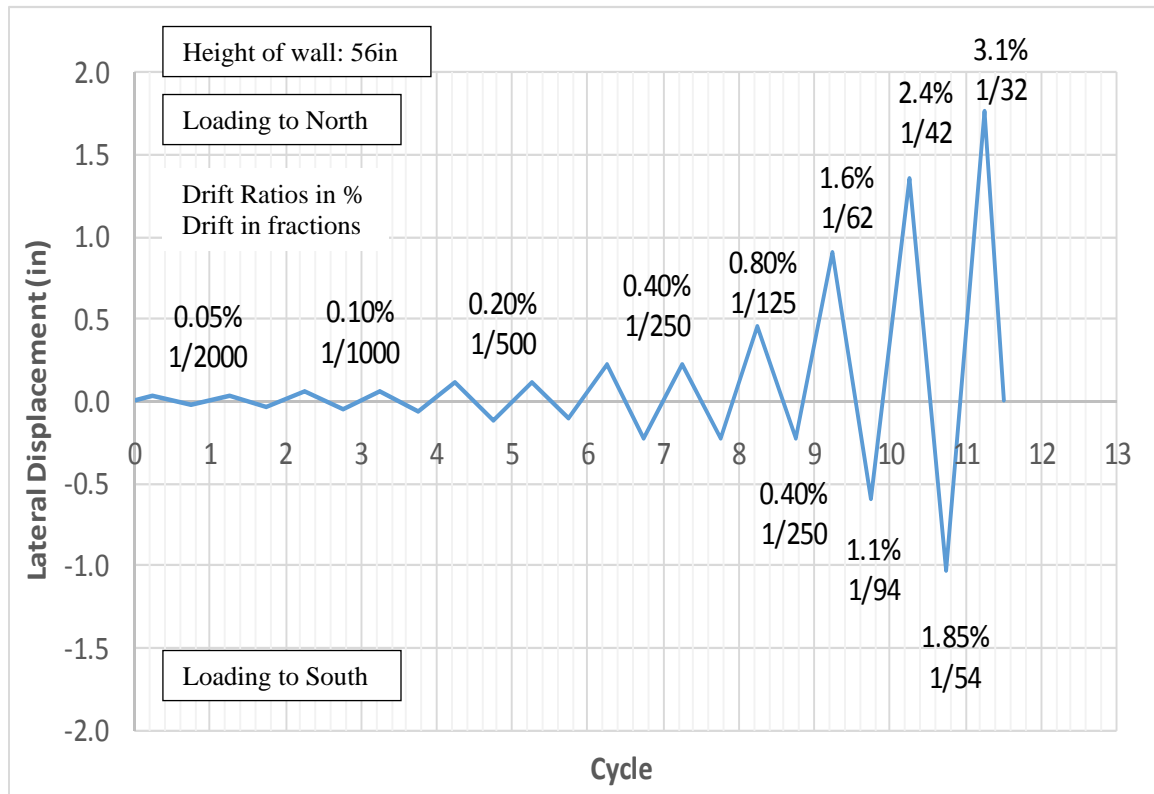


***Figure 6.64 History of hysteretic cycle displacement applied to the specimen.***

### 6.4.2.2.3 Test Results and Comparisons

**6.4.2.2.3.1    Response of the specimen Shear force vs. Lateral Displacement**

The retrofitted masonry wall behaved linearly for the first 6 cycles up to deflection of 0.11 in. in both direction of loading as shown in Figure 6.65. No sliding was observed. The measured load was 136kips to north and 130kips to the south. The measured secant linear stiffness to replace the peak load was 1236kip/in for the north direction and 1.182 kip/in for the south direction. The existing crack widths did not increase. No pinching was observed. However, in the 5th cycle sudden in.popsin. indicated the beginning of the debonding of the CFRP strips.
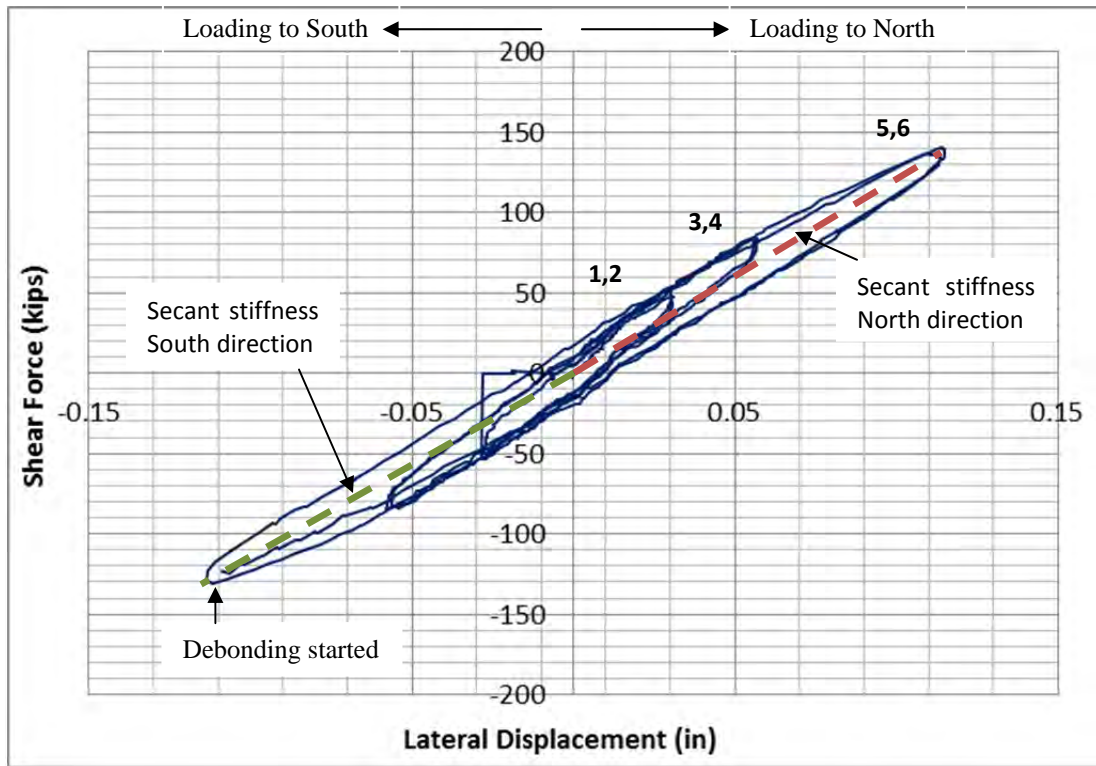


***Figure 6.65 Shear force vs. Lateral displacement of the first 6 cycles – Linear range.***

296

During the 7th cycle, more 'poppingin. was heard indicating further debonding of the CFRP sheets. Nonlinear response was noted at about 0.12 in. lateral deformation in both directions, with a gradual degradation of the stiffness as is shown in Figure 6.66.
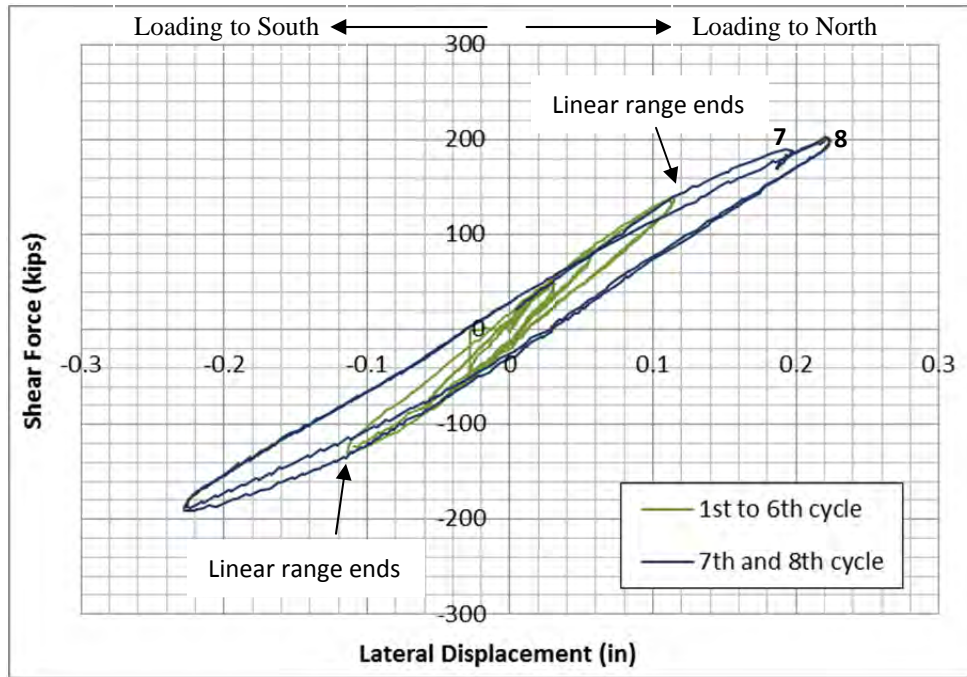


*Figure 6.66 Shear force vs. Lateral displacement of the first 8 cycles.*

In the 9th cycle, the maximum lateral load of 284kips under loading to north was reached at a displacement of 0.45 in. (Figure 6.67). When the specimen was loaded to south, the test was stopped because the maximum tension load of the lateral actuator was reached measuring at 191kips and the lateral displacement was 0.23 in.

In the 10th hysteretic cycle to the north, significant sliding at top of the masonry wall was noted. No sliding between the concrete ring and the CMUs of the masonry wall was observed. Loading in the south was reversed when the capacity of the actuator (200kips) was reached. Larger displacements to south occurred in each cycle due slipping

297

at the top of the wall. In the 11th cycle, the lateral load varied suddenly. This variation was due to a drop axial from 140kips to about 100kips as it can be seen in Figure 6.67. The axial load was increased to 140kips and the test continued. The maximum lateral displacement to the south was 1.04 in. and the shear force measured was 191kips. There was a gradual degradation of stiffness and shear capacity under loading to the north due to sliding effects, debonding of the CFRP material, and yielding of the reinforcement in the wall.
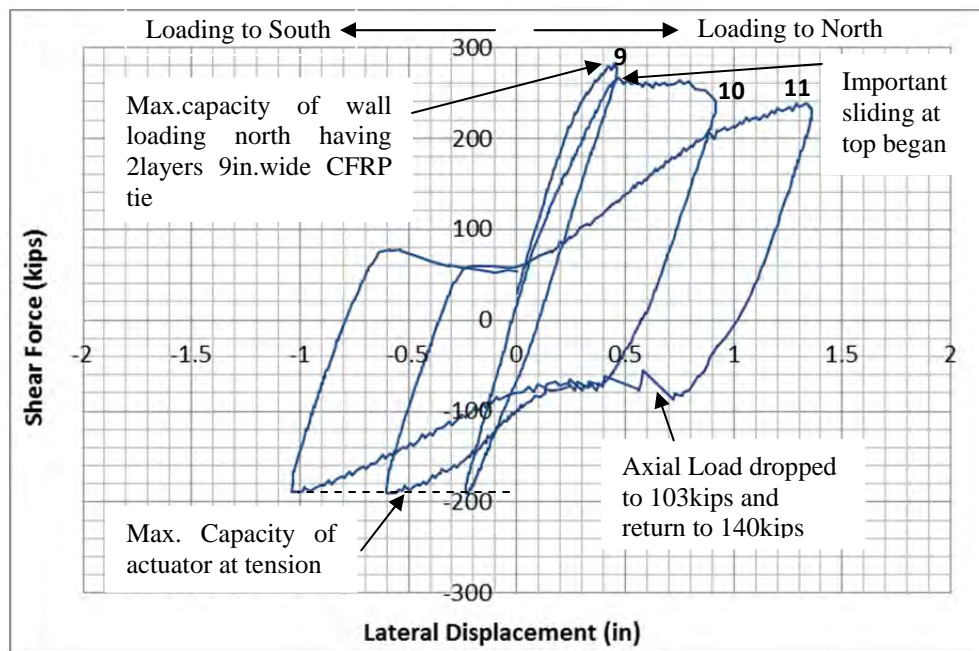


*Figure 6.67  Shear force vs. lateral displacement of 9th, 10th and 11th cycle.*

Failure occurred in the 12th cycle under loading to north (Figure 6.68). The top CFRP anchors located at the north end of the wall fractured. Detail of this mechanism of failure by the anchor rupture is explained in 6.4.2.2.3.2. The maximum displacement reached was 1.76 in. and the shear measured was 128kips. Before failure, there was a drop in the axial load of 20kips when the CFRP anchor ruptured, producing a drop in the

298

shear force from 204kips to 128kips and an increase in the lateral displacement from 1.40 to 1.76 in. due sliding at the top of the masonry wall.
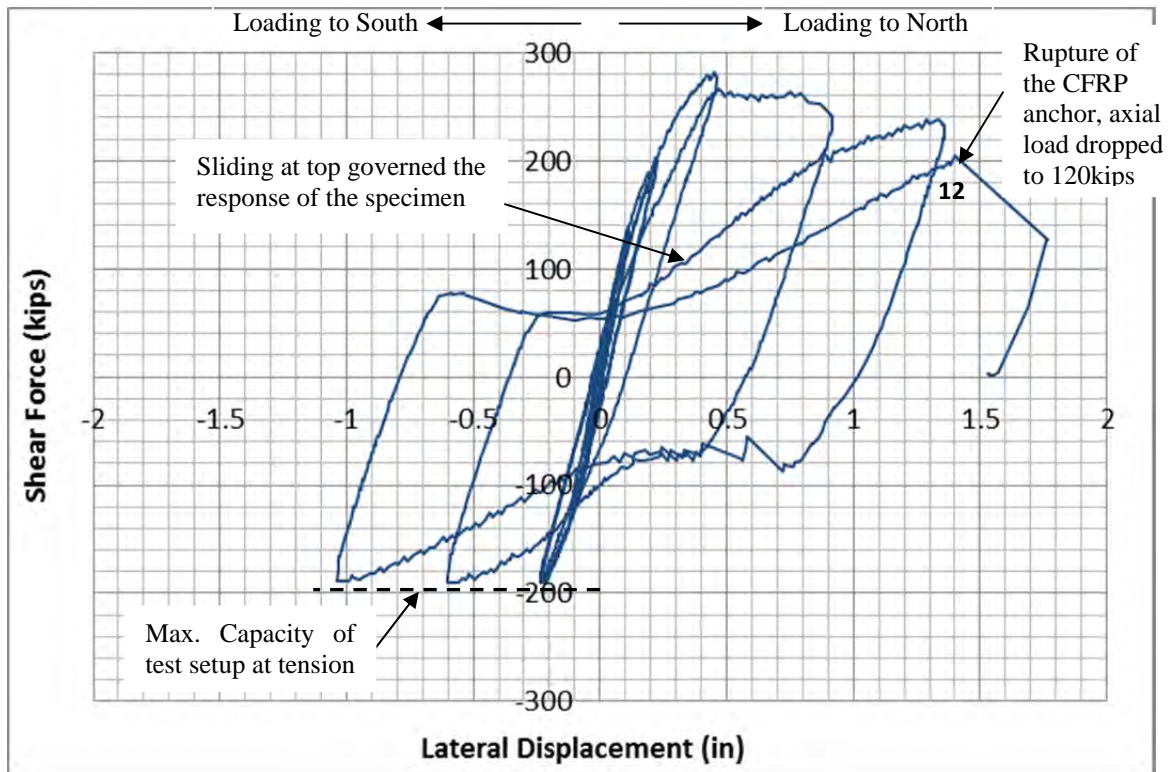


*Figure 6.68 Shear force vs. Lateral displacement of RMW-R2.*

The existing crack in the bottom-left corner of the wall opened when the specimen was loaded to the south. This crack was located close to the end of the CFRP tension tie as Figure 6.69 – left shows. Additionally, Figure 6.69-right shows the existing crack located on the bottom-right corner close to the edge of the U-wrap. The crack opened when the specimen failed in the 12th hysteretic cycle, loading to north.

*Figure 6.69 Existing cracks opened after reach maximum south (left) and north (right) lateral displacement*

The sliding displacement at the top of the wall was important. Sliding at bottom of the specimen was not significant. Figure 6.70 shows comparisons between the total lateral displacements of the specimen including sliding, and the lateral displacement of the wall without the effect of the sliding. Sliding at top was about 50% of the total lateral displacement in the last 3 cycles of the test.
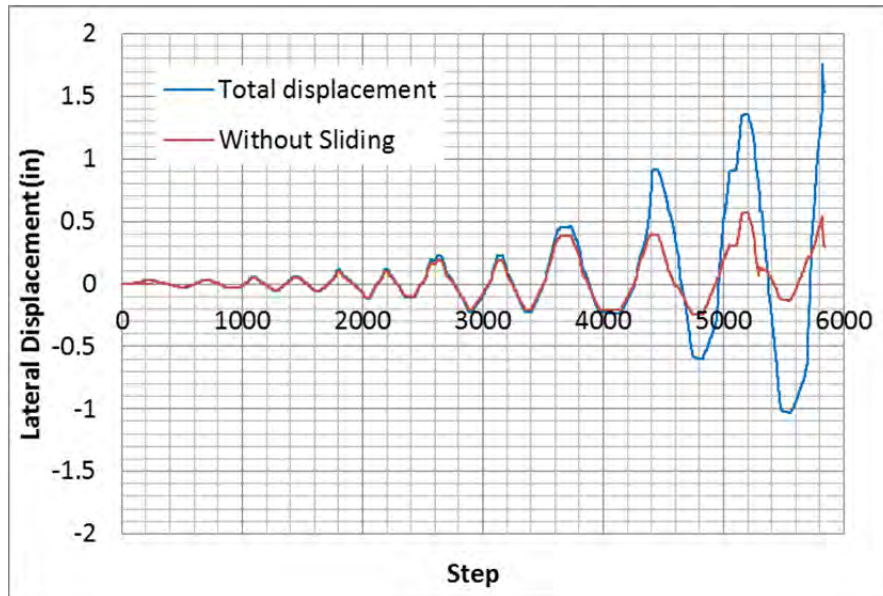
*Figure 6.70 Comparison between the histories of lateral displacements of the specimen with and without total sliding.*

Figure 6.71 shows the response of the specimen without sliding at bottom and top of the masonry wall. The overall nonlinear response of the specimen was governed primarily by sliding at the top.
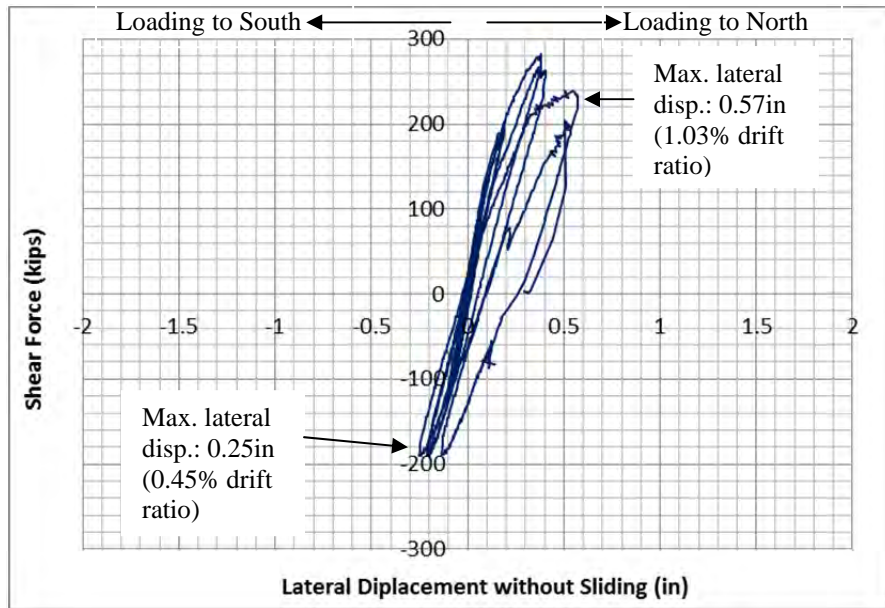
*Figure 6.71 Shear response of the specimen without total sliding.*

Figure 6.72 shows the envelopes curves from the response of RWM-R2 loaded to north (blue line) and south (red line). It can be seen that the response loading to north has slightly larger stiffness than loading to south. It is explained because of the diagonal tie with larger amount of CFRP sheet (2layers of 9 in. wide).
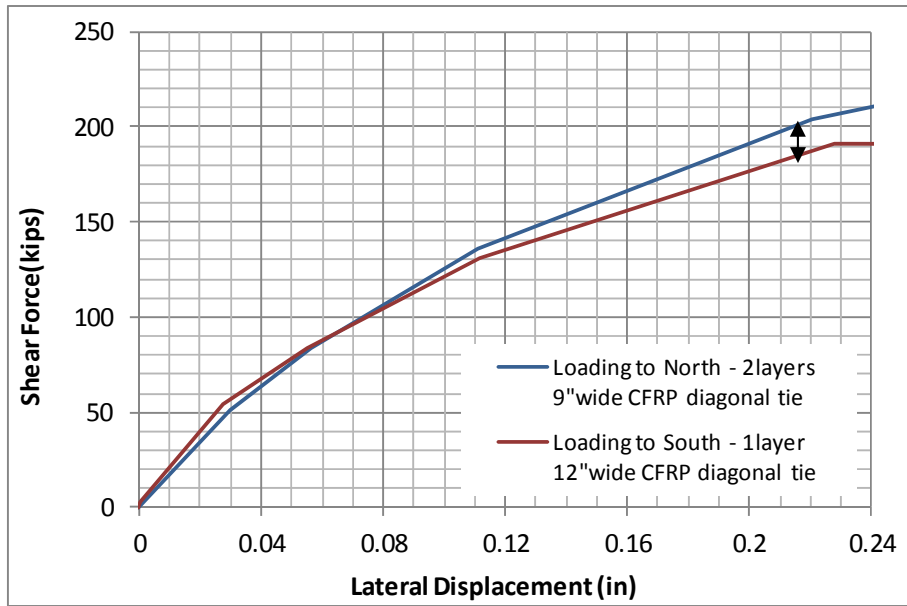
*Figure 6.72 Differences between the behaviors of the two diagonal ties.*

**6.4.2.2.3.2   Response of the Two 9in. wide layers of CFRP Diagonal Tie**

CFRP diagonal strips worked as axial tension punctual brace when the masonry wall was loaded to the north. In the 7th hysteretic cycle, some noise was heard indicating the beginning of the debonding. The CFRP anchors transferred tension from the CFRP diagonal strips to the top and bottom support of the wall. The maximum strain measured was 0.0052 (Figure 6.73 ) on the front face of specimen which is slightly above 50% of the strain capacity of the CFRP according to the producer's specification. The maximum strain deformation measured on the CFRP strip on the back face was 0.0039(Figure 6.74).

Compressive strains in the CFRP strips were measured under loading to the south. In the 11th hysteretic cycle, the CFRP strip buckled as is shown in Figure 6.75. The maximum strain in compression prior to buckling was 0.0016. However, when the buckling occurred CFRP on front face of the wall, the compressive strain was 0.0027 (Figure 6.73) and 0.0014 on the back face of the wall (Figure 6.74). It was observed also that the strain measured was longer on the bottom part of the diagonal ties, having concentration of compression stress on this region.
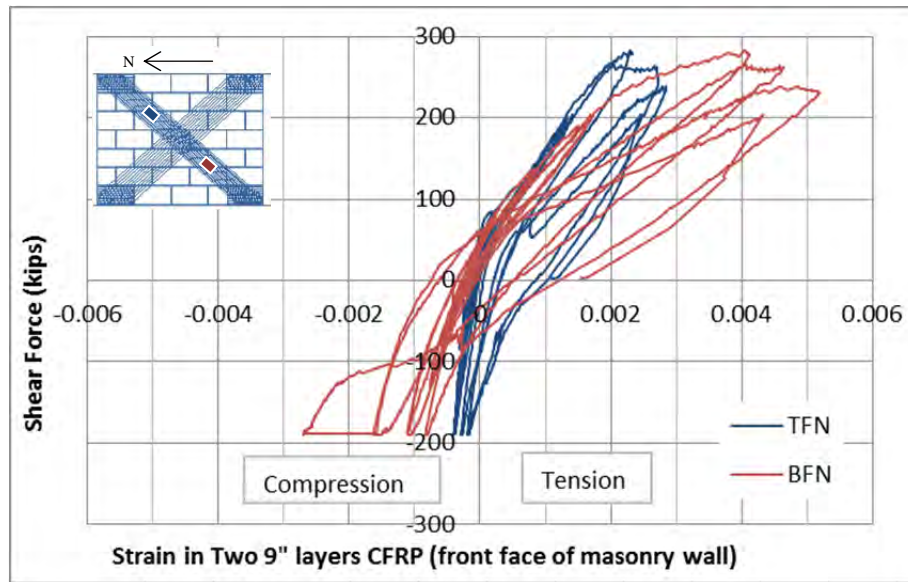
*Figure 6.73 Strain deformation of the two 9in. layers CFRP sheet on west face of the masonry wall*
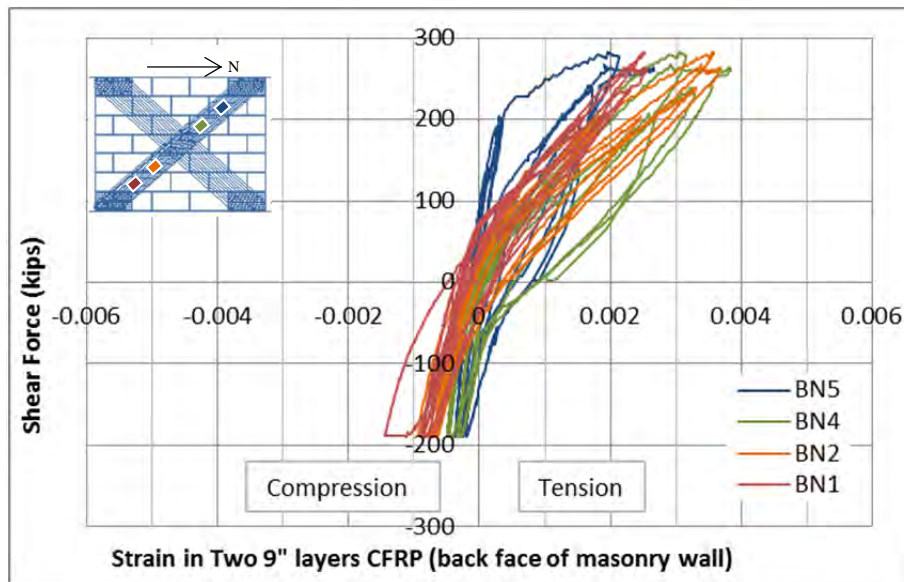


*Figure 6.74 Strain deformation of the two 9in. layers CFRP sheet on east face of the masonry wall.*

305

Failure occurred during the 12<sup>th</sup> cycle of the test. It was due to rupture of the CFRP anchors installed on the top north corner of the masonry wall Figure 6.76. Those CFRP anchors provided restraint against the sliding between the wall line and the top concrete beam. The CFRP anchors carried the axial load from the debonded CFRP diagonal ties (2 x two 9in.CFRP sheets), and a tension due to the correspondent diagonal component of the force produced during sliding. The sliding measured at failure was 1.24 in.
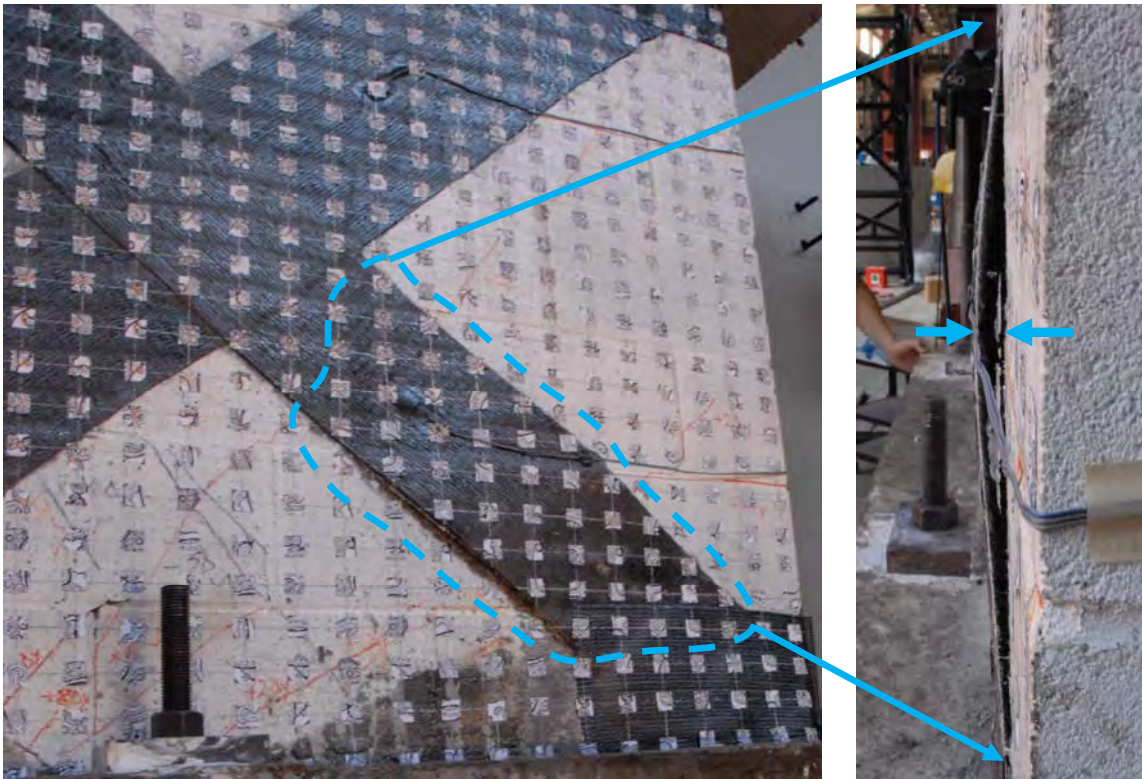


*Figure 6.75 Buckling presented on 9in.wide CFRP sheet at 11<sup>th</sup> cycle.*
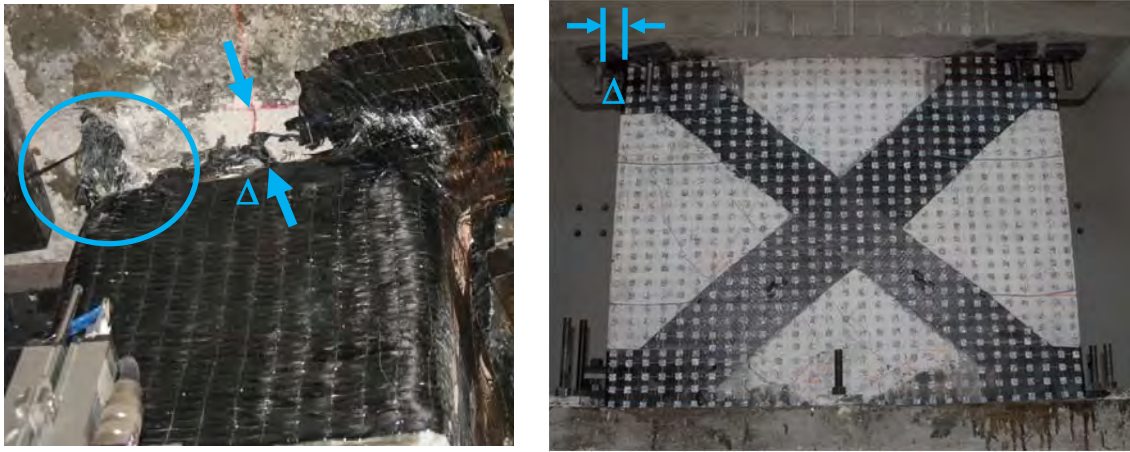
***Figure 6.76 Amount of slip following rupture of CFRP anchors***

It was observed during the test that the CFRP anchor provided resistance against the sliding at top of wall. Figure 6.77 shows a body diagram of the forces implied to the behavior of the CFRP anchors when the specimen was loading to north direction. There are two types of forces applied to the anchor. They are: pulling loads due the tension load from the diagonal ties, and the sliding forces due the lateral load from the top concrete beam. Each of these forces is divided by the correspondent number of anchors. Using the parallel and perpendicular forces component respectively to the direction of the anchor, the CFRP anchor resists two types of load: pulling load (parallel to the anchor's direction) and shear force (perpendicular to the anchor's direction). It is not considered the dowel effect on the sliding.
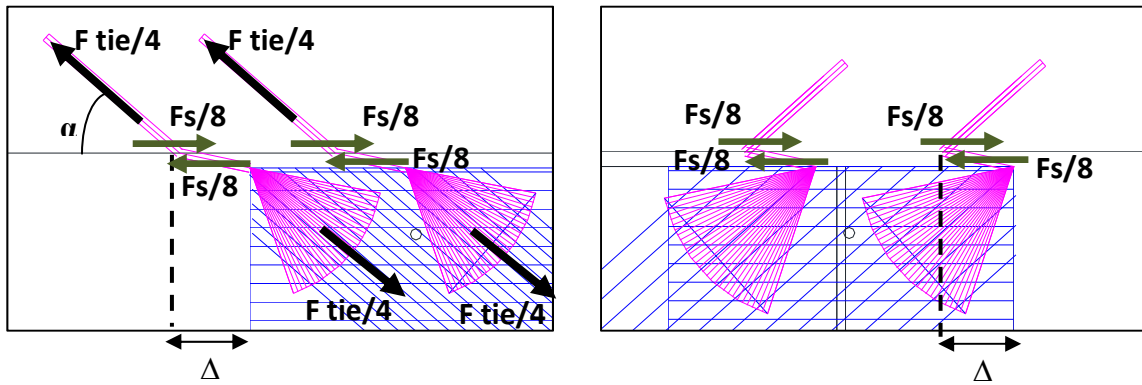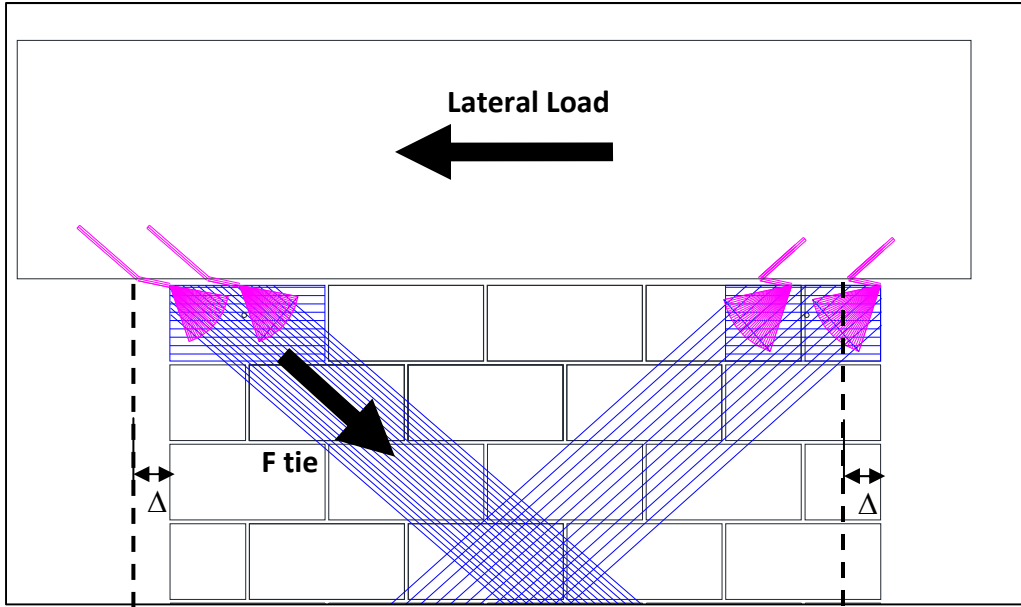
*Figure 6.77  Forces applied to the CFRP anchor*

Equation 6-1 and Equation 6-2 show the developed formulas for the two types of forces applied in the CFRP anchor in base of the body diagram of forces for the north corner:

$$F\ tension\ tie/4 + (F\ sliding/8)cos\alpha = CFRP\ anchor\ Pulling\ Force$$

**Equation 6-1**

$$(F\ sliding/8)sin\alpha = CFRP\ anchor\ Shear\ Force$$

**Equation 6-2**

Figure 6.77 also shows the body diagram for the south top corner of the masonry wall. It is considered that the CFRP diagonal ties had not tension pulling loads for this case. Therefore forces due sliding were considered only. It is deduced that the forces applied to the south CFRP anchors (or north CFRP anchors when it is loading to south) are due the sliding.

Equation 6-3 and Equation 6-4 show the developed formulas by the body force diagram in order to calculate the forces applied to the CFRP anchor in the south corner.

$$F\ sliding/8\ cos\alpha = CFRP\ anchor\ Pulling\ Force$$

**Equation 6-3**

$$F\ sliding/8\ sin\alpha = CFRP\ anchor\ Shear\ Force$$

**Equation 6-4**

It is concluded that the CFRP anchors had a very important role for the resistance of the masonry wall against its sliding at top. The resistance capacity of the CFRP anchors under pulling and shear forces are explained in Chapter 3.

**6.4.2.2.3.3  Response of the 12in.wide CFRP Diagonal Tie**

CFRP diagonal strips worked as axial tension brace when the masonry wall was loaded to the south. Debonding of the CFRP diagonal strips appeared at the $5^{th}$ cycle. This was noticed by a noise heard, being this more clear on the $9^{th}$ cycle and further. In the $11^{th}$ hysteretic cycle the maximum strain was reached in tension, 0.0023 and 0.0036 for the front and back face of the wall respectively. The pattern of the strain deformation is shown in Figure 6.78 and Figure 6.79.

Compression strains reached 0.002 (20% of the maximum tensile strain capacity). This was measured on the lower strain gage applied on the CFRP diagonal strip. The strain deformation in compression was larger for the bottom part of the CFRP diagonal strip, indicating that there was a major concentration of stress at the bottom tie. It is observed that the strain gages near the bottom exhibited larger strain than the gages near the top.
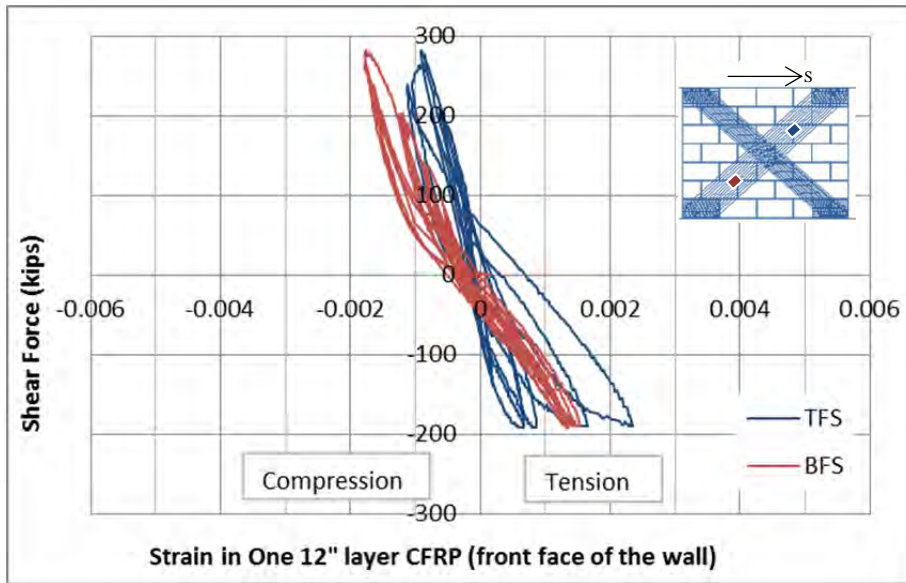
*Figure 6.78 Strain deformation of the one 12 in. layer CFRP sheet on west face of the masonry wall*
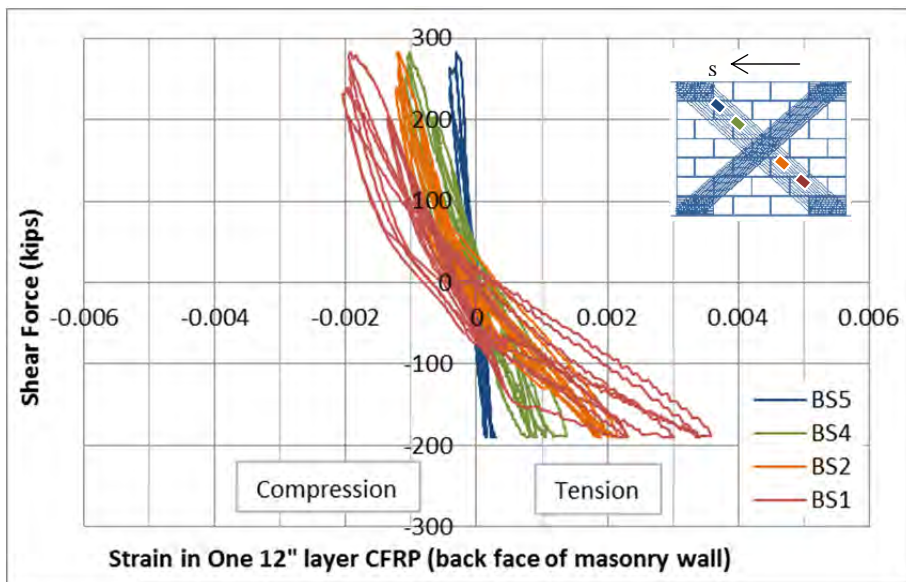


*Figure 6.79 Strain deformation of the one 12 in. layer CFRP sheet on east face of the masonry wall*

The sliding observed was 0.88in and the CFRP anchors close to the rupture as it can be seen in Figure 6.80. Buckling was observed specially in the 12$^{th}$ cycle. Figure 6.81 shows the front face of the masonry wall with the inferior part of the diagonal tie with portions of the CFRP strips buckled. It was observed that CFRP anchor carried out load from sliding. The resistance of those CFRP anchor was explained in 6.4.2.2.3.2.
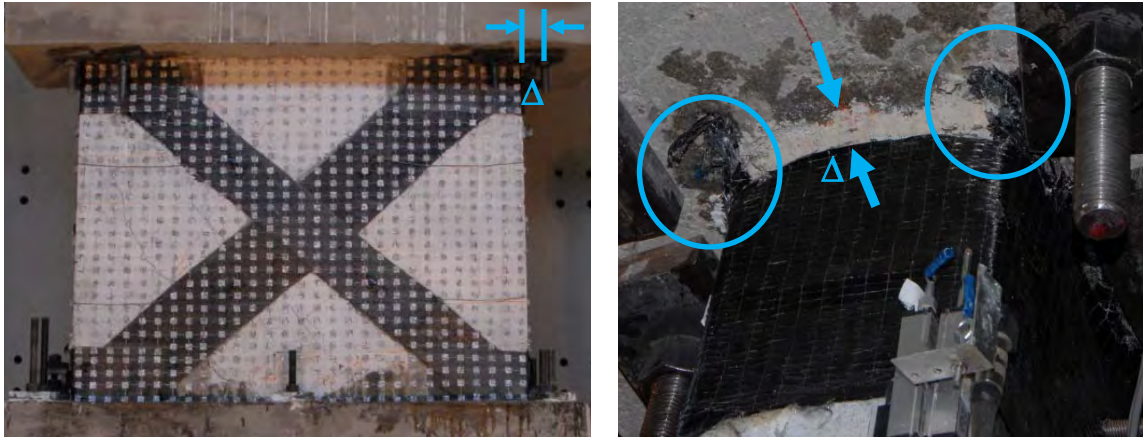


***Figure 6.80 Condition of the specimen at maximum south lateral displacement (left) and sliding at top with the CFRP anchors close to the rupture (right).***
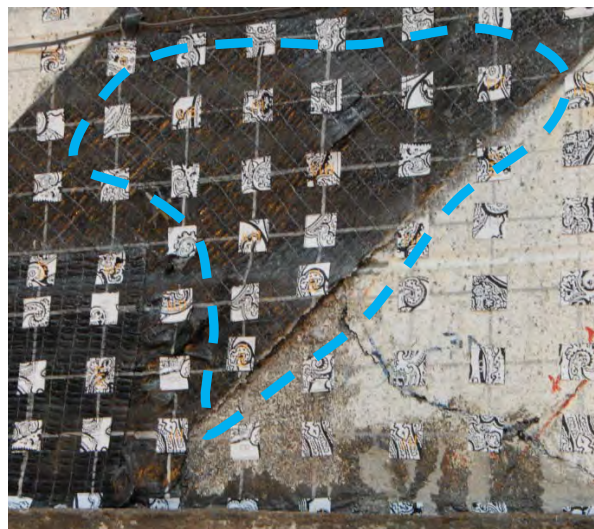


***Figure 6.81 Buckling presented on 12 in.wide CFRP sheet at 12$^{th}$ cycle.***

## 6.5    SUMMARY

The histories of shear force vs. drift for each specimen (RMW, RMW-R1 and RMW-R2) are presented. Further detailed comparisons are shown and explained in next Chapter 7.

Figure 6.82 shows the hysteretic response in the linear range for the three different specimens tested. It can be seen that for RMW-R2 has less stiffness than the as-built masonry wall RMW, even though the masonry wall was retrofitted with CFRP diagonal ties and a lower aspect ratio than the as-built column. It is also observed that stiffness of RMW-R1 is lower than RMW-R2 because of the CFRP diagonal ties increase the stiffness of the wall.
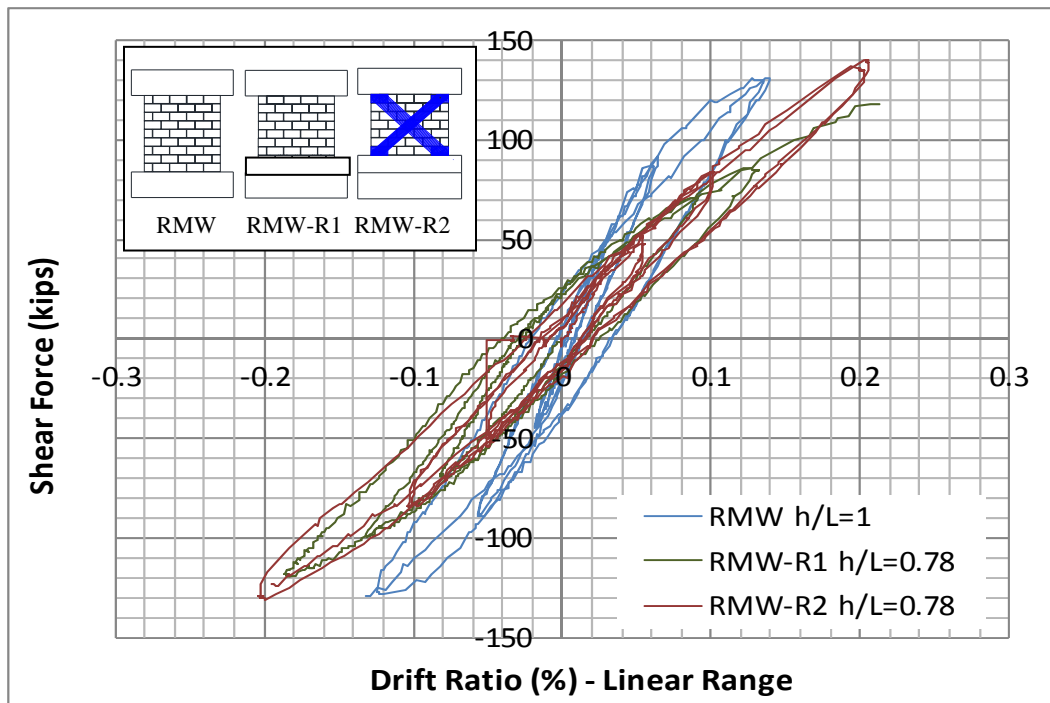


*Figure 6.82 Shear force vs. drift ratio on linear range of RMW, RMW-R1 and RMW-R2*

Figure 6.83 shows a comparison between the behavior of RMW and RMW-R2. Values of lateral displacement were normalized by drift ratios since both specimens had different aspect ratios. It can be observed that the retrofitted wall had higher shear capacity because its aspect ratio was reduced from h/L=1 of the as-built column to h/L=0.78 and sliding was prevented by the CFRP anchors. Drift capacity of the retrofitted wall was larger despite its lower aspect ratio.
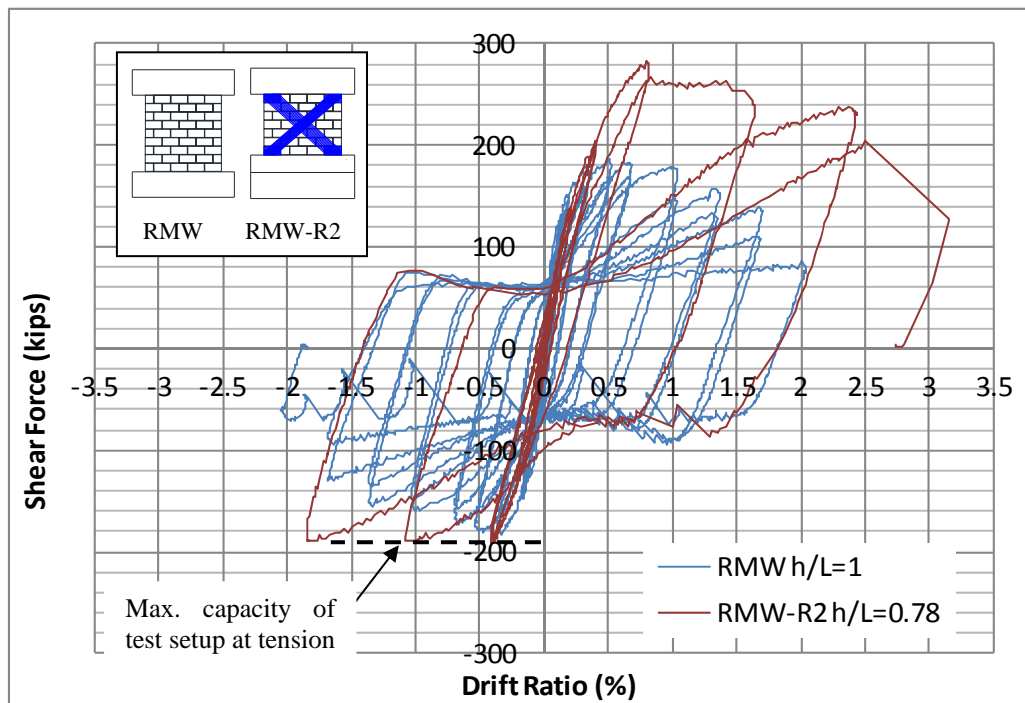


*Figure 6.83 Shear force vs. drift ratio of RMW and RMW-R2.*

Figure 6.84 shows the shear force vs. drift ratio after sliding deformation was removed. It can be seen that the retrofitted wall developed larger deformations than the as-built wall. The increased strength and stiffness of RMW-R2 can be attributes to the greater forces carried by the CMU wall, the diagonal ties, and wall reinforcement when sliding is prevented.
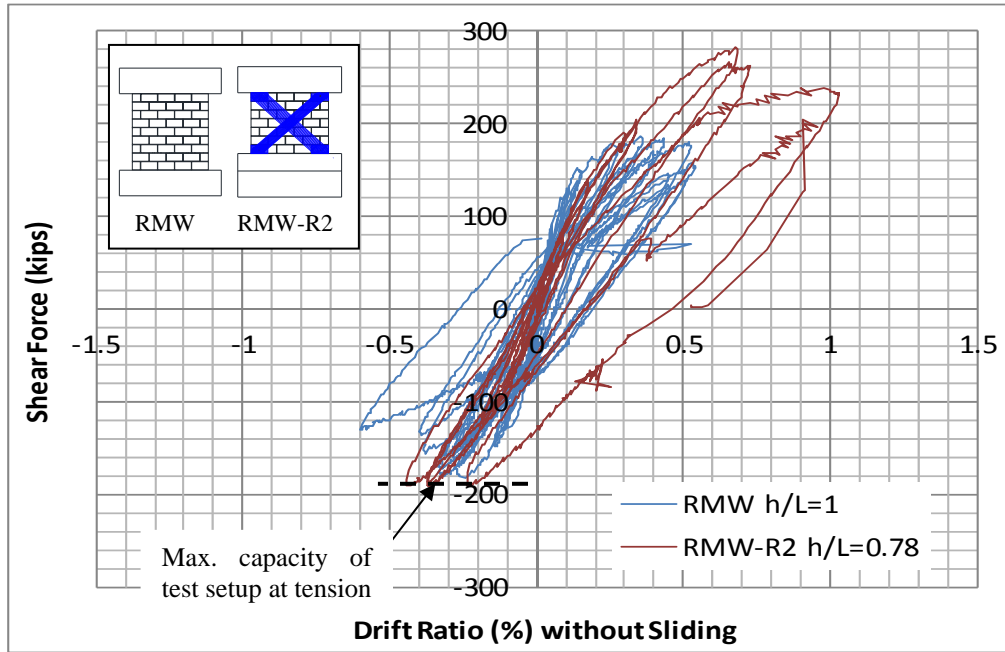
*Figure 6.84 Shear force vs. drift (without sliding) of RMW and RMW-R2.*

# CHAPTER 7

# Modeling Performance of Rehabilitated Columns and Masonry Wall for Analysis and Design

## 7.1 SCOPE

This chapter is focused on the structural performance assessment of the reinforced concrete members. Comparisons between the different lateral load vs. lateral displacement curves obtained on the tests shown in Chapter 4 and Chapter 5 are presented. Backbone curves were constructed following the procedures of ASCE41-07 and the proposed update to ASCE41-13. Using these normalized backbone curves, shear resistance values and ductility are compared through graphs.

Idealized force-displacement curves and elasto-plastic curves are proposed based on the ASCE41-13 backbone curves. The curves are normalized with respect to load at yield obtained from the idealized curves. These converted data are presented for use for computer models.

One of the developed behavioral models was used into a nonlinear structural analysis of the retrofit of one existing building. The results are compiled in Appendix J.

317

**7.2    DIFFERENCES IN BACKBONE CURVES ASCE41-07 AND ASCE41-13**

A timeline of structural assessment guides for the last 20 years helps to understand the philosophy behind design guidelines. The assessment procedures were developed first in FEMA 273 (1997), followed by FEMA 356 (2000) and ATC-40. FEMA 356 was updated by SEI producing ASCE41-07. The latest update will be ASCE41-13. The type of assessment in ASCE41-13 was changed using recent data reported in the literature. The definition of backbone curve using experimental data will also be changed. The two assessments guides: ASCE41-07 and ASCE41-13 will be discussed in this chapter.

ASCE41-07 and its update ASCE 41-13 define alternative modeling parameters and acceptance criteria from experimental data on the cycle response of member. Guidance for developing appropriate data to evaluate members not defined in the ASCE41 provisions will be discussed, particularly members retrofitted with CFRP or mechanical splices.

**7.2.1    Backbone Curves**

Figure 7.1 shows both definitions of backbone curves developed by ASCE41-07 and ASCE41-13. ASCE41-07 backbone curves were drawn through the intersection of the first cycle curve of the (i)th deformation step with the second cycle curve of the (i-1)th deformation step, for all i steps. The proposal of ASCE41-13 defines the backbone curve as the focus of point at peak displacement during the first cycle of each increment of loading.  Both procedures are indicated in Figure 7.1.

318
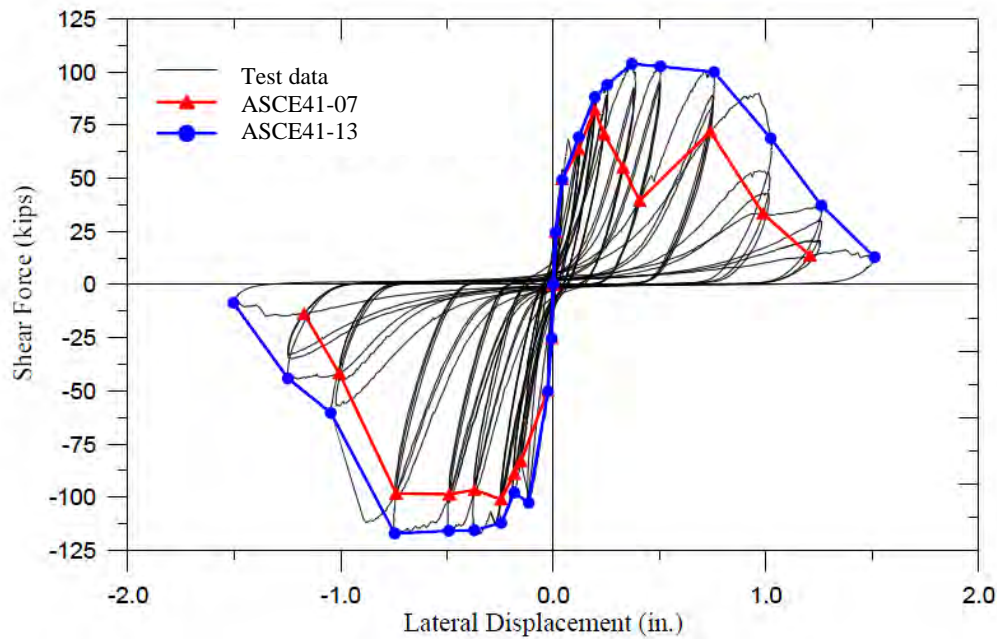
*Figure 7.1 Backbone curves following ASCE41-07 and ASCE41-13 (Elwood, et al.; 2007)*

It can be seen that backbone curve ASCE41-07 is very conservative in comparison with the backbone curve using ASCE41-13. Values of shear capacity and ductility are reduced using ASCE41-07 and can be considered as part of a lower bound approach. However, the backbone curve using ASCE41-13 results in higher shear forces and large ductility and represents an upper bound approach.

Lower bound methods are very useful for the design and construction of new structures. There many load factors proposed by LRFD in order to meet minimum provisions of design. Additionally the many uncertainties which occur in the design of a new structure are indirectly taken into account following lower bound solutions. The use of lower bound methods may not be practical for repair and rehabilitation purposes because they may be unnecessarily conservative and result in higher construction costs.

319

In many cases the required design forces in the members could be quite high if the structure or the member is required to remain elastic.

Instead, an upper bound method may be more appropriate for retrofit purposes. Design of retrofitted elements is focused on an individual member of the structure. Yield and ultimate capacity and deformation of each member are considered. Upper bound methods are very usable for non-linear procedures and provide adequate structural assessment of RC concrete members. In the retrofitted member is permitted to dissipate energy by inelastic deformation, the force levels on the structure are reduced. The economic advantages are clear, provided that the critical regions can be designed to dissipate energy satisfactorily before loss of strength or ductility.

Additionally, the trend in structural seismic evaluation and design is toward deformation-based approaches and performance-based design and assessment techniques. Therefore, upper bound methods are more applicable to retrofit design. For this study the backbone ASCE41-13 curves are used to provide new idealized force-displacement and elasto-plastic curves for critical zones (hinges) of columns and masonry wall retrofitted using mechanical couplers or CFRP materials.

**7.2.2 Idealized Curves for modeling parameters and analysis considerations**

The capacity of existing buildings under seismic loading is determined from nonlinear static and dynamic analyses. Nonlinear modeling of behavior of structural members or components is presented in FEMA 356 and ASCE41-07. Three types of modeling which consist of a series of linear segments (Figure 7.2) are presented. It can be seen that Type 1 curve is appropriate for ductile members with some residual capacity. A Type 2 curve is appropriate for members with some ductility, however, lateral large deformations capacity is lost at a point 3. Finally, Type 3 curve is used to represent the response of brittle members or components. It is important to note that Type 1 and Type 2 curves are ductile because deformation at "e" (point 2) is at least two times the deformation at "g" (point 1) (e >2g).
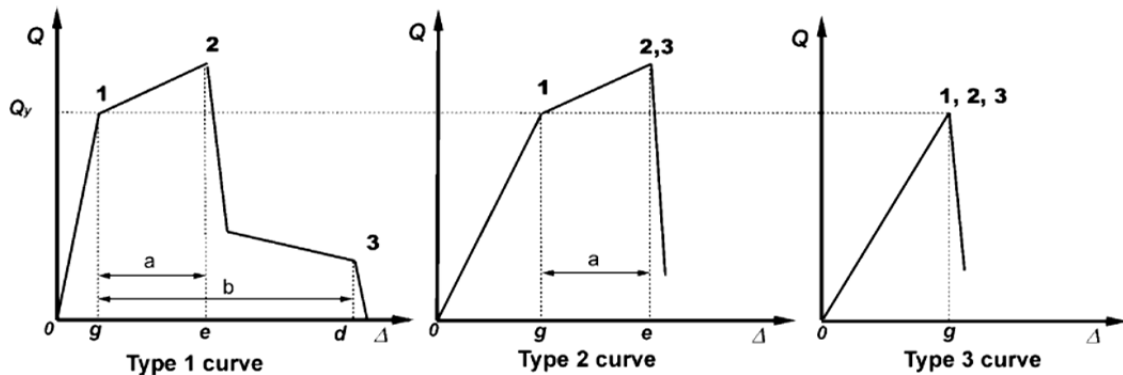


*Figure 7.2  Revised component force-deformation curves proposed for ASCE41-07*

Since the curves in Figure 7.2 were developed using data from ASCE41-07 axial-bending tests, type 2 and type 3 curves are modified. Figure 7.3 shows the types of curves with extended deformation capacity from point e to point f.
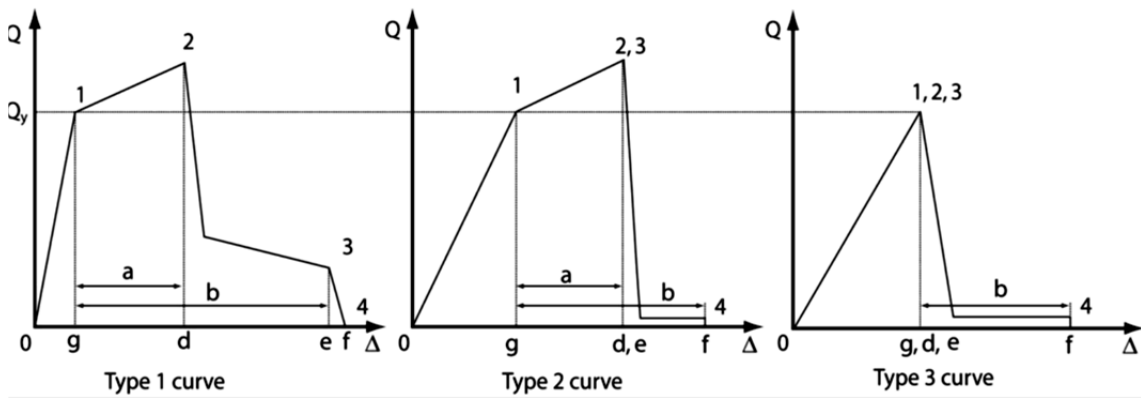
*Figure 7.3  Revised component force-deformation curves proposed for ASCE41-13*

Figure 7.4 shows the generalized component force-deformation relation for depicting modeling, for behavior under singular axial, bending and shear deformation. They are normalized as a function of the yield strength Qy, deformation parameters a and b, and the residual strength parameter c. However, recent experimental data suggest that the sudden drop in strength from point C to D is no realistic and very problematic for computer modeling of nonlinear response. Because of this problem, ASCE41-13 provisions recommends the use of a modified slope to represent the degrading response which is shown by dashed line from points C to E. Figure 7.4 also shows the difference between the actual ASCE41-07 and the updated ASCE41-13, considering a tri-linear curve.

322
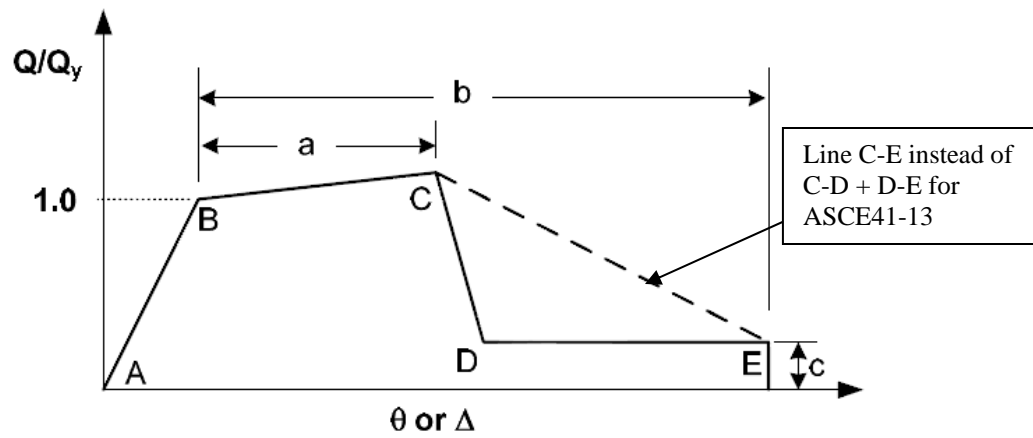
*Figure 7.4  Modified force-deformation response curve for ASCE41-07 and the change for ASCE41-13*

**7.3   MODELING BEHAVIOR  AND SEISMIC PERFORMANCE**

**7.3.1   Columns**

An idealized force-displacement curve for the retrofitted columns was based on the backbone curve obtained using the ASCE41-13 provisions. In addition, a bilinear elasto-plastic curve was developed.

Figure 7.5  shows the first method, which follows the provisions of ASCE41-07 and ASCE41-13 section 3.3.3. This method consists of the selection of three lines to represent response as shown in Figure 7.5. The first line represents the elastic and linear behavior of the member, defined as the line which joins the origin of coordinates and approximately 60% of the yielding of the member (0.6Vy). The slope of the elastic curve is the effective stiffness (Ke). The second extends from the point of yielding of the member to the point of maximum capacity of the member. The slope is a fraction ($\alpha_1$) of the effective stiffness. The descending branch represents degradation of the capacity due to sliding, lifting, shear deformation. To define Vy and $\Delta$y, the dissipation of energy, from the backbone curve (area under the curve) is used. The idealized force-displacement curve (tri-linear curve) should have the same value of dissipated energy (area enclosed) as the backbone curve.

**Base shear**

$V_d$

$V_y$

$0.6V_y$

$\alpha_1 K_e$

$\alpha_{P-\Delta} K_e$

$\alpha_e K_e$

Actual force-displacement curve

$\alpha_2 K_e$

$K_e$

$\Delta_y$

$\Delta_d$
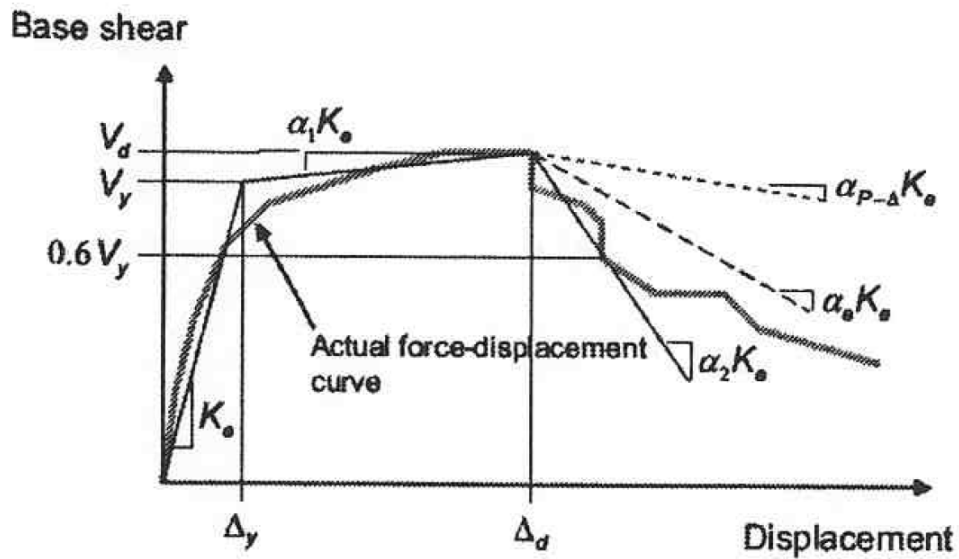
Displacement

***Figure 7.5  Idealized Force-Displacement Curve (ASCE41-07 and ASCE41-13)***

Figure 7.6 shows an elasto-plastic (bilinear) approximation of the measured response. This procedure is used in retrofit research. The first line starts from the origin and extends through the backbone curve at a point at half the maximum measured shear load (Vr). The second line extends horizontally to point near the measured peak deformation. Once again, they are under the backbone curve should be the same as that under the bi-linear approximation. Elwood (Elwood, et.al, 2006) defined for retrofit purposes the value of Kr as the effective stiffness of columns.

325
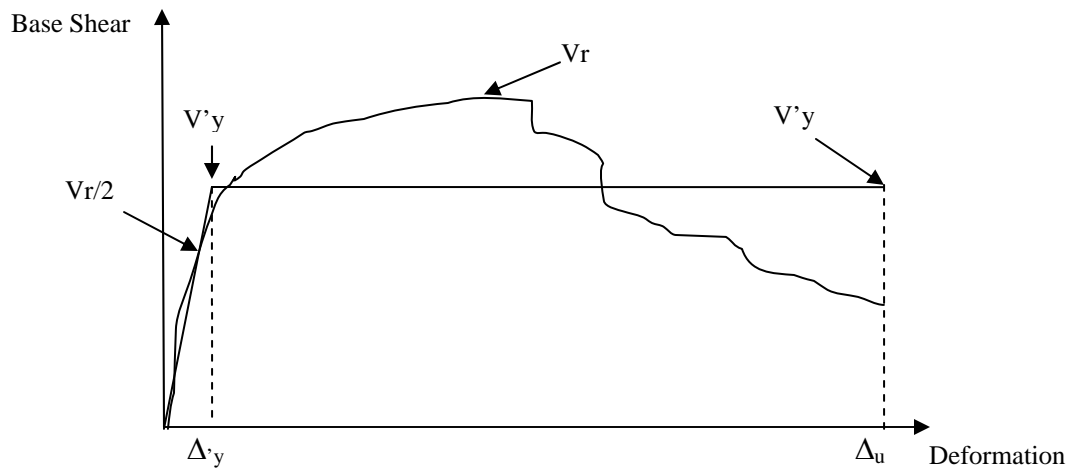
*Figure 7.6  Idealized Elasto-Plastic Curve (He, et.al. , 2013)*

Figure 7.7 shows the idealized elasto-plastic curve when the backbone curve has its last part a very pronounced degradation of base shear. It may be hard to have a good approximation of elasto-plastic curve having a very low shear force as it is shown in Figure 7.6. The elasto-plastic curve may not represent accurately the behavior of the retrofitted column. Because of this, the extension of the elasto-plastic curve is limited until the deformation when the capacity reaches for second time 0.8Vr. The energy are compared until the displacement correspondent 0.8Vr ($\Delta_{0.8}$) to and obtained the value of V'y. This procedure is most common for wall cases. It is explained with better details in the next section.
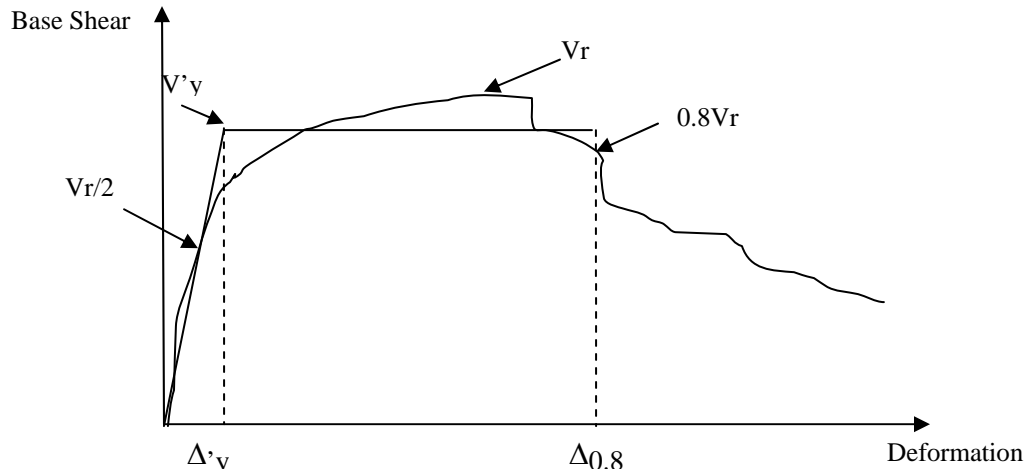
*Figure 7.7 Idealized Elasto-Plastic Curve for backbone curve with pronounced negative slope at last capacity*

### 7.3.2 Masonry Wall

Two methods are used to define the modeling parameters or behavioral model for the retrofitted masonry wall. The first method is the Idealized Force-Displacement Curve which consists of the same procedure used for the retrofitted column. The second method consists of a bi-linear Elasto-Plastic Curve.

Figure 7.8 shows different cases of elasto-plastic curves used for masonry walls. Shedid (2008) defined several bilinear curves for computational models. The one is used for wall tested in this research is based on a maximum deformation corresponding to the deformation when the strength degrades to 80% of the maximum measured capacity (Vmax and $\Delta_{y0.8u}$). The first line is defined by the point of the backbone curve when the first internal steel bar reaches the yielding. However, for retrofitted members, a value of

327

Vmax/2 is used instead for the point of intersection.. The second line is horizontal finishing at 0.8Vmax. The dissipated energy under the backbone curve to $\Delta_{y0.8u}$ is used to determine the value of Vy that has the same dissipated energy as that under the backbone curve.
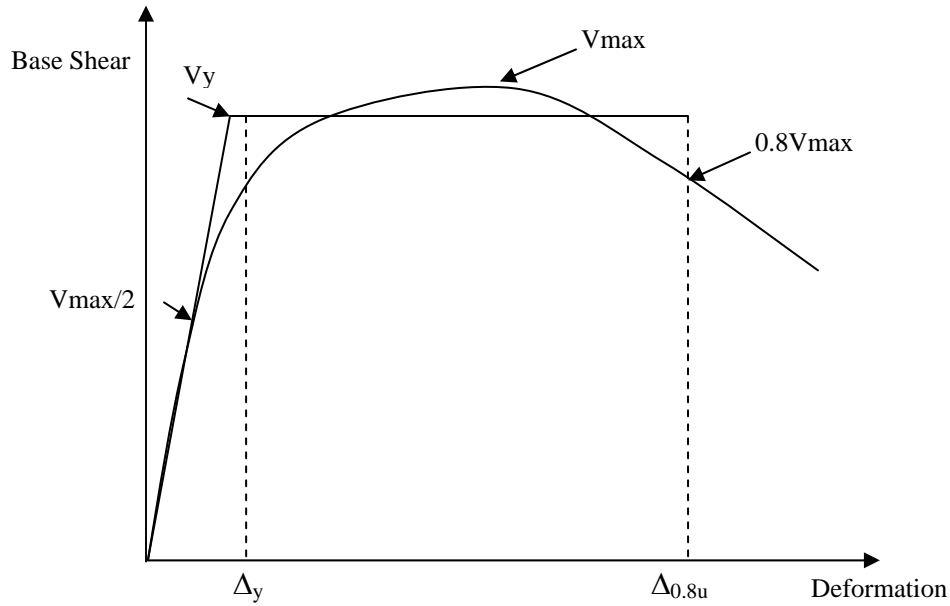


*Figure 7.8  Idealized Elasto-Plastic Curve*

## 7.4 COLUMN CASES

### 7.4.1 Backbone ASCE41-07 and ASCE41-13 curves

A set of 10 graphs of shear force vs. lateral displacement are presented with the backbone curves shown for the strengthened specimens tested. Each graph shows the backbone curves following the provisions of ASCE41-07 (yellow) and ASCE41-13 (red).

Loading protocols applied to the tests were appropriate to build the ASCE41-07 and ASCE41-13. For every specimen, ASCE41-07 and ASCE41-13 backbone curves were built without problems until no mayor failure occurred.

The first 7 graphs are from tests conducted in this study. Figure 7.9 and Figure 7.10 show the results from tests of experiments made to existing specimens RC-1 and RC-2. Figure 7.11, Figure 7.12 and Figure 7.13 show the performance specimen of RC-1R and the behavior of the top and bottom hinge regions. Figure 7.14 and Figure 7.15 show the behavior of RC-2R-SMS and RC-2R-LMS respectively. Figure 7.16 shows the behavior of specimen 2-A-S8-M tested by Kim 2008. Figure 7.17 shows specimen FC-17 tested by Aboutaha 1994, and finally Figure 7.18 shows the test results of Column 2-R tested by He 2013. The tests made by Kim and Aboutaha were conducted at Ferguson Structural Engineering Laboratory. The test from He was conducted in Missouri University. Details of the specimens 2-A-S8-M, FC-17 and Column 2-R are listed in Chapter 2. Those three additional tests are used for comparison with the procedures proposed in this research.
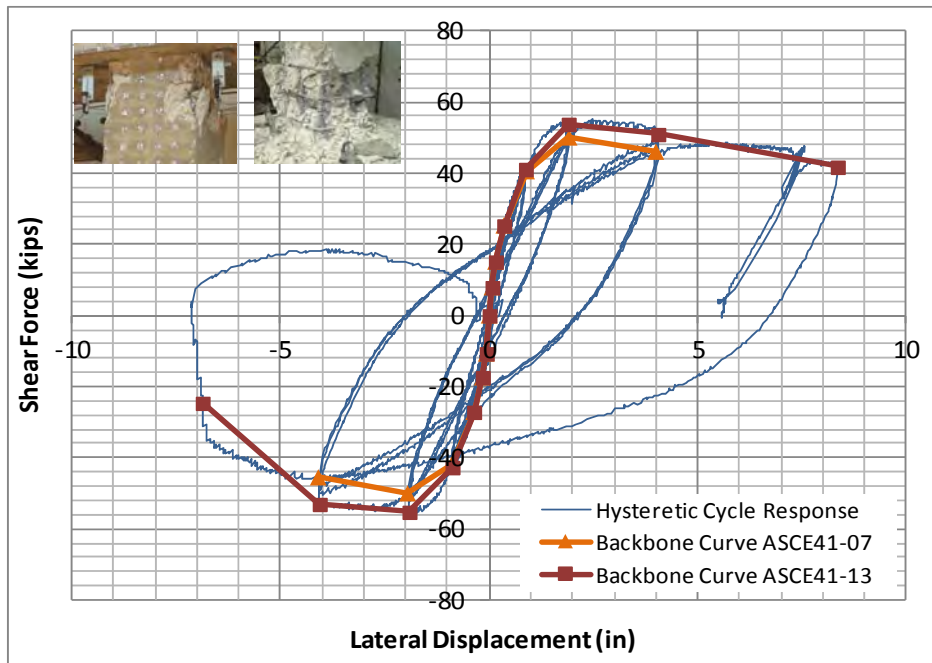
*Figure 7.9  Backbone curves following for RC-1*
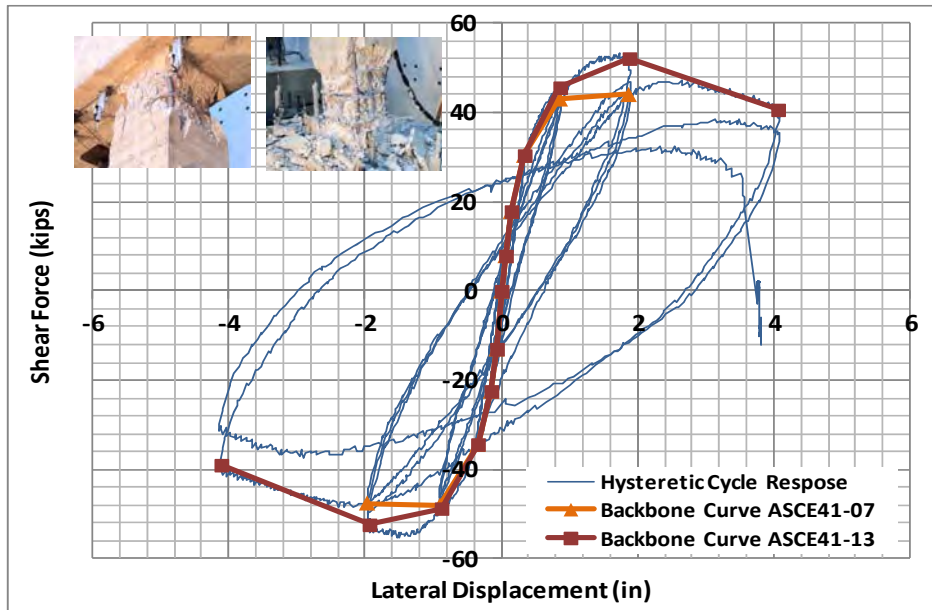


*Figure 7.10  Backbone curves following for RC-2*

330
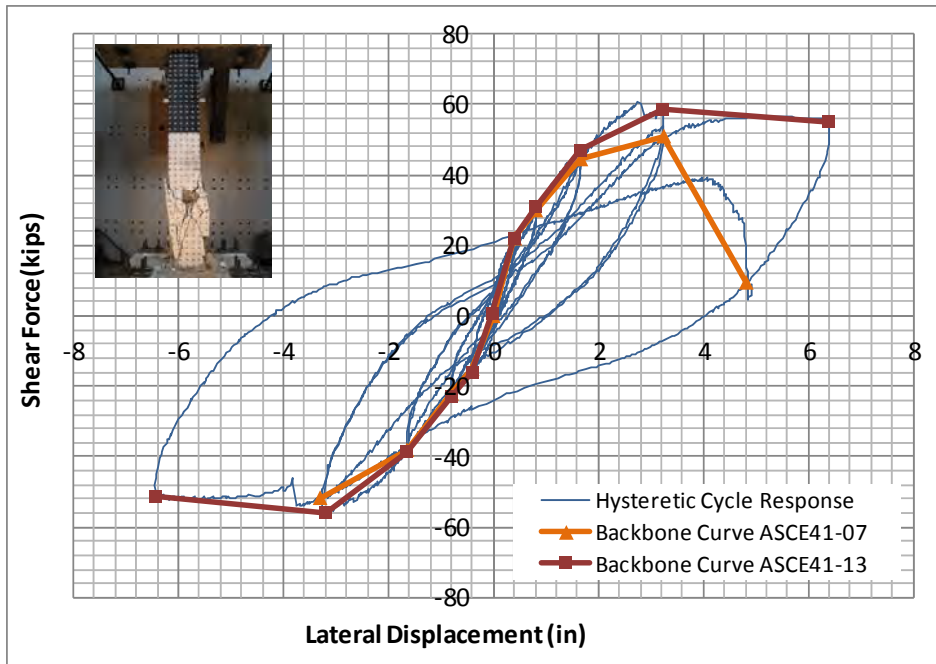
*Figure 7.11  Backbone curves RC-1R*
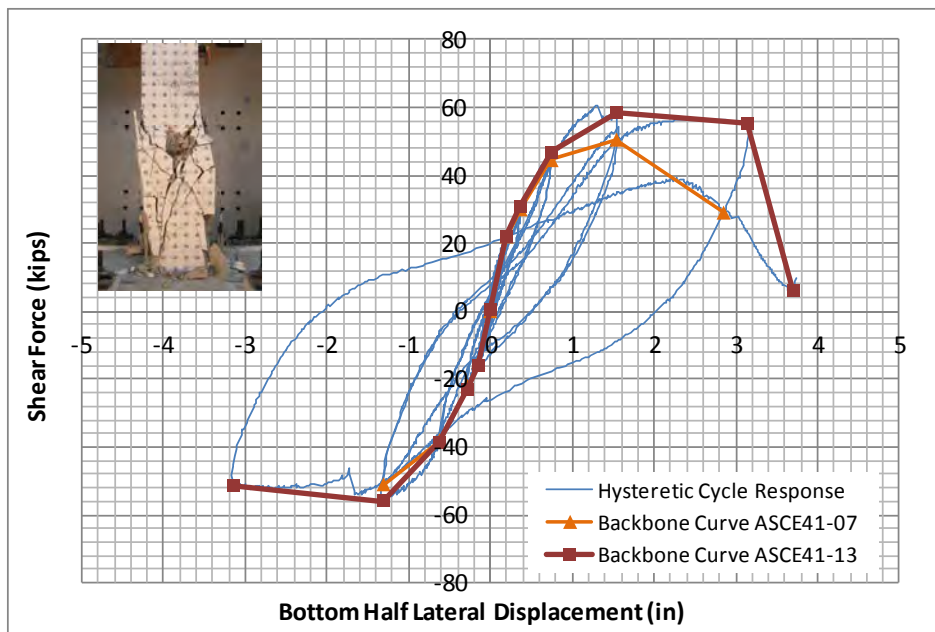
*Figure 7.12 Backbone curves for RC-1R-Bottom Half*
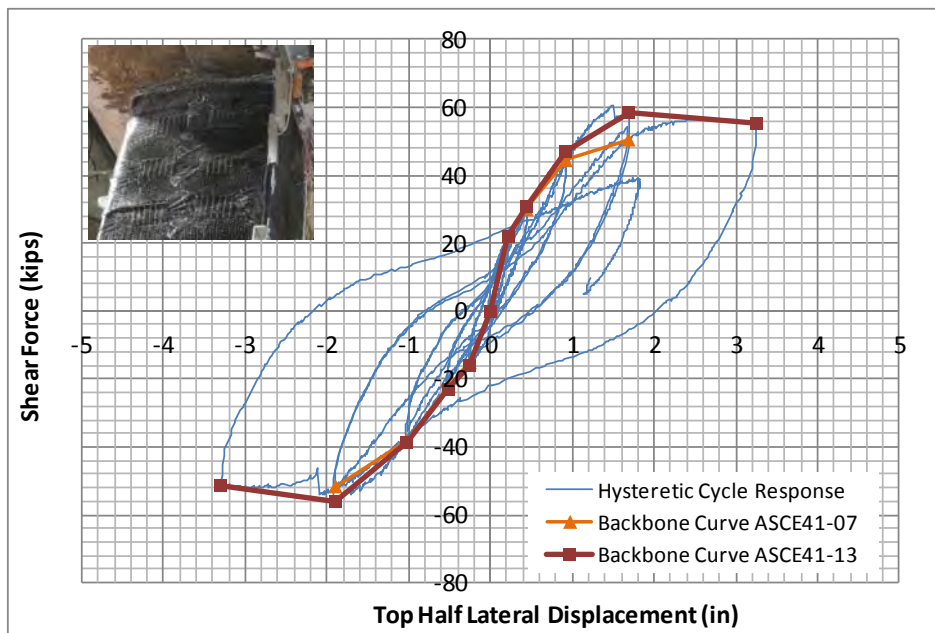


*Figure 7.13 Backbone curves for RC-1R-Top Half*

332
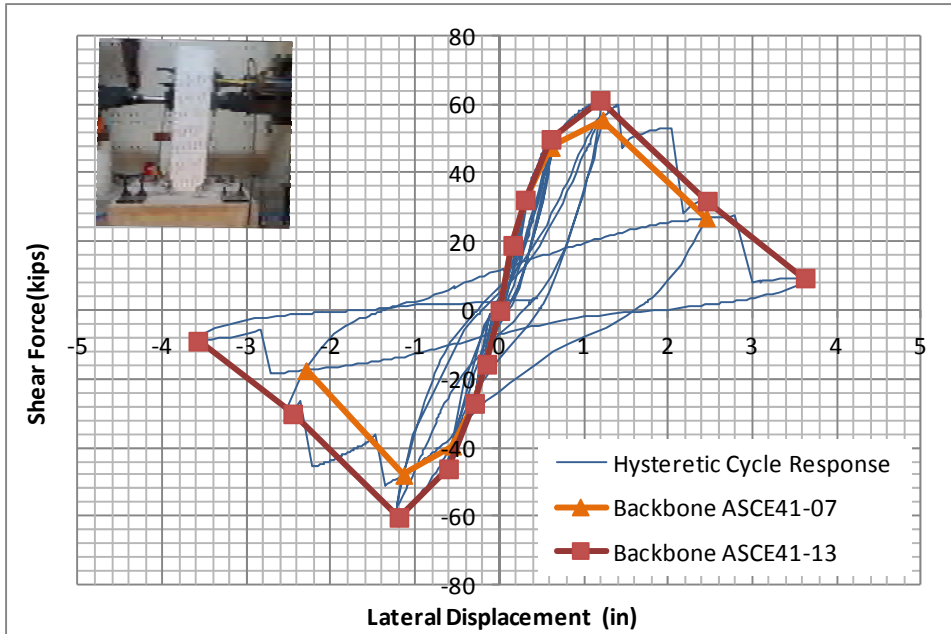
*Figure 7.14  Backbone curves for RC-2R-SMS*
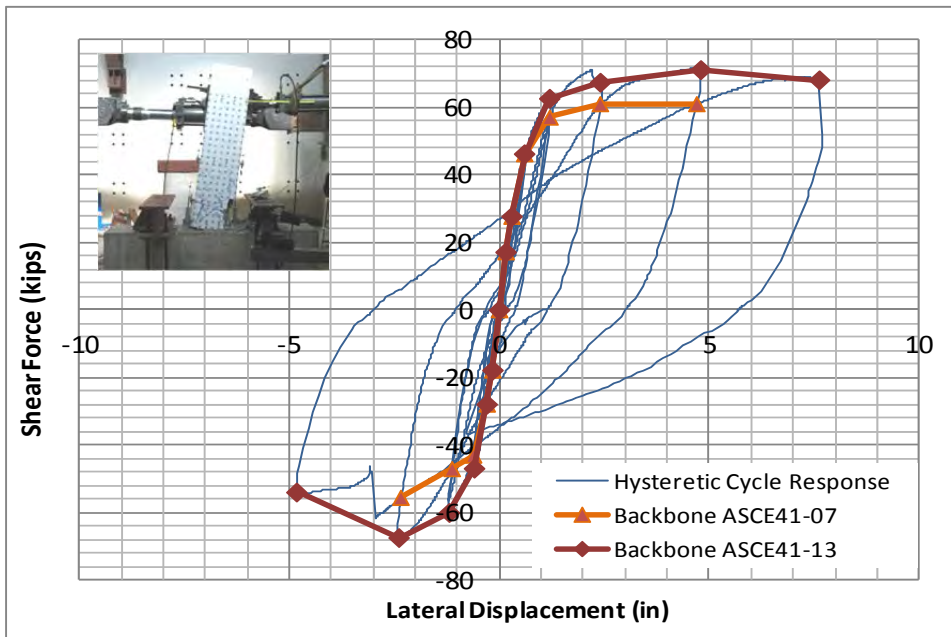


*Figure 7.15  Backbone curves for RC-2R-LMS*

333
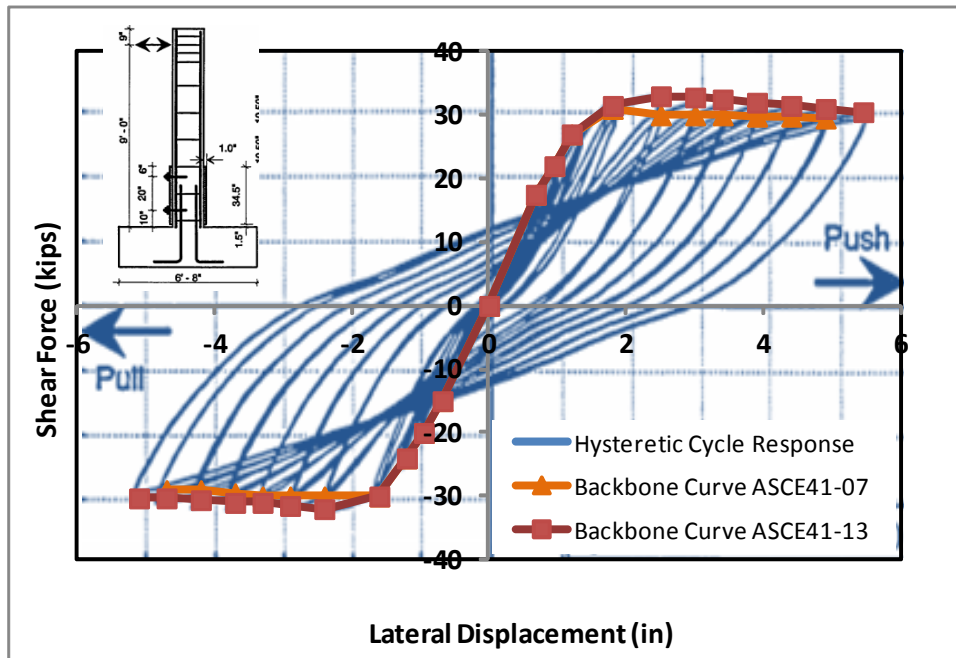
*Figure 7.16  Backbone curves for FC-17 (Aboutaha)*
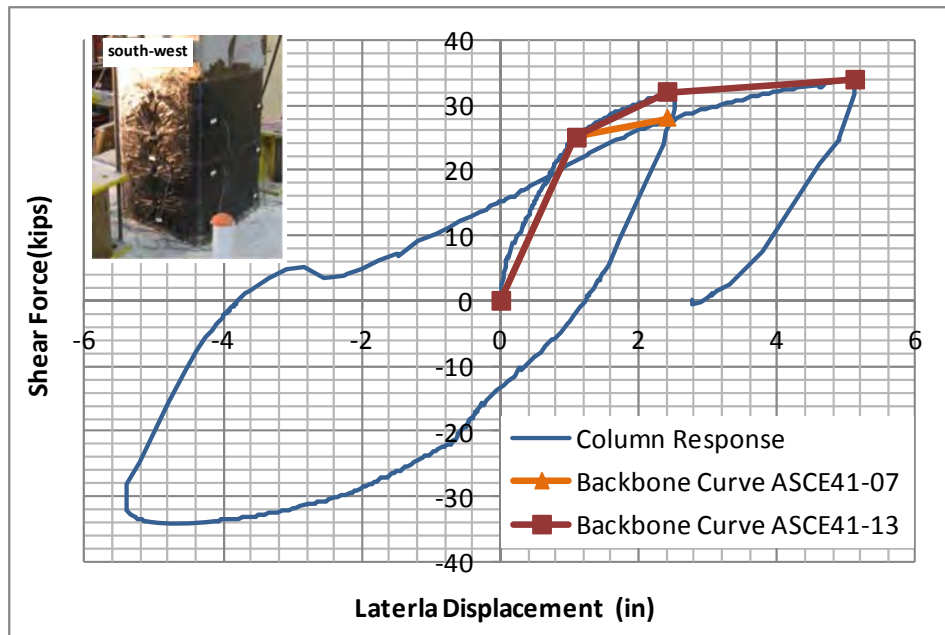


*Figure 7.17  Backbone curves for 2-A-S8 (Kim)*

334
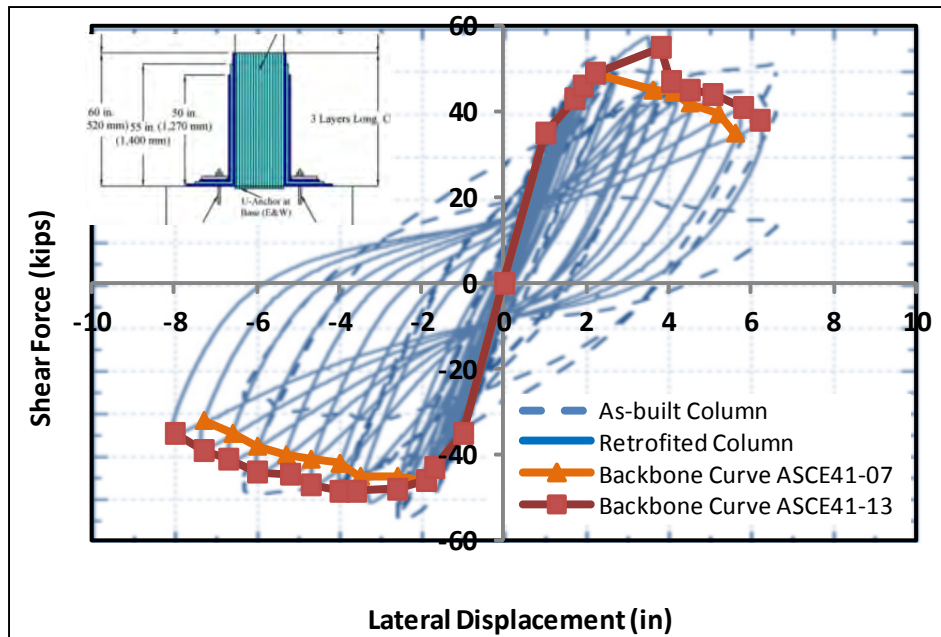
***Figure 7.18  Backbone curves for Column 2-R (He)***

The Table 7-1 shows the values of maximum shear force and the lateral displacement for case. It is seen that provisions given in ASCE41-13 to build the backbone curves are less conservative than ASCE41-07. The differences in shear force between both provisions vary from 1.06 to 1.21 and for lateral displacement vary from 1.1 to 2.1. These comparisons are useful to understand the differences between the two types of backbone curves. For maximum shear forces (Vmax) the differences are not large, between backbone curves of ASCE41-07 and the proposed ASCE41-13 and it is not too conservative. However, for maximum displacement, the differences can be from 1.1 (almost the same) to 2.1, being too conservative for ASCE41-07 provisions for building backbone curves.

## Table 7-1  Summary of maximum values of shear forces and lateral displacement by ASCE41-07 and ASCE41-13

| | ASCE41-07 | | ASCE41-13 | | Ratio for | Ratio for |
|---|---|---|---|---|---|---|
| | Vmax (kips) | Max Disp. (in) | Vmax (kips) | Max Disp. (in) | Vmax (x) | Max Disp.(*) |
| RC-1 | 50.00 | 4.10 | 55.23 | 8.35 | 1.10 | 2.04 |
| RC-2 | 48.00 | 1.97 | 52.32 | 4.11 | 1.09 | 2.09 |
| RC-1R | 51.60 | 4.82 | 58.45 | 6.43 | 1.13 | 1.33 |
| RC-1R Bottom Half | 51.00 | 1.54 | 58.45 | 3.15 | 1.15 | 2.04 |
| RC-1R Top Half | 51.60 | 1.89 | 58.45 | 3.30 | 1.13 | 1.74 |
| RC-2R-SMS | 55.50 | 2.45 | 61.28 | 3.62 | 1.10 | 1.48 |
| RC-2R-LMS | 61.00 | 4.70 | 71.08 | 7.62 | 1.17 | 1.62 |
| FC-17 | 31.00 | 4.90 | 33.00 | 5.45 | 1.06 | 1.11 |
| 2-A-S8-M | 28.00 | 2.40 | 33.88 | 5.11 | 1.21 | 2.13 |
| Column 2-R | 49.00 | 7.30 | 55.00 | 8.00 | 1.12 | 1.10 |

(x)Ratio for Vmax = Vmax(ASCE41-07) / Vmax(ASCE41-07)
(*)Ratio for Max.Disp. = Max.Disp.(ASCE41-07) / Max.Disp.(ASCE41-07)

### 7.4.2 Comparisons of ASCE41-07 and ASCE41-13 backbone curves

#### 7.4.2.1 *Normalization of shear capacity for column tests using exiting (as-built) computed strength*

To compare the effectiveness of the retrofit procedures using carbon fiber and mechanical splices, the shear capacity vs. lateral displacement are compared for the different tests. The value of the measured experimental lateral capacity is normalized using the nominal lateral capacity of the as-built confined section of each retrofitted or existing column. To calculate the nominal capacity, the measured dimensions and material properties were used. Details of the calculations are presented in Appendix A. and include the moment-curvature, moment-axial load interaction diagrams and shear capacity for unconfined and confined sections. The lateral displacement was normalized calculating the drift ratio for each column case.

Figure 7.19 shows the normalized backbone curves following the provisions of ASCE41-07, and Figure 7.20 shows the correspondent for ASCE41-13.

337
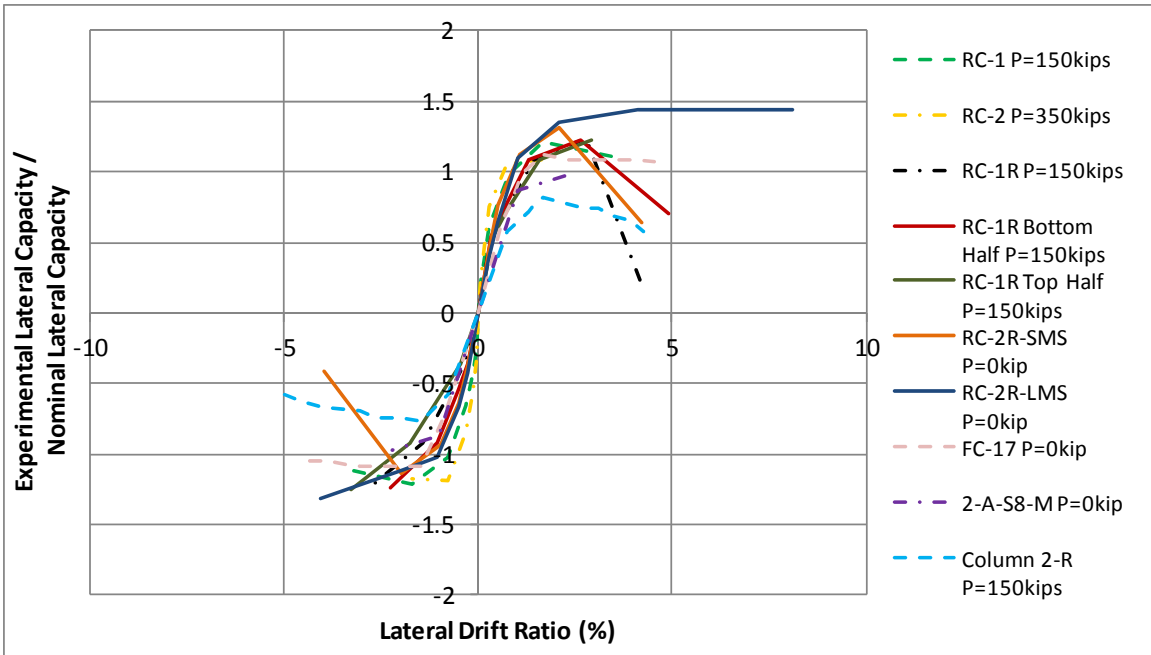
*Figure 7.19  Normalized ASCE41-07 backbone curves (as-built)*
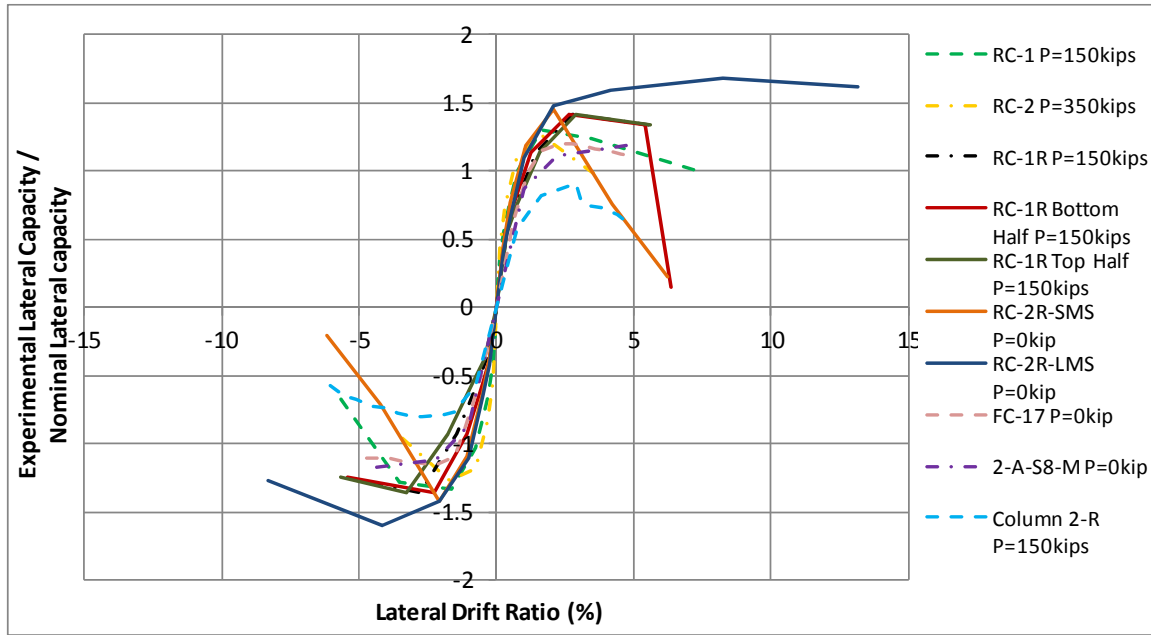


*Figure 7.20  Normalized ASCE41-13 backbone curves (as-built)*

338

Figure 7.21 shows the normalized ASCE41-13 backbone curves of existing column RC-1 and after retrofitting RC-1R. Additionally, the backbone curves for RC-1R Bottom Half and RC-1R Top Half are plotted separately to compare different types of retrofitting, short mechanical splices (RC-1R Bottom Half) and CFRP jacketing. (RC-1R Top Half). In all cases the axial load was 150kips.

The retrofitted columns were less stiff than the existing column. This difference is more pronounced in the negative quadrant of the graph, and indicates the reduction due to loading in the opposite direction. RC-1R Bottom Half exhibited larger stiffness than RC-1R Top Half. This was expected since the section of RC-1R Bottom Half was increased from the original 16in x 16in to 18in x 18in in order to have enough clear cover for the 2.1in. external diameter of the short mechanical splice, and RC-1R Top Half dimension was unchanged but had a CFRP jacket.

Retrofitted columns had higher values of normalized shear capacity, indicating that rehabilitation techniques can increase the strength of the members. Values of ultimate drift ratio are comparables. It should be mentioned that the hinge zone of failure for RC-1R was close to the inflection point between the Top and Bottom Half. This was the weakest zone of the retrofitted column because of the poor as-built column concrete and insufficient transverse reinforcement in that portion of column. Therefore it can be expected larger deformation for the top and bottom hinge zone of RC-1R, RC-1R Bottom Half and RC-1R Top Half.
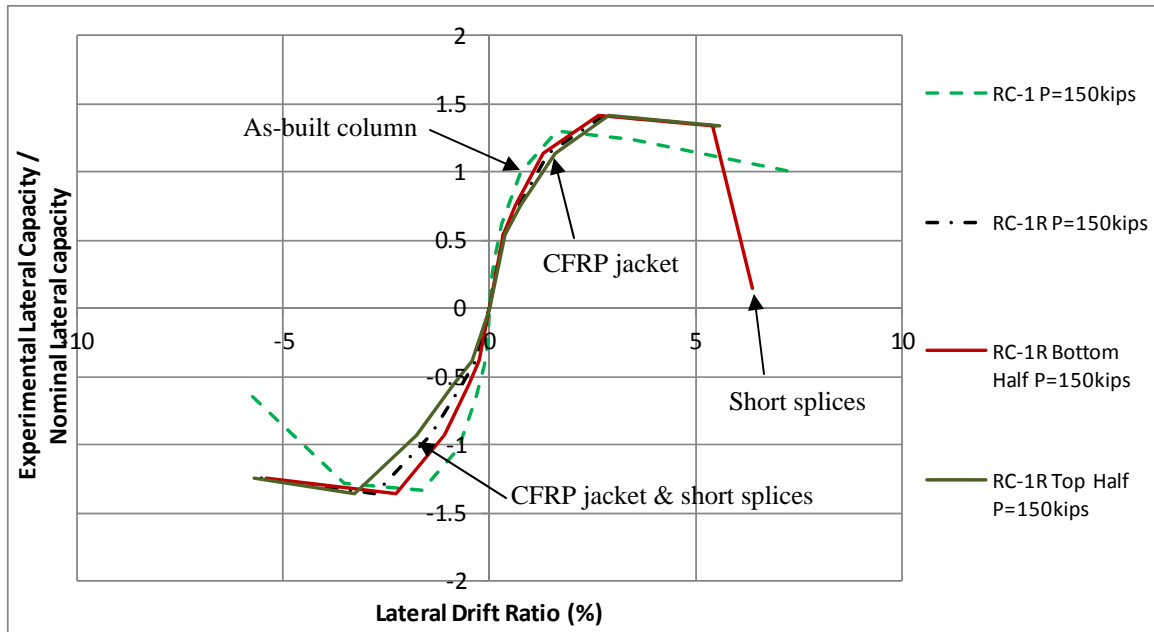
*Figure 7.21 Comparison of the normalized ASCE41-13 backbone curves of RC-1 and its correspondent retrofitted columns RC-1R, RC-1R Top Half and RC-1R Bottom Half*

Figure 7.22 shows a comparison among the normalized ASCE41-13 backbone curves of existing RC-2 and retrofitted columns RC-2R-SMS and RC-2R-LMS. It should be mentioned that RC-2 was subjected to 350 kips axial load and retrofitted cases had no axial load. The retrofitted columns were tested under cycled lateral load only which represents the worst case for tension force in the column bars with mechanical splices in the hinge region.

In Figure 7.22, the two retrofitted columns had slightly higher initial stiffness and they developed considerately larger lateral deformations and higher lateral load capacity than the as-built column RC-2. It was also observed in Figure 7.22 that the two retrofitted columns had the same behavior in the elastic region. However RC-2R-LMS reached higher lateral capacity and considerable larger deformation as would be expected since the short mechanical splices are nor intended for the use where large ductility is desired.

340
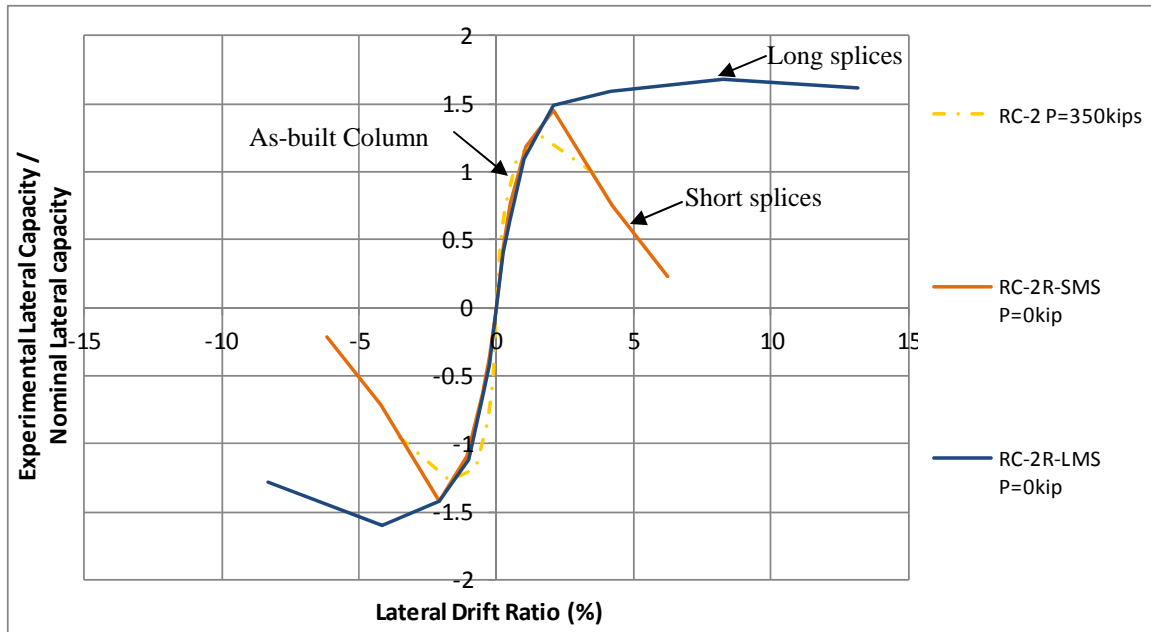
*Figure 7.22 Comparison of the normalized ASCE41-13 backbone curves among RC-2 and its correspondent retrofitted columns RC-2R-SMS and RC-2R-LMS*

Figure 7.23 shows the comparisons among the retrofitted column cases with the same axial load applied P=150kips. It is appreciated that the retrofitted column with the short mechanical splices and also the retrofitted column with the CFRP jacketing were considerable more efficient than Column 2-R with higher normalized lateral capacity. It is also shown in Figure 7.23 than the drift ratio of Column 2-R is shorter than retrofitted column RC-1R Top Half, RC-1R Bottom Half, as well RC-1R. The hinge from RC-1R Top Half and RC-1R Bottom Half had better efficient compared with the proposed with Column 2-R. It can be explained since Column 2-R replaced important part of its core with repair mortar instead of new concrete. This mortar made Column 2-R to have a weak core section despite the two direction CFRP jacket around the hinge zone of this column.
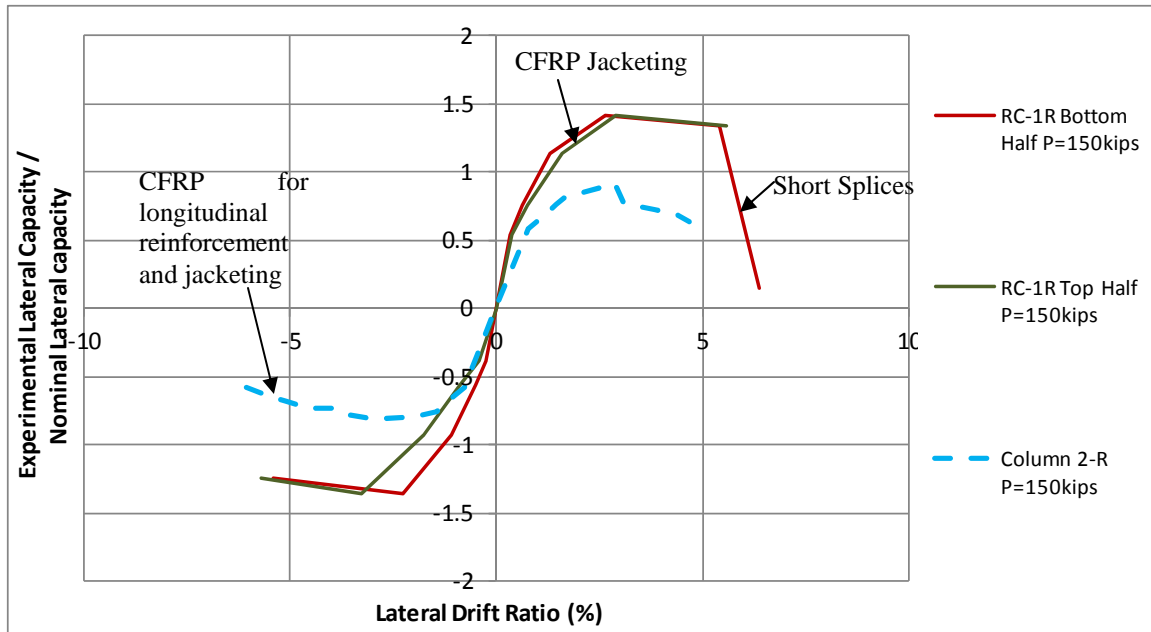
*Figure 7.23 Comparison of the normalized ASCE41-13 backbone curves among retrofitted columns with same axial load applied P=150kips*

Figure 7.24 shows the retrofitted column cases with no axial load applied. Normalized backbone curves of RC-2R-SMS and RC-2R-LMS have same stiffness at comparison with the retrofitted with the CFRP jacket on 2-A-S8-M or steel jacket on FC-17. However, these retrofitted columns using the mechanical splices reached larger value of drift ratio and higher normalized lateral load capacity.
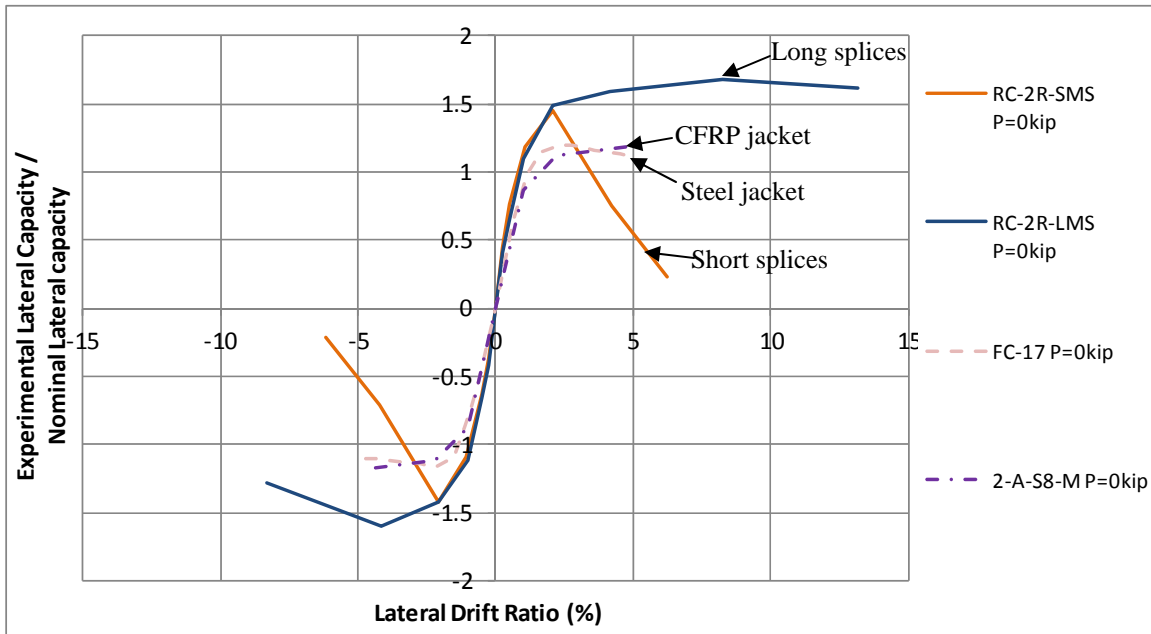
***Figure 7.24 Comparison of the normalized ASCE41-13 backbone curves among retrofitted columns with no axial load applied P=0kip***

Table 7-2 shows peak values of normalized lateral load capacity and percentage of drift ratios. It is noticed the effectiveness of the procedures proposed in this research using the innovative materials and devices as the CFRP and the mechanical splices. These material and devices were applied in appropriated location on the hinge zones of the column. This procedure made the retrofitted columns reach high performance in shear force and lateral deformation under constant axial load and cycle lateral loads.

***Table 7-2  Summary of peak values of normalized shear capacity and drift***

***ratios for each backbone curve ASCE41-13***

| | Related with as-built nominal capacity of specimen | Related with height of specimens | |
|---|---|---|---|
| | Calculated Nom.Lat.Cap. | Exp.Lat.Load / Nom.Lat.Cap. | Drift.Ratio % |
| RC-1 P=150kips | 41.20 | 1.30 | 7.20 |
| RC-2 P=350kips | 41.20 | 1.26 | 3.50 |
| RC-1R P=150kips | 41.20 | 1.42 | 5.51 |
| RC-1R Bottom Half P=150kips | 41.20 | 1.42 | 6.38 |
| RC-1R Top Half P=150kips | 41.20 | 1.42 | 5.60 |
| RC-2R-SMS P=0kip | 42.20 | 1.43 | 6.25 |
| RC-2R-LMS P=0kip | 42.20 | 1.68 | 13.14 |
| FC-17 P=0kip | 27.50 | 1.19 | 5.05 |
| 2-A-S8-M P=0kip | 28.70 | 1.18 | 4.73 |
| Column 2-R P=150kips | 60.30 | 0.91 | 4.70 |

### 7.4.2.2 *Normalization of shear capacity for column tests using computed strength of actual retrofitted column*

The value of the measured experimental lateral capacity is normalized using the nominal lateral capacity of the retrofitted column. To calculate the nominal capacity, the dimension and material properties for the retrofitted and axial load applied. However, for the columns retrofitted with steel and CFRP jacketing, the compressive strength of the column was considered the same of as-built column. Where spalled cover and damaged concrete core were removed, it was not possible to measure the value of f'c for the concrete. In order to calculate the nominal lateral capacity, it was assumed that the f'c was the original as-built strength and that only the internal transverse reinforcement as internal confinement of the retrofitted column was considered.

Details of the calculations are presented in Appendix A and include the moment-curvature, moment-axial load interaction diagrams, and shear capacity for unconfined and confined section. The lateral displacement was normalized calculating the drift ratio for each column case.

Figure 7.25 shows the resulting normalized backbone curves following the provisions of ASCE41-07, and Figure 7.20 shows the correspondent for ASCE41-13.
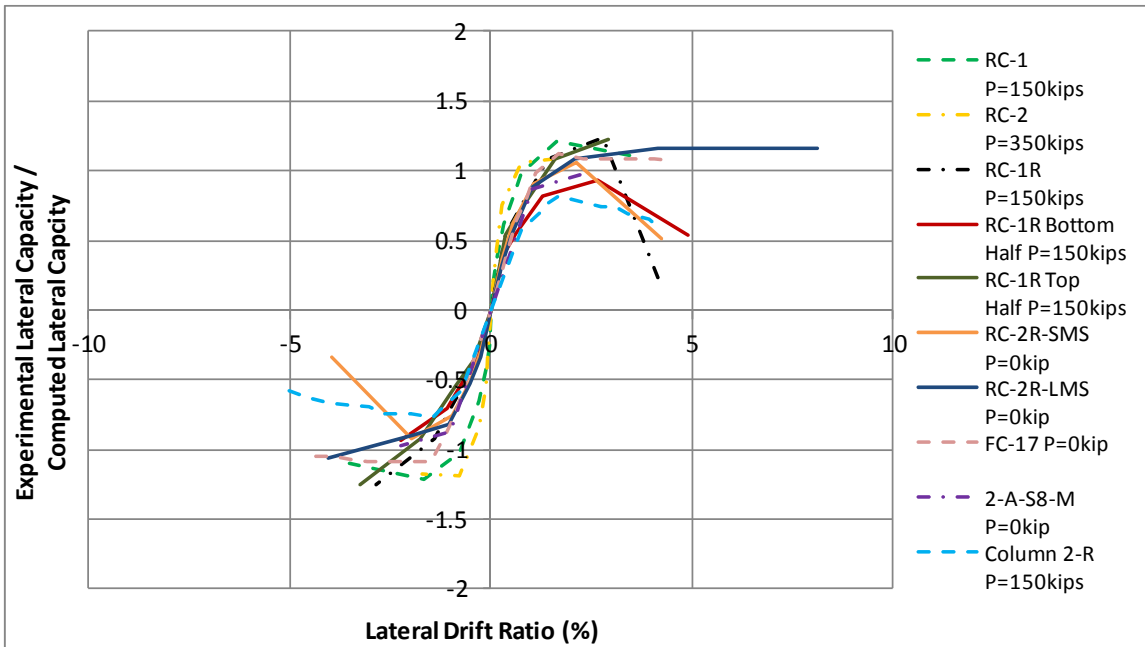
*Figure 7.25  Drift ratio vs. normalized shear force - ASCE41-07 for each column case*
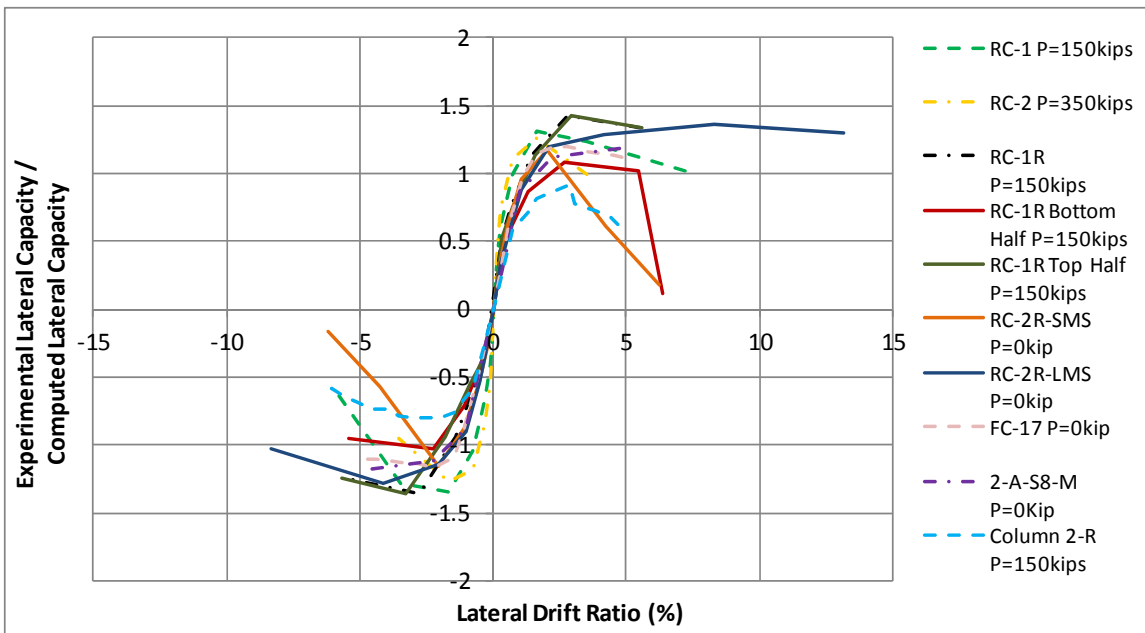


*Figure 7.26  Comparison of drift ratio vs. normalized shear force - ASCE41-13*

Table 7-3 shows peak values of normalized lateral load capacity and percentage of drift ratios.

*Table 7-3  Summary of peak values of normalized shear capacity and drift ratios for each backbone curve ASCE41-13*

| | Related with the nominal capacity of each specimen | Related with height of specimens |
| --- | --- | --- |

| | Calculated Actual Capacity | Exp.Lat.Load / Actural Cap. | Drift.Ratio % |
| --- | --- | --- | --- |
| RC-1 P=150kips | 41.20 | 1.30 | 7.20 |
| RC-2 P=350kips | 41.20 | 1.26 | 3.50 |
| RC-1R P=150kips | 41.20 | 1.42 | 5.51 |
| RC-1R Bottom Half P=150kips | 54.30 | 1.08 | 6.38 |
| RC-1R Top Half P=150kips | 41.20 | 1.42 | 5.60 |
| RC-2R-SMS P=0kip | 52.40 | 1.17 | 6.25 |
| RC-2R-LMS P=0kip | 52.40 | 1.36 | 13.14 |
| FC-17 P=0kip | 27.50 | 1.20 | 5.05 |
| 2-A-S8-M P=0kip | 28.70 | 1.18 | 4.73 |
| Column 2-R P=150kips | 60.30 | 0.91 | 4.70 |

### 7.4.3 Idealized Force-Displacement curves and Elasto-Plastic curves for columns

As it was discussed in 7.3.1, two types of behavioral models for the hinge zones are proposed. Elasto-Plastic Curve and Force-Displacement curve. Idealized curves were based on the backbone curves, and normalized to the measured value of yielding for each section Q/Qy. The resulting curves are named this curves: Generalized Force-Deformation for Concrete Elements or Components in ASCE41-13.

#### 7.4.3.1 RC-1R Top Half

This hinge zone consists of concrete core with internal cracks, spalled concrete cover replaced by repair mortar; and a CFRP jacket with CFRP anchors on one face. Figure 7.27 shows the retrofitted hinge zone of RC-1R (represented by RC-1R Top Half). The proposed idealized curves consider the action of constant axial load P/Ag x f'c = 0.20; and a point of inflection at the mid-height of the column.
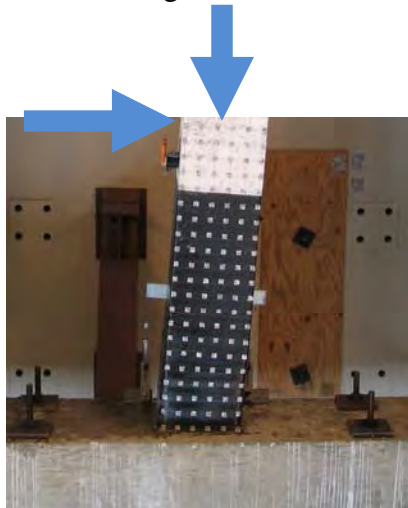


***Figure 7.27  Hinge zone with CFRP jacketing under constant axial load (RC-1R Top Half)***

Figure 7.28 shows the idealized curves for the backbone curve using ASCE41-13 for RC-1R Top Half. Each curve has the same effective stiffness and maximum displacement. However the values of Vy differ. The Force-Displacement curve Vy is higher than Elasto-Plastic V'y. However, both areas under the curves will be the same.
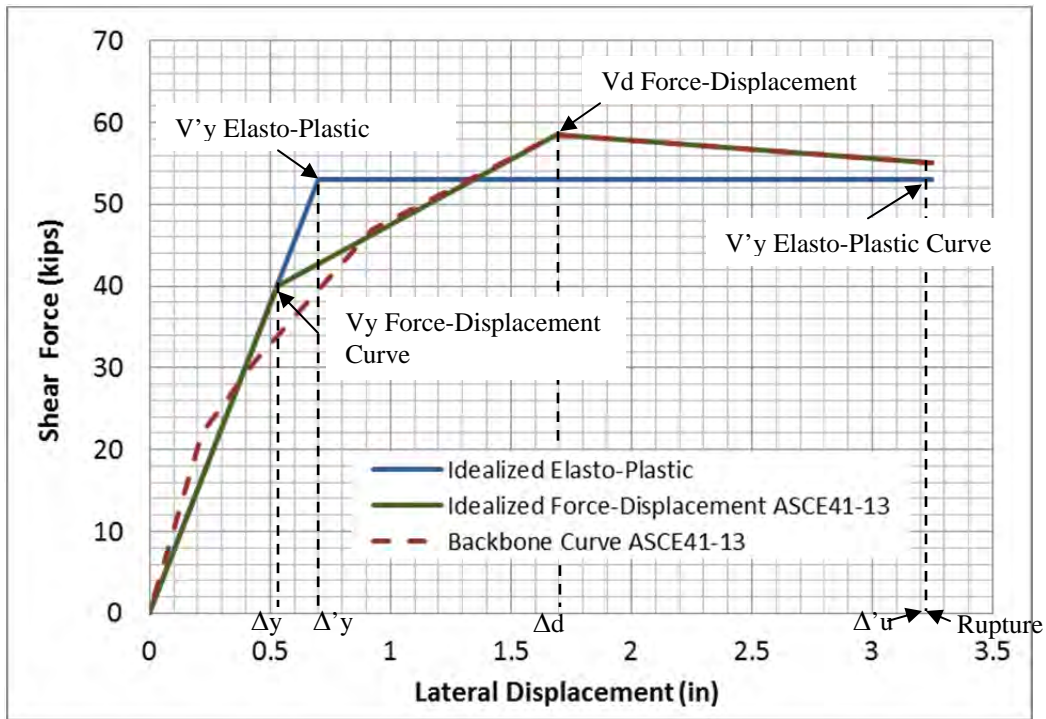


*Figure 7.28  Idealized Curves for RC-1R Top Half*

Table 7-4 and Table 7-5 show the coordinates of each point for the idealized elasto-plastic and force-displacement curve. Table 7-6 shows the values of initial stiffness and displacement ductility calculated from both idealized curves.

*Table 7-4  Idealized elasto-plastic curve main values for RC-1R Top Half*

|        | Δ(in) | V (kips) |      |
|--------|-------|----------|------|
| **Origin** | 0 | 0 |      |
| **Δ'y** | 0.70 | 53.00 | **V'y** |
| **Δ'u** | 3.25 | 53.00 | **V'y** |

*Table 7-5  Idealized force-displacement curve main values for RC-1R Top Half*

|          | Δ(in) | V (kips) |      |
|----------|-------|----------|------|
| **Origin** | 0.00 | 0.00 |      |
| **Δy** | 0.53 | 40.00 | **Vy** |
| **Δd** | 1.69 | 58.45 | **Vd** |
| **Rupture** | 3.25 | 55.14 |      |

*Table 7-6  Effective Stiffness (Keff) and Displacement Ductility for RC-1R Top Half*

| Elasto-Plastic |       |        |
|----------------|-------|--------|
| **K eff** | 76 | kip/in |
| **μ** | 4.64 |        |
| **Force-Displacement** |       |        |
| **K eff** | 75 | kip/in |
| **μ** | 6.13 |        |

For Elasto-Plastic Curve: μ = Δ'u / Δ'y ;

For Force-Displacement Curve: μ = Rupture / Δy

Figure 7.29 shows the generalized curves for each method. Table 7-7 and Table 7-8 show the coordinate points for each generalized curve.

350
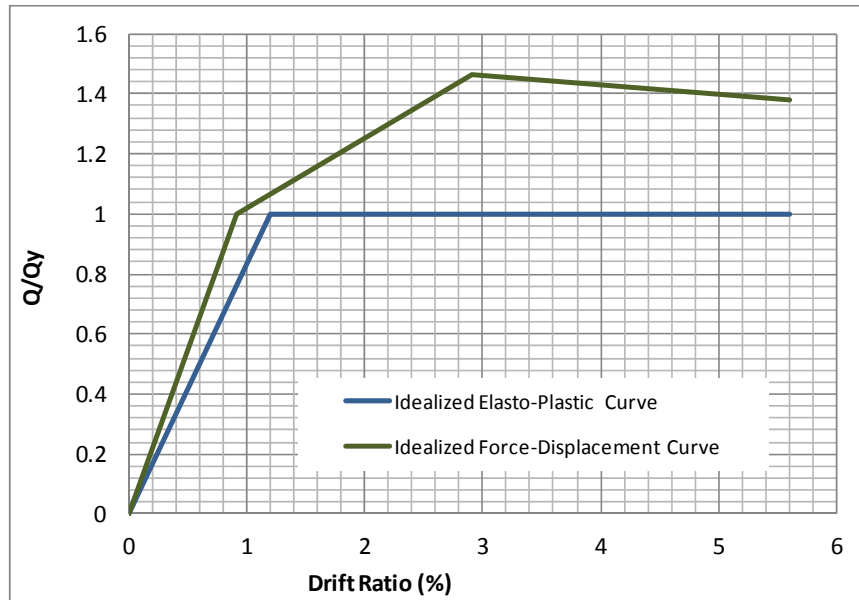
***Figure 7.29  Generalized force-deformation curves for RC-1R Top Half***

***Table 7-7  Coordinate point values for the generalized force deformation from the elasto-plastic curve***

|  | Drift (%) | Q/Qy |  |
|---|---|---|---|
| **Origin** | 0 | 0 |  |
| **Δ'y** | 1.21 | 1.00 | **V'y** |
| **Δ'u** | 5.60 | 1.00 | **V'y** |

***Table 7-8  Coordinate point values for the generalized force deformation from the force-displacement curve***

|  | Drift (%) | Q/Qy |  |
|---|---|---|---|
| **Origin** | 0.00 | 0.00 |  |
| **Δy** | 0.91 | 1.00 | **Vy** |
| **Δd** | 2.91 | 1.46 | **Vd** |
| **Rupture** | 5.60 | 1.38 |  |

351

### 7.4.3.2 RC-1R Bottom Half

This hinge zone includes short mechanical splices, new longitudinal and transverse reinforcement and new concrete replacing the crushed core and buckled longitudinal bars. Figure 7.30 shows the retrofitted hinge zone of RC-1R (represented by RC-1R Bottom Half). The proposed idealized curves consider a constant axial load P/Ag x f'c = 0.12 and a point of inflection at column mid-height.
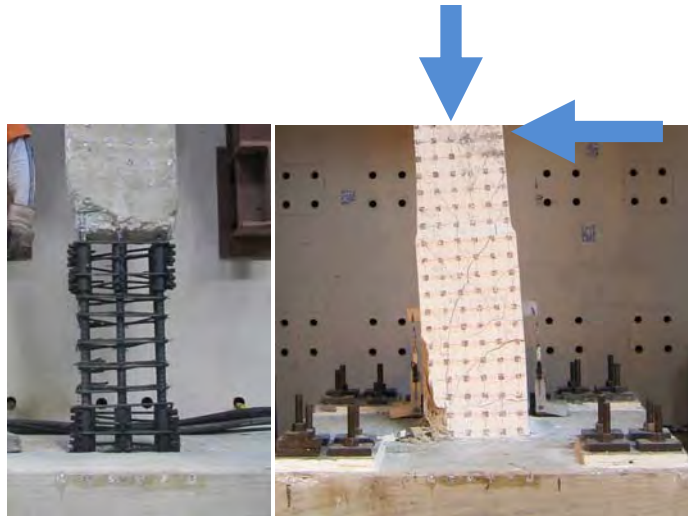


***Figure 7.30  Hinge zone with short mechanical splice under constant axial load (RC-1R-Bottom Half)***

Figure 7.31 shows the idealized curves for the RC-1R Bottom Half backbone curve ASCE41-13. The tendency of each graph can be seen, having same effective stiffness and maximum displacement. Both Force-Displacement and Elasto-Plastic curves have the same value of V'y.
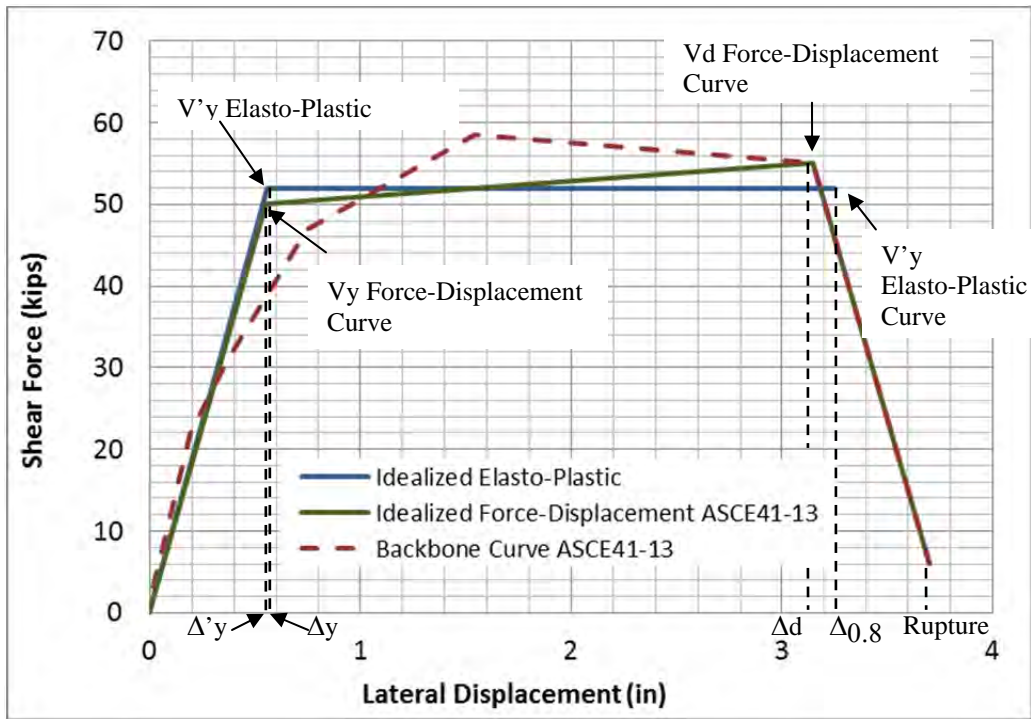
***Figure 7.31  Idealized Curves for RC-1R Bottom Half***

Table 7-9 and Table 7-10 show the coordinates of each point for the idealized elasto-plastic and force-displacement curve. Table 7-11 shows the values of initial stiffness and displacement ductility calculated from both idealized curves. It is noticed that Keff for elasto plastic curve is the same compared with Keff for force-displacement curve. A similar comparison is observed with the values of μ for elasto-plastic curve is less than force-displacement curve case.

*Table 7-9  Idealized elasto-plastic curve main values for RC-1R Bottom Half*

|  | Δ(in) | V (kips) |  |
|---|---|---|---|
| **Origin** | 0 | 0 |  |
| **Δ'y** | 0.56 | 51.50 | **V'y** |
| **Δ0.8** | 3.25 | 51.50 | **V'y** |

*Table 7-10  Idealized force-displacement curve main values for RC-1R Bottom Half*

|  | Δ(in) | V (kips) |  |
|---|---|---|---|
| **Origin** | 0.00 | 0.00 |  |
| **Δy** | 0.55 | 50.00 | **Vy** |
| **Δd** | 3.15 | 55.14 | **Vd** |
| **Rupture** | 3.70 | 6.00 |  |

*Table 7-11  Effective Stiffness (Keff) and Displacement Ductility for RC-1R Bottom Half*

| Elasto-Plastic | | |
|---|---|---|
| **K eff** | 92 | kip/in |
| **μ** | 5.80 |  |
| Force-Displacement | | |
| **K eff** | 91 | kip/in |
| **μ** | 6.73 |  |

For Elasto-Plastic Curve: $\mu = \Delta_{0.8} / \Delta'y$ ;

For Force-Displacement Curve: $\mu = $ Rupture $/ \Delta y$

Similar procedure was operated for this hinge zone. The values of the idealized curves were normalized to each Vy respectively. Figure 7.32 shows the generalized curves for each method. Table 7-12 and Table 7-13 show the coordinate points for each generalized curve.
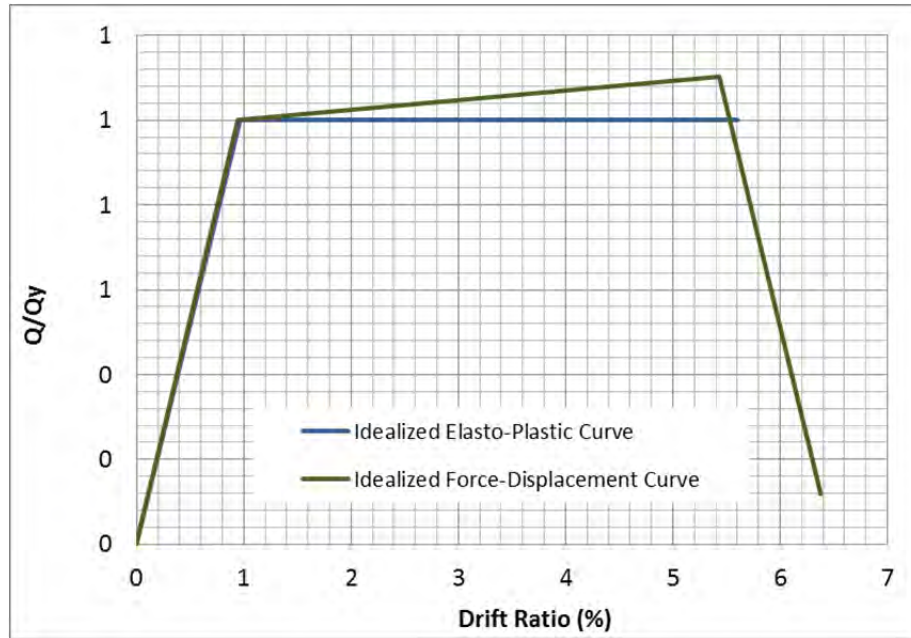


*Figure 7.32  Generalized force-deformation relations for RC-1R Bottom Half*

*Table 7-12  Coordinate point values for the generalized force deformation from the elasto-plastic curve for RC-1R Bottom Half*

|          | Drift (%) | Q/Qy |      |
|----------|-----------|------|------|
| **Origin** | 0 | 0 | |
| **Δ'y** | 0.97 | 1.00 | **V'y** |
| **Δ0.8** | 5.60 | 1.00 | **V'y** |

355

***Table 7-13  Coordinate point values for the generalized force deformation from the force-displacement curve RC-1R Bottom Half***

|  | Drift (%) | Q/Qy |  |
|---|---|---|---|
| **Origin** | 0.00 | 0.00 |  |
| **Δy** | 0.95 | 1.00 | **Vy** |
| **Δd** | 5.43 | 1.10 | **Vd** |
| **Rupture** | 6.38 | 0.12 |  |

### 7.4.3.3  RC-2R-SMS

This hinge zone includes short mechanical splices, new longitudinal and transversal reinforcement and new concrete replacing the crushed core and buckled longitudinal bars. Figure 7.30 shows the retrofitted hinge zone of RC-2R-SMS. The proposed idealized curves consider no axial load P/Ag x f'c = 0; and a point of inflection at column mid-height.
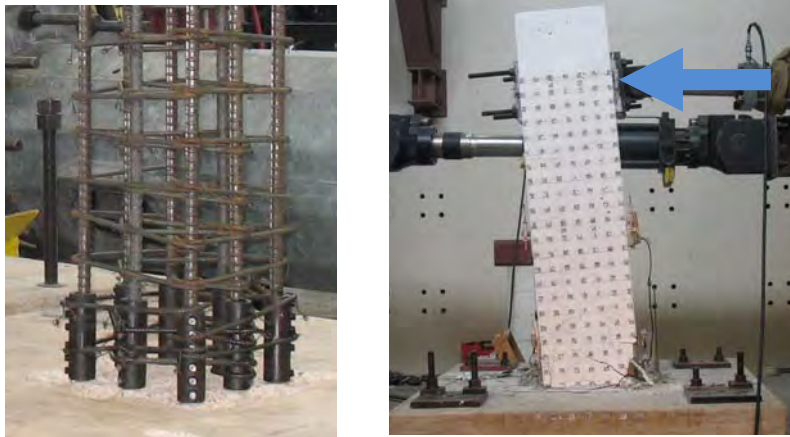


***Figure 7.33  Hinge zone with short mechanical splice. No axial load applied. (RC-2R-SMS)***

Figure 7.34 shows the idealized curves for the RC-2R-SMS backbone curve ASCE41-13. It can be seen the tendency of each graph, having similar effective stiffness and V'y with Vy values. It should be explained that the maximum displacement considered for the idealized elasto-plastic curve was the second last one point of the backbone curve. The last point of the backbone curve represented a high loss of shear force in order to compare the energy dissipated considering large deformation. The plateau of this curve was going to be by lower V'y value, obtaining a no representative elasto-plastic curve for this system.
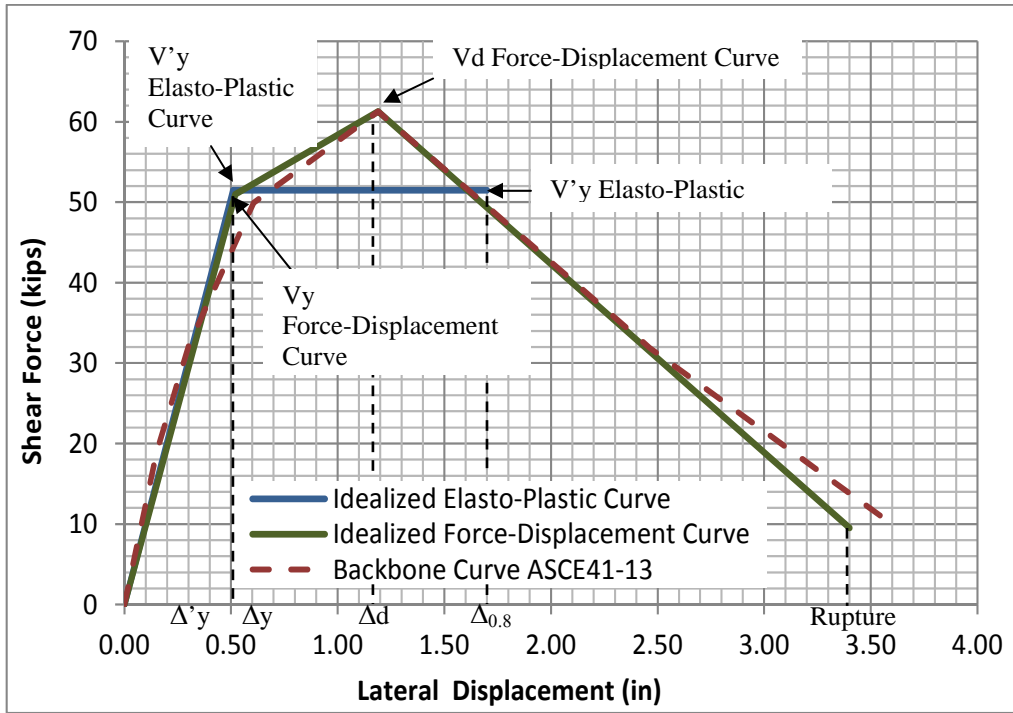
*Figure 7.34  Idealized Curves for RC-2R-SMS*

Table 7-14 and Table 7-15 show the coordinates of each point for the idealized elasto-plastic and force-displacement curve. Table 7-16 shows the values of initial stiffness and displacement ductility calculated from both idealized curves. It is noticed that Keff for elasto plastic curve is higher than Keff for force-displacement curve. However, value of μ for elasto-plastic curve is less than force-displacement curve case.

*Table 7-14  Idealized elasto-plastic curve main values for RC-2R-SMS*

|  | Δ(in) | V (kips) |  |
|---|---|---|---|
| **Origin** | 0.00 | 0 |  |
| **Δ'y** | 0.51 | 51.50 | **V'y** |
| **Δ0.8** | 1.70 | 51.50 | **V'y** |

358

**Table 7-15  Idealized force-displacement curve main values for RC-2R-SMS**

|  | Δ (in) | V (kips) |  |
|---|---|---|---|
| **Origin** | 0.00 | 0.00 |  |
| **Δy** | 0.52 | 51.00 | **Vy** |
| **Δd** | 1.19 | 61.28 | **Vd** |
| **Rupture** | 3.40 | 9.50 |  |

**Table 7-16  Effective Stiffness (Keff) and Displacement Ductility for RC-2R-SMS**

| Elasto-Plastic | | |
|---|---|---|
| **K eff** | 101 | kip/in |
| **μ** | 3.33 | |
| **Force-Displacement** | | |
| **K eff** | 98 | kip/in |
| **μ** | 6.54 | |

For Elasto-Plastic Curve: $\mu = \Delta_{0.8} / \Delta'y$ ;

For Force-Displacement Curve: $\mu = Rupture / \Delta y$

Similar procedure was operated for this hinge zone. The values of the idealized curves were normalized to V'y and Vy respectively. Figure 7.35 shows the generalized curves for each method. Table 7-17 and Table 7-18 show the coordinate points for each generalized curve.
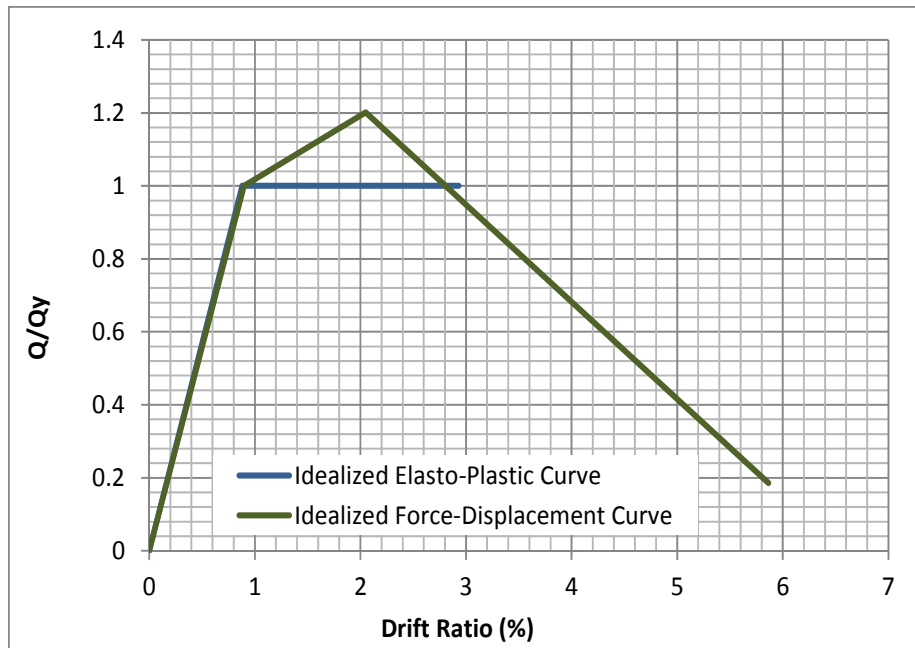
*Figure 7.35  Generalized force-deformation relations for RC-2R-SMS*

*Table 7-17  Coordinate point values for the generalized force deformation from the elasto-plastic curve for RC-2R-SMS*

|         | Drift (%) | Q/Qy |      |
|---------|-----------|------|------|
| Origin  | 0.00      | 0    |      |
| Δ'y     | 0.88      | 1.00 | V'y  |
| Δ0.8    | 2.93      | 1.00 | V'y  |

*Table 7-18  Coordinate point values for the generalized force deformation from the force-displacement curve RC-2R-SMS*

|  | Drift (%) | Q/Qy |  |
|---|---|---|---|
| **Origin** | 0.00 | 0.00 |  |
| **Δy** | 0.90 | 1.00 | **Vy** |
| **Δd** | 2.05 | 1.20 | **Vd** |
| **Rupture** | 5.86 | 0.19 |  |

### 7.4.3.4   RC-2R-LMS

This hinge zone includes large mechanical splices, new longitudinal and transversal reinforcement and new concrete replacing the crushed core and buckled longitudinal bars. Figure 7.36 shows the retrofitted hinge zone of RC-2R-LMS. The proposed idealized curves consider no axial load P/Ag x f'c = 0; and a point of inflection at column mid-height.
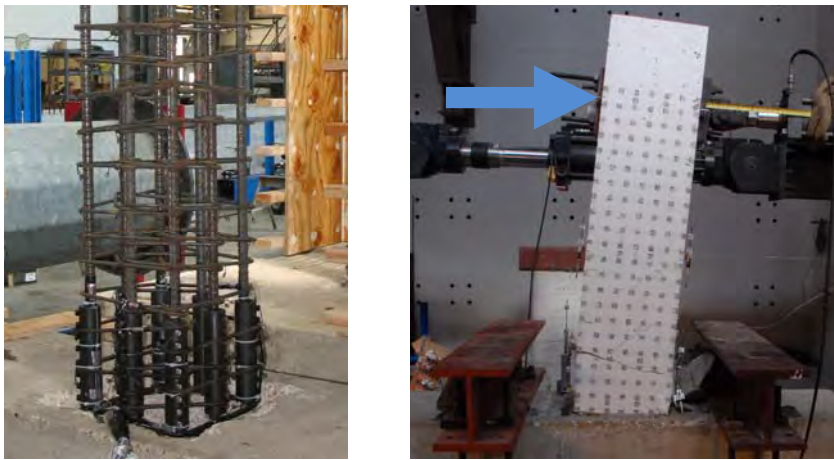


***Figure 7.36  Hinge zone of the large mechanical splice. No axial load applied.(RC-2R-LMS)***

Figure 7.37 shows the idealized curves for the backbone curve RC-2R-LMS. It can be seen the tendency of each graph, having same effective stiffness and maximum displacement. However they differ the values of V'y and Vy. Force-Displacement curve Vy is lower than Elasto-Plastic V'y.
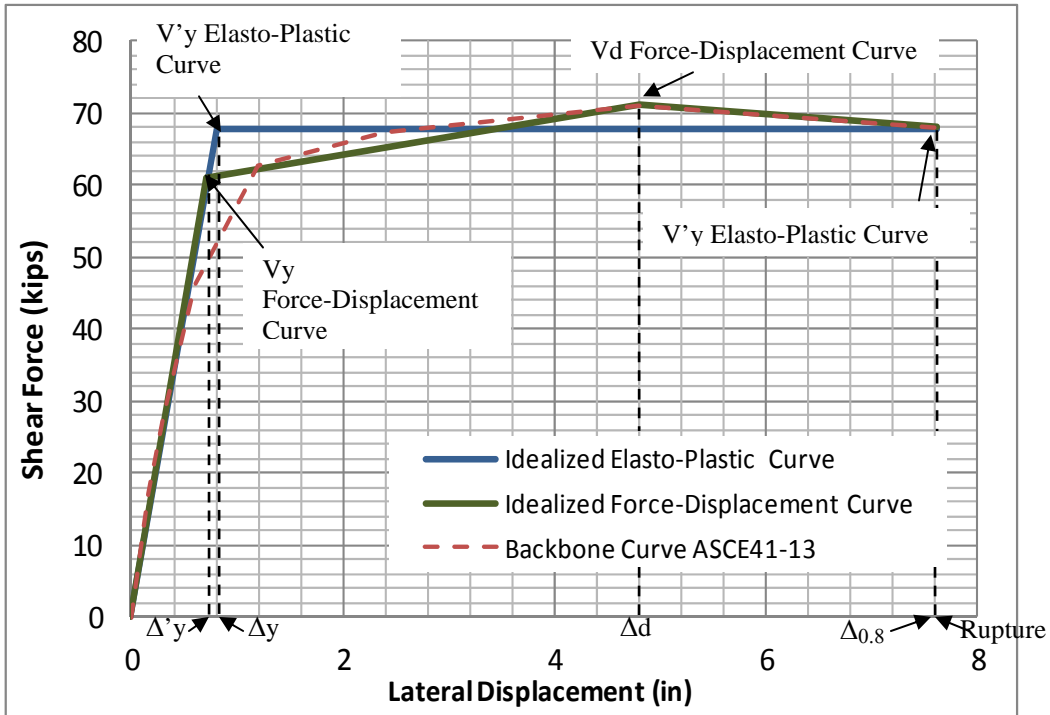
*Figure 7.37 Idealized Curves for RC-2R-LMS*

Table 7-19 and Table 7-20 show the coordinates of each point for the idealized elasto-plastic and force-displacement curve. Table 7-21 shows the values of initial stiffness and displacement ductility calculated from both idealized curves. It is noticed that Keff for elasto plastic curve is similar than Keff for force-displacement curve. However, value of μ for elasto-plastic curve is less than force-displacement curve case.

363

**Table 7-19  Idealized elasto-plastic curve main values for RC-2R-LMS**

|  | Δ(in) | V (kips) |  |
|---|---|---|---|
| **Origin** | 0 | 0 |  |
| **Δ'y** | 0.80 | 67.70 | **V'y** |
| **Δ'u** | 7.62 | 67.70 | **V'y** |

**Table 7-20  Idealized force-displacement curve main values for RC-2R-LMS**

|  | Δ(in) | V (kips) |  |
|---|---|---|---|
| **Origin** | 0 | 0 |  |
| **Δy** | 0.70 | 61.00 | **Vy** |
| **Δd** | 4.80 | 71.08 | **Vd** |
| **Rupture** | 7.62 | 68.05 |  |

**Table 7-21  Effective Stiffness (Keff) and Displacement Ductility (μ) for RC-2R-LMS**

| Elasto-Plastic | | |
|---|---|---|
| **K eff** | 85 | kip/in |
| **μ** | 9.53 | |
| **Force-Displacement** | | |
| **K eff** | 87 | kip/in |
| **μ** | 10.89 | |

For Elasto-Plastic Curve: μ = Δ'u / Δ'y

For Force-Displacement Curve: μ = Rupture / Δy

364

The values of the idealized curves were normalized to each V' and Vy respectively. Figure 7.38 shows the generalized curves for each method. Table 7-22 and Table 7-23 show the coordinate points for each generalized curve.
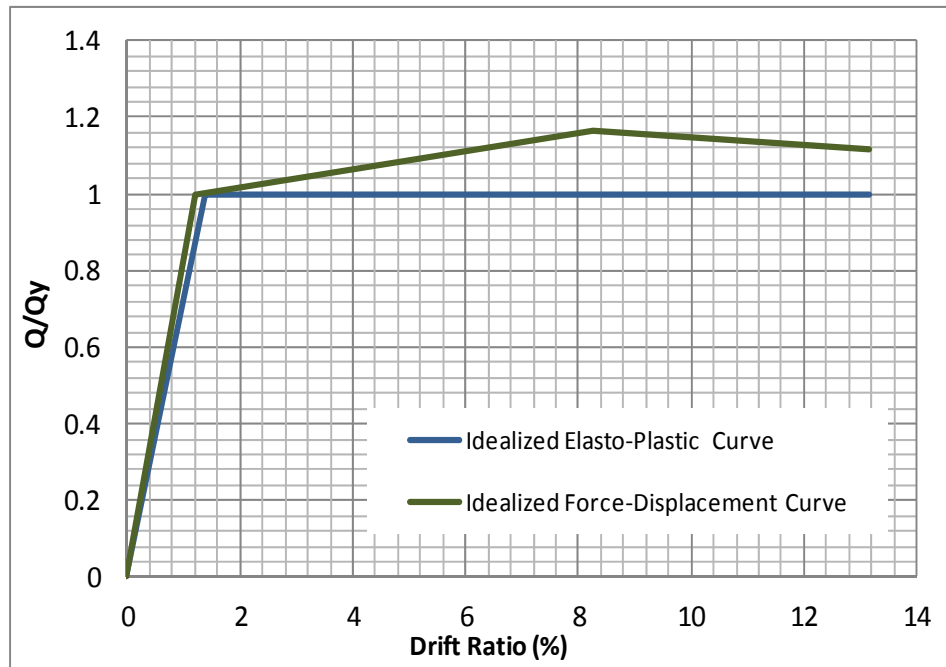


*Figure 7.38  Generalized force-deformation relations for RC-2R-LSMS*

*Table 7-22  Coordinate point values for the generalized force deformation from the elasto-plastic curve for RC-2R-LMS*

|        | Drift (%) | Q/Qy |      |
|--------|-----------|------|------|
| Origin | 0         | 0    |      |
| Δ'y    | 1.38      | 1.00 | V'y  |
| Δ'u    | 13.14     | 1.00 | V'y  |

*Table 7-23  Coordinate point values for the generalized force deformation from the force-displacement curve RC-2R-LMS*

|  | Drift (%) | Q/Qy |  |
|---|---|---|---|
| **Origin** | 0 | 0 |  |
| **Δy** | 1.21 | 1.00 | **Vy** |
| **Δd** | 8.27 | 1.17 | **Vd** |
| **Rupture** | 13.14 | 1.12 |  |

### 7.4.4 Comparison of idealized force-displacement curves and elasto-plastic curves into Generalized Relations

There are presented comparisons among the different generalized relations based in the elasto-plastic and force displacement curves made in this research. Figure 7.41 shows the Type 2 curve used to build the Generalized Relations in Q/Qy vs Drift (%) and their parameters. The parameters proposed for each proposed rehabilitation method are listed in Table 7-24 and Table 7-25.
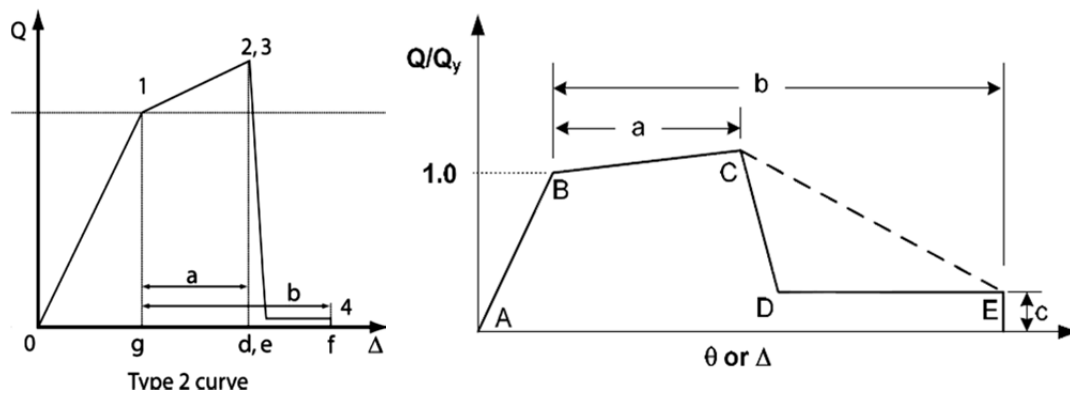


***Figure 7.39  Parameter for Type 2 curve (left) and Generalized Relations for computer modeling (right)***

Figure 7.40 shows comparisons of the elasto-plastic curves for each hinge zone using the rehabilitation method proposed in this research. It should be mentioned that in the test with axial load failure of their test occurred out of the hinge zone assessed, so the ductility of the hinge will be higher than indicated.
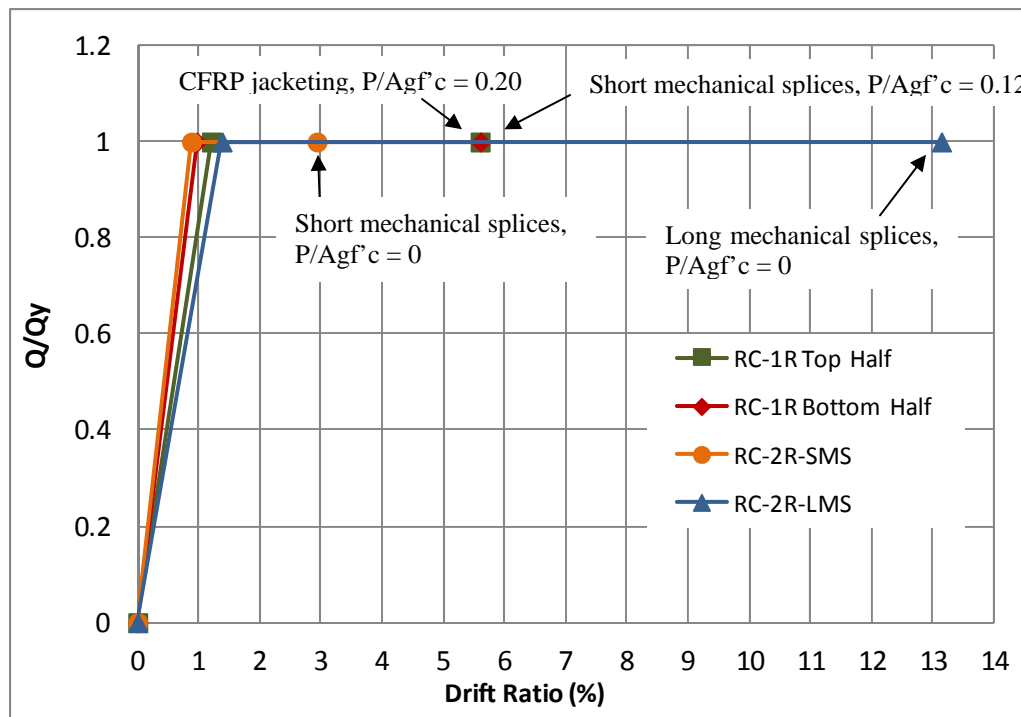
*Figure 7.40  Generalized force-deformation relations from elasto-plastic curves.*

Table 7-24 shows a summary of the parameters correspondent for Type 2 curve. According with ASCE41-13, the structural behavior can be classified either deformation control or force-control. It is presented in Table 7-24 the proposed parameter to ASCE41-13 for this type of rehabilitation method applied to severely damage column. Type 2 curve was used because the specimen has residual strength and also large ductility (e>2g), considering the structural behavior as deformation-control. Since the generalized force-deformation relation was made from the elasto-plastic curves, values of "e" and "d" are the same. As well the parameter "a" and "b" have same values. Parameter "c" has the same value 1.00 for each rehabilitation method.

*Table 7-24  Summary of Type 2 Elasto-Plastic curves for different rehabilitation methods*

| Rehabilitation Method | P/Ag f'c | g | e | d | e > 2g ? | a | b | c |
|---|---|---|---|---|---|---|---|---|
| CFRP Jacket wich anchor | 0.2 | 1.21 | 5.60 | 5.60 | Yes | 4.39 | 4.39 | 1.00 |
| Short mechanical splices | 0.12 | 0.95 | 6.38 | 6.38 | Yes | 5.43 | 5.43 | 1.00 |
| Short mechanical splices | 0 | 0.78 | 4.24 | 4.24 | Yes | 3.47 | 3.47 | 1.00 |
| Long mechanical splices | 0 | 1.38 | 13.14 | 13.14 | Yes | 11.76 | 11.76 | 1.00 |

Figure 7.41 shows comparisons of the 4 generalized force-deformation relations for each rehabilitation method proposed in this research. The shape of the graphs of the generalized relations best described by to Type 2 curve since a tri-linear curve was used. It should be mentioned that the short splice rehabilitation with axial load may provide a larger drift ratio since the failure in this test did not occur in the hinge zone assessed. The same observation is valid of the CFRP jacket rehabilitation.
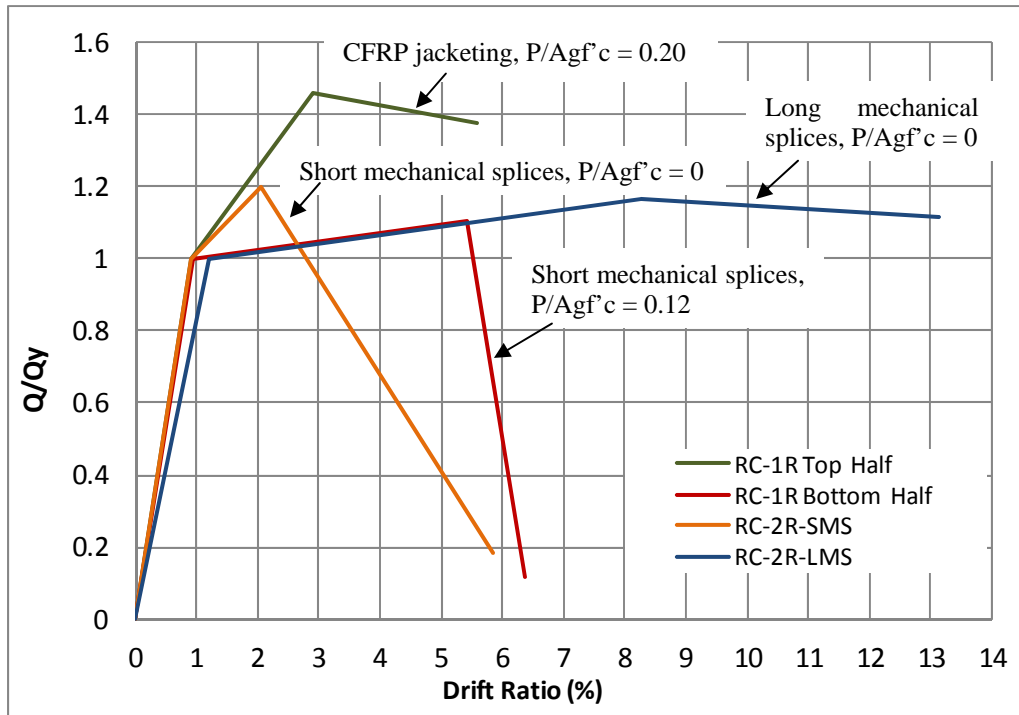
***Figure 7.41  Generalized force-deformation relations from force-displacement curves.***

Table 7-25 shows a summary of the parameters need to describe a Type 2 curve. According to ASCE41-13, the structural behavior can be classified either deformation control or force-control. In Table 7-25, the proposed parameter to ASCE41-13 for each type of rehabilitation method applied to severely damage columns. As it was explained in previous paragraph, Type 2 curve was used because the specimen has residual strength and also large ductility (e>2g), considering the structural behavior as deformation-control.

**Table 7-25  Summary of Type 2 Force-Displacement curves for different rehabilitation methods**

| Rehabilitation Method | P/Ag f'c | g | e | d | e > 2g ? | a | b | c |
|---|---|---|---|---|---|---|---|---|
| CFRP Jacket wich anchor | 0.2 | 0.91 | 2.91 | 5.60 | Yes | 2.00 | 2.69 | 1.38 |
| Short mechanical splices | 0.12 | 0.95 | 5.43 | 6.38 | Yes | 4.48 | 0.95 | 0.12 |
| Short mechanical splices | 0 | 0.90 | 1.19 | 3.40 | Yes | 0.29 | 2.21 | 0.19 |
| Long mechanical splices | 0 | 1.21 | 8.27 | 13.14 | Yes | 7.07 | 4.87 | 1.12 |

## 7.5    MASONRY WALL CASES

### 7.5.1    Backbone ASCE41-07 and ASCE41-13 curves

Results from four different tests are presented. Two tests, RMW and RMW-R2, were in Ferguson Structural Engineering Laboratory – UT Austin. For comparison 2 are included: A shake table test at the University of California San Diego (UCSD), and a test at Washington State University (WSU). Details of specimens are listed in Chapter 6 (UCSD) and Appendix A (WSU).

In order to understand better the behavior of this type of masonry wall, the results of Shake Table test UCSD W-2 and RMW which have same aspect ratio (h/L=1) are compared. The results of WSU Specimen 6 are compared to RMW-R2 because both have the same aspect ratio (h/L=0.78) and the same type of reinforcement.

Loading protocols applied to the tests were appropriate to build the ASCE41-07 and ASCE41-13. For every specimen, ASCE41-07 and ASCE41-13 backbone curves were built without problems until no mayor failure occurred.

Each graph shows the backbone curves following the provisions of ASCE41-07 and ASCE41-13. The orange line represents the curve correspondent to ASCE41-07 and the brown line represents the curve correspondent to ASCE41-13.
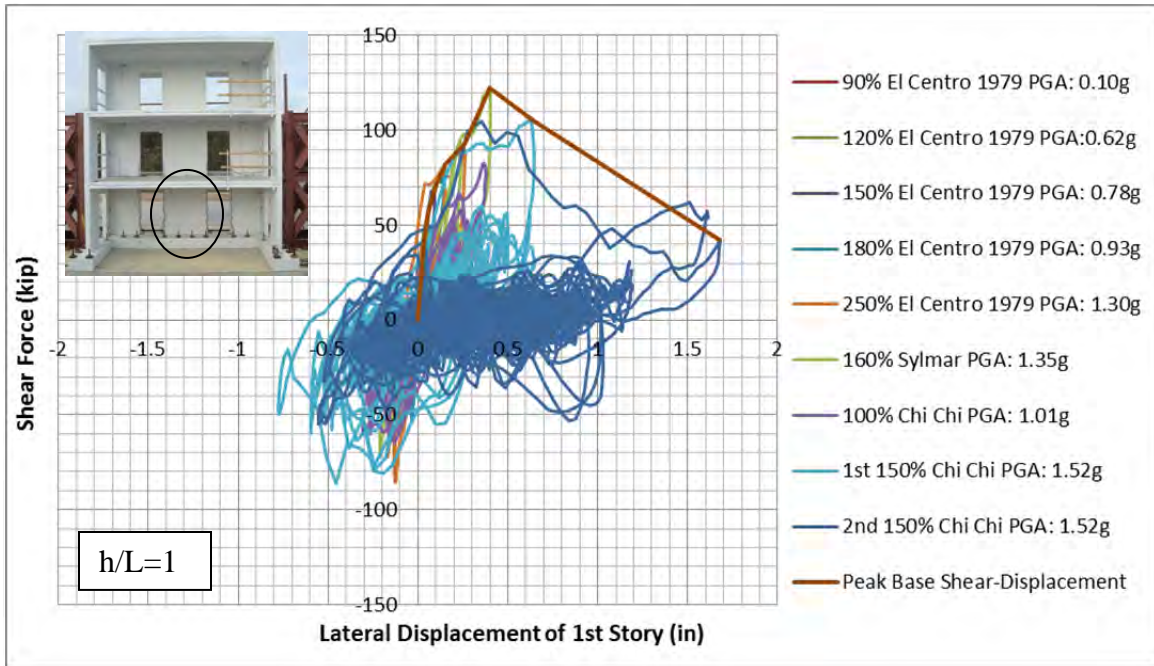
*Figure 7.42  Backbone curve for UCSD W-2*
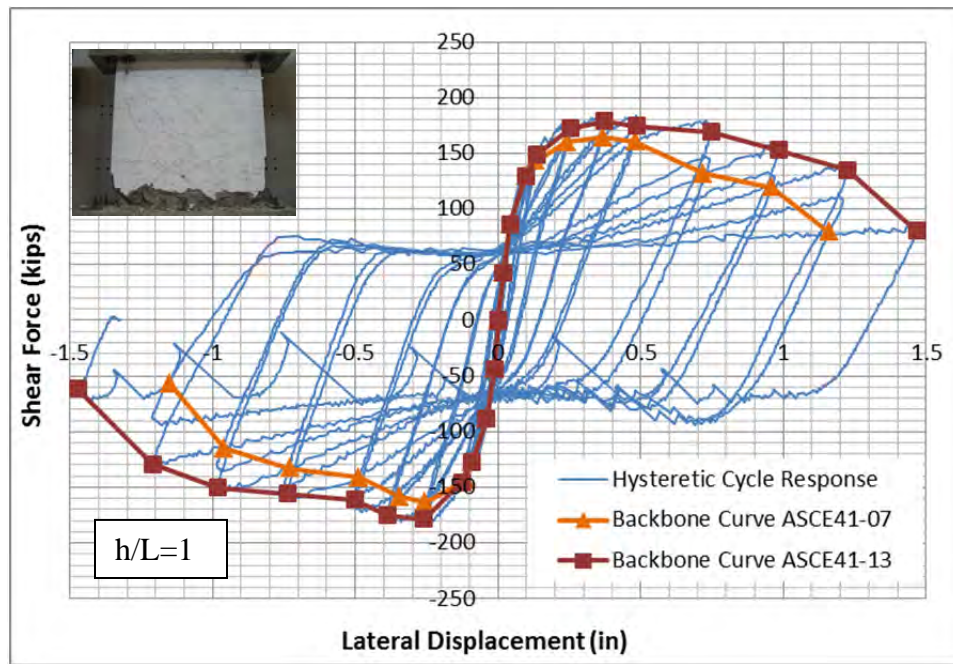


*Figure 7.43  Backbone curves for RMW*

373
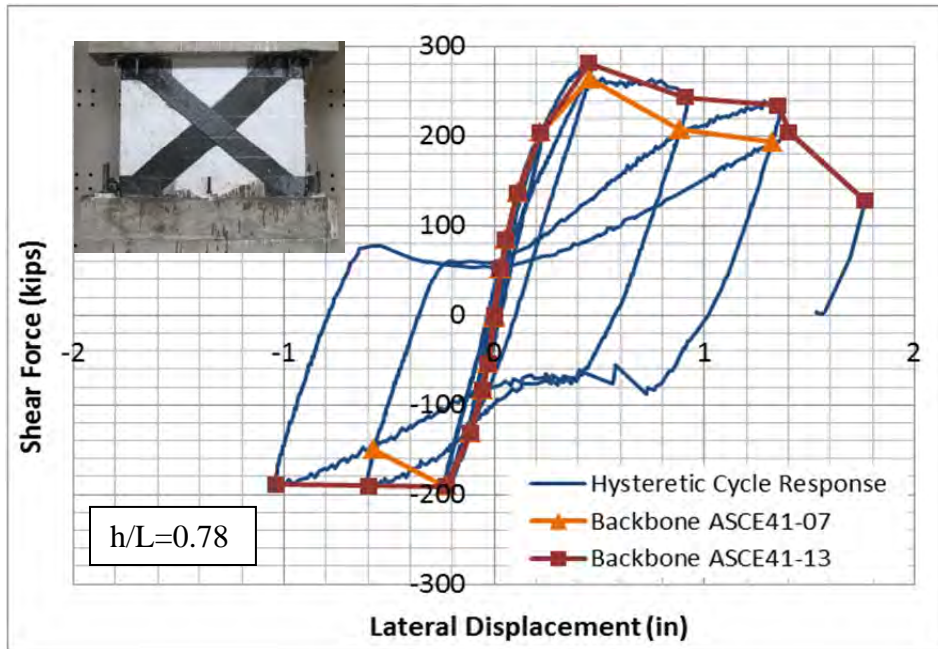
*Figure 7.44  Backbone curves for RMW-R2*
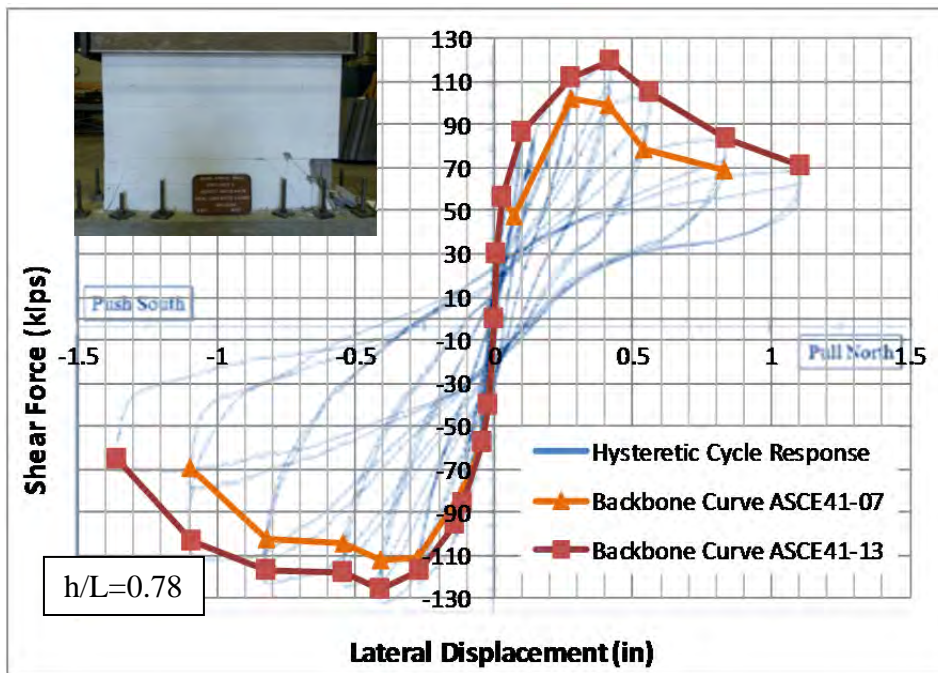


*Figure 7.45  Backbone curves following for WSU Specimen 6*

374

The Table 7-1 shows the values of maximum shear force and the maximum lateral displacement for case. It is seen that provisions given in ASCE41-13 to build the backbone curves are less conservative than ASCE41-07. The differences in shear force between both provisions vary from 1.1% to 1.3% and for lateral displacement vary from 1.2% to 1.3%.

*Table 7-26  Summary of maximum values of shear forces and lateral displacement by ASCE41-07 and ASCE41-13*

| | ASCE41-07 | | ASCE41-13 | | Ratio for | Ratio for |
|---|---|---|---|---|---|---|
| | Vmax (kips) | Max Disp. (in) | Vmax (kips) | Max Disp. (in) | Vmax (x) | Max.Disp.(*) |
| UCSD W-2 | x | x | 122.32 | 1.680 | x | x |
| RMW | 164.00 | 1.16 | 178.73 | 1.47 | 1.1 | 1.3 |
| RMW-R2 | 263.82 | 1.32 | 281.43 | 1.76 | 1.1 | 1.3 |
| WSU Specimen 6 | 111.70 | 1.10 | 125.52 | 1.36 | 1.1 | 1.2 |

(x) Ratio for Vmax = Vax(ASCE41-13) / Vmax(ASCE41-07)

(*) Ratio for Vmax = Max.Disp.(ASCE41-13) / Max.Disp.(ASCE41-07)

**7.5.2 Comparisons among ASCE41-07 and ASCE41-13 Backbone curves from the different masonry wall cases - Normalization of shear load using the as-built wall nominal lateral capacity**

The value of the measured experimental lateral capacity is normalized using the nominal lateral capacity of each specimen. To calculate the nominal lateral capacity, the as-built material properties and applied axial load were considered.

Details of the calculation are presented in Appendix A including the moment-axial load interaction diagram; and shear capacity. The lateral displacement was normalized using the drift ratio for each masonry wall case.

Figure 7.25 shows the normalized backbone curves following the provisions of ASCE41-07, and Figure 7.20 shows the corresponding curves for ASCE41-13.
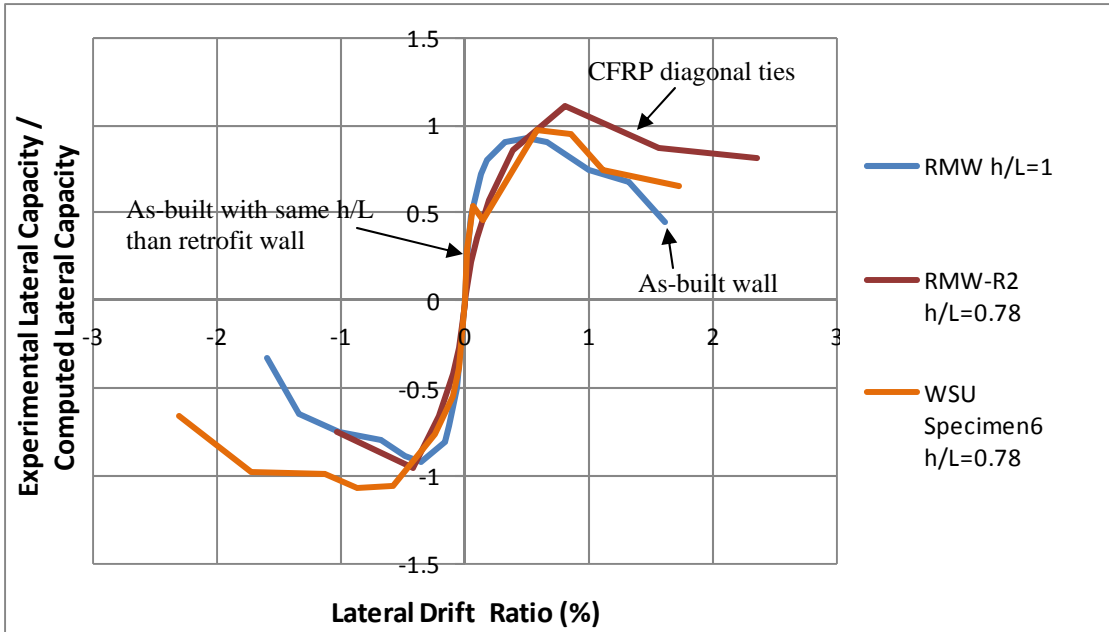
*Figure 7.46  Normalized ASCE41-07 backbone curves*
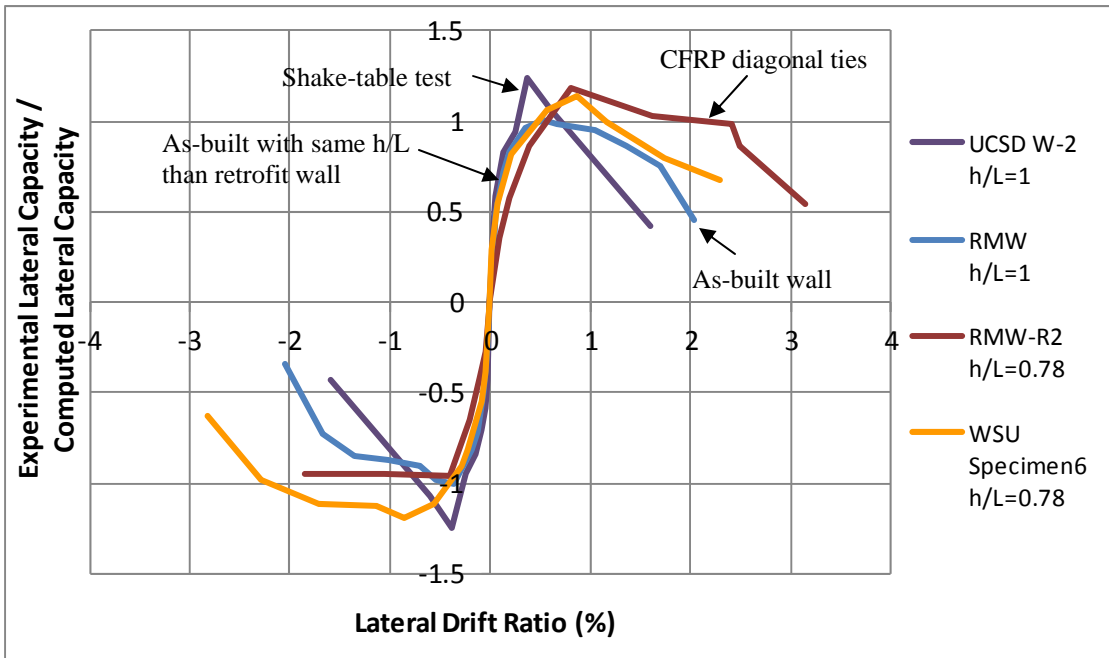


*Figure 7.47  Normalized ASCE41-13 backbone curves*

377

It can be seen that the initial stiffness for retrofitted masonry wall is larger than the same aspect ratio WSU Specimen 6. Also, compared with UCSD W-2 and the as-built masonry wall RMW the stiffness for RMW-R2 is reduced. It was expected that RMW-R2 would have a higher initial stiffness since lower aspect ratio but previous loading reduced the stiffness.

It is also observed that the retrofit masonry wall RMW reached a higher peak shear capacity, since the aspect ratio of RMW-R2 (h/L=0.78) was less than that of RMW (h/L=1).

Table 7-27 shows peak values of normalized lateral load capacity and percentage of drift ratios.

*Table 7-27  Summary of maximum values of normalized shear forces and drift ratios for each backbone curve ASCE41-13*

| | Related with as-built nominal capacity of | Related with height of specimens | |
| --- | --- | --- | --- |
| | Calculated Nom.Lat.Cap. | Exp.Lat.Load / Nom.Lat.Cap. | Drift.Ratio % |
| RMW P=140kips | 178.00 | 1.00 | 2.04 |
| RMW-R2 P=140kips | 237.00 | 1.19 | 3.15 |
| UCSD W-2 P=56kips | 98.00 | 1.24 | 1.60 |
| WSU Spec.6 P=86kips | 105.00 | 1.20 | 2.83 |

### 7.5.3 Idealized Force-Displacement curves and Elasto-Plastic ASCE41-13 curves for masonry wall RMW-R2

As it was discussed in 7.3.1, two types of behavioral models for the retrofitted masonry walls were proposed in this research: Elasto-Plastic and Force-Displacement models. First idealized curves were developed from the backbone curves, and then they were normalized by the shear at yielding for each section $Q/Q_y$. Lateral deformation is represented by drift ratios.

The proposed idealized curves consider the action of constant axial load $P/A_g$ x f'm = 0.08 and lateral load as shown in Figure 7.27.
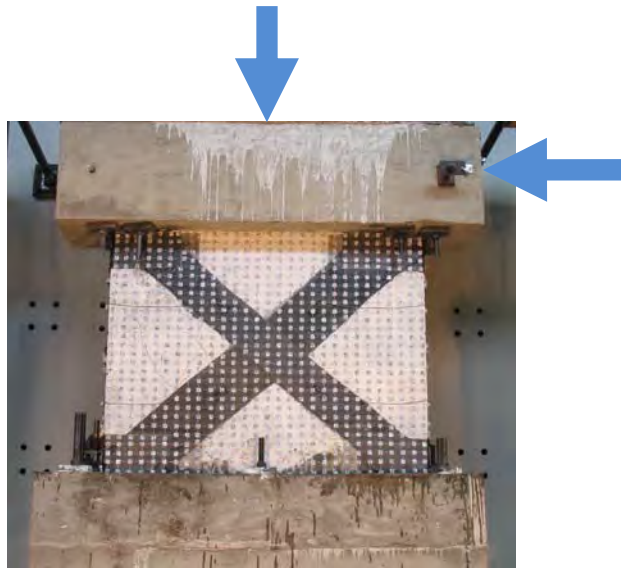


*Figure 7.48  Hinge zone of CFRP jacketing. Constant axial load and cycle lateral load are applied*

Figure 7.28 shows the idealized curves for the backbone curve ASCE41-13 RMW-R2. It can be seen the tendency of each graph, having effective stiffness and maximum displacement. However they have different values of Vy. Force-Displacement curve Vy is lower than Elasto-Plastic V'y. Table 7-28 and Table 7-29 show the coordinates of each point for the idealized elasto-plastic and force-displacement curve. Table 7-30 shows the values of initial stiffness and displacement ductility calculated from both idealized curves. It is noticed that Keff for elasto plastic curve is lightly higher at comparison with Keff for the force-displacement curve. However, value of μ for elasto-plastic curve is less than force-displacement curve case. This is explained because the methodology to draw the elasto-plastic curve consists to work until the displacement correspondent to 80% of the maximum shear capacity of the specimen. The maximum displacement considered for force-displacement curve is correspondent to the maximum measured displacement in the test.
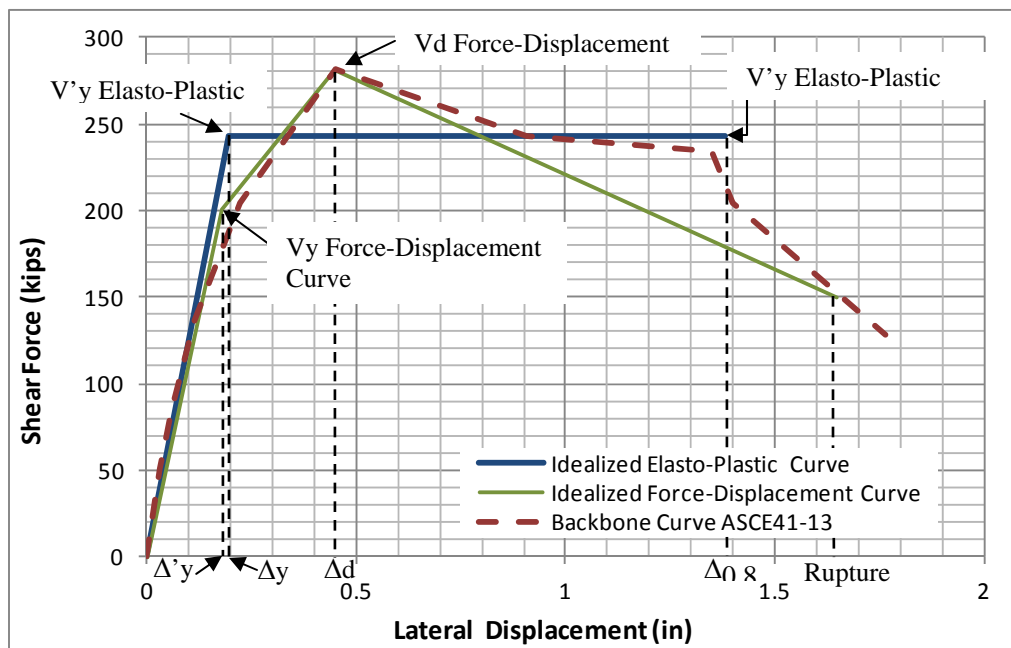


***Figure 7.49 Idealized Curves for RMW-R2***

**Table 7-28  Idealized elasto-plastic curve main values for RMW-R2**

|  | Δ(in) | V (kips) |  |
|---|---|---|---|
| **Origin** | 0 | 0 |  |
| **Δ'y** | 0.20 | 243.00 | **V'y** |
| **Δ0.8** | 1.38 | 243.00 | **V'y** |

**Table 7-29  Idealized force-displacement curve main values for RMW-R2**

|  | Δ(in) | V (kips) |  |
|---|---|---|---|
| **Origin** | 0 | 0 |  |
| **Δy** | 0.18 | 200.00 | **Vy** |
| **Δd** | 0.45 | 281.43 | **Vd** |
| **Rupture** | 1.65 | 150.00 |  |

**Table 7-30  Effective Stiffness (Keff) and Displacement Ductility ($\mu$) for specimen RMW-R2**

| Elasto-Plastic | | |
|---|---|---|
| **K eff** | 1246 | kip/in |
| **μ** | 7.08 |  |
| **Force-Displacement** | | |
| **K eff** | 1111 | kip/in |
| **μ** | 9.17 |  |

For Elasto-Plastic Curve: $\mu = \Delta_{0.8} / \Delta'y$ ;

For Force-Displacement Curve: $\mu = \text{Rupture} / \Delta y$

The values of the idealized curves were normalized to each Vy respectively. Figure 7.38 shows the generalized curves for each method. Table 7-22 and Table 7-23 show the coordinate points for each generalized curve.
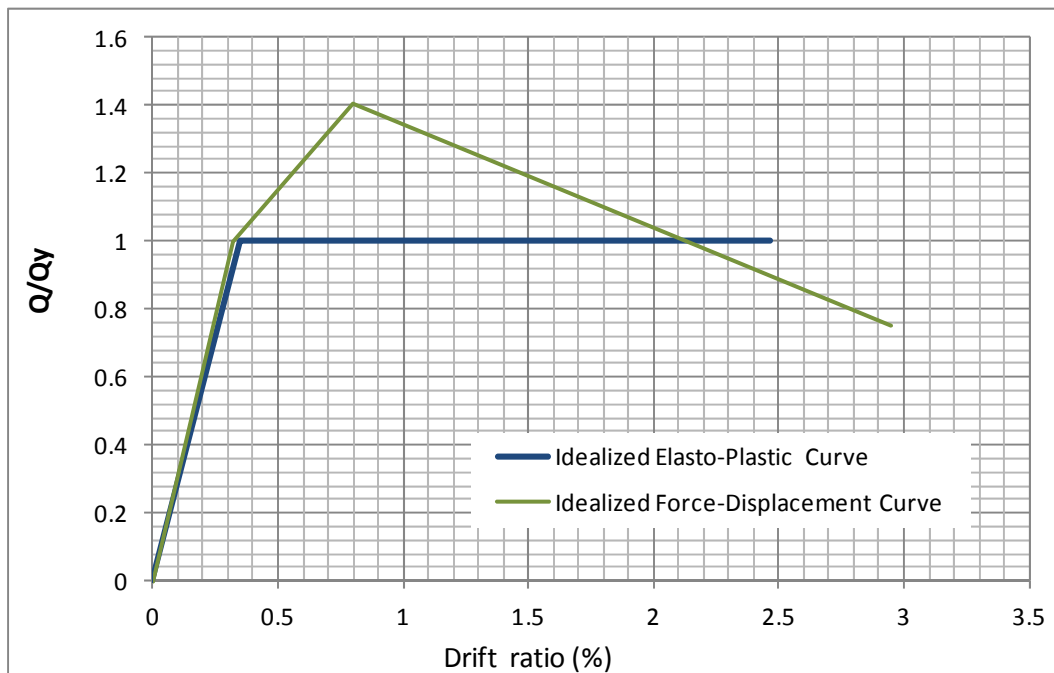
*Figure 7.50  Generalized force-deformation curves for RMW-R2*

*Table 7-31  Coordinate point values of the generalized force deformation from the elasto-plastic curve*

|  | Drift | Q/Qy |  |
|---|---|---|---|
| **Origin** | 0 | 0 |  |
| **Δ'y** | 0.35 | 1.00 | **V'y** |
| **Δ0.8** | 2.46 | 1.00 | **V'y** |

*Table 7-32  Coordinate point values for the generalized force deformation from the force-displacement curve*

|  | Drift (%) | Q/Qy |  |
|---|---|---|---|
| **Origin** | 0 | 0 |  |
| **Δy** | 0.32 | 1.00 | **Vy** |
| **Δd** | 0.80 | 1.41 | **Vd** |
| **Rupture** | 2.95 | 0.75 |  |

According with ASCE41-13, the structural behavior can be classified either deformation control or force-control. It is presented in Table 7-33 the proposed parameter to ASCE41-13 for this type of rehabilitation method applied to masonry wall. Type 2 curve was used because the specimen has residual strength and also large ductility (e>2g), considering the structural behavior as deformation-control. Figure 7.51 shows the location of each point that define the parameters.

*Table 7-33  Parameters of Type 2 curves for RMW-R2*

| Elasto-Plastic | | | | | | |
|---|---|---|---|---|---|---|
| **g** | **e** | **d** | **e > 2g ?** | **a** | **b** | **c** |
| 0.35 | 2.46 | 2.46 | Yes | 2.12 | 2.12 | 1.00 |
| **Force-Displacement** | | | | | | |
| **g** | **e** | **d** | **e > 2g ?** | **a** | **b** | **c** |
| 0.32 | 0.80 | 2.95 | Yes | 0.48 | 2.14 | 0.75 |
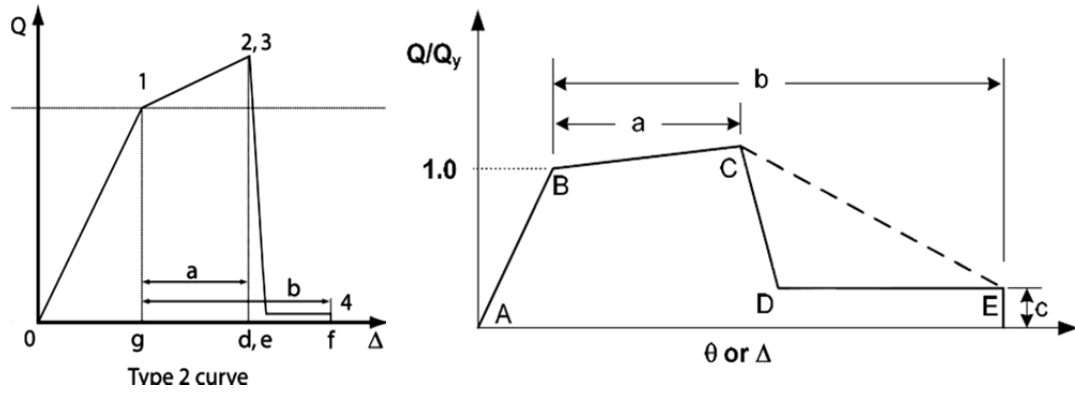
*Figure 7.51  Parameter for Type 2 curve (left) and Generalized Relations for computer modeling (right)*

# CHAPTER 8

# Summary and Conclusions

## 8.1 SUMMARY OF TEST OBSERVATIONS

### 8.1.1 Use of mechanical splices

Mechanical splices are frequently used in new construction. However, their use is limited and not always practical for retrofitted structures. If the bars to be joined do not need to be threaded in order to be connected with a special mechanical splice, such mechanical splices can be useful.

Mechanical splices are generally most economical when traditional lap splices are too large and difficult to utilize. Mechanical splices are used to connect bars to transfer tension or compression forces and need to have sufficient strength so that yielding and failure will occur in the bars. The mechanical couplers used in this study gripped the spliced bars using bolts tightened to a specified torque.

For seismic applications, ACI 318 code provisions require that mechanical splice systems should develop at least 1.25fy. ACI318 also defines Type 1 and Type 2 splices. A Type 2 splice is used in hinged regions of the concrete member where high force and large deformation are needed. A Type 1 splice is allowed to connect bars in zones of low deformation. ACI318 specifies that Type 2 splices must develop a fracture stress higher than 1.25fy and the specified ASTM ultimate strength. Type 1 splices must develop the specified tensile strength of the bar. AASTHO provisions indicate that Type 2 splices should develop a stress at rupture higher than 1.35fy in order to be used in bridges.

Two types of splices were studied: short mechanical splices (SMS) and long mechanical splices (LMS) meeting ACI requirements for Type 1 and Type 2 splices. The length of the short splice (SMS) was 6.8 in., and the long splice (LMS) was 10 in. The end bolt had pointed end in the SMS splice and a rounded end in the LMS splice. With a pointed end, the area of the bar was reduced more than with a round end. Bar fractures were observed at the location of the pointed bolt. With a rounded end, bar fracture occurred away from the splice. Therefore the rounded end meets Type 2 splice requirements and is more appropriate for seismic strengthening of concrete members.

In the tests conducted on mechanical coupler, it was observed that the measured maximum stress in the long splices met the requirements for ACI-318 and AASTHO for Type 2 splices and would meet all the requirements for Type 1 splices. However, the measured maximum stresses in the short splices indicated that they can meet Type 1 splice requirements for A-706 and A-615 bars, but would not meet the requirement for a Type 2 splice if A-615 bars are used. Short splices would meet the requirements when A-706 is used.

### 8.1.2   Use of CFRP materials

CFRP materials were used for confinement of column hinge regions and as tension ties in a masonry wall. The CFRP jacket confines the column and provides extra shear capacity so that the jacketed column section is stronger in shear than the original column.

In addition to the jacket, CFRP anchors helped confine the square column section. For the masonry wall, the diagonal ties across the wall provided a tension brace to improve capacity after the cracks in the concrete masonry units lowered the shear capacity of the wall. The force in the tension tie was transferred from the CFRP sheet to an anchor that extended into the supporting members at the top and bottom of the wall. For the masonry wall case, the anchors were installed parallel to the axis of CFRP tie. The capacity of the anchor was determined by the tension strength of the anchor and adherence between the interior surface of the hole and the anchor.

For optimal use of CFRP materials, it is very important that strict quality control be carried out in the application of the CFRP. Without high quality installation, the capacity of the CFRP is compromised and may not reach the capacity desired.

### 8.1.3  Column strengthening and repair

Two as-built columns (RC-1 and RC-2) had low compressive concrete strength and poorly detailed transverse reinforcement, characteristics that were not appropriate for concrete structures in high seismic zones. The as-built columns failed because they were not capable of carrying axial load and large lateral displacement at the same time. Crushed concrete, buckled bars and open ties were observed in bottom hinge of RC-1 and both extremes of RC-2. The maximum lateral load reached for RC-1 with low axial load (150 kips) was 53kips at 1.6% drift ratio, and the failure occurred at 7% drift ratio and a lateral load of 41kips. The maximum load reached for RC-2 with high axial load (350kips) was 52kips at 1.6% drift ratio, and the failure occurred at 3.5% drift ratio and the lateral load was 25kips.

Two different types of repair were used for RC-1. The hinge zone at the top of the column was strengthened with a CFRP jacket, and the bottom hinge was repaired using short mechanical splices to replace the buckled bars.

In the top of the column, the CFRP jacket confined the column. Before installing the jacket, loose concrete was removed and mortar was used to replace any concrete removed. There was no attempt to inject epoxy into the cracks at the top of the column. The damaged region was wrapped with two layers of CFRP sheets that extended over the length of hinge zone.

In the bottom of column, new concrete was placed in the region where the bars were removed. The strength of the new concrete was higher than the original column concrete and the cross section was increased to provide sufficient cover over the mechanical splices. Concrete and reinforcement were replaced in the heavily damaged bottom hinging region.

Failure occurred in the existing column section above the zone where the new concrete was cast (above the mechanical splices). The concrete crushed under the axial load and the bars bent. The maximum lateral capacity for the repaired column was 61 kips at 2.8% drift ratio. The repaired specimen was not able to sustain axial load ((P/Agf'c=0.20) after a drift ratio of 5.5% was reached and a lateral load of 57kips. The top hinge zone showed no damage. No bars fractured in the splice region at bottom of column.

Specimen RC-2 was divided into two cantilever columns and tested without axial load (P/Agf'c=0). Lateral load was applied at the mid-height of the original column. The existing column was removed and protruding existing bars were left at bottom and top of column. One half of the column was retrofitted using short mechanical splices, and the second with long mechanical splices.

In the specimen with short splices, the maximum lateral shear force applied was 61kips at 2.1%. The first bar fracture at the splice occurred at a drift of 2.4%. After the existing bars ruptured progressively, the maximum drift ratio was 6% and the lateral load was 10kips. For the column with long splices, the failure occurred due to the rupture of a longitudinal bar from the existing column. The maximum lateral shear force prior to bar fracture was 72kips at 8% drift ratio. The maximum drift ratio was 13% and the lateral load was 68kips. In both columns, flexural failure produced the collapse.

### 8.1.4 Strengthening of the masonry wall

The study of a shake-table test of a three story structure (tested at UC San Diego) helped to define the type and level of damage which could be observed in a reinforced masonry wall. It was observed that sliding of a wall led to the degradation of the stiffness of the structure and reduced the shear capacity of the three-story structure.

An isolated reinforced masonry wall with similar restraints to that of wall in the three-story structure was tested. The isolated wall was subjected to constant axial load (P/Agf'm = 0.08, h/L=1) and lateral cyclic load. Diagonal cracks formed in the wall and large sliding deformations occurred at the bottom of wall. Crushing of the concrete masonry units occurred in the bottom two courses of the wall. The vertical bars in the wall were bent due the high shear deformation. The maximum shear strength was 179kips at 0.5% drift ratio. The specimen was not able to support the axial load producing a collapse at 2% drift ratio.

The damaged concrete blocks at the bottom of the masonry wall were encased in a reinforced concrete ring. The concrete ring reduced the height of the wall. The aspect ratio was reduced from h/L= 1 to 0.78. The stiffness of the shortened wall was less compared to that of the as-built specimen. Extensive diagonal shear cracks in the damaged wall reduced the stiffness.

To strengthen this wall, CFRP sheets were attached to the wall along the diagonals to produce a tension brace or tie, and CFRP anchors were installed at the ends of the sheets to transfer the tie forces to the top and bottom supports of the wall. The CFRP diagonal ties, anchors and U-wraps were applied on both faces of the masonry wall. Two layers of CFRP 9 in. wide were applied along one diagonal and one layer of CFRP 12 in. wide was placed along the other diagonal on both faces.

Considerable sliding displacement occurred at the top of the strengthened wall. Sliding at top was about 50% of the total lateral displacement. Sliding at bottom of the wall was not significant. The maximum shear capacity prior to sliding was 284kips at 0.8% drift. Failure occurred due to rupture of the CFRP anchors installed at the top of the masonry wall at a lateral load 128kips and the maximum drift ratio was 3.1%.

## 8.2 CONCLUSIONS

The research represents a unique project for repair of severely damaged concrete members efficiently and with attractive cost-time benefits. The use of innovative materials and devices was very important for developing these new methods. The test results were evaluated using the provisions of ACI 318 for buildings, AASTHO for bridges, and ASCE41-13 for rehabilitated members.

The rehabilitation methods produced retrofitted members that were less stiff than the existing elements. However, retrofitted columns and the masonry wall had higher normalized shear capacities. Shear forces for columns were normalized by two methods: nominal lateral capacity of as-built columns, and the computed lateral capacity of actual columns. Shear forces for masonry wall were normalized by the computed lateral capacity of actual walls. Values of drift at peak load were comparables. The existing bars had larger deformation and the bond between the bars and the concrete was reduced considerably prior rehabilitation. For case of the wall, the severe cracking of the wall reduced the stiffness.

The ultimate drift ratio of the test for retrofitted columns reached values larger than 2% which is the acceptable lateral drift capacity recommended by ASCE07-05 for occupancy category I and II. Retrofitted columns exhibited good performance at 1% drift that is appropriate for occupancy category IV. For the retrofitted masonry wall, an acceptable drift of 0.70% (prior to sliding) was reached correspond for occupancy category IV.

The existing bars must carry tension under bending effects. The mechanical splices could be used for rehabilitation by connecting new bars to protruding bars that were previously yielded. The tests showed that such connections are reliable. However,

392

they are the weakest element in the column because they are likely to rupture first under large deformations; especially last bolt of a coupler with a pointed end that reduces the area of the bar. There is no problem for a long splice because the last bolt has a round end.

With couplers it may not be necessary to remove the entire concrete member to replace it. Couplers will still be needed to connect the new concrete member to the existing elements. By removing only damaged concrete and buckled bar, the volume of material is not as large as it will be when demolishing an entire member and building a new one. The retrofit cost is likely to be reduced in proportion to the volume of the concrete replaced in the member. So the cost of replacing damaged areas only should be attractive.

In the case of walls, the sliding effect is very important. The structure may not collapse as was the case of the three-story structure tested on a shake table; however, non-structural elements may be damaged rendering the structure unusable. Structures such as hospitals that have many pipes and equipment installations on their walls would be most vulnerable. A possible solution to avoid wall sliding is the addition of CFRP anchors. The response of the strengthened wall demonstrated that development of the required tension force in the diagonal CFRP brace can be achieved, and the prevention of sliding depends entirely on the CFRP anchors.

Sliding provides energy dissipation that allows the structure remain properly. However actual shear capacity of the wall cannot be predicted because sliding. CFRP anchors predict a no occurrence of sliding until the anchor resistance level. Above that force, sliding may occur.

The proposed rehabilitation methods can be implemented rapidly and may cost less than others traditional techniques. However, to avoid vulnerability of the structure during the construction, these must be planning for the use of jacks or supported to the structure when the columns are being rehabilitated. Since the columns are going to be cut at the affected zone, the extra supports will carry the axial loads provisionally. It is very important to assure both lateral and vertical stability of the structure during the process of rehabilitation of columns.

It was observed that the method for developing models for the behavior of new existing, or repaired element, varies. ASCE41-07 procedures produce very conservative models for shear capacity and drift ratios. However, ASCE41-13 considers an envelope of shear-displacement data. While conservative models may be appropriate for new construction, they may result in excessive requirements for rehabilitation that could lead owners to reject improvements in their buildings - an outcome that does not reduce risk to the public.

The proposed rehabilitation methods performed well. Higher shear capacity and larger displacement were reached using the methodologies proposed in this research. Additionally, the inclusion of short and long mechanical splices to rehabilitate columns with poor lap splices had better performance in lateral capacity and displacement than the use of steel or CFRP jacket with anchors.

## 8.3  RECOMMENDATION FOR FUTURE RESEARCH

More test data is recommended to optimize mechanical splices. The behavior of short splices might be improved if the pointed end of the last bolt is replaced with a rounded end. The reduction of the bar area will not be as great and the splice may meet the requirement for Type 2 splices using A615 bars.

It is also recommended that long mechanical splices using previously yielded bars and new bars be tested. Despite the fact that long mechanical splices performed adequately under high loads and large deformations, previously yielded bars were not tested in the long splices.

Various geometries of transverse reinforcement need to be studied. The location of the bolts in the splices made it difficult to install transverse reinforcement around the splices. By dividing the ties in two parts, installation time will be reduced and the rehabilitation will be more efficient.

The failure of one of the retrofitted column in a zone of poor quality existing concrete highlighted the need to consider all possible failure modes and to study the jacketing of all segments of an existing column that have low compressive concrete capacity or inadequate transverse reinforcement using a CFRP jacket over the entire length of the column.

More study of the CFRP anchors used in masonry wall strengthening effects is needed especially to control sliding.

# APPENDIX A

# Capacity of the Retrofitted Concrete Members

## A.1 RC-1R-Bᴏᴛᴛᴏᴍ Hᴀʟꜰ
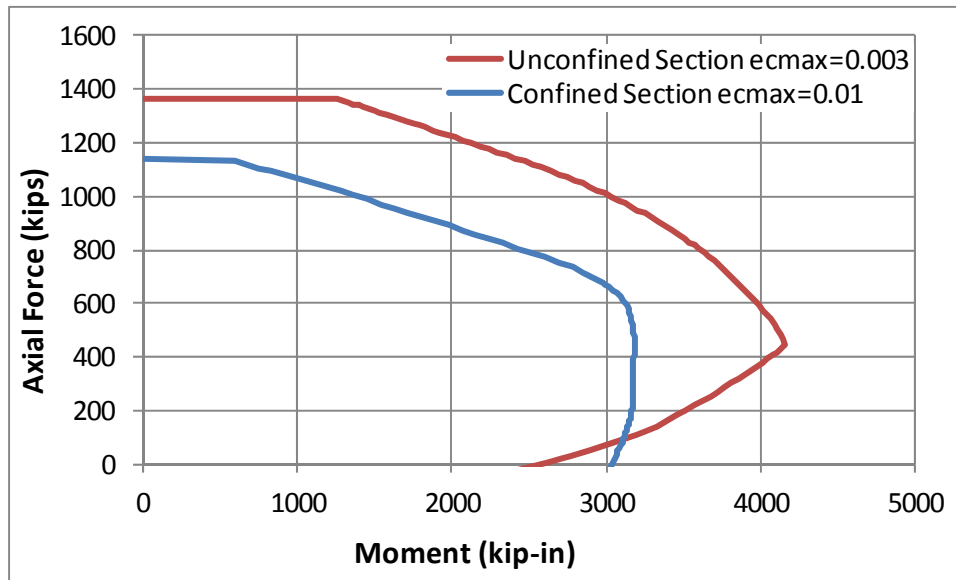


*Figure A.1  Moment vs. axial force for RC-1R Bottom Half*

*Table A-1  Shear force capacity for normalization RC-1R Bottom Half*

|  | H | 58 in |
|---|---|---|
|  | Axial Load | 150 kips |
| confined | Mn | 2390 kips-in |
| Vn = Mn / H | Vn | 41.2 kips |
| unconfined | Mn | 2690 kips-in |
| Vn = Mn / H | Vn | 46.4 kips |
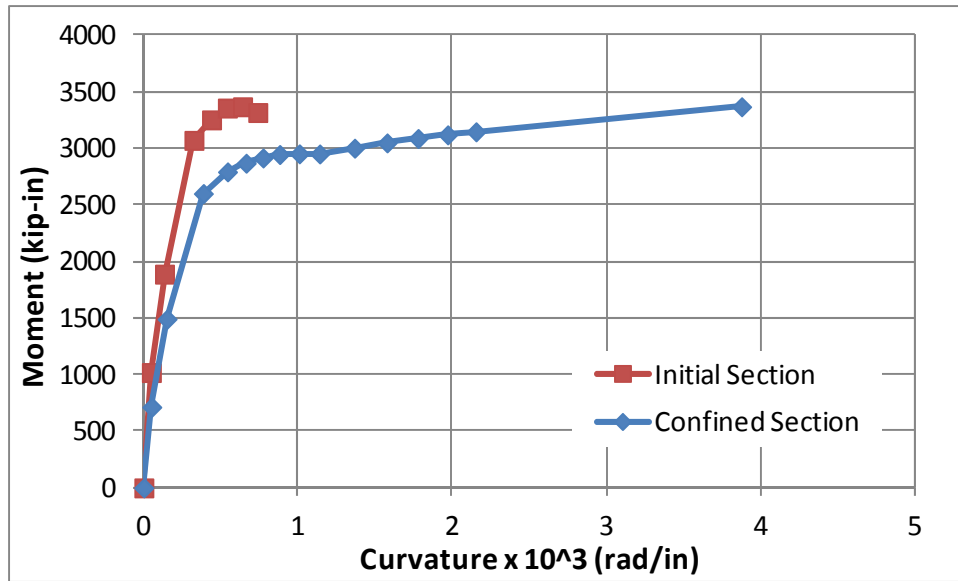
*Figure A.2 Moment vs. curvature at 150kip axial force for RC-1R Bottom Half*
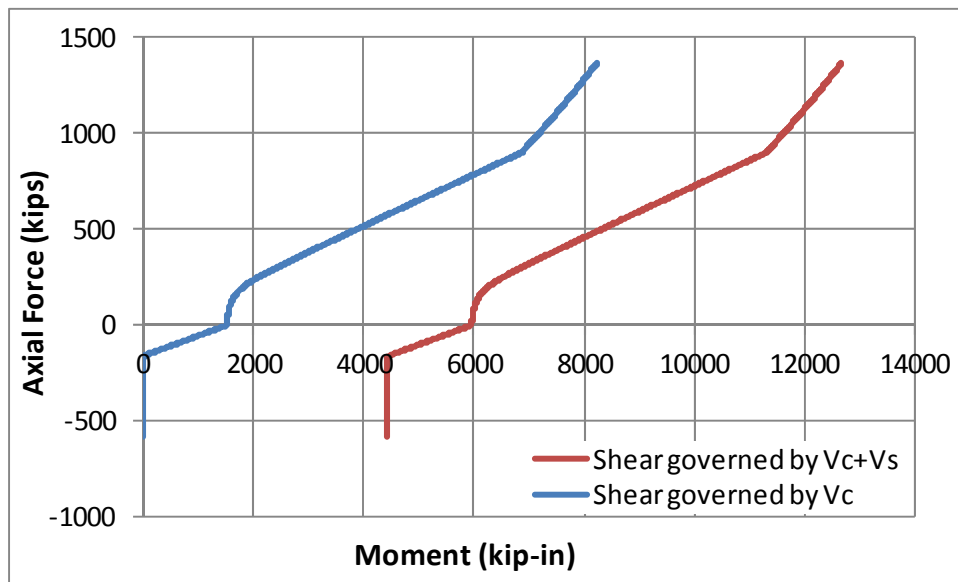


*Figure A.3 Shear governed by Vc and Vs for RC-1R Bottom Half*

*Table A-2 Calculation of Vs and Vc for RC-1R Bottom Half*

| | | |
|---|---|---|
| $A_v$ | 0.385 | in.$^2$ |
| L | 116 | in. |
| $b_w$ | 18 | in. |
| $\rho_w$ | 0.010215517 | |
| d | 11.6 | in. |
| h | 18 | in. |
| $A_g$ | 324 | in.$^2$ |
| s | 3.5 | in. |
| $f'_c$ | 4000 | psi |
| $f_y$ | 60 | ksi |
| | | |
| **Calculate:** | | |
| $V_s$ | 76.56 | kips |
| $V_c$ | 25.09 | kips |
| **M governed by Vs:** | 4440.48 | kip-in. |

# Table A-3 Properties of concrete for Scott, Park & Priestley for RC-1R Bottom Half

| | | |
|---|---:|---|
| Concrete compressive strength, $f'_c =$ | 4000 | psi |
| Spacing of hoops or ties, $s_h =$ | 3.5 | in. |
| $\rho_s$ | 0.015 | |
| $b''$ | 13.84 | in. |
| $fy$ | 60 | ksi |
| **Calculate:** | | |
| $E_T$ (Modulus) | 3265306.122 | psi |
| K | 1.225 | |
| $\varepsilon_o$ | 0.00245 | in./in. |
| | | |
| **Tension** | | |
| $f_r$ | -500 | psi |
| $\varepsilon_r$ | -0.000153 | in./in. |
| | | |
| **Compression** | | |
| $\varepsilon_{50u}$ | 0.003666667 | in./in. |
| $\varepsilon_{50h}$ | 0.022371059 | in./in. |
| $\varepsilon_{50c}$ | 0.026037726 | in./in. |
| $0.5f'_c$ | 2000 | psi |
| $Z_m$ | 21.20 | |
| | | |
| **Unconfined Concrete Linear Curve Fit** | | |
| m | -1643835.616 | |
| b | 8027.39726 | |
| $\varepsilon_{cu}$ | 0.004396667 | |
| | | |
| **Confined Concrete Linear Curve Fit** | | |
| $\varepsilon_{cu}$ | 0.040190361 | |
| Max. compressive stress | 4.90 | ksi |

*Figure A.4 Stress vs. Strain of concrete in compression for RC-1R Bottom Half*

## A.2 RC-1R-Top Half
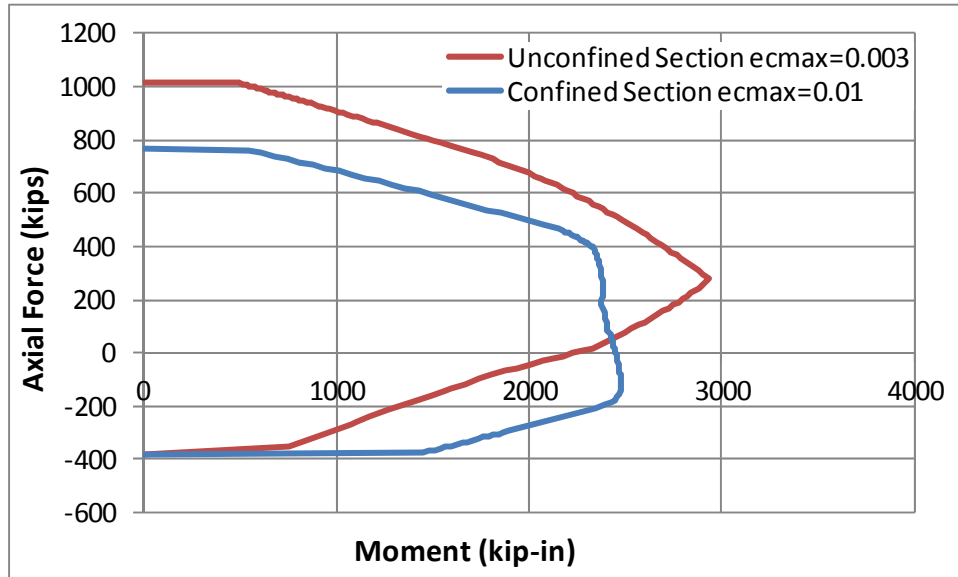


*Figure A.5  Moment vs. axial force for RC-1R Top Half*

*Table A-4  Shear force capacity for normalization RC-1R Top Half*

|  |  | | |
|---|---|---|---|
|  | H | 58 | in |
|  | Axial Load | 150 | kips |
| confined | Mn | 2390 | kips-in |
| Vn = Mn / H | Vn | 41.2 | kips |
| unconfined | Mn | 2690 | kips-in |
| Vn = Mn / H | Vn | 46.4 | kips |
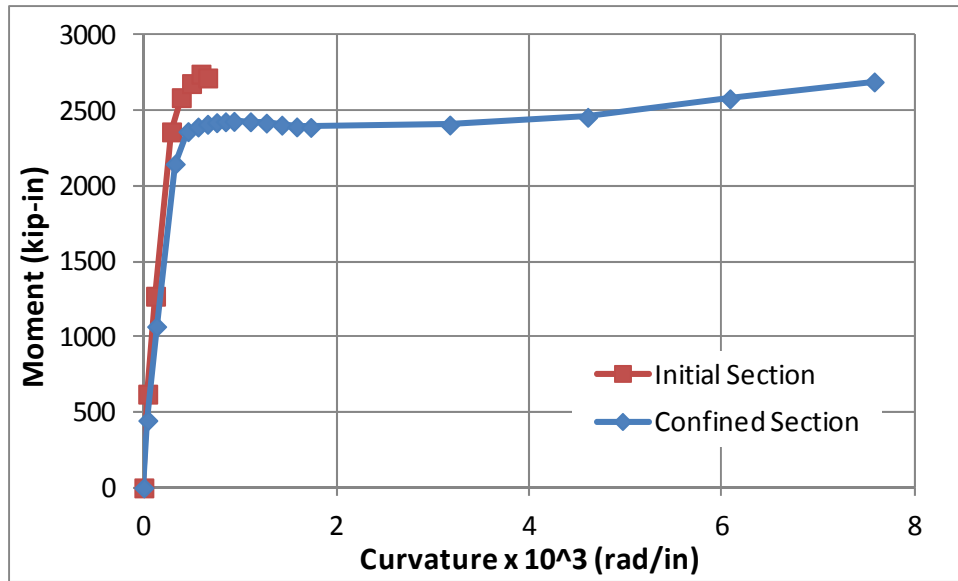
*Figure A.6  Moment vs. curvature at 150kip axial force for RC-1R Top Half*
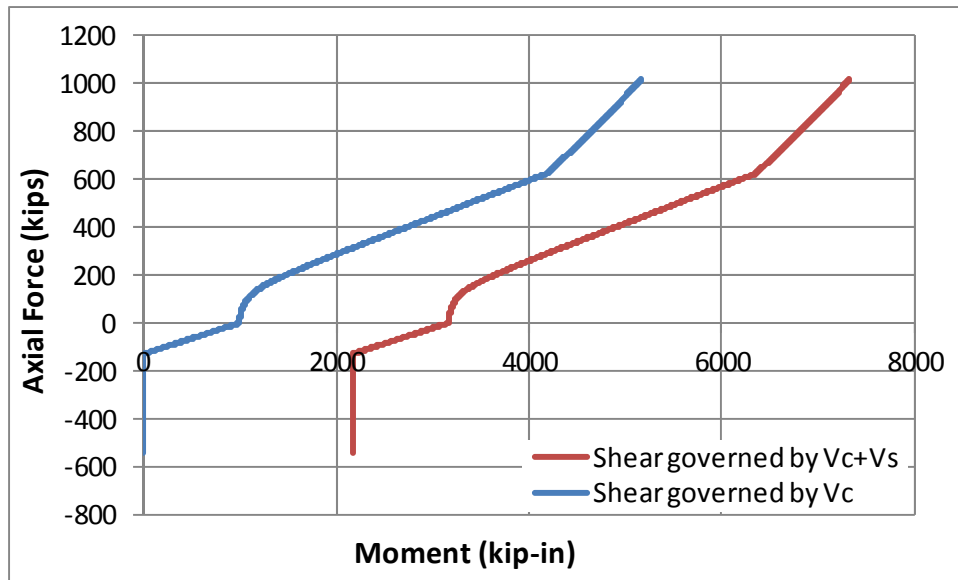


*Figure A.7  Shear governed by Vc and Vs for RC-1R Top Half*

*Table A-5 Calculation of Vs and Vc for RC-1R Top Half*

| | | |
|---|---|---|
| $A_v$ | 0.385 | in.$^2$ |
| L | 100 | in. |
| $b_w$ | 16 | in. |
| $\rho_w$ | 0.010972222 | |
| d | 11.25 | in. |
| h | 16 | in. |
| $A_g$ | 256 | in.$^2$ |
| s | 6 | in. |
| $f'_c$ | 3000 | psi |
| $f_y$ | 60 | ksi |
| | | |
| Calculate: | | |
| $V_s$ | 43.31 | kips |
| $V_c$ | 18.73 | kips |
| M governed by Vs: | 2165.63 | kip-in. |

## Table A-6 Properties of concrete for Scott, Park & Priestley for RC-1R Top Half

| | | |
|---|---|---|
| *Concrete compressive strength, f'$_c$=* | 3000 | psi |
| *Spacing of hoops or ties, s $_h$ =* | 6 | in. |
| $\rho_s$ | 0.00875 | |
| b" | 13 | in. |
| fy | 60 | ksi |
| **Calculate:** | | |
| E$_T$ (Modulus) | 2553191.489 | psi |
| K | 1.175 | |
| $\varepsilon_o$ | 0.00235 | in./in. |
| | | |
| **Tension** | | |
| f$_r$ | -428.5714286 | psi |
| $\varepsilon_r$ | -0.000168 | in./in. |
| | | |
| **Compression** | | |
| $\varepsilon_{50u}$ | 0.0045 | in./in. |
| $\varepsilon_{50h}$ | 0.009659738 | in./in. |
| $\varepsilon_{50c}$ | 0.014159738 | in./in. |
| 0.5f'$_c$ | 1500 | psi |
| Z$_m$ | 42.34 | |
| | | |
| **Unconfined Concrete Linear Curve Fit** | | |
| m | -697674.4186 | |
| b | 4639.534884 | |
| $\varepsilon_{cu}$ | 0.00579 | |
| | | |
| **Confined Concrete Linear Curve Fit** | | |
| $\varepsilon_{cu}$ | 0.0212 | |
| Max compressive stress | 3.523 | ksi |
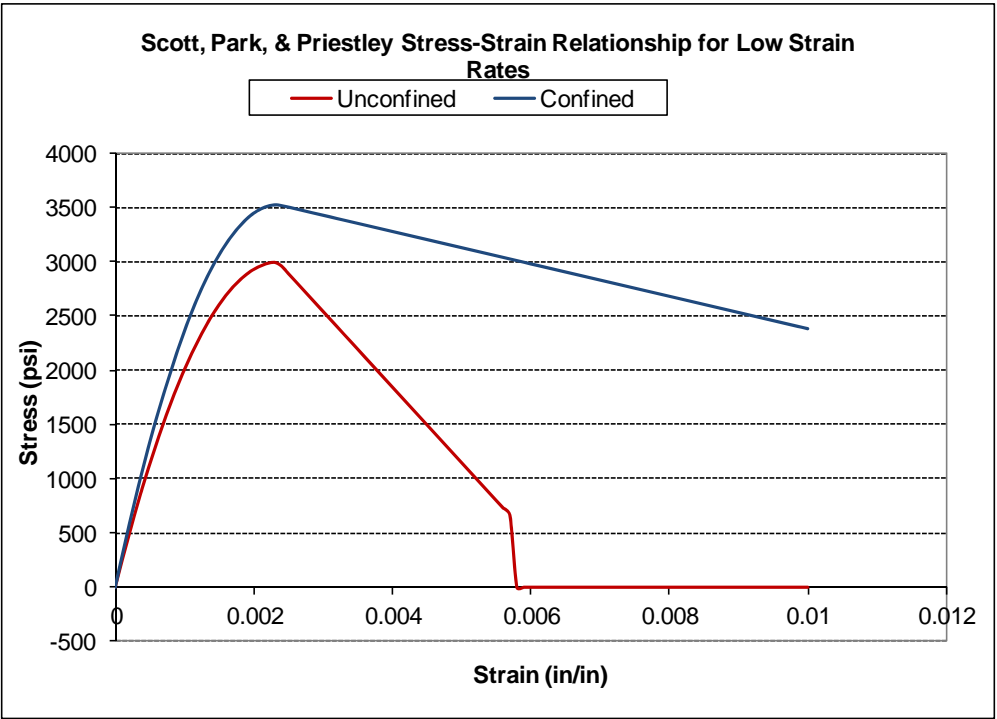
*Figure A.8  Stress vs. Strain of concrete in compression for RC-1R Top Half*

## A.3 RC-2R-SMS
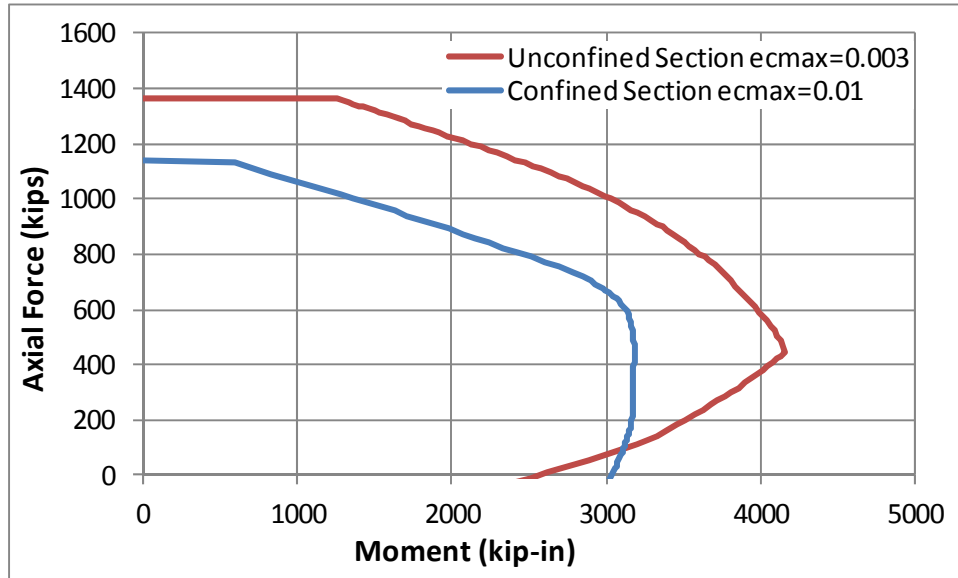


*Figure A.9  Moment vs. axial force for RC-2R-SMS*

*Table A-7  Shear force capacity for normalization RC-2R-SMS*

|  |  |  |  |
|---|---|---|---|
| | H | 58 | in |
| | Axial Load | 0 | kips |
| confined | Mn | 2450 | kips-in |
| Vn = Mn / H | Vn | 42.2 | kips |
| unconfined | Mn | 2230 | kips-in |
| Vn = Mn / H | Vn | 38.4 | kips |
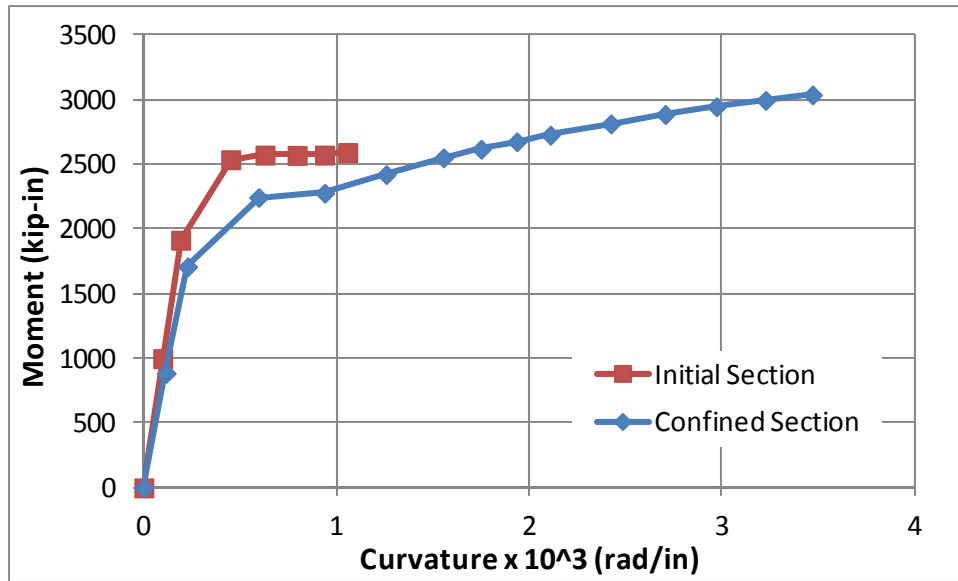
*Figure A.10  Moment vs. curvature at 0kip axial force for RC-2R-SMS*
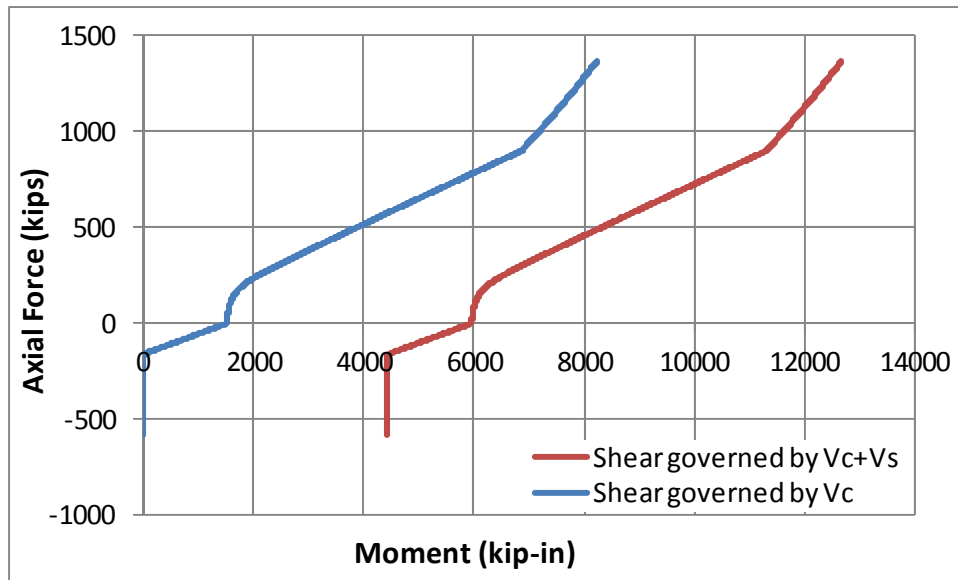


*Figure A.11  Shear governed by Vc and Vs for RC-2R-SMS*

*Table A-8 Calculation of Vs and Vc for RC-2R-SMS*

| | | |
|---|---|---|
| $A_v$ | 0.385 | in.$^2$ |
| L | 116 | in. |
| $b_w$ | 18 | in. |
| $\rho_w$ | 0.010215517 | |
| d | 11.6 | in. |
| h | 18 | in. |
| $A_g$ | 324 | in.$^2$ |
| s | 3.5 | in. |
| $f'_c$ | 4000 | psi |
| $f_y$ | 60 | ksi |
| | | |
| **Calculate:** | | |
| $V_s$ | 76.56 | kips |
| $V_c$ | 25.09 | kips |
| **M governed by Vs:** | 4440.48 | kip-in. |

### Table A-9 Properties of concrete for Scott, Park & Priestley for RC-2R-SMS

| | | |
|---|---|---|
| Concrete compressive strength, $f'_c =$ | 4000 | psi |
| Spacing of hoops or ties, $s_h =$ | 3.5 | in. |
| $\rho_s$ | 0.015 | |
| $b''$ | 13.84 | in. |
| $fy$ | 60 | ksi |
| **Calculate:** | | |
| $E_T$ (Modulus) | 3265306.122 | psi |
| K | 1.225 | |
| $\varepsilon_o$ | 0.00245 | in./in. |
| | | |
| **Tension** | | |
| $f_r$ | -500 | psi |
| $\varepsilon_r$ | -0.000153 | in./in. |
| | | |
| **Compression** | | |
| $\varepsilon_{50u}$ | 0.003666667 | in./in. |
| $\varepsilon_{50h}$ | 0.022371059 | in./in. |
| $\varepsilon_{50c}$ | 0.026037726 | in./in. |
| $0.5f'_c$ | 2000 | psi |
| $Z_m$ | 21.20 | |
| | | |
| **Unconfined Concrete Linear Curve Fit** | | |
| m | -1643835.616 | |
| b | 8027.39726 | |
| $\varepsilon_{cu}$ | 0.004396667 | |
| | | |
| **Confined Concrete Linear Curve Fit** | | |
| $\varepsilon_{cu}$ | 0.040190361 | |
| Max. compressive stress | 4898 | psi |

*Figure A.12  Stress vs. Strain of concrete in compression for RC-2R-SMS*

## A.4   RC-2R-LMS
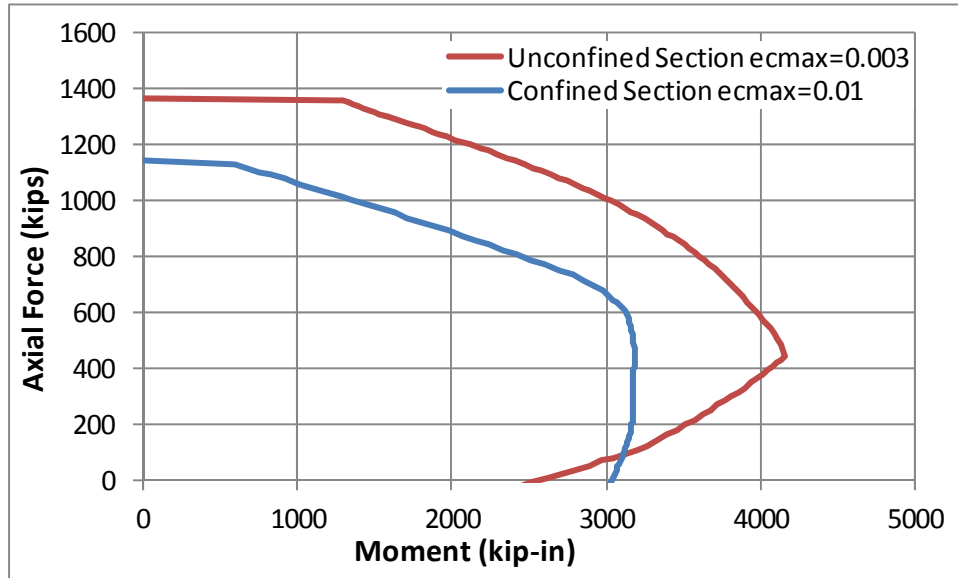


*Figure A.13  Moment vs. axial force for RC-2R-LMS*

*Table A-10  Shear force capacity for normalization RC-2R-SMS*

|  | H | 58 | in |
|---|---|---|---|
|  | Axial Load | 0 | kips |
| confined | Mn | 2450 | kips-in |
| Vn = Mn / H | Vn | 42.2 | kips |
| unconfined | Mn | 2230 | kips-in |
| Vn = Mn / H | Vn | 38.4 | kips |
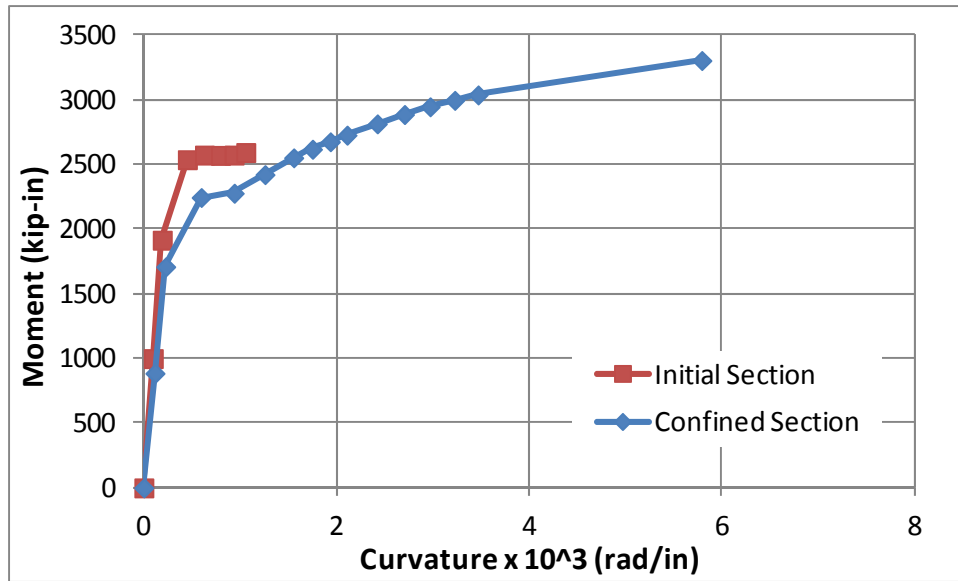
*Figure A.14  Moment vs. curvature at 0kip axial force for RC-2R-LMS*
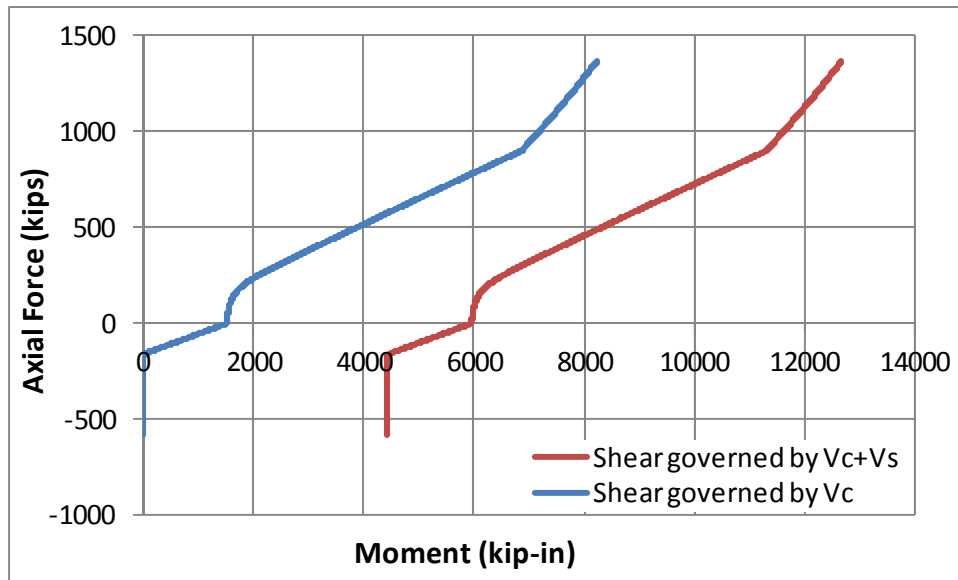


*Figure A.15  Shear governed by Vc and Vs for RC-2R-SMS*

412

*Table A-11 Calculation of Vs and Vc for RC-2R-SMS*

| | | |
|---|---:|---|
| $A_v$ | 0.385 | in.$^2$ |
| L | 116 | in. |
| $b_w$ | 18 | in. |
| $\rho_w$ | 0.010215517 | |
| d | 11.6 | in. |
| h | 18 | in. |
| $A_g$ | 324 | in.$^2$ |
| s | 3.5 | in. |
| $f'_c$ | 4000 | psi |
| $f_y$ | 60 | ksi |
| | | |
| **Calculate:** | | |
| $V_s$ | 76.56 | kips |
| $V_c$ | 25.09 | kips |
| **M governed by Vs:** | 4440.48 | kip-in. |

### Table A-12 Properties of concrete for Scott, Park & Priestley for RC-2R-SMS

| | | |
|---|---|---|
| Concrete compressive strength, $f'_c =$ | 4000 | psi |
| Spacing of hoops or ties, $s_h =$ | 3.5 | in. |
| $\rho_s$ | 0.015 | |
| $b''$ | 13.84 | in. |
| $fy$ | 60 | ksi |
| **Calculate:** | | |
| $E_T$ (Modulus) | 3265306.122 | psi |
| K | 1.225 | |
| $\varepsilon_o$ | 0.00245 | in./in. |
| | | |
| **Tension** | | |
| $f_r$ | -500 | psi |
| $\varepsilon_r$ | -0.000153 | in./in. |
| | | |
| **Compression** | | |
| $\varepsilon_{50u}$ | 0.003666667 | in./in. |
| $\varepsilon_{50h}$ | 0.022371059 | in./in. |
| $\varepsilon_{50c}$ | 0.026037726 | in./in. |
| $0.5f'_c$ | 2000 | psi |
| $Z_m$ | 21.20 | |
| | | |
| **Unconfined Concrete Linear Curve Fit** | | |
| m | -1643835.616 | |
| b | 8027.39726 | |
| $\varepsilon_{cu}$ | 0.004396667 | |
| | | |
| **Confined Concrete Linear Curve Fit** | | |
| $\varepsilon_{cu}$ | 0.040190361 | |
| Max. compressive stress | 4898 | psi |

*Figure A.16  Stress vs. Strain of concrete in compression for RC-2R-SMS*

*Table A-13  Shear force capacity for normalization RC-1R*

| | H | 116 | in |
|---|---|---|---|
| | Axial Load | 150 | kips |
| confined | Mn | 2390 | kips-in |
| Vn = 2Mn / H | Vn | 41.2 | kips |
| unconfined | Mn | 2690 | kips-in |
| Vn = 2Mn / H | Vn | 46.4 | kips |

*Table A-14  Shear force capacity for normalization RC-1*

| | H | 116 | in |
|---|---|---|---|
| | Axial Load | 150 | kips |
| confined | Mn | 2390 | kips-in |
| Vn = 2Mn / H | Vn | 41.2 | kips |
| unconfined | Mn | 2690 | kips-in |
| Vn = 2Mn / H | Vn | 46.4 | kips |

*Table A-15  Shear force capacity for normalization RC-2*

| | H | 116 | in |
|---|---|---|---|
| | Axial Load | 350 | kips |
| confined | Mn | 2390 | kips-in |
| Vn = 2Mn / H | Vn | 41.2 | kips |
| unconfined | Mn | 2690 | kips-in |
| Vn = 2Mn / H | Vn | 46.4 | kips |

***Table A-16  Shear force capacity for normalization FC-17 (Aboutaha, 1994)***

|  | H | 108 | in |
|---|---|---|---|
|  | Axial Load | 0 | kips |
| confined | Mn | 2970 | kips-in |
| Vn = Mn / H | Vn | 27.5 | kips |
| unconfined | Mn | 2320 | kips-in |
| Vn = Mn / H | Vn | 21.5 | kips |

***Table A-17  Shear force capacity for normalization 2-A-S8-M (Kim, 2008)***

|  | H | 108 | in |
|---|---|---|---|
|  | Axial Load | 0 | kips |
| confined | Mn | 3100 | kips-in |
| Vn = Mn / H | Vn | 28.7 | kips |
| unconfined | Mn | 2490 | kips-in |
| Vn = Mn / H | Vn | 23.1 | kips |

***Table A-18  Shear force capacity for normalization WSU Column 2R (He, 2013)***

|  | H | 132 | in |
|---|---|---|---|
|  | Axial Load | 0 | kips |
| confined | Mn | 7960 | kips-in |
| Vn = Mn / H | Vn | 60.3 | kips |
| unconfined | Mn | 6800 | kips-in |
| Vn = Mn / H | Vn | 51.5 | kips |

## A.5 RMW-R2
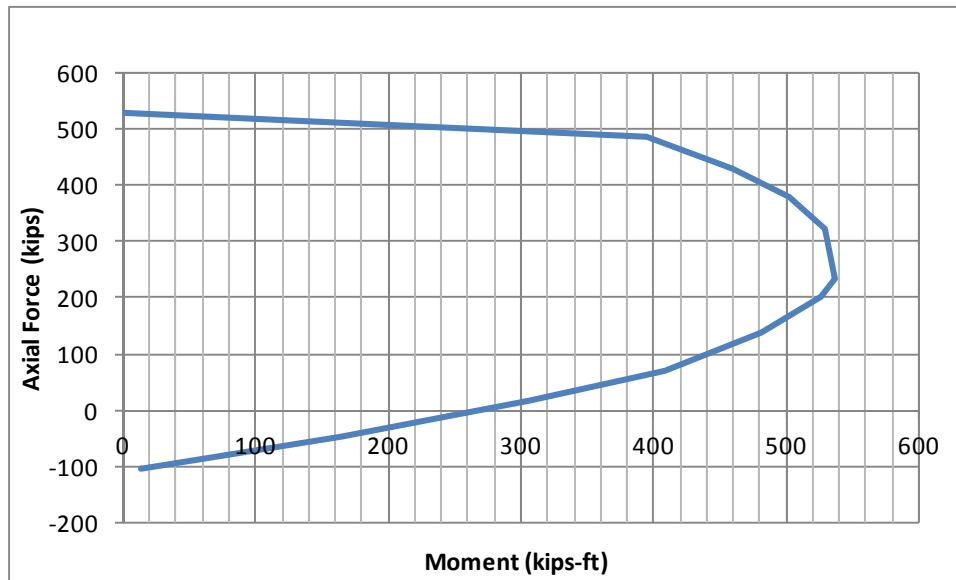


*Figure A.17 Moment vs. axial force for RMW-R2*

*Table A-19 Shear capacity calculated by flexural effects*

| | |
|---|---:|
| H in | 56 |
| Pn kip | 139 |
| Mn kip-ft | 481 |
| | |
| Vn = Mn / (H/2) | |
| **Vn kip** | **205.93** |

Following 2008 MSJC, shear capacity is governed by:

1. Considering flexural, shear and axial forces:

$$V_{nm} = \left[ 4.0 - 1.75 \left( \frac{M_u}{V_u \, d_v} \right) \right] A_n \sqrt{f'_m} + 0.25 \, P_u$$

418

2. Considering internal reinforcement:

$$V_{ns} = \left(\frac{1}{2}\right) A_v \, f_y \, \frac{d}{s} =$$

**Table A-20  Contribution of the bending, shear and axial force Vnm, and internal reinforcement Vn to the lateral capacity of RMW-R2**

| | |
|---|---|
| Vnm | 75.39 lb |
| Vns | 48.75 kip |
| **Vn** | **124.14 kip** |

**Table A-21  Contribution of the 2layers 9"width CFRP diagonal tie to the lateral capacity of RMW-R2 loading to North**

| CFRP CONTRIBUTION FOR SHEAR | |
|---|---|
| **Pushing - North** | |
| Ultimate strength | 106 ksi |
| angle sheet | 42 |
| Width | 18 in |
| tickness | 0.08 in |
| CFRP MATERIAL / Sheet | 1.44 in2 |
| CFRP sheet capacity | 152.64 kips |
| **Vfrp Horizontal Component** | **113.43** kips |

*Table A-22  Contribution of the 1layer 12"width CFRP diagonal tie to the lateral capacity of RMW-R2 loading to South*

| CFRP CONTRIBUTION FOR SHEAR | |
|---|---|
| **Pull - South** | |
| Ultimate strength | 106 ksi |
| angle sheet | 41 |
| Width | 24 in |
| tickness | 0.04 in |
| CFRP MATERIAL / Sheet | 0.96 in2 |
| CFRP sheet capacity | 101.76 kips |
| **Vfrp Horizontal Component** | **76.80** kips |

*Table A-23  Lateral capacity of the specimen*

| Loading to North | Vn = Vnm + Vns + Vfrp |
|---|---|
| | Vn                237.6 kip |
| Loading to South | Vn = Vnm + Vns + Vfrp |
| | Vn                200.9 kip |

**Table A-24  Pulling out capacity of the CFRP anchors by the amount of CFRP strip material used**

| CFRP ANCHORS Pushing - North | | CFRP ANCHORS Pull - South | |
|---|---|---|---|
| Ultimate strength | 106 ksi | Ultimate strength | 106 ksi |
| angle sheet | 42 | angle sheet | 41 |
| Width | 7.5 in | Width | 5 in |
| tickness | 0.04 in | tickness | 0.04 in |
| CFRP MATERIAL / STRIP | 0.6 in2 | CFRP MATERIAL / STRIP | 0.4 in2 |
| # ANCHOR | 4 | # ANCHOR | 4 |
| | | | |
| **CFRP anchor resistance** | 151.24 kips | **CFRP anchor resistance** | 102.40 kips |

**Table A-25  Pulling capacity of the CFRP anchors by dimension of drilled hole and concrete of top and bottom beams**

$$P_n = 4\sqrt{f_c} \times h_c \times (d + h_c) \times \pi + 22\sqrt{f_c} \times h_c \times (h - h_c) \quad h > 2 in.$$

$P_n$ : tensile strength of CFRP anchor. lb

$f_c$ : compressive strength of concrete. psi

$d$ : hole diameter. in.

$h$ : embedment depth of CFRP anchor. in.

$h_c$ : concrete cone depth. 2 in.

$$d_{\substack{anchor \\ hole}} \geq \sqrt{\frac{11.2 \cdot w_{frp} \cdot t_{frp}}{\pi}}$$

**Table A-26  Capacity of the CFRP anchors for loading to north**

| Push North direction | | |
|---|---|---|
| w frp | | 7.5 in |
| t frp | | 0.04 in |
| | | |
| minimum d anchor hole | | 1.03 in |
| **Push North direction** | | |
| | f'c | 4000 psi |
| | d | 1 in |
| (depth) | h | 8 in |
| | hc | 2 in |
| | | |
| | Pn | 35771.24 lb |
| | | 35.77 kips |
| total 4 anchors | | 143.08 kips |
| Length Fan | | 6 in |
| depth | | 8 in |
| total length CFRP strip anchor | | 14 in |

**Table A-27  Capacity of the CFRP anchors for loading to south**

| Pull South direction | | |
|---|---|---|
| w frp | | 5 in |
| t frp | | 0.04 in |
| | | |
| minimum d anchor hole | | 0.84 in |
| **Pull South direction** | | |
| | f'c | 4000 psi |
| | d | 1 in |
| (depth) | h | 5 in |
| | hc | 2 in |
| | | |
| | Pn | 20269.92 lb |
| | | 20.27 kips |
| total 4 anchors | | 81.08 kips |
| Length Fan | | 7 in |
| depth | | 5 in |
| total length CFRP strip anchor | | 12 in |

# APPENDIX B

# Retrofit Process for RC-1R and Additional Graphs of Test Results

**B.1** **RETROFIT PROCESS**



*Figure B.1  Severely damaged column RC-1 removed from the test setup*
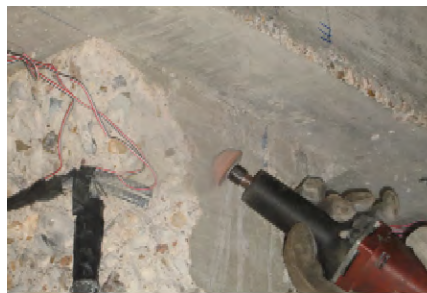


*Figure B.2  Preparing surface to application of repair mortar*

*Figure B.3 . Mixing repair mortar with water to apply on the damage top of column*



*Figure B.4  Application of the mortar on the column replacing the cover*

*Figure B.5  Condition of the top of column after the mortar dried*

*Figure B.6  Mixing epoxy to application of CFRP materials*



*Figure B.7  Application of epoxy into the drilled holes for the CFRP anchors*

*Figure B.8  Saturation of epoxy to the CFRP sheet*
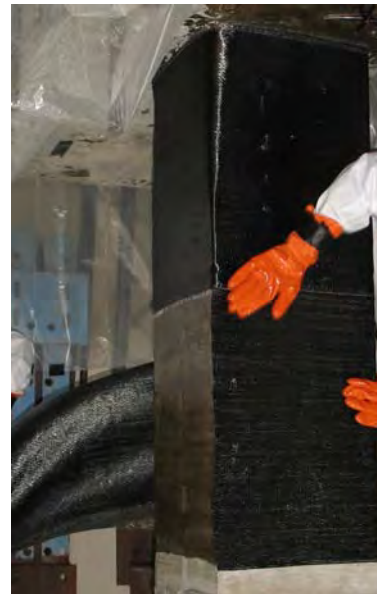


*Figure B.9  Application of 2 layers CFRP jacket (left) and 1 layer CFRP jacket (right)*

*Figure B.10  Application of the CFRP anchor (left) and spreading the fan on the surface (right)*



*Figure B.11  Application of the CFRP patch on the fans of the anchors*

*Figure B.12 Buckled bars and opened ties in bottom of column (left) and removing of the damaged bars (right)*



*Figure B.13  Protruded bars to installation of the splices*

*Figure B.14  Alignment of existing column with the new bar to be installed (left) and short splices with the new longitudinal bars to be joined with the existing bars (right)*

*Figure B.15  New bars applied together with the splices*



*Figure B.16  Tightening of the bottom bolts of splices using ratchet wrench*

*Figure B.17  Form for the casting of concrete in bottom of column*



*Figure B.18  Casting of concrete: slump 6.5in*

*Figure B.19  Placing of concrete in form*



*Figure B.20  Edge of new and existing concrete*

*Figure B.21  Specimen RC-1R after removal of the form.*

## B.2  ASCE41-13 BACKBONE CURVES FOR EACH DIRECTION
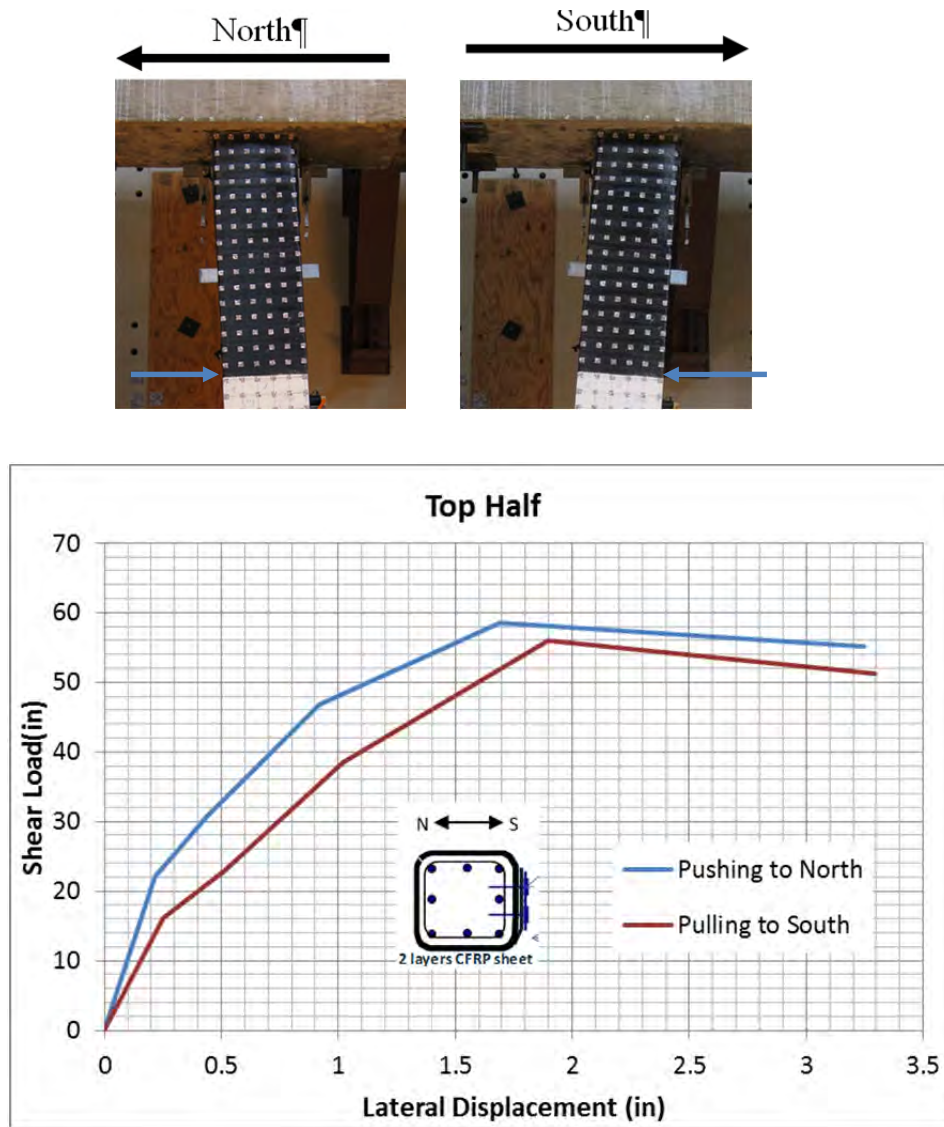


*Figure B.22  ASCE41-13 backbone curve for each direction of load, RC-1R Top Half*
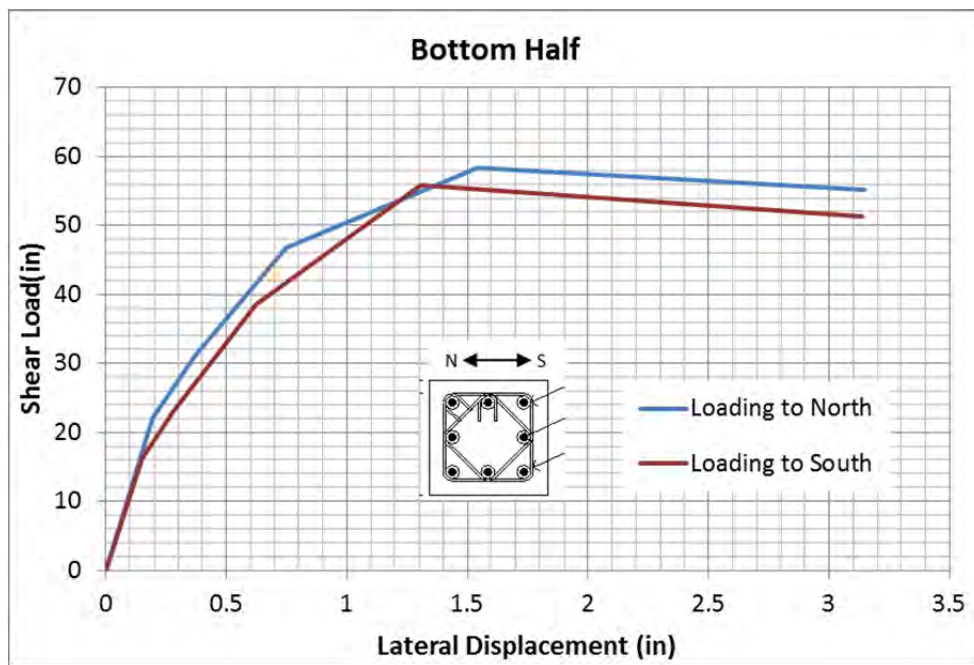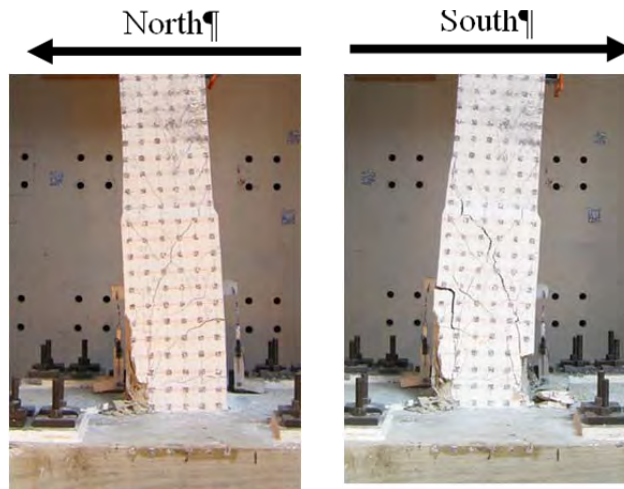
*Figure B.23  ASCE41-13 backbone curve for each direction of load, RC-1R Bottom Half*

# APPENDIX C

# Retrofit Process for RC-2R-SMS and RC-2C-LMS and Additional Graphs of Test Results

**C.1   RETROFIT PROCESS**



*Figure C.1   Severely damaged column RC-2 removed from the test setup*
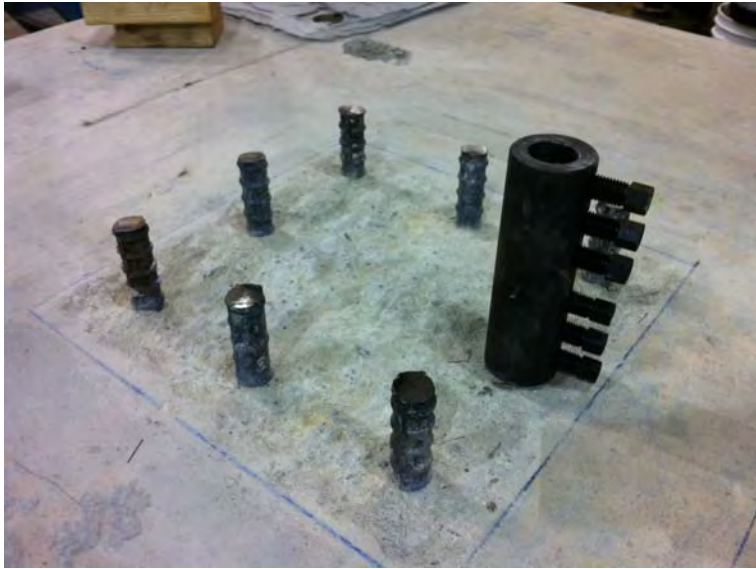
*Figure C.2  Concrete and bent bar removed*



*Figure C.3  Removing concrete for installation of mechanical couplers*

*Figure C.4  Protruding bars prior to installation of short splices (left) and long splices (right)*



*Figure C.5  Short (left) and long (right) mechanical splices in place.*

*Figure C.6  Grinding of bar end prior to inserting the bar into the splice*



*Figure C.7  Tightening of the splice bolts using impact wrench*

*Figure C.8  Reinforcement cages for columns*



*Figure C.9  Forms for the specimens*

*Figure C.10  Concrete placement: slump 3.5in*



*Figure C.11  Placement of concrete in forms*

*Figure C.12  RC-2R-SMS (left) and RC-2R-LMS (right) after removing the forms*

# APPENDIX D

# Retrofit Process for RMW-R1 and RMW-R2

**D.1    PROCESS TO REPAIR THE MASONRY WALL**



*Figure D.1   Condition of RMW after initial tests*

*Figure D.2  Installation of the reinforcement for the concrete ring (RMW-R1)*



*Figure D.3  Form for the concrete ring*

*Figure D.4  Concrete placement, slump: 6.5in*



*Figure D.5  Placement of the concrete ring*

*Figure D.6  Concrete ring after removal of form (left) and corner before repair with mortar (right)*



*Figure D.7  Mixing of dry mortar mix with water(left) and corner toe after mortar applied (right)*

*Figure D.8  Drilling the holes for CFRP anchor application (left) and drilled holes with rounded edges (right)*



*Figure D.9  Cleaning the surface prior to application of CFRP sheet*

*Figure D.10  CFRP anchors for the bottom corners*
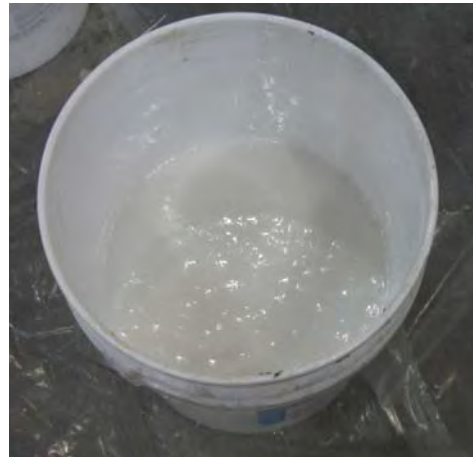


*Figure D.11  Mixing components to prepare epoxy for CFRP application*

*Figure D.12 Application of the epoxy on front surface*



*Figure D.13  Application of the epoxy on the back surface*

*Figure D.14  Application of the epoxy on CFRP strips*



*Figure D.15  Application of CFRP strip on back side*

451

*Figure D.16  Saturation of CFRP anchor with epoxy*



*Figure D.17  Insertion of CFRP anchor into the drilled hole*

*Figure D.18  Saturation of CFRP diagonal strips with epoxy*



*Figure D.19  Installation of CFRP anchor*

*Figure D.20  Application of the epoxy on the strip for the CFRP U-patch*



*Figure D.21  Application of the CFRP U-patch over the fan anchors*

# APPENDIX E

# Quality Control of the Material Used

**E.1 COMPRESSION STRENGTH OF CONCRETE FOR RC-1R**

Standards ASTM C39 / C39M was used to determine compressive strength of cylindrical specimens.

*Table E-1 Compressive strength of cylinders for RC-1R*

|  | Load (kip) | Strength (ksi) |
|---|---|---|
| Cylinder 1 | 51.91 | 4.13 |
| Cylinder 2 | 49.57 | 3.95 |
| Cylinder 3 | 37.63 | 3.00 |
| Cylinder 4 | 58.28 | 4.64 |
| Cylinder 5 | 54.26 | 4.32 |
| Cylinder 6 | 55.38 | 4.41 |
| Cylinder 7 | 47.65 | 3.79 |
| Cylinder 8 | 50.18 | 4.00 |
|  | **Average** | 4.03 |
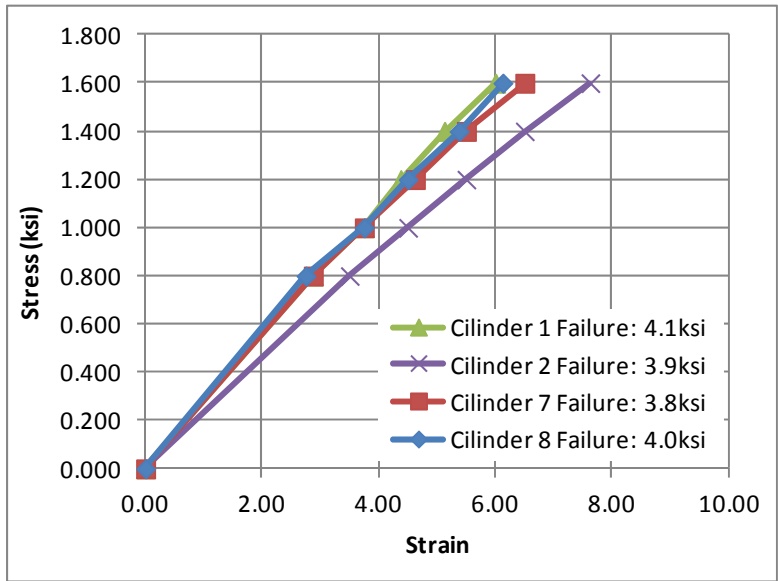
*Figure E.1  Stress vs. Strain for test of concrete cylinders for RC-1R*



*Figure E.2  Compressive test of concrete cylinder in universal machine*

### E.2    COMPRESSION STRENGTH OF CONCRETE FOR RC-2R-SMS
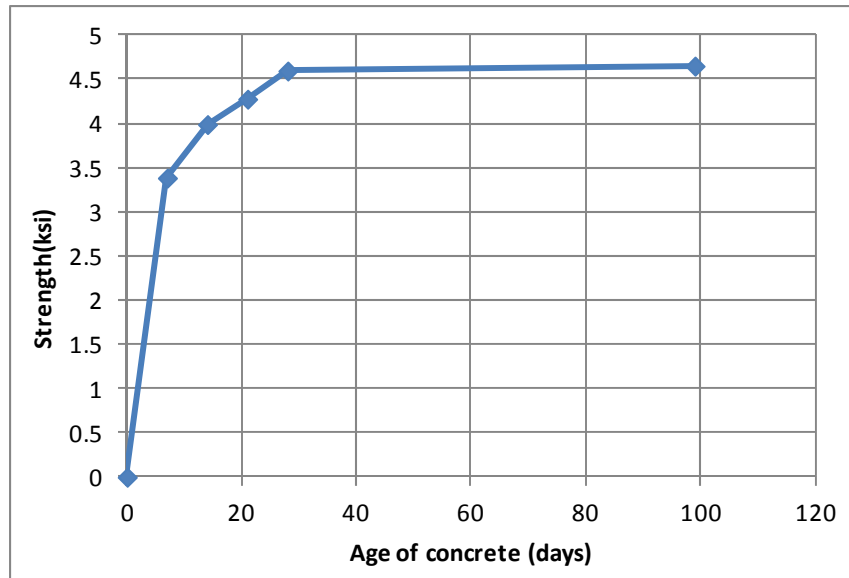


*Figure E.3  Compressive stress of the concrete cylinders by age for RC-2R-SMS*

*Table E-2 Compressive strength of the cylinders for RC-2R-SMS*

|  | Time (days) | Load (kip) | Strength (ksi) |
|---|---|---|---|
| Cylinder 1 | 7 | 42.50 | 3.38 |
| Cylinder 2 | 14 | 50.10 | 3.99 |
| Cylinder 3 | 21 | 53.70 | 4.28 |
| Cylinder 4 | 28 | 57.70 | 4.59 |
| Cylinder 5 | 99 | 58.40 | 4.65 |
| Cylinder 6 | 99 | 59.90 | 4.77 |
|  |  | Average | 4.67 |

## E.3    COMPRESSION STRENGTH OF CONCRETE FOR RC-2R-LMS
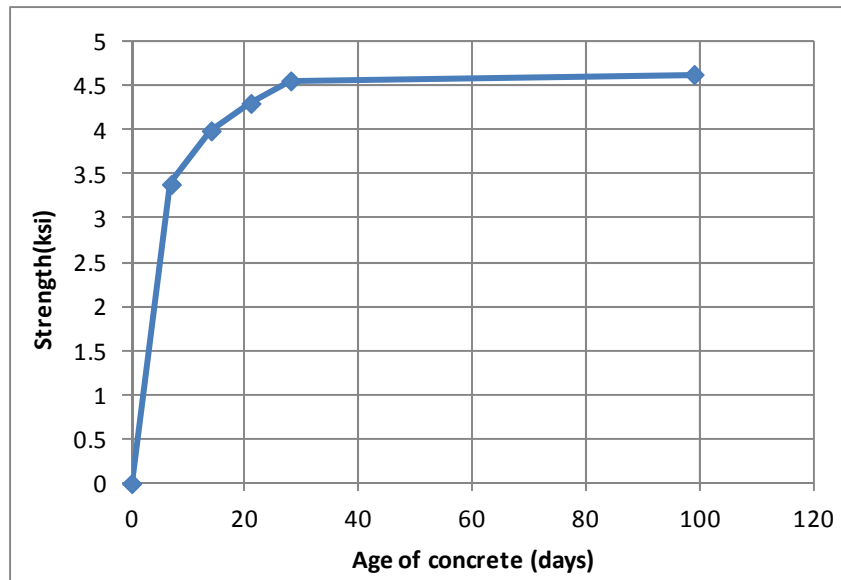


*Figure E.4  Compressive strength of the concrete cylinders by age for RC-2R-SMS*

*Table E-3 Compressive strength of the cylinders for RC-2R-LMS*

|            | Time (days) | Load (kip) | Strength (ksi) |
|------------|-------------|------------|----------------|
| Cylinder 1 | 7           | 42.50      | 3.38           |
| Cylinder 2 | 14          | 50.10      | 3.99           |
| Cylinder 3 | 21          | 54.00      | 4.30           |
| Cylinder 4 | 28          | 57.20      | 4.55           |
| Cylinder 5 | 99          | 58.10      | 4.63           |
|            |             | Average    | 4.59           |

## E.4   COMPRESSION STRENGTH OF CONCRETE RING IN RMW-R1

*Table E-4 Compressive strength capacity of the cylinder for RMW-R1 Concrete Ring*

| Average Diameter |
|---|
| 4.000 in |
| Area |
| 12.57 in2 |

|  | Load (kip) | Stress (ksi) |
|---|---|---|
| Cilinder 1 | 49.97 | 4.0 |

## E.5 TENSION TEST FOR STEEL BAR COUPONS

Tensile properties of #8 bars were determined according to ASTM A370-12.

*Table E-5 Axial force at rupture of bar A-615 Grade 60 for RC-1R Bottom Half*

**Bars #8**                    0.79 in2

|         | Load (kip) | Strength (ksi) |
|---------|------------|----------------|
| Bar 1   | 87.4       | 110.63         |
| Bar 2   | 82         | 103.80         |
|         | Average    | 107.22         |

*Table E-6 Axial force at rupture of bar A-615 Grade 60 for RC-2R-SMS and RC-2R-LMS*

**Bars #8**                    0.79 in2

|         | Load (kip) | Strength (ksi) |
|---------|------------|----------------|
| Bar 1   | 88.9       | 112.53         |
| Bar 2   | 87.5       | 110.76         |
| Bar 3   | 87.5       | 110.76         |
| Bar 4   | 82.3       | 104.18         |
| Bar 5   | 82         | 103.80         |
| Bar 6   | 83         | 105.06         |
|         | Average    | 107.85         |
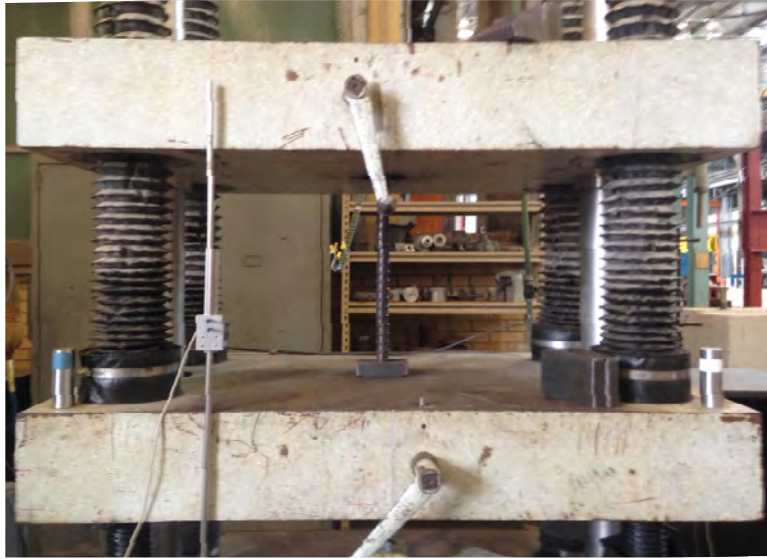
*Figure E.5  Axial tension test for steel bars*

## E.6   CFRP MATERIALS

Standard ASTM D7565 / D7565M - 10 was used for reference to obtain the tensile force capacity and ultimate tensile strain of CFRP material.
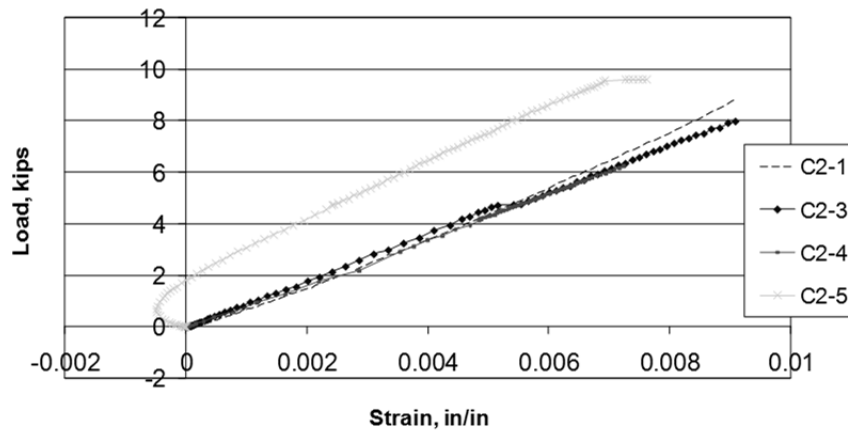


*Figure E.6  Measured strain on CFRP coupons (Pham 2009)*

*Table E-7 Summary of results of tests performed*

| Coupon | Width | Thickness | Ultimate load | Ultimate stress | Ultimate strain | Average E |
|--------|-------|-----------|---------------|-----------------|-----------------|-----------|
|        | in    | in        | Kip           | ksi             | in/in           | ksi       |
| C2-1   | 2     | 0.04      | 8.4           | 105.00          | -               | -         |
| C2-2   | 2     | 0.04      | 8.94          | 111.75          | 0.0091          | 12280     |
| C2-3   | 2     | 0.04      | 8.05          | 100.63          | 0.0091          | 11058     |
| C2-4   | 2     | 0.04      | 6.26          | 78.25           | 0.0072          | 10868     |
| C2-5   | 2     | 0.04      | 9.6           | 120.00          | 0.0076          | 15789     |
| C2-6   | 2     | 0.04      | 8.85          | 110.63          | -               | -         |
| C2-7   | 2     | 0.04      | 9.19          | 114.88          | -               | -         |
|        |       |           | **Average**   | **106.00**      | **0.00825**     | **11402** |

*Figure E.7  Rupture of the coupon*

*Table E.8 CFRP sheet properties provided by the manufacturer*

| Property | ASTM Method | Typical Test Value | Design Value |
|---|---|---|---|
| Ultimate tensile strength (ksi) | D-3039 | 143 | 121 |
| Elongation at crack failure | D-3039 | 1.00% | 0.85% |
| Tensile modulus (ksi) | D-3039 | 13900 | 11900 |
| Laminate thickness (in) | D-3039 | 0.04 | 0.04 |

463

*Table E.9 Epoxy properties provided by the manufacturer*

| Property | ASTM Method | Typical Test Value |
|---|---|---|
| **Tensile strength (ksi)** | D-638, Type 1 | 10.5 |
| **Tensile modulus (ksi)** | D-638, Type 1 | 461 |

## E.7   REPAIR MORTAR

*Table E.10 Properties provided by the manufacturer*

| Setting time, ASTM C191 | |
|---|---|
| Initial | Approx. 20 min. |
| Final | 20 - 40 min. |
| **Approx. water content / 60# bag** | 1 3/8 gal (5.2 L) |
| **Consistency** | gel-like |
| **Unit weight, lb/cu ft (kg/m3)** | 128 (2051) |
| **Compressive strength, ASTM C109 modified** | |
| 3 hours | 2000 psi (13.8 MPa) |
| 24 hours | 4000 psi (27.6 MPa) |
| 7 days | 5000 psi (34.5 MPa) |
| 28 days | 6000 psi (41.4 MPa) |
| **Slant shear, ASTM C882 modified** | |
| 24 hours | 1000 psi (6.9 MPa) |
| 7 days | 1500 psi (10.3 MPa) |
| 28 days | 2500 psi (17.2 MPa) |
| **Length change, ASTM C157 (typical)** | |
| 28 days, air | -0.10% |
| 28 days, water | 0.10% |

Compressive strengths of 2-in. mortar cubes were determined according to ASTM C780-11, which refers in turn to ASTM C109-11.

*Table E.11 Compressive strength of the repair mortar cubes for RC-1R Top Half*

| Cube Length | |
|---|---|
| | 2 in |
| Area | |
| | 4.00 in2 |

| | Load (kip) | Stress (ksi) |
|---|---|---|
| Cube 1 | 17 | 4.3 |
| Cube 2 | 16 | 4.0 |
| Cube 3 | 18 | 4.5 |
| | Average | 4.3 |

*Table E.12 Compressive strength of the repair mortar cubes for RMW-1R*

| Cube Length | |
|---|---|
| | 2 in |
| Area | |
| | 4.00 in2 |

| | Load (kip) | Stress (ksi) |
|---|---|---|
| Cube 1 | 15 | 3.8 |
| Cube 2 | 17 | 4.3 |
| Cube 3 | 16 | 4.0 |
| | Average | 4.0 |

*Figure E.8  Mortar cubes for compressive test*

# APPENDIX F

# Test Setup of Specimens

## F.1 RC-1R



*Figure F.1  Placement of L-frame setup on specimen RC-1R*

***Figure F.2  Lateral braces to prevent the out-of-plane deformation and stabilization of
L-frame setup***

## F.2 RC-2R-SMS AND RC-2R-LMS



*Figure F.3  View of specimen RC-2R-SMS showing test setup and instrumentation*

*Figure F.4  View of specimen RC-2R-LMS showing test setup and instrumentation*

*Figure F.5  Installation of rods on RMW-R2 and the L-frame setup*

# APPENDIX G

# Extension of the Test of RC-1R for Different Levels of Axial Load

## G.1 PROTOCOL OF LOAD

The graph of the protocol of deformation for this test for specimen RC-1R is shown in Figure G.1. In the cyclic loading test, specimen RC-1R was subjected to two cycles of lateral displacements at drifts of: $\pm 1/250$, $\pm 1/125$, $\pm 1/63$, $\pm 1/32$ and one cycle $\pm 1/17$ and finally pushed to north direction until the column could not hold the axial load (point (a) in Figure G.1). Afterwards the axial load applied to the column was reduced to 75 kips and the column pushed to north direction to (b), the axial load was further reduced to 35kips to (c), and finally the axial load was reduced to 5kips with failure at (d). The test was by displacement control.
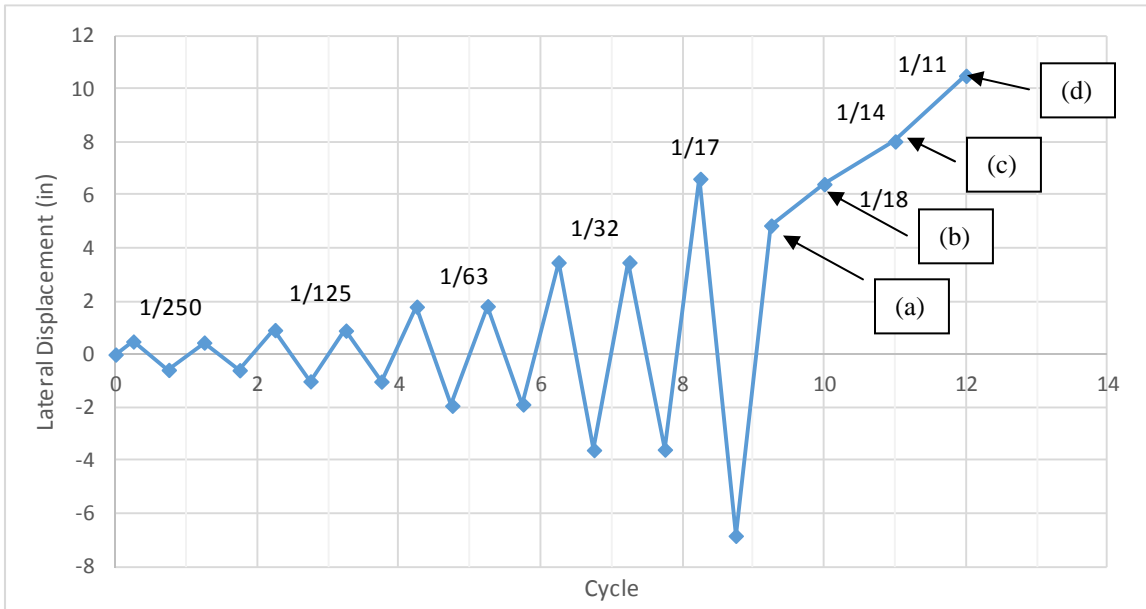
*Figure G.1 Load cycling for specimen RC-1R*

## G.2 RESULTS

The deformation presented was more predominant in the hinge zone, having larger lateral deformation at this level in comparison with the other levels of the specimen (Table G-1).. Condition of the column is shown in Figure G.2. Response of RC-1R under shear force and axial load is shown in Figure G.3 and Figure G.4

474
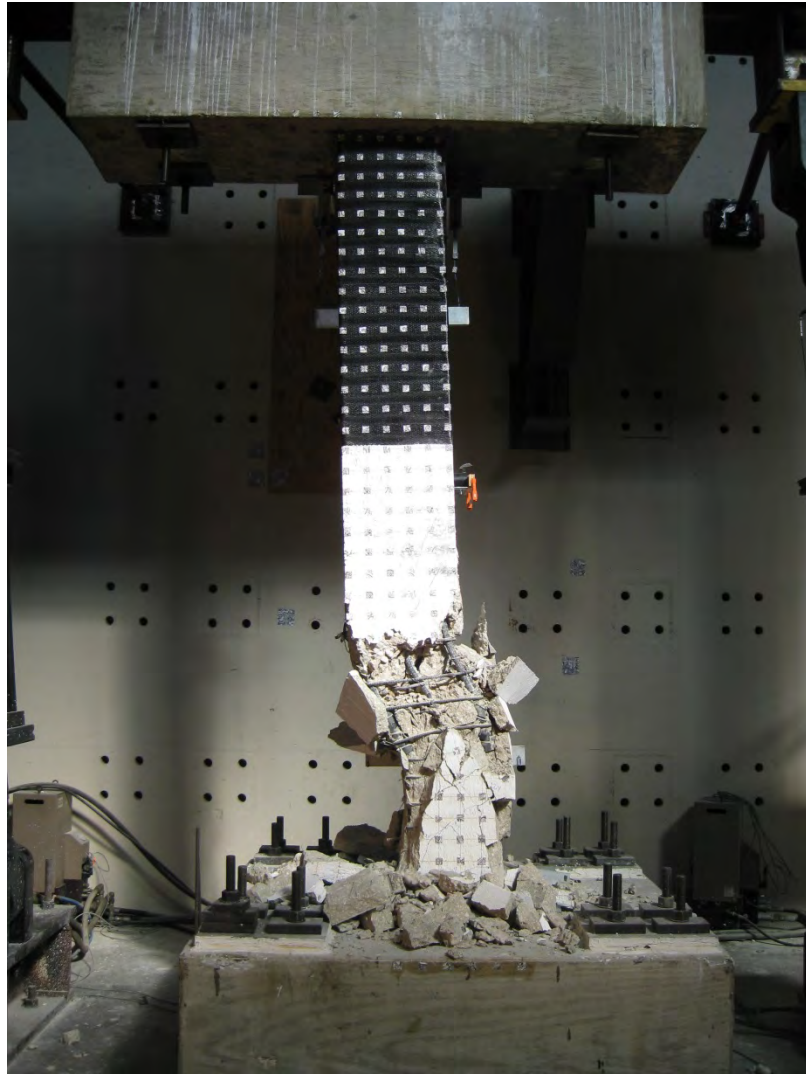
*Figure G.2 Condition of the specimen at maximum lateral displacement.*
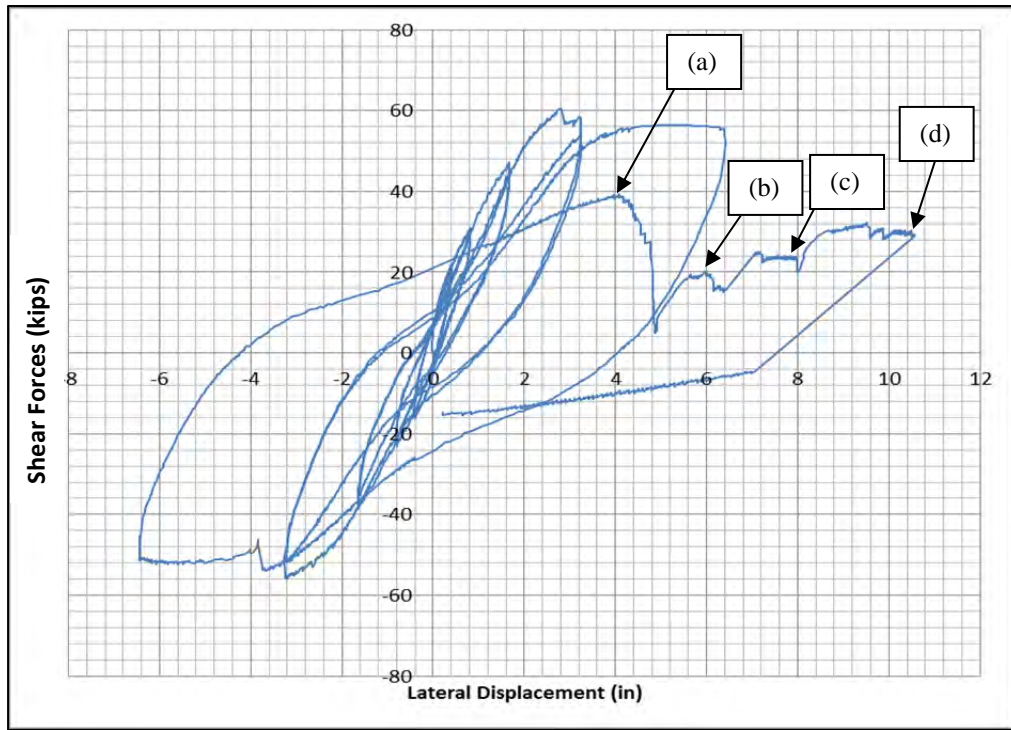
*Figure G.3 Shear-displacement response of column RC-1R*
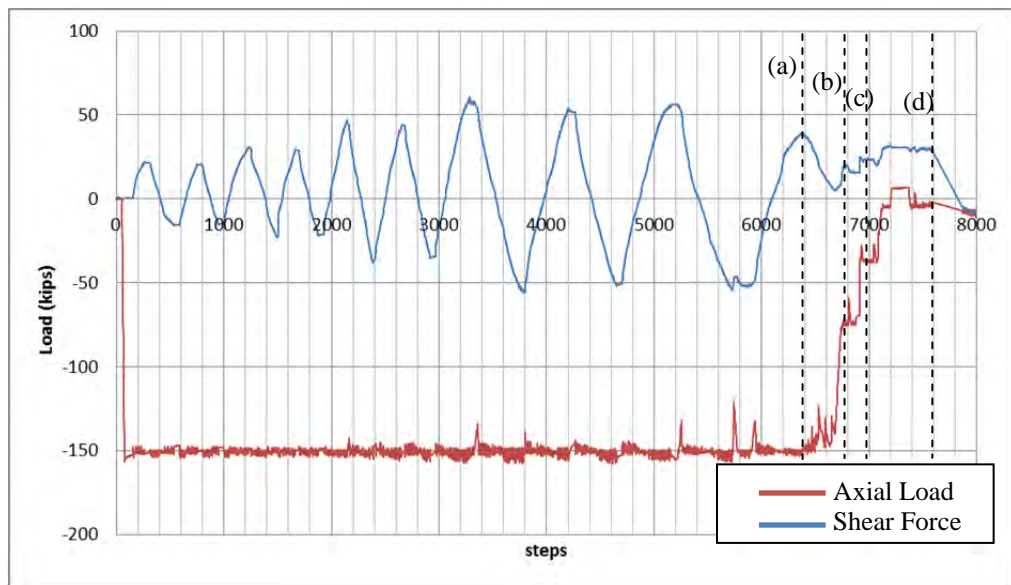


*Figure G.4 History of lateral and axial load for the test*

476

***Table G-1 Displacement and shear forces measured for each reduction of axial load during the test.***

| Step | Axial Load (kips) | Displacement (in) | Shear Force (kips) |
|------|-------------------|-------------------|--------------------|
| a | 150.00 | 4.20 | 39.00 |
| b | 75.00 | 6.10 | 19.37 |
| c | 37.00 | 8.00 | 24.00 |
| d | 5.00 | 10.60 | 32.30 |

When the axial load was reduced to the 75kips, the cover spalled specially at the west and east faces of the column at the zone of the shear hinge, being exposed the top mechanical splice. It was noticing that one stirrup with 135deg hooks began to be opened; it was located just above the superior level of mechanical splices. The concrete keep being crushed at the shear hinge region.

When the axial load was reduced to 37.5 kips, crushing of the concrete at the hinge region kept increasing starting to lose compression capacity the concrete and the longitudinal reinforcement started to provide entirely the resistance capacity under axial and flexural effects; and the transversal reinforcement began to provide the resistance capacity under shear effects to the specimen. The concrete cover of north and south face of bottom part of the column felt down.

Finally, the axial load was reduced until 5kips to continue the test. Most of the lateral deformation occurred on the hinge region (Figure G.5).
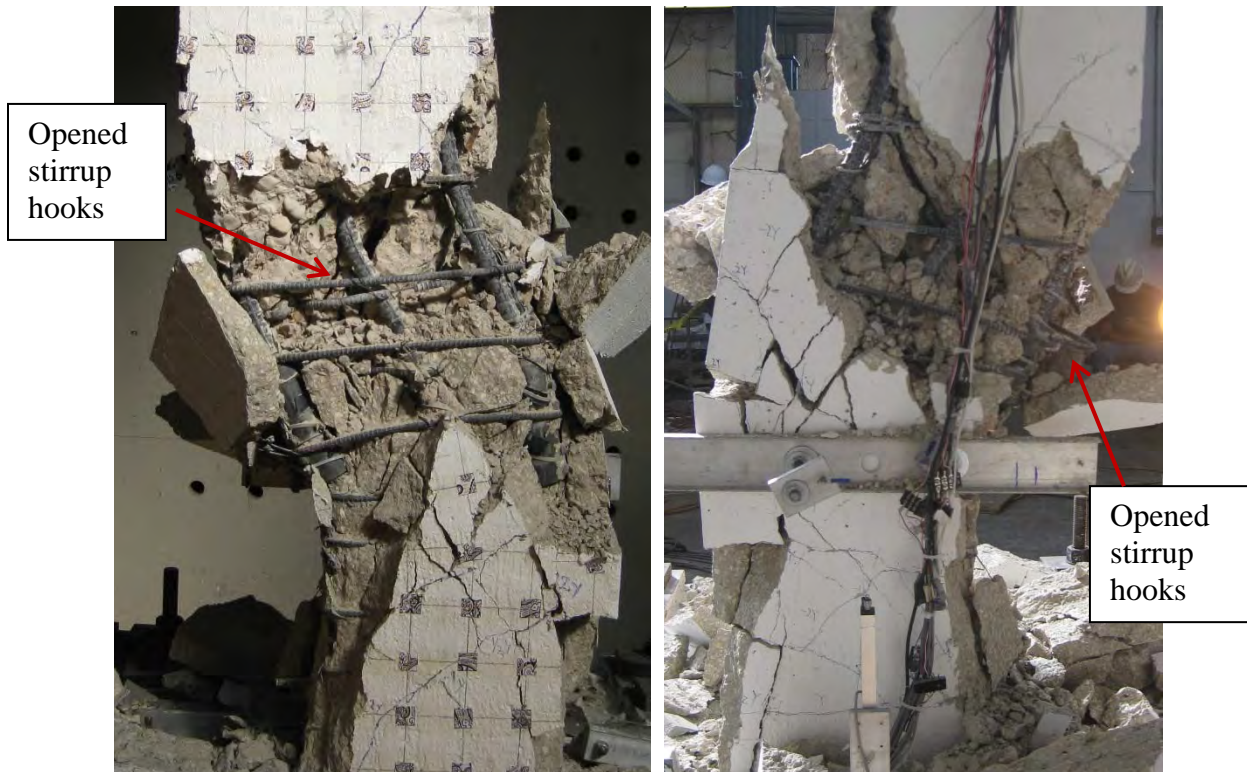
*Figure G.5 West (left) and East (right) faces of the specimen at hinge region.*

The CFRP jacketing system performed tremendous very well during the test. No damaged was presented either at the maximum load and lateral displacement applied to the column. The CFRP anchors remained into the concrete column. There was presented some debonding on the 2 layers zone of CFRP sheers (Figure G.6). They were recognized by knocks on the surface of this zone. The corners did not presented signal of cutting of the CFRP because the fill drilled on along those corners regions of the column. Lifting was presented on the top of the column.

478
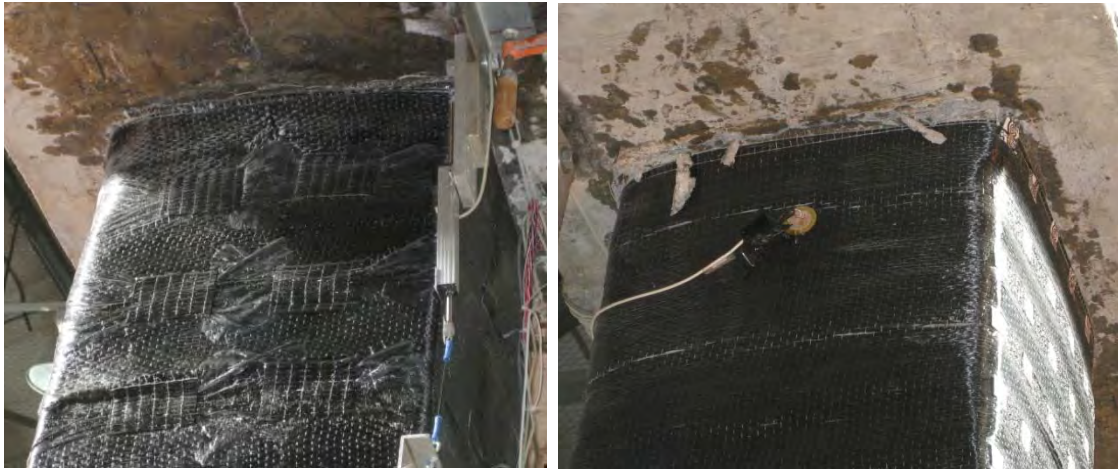
*Figure G.6 CFRP jacket in good conditions at the maximum lateral deformation reached.*

After the finishing the test, the CFRP jacketing was removed to assess the condition of the column at top. Figure G.7 shows that the cover was crushed having different patterns of cracks. Additionally, the condition of the CFRP anchors was checked as it can be seen in Figure G.8. Anchorage remained in good condition too.

*Figure G.7  Condition of top of column after the removing of CFRP jacket*



*Figure G.8  Condition of CFRP anchor after test*

# APPENDIX H

# Vision System Used for Measurement of Displacements

## H.1 DATA ACQUISITION

Cameras with high resolution were used. They captured pictures of the specimen when it was loaded and deformed. The pictures were collected into the computer which monitored the displacement of the target pasted on the surface of each specimen. Figure H.1 shows the cameras and computers from the data acquisition system. Vision System was developed at FSEL with the capability to measure deformations on the column surface.



***Figure H.1 Data acquisition system – High resolution cameras (right) and two PCs for each camera used (left)***

## H.2 SPECIMEN MS-L1

Figure H.2 shows the strains calculated from the measurement of displacement using the Vision System. It can be seen the tendency of the increment of strain when the specimen was loaded. Strain of top half (y00-y05), bottom half (y05-11), at the middle (y07-y05) and the total splice (y11-y00) are shown.
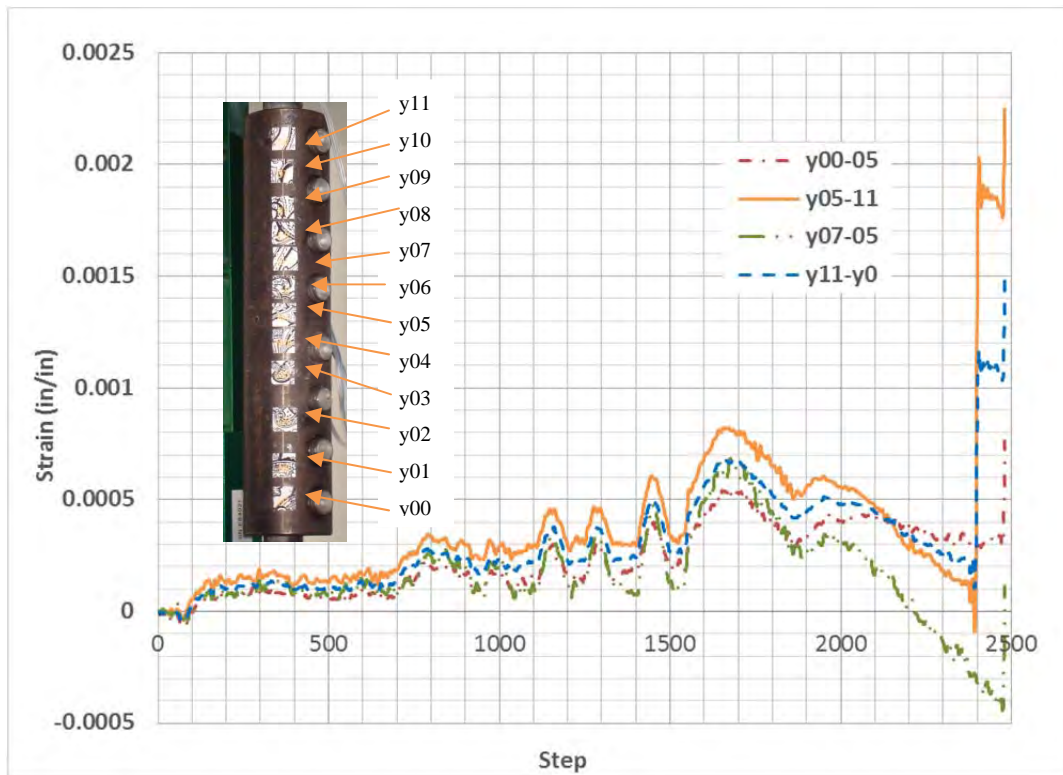


*Figure H.2 Strain measured by Vision System MS-L1.*

Figure H.3 shows the strain between targets. It can be seen that is difficult to define the behavior of the splice along its longitudinal axis. The strains were measured in the second peak displacement around step 1660.
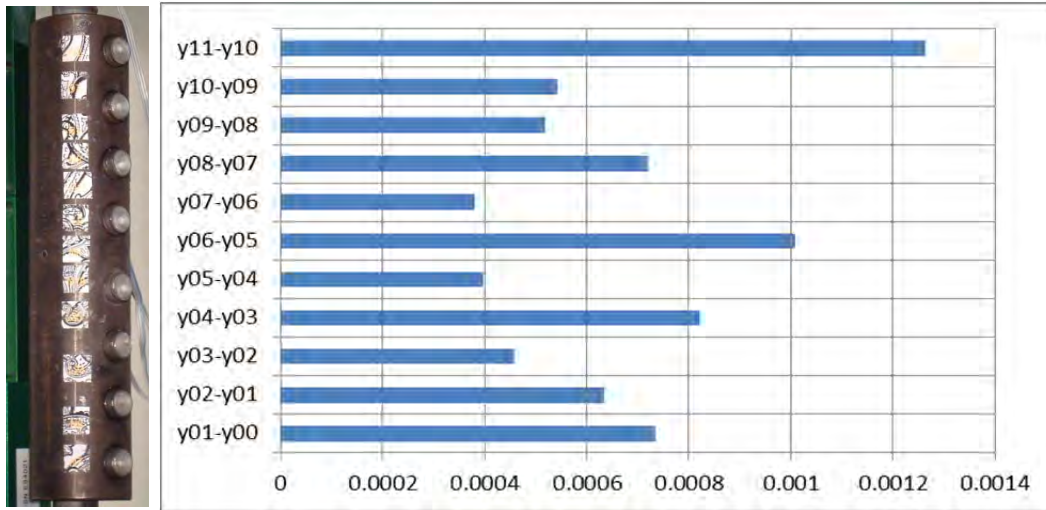


*Figure H.3   Strain reached at each gap between targets at failure*

## H.3 SPECIMEN MS-S1

Vision system was used also to measure the strain in the specimen MS-S1 for the tension cycle tests. It was the first test having a short coupler.

Figure H.4 shows the strain calculated from the measured displacements of target y06 and y00; and between targets y04 and y02. It can be noticed the tendency to increase when is loaded. However, the measurement was not able to capture a the strain value with precisely.
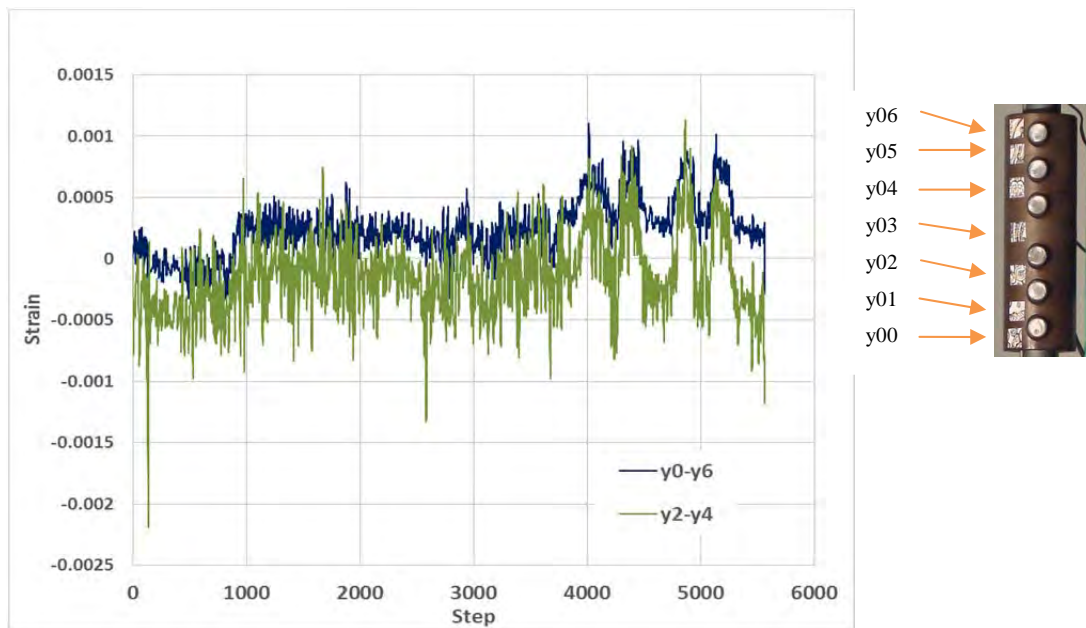


***Figure H.4  History of deformation strain (in/in) measured from both extreme targets (y00-y06) and middle of the slice (y02-y04)***

Figure H.5 shows the strain between targets y0-y3 (bottom half) and y3-y6 (top half). There was the same trouble with the sensitive of measurement of displacement of the targets. However, it can be noticed the tendency of increment of strain under the applied tension load.
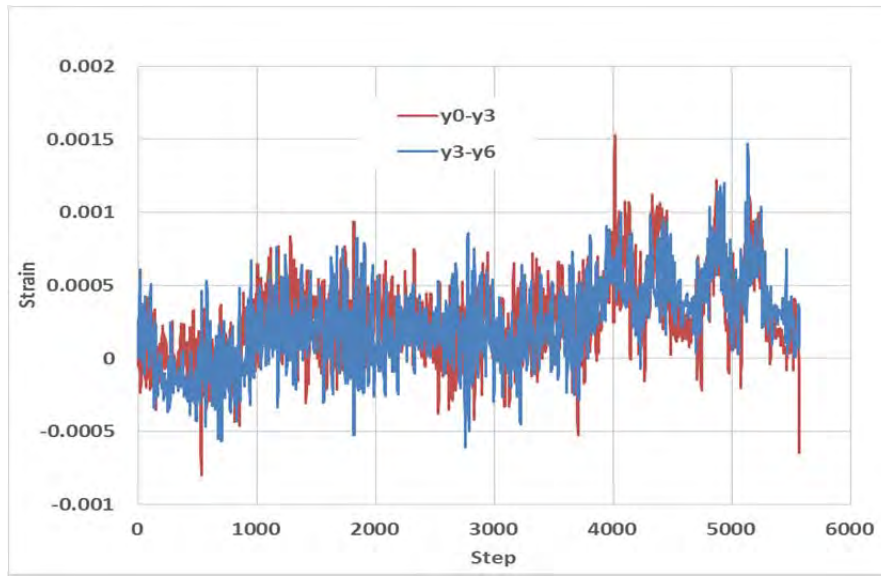


***Figure H.5  History deformation strain of top (y00-y03) and bottom half of the splice (y03-y06)***

485

## H.4 RETROFITTED COLUMN RC-1R

Vision System was used to calculate the curvatures at selected locations in specimen RC-1R. The curvatures were calculated from the measurement of displacements of each target.

In Figure H.6, the curvature along the specimen is plotted. It is observed that the bottom of the column has less rotation than the top. The increased section in the bottom increased the stiffness relative to that at the top of the column. Curvatures in bottom are the same for both cases of loading (north and south). It can be seen also that when the specimen is loaded to south and the zone with the CFRP anchors at top is in tension, the curvature is less than the opposite case (specimen is loaded to north and the face is in compression). This indicates that the CFRP anchors helped to stiffen that portion of column.

Figure H.7 shows the deformation of RC-1R at the peak of each cycle. The % drift ratio reached is shown in the figure.

Figure H.8 and Figure H.9 show the moment-curvature relationship at top of column. The curvature of the sections at 3.5in and 16in below the concrete beam are plotted. The difference in curvatures between loading to the north and south can be observed.

Figure H.10 and Figure H.11 show moment-curvature relationships of section at the bottom of column, one 3.5in above the foundation and the second 14.5in above the foundation also. The curves are nearly the same in each direction.
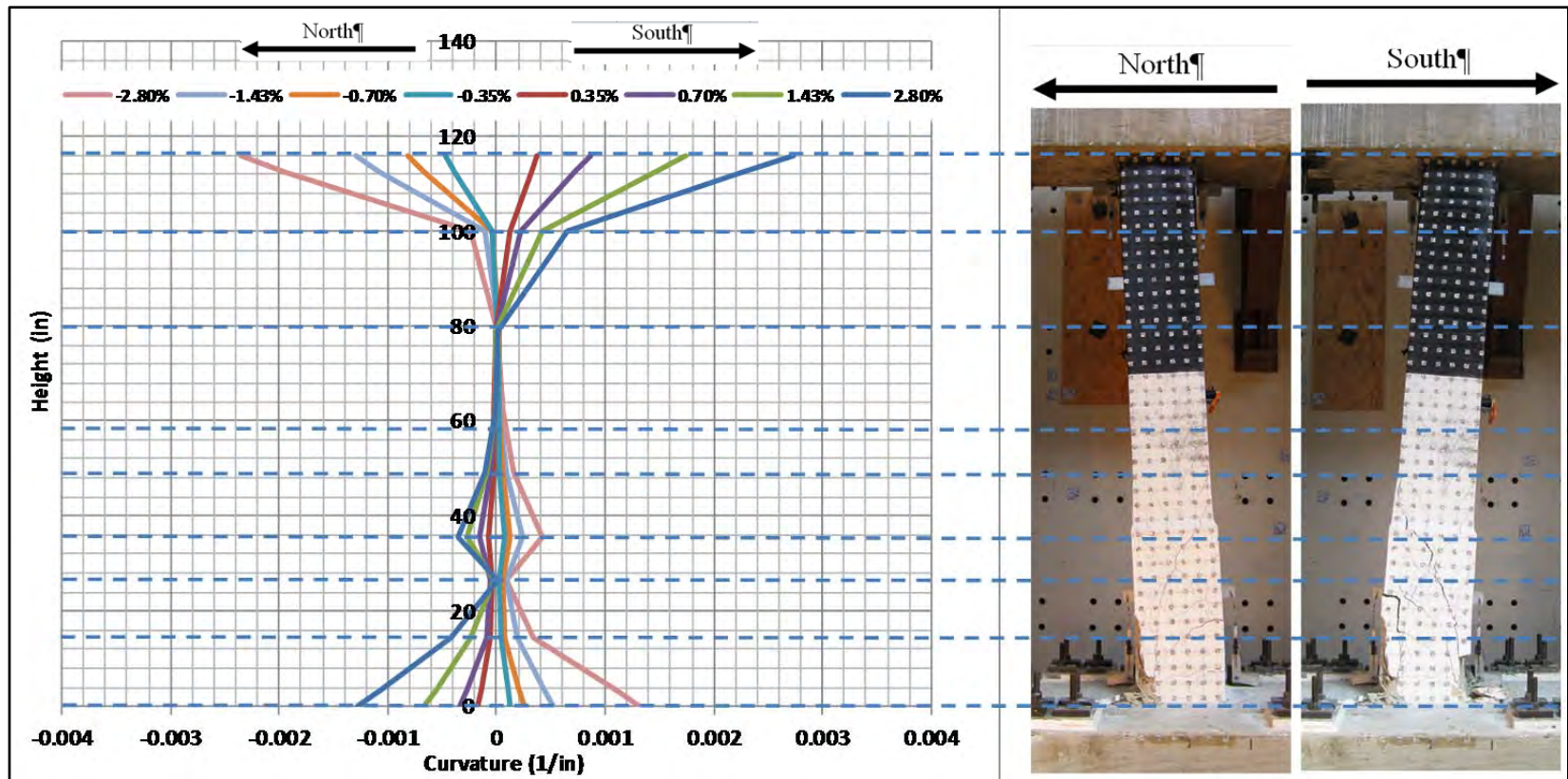
*Figure H.6  Measured curvature for RC-1R*
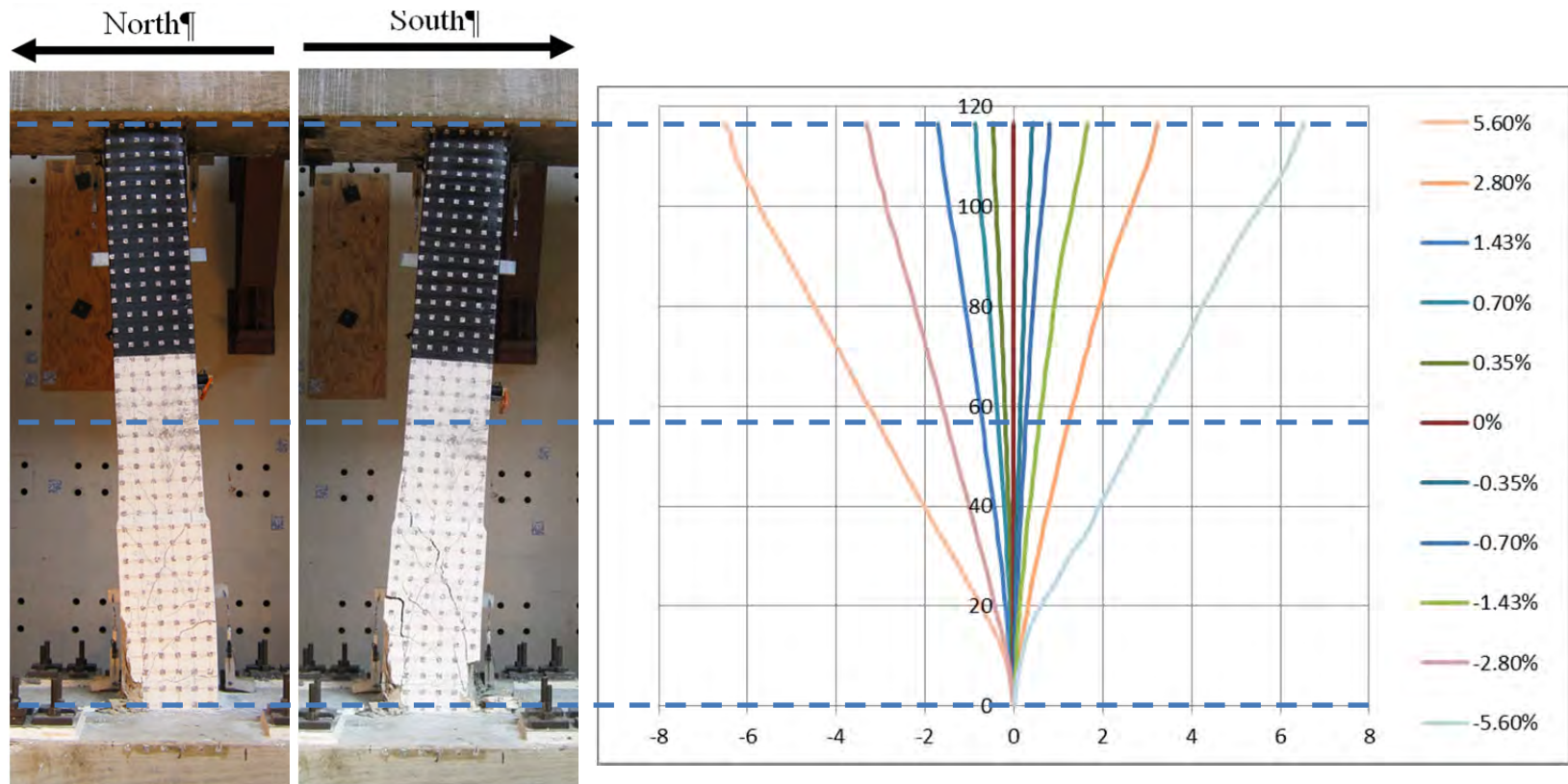
*Figure H.7  Measured lateral displacement for RC-1R*
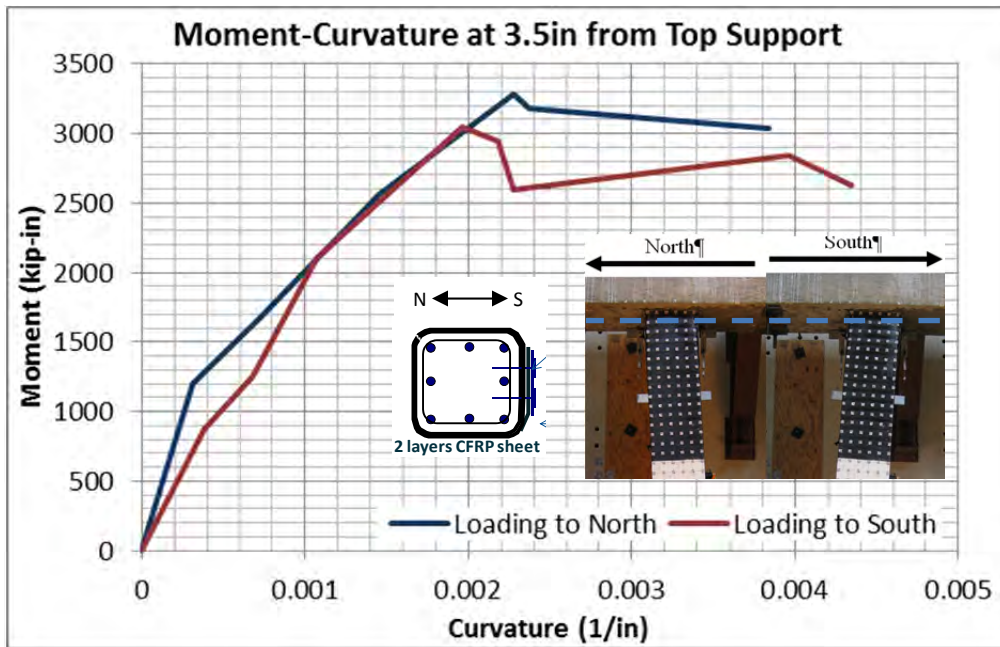
*Figure H.8. Moment vs. curvature in 3.5in from top of RC-1R*
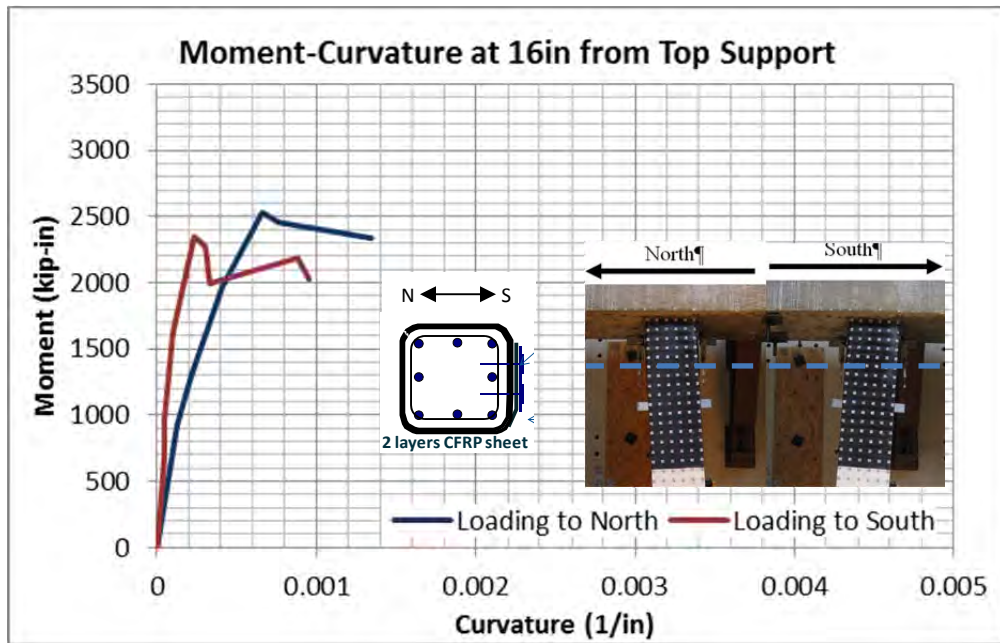


*Figure H.9  Moment vs. curvature in 3.5in from top of RC-1R*

489
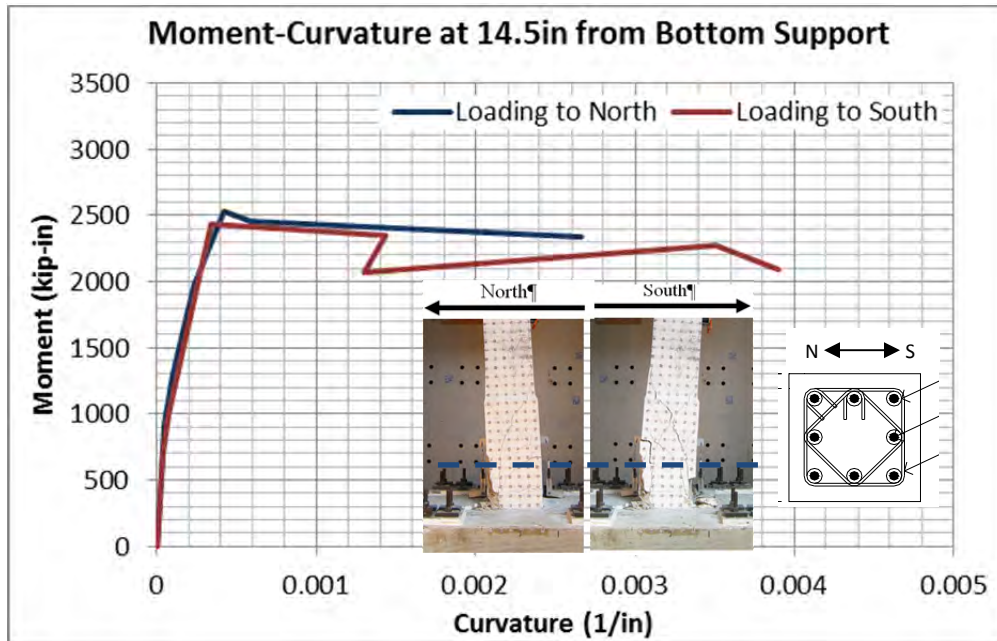
*Figure H.10. Moment vs. curvature in 14.5in from base of RC-1R*
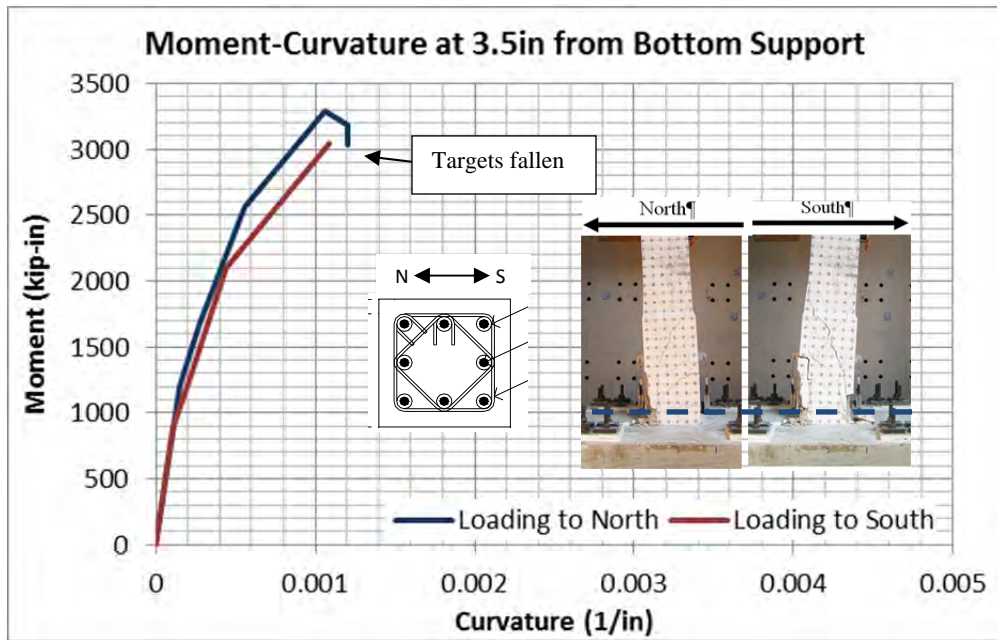


*Figure H.11  Moment vs. curvature in 3.5in from base of RC-1R*

490

## H.5   RETROFITTED COLUMN RC-2R-SMS

The curvature calculated from the displacement of Vision System targets are plotted at the peak of each cycle represented by % drift in Figure H.12. In general they were symmetric since the cross-section was symmetric also. As expected, larger rotations developed at the bottom.
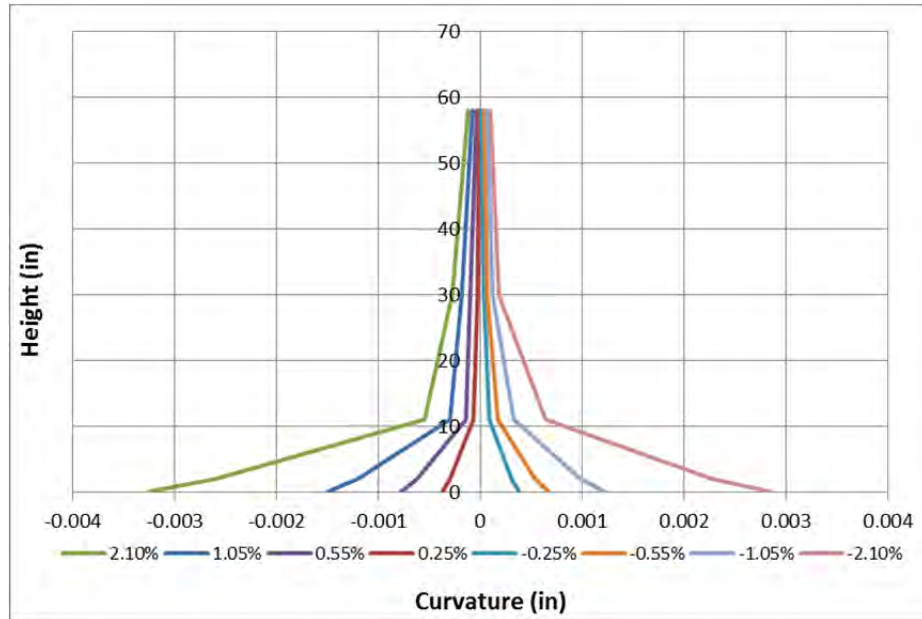


***Figure H.12   Measured curvature for RC-2R-SMS***

Figure H.13 shows the graphs of moment-curvature at two levels. The first at 2" above the foundation and the second was at a level 1" above the short splices. It can be seen that the curves are also symmetric.
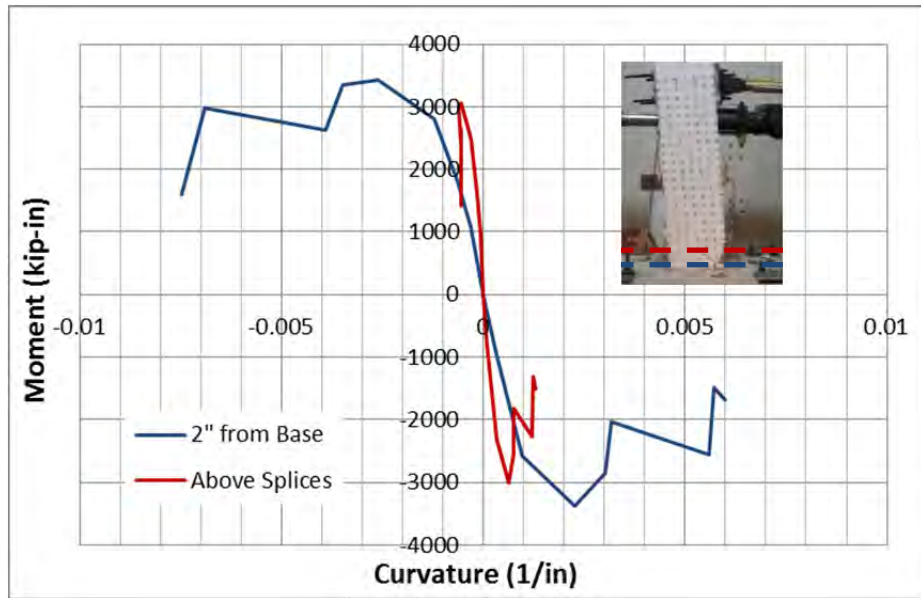
*Figure H.13. Moment vs. curvature in RC-2R-SMS*

## H.6 RETROFITTED COLUMN RC-2R-LMS

In Figure H.14, curvatures are plotted for RC-2R-LMS, rotations close to the base are larger than at the top.
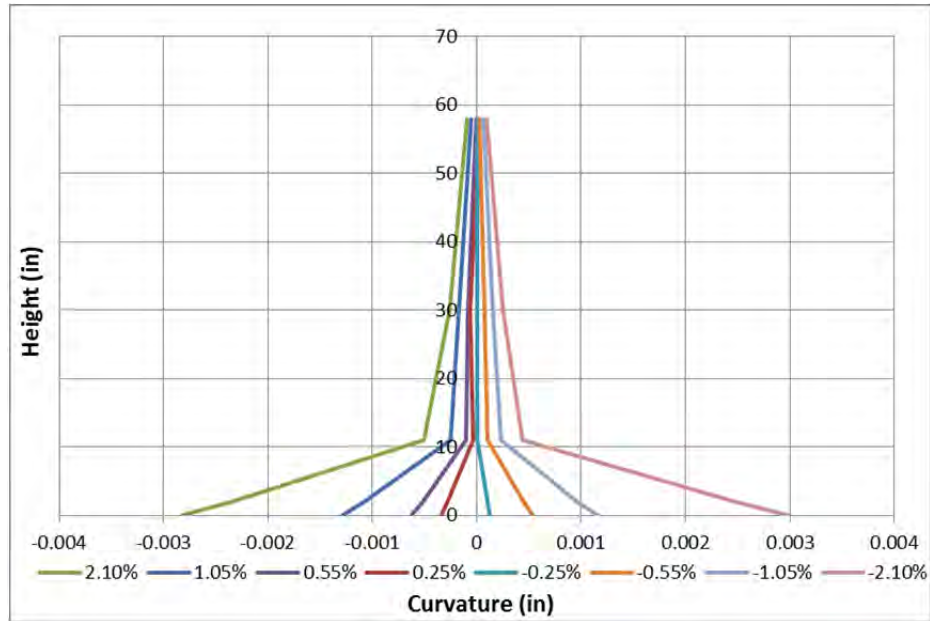


*Figure H.14  Measured curvature for RC-2R-LMS*

Figure H.15 shows the graphs of moment-curvature at two levels. The first at 2" above the foundation and the second was at a level 1" above the long splices. It can be seen that the curves are also symmetric.
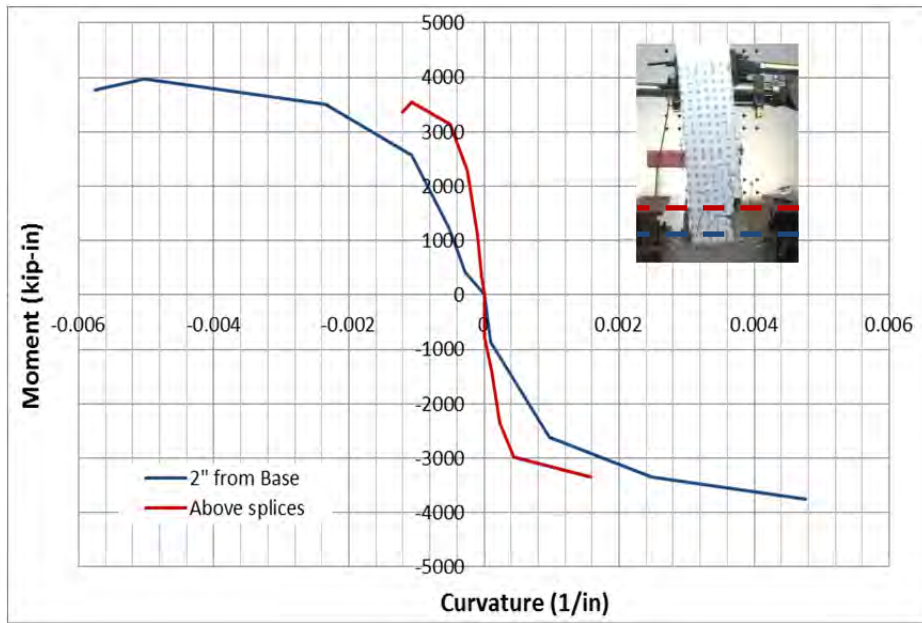
*Figure H.15. Moment vs. curvature in RC-2R-LMS*

# APPENDIX I

# Test Program Mechanical Splices

## I.1 FIRST SET OF MECHANICAL SPLICES

### I.1.1 Specimen 2 - Long Mechanical Splice MS-L2

MS-L2 was formed by a long mechanical splice and two #8 bars. During torqueing of the last rounded end bolt, the coupler cracked to the third bolt as shown in Figure I.1. Tightening of the rounded point bolt was stopped before the bolt head fractured. It was subsequently found that the steel and this coupler did not meet the standards of the manufacturer as is not being used to manufacture couplers. Even though the coupler was cracked, it performed very well and was therefore included in the Appendix I.



***Figure I.1 Crack in coupler after bolt tightening.***

### I.1.1.1 Dimensions of the specimen MS-L2

Specimen MS-L2 has the same dimensions as MS-L1 discussed in Chapter 3. Figure I.2 shows a sketch of the specimen MS-L2. Each bar connected with mechanical splice has a length of 5 into the splice, similar than MS-L1 case. The total length of the specimen between clamps of the universal machine was 30 in length.
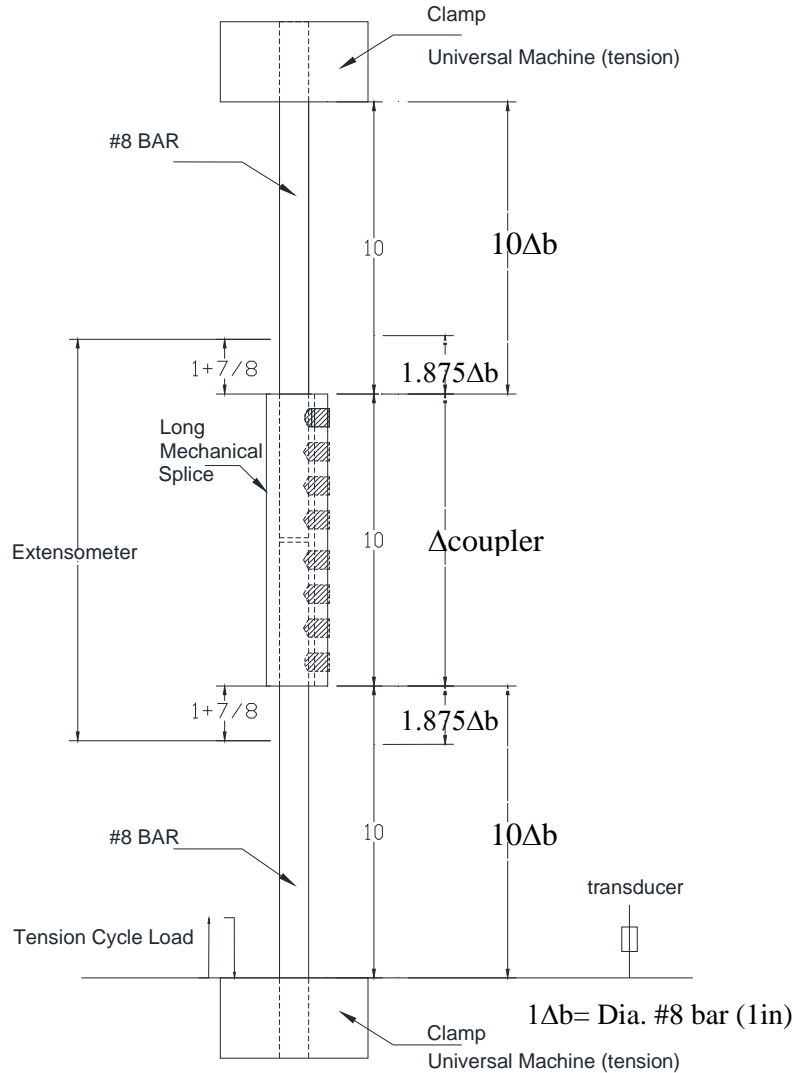


**Figure I.2 Sketch of MS-L2 in test machine**

### I.1.1.2  Instrumentation for the test for MS-L2

Having the measuring of deformation and observed the pattern of failure from the first test for one long mechanical splice, the objectives of measurement were to determinate:

a) General behavior of the mechanical splice and the bars, Axial load vs. Deformation of the specimen formed by the long mechanical splice and the two bars.

b) Mechanical behavior pattern under axial load for the deformation before failure of the mechanical splice and the portion of bar next to the splice. An extensometer has been used being 16"lenght with 2" gage. The length of the stroke extended to measure the mechanical splice and bar deformation is 14in ($3.75\Delta b + \Delta coupler$) as Figure I.2 shows. The distance between the exterior edge of the splice and the extreme of the extensometer was $1.875\Delta b = 1 + 7/8$ in. Similar than MS-L1, the extensometer has been removed previous the failure of the bar. Figure I.3 also shows the location of this extensometer.
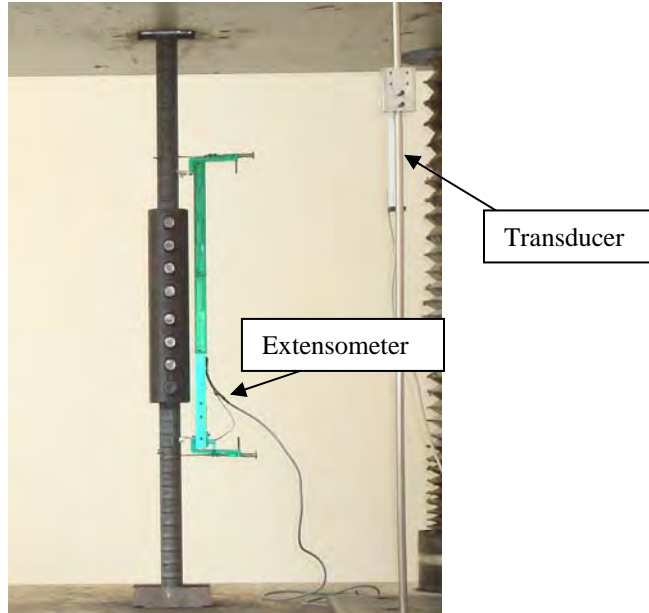
*Figure I.3  Instrumentation for Test*

### I.1.1.3   *Protocol of the test to MS-L2*

The specimen was subjected to two cycles of tension load of 20, 40, 50, and a final load to failure. The loading protocol for this test was established to capture the deformation under the linear range of behavior of the mechanical splice with the crack together with the bars, cycle deformation for pattern after the yielding and previous the hardening.
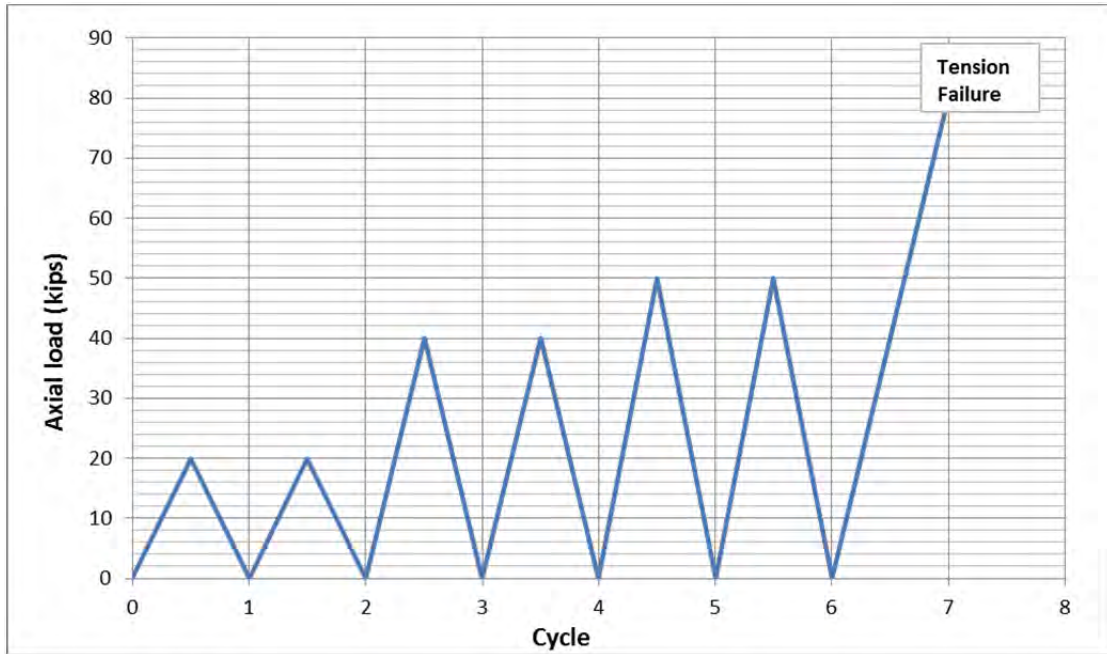
*Figure I.4  Protocol of load to the cycle tension axial load test for MS-L2*

### I.1.1.4   Results of the Cyclic Tension Axial Load Test for specimen MS-L2

The load rate applied for the two first cycles to 20kips, was approximately 7 kips/min; for the second set for 40kips load the speed was approximately 13 kips/min, the third set to 50kips the load rate was 17 kips/min. For the last cycle which was taken the failure, the speed was 3 kip/min.

Despite to have crack on the splice, there was not presented any fracture of any part of the long mechanical splice while the test. Figure I.5 shows the condition of the bolts and the crack did not have a larger opening than previous the test.

The extensometer's reading showed a linear response expected, indicating the need to correct the first measuring from the linear potentiometer. However the reading from the linear potentiometer indicates a pattern of two lines for the deformation before the yielding as Figure I.8 shows. It occurs by the crack on the splice and the condition of the bolt which is half of way tight. Despite that he bolts behaved as one piece together with the mechanical splice, it produced an unexpected deformation before the yielding.

The extensometer was removed at 40kips loading. The graph in Figure I.7 shows the pattern of deformation of the splice and the part of the bars next to the splice. The system reached the yielding at the load of 47kips, the yielding displacement was 0.35 in measured from the linear potentiometer and the hardening started at 0.50 in. The failure of the system was presented by the fracture of the bar at 4 in above the contact zone with the mechanical splice as Figure I.6 show. The failure was reached at 75.8 kips as maximum axial load and 2.15 in measured by the linear potentiometer.

No larger or wider cracks
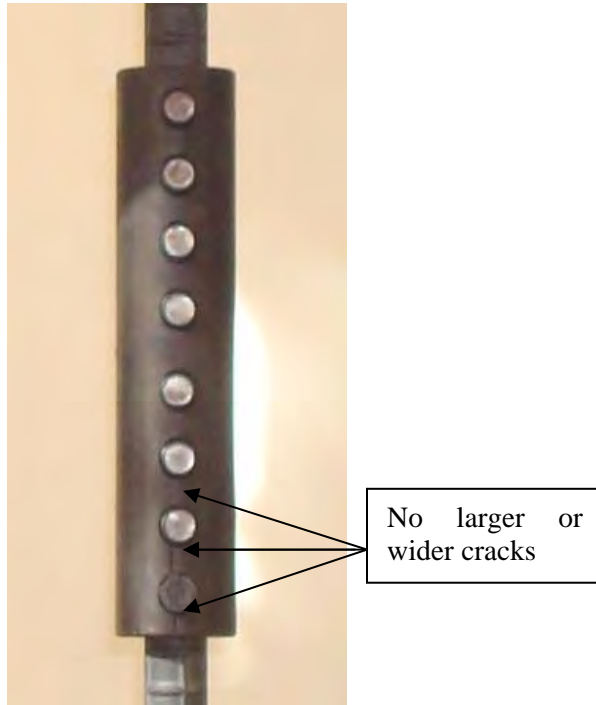
*Figure I.5 MS-S2 loaded 50Kips, bolt are in good conditions.*



LOAD: 75.80 Kips

4in

*Figure I.6 MS-L1 failure pattern.*
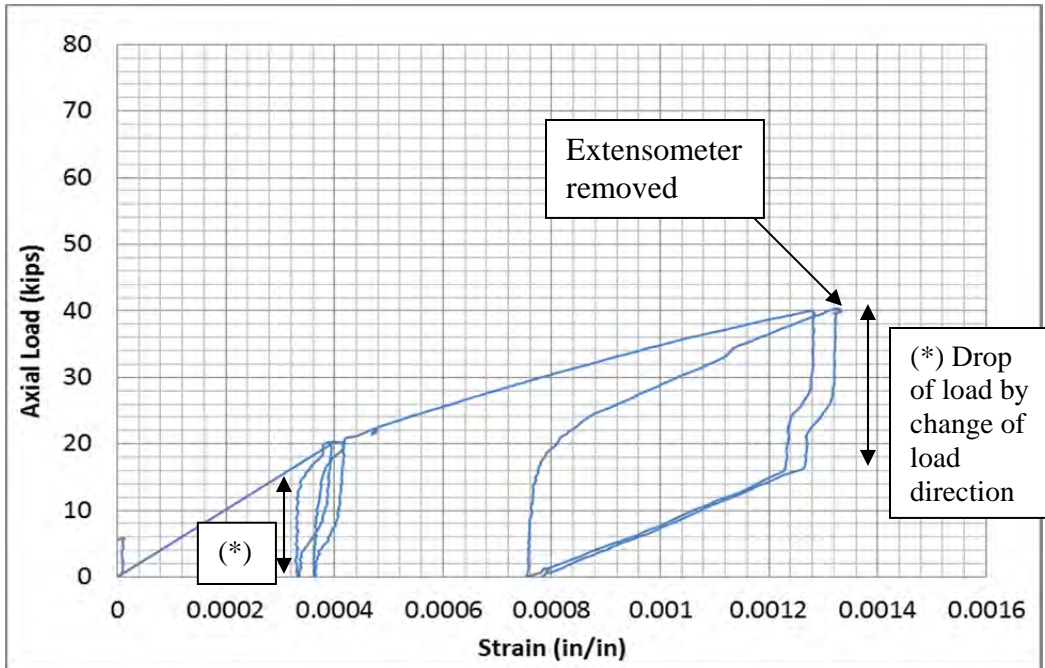
*Figure I.7  Deformation measured from the extensometer on MS-L2.*
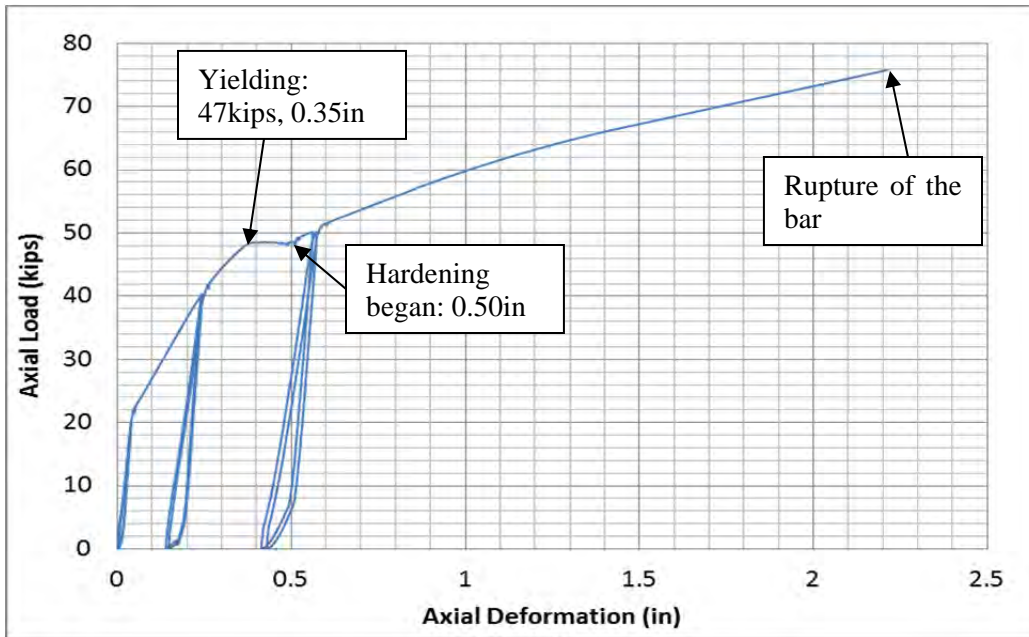


*Figure I.8  Deformation of the specimen MS-L2 measured by linear potentiometer*

502

### I.1.2 Specimen 3 - Short Mechanical Splice MS-S1

#### *I.1.2.1 Dimensions of the specimen MS-S1*

The sketch for specimen MS-S1 shows that each bar is inserted 3.4in into the sleeve (Figure I.9).
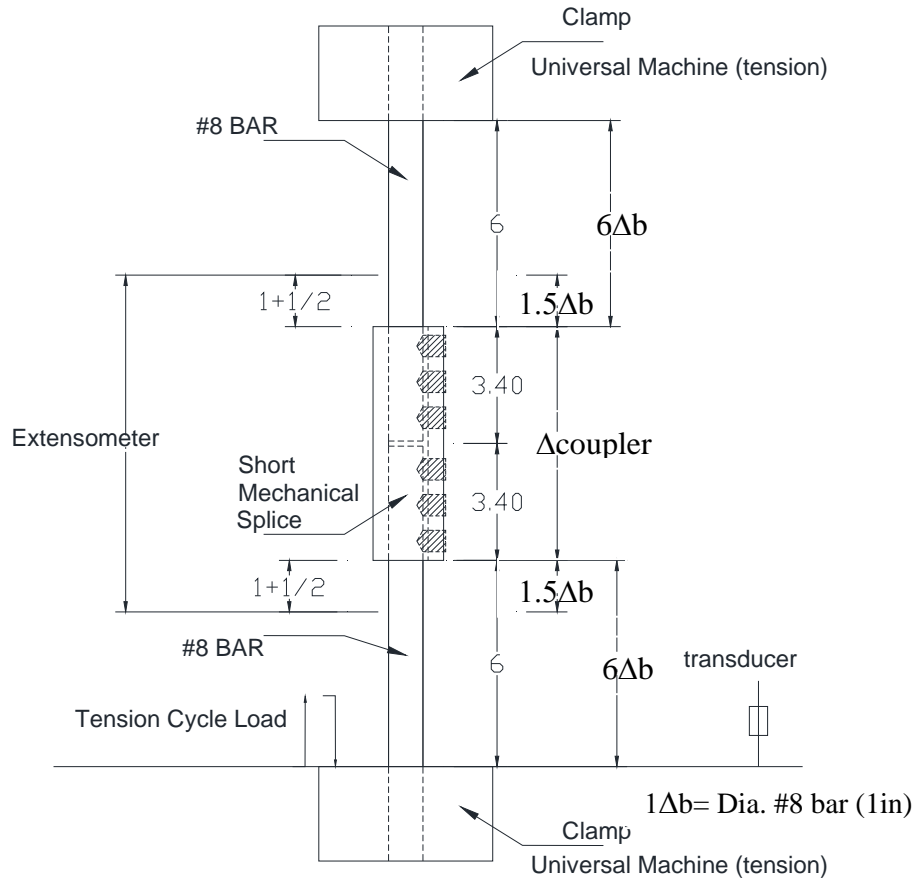


*Figure I.9 Sketch of the specimen MS-S1*

#### *I.1.2.2 Instrumentation for the test for MS-S1*

Since this was the first test to the short mechanical splices, the objectives were to determine:

503

a) General behavior of the specimen MS-S1, Axial load vs. Deformation of the specimen formed by the short mechanical splice and the two bars.

b) Differences of strain deformations on the bar and on the mechanical splice, one of the middle of this splice and other at level of the gap between the first and second bolt from top of the splice (Figure 3.38).

c) Deformation and strain along the mechanical splice. A system of cameras and paper target called Vision System were used. Measurement and details are shown in Appendix E. The targets can be seen in Figure 3.38
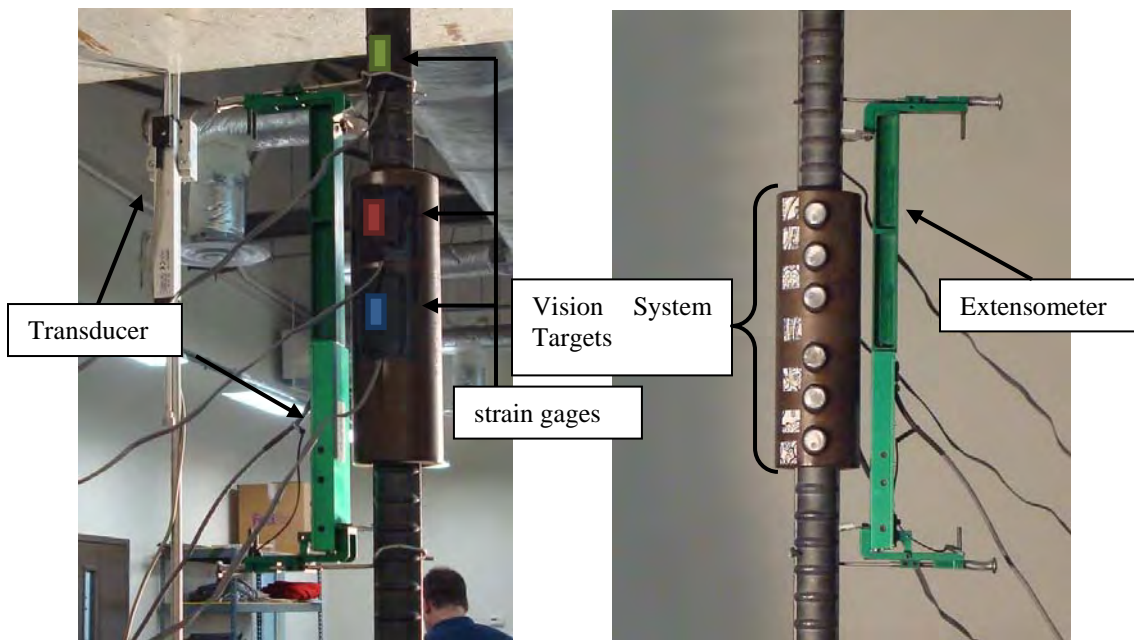


*Figure I.10  Instrumentation for MS-S1 test.*

### I.1.2.3   Protocol of the test to MS-S1

The specimen was subjected to two cycles of tension load of 20, 30, 40, 50, 60 kips and a final pushing load to failure. The loading protocol was established to capture the deformation in the linear range of behavior of the mechanical splice and bars, even posterior to the yielding and hardening. Figure I.11 shows the graph for the tension cycle test protocol for MS-S1.
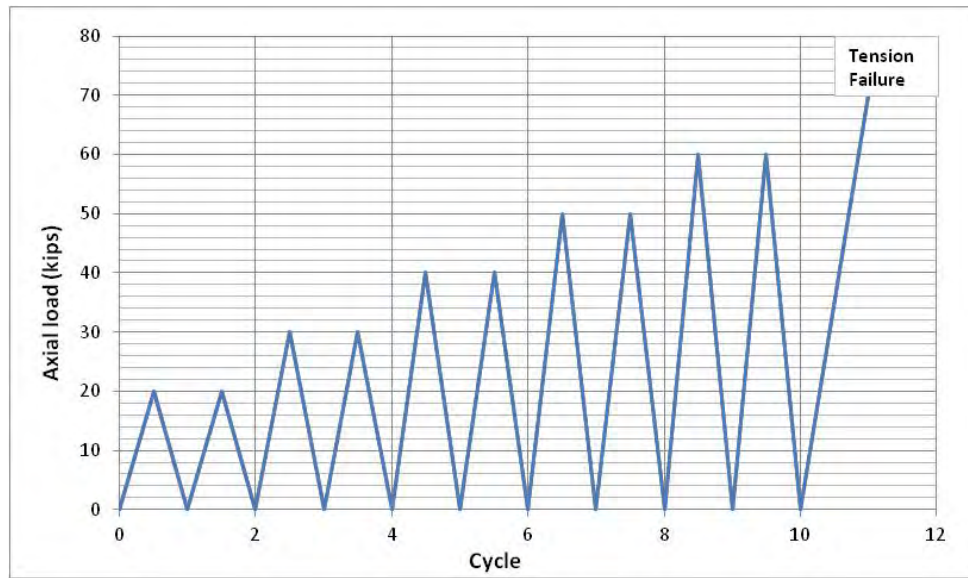


***Figure I.11  Protocol of load to the cycle tension axial load test of MS-S1.***

### I.1.2.4   Results of the Cyclic Tension Axial Load Test for specimen MS-S1

The load rate applied for the two first cycles to 20kips, was 6.7 kips/min; for the second set to 30kips load rate was approximately 5 kips/min, this last one faster specially for the short deformation, the third set to 40kips was 6.7 kips/min. The load rate to 50kips load was 5kip/min and for the cycle tension loading of 60kips the load rate was 7.5kip/min. For the last cycle which was taken to failure, the speed was 6 kip/min.

505

Similar than the cases of the long mechanical splices cases, while the test were performed, there was not presented any fracture of any part of the long mechanical splice. However, the pattern of deformation measured from the linear potentiometer presented a curve not related with the linear stiffness of the system as Figure I.15 shows at the first loads of the test. It can be noticed in Figure I.14 that the reading from the extensometer showed a linear response expected, indicating the needed to correct the first measuring from the linear potentiometer. This disruption was due the accommodation of the bars and the two extreme clamps of the universal test machine, same explanation for MS-L1 case. It was corrected for the envelope curve of this graph. The bolts behaved as one piece together with the mechanical splice.

The specimen started to yield at 40kip load, and measured from the extensometer the yielding displacement was 0.0018, the graph in Figure I.14 shows the pattern of deformation of the splice and the part of the bars next to the splice, measured through the extensometer. It was heard a sound from the specimen after the yielding. This sound appeared that the bar was broke internally, however no damage was found at this point.

The hardening started at 0.0052 of deformation read from the extensometer. The failure of the system was presented by the fracture of the bar at the contact zone with the mechanical splice as Figure I.12 and Figure I.13 show. The failure was reached at 68.98 kips as maximum axial load and 0.022 measured by the extensometer and 1.46 in measured by the transducer after the correction by the first deformation disruption or phasing, the envelope curves plotted in Chapter 3 contains this phase corrected. It can be also noticed that the bar failure occurred where the bar suffered a reduction of area in approximately 10% by the tightening of the bolt into the bar, as Figure I.12 shows.

*Figure I.12  Specimen MS-S1 after failure*
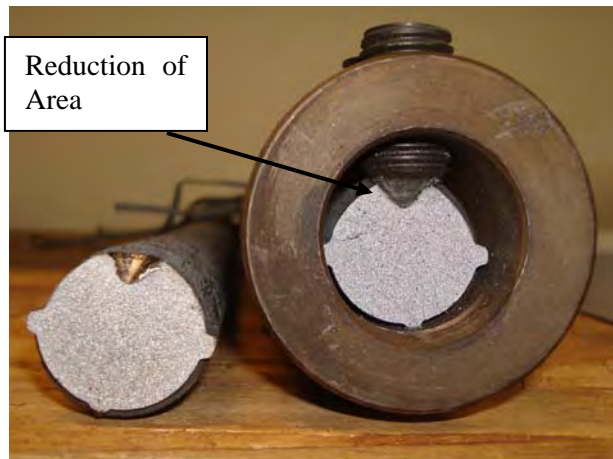


*Figure I.13 Cross Section of the bar with reduced area by the bolt tighten MS-S1*
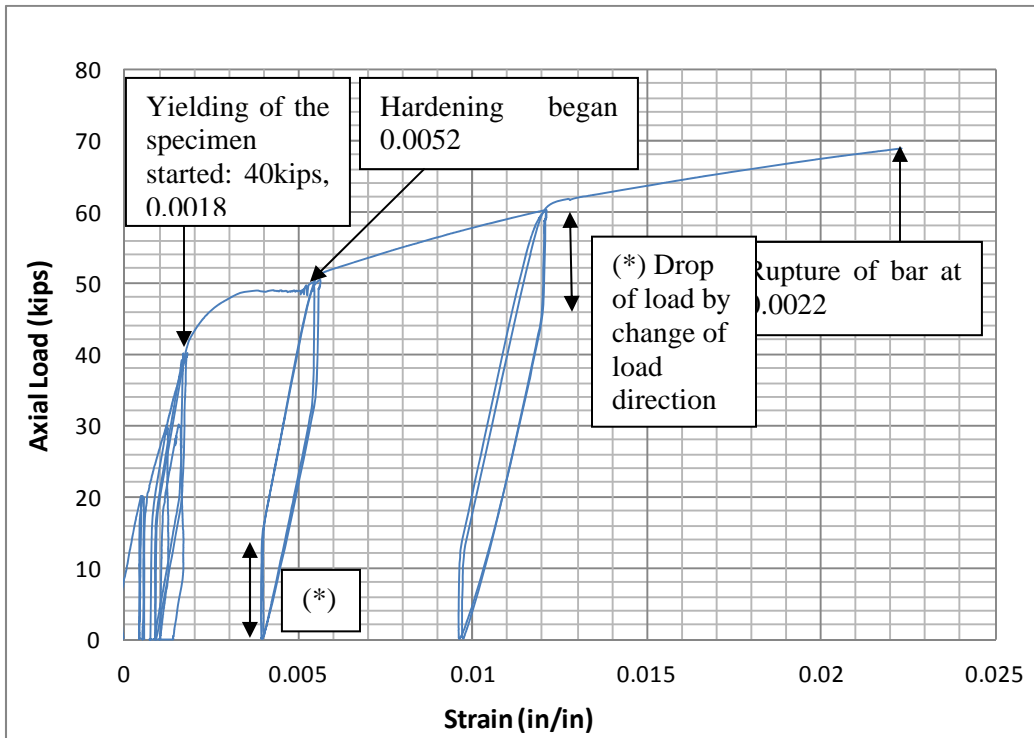
*Figure I.14  Deformation measured by the extensometer on specimen MS-S1*
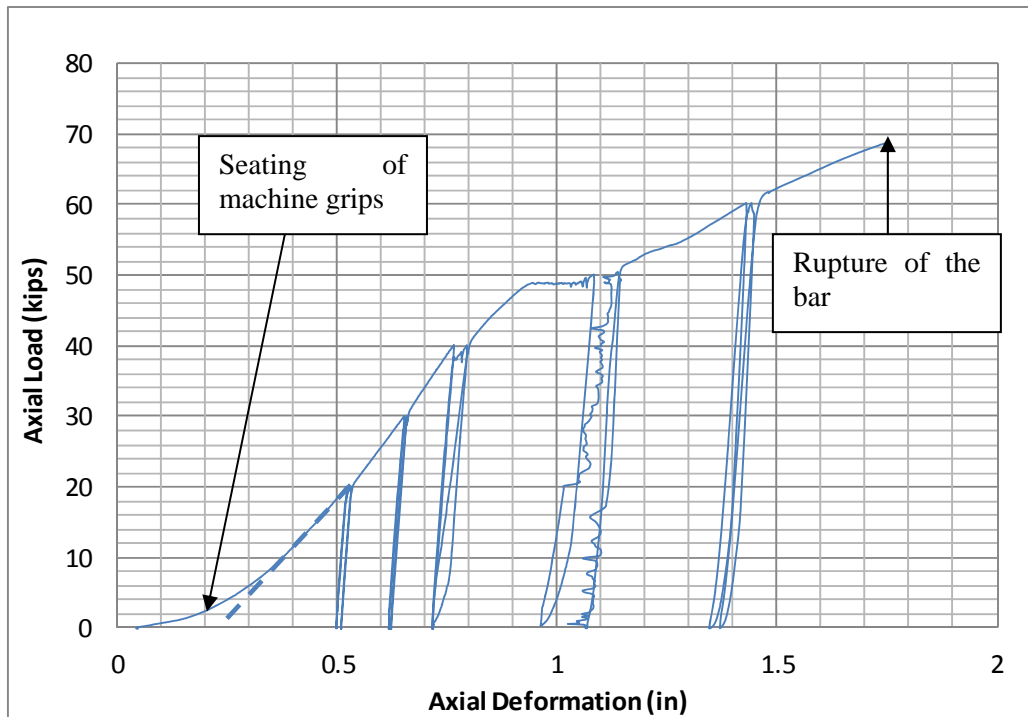
***Figure I.15  Displacement measured by the transducer for MS-S1***

The strain measured from the top bar presented similar pattern of deformation as the long mechanical splice case and values. Figure I.16 shows graph Axial Load vs. Strain, obtaining at strain value at yielding of 0.0024, close than the theoretical value of 0.0021 for steel Grade 60, and at the beginning of the hardening 0.011. Since there was not presented any quite difference on strain deformation pattern, neither of value for each face of the bar at MS-L1 case, indicating that the bolts on the splice do not make differences on strain at the bars, there was located one strain gage only at the face of the contact friction of the bar with the splice, as it can be seen at Figure I.10.
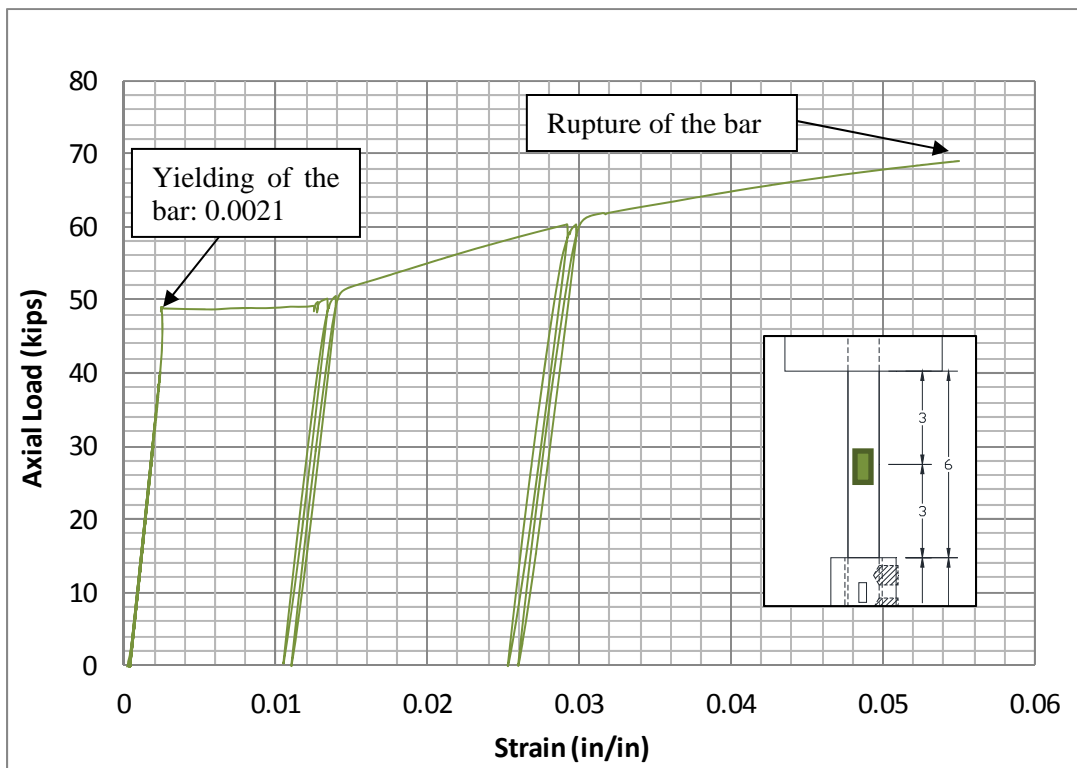
*Figure I.16  Strain deformation of the bar measured by straingage in MS-S1*

Figure I.17 shows the different behavior for strain deformation on the middle of the strain in comparison with another location, especially for deformation after the yielding of the system MS-S1. Strain between the $1^{st}$ and $2^{nd}$ bolts present similar initial stiffness than the middle of the splice. The strain also between the $1^{st}$ and $2^{nd}$ bolts presents a no-linear behavior under high loads specially after the yielding of the system, even presented compression strain when the system is unloading as Figure I.17 shows also. However the strain measured on the middle of the splice is constantly linear for all the developed of the test. The explanation is quite similar than MS-L1 case, because on the middle of the splice, both bars gathered by the splice are separated by a gap of less than 0.1in, no contact between both bars. The cross section area of the system at this level is provided only by the mechanical splice, being large area enough to be under its

510

yielding axial force value, for this case approximately 3times larger than yielding force value read. Instead, at other location, the cross section is formed by the splice and bar cross section, having a complex cross section. There was not compression strain presented on both locations for the strain gages.

No strain gage presented a strain value higher than 0.0021 for strain as Figure I.16 shows, the maximum values reached were 0.00057 between the third and second bolt, and 0.0011 at the middle of the splice. This indicates that the splice did not reach the yielding. It can be explained because the cross section area on both places has larger area than the bar only.
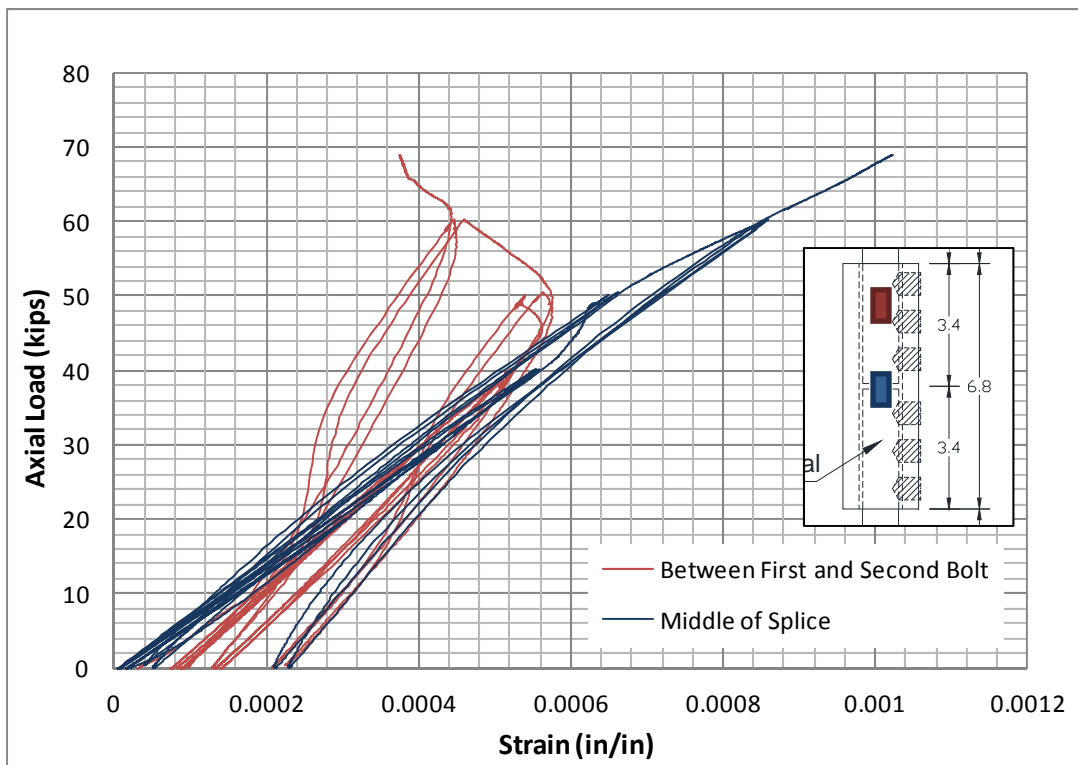


*Figure I.17  Strain on the short mechanical splice measured by strain gages.*

### I.1.3 Specimen 4 Short Mechanical Splice MS-S2

#### I.1.3.1 *Dimensions of the specimen MS-S2*

Figure I.18 shows a sketch of specimen MS-S2. Similar than MS-S1 case, each bar connected with mechanical splice has a length of 3.4 into the splice, The total length of the specimen between clamps or the clear space between heads of the universal machine was 18.8 in length.
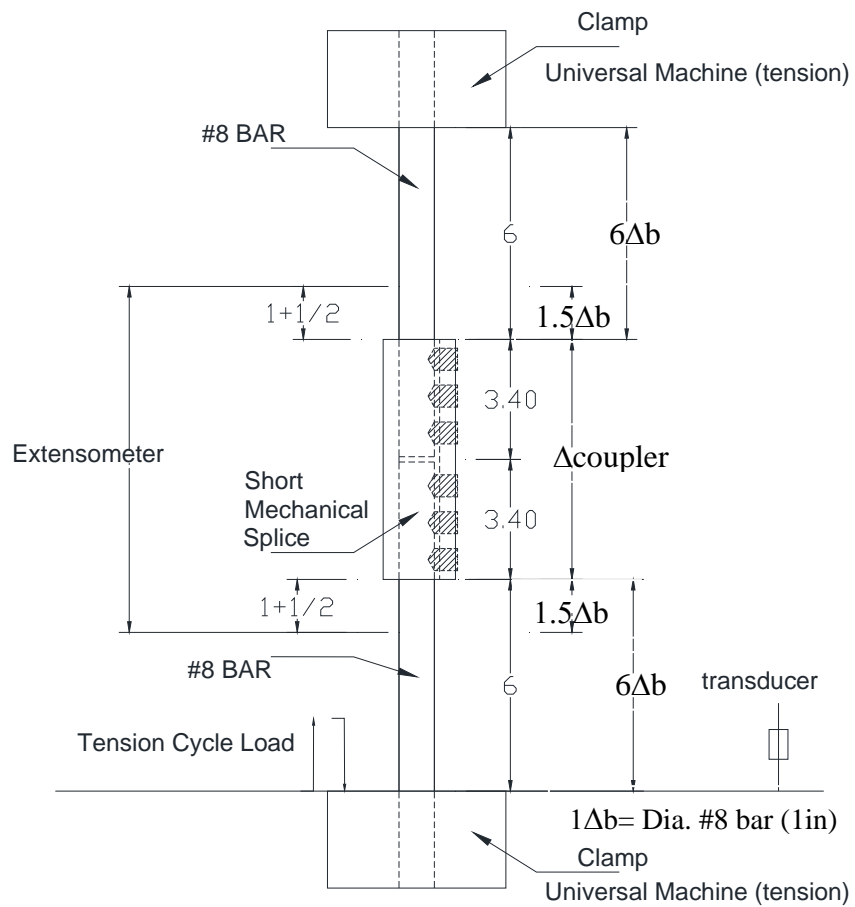


*Figure I.18 Scheme of the specimen MS-S2*

### I.1.3.2   Instrumentation for the test for MS-S2

The objective was to measure the following deformations (Figure I.19):

a)  General behavior of the specimen MS-S2, Axial load vs. Deformation of the specimen.

b)  Differences of strain deformation on the mechanical splice, one of the middle of this splice and other at level of the gap between the first and second bolt from top of the splice. strain gages were applied on the mechanical splice as Figure I.19 shows
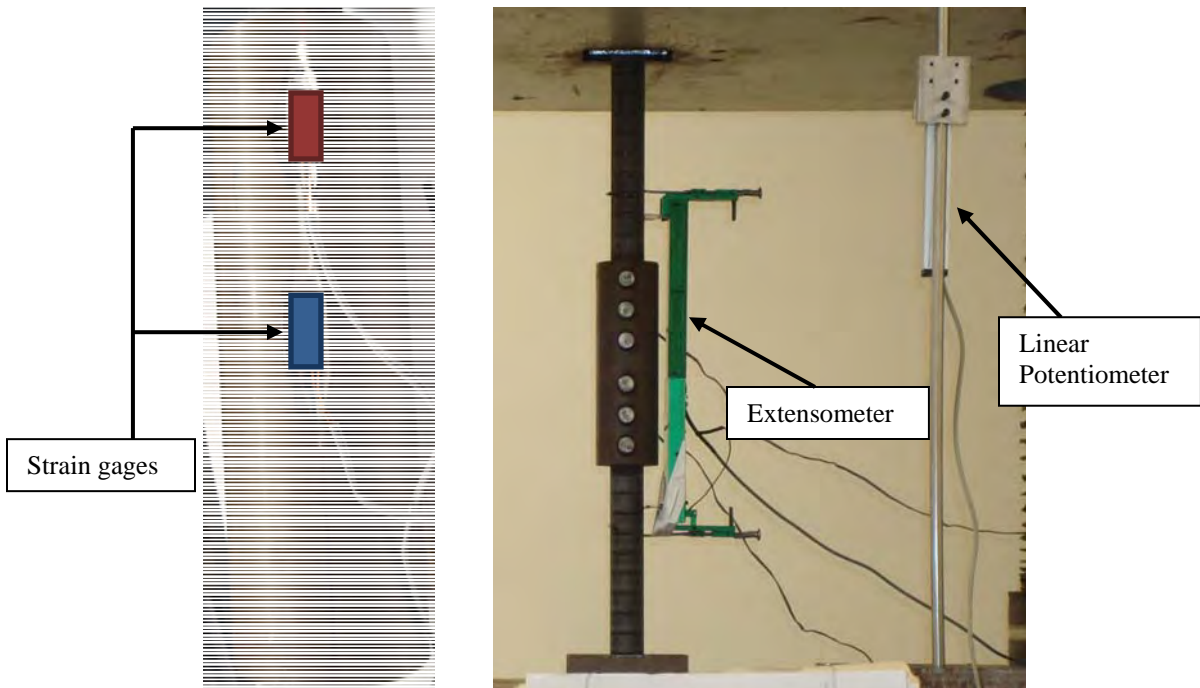


*Figure I.19  Instrumentation for MS-S2 test*

### I.1.3.3    Protocol of the test to MS-S2

The specimen was subjected to two cycles of tension load of 20, 30, 40, 50, 60 kips and a final load to failure. Figure I.20 shows the graph for the tension cycle test protocol for this specimen.
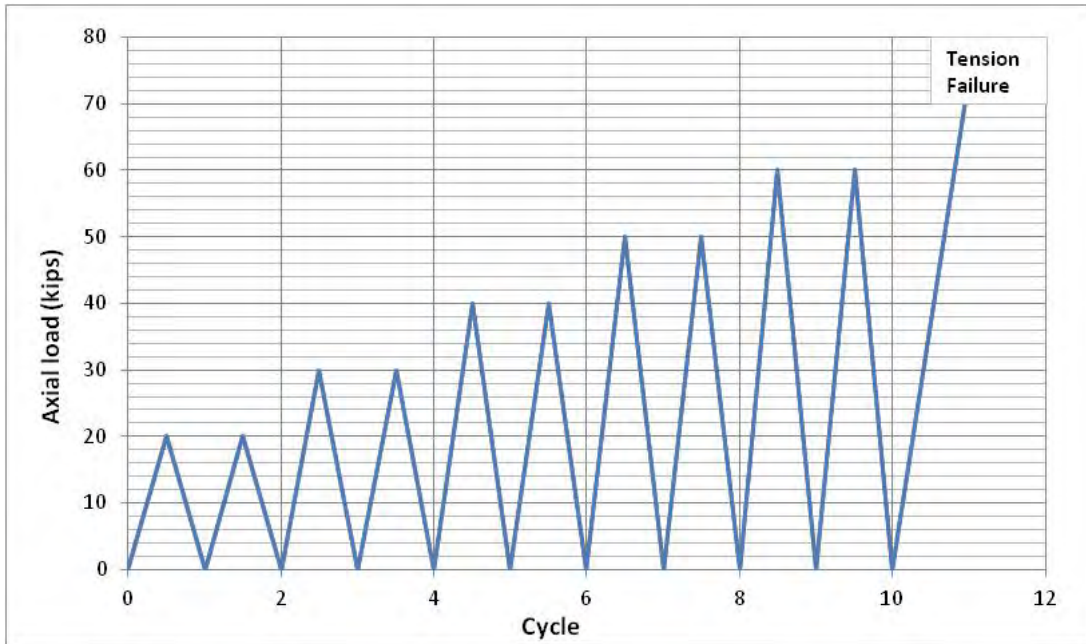


***Figure I.20  Load protocol for the cycle tension axial load test in MS-S2***

### I.1.3.4    Results of the Cyclic Tension Axial Load Test for specimen MS-S2

The load rate applied for the two first cycles to 20kips, was 7 kips/min; for the second set to 30kips load the speed was approximately 10 kips/min, the third set to 40kips load the speed was 13 kips/min. The speed loading for the 50kips load set was 10 kip/min and for the cycle tension loading of 60kips the speed loading was 10 kip/min also. For the last cycle which was taken to failure, the speed was 5 kip/min.

Similar than MS-S1, there was not presented any fracture of any part of the long mechanical splice during the test. At the beginning of the test, the pattern of deformation measured using the linear potentiometer presented a curve not related with the linear stiffness of the system as Figure I.24 shows. The extensometer indicated a linear response expected. This disruption was produced by the accommodation of the bars and the two extreme clamps of the universal test machine, same problem appeared at MS-S1. It was corrected for the envelope curve of this graph. The bolts behaved as one piece together with the mechanical splice.

The system reached yield at 49kip, and measured from the extensometer the yielding displacement was 0.009in, the graph in Figure I.23 shows the pattern of deformation of the splice and the part of the bars next to the splice. The hardening started at 0.027 in of deformation read from the extensometer. The extensometer was removed at 65.7 kips axial load. The failure of the system was presented by the fracture of the bar as Figure I.21 and Figure I.22 show. The failure was reached at 73.3 kips as maximum axial load and 2.06in measured by the transducer after the correction by the first deformation disruption or phasing, where the Figure I.26 shows the envelope curves with en phase corrected.
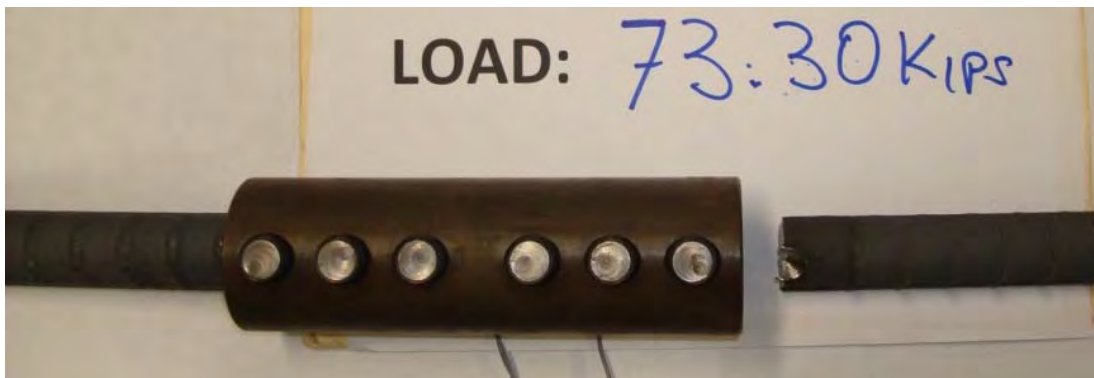


*Figure I.21  Rupture of the bar on the specimen MS-S2*

515

***Figure I.22  Cross section of the bar broken of MS-S2***
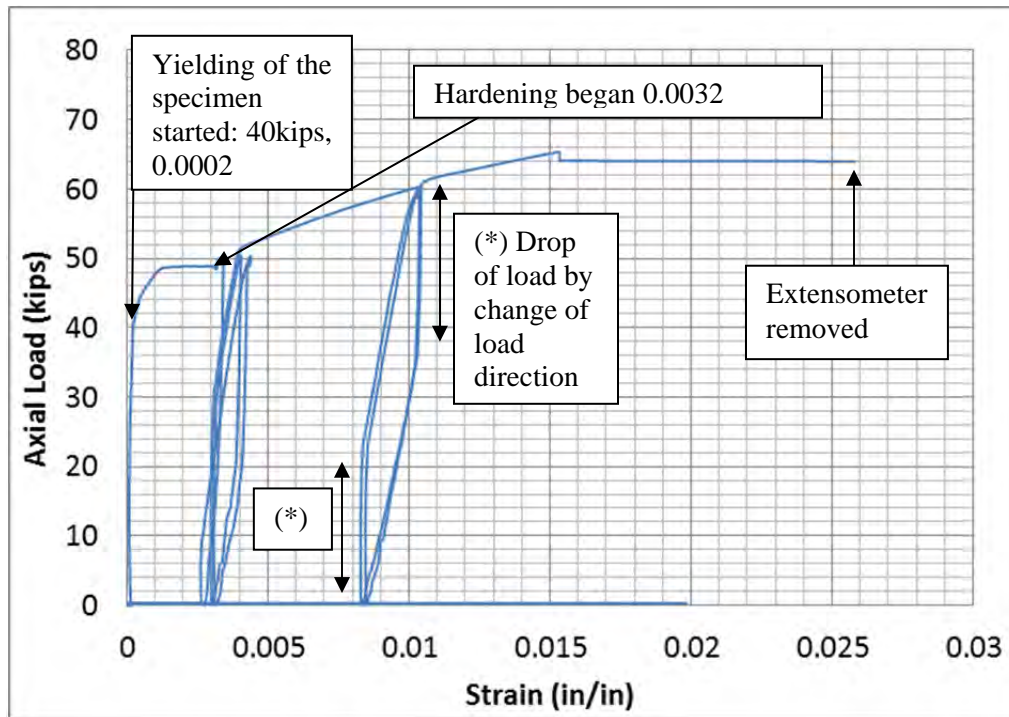


***Figure I.23  Deformation measured from the extensometer on specimen MS-S2***
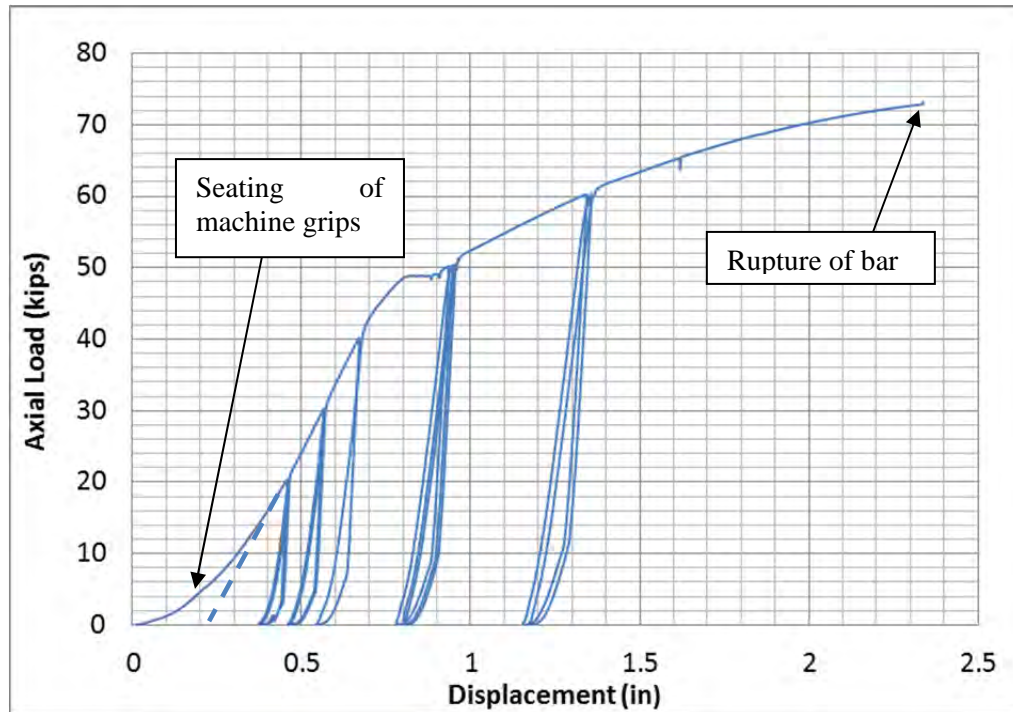
***Figure I.24  Displacement measured by the transducer in MS-S2***

Figure I.25 shows the different behavior for strain deformation on the middle of the strain in comparison with another location, especially for deformation after the yielding of the specimen. Strain between the $1^{st}$ and $2^{nd}$ bolt present similar initial stiffness than the middle of the splice, being the first one 25% higher than the second one. The strain between the $1^{st}$ and $2^{nd}$ bolt presents a no-linear behavior under high loads specially after the yielding of the system. However the strain measured on the middle of the splice is constantly linear for all the developed of the test. Because on the middle of the splice, both bars gathered by the splice are separated by a gap of less than 0.1in, no contact between both bars. The cross section area of the system at this level is provided only by the mechanical splice, being large area enough to be under its yielding axial force value, for this case approximately 3times larger than yielding force value read. Instead, at other location, the cross section is formed by the splice and bar cross section, having a

517

complex cross section behaving as Figure I.16 shows. There was not compression strain presented on both locations for the strain gages.

No location presented a value higher than 0.0014 for strain as Figure I.25 shows, this indicates that the splice did not reach the yielding. The maximum values reached were 0.00084 between the third and second bolt, and 0.00143 at the middle of the splice. This indicates that the splice did not reach the yielding. It can be explained because the cross section area on both places has larger area than the bar as is was described at the MS-L1 case.
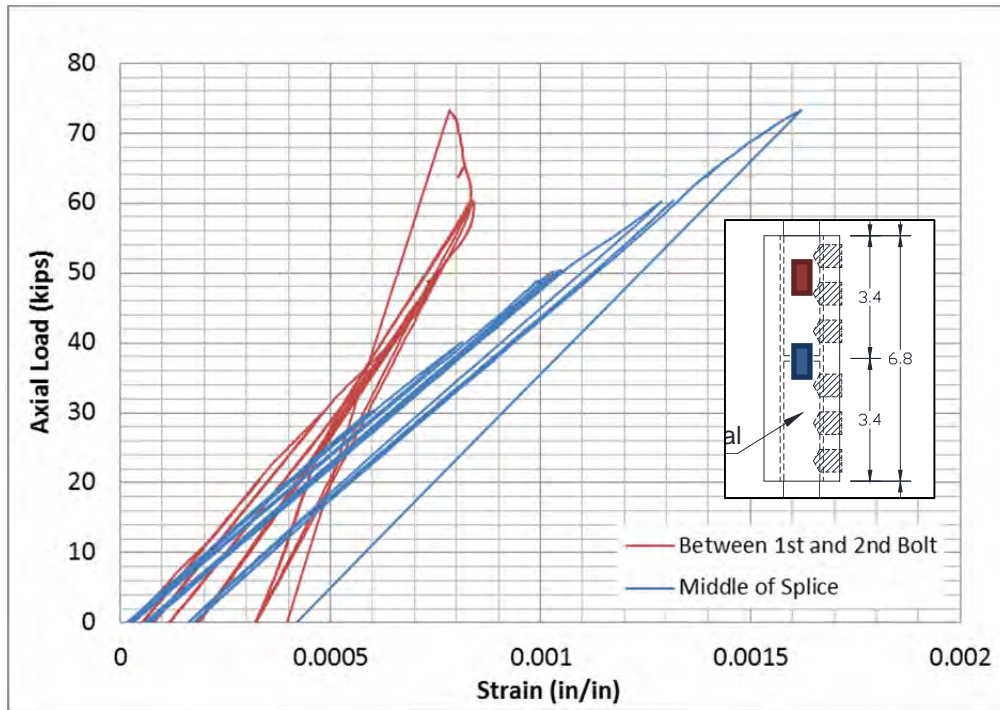


*Figure I.25  Strain measured on the splice in MS-S2*

### I.1.3.5   Summary of results for the Tension Cycle Axial Load Test

It is shown Figures where it can be seen the differences among the responses of each four specimens tested under tension cycle loads. The Figure I.26 shows the measurements of top platform of the universal machine, considering the deformation of the total length of each mechanical splice until the failure. It can be seen that the long mechanical splices present larger failure displacement than the short mechanical splices cases.
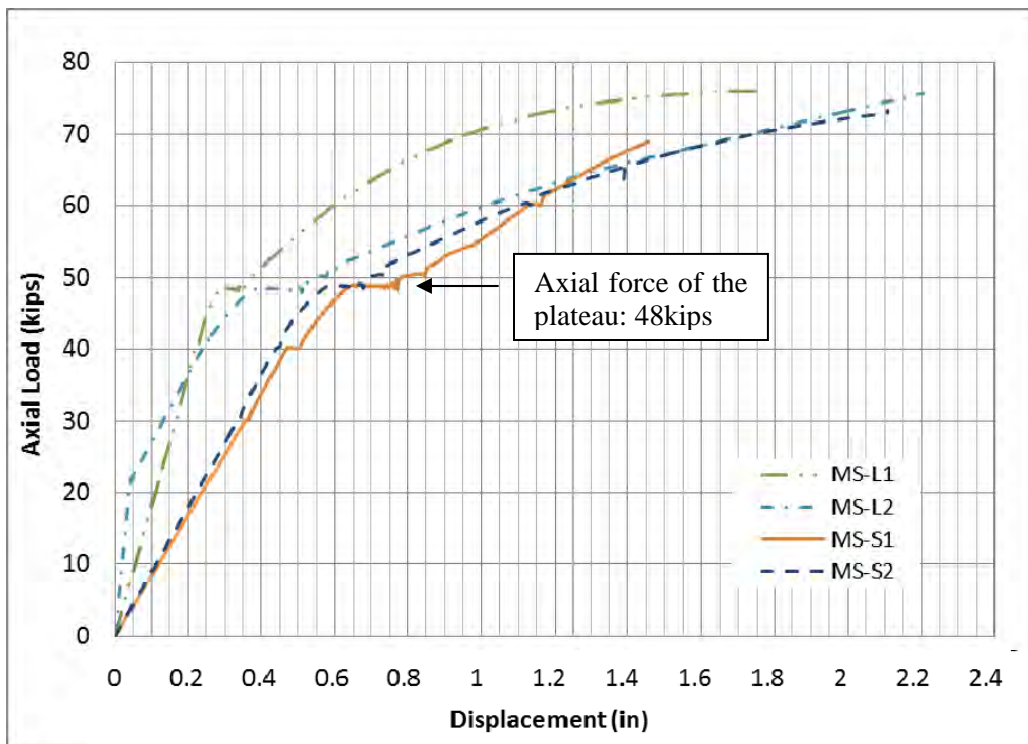


*Figure I.26  Peak cycles displacement of the universal machine*

519

Figure I.27 shows the pattern of deformation of the mechanical splice and a short portion of bars. It can be seen that the load of yielding response in tension is similar per each case of mechanical splice, having the yielding response displacement very similar among each other.
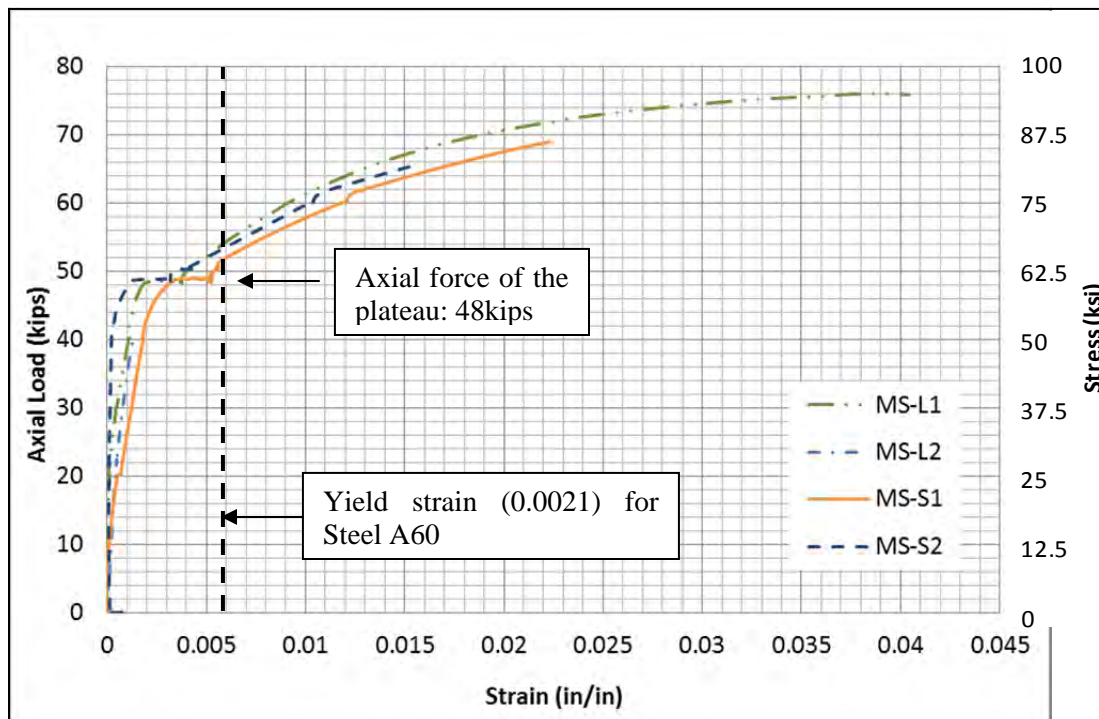


*Figure I.27  Peak cycle load-strain of each specimen from extensometer*

Figure I.28 and Figure I.29 shows the different responses of strain deformation of the mechanical splices. The strain measured on the middle of the splices presented linear response primarily. However the responses for the strain at level of the gap between the last two bolts of the splice presented linear response at the first loads and afterwards they presented nonlinear responses under higher tension loads applied.

520
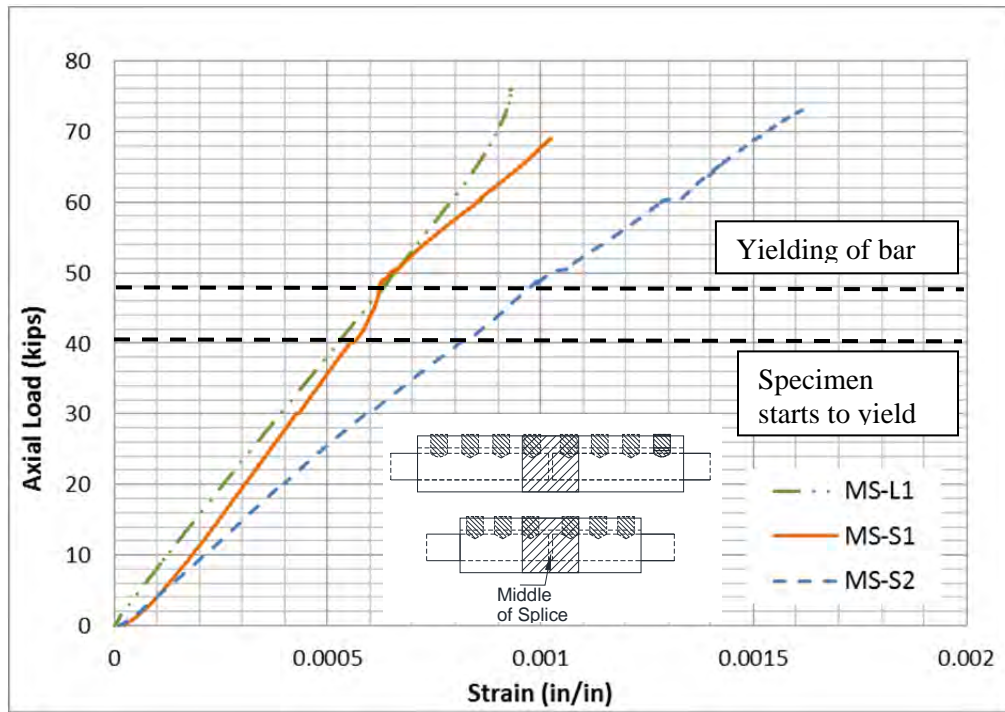
***Figure I.28  Peak cycle strain deformation at the middle of the mechanical splices***
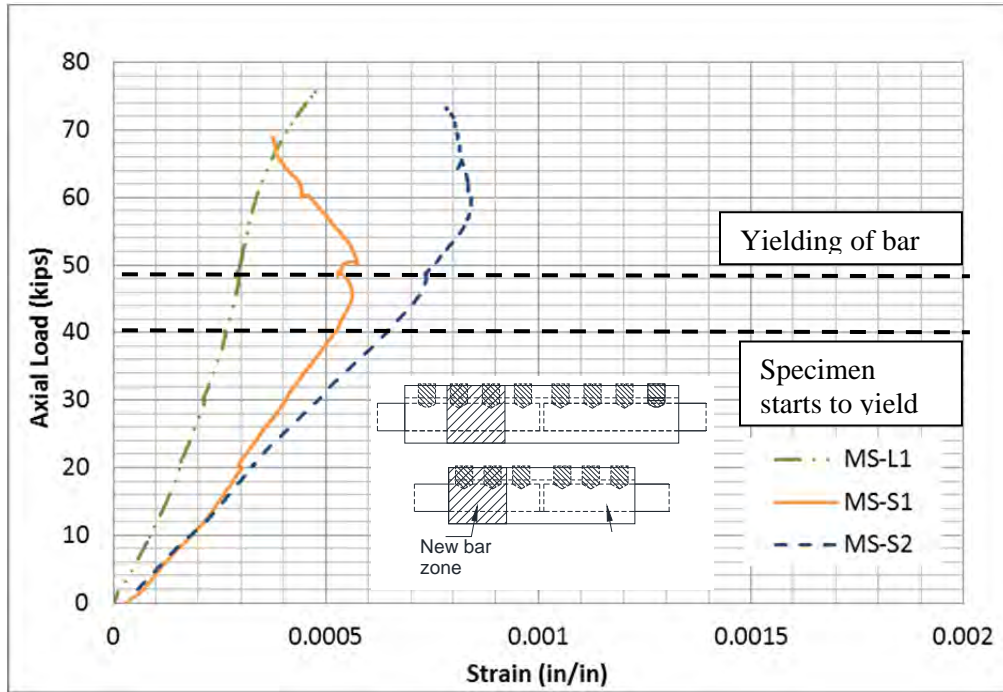
*Figure I.29  Peak cycle strain deformation measured between the second and third bolt for long splices and between the first and second bolt for short splices*

*Table I-1  Yield Strain and Maximum strain (extensometer)*

| Specimen | Yield Strain Tension | Maximum Strain Extensometer (*) |
|---|---|---|
| MS-L1 | 0.00223 | X |
| MS-L2 | X | X |
| MS-S1 | 0.00388 | 0.02713 |
| MS-S2 | 0.00120 | X |

**(x) Extensometer removed or no installed**

522

### I.1.4 Specimen 5 - Long Mechanical Splice MS-L3

#### *I.1.4.1 Characteristics of the specimens*

This specimen consists in two new steel bars #8 and one long mechanical splices. While the process of the construction of MS-L3, three bolts with point ending were broken on the neck at 0.2in inferior level high than the appropriate locate which is immediately under the head, it means between the tread and head of the bolt as Figure I.31 shows. It can be seen in Figure I.30 the location of the bolts broken on the tread.



*Figure I.30 Condition of MS-L3 after the tightening*



*Figure I.31  Thread of the bolt broken*

Figure I.32 shows a sketch of the specimen MS-L3. The bars connected with mechanical splice have a length of 5 into the splice. The total length of the specimen MS-L3 between clamps or the clear space between heads of the universal machine was 14.6in length.
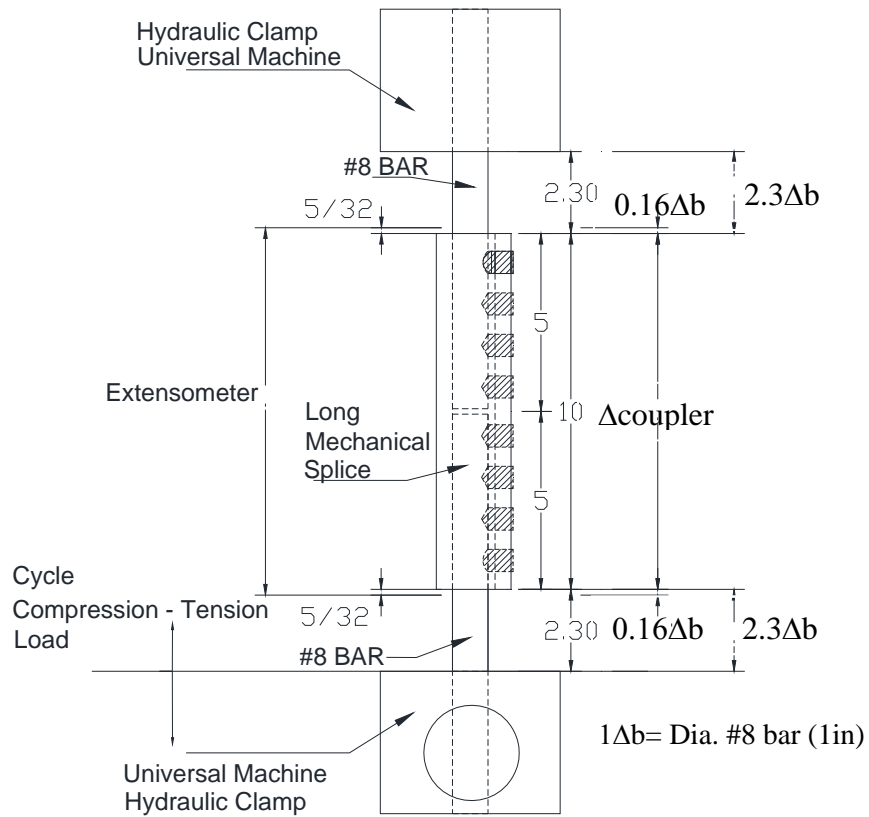


*Figure I.32  Sketch of specimen MS-L3*

### I.1.4.2 Instrumentation for the test

Since it was the first test made, the objectives were to look for (Figure I.33):

a) General behavior of the specimen MS-L3, Axial load vs. Deformation of the specimen formed by the long mechanical splice plus the two new bars.

b) Differences of strain deformation on the mechanical splice, one on the middle of the coupler and other at level of the gap between the second and third bolt from top of the splice. Strain gages were applied on the mechanical splices as Figure I.33 shows the location of them. One strain gage is located at the middle of the splice and the second between the $2^{nd}$ and $3^{rd}$ bolt of the bottom part of the long mechanical splice.
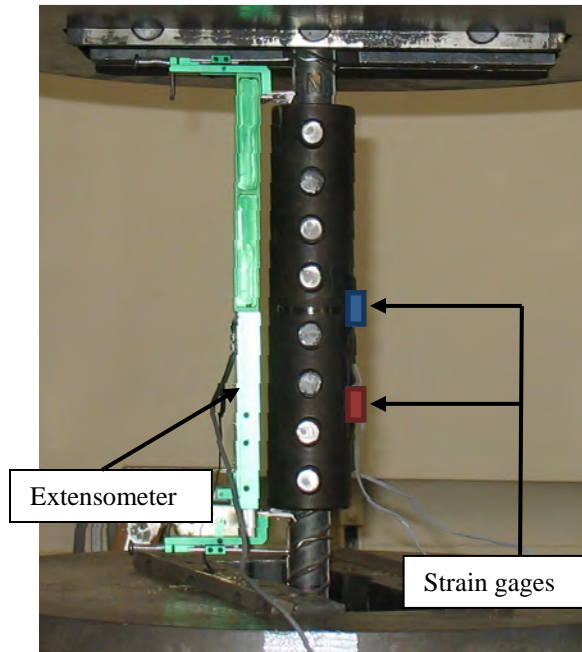
*Figure I.33  Instrumentation for MS-L3 Test – No strain gages on bars*

### I.1.4.3    *Protocol of the test to MS-L3*

To define the sequence and peaks for each cycle, the envelope curve for MS-L1 axial tension test as shown in Figure I.34 was used. The objective was to measure the pattern of deformation in the linear range before yielding, after yielding, and in the strain hardening range.
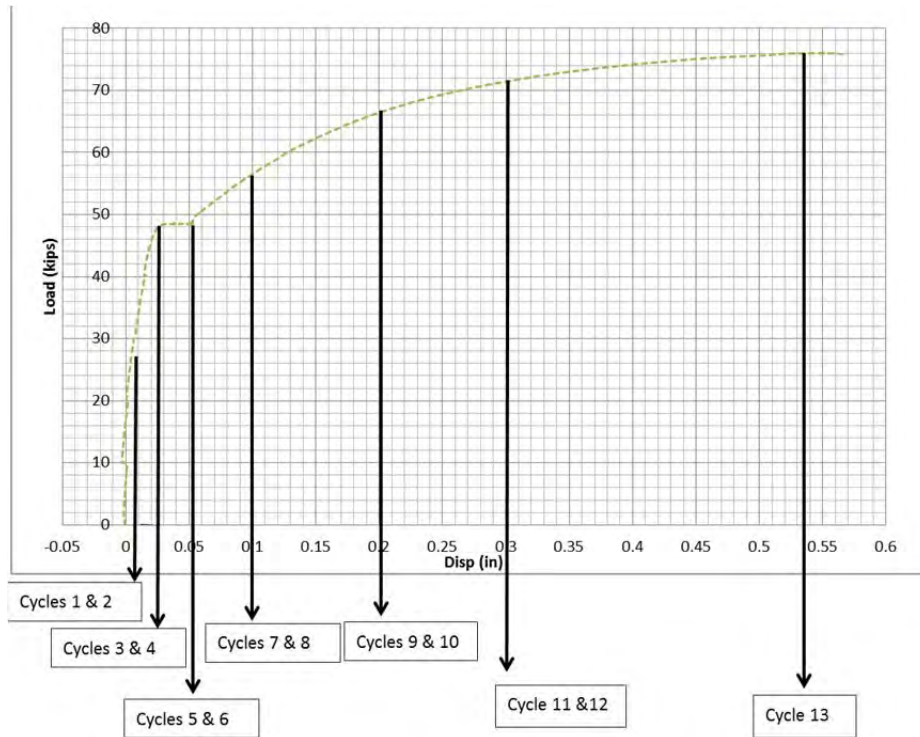
*Figure I.34 Envelope Curve for MS-L1 to define peak deformation for each cycle.*

The deformation levels were based on multiples of displacement yielding (Figure I.35.). The value of deformation yielding $\delta y$ was 0.025in. The maximum compression deformation was -1 $\delta y$ (0.25in) for all cycles. The graph of the protocol of deformation for this test MS-L3 is showed in Figure I.35.

527
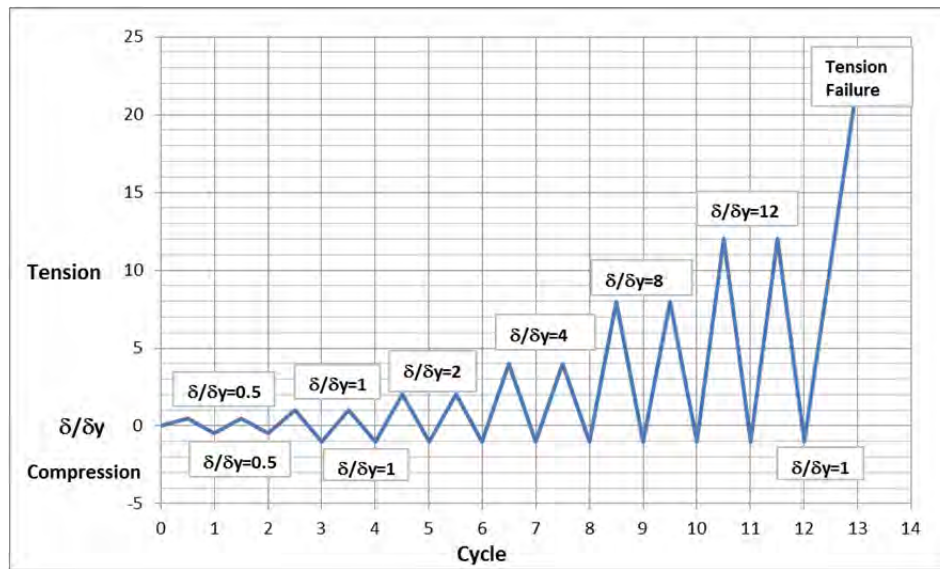
*Figure I.35  Protocol of load for test of specimen MS-L3*

The test was controlled directly by the measurement of the stroke. The universal machine operation is controlled by the increment of tension or compression loads.

In this test machine the extensometer and head deformation (stroke) gave nearly identical results in the linear range of the bars.

*I.1.4.4   Results of the Cyclic Compression-Tension Axial Load Test*

The cycle load were applied without disruption rate of loading in last cycle was 7 kips/min, and the displacement rate was 0.095in/min. During the test, there was not presented any fracture of any part of the long mechanical splice. The bolts behaved as one piece together with the mechanical splice. The broken thread of the three bolts of the mechanical splice did not present failure or rupture.

The system reached the yielding under tension loads at 61 kips, The yielding displacement measured from the extensometer was 0.0014. Under compression load, the yielding load for the long mechanical splice and the portion of bars between the extensometer was 48kips and 0.0078 deformation measured by the extensometer. This instrument was removed after some higher load, at the 13th cycle to prevent damage of this instrument could suffer by the brittle failure of the specimen. The failure of the system was presented by the fracture of the bar in the contact zone with the last bolt of the mechanical splice as Figure I.36 and Figure I.37 show. The failure was reached at 85.80 kips as maximum axial load and 1.14 in measured by the stroke of the universal machine.



*Figure I.36 Failure pattern, rupture of the bar of MS-L3*

*Figure I.37 Bar broken in the contact zone of rounded point bolt for MS-L3*
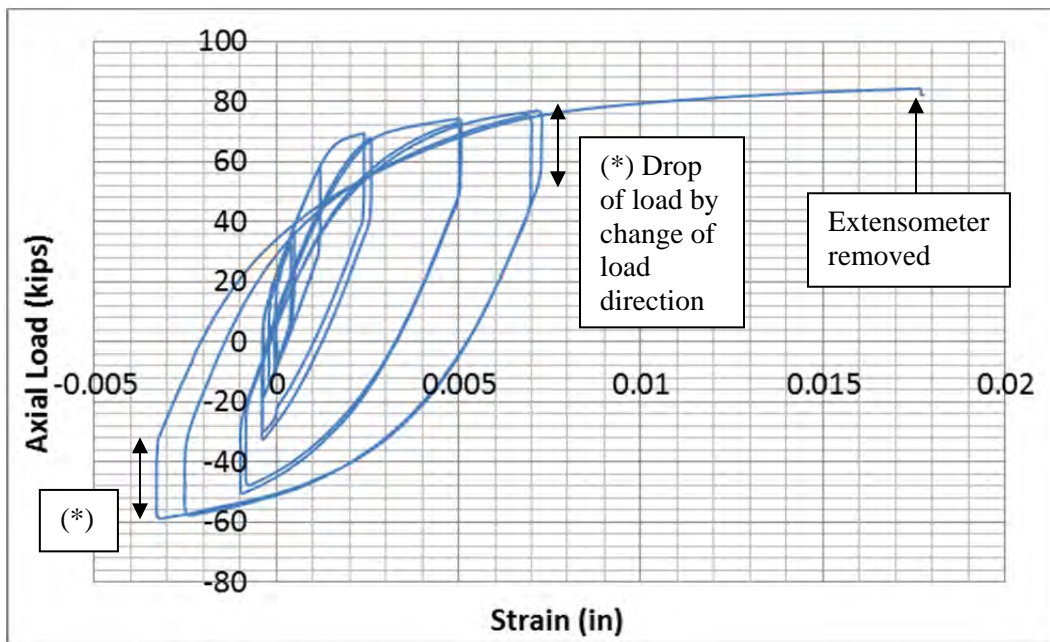


*Figure I.38  Strain deformation measured by extensometer on the specimen*
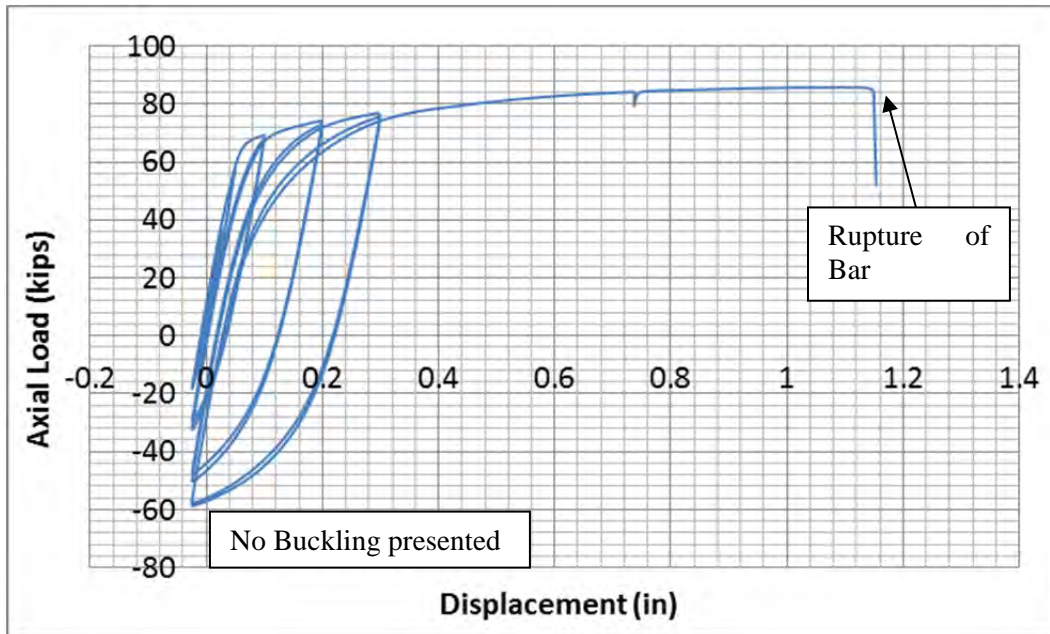
*Figure I.39  Displacement measured by the stroke of the universal machine t*

Strains measured at the middle and between the $2^{nd}$ and $3^{rd}$ bolt of the mechanical splices indicate different behaviors as Figure I.40 shows. Strain between the $2^{nd}$ and $3^{rd}$ bolts present 25% higher initial stiffness than the middle of the splice. The strain also between the $2^{nd}$ and $3^{rd}$ bolts presents a no-linear behavior under high loads specially after the yielding of the system. However the strain measured on the middle of the splice is linear; it only presents a no linear behavior before the failure. The difference mentioned can be explained because on the middle of the splice, both bars gathered by the splice are separated by a gap of less than 0.1in, no contact between both bars. The cross section area of the system at this level is provided only by the mechanical splice, being large area enough to be under its yielding axial force value, for this case approximately 3times larger than yielding force value read. Instead, at other location, the cross section is formed by the splice and bar cross section.

531

No location presented a value higher than 0.0021 for strain as Figure I.40 shows, this indicates that the splice did not reach the yielding. The maximum values reached were 0.00072 for tension loads and 0.0004 for compression loads at he zone between the third and second bolt; and 0.0011 for tension loads and 0.0007 for compression at the middle of the splice. This indicates that the splice did not reach the yielding. It can be explained because the cross section area on both places has larger area than the bar as is was described at the MS-L1 case.
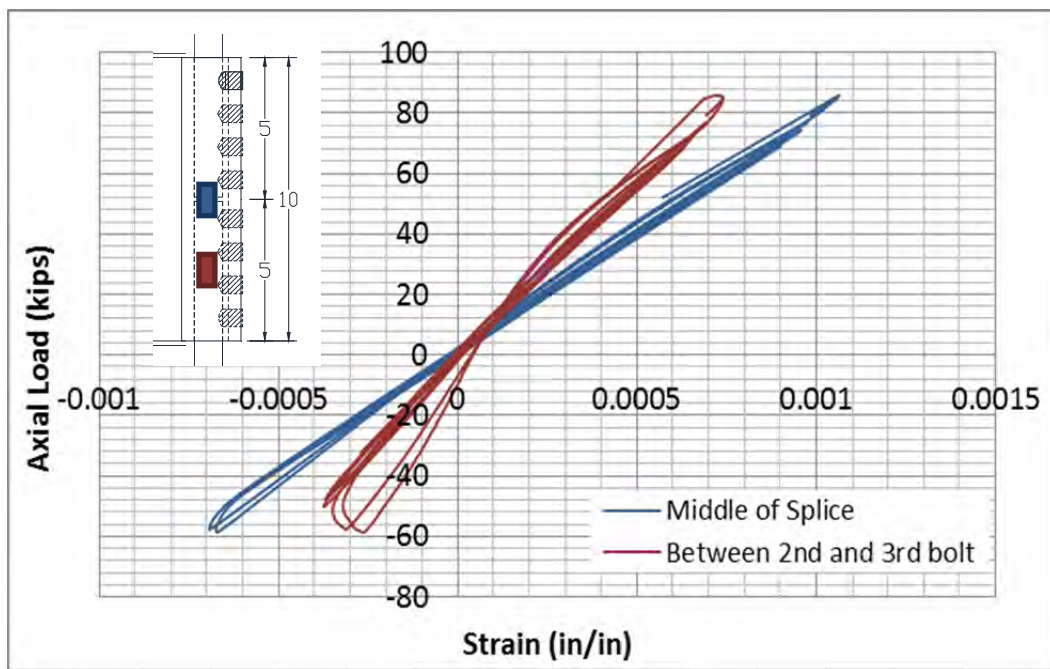


*Figure I.40  Deformation measured for the system and the mechanical splice MS-L3*

### I.1.5 Specimen 6 Long Mechanical Splice MS-L4

#### I.1.5.1 *Characteristics of the specimens*

This specimen consists in two new steel bars #8 and one long mechanical splices. Every bolt has been applied as instructions without ruptures as the case of MS-L3 as Figure I.42 shows. The head of each bolt has been removed though the torque of this bolt, which location of cutting was between the thread and the head as Figure I.41 shows.



*Figure I.41 Bolt's head removed from the edge of the thread*



*Figure I.42  Bolts of MS-L4 applied with shear cutting on the thread*

Figure I.43 shows a sketch of the specimen MS-L4. The bars connected with mechanical splice have a length of 5 in into the splice, 2 in additional external length and 6.5in additional for clamping to the universal machine. The total length of the specimen MS-L4 between clamps or the empty room of the universal machine was 14in length.
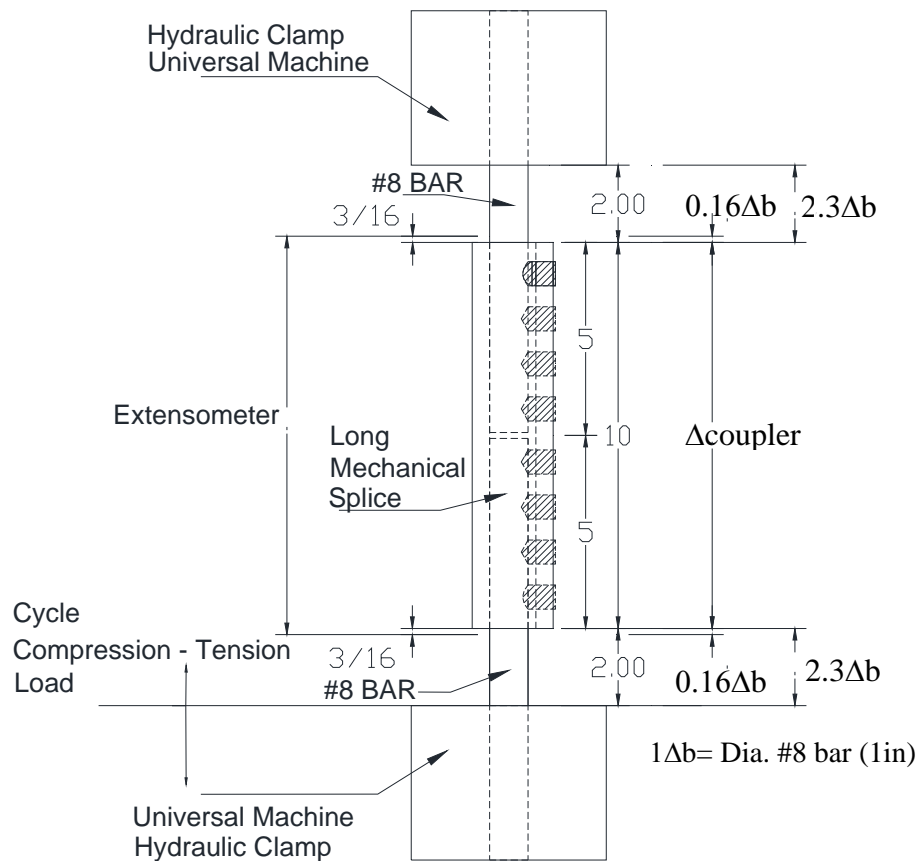


*Figure I.43  Sketch of the specimen MS-L4*

### I.1.5.2 Instrumentation for the test

Measurement of deformation and strain located at the same locations than previous specimen, having the extensometer a slightly shorter than MS-L3 case (Figure I.44)

a) General behavior of the specimen MS-L4, Axial load vs. Deformation of the specimen formed by the long mechanical splice plus the two new bars.

b) Differences of strain deformation on the mechanical splice, one of the middle of this splice and other at level of the gap between the second and third bolt from top of the splice.
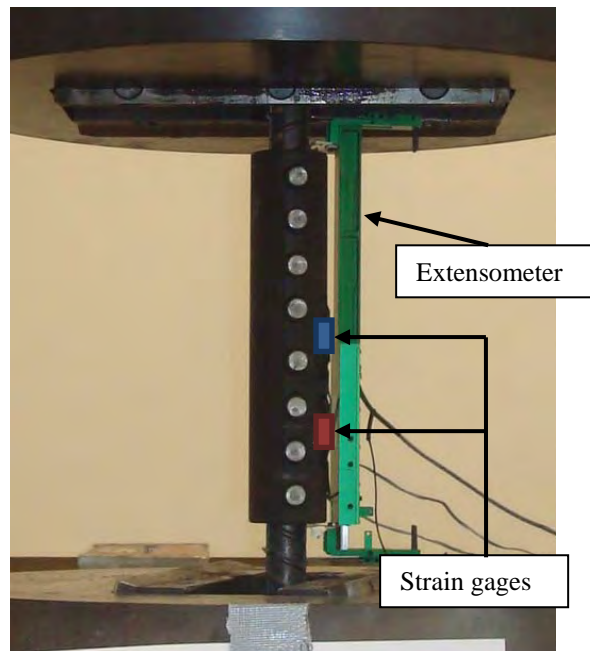


*Figure I.44  Instrumentation for MS-L3*

### I.1.5.3  Protocol of the test to MS-L4

The tests for the second set of specimens were performed by displacement control. The objective was to measure the pattern of deformation for the linear behavior before the yielding, behavior after the yielding and hardening. The test was controlled indirectly by the measurement of the stroke, as MS-L3 test.

Since the last test MS-L3 did not show problems for buckling, it was decided to increase the compression deformation until $2\delta y$. Therefore, in the cyclic loading test, the current specimen was subjected to two cycles of tension compression deformation of $\pm 0.5\ \delta y$ and $\pm\ 1\ \delta y$, then two cycles of $+2\ \delta y$, $+4\ \delta y$, $+8\ \delta y$, $+12\ \delta y$, considering at all cycles a maximum of $-2\delta y$ for compression deformation; and finally increase the deformation until de failure. Similar than MS-L3, the value of deformation yielding $\delta y$ was considerate 0.025in measured by the tension axial cycle load test or MS-L1. The graph of the protocol of deformation for this test MS-L3 is showed in Figure I.45.
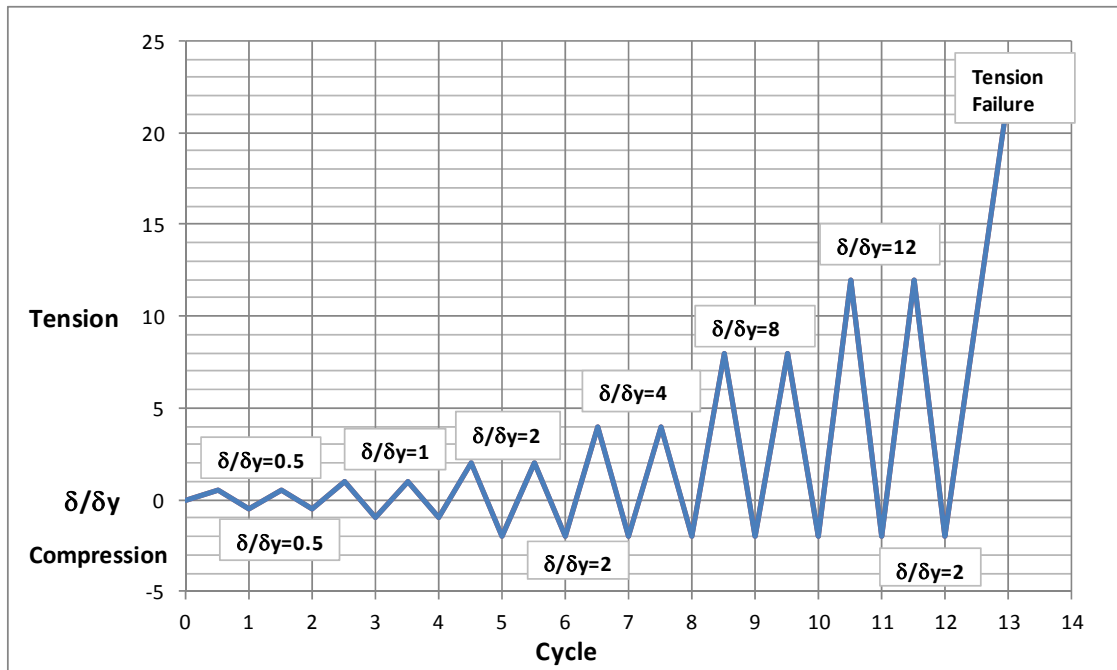
*Figure I.45  Protocol of load for test of specimen MS-L4*

### I.1.5.4   Results of the Cyclic Compression-Tension Axial Load Test

There was not disruption while the application of the load. The load rate average applied was faster than MS-L3 case 20 kips/min, and measured by displacement 0.24in/min. Both the extensometer and the stroke measurement presented linear behavior for initial displacement. The diphase did not appear for this specimen MS-L4. During the test, there was not presented any fracture of any part of the long mechanical splice. The bolts behaved as one piece together with the mechanical splice.

The system reached the yielding under tension loads at 52 kips load, and measured from the stroke the yielding displacement was 0.064. as they can be seen in Figure I.48. The yielding displacement measured from the extensometer was 0.00164 as Figure I.47 shows. Under compression load, the yielding load for the long mechanical

537

splice and the portion of bars between the extensometer was 44 kips and 0.00042 deformation measured by the extensometer.

There was heard a sound similar than a rupture of bar, however no damage was visible on the test at the 9$^{th}$, 11$^{th}$ and 12$^{th}$ cycle. The extensometer was removed after some load higher, at the 13$^{th}$ cycle to prevent damage of this instrument could suffer by the brittle failure of the specimen. The type of failure of the system was similar than MS-L3 case, it was presented by the fracture of the bar in the contact zone with the last bolt of the mechanical splice as Figure I.46 shows. The failure was reached at 86 kips as maximum axial load and 0.98 in measured by the stroke of the universal machine.



*Figure I.46 Failure pattern for MS-L4*
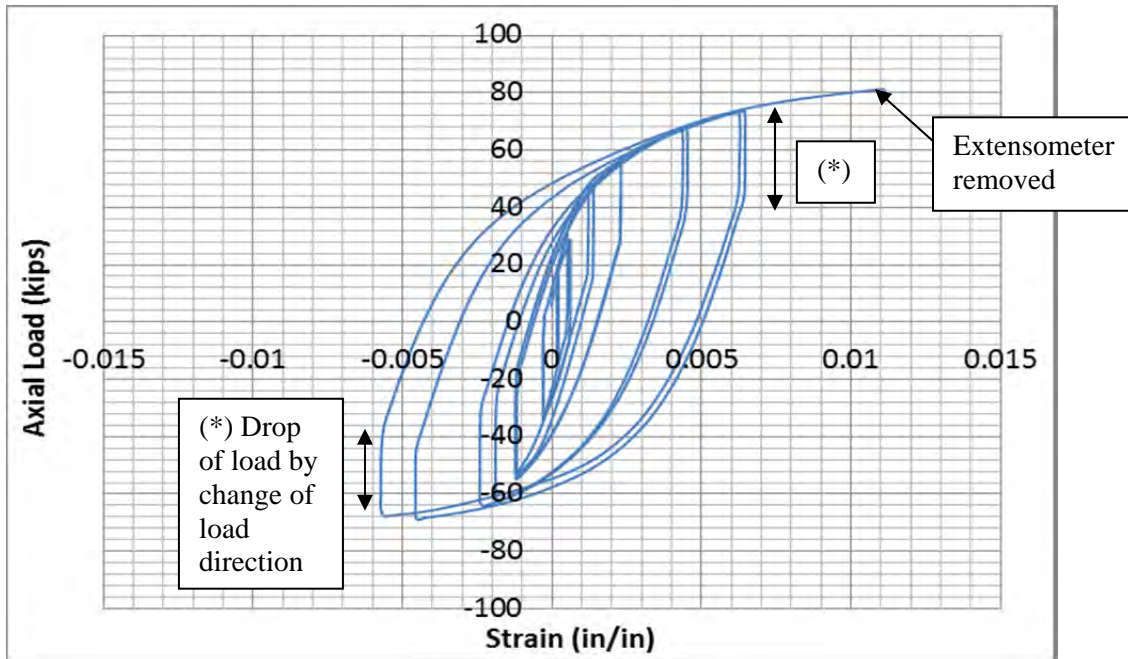
*Figure I.47  Deformation measured by the extensometer for specimen MS-L4*
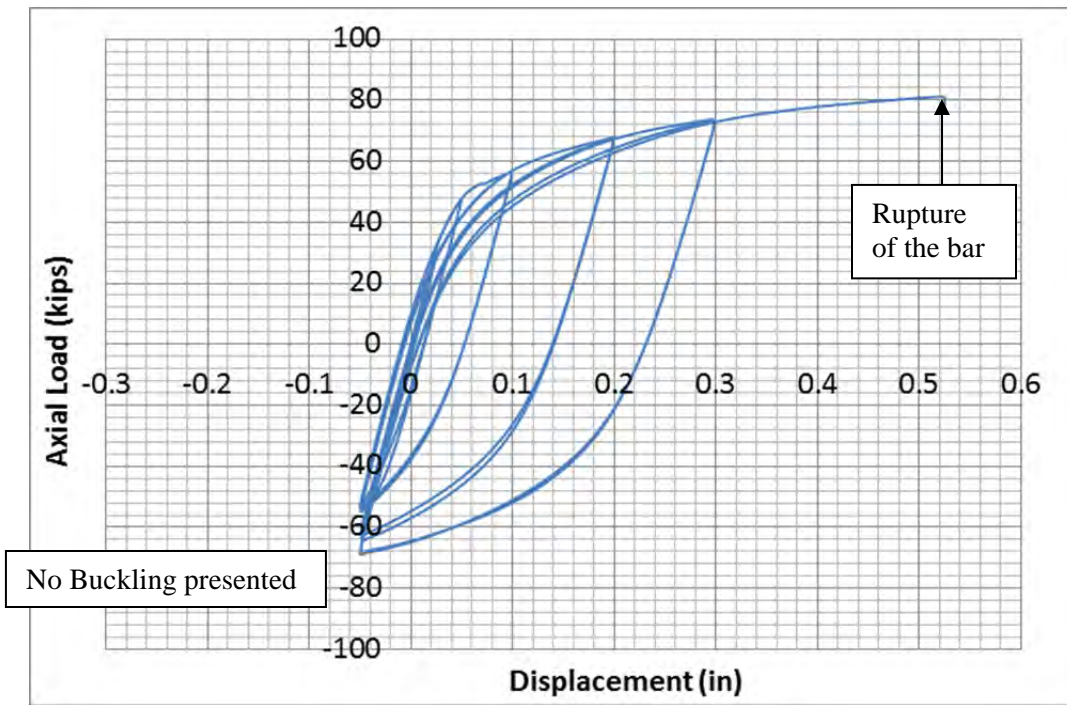


*Figure I.48  Displacement measured by the stroke of the universal machine for MS-L4*

539

Pattern of strain deformation was similar than MS-L3 case. Strains measured at the middle and between the $2^{nd}$ and $3^{rd}$ bolt of the mechanical splices indicate different behaviors as Figure I.49shows. Strain between the $2^{nd}$ and $3^{rd}$ bolts present 30% higher initial stiffness than the middle of the splice. The strain also between the $2^{nd}$ and $3^{rd}$ bolts presents a no-linear behavior under high loads specially after the yielding of the system. However the strain measured on the middle of the splice is linear; it only presents a no linear behavior before the failure. The difference mentioned can be explained because on the middle of the splice, both bars gathered by the splice are separated by a gap of less than 0.1in, no contact between both bars. The cross section area of the system at this level is provided only by the mechanical splice, being large area enough to be under its yielding axial force value, for this case approximately 3times larger than yielding force value read. Instead, at other location, the cross section is formed by the splice and bar cross section.

No location presented a value higher than 0.0021 for strain as Figure I.49 shows, this indicates that the splice did not reach the yielding. The maximum values reached were 0.00052 for tension loads and 0.00091 for compression loads at the zone between the third and second bolt; and 0.001 for tension loads and 0.0011 for compression at the middle of the splice. This indicates that the splice did not reach the yielding. It can be explained because the cross section area on both places has larger area than the bar as is was described at the MS-L1 case.
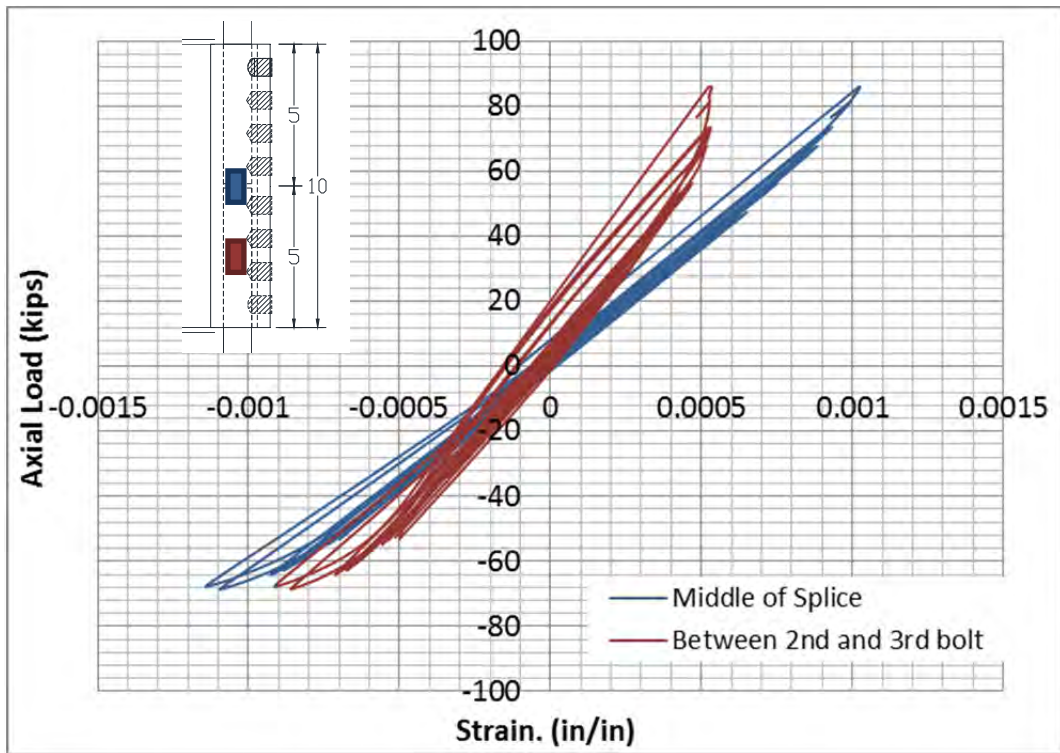
*Figure I.49  Strain deformation on the short mechanical splice of MS-L4*

### I.1.6 Specimen 7 Short Mechanical Splice MS-S3 – Additional information

#### I.1.6.1 *Results of Cyclic Compression-Tension Test*

Axial load vs. deformation of the specimen measured by the stroke of the universal machine is shown in Figure I.50.
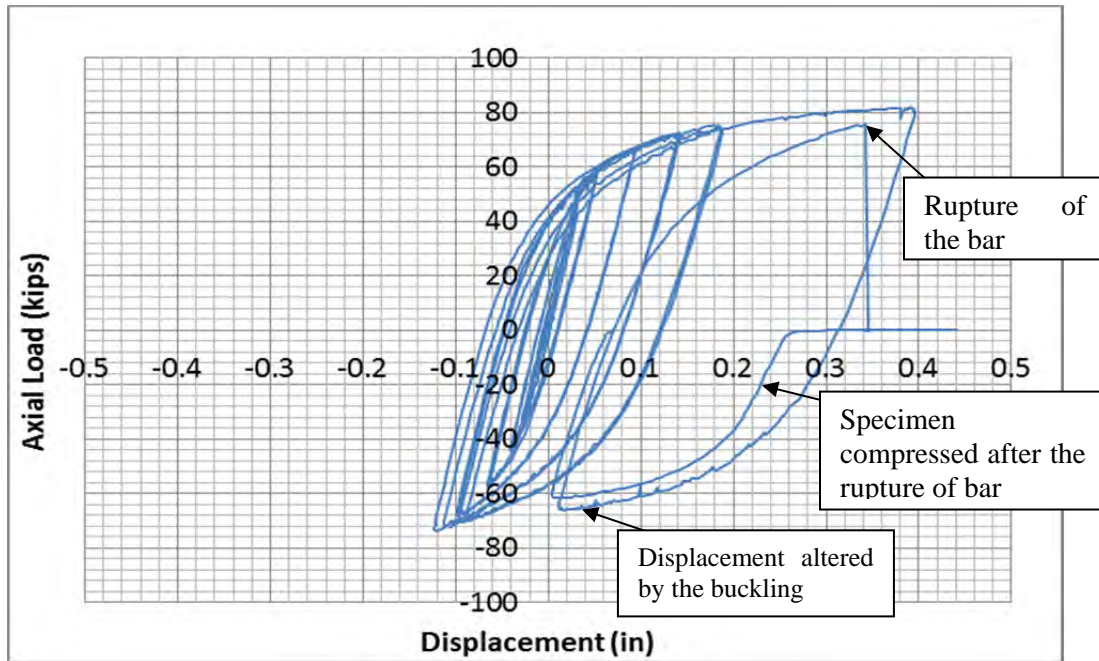


*Figure I.50  Deformation measured by stroke of the universal machine*

The stiffness of the top and bottom zone of the splice is higher than the middle part for tension and compression loads. For the zone above the middle of the splice, the stiffness is 40% higher than in the middle, both for tension loads as Figure I.51 shows. For the zone below the middle, the stiffness is 30% higher even than the middle for tension loads. For compression loads, both, above and below the middle behavior were similar, having the below shorter deformation for the buckling effect on the specimen. Those differences are due the different cross section areas at each location of the strain gages, as it was explained at MS-L1 case.

542

No location presented a value higher than 0.0021 for strain, this indicates that the splice did not reach the yielding. The maximum values reached were 0.00038 for tension loads and 0.00035 for compression loads at the zone between the third and second bolt at the new bar zone of the splice; 0.0005 for tension loads and 0.00034 for compression loads at the zone between the third and second bolt at the previously yielded bar zone of the splice; and 0.0008 for tension loads and 0.0010 for compression at the middle of the splice. It can be explained because the cross section area on both places has larger area than the bar as is was described at the MS-L1 case. In addition, the reason for the strains at the previously yielded bar are larger than the new bar zone is because the bar used for the bottom part was previously deformed 4δy at tension and 3δy compression, being a weak zone at comparison with the top part of the splice formed by a new steel bar.
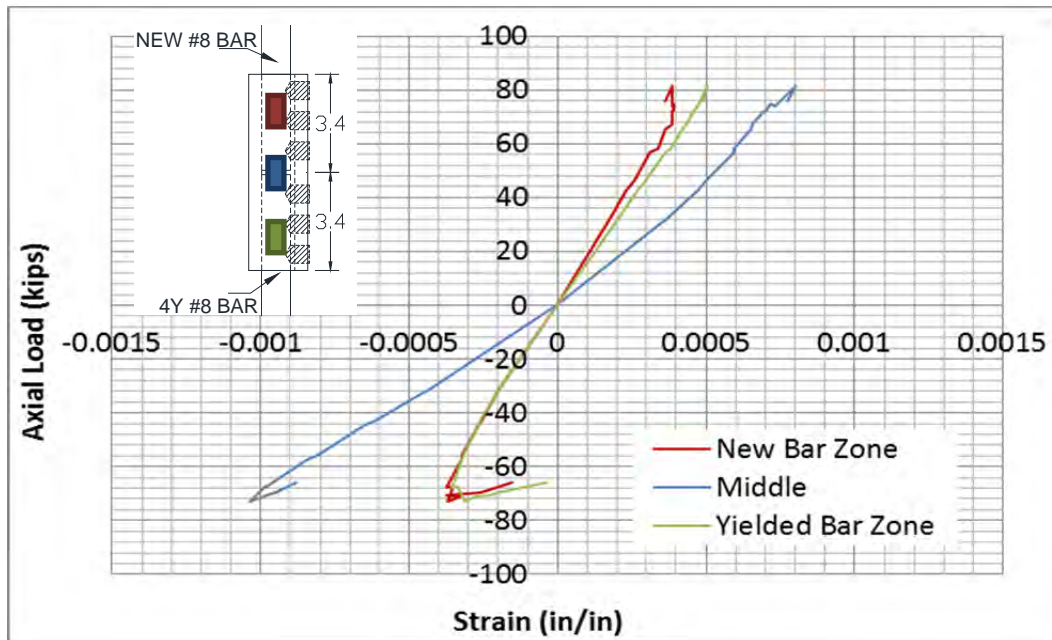


*Figure I.51  Peak strain on the short mechanical splice in specimen MS-S3*

### I.1.7 Specimen 8 Short Mechanical Splice MS-S4

#### *I.1.7.1 Characteristics of the specimen*

This specimen consists in one steel bar yielded previously reaching 1.5 times tension and compression yielding deformation (Appendix I) located above the middle of the splice, one new steel bar #8 located below the middle of the splice, (opposites places for bars at comparison of specimen MS-S3) and one short mechanical splices as they can be seen in Figure I.53. It was switched the location of the bars in order to study the possible effects of different location of bars loaded at the universal machine. For retrofit purposes, the mechanical splice will gather an old bar previously deformed together with a new bar, providing continuity of reinforcement. No bolts applied have been broken on the thread area or neither the splice broken as it can be seen in Figure I.52.



*Figure I.52 No bolt broken on its thread area in specimen MS-S4*

Figure I.53 shows the sketch for the specimen MS-S4. Each bar connected with mechanical splice has a length of 3.4 in into the splice. The total length of the specimen between clamps clear space between heads machine was 10.8 in length.
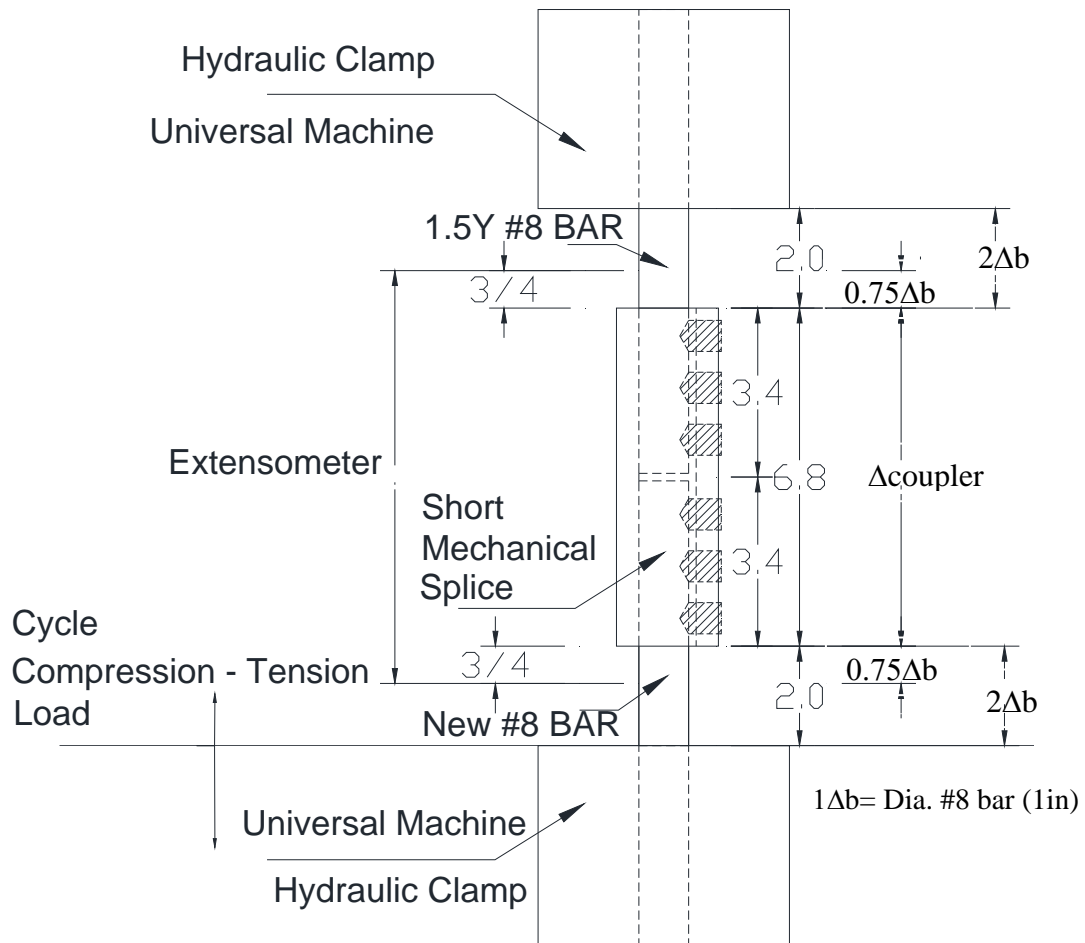
*Figure I.53  Dimensions for Specimen MS-S4*

### I.1.7.2   Instrumentation for the test

Measurement of deformation and strain located at the same locations than previous specimen MS-S3 (Figure I.54):

a) General behavior of the mechanical splice, Axial load vs. Deformation of the specimen formed by the short mechanical splice plus the previously deformed bar and the new steel bar.

b) Differences of strain deformation on the mechanical splice. One strain gage is located at the middle of the splice; the second one between the first and second bolt of the top part of the short mechanical splice where is applied the previously yielded bar; and the third strain gage is placed at the exact opposite location between the first and second bolt of the bottom part of the short mechanical splice where is applied the new bar. The line of application of gages was 0.5in next the edge line of the splice's bolts as Figure I.54 shows.



Extensometer

strain gages
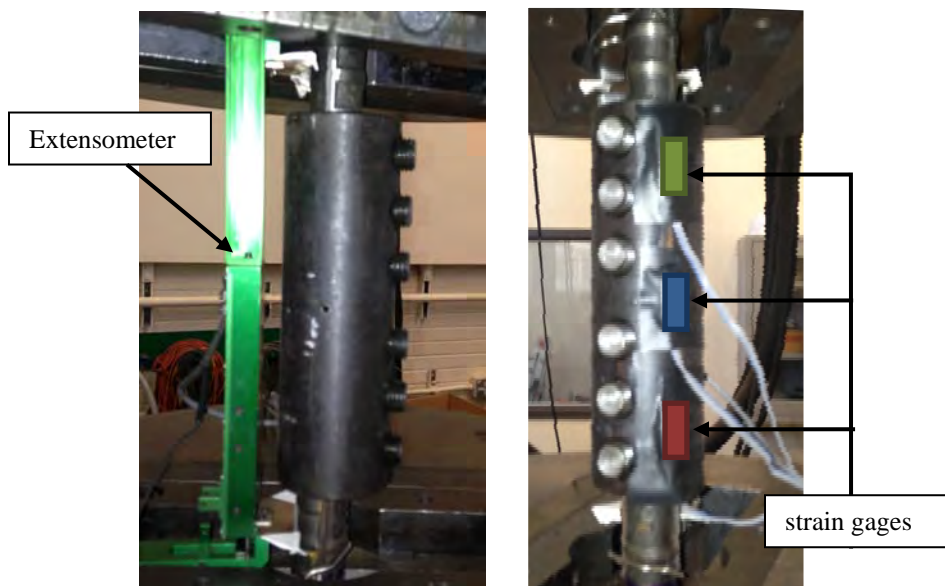
*Figure I.54  Instrumentation for the test of specimen MS-S4*

### I.1.7.3   *Protocol of the test to MS-S4*

The specimen was subjected to two cycles of tension compression deformation of $\pm 0.25\ \delta y$, $\pm 0.5\ \delta y$, $\pm 1\ \delta y$, $\pm 2\ \delta y$, one cycle $\pm 3\delta y$ each; and finally the deformation was increase by tension load until de failure. The value of deformation yielding $\delta y$ was considerate the average value measured by the extensometer in MS-S1, 0.0027in, and

MS-2 tests 0.009 in. The yielding deformation considerate was δy 0.018in. The graph of the protocol of deformation for this test MS-S4 is showed in Figure I.55.

The tests for the second set of specimens were performed by displacement control. It was controlled indirectly by the measurement of the extensometer. The universal machine operation is controlled by the increment of tension or compression loads. However the monitored displacement measured by the extensometer indicated the peak of each cycle, pausing the test in order to change the direction of the load.
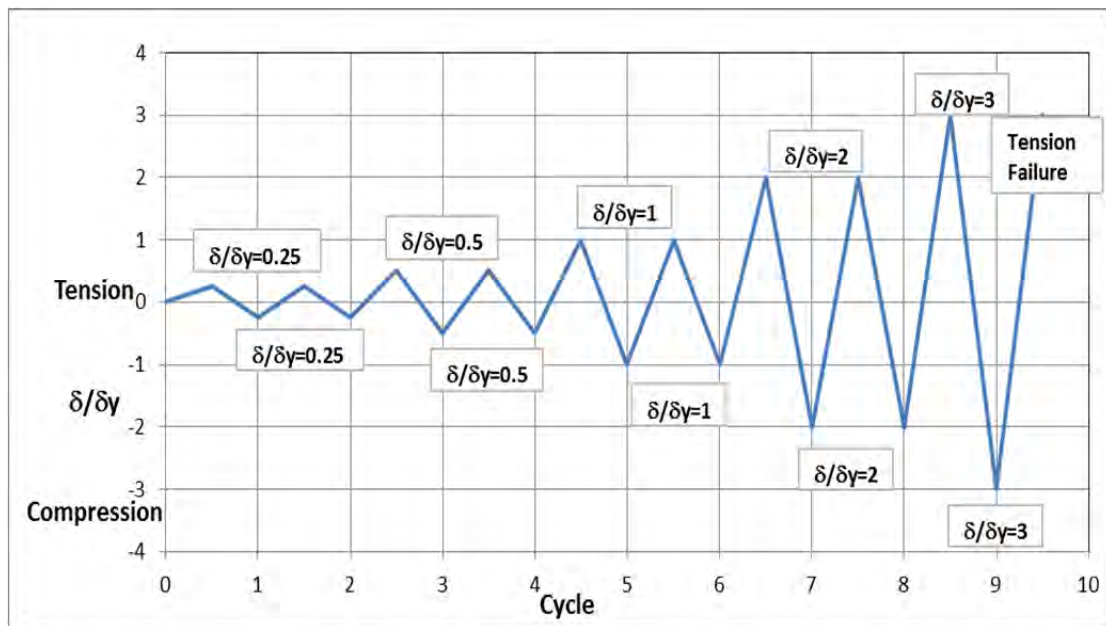


*Figure I.55  Protocol of load for test of specimen MS-S4.*

### I.1.7.4   Results of the Cyclic Compression-Tension Axial Load Test

There was not disruption while the application of the load. The speed load average of the application of the load on the test was 28 kips/min, and measured by displacement 0.015in/min. Those averages of load speed were applied for compression and tension loads. The extensometer and the stroke measurement presented linear

behavior for initial displacement. The Diphase presented on the First Set Specimen Test did not appear for this specimen MS-S4 test. During the test, there was not presented any fracture of any part of the long mechanical splice. The bolts behaved as one piece together with the mechanical splice. No buckling presented while the test was performed.

The system reached the yielding under tension loads at 45 kips load, and measured from the extensometer the yielding displacement was 0.0022 , same value than the case for tension cycle loads tests as it can be seen in Figure I.58. The yielding displacement measured from the stroke was 0.046in, as Figure I.59 shows, very similar value than MS-S3 specimen. Under compression load, the yielding load for the long mechanical splice and the portion of bars between the extensometer was 49 kips and 0.0011 deformation measured by the extensometer and 0.038in measured from the stroke. The maximum displacement in tension (+3δy) the load measured for was 66.98 kips and for max compression deformation loads 77.58 kips (-3.5δy).

The failure of the system was presented by the fracture of the previously yielded bar in the contact zone with the last bolt of the mechanical splice as Figure I.57 shows. The failure was reached increasing the tension loads to reach the peak +3δy for second time, cycle #10 as Figure I.55 shows. The rupture of the bar previously deformed produced the failure of MS-S4. The tension load value at failure was 67.35kips at kips as maximum axial load and 0.038in measured by extensometer and 0.95in measured by the stroke of the universal machine.
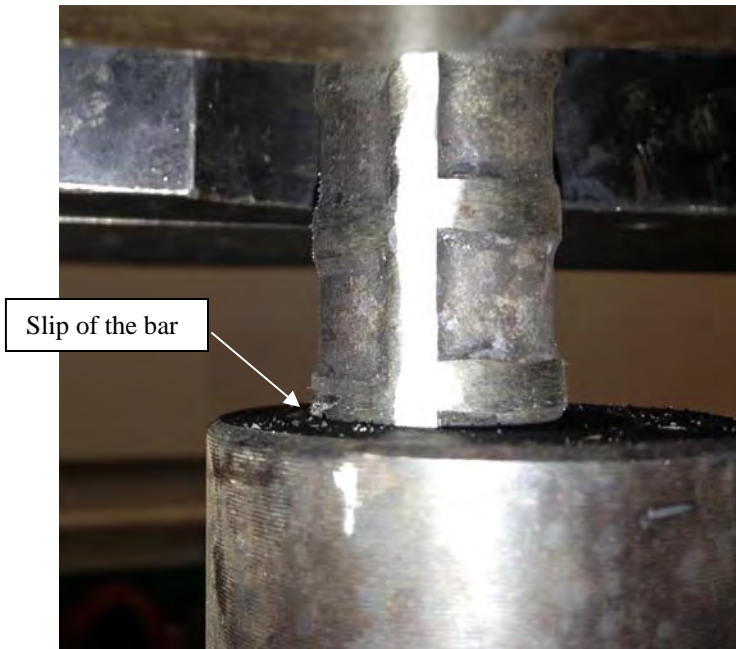
*Figure I.56  Evidence of the slip of the bar into the splice*



*Figure I.57 Failure pattern of the specimen MS-S4*

549
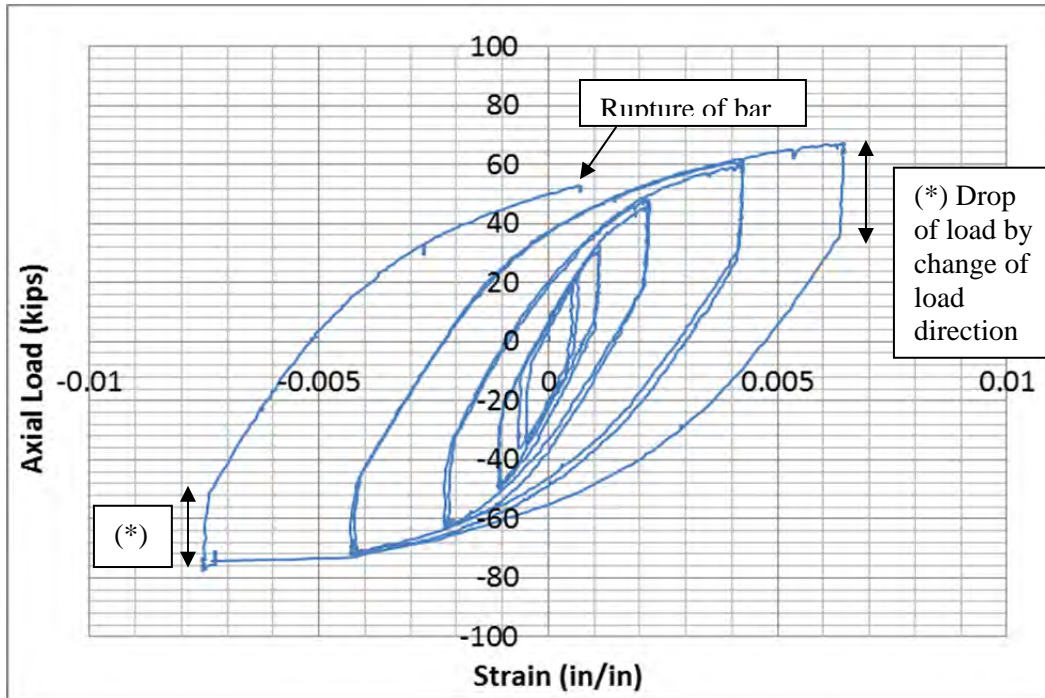
*Figure I.58  Strain deformation measured by the extensometer for MS-S4*
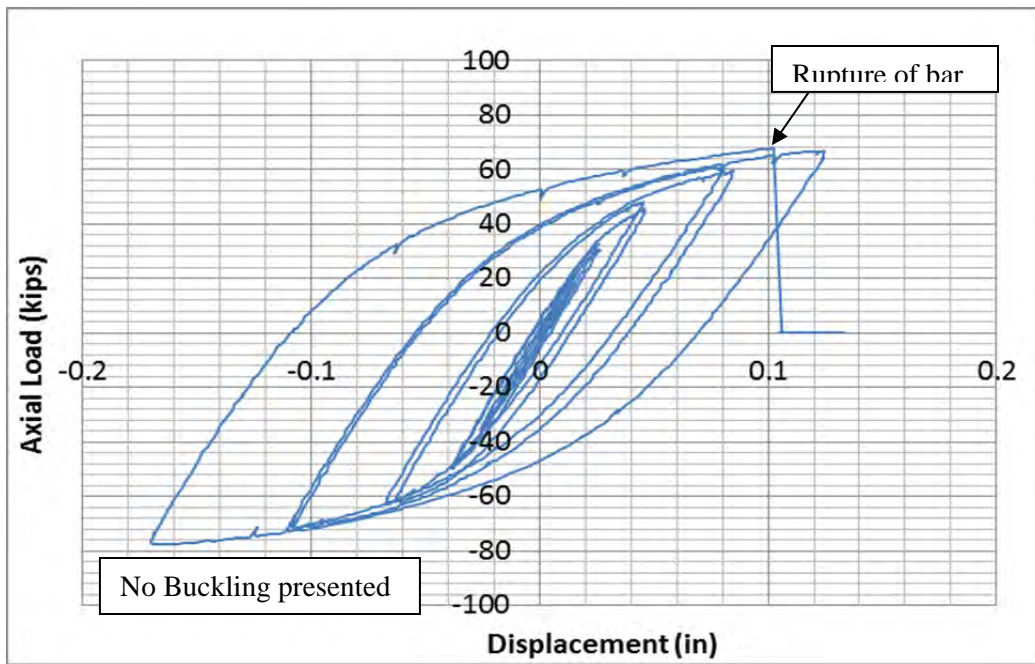


*Figure I.59  Deformation measured for by the stroke for MS-S4*

The strain at top (yielded bar zone) and bottom (new bar zone) presented different pattern of deformation different than the middle one as Figure I.60 shows, similar than specimen MS-S3. The strain at bottom behavior was linearly for tension and compression loads; however it presented a no-linear behavior under high compression loads. The strain at top presented linear behavior during the entire cycle test, however it presented different stiffness for tension and compression behaviors, being the tension stiffness less than compression one. The strain measured on the middle of the splice is linear presenting a nonlinear behavior on large compression deformations.

The stiffness of the top and bottom zone of the splice is higher than the middle part for tension and compression loads. For top part, the stiffness is 80% higher than the middle for tension loads as Figure I.61 shows. For bottom part, the stiffness is 50% higher even than the middle for tension loads. For compression loads, both, above and below the middle behavior were similar, same characteristic presented at MS-S3. Those differences are due the different cross section areas at each location of the strain gages, as it was explained at MS-L1 case.

No location presented a value higher than 0.0021 for strain as Figure I.60 shows, this indicates that the splice did not reach the yielding. The maximum values reached were 0.00017 for tension loads and 0.00019 for compression loads at the zone between the third and second bolt at the yielded bar zone of the splice; 0.00041 for tension loads and 0.00018 for compression loads at the zone between the third and second bolt at the previously new bar zone of the splice; and 0.00097 for tension loads and 0.0019 for compression at the middle of the splice. It can be explained because the cross section area on both places has larger area than the bar as is was described at the MS-L1 case.
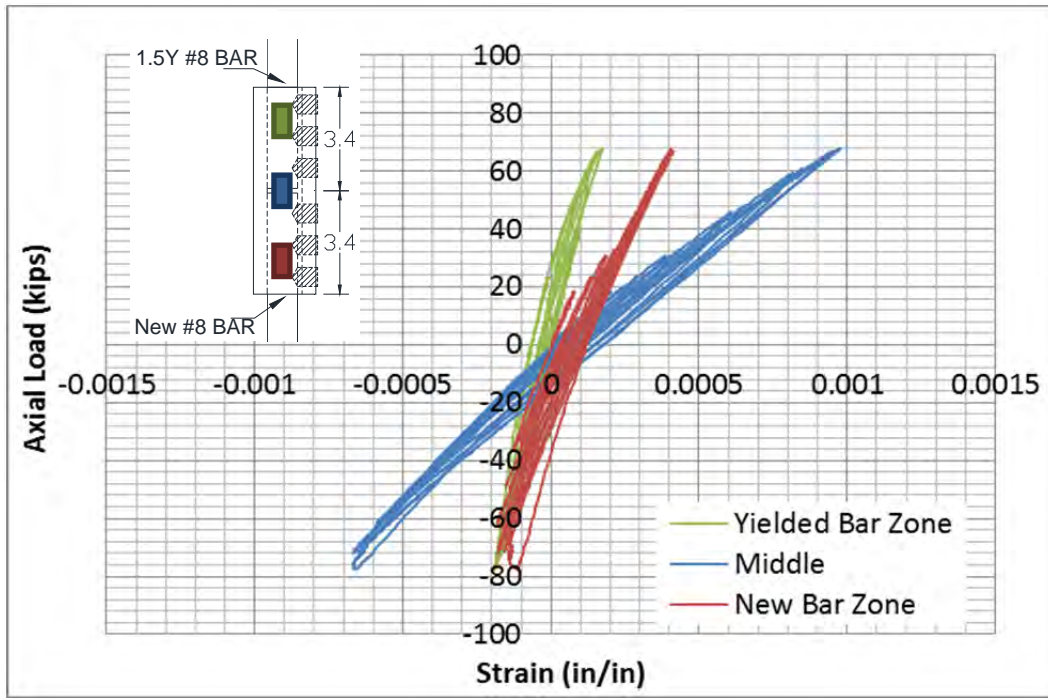
*Figure I.60  Strain at the three different locations on the mechanical splice of MS-S4.*
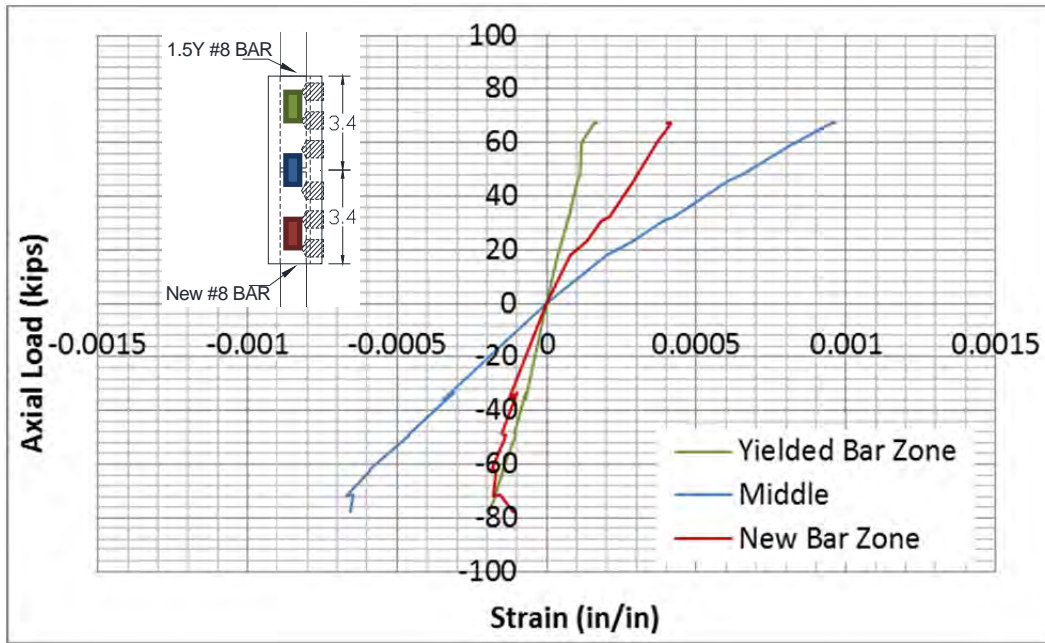
*Figure I.61  Peak cycle strain for the short mechanical splice at MS-S4*

553

## I.1.8    Specimen 9 Short Mechanical Splice MS-S5

### I.1.8.1    *Characteristics of the specimen*

This specimen consists in one new steel bar #8, a steel bar yielded previously reaching 4times tension yielding deformation and 3 times compression yielding deformation (Appendix I) and one short mechanical splices. For retrofit purposes, the mechanical splice will gather an old bar previously deformed together with a new bar, providing continuity of reinforcement. While the process of the construction of MS-S5, one bolt with point ending was broken on the thread area. It can be seen in Figure I.62 the location of the bolt broken on the tread.
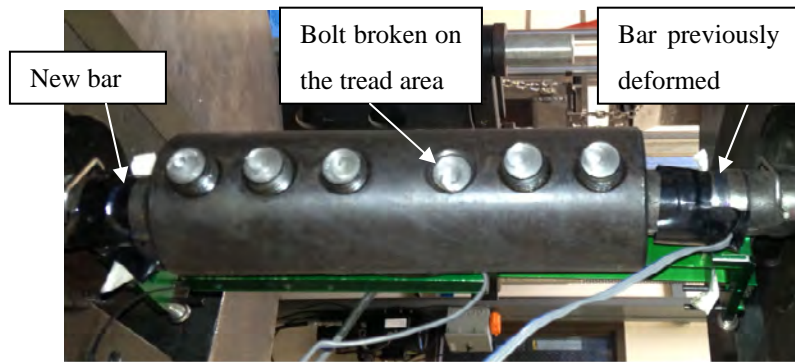


*Figure I.62 Specimen MS-S5 to be tested*

Figure  I.63 shows the sketch for the specimen MS-S5. Each bar connected with mechanical splice has a length of 3.4in into the splice, having 2.1in extra from the edge of the splice to the edge of the clamps. The total length of the specimen between clamps of the universal machine was 11in length. The previously yielded bar was applied at the top and the new bar the bottom of the short mechanical splice.

Hydraulic Clamp

Universal Machine

4Y #8 REBAR

1+1/16

Extensometer

Short
Mechanical
Splice

Cycle
Compression - Tension
Load

1+1/16

NEW #8 BAR

2.1

1.06Δb

2.1Δb

3.4

6.8    Δcoupler

3.4

2.1    1.06Δb    2.1Δb

1Δb= Dia. #8 bar (1in)

Universal Machine

Hydraulic Clamp
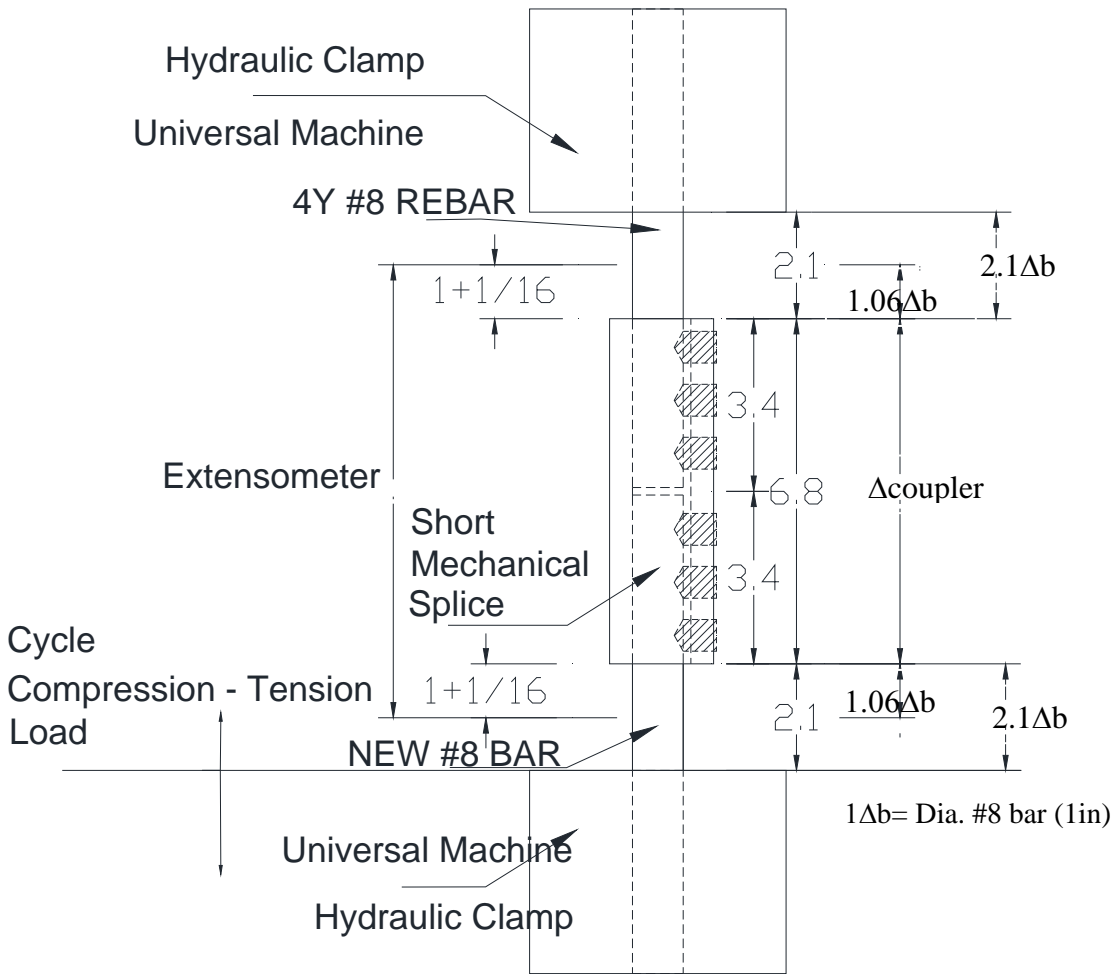
*Figure  I.63  Dimensions of specimen MS-S5*

### I.1.8.2    Instrumentation for the test

Measurement of deformation and strain located at the same locations than previous specimen (Figure I.64):

   a)   General behavior of the specimen MS-S5, Axial load vs. Deformation of the system mechanical splice and the steel bars.

b) Differences of strain deformation on the mechanical splice and the two bar which form the specimen MS-S5. Figure I.64 shows that one strain gage is located at the middle of the splice, other on the surface of the previously yielded bar 1in from the top edge of the splice, and the third strain gage was located 1 in below the bottom edge of the splice on the surface of the new bar. The line of application of gages was in the opposite face of the axis of the splice's bolts.
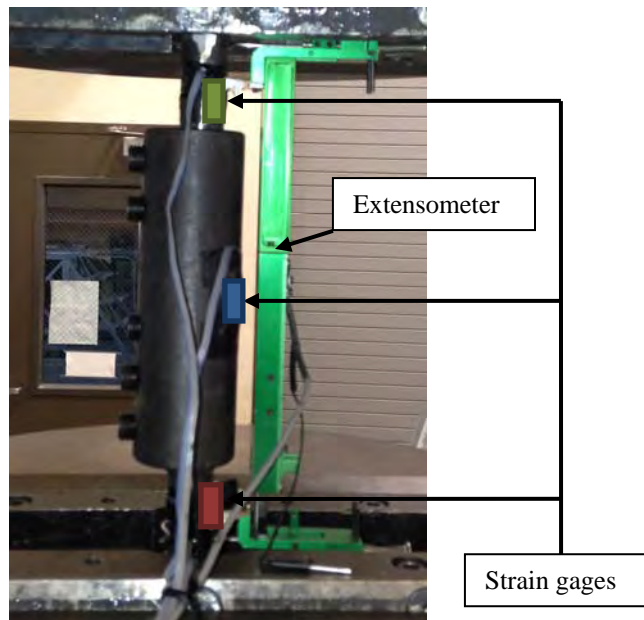


*Figure I.64  Instrumentation for test of specimen MS-S5*

### I.1.8.3  *Protocol of the test to MS-S5*

In the cyclic loading test, the specimen was subjected to two cycles of tension compression deformation of $\pm 0.25\ \delta y$, $\pm 0.5\ \delta y$, $\pm 1\ \delta y$, $\pm 2\ \delta y$, $\pm 3\ \delta y$, $\pm 4\ \delta y$, then two cycles of $+8\ \delta y$, considering at all cycles a maximum of $-6\delta y$ for compression deformation; and finally increase the deformation until de failure. The yielding

deformation considerate was δy 0.018in. The graph of the deformation protocol is shown in Figure I.65

This test was performed by displacement control too. The test was controlled indirectly by the measurement of the extensometer. The universal machine operation is controlled by the increment of tension or compression loads. However the monitored displacement measured by the extensometer indicated the peak of each cycle, pausing the test in order to change the direction of the load.
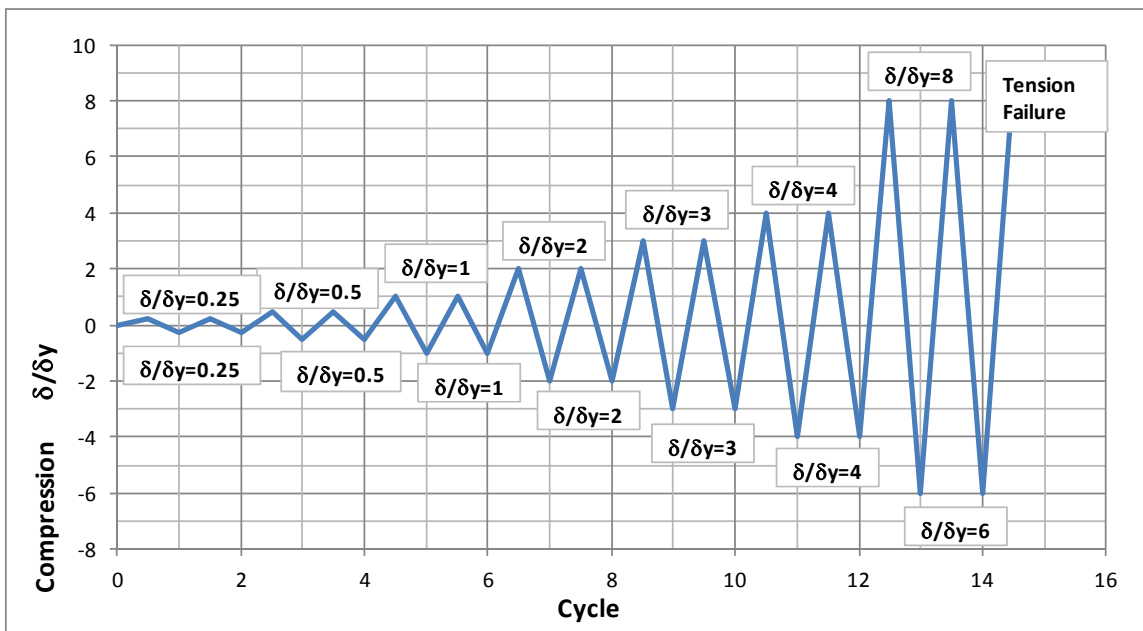


*Figure I.65  Protocol of load for test of specimen MS-S5*

### I.1.8.4   *Results of the Cyclic Compression-Tension Axial Load Test*

There was not disruption while the application of the load. The speed load average of the application of the load on the test was 14 kips/min, and measured by displacement 0.04 in/min. Those averages of load speed were applied for compression and tension loads. The extensometer and the stroke measurement presented linear

557

behavior for initial displacement. The Diphase presented on the First Set Specimen Test did not appear for this specimen MS-S5 test.

The system reached the yielding under tension loads at 51 kips load, and measured from the extensometer the yielding displacement was 0.0020, same value than the case for tension cycle loads tests as it can be seen in Figure I.68. The yielding displacement measured from the stroke was 0.053in, as Figure I.69 shows. Under compression load, the yielding load for the long mechanical splice and the portion of bars between the extensometer was 44kips and 0.0020 deformation measured by the extensometer and 0.0451in measured from the stroke. The maximum displacement in tension deformation (+8δy) the load measured for was 76.01 kips and for max compression deformation (-6δy).the load was 60.25 kips Buckling was presented on the bottom bar as Figure I.66 shows. This buckling appear when it was applied a compression load to reach -6δy deformation.

The failure of the specimen was due the fracture of the bolts that tight the bars together with the splice. The bolts receive shear force due the axial tension and compression loads applied to the specimen MS-S5. The bolts also had important shear deformation in the gap between the internal surface of the splice and the bars. The sequence of rupture of the bolts is showed in Figure I.69. The first bolt broken by shear was the $3^{er}$ bolt (next to the bottom edge of the splice), the tension load applied was 56.62 kips, having a deformation of 0.0306 measured by the extensometer and 0.481in measured by the stroke. The load dropped until cero load capacity, increasing the load again to observe the maximum capacity of the two rest bolts, reaching a tension load capacity of 21.73 kips, having the $2^{nd}$ bolt broken and the total disconnection of the bar with the splice. Only the $1^{st}$ bolt (next to the middle of the splice) remained together with the splice without rupture as it can be seen in Figure I.67.

558

*Figure I.66 Buckling presented in new bar on the specimen MS-S5*



*Figure I.67 Bolts broken on the thread between the internal surface of the splice and the new steel bar.*
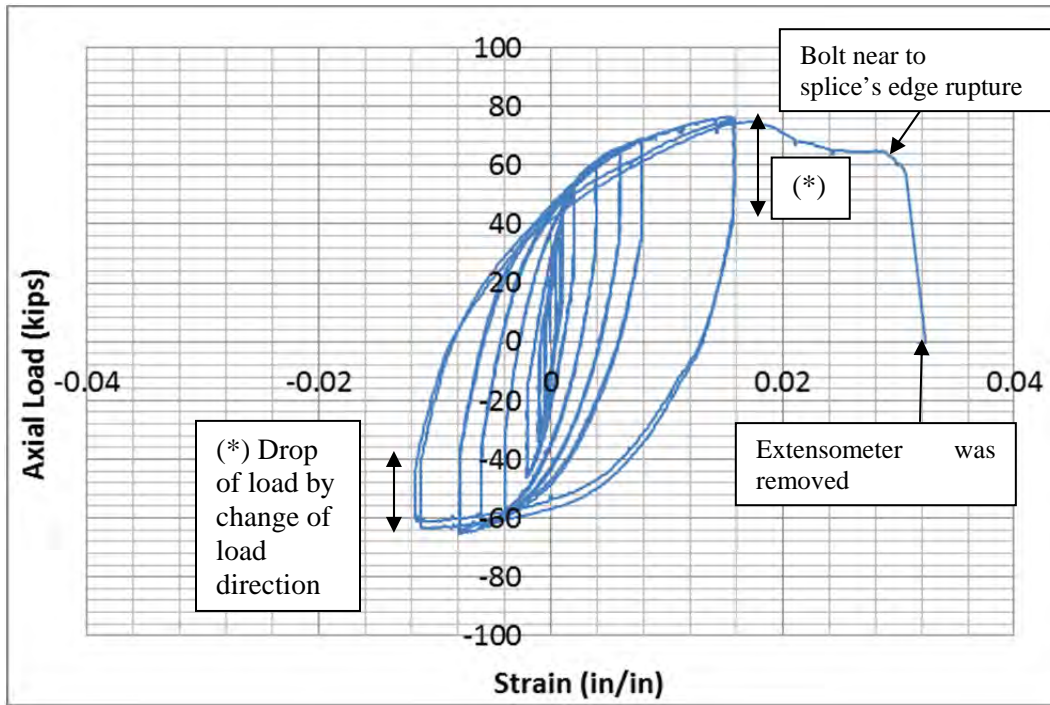
*Figure I.68  Deformation measured by the extensometer on specimen MS-S5*

The chart contains the following labels:
- 3 bolts having high shear deformation
- Bolt near to splice's edge rupture
- Behavior of 2 rest bolts
- 2nd bolt rupture
- Displacement altered by the buckling presented

Axis labels: Axial Load (kips) — vertical; Displacement (in) — horizontal
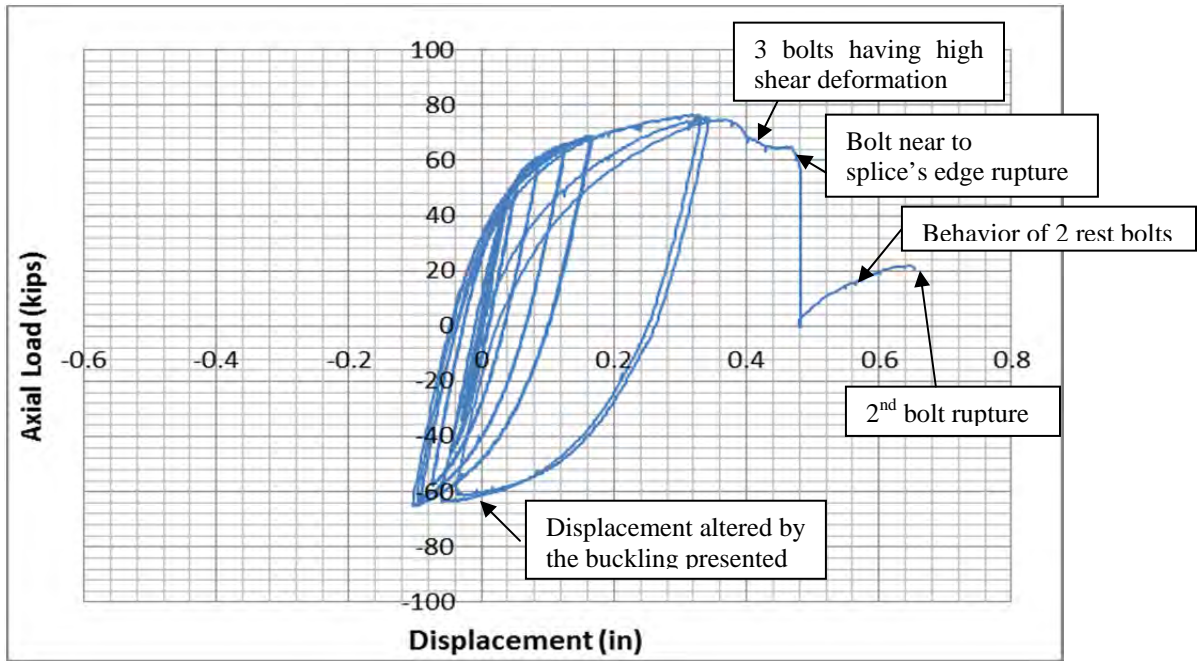
*Figure I.69  Displacement measured by the stroke for test of specimen MS-S5*

The strain measured on the middle of the splice is linear presenting a nonlinear behavior on large compression deformations, especially for -6 δy. The strain measured on the middle of the splice did not reach the yielding strain for steel A60: 0.0021, as it can be seen in Figure I.68. The maximum deformation under tension loads was 0.00097  and for compression loads 0.0019 .

The strain measured on the bars, both presented bilinear behavior as they can be seen in Figure I.71 and Figure I.72. Both the previously yielded and new bars had similar deformation and stiffness under tension loads, however for compression loads the previously yielded bar presented less stiffness and larger strain deformation than the new bar. This induce the conclusion that the previously yielded bar had reduced compression

561

capacity at comparison than a new bar. The previously yielded bar was tested until 4 times yielding deformation under tension loads and 3times yielding deformation under compression loads, this previous its application into the short mechanical splice.

The bottom bar has been buckled as Figure I.66 shows. The buckling appeared when the specimen was being loaded in order to reach 0.105 in compression deformation. It can be seen in Figure I.72 that the strain deformation was disrupted by the buckling effect on the bar.
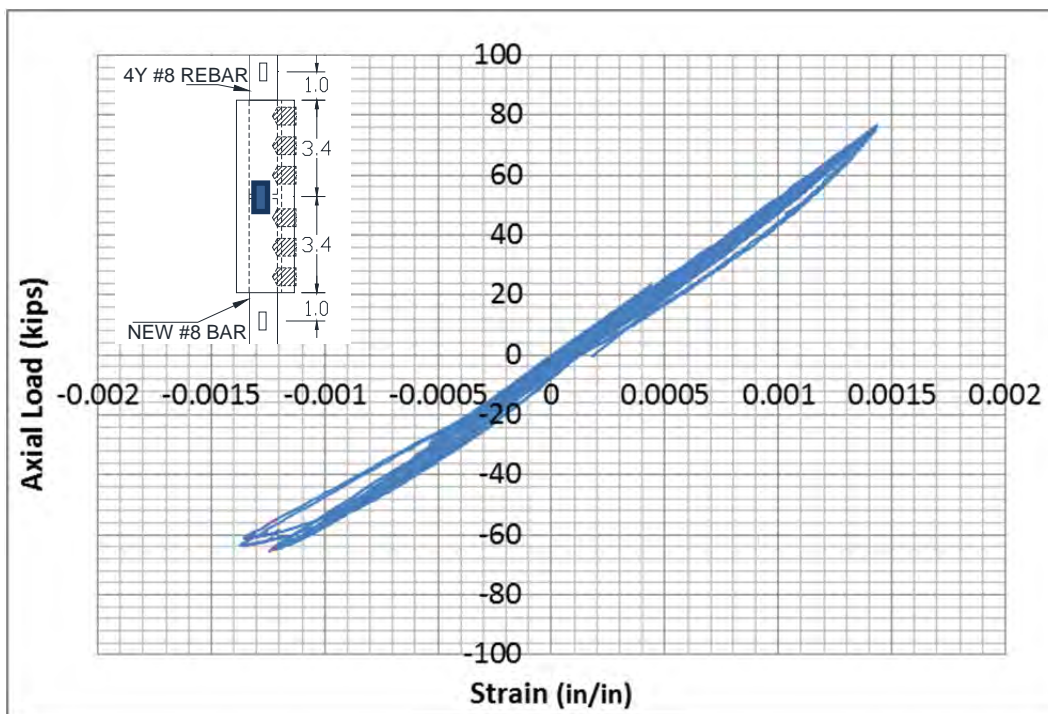


*Figure I.70  Strain measured at the middle of the splice*
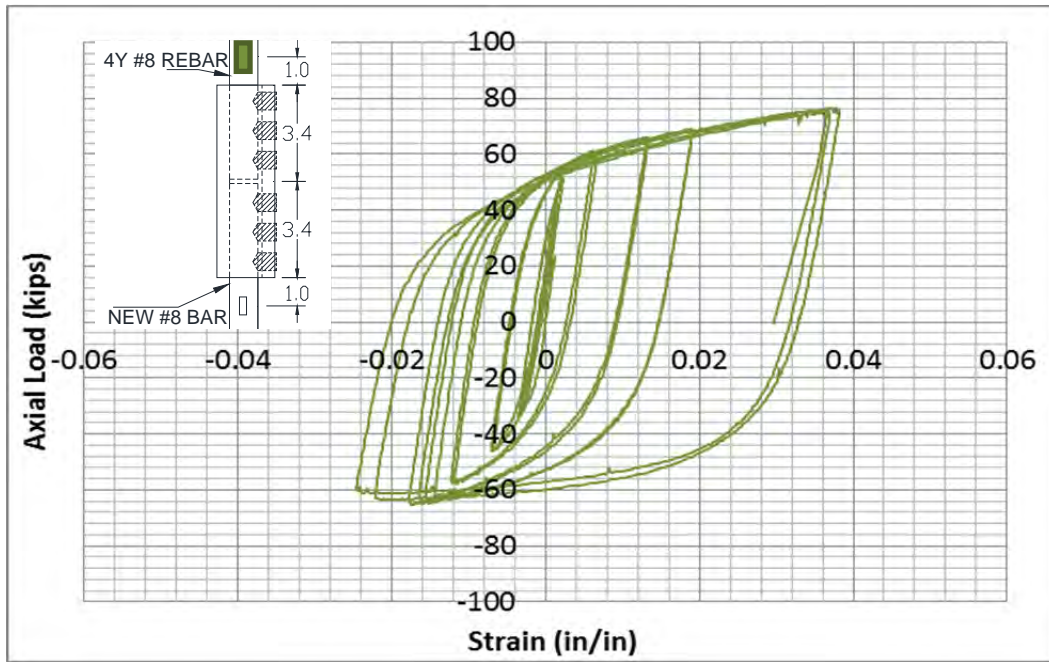
*Figure I.71  Strain measured on the top bar (previously yielded)*
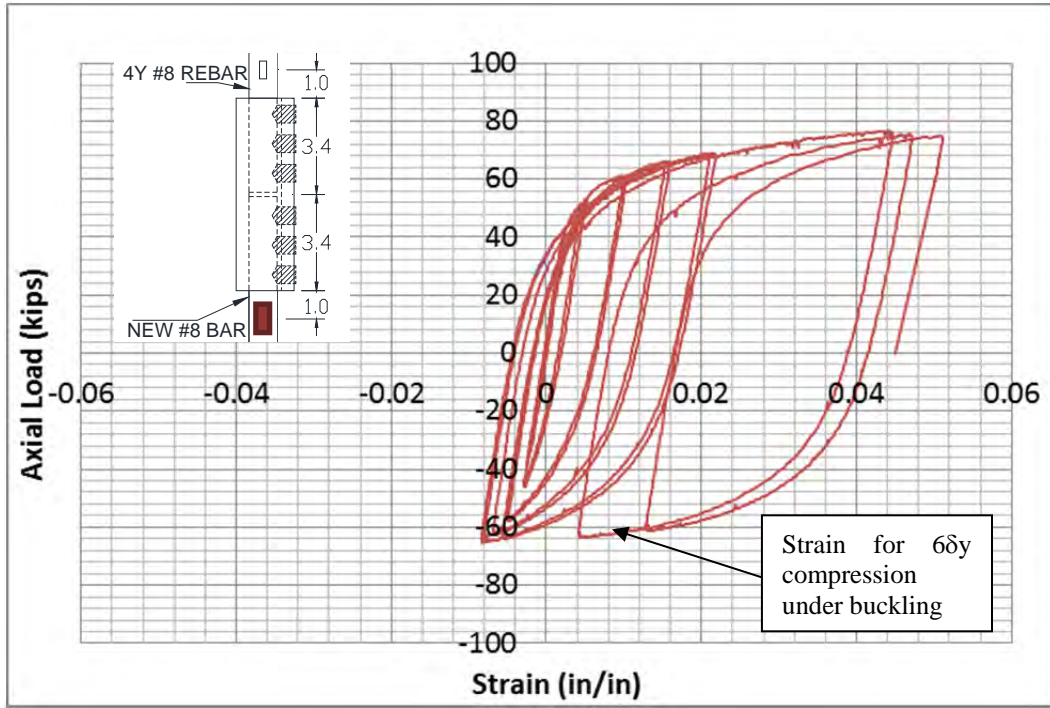
*Figure I.72  Strain measured on the bottom bar (new steel bar)*
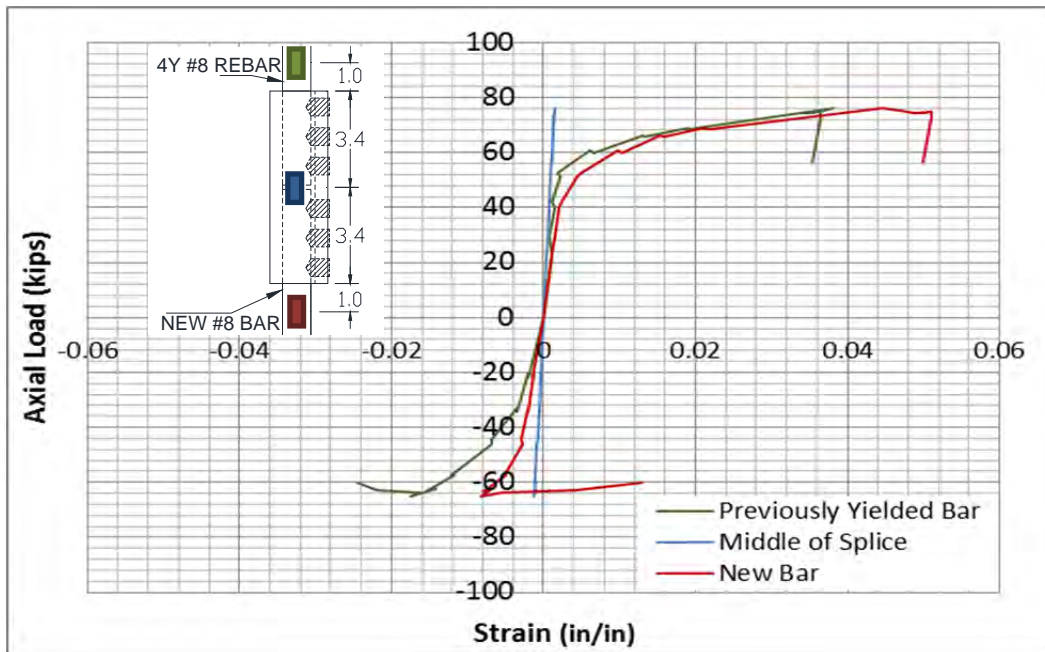
*Figure I.73  Peak cycle strain measure.*

### I.1.9    Specimen 10 Short Mechanical Splice MS-S6

#### I.1.9.1    *Characteristics of the specimen*

This specimen consists in one new steel bar #8, a steel bar yielded previously reaching 1.5 times tension yielding deformation and 3 times compression yielding deformation (Appendix I) and one short mechanical splices. For retrofit purposes, the mechanical splice will gather an old bar previously deformed together with a new bar, providing continuity of reinforcement. While the process of the construction of MS-S6, one bolt with point ending was broken on the thread area. It can be seen in Figure I.74 the location of the bolt broken on the tread.



New bar

Bolt broken on the tread area

Bar previously deformed
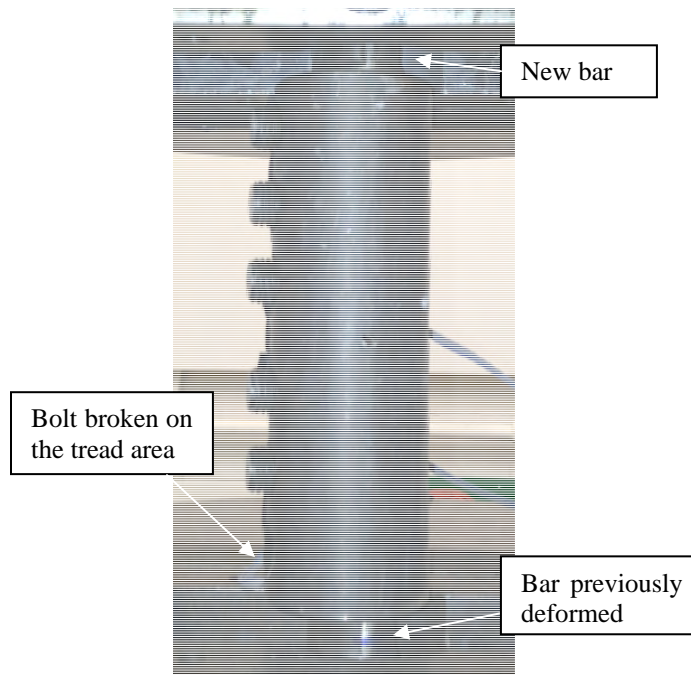
*Figure I.74 Specimen MS-S6*

In order to review the effect of the failure of the bolts produced by the larger tension and compression deformation applied in specimen MS-S5 and also to prevent the buckling to study the specimen under high compression axial load, the specimen had short steel bars applied into the short mechanical splice. Figure I.75 shows the scheme for

566

the specimen MS-S6. Each bar connected with mechanical splice has a length of 3.4 in at the interior of the splice, having a extra 1.25 in from the edge of the splice to the edge of the clamps. The total length of the specimen between clamps or the empty room of the universal machine was 11.3 in length. It is used short length pieces of bar at comparison than previous cases that have around 1in larger. Since the clear room of the universal machine has a short distance, 13.in length, there is no enough gap to locate a extensometer.
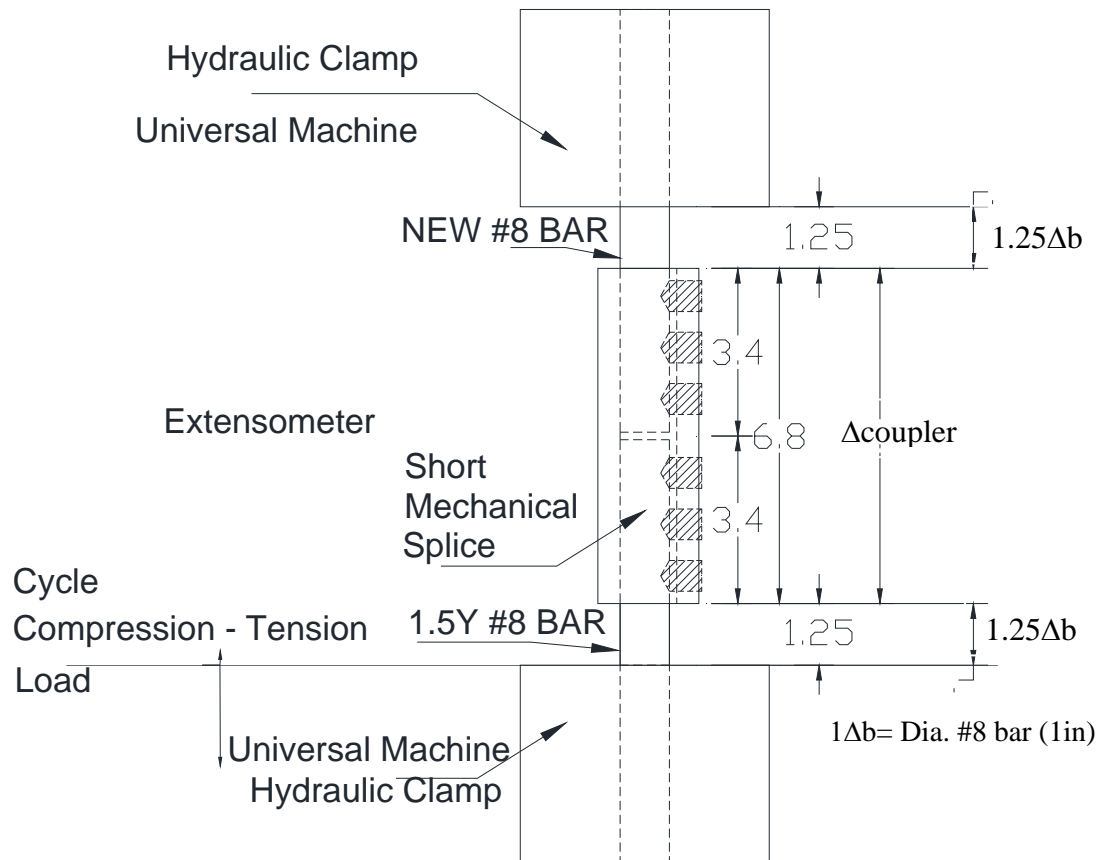


*Figure I.75  Dimensions of specimen MS-S6*

### I.1.9.2  Instrumentation for the test

The objectives of measurement for this test were (Figure I.76.):

a) General behavior of the specimen MS-S6, Axial load vs. Deformation of the specimen.

b) Differences of strain deformation on the mechanical splice. One strain gage is located on the middle of the splice; the second one between the first and second bolt of the top part of the short mechanical splice where is applied the new bar, and the third strain gage is placed at the exact opposite location, it is between the first and second bolt of the bottom part of the short mechanical splice where the previously yielded bar is applied into the short mechanical splice. The location of the strain gages is shown in Figure I.76.



Strain gages
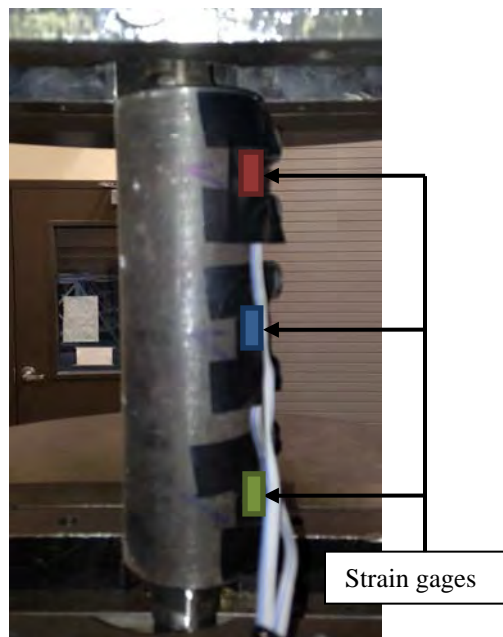
**Figure I.76  Instrumentation for test of specimen MS-S6**

### I.1.9.3  *Protocol of the test to MS-S6*

In the cyclic loading test, the specimen MS-S6 was subjected to two cycles of tension compression deformation of ±0.25 δy, ±0.5 δy, ± 1 δy, ± 2 δy, ± 3 δy, ±4 δy, then one cycles of ±6 δy; and finally increase the deformation to failure. The yielding deformation considerate was δy 0.018in. The graph of the protocol of deformation for this test MS-S6 is showed in Figure I.65

The test was controlled indirectly by the measurement of the stroke in the universal machine at its bottom cylinder. The universal machine operation is controlled by the increment of tension or compression loads.
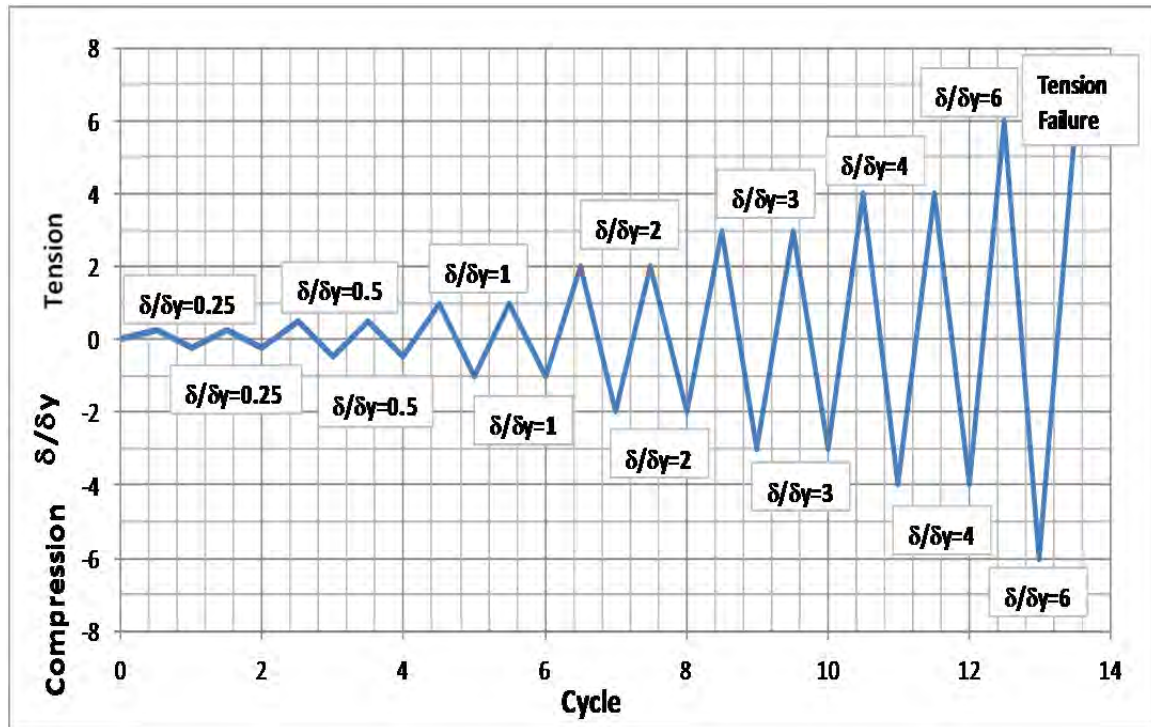


*Figure I.77  Protocol of load for test of specimen MS-S5*

### I.1.9.4   Results of the Cyclic Tension Axial Load Test

There was not disruption while the application of the load. The load ratio average of the application of the load on the test was 32 kips/min, and measured by displacement 0.041in/min. That average load ratio was applied for compression and tension loads.

The stroke measurement presented linear behavior for initial displacement. During the test, there was not presented any fracture of any part of the long mechanical splice. The bolts behaved as one piece together with the mechanical splice. No buckling presented while the test was performed.

The system reached the yielding under tension loads at 43 kips, the yielding displacement measured from the stroke was 0.040in, as Figure I.80 shows. Under compression load, the yielding load for the long mechanical splice and the portion of bars between the extensometer was 52 kips and 0.036 in deformation measured by the stroke. For the maximum displacement in tension ($+6\delta y$), the load measured was 65.96 kips and for max compression deformation loads 78.01 kips ($-6y$).

The failure of the system was presented by the fracture of the previously yielded bar in the contact zone with the last bolt of the mechanical splice as Figure I.79 shows. The failure was reached increasing the tension loads to reach the peak $+6\delta y$ for second time, cycle #12 as Figure I.77 shows. The rupture of the bar previously deformed produced the failure of MS-S6. The tension load value at failure was 65 kips and 0.095in measured by the stroke of the universal machine.
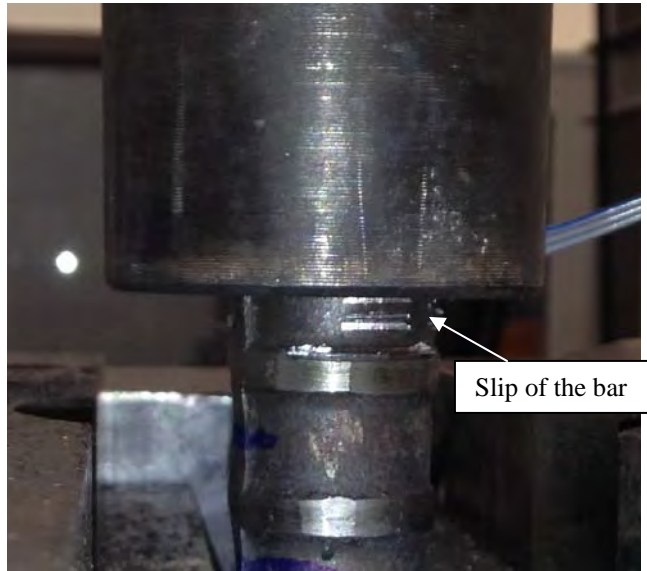
*Figure I.78 Slip of the yielded bar, marks of the interior threads of the splice are seen.*



*Figure I.79 Failure pattern of specimen MS-S6*
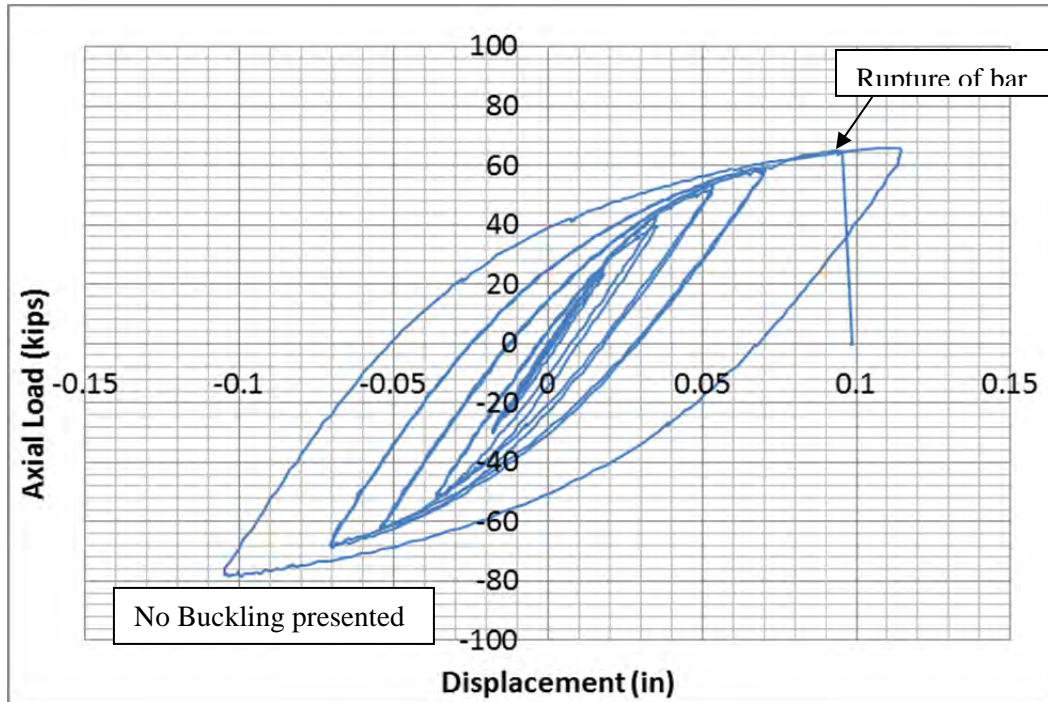
*Figure I.80  Deformation measured for the system and the mechanical splice MS-S1*

The strain at top (yielded bar zone) and bottom (new bar zone) presented different pattern of deformation different than the middle one as Figure I.81 shows. The strain at bottom behavior was linearly for tension loads; however it presented a no-linear behavior under compression loads having tension deformation. Similar pattern top part of splice presented, having same deformation under tension loads and also tension deformation under compression loads. The strain measured on the middle of the splice was linear presenting a nonlinear behavior on large compression deformations. This effect can be explained considering the location of the gages next to the edge of the bolts. The stiffness of the top and bottom zone of the splice is higher than the middle part for tension loads. For top part and bottom part, the stiffness is 55% higher than the middle for tension loads as Figure I.82 shows.

572

No strain had a value higher than 0.0021 for strain as Figure I.60 shows, this indicates that the splice did not reach the yielding. The maximum values reached were 0.00057n/in for tension loads and 0.00003 for compression at the zone between the third and second bolt at the yielded bar zone of the splice; 0.00066 for tension loads and 0.000004 for compression at the zone between the third and second bolt at the previously new bar zone of the splice; and 0.00106 for tension loads and 0.00053 for compression at the middle of the splice.
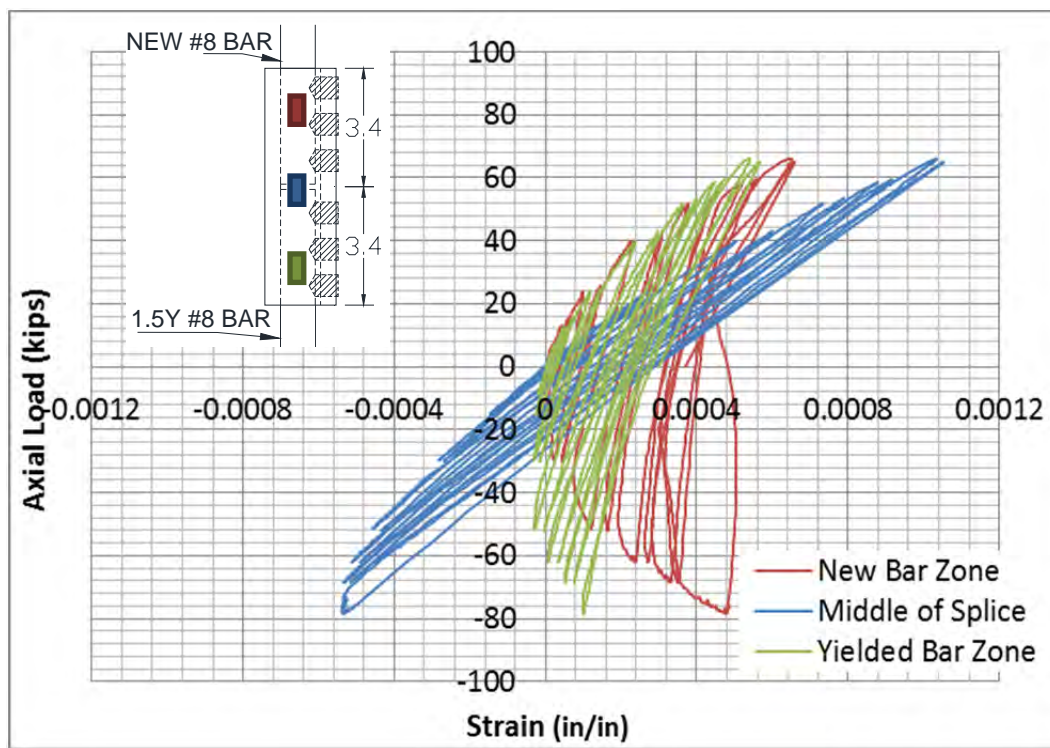


*Figure I.81  Strain at the three different locations on the mechanical splice of MS-S6*
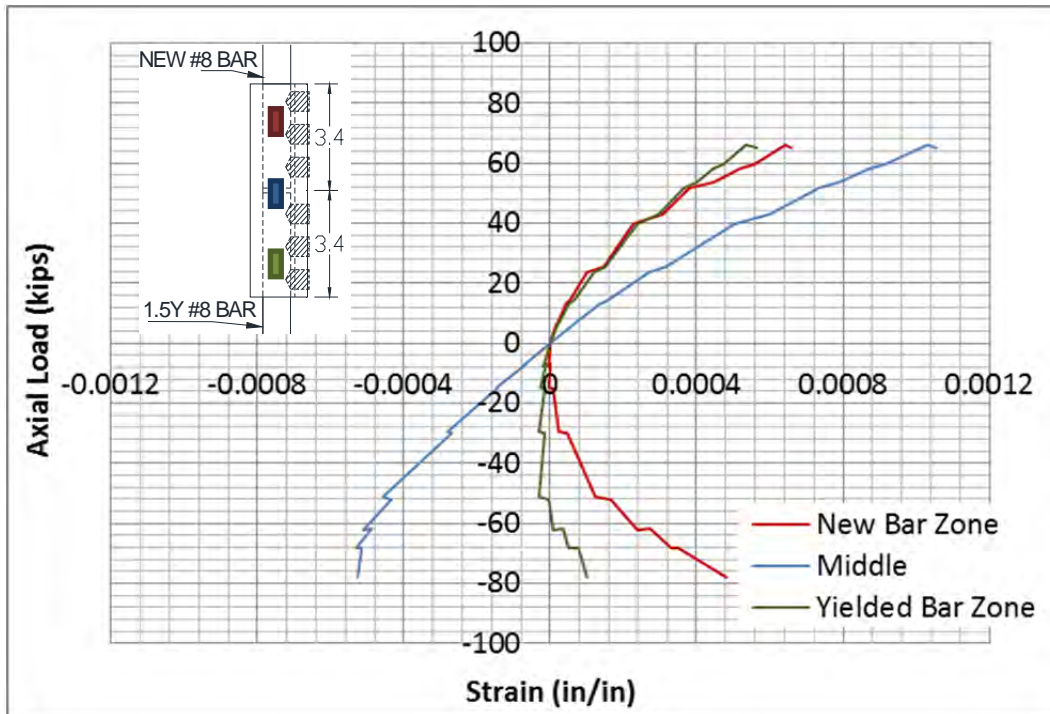
*Figure I.82  Peak cycle strain for the short mechanical splice at MS-S6*

APPENDIX J

# Non-linear Static Analysis of Existing Building Using Behavioral Models Developed

## J.1 INTRODUCTION

Inclusion of behavioral models of new retrofit procedures into current Performance Based Seismic Design procedure (ASCE 41) for strengthening of existing or repaired damaged buildings was proposed. The models are used to perform a nonlinear static analysis of an existing structure in which the columns have been strengthened using long mechanical splices. The objective of this non-linear static analysis is to demonstrate how these methodologies of retrofit can be used in design.

## J.2 STRUCTURE

An evaluation of an existing building shown in Figure J.1 was performed to determine its ability to resist seismic forces. The structure has a basement and 5 stories. The structural system in the North-South direction is formed by concrete frames with three different sizes of rectangular columns. The East-West direction is formed principally by shear walls formed by the 8 external towers. The assessed direction was the north-south direction.

The height of the basement and 1$^{st}$ story is 144in and the rest of stories are 165in high. The area of the floors is 245ft x 90ft. The basement is surrounded by retaining walls.

*Figure J.1  Aerial view of the Science Building*

The north-south direction lateral force resisting system consists of 3 frames along three different axes (Figure J.2). Three types of columns were used. Figure J.3 shows a typical section 2.10x2 (34"x24" cross section). This column was included in every frame also for a total of 20 columns. Four columns 2.6x1.6 (30"x18") and one 2x1.6 (24"x18") also were used.
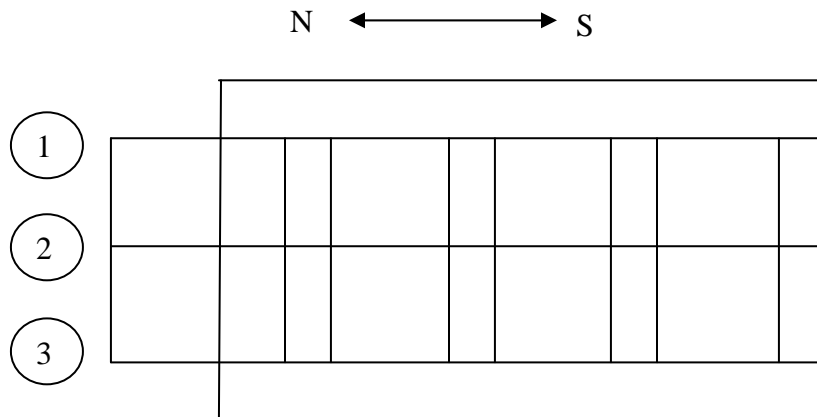
*Figure J.2  Plan scheme of the principal axes of the structure in north-south direction*
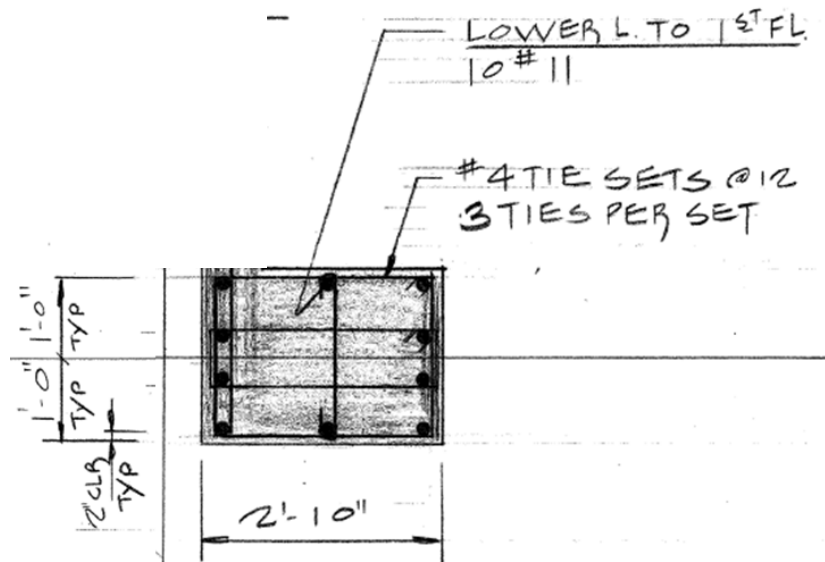


*Figure J.3  Transverse section of column 2.10 x 2*
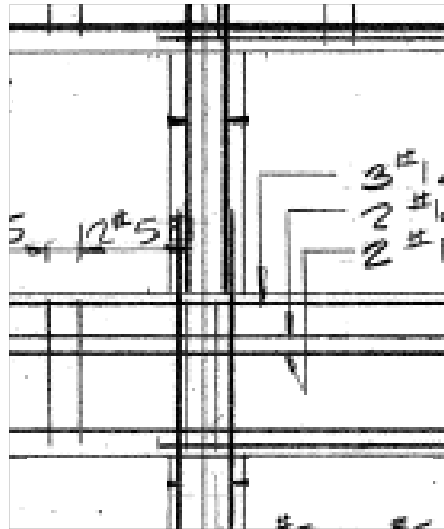
*Figure J.4  Short lap splice located on the bottom of columns in basement and 1<sup>st</sup> story.*

The compressive strength of concrete girders, shear walls, and columns was determined to be 5000 psi from the structural drawings. Available drawings did not include specifications for the yield strength of the reinforcing bars and tendons and thus could not be determined without testing of the reinforcement currently in the building. Since this proposition proved to be infeasible, the date of the structural drawings allowed for the determination that the minimum yield strength of 60,000 psi was applicable for the reinforcing steel.

Several deficiencies in the building were identified In the North-South direction. Short lap splices are located at the bottom of the columns of the basement and the first story and the columns does not have a sufficient amount of transversal reinforcement. The lateral force resisting system does not have enough strength to withstand a design earthquake.

A nonlinear static procedure (NSP) was used to analyze the existing structure.

## J.3    NON-LINEAR STATIC ANALYSIS - PUSHOVER

A 3D computer model of the building was created by the program Structural Analysis Program (SAP 2000 v.15). The computer model developed only utilized the elements which were determined to have a significant contribution to the lateral force resisting system. Every floor of the structure was considered as rigid in order to constrain displacement.
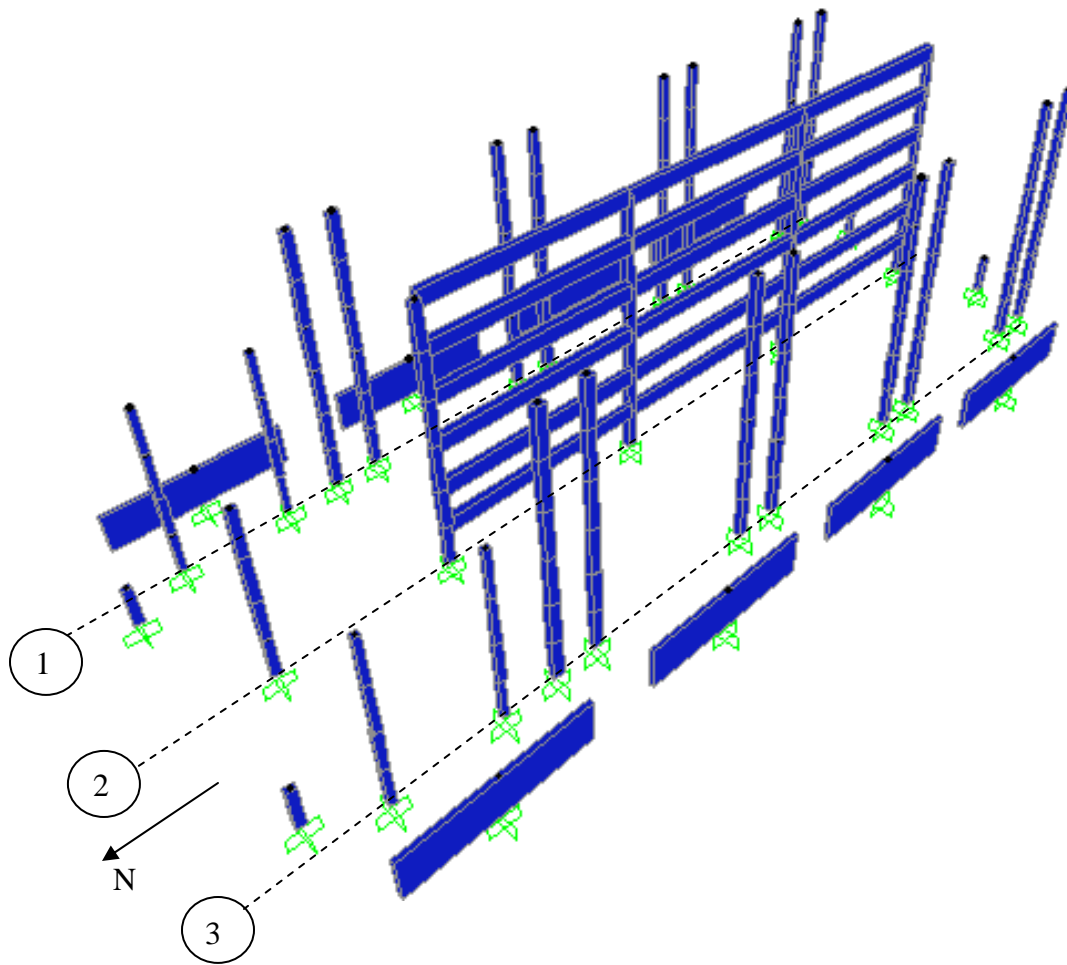


*Figure J.5  3D View of the structure*

Since the floor slabs were not modeled, the dead and live loads of the structure had to be manually computed and entered into the computer model. Point loads were added to the column and shear walls at each level, representing the dead load carried by each element. The load schedule shown in the existing building drawings was used as a guide for live loads.

In a nonlinear static analysis, seismic forces are not directly applied. Instead, the structure is subjected to lateral displacements, and the lateral capacity is measured. The computer model was analyzed for a total of seven different load cases. These included 5 first-order linear-elastic analyses cases, and 2 first-order nonlinear static analyses cases. These seven different load cases are shown in Table J-1.

In order to properly capture the effects of gravity loads, a non-linear analysis was first performed using only those loads. From that point in the structural response, the non-linear analysis was continued with the application of lateral displacement to the structure.

*Table J-1  Type of load and description*

| Case No. | Analysis Case | Type | Description |
|---|---|---|---|
| 1 | **Dead Load** | 1$^{st}$ order linear static | Gravity loads due to self weight of building components |
| 2 | **Live load** | 1$^{st}$ order linear static | Live loads on floor slab |
| 3 | **Modal** | Linear elastic | Modal analysis of building |
| 4 | **Gravity** | 1$^{st}$ order nonlinear static | Nonlinear analysis of full dead load along with 25% of live load |
| 5 | **UNIF X** | 1$^{st}$ order linear elastic | Linear analysis of floor displacements at each level. Performed for the following Analysis Case. |
| 6 | **Pushover UNIF X-dir** | 1$^{st}$ order nonlinear static | Nonlinear static analysis of later loads assuming a uniform distribution of lateral forces at each level proportional to the total mass at each level. |
| 7 | **Pushover MODE X-dir** | 1$^{st}$ order nonlinear static | Nonlinear static analysis of lateral forces assuming a modal shape of displacement |

## J.3.1    As-built Building with poor lap splices

The definition of backbone curves for concrete members was found in accordance with the requirements of ASCE41-07, section 6. The typical backbone curves for moment hinging without lap splices in this building are shown in Figure J.6 and with lap splices in Figure J.7. The value of the individual scale factor (Yielding moment) defined the backbone curves for each element.

581
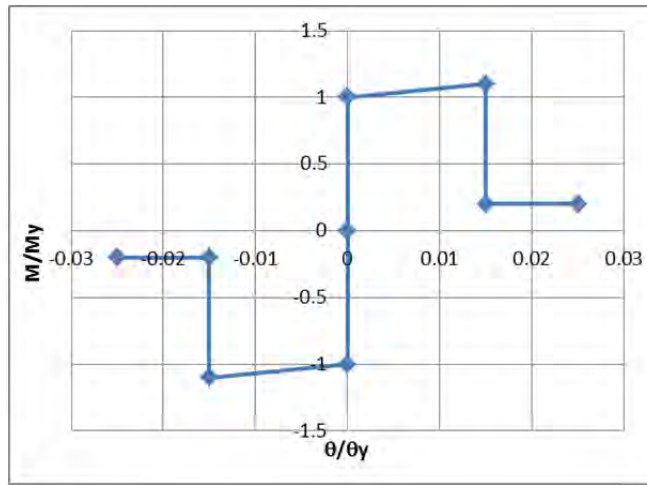
*Figure J.6  Typical backbone curve for moment-rotation for hinge without lap splice*
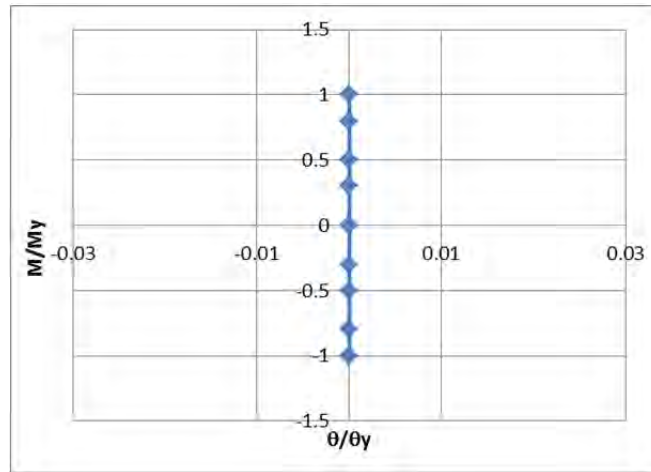


*Figure J.7  Typical backbone curve for moment-rotation for hinge with poor lap splice*

The results of the pushover analysis revealed that the structure begins to lose stiffness once the control node at the top of the building has displaced by roughly 2 in. horizontally in the north-south direction, and a peak base shear is reached of between 1900 kips for Unif. Dir.X type of load, and 1500 kips for Mode Dir.X type of load. Because of the poor lap splices, the structure has a sudden loss of lateral capacity at a displacement of 3.5 in. The ultimate lateral displacement reached in both types of

582

analysis was 16.5in. of deformation at the control node. The results of the pushover curve for two different load distributions are shown in Figure J.8
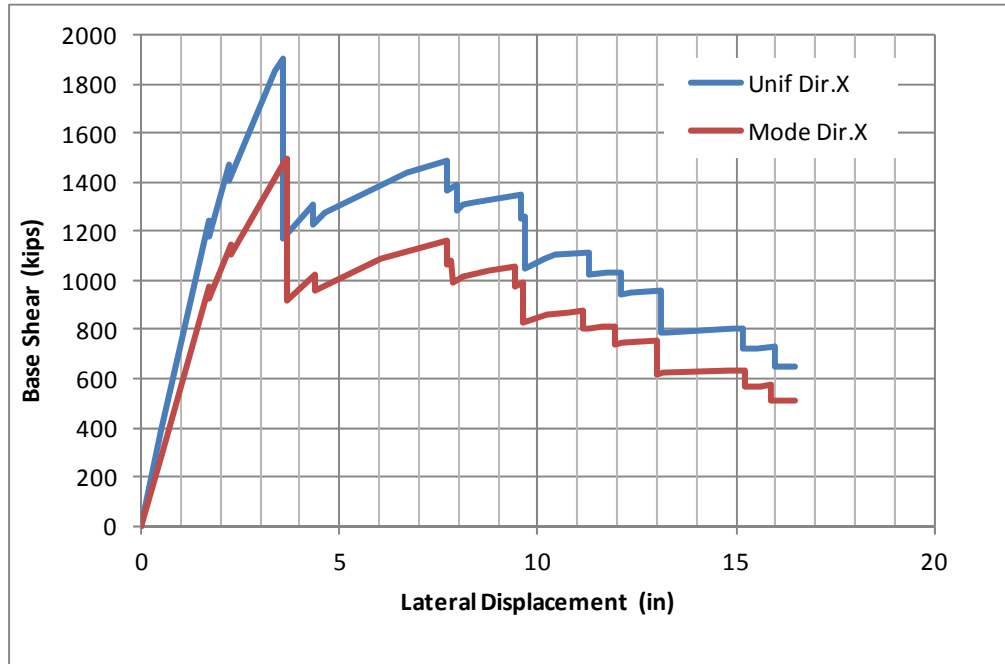


*Figure J.8 Capacity curves of the as-built structure for the two types of pushover analysis*

Figure J.9 shows the structure deformed 3.6in at roof. The maximum lateral capacity (Base Shear) is reached. It can be seen that the hinges in the bottom of columns of the first story collapsed (red point). The rest of columns remain with acceptable deformations and reached the immediate occupancy level of behavior in the worst case scenario (blue points), and the other reached the yielding only (pink points).

**Failure of hinges**

**Failure of hinges**

**Failure of hinge**
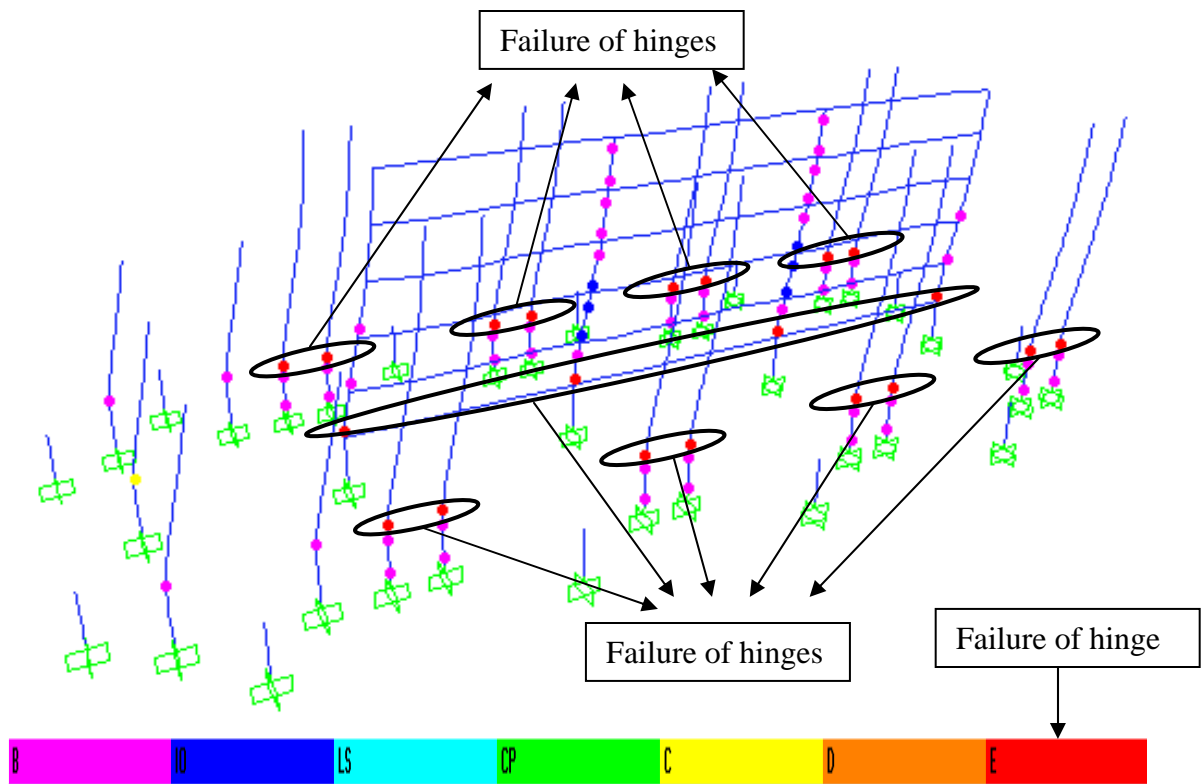
*Figure J.9 Level of damaged hinges at 3.6in lateral displacement, maximum lateral capacity*

## J.3.2 Retrofitted Building replacing the poor lap splices zones with long mechanical splices.

The bottom of columns in the first story will be replaced. Instead of lap splices, it with long mechanical splices. Figure J.10 shows a detail of the retrofit. The concrete over the length of the splices will be removed and the bars cut to permit installation of the long splice.
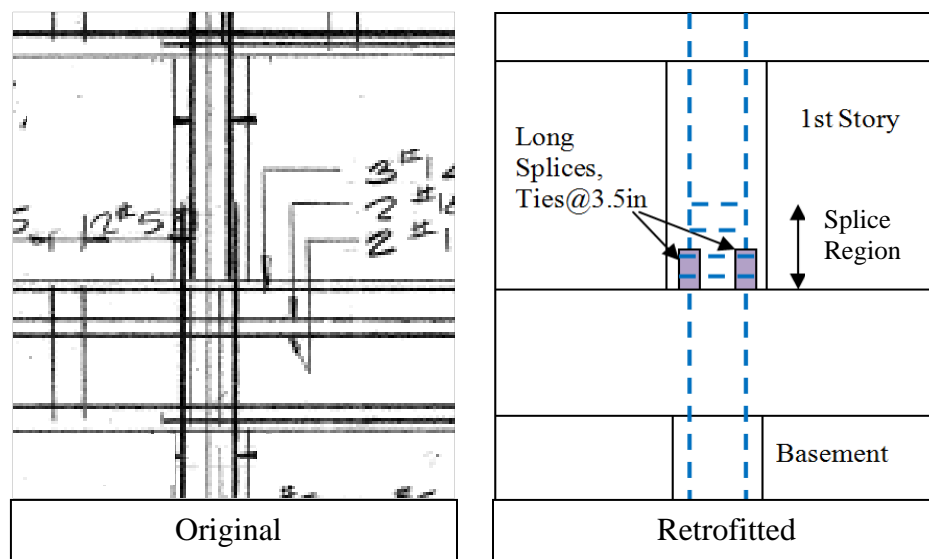


*Figure J.10 Scheme of strengthening of the columns in first story.*

Figure J.11 shows the characteristic of the hinge with long mechanical splices and the sufficient transverse reinforcement.

585
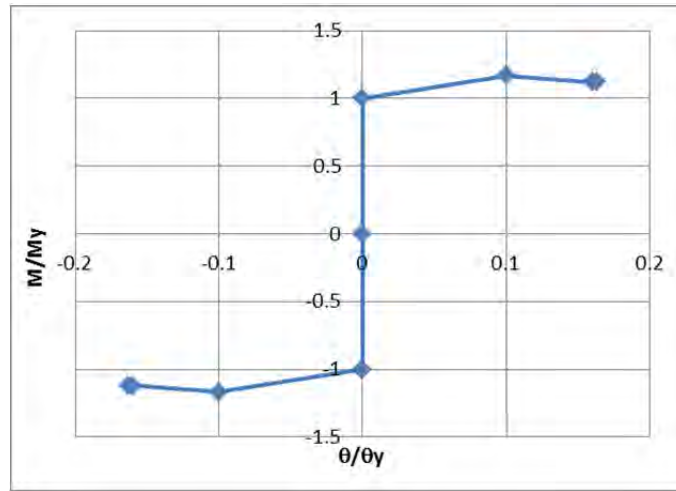
*Figure J.11  Typical backbone curve for moment-rotation for hinge without lap splice*

The pushover curve in the North-South direction was recalculated. The results of the pushover analysis revealed that the structure begins to lose stiffness once the control node at the top of the building has displaced by roughly 4in. horizontally in the north-south direction, and a peak base shear is reached of between 2450kips for Unif. Dir.X type of load, and 1900 kips for Mode Dir.X type of load. The lateral displacement reached in the calculation in both type of analysis was 35in. The results of the pushover curve for two different load distributions are shown in Figure J.12.

586
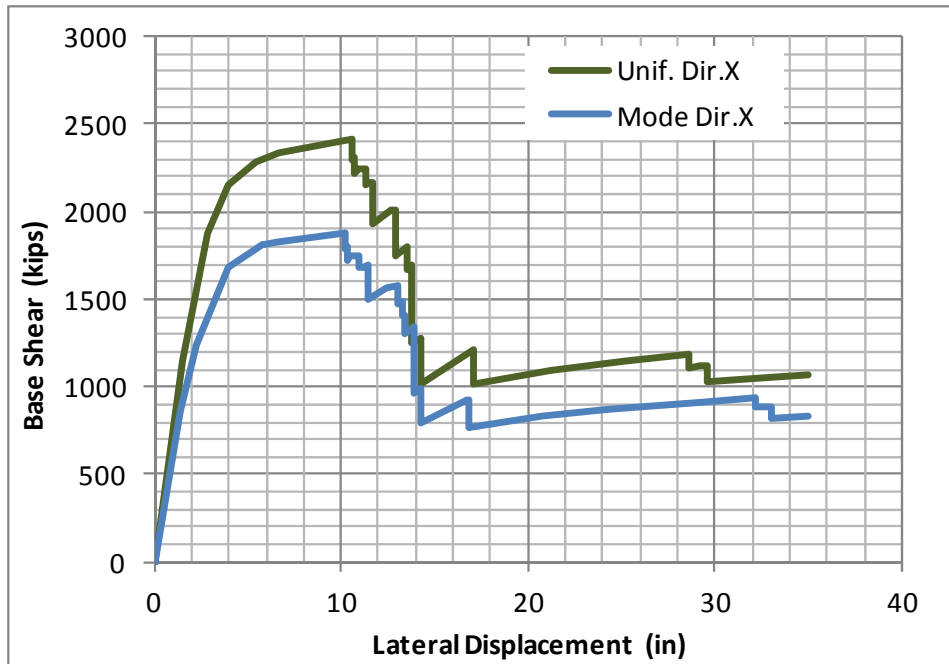
*Figure J.12 Capacity curves of the retrofitted structure for the two types of pushover analysis*

Figure J.13 shows that the peak shear capacity was reached at a deformation of 10.6in at the roof level. It can be seen that the hinges in the bottom of columns of the first story are at immediate occupancy level (blue point). The rest of columns remain with acceptable conditions, and reached the immediate occupancy level of behavior in the worst case scenario (blue points), and the other columns at that level were below failure, hinges only reached the yielding (pink points). In the center axis of the structure, two columns in second story developed a hinge close to collapse.
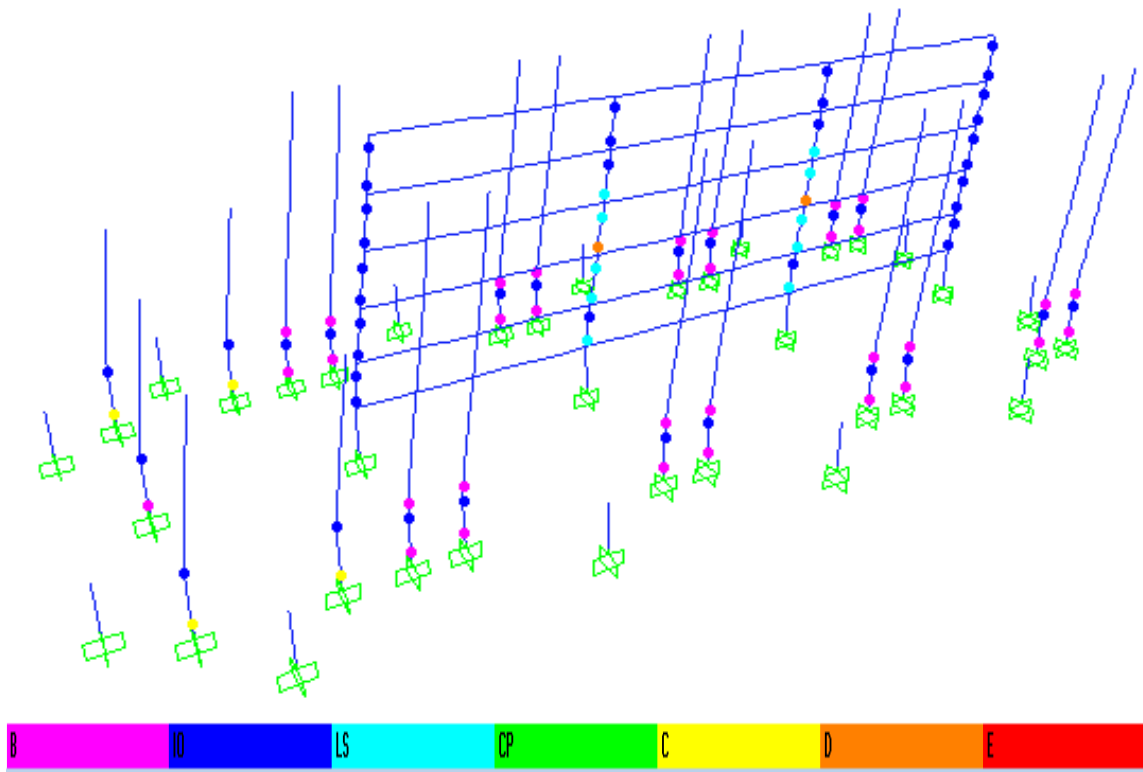
*Figure J.13 Level of damaged hinges at 10.6in lateral displacement, maximum lateral capacity*

Figure J.14 and Figure J.15 show the comparison of capacity between the as-built and retrofitted structure. Figure J.14 shows the analysis results of Unif.Dir.X loading. The retrofitted structure reaches 32% higher base shear capacity than the original structure. Besides, the retrofitted structure is able to develop larger deformation than the as-built structure before the capacity drops.
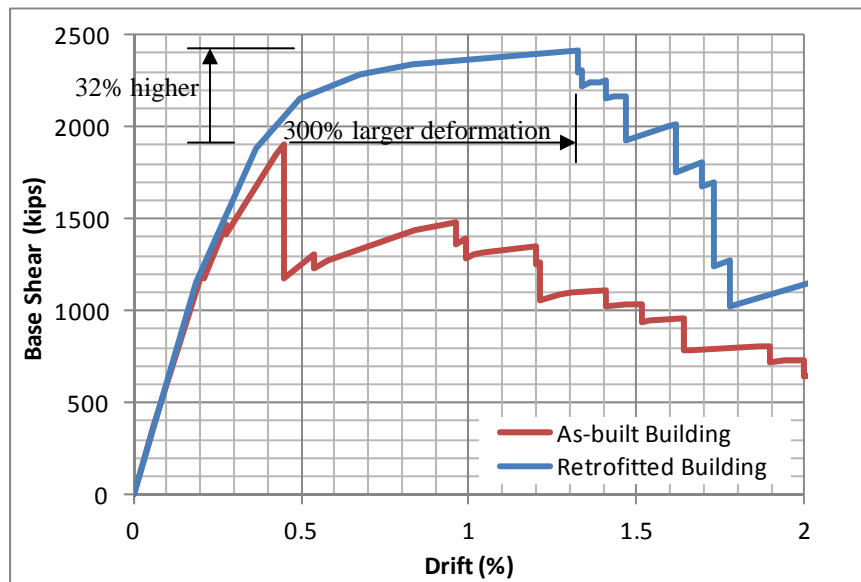


***Figure J.14 Comparison of the pushover capacity curve calculated with uniform distribution of loads for As-built and Retrofitted Structure***

Figure J.15 shows the analysis results of Mode Dir.X loading. The same tendency of considerable increase in capacity can be seen. The retrofitted structure had a higher base shear capacity than the original structure. Additionally, the retrofitted structure was able to develop larger deformation than the as-built structure before the lateral load dropped.
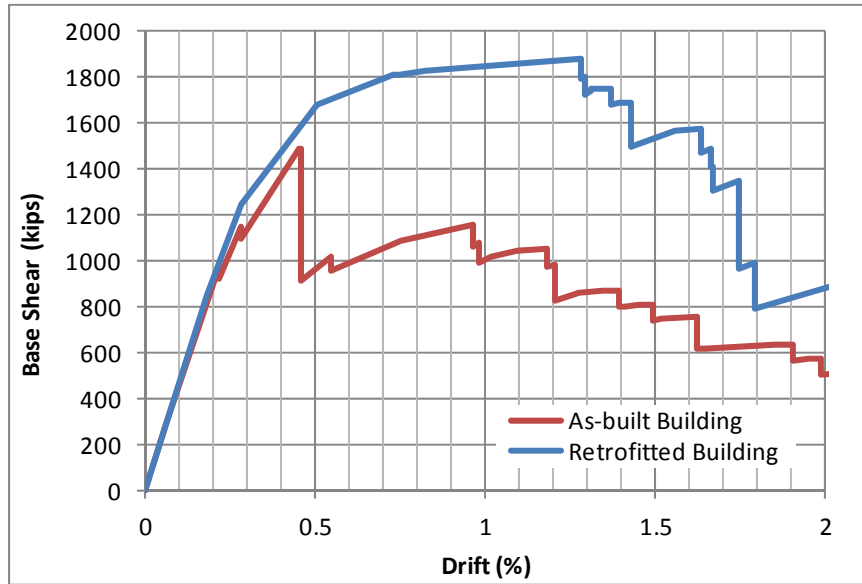
*Figure J.15 Comparison of the pushover capacity curve calculated with modal distribution of loads for As-built and Retrofitted Structure*

# REFERENCES

Aboutaha.;(1994). "Seismic Retrofit of non-ductile reinforced concrete columns using rectangular steel jackets" Ph.D. Disertation The University of Texas at Austin. USA, 367pp

Ahmadi.;(2012) "Displacement-based Seismic Design and Tools for Reinforced Masonry Shear-Wall Structures" Ph.D. Disertation The University of Texas at Austin. USA, 692pp

American Concrete Institute, (2008). "Guide for the Design and Construction of Externally Bonded FRP Systems for Strengthening Concrete Structures (ACI 440.2R-08)." Farmington Hills, Michigan, USA.

Akyuz, O. and Ozdemir, G., (2004). "Mechanical Properties of CFRP Anchorages", *13th World Conference on Earthquake Engineering, Vancouver, B.C., Canada,* August 1-6, 2004, Paper No. 3349.

American Concrete Institute, (2008). "Guide for the Design and Construction of Externally Bonded FRP Systems for Strengthening Concrete Structures (ACI 440.2R-08)." Farmington Hills, Michigan, USA.

ASCE41-07/SEI, "Seismic Rehabilitation of Existing Buildings" America Society of Cicil Engineers, Reston, Virginia. USA

ASTM International, (2007). "Standard Test Method for Flexural Strength of Concrete Using Simple Beam With Center-Point Loading, (C293-07)," ASTM International, West Conshohocken, PA, USA.

ASTM International, (2007). "ASTM D 3039/D3039M Standard Test Method for Tensile Properties of Polymer Matrix Composite Materials." ASTM International, West Conshohocken, PA, USA.

ASTM International, (2010). "Standard Test Method for Testing Mechanical Splices for Steel Reinforcing Bars (A1034/A1034M)," ASTM International, West Conshohocken, PA, USA.

Bett B., et al.; (1985). "Behavior of Strengthened and Repaired Reinforced Concrete Columns under Cyclic Deformations" Report Research Project, National Science Foundation, The University of Texas at Austin. USA.

Ceroni, F. and Pecce, M., (2006). "Bond Tests on Concrete and Masonry Blocks Externally Bonded with FRP", Composites in Civil Enginnering Miami, Florida, USA December 13-15, 2006, Paper No. 1.

El-Dakhani, W.; et al. (1996). "Design And Retrofit Of Concrete Masonry-Infilled Steel Frames Using Gfrp Laminates," Earthquake Spectra, V. 12, No. 1, Feb., pp. 1-11.

Elwood, et al..;(2007). "Update to ASCE/SEI 41 Concrete Provisions." ASCE/SEI 41 Seismic Rehabilitation of Existing Buildings" PEER Report 02. USA.

592

Elwood, K.; Eberhard, M.; (2006) "Effective Stiffness of Reinforced Concrete Columns" PEER publication. Research Digest No. 2006-1 USA.

Elwood K., et al..;(2007). "Update to ASCE/SEI 41 Concrete Provisions." ASCE/SEI 41 Seismic Rehabilitation of Existing Buildings" Earthquake Spectra, V. 23, No. 3, August 2007, pp. 493-523

Guimaraes G.; et.al, (2007). "Experimental Study on Bond Between Carbon Fiber Composites and Concrete" 8th International Symposium on Fiber-Reinforced Polymer (FRP) Reinforcement for Concrete Structures, Patras, Greece, July 16-18, 2007. Paper No. 2-7.

He R.; et al.; (2013). "Rapid repair of a severely damaged RC column having fractured bars using externally bonded CFRP" Composites Structures 101 (2013) pp 225-242

Karantzikis, M. (2007), "Structural Strengthening with FRPs in Greece", 8th International Symposium on Fiber-Reinforced Polymer (FRP) Reinforcement for Concrete Structures, Patras, Greece, July 16-18, 2007. Paper No. 15-1.

Kim, I., (2006). "Rehabilitation of Poorly Detailed RC Structures Using CFRP Materials" M.S.E. thesis. The University of Texas at Austin.USA, 142pp.

Kim, I., (2008). "Use of CFRP to Provide Continuity in Existing Reinforced Concrete Members Subjected to Extreme Loads", Ph.D Dissertation, The University of Texas at Austin, USA, 478 pp.

Klamer, E.L., Hordijk, D.A. and Janssen, H.J.M. "The Influence of Temperature on the Debonding of Externally Bonded CFRP", (2005). 7th International Symposium on Fiber-Reinforced Polymer (FRP) Reinforcement for Concrete Structures, Kansas City, Missouri, U.S.A. November 6-9, 2005. Vol.2  Paper Sp-230-88.

Kobayashi, K., Fujii S., Yabe Y., Tsukagoshi H., and Sugiyama T. (2001). "Advanced wrapping system with CF anchor –Stress Transfer Mechanism of CF Anchor." 5th International Symposium on Fiber-Reinforced Polymer (FRP) Reinforcement for Concrete Structures, Cambridge, UK, 379- 388.

Krawinkler, H., (1996). "Cyclic Loading Histories for Seismic Experimentation on Structural Components," Earthquake Spectra, V. 12, No. 1, Feb., pp. 1-11.

LeBorgne M.;(2012). "Modeling The Post Shear Failure Behavior Of Reinforced Concrete Columns" Ph.D. Disertation The University of Texas at Austin. USA, 301pp

Matamoros, A; et al. (2004). "Performance Of Mechanical Splices Within The Plastic Hinge Region Of Beams Subject To Cyclic Loading", 13th World Conference on Earthquake Engineering, Vancouver, B.C., Canada, August 16, 2007. Paper No. 1073

Melek M.; Wallace J.; Conte J.; (2003). "Experimental Assessment of Columns with Short Lap Splices Subjected to Cyclic Loads" Pacific Earthquake Engineering Researh Center PEER. Report 2003/04 USA.

Orton, S.L., (2007). "Development of a CFRP system to Provide Continuity in Existing Reinforced Concrete Buildings Vulnerable to Progressive Collapse". Ph.D. Dissertation, The University of Texas at Austin, USA, 363 pp

Pampanin, S.; Akgusel U.; (2011). "Performance-Based Seismic Retrofit of Existing Reinforced Concrete Frame Building using Fiber-Reinforced Polymers: Challenges and Solutions" Structural Engineering International SEI V. 3, pp. 260-270.

Paul, A. (2007). "FRP Stitching of Segmental Post-Tensioned Concrete Box Girder Bridge Joints"; 8th International Symposium on Fiber-Reinforced Polymer (FRP) Reinforcement for Concrete Structures, Patras, Greece, July 16-18, 2007. Paper No. 15-3.

Pham, L.T.;(2009). "Development of a Quality Control Test For Carbon Fiber Reinforced Polymer Anchors" M.S.E. Thesis The University of Texas at Austin. USA, 84pp

Pekelnick, Poland.;(2012). "ASCE41-13: Seismic Evaluation and Retrofit of Exisiting Building" SEAOC 2012 Convention Proceedings. USA.

Pekelnick, Poland.;(2012). "ASCE41-13: Seismic Evaluation and Retrofit of Exisiting Building" SEAOC 2012 Convention Proceedings. USA.

Ruangrassamee A.; Mounnarath P.; (2008). "Monotonic And Cyclic Behaviors Of Energy-Dissipating Threaded Mechanical Splices", 14th World Conference on Earthquake Engineering, Beijing, China, October 12-17 2008

Saatcioglu, M; Serrato F. Foo F.; "Seismic Performance of Masonry Infill Walls Retrofitted With CFRP Sheets", (2005). 7th International Symposium on Fiber-Reinforced Polymer (FRP) Reinforcement for Concrete Structures, Kansas City, Missouri, U.S.A. November 6-9, 2005. Vol.2  Paper Sp-230-20.

Shadravan, B. and Saatcioglu, M., (2007). "An Investigation On The Bond Length of FRP Sheets on Concrete Substrate", 8th International Symposium on Fiber-Reinforced Polymer (FRP) Reinforcement for Concrete Structures, Patras, Greece, July 16-18, 2007. Paper No. 2-15.

Sullivan T.; Calvi G. and Priestley, M., (2004). "Initial Stiffness Versus Secant Stiffness In Displacement Based Design", 13th World Conference on Earthquake Engineering, Vancouver, B.C., Canada, August 16, 2007. Paper No. 2888

Sherman, J.; (2011). "Effects Of Key Parameters On The Performance Of Concrete Masonry Shear Walls Under In-Plane Loading" M.S.E. Thesis Washington State University. USA, 132pp

Stavridis A.; Mavros M.; Liu Y.; Shing B; (2011). "Shake-Table Test of a Full-Scale Three-Story Reinforced Masonry Structure" UC San Diego USA

Sungjin B.; Mieses A.; and Bayrak O., (2005). "Inelastic Buckling of Reinforcing Bars" Journal of Structural Engineering ASCE, V. 131, No. 2, February., pp. 314-321.

Taghdi M; et al. (2000). "Seismic Retrofitting Of Low-Rise Masonry And Concrete Walls Using Steel Strips" Journal of Structural Engineering ASCE, V. 126, No. 9, September, pp. 1017-1025.

596

# VITA

Guillermo Huaco was born in Lima, Peru on September 11, 1977. After completing his work at San Antonio High School in 1993, he attended the National University of Engineering in Lima, Peru. In December 2000, he received a Bachelor of Science from the National University of Engineering.

He studied Master courses in Structural Engineering at the National University of Engineering in Lima from 2002 to 2003. He also completed a postgraduate program at the Institute of Earthquake Engineering and Engineering Seismology IZZIS – Skopje, F.Y.R. Macedonia (Ex-Yugoslavia) in 2005. He studied Risk Management, Disaster Mitigations and Repair of Infrastructure at The Ministry of Land and Construction JAPAN & JICA - Osaka Japan in 2007.

During the following years he was employed as a teacher and research assistant at the National University of Engineering in Lima, Peru. He also spent time as an engineer at Fenix South America Consulting, Steel Deck Enterprises and SC Engineering in Lima Peru. In January, 2008, he entered the Graduate School at the University of Texas at Austin. He completed his Master of Science degree in Engineering in December of 2009, and he began to work on his Ph.D. under the supervision of James O. Jirsa.

Permanent Address:
    Los Amancáes 315  Urb. Jardines Virú Bellavista
    Lima, Peru.
    Phone: 51-14518622
Email: guillermohuaco@utexas.edu

.